



eReefs Marine Modelling: Final Report

M. Herzfeld, J. Andrewartha, M. Baird, R. Brinkman, M. Furnas, P. Gillibrand, M. Hemer, K. Joehnk, E. Jones, D. McKinnon, N. Margvelashvili, M. Mongin, P. Oke, F. Rizwi, B. Robson, S. Seaton, J. Skerratt, H. Tonin, K. Wild-Allen

January 2016

Contents

Executive Summary	6
Technical Summary	12
1. Introduction	17
2. Background	20
2.1 Hydrodynamics.....	20
2.2 Sediment Transport	21
2.3 Biogeochemistry	22
3. Modelling framework	24
4. Methods.....	25
4.1 Whole of GBR Hydrodynamic Model	25
4.1.1 Bathymetry analysis	29
4.1.2 TRIKE.....	31
4.1.3 River inflow	34
4.1.4 Dual relaxation.....	39
4.2 Further develop HD model.....	44
4.2.1 Sub-grid scale development.....	44
4.2.1.1 Background.....	44
4.2.1.2 Methods	44
4.2.1.3 Results	50
4.2.1.4 Comments.....	59
4.2.2 SHOC Performance development.....	60
4.2.2.1 Overview.....	60
4.2.2.2 4km Models	61
4.2.2.3 1km Models	63
4.3 Data assimilation	65
4.3.1 Introduction.....	65
4.3.2 Hydrodynamic DA Methodology.....	65
4.3.3 Hydrodynamic Observations	66
4.3.4 Hydrodynamic model error and uncertainty.....	68
4.3.5 Hydrodynamic model perturbations.....	70
4.3.6 DA Algorithms applied to GBR4 hydrodynamics.....	82
4.3.7 Data Assimilation Pilot Summary.....	91
4.3.8 GBR4 Hydrodynamic model 4 year reanalysis.....	92
4.3.9 BGC Data Assimilation	98
4.4 GBR-wide Wave Model	109

4.4.1 Introduction	109
4.4.2 WaveWatch III implementation.....	110
4.4.3 SWAN implementation.....	118
4.5 Transport model	126
4.5.1 Background.....	126
4.5.2 Semi-Lagrangian transport model	126
4.5.3 FFSL transport model.....	131
4.6 Sediment transport model	146
4.6.1 Initial conditions.....	146
4.6.2 Forcing.....	147
4.6.3 Catchment loads	148
4.6.4 Calibration strategy	149
4.7 Biogeochemical Model.....	151
4.7.1 Introduction	151
4.7.2 Model description.....	152
4.7.3 Biogeochemical cycling in the GBR	154
4.7.4 Biogeochemical model process enhancement.....	176
4.7.5 Whole of GBR biogeochemical model simulations.....	194
4.7.6 1km near real time BGC Model.....	219
4.8 Develop and test relocatable coastal model platform	220
4.8.1 Motivation	220
4.8.2 Framework.....	221
4.8.3 Tracer definition.....	223
4.8.4 Tracer attribute prescription	223
4.8.5 Global parameter specification.....	223
4.8.6 BGC process definition	224
4.8.7 BGC 'Universal' parameterisations	225
4.8.8 Sediment model parameterisation	238
4.8.9 Testing of temporal inflow boundary requirements.....	241
4.8.10 Grid generation.....	242
4.8.11 ROBUST settings.....	248
4.8.12 Two-way nesting	249
4.8.13 Waves.....	252
4.8.14 RECOM workflow	252
5. Validation.....	258
5.1. GBR4 Hydrodynamics.....	258

5.1.1 Calibration	261
5.1.2 Cyclone Yasi	264
5.1.3 ARGO	267
5.1.4 Currents.....	268
5.1.5 GHR SST	270
5.1.6 Validation.....	271
5.1.7 Open boundary specification.....	276
5.1.8 Open boundary data	279
5.1.9 Short wave parameters	281
5.1.10 River input	282
5.1.11 Open ocean mean flow.....	283
5.1.12 Climatology	287
5.1.13 Other sensitivities.....	289
5.2. GBR1 Hydrodynamics.....	290
5.2.1 Resolution improvements	290
5.2.2 NRT comparisons	291
5.3 Hydrodynamic analysis	302
5.3.1 Catchment connectivity using passive tracers.....	302
5.3.2 Temperature Exposure	305
5.3.3 Coral Sea Connections	310
5.3.4 Decorrelation length scales.....	312
5.3.5 Submesoscale Coherent Vortices.....	314
5.4 Sediment Transport	318
5.4.1 Assimilation of the remote sensing TSS	318
5.4.2 Model vs coastal records.....	323
5.4.3 Model vs GBROOS data	326
5.4.4 GBR1: 1 km GBR sediment model.....	329
5.4.5. Baseline Scenario	333
5.4.6. Perturbation scenarios	339
5.4.7 Conclusion	342
5.5 Biogeochemistry.....	343
Scope of BGC model Validation.....	343
5.5.1 Mass Conservation.....	344
5.5.2 Comparison of Model with Climatology.....	345
5.5.3 Observations used for Model Comparison.....	354

5.5.4 Skill assessment of biogeochemical model against water quality time series observations	357
5.5.5 Skill assessment of biogeochemical model against glider data	386
5.5.6 Trichodesmium	389
5.5.7 Emergent properties	395
5.5.8 Regional budgets.....	400
5.5.9 Primary production and zooplankton grazing	402
5.5.10 Summary of the 4 km BGC model Skill assessment against Observations	408
5.5.11 Comparison of the 4 km and 1 km BGC configurations	410
5.5.12 Demonstration scenarios	427
5.6 RECOM	431
5.6.1 Fitzroy Estuary.....	431
5.6.2 Heron Island.....	446
5.6.3 Whitsundays.....	460
5.6.4 Summary and recommendations.....	470
6. Summary	473
7. References.....	475
8. Publications.....	493
8.1 Presentations	494

Citation

Herzfeld, M., J. Andrewartha, M. Baird, R. Brinkman, M. Furnas, P. Gillibrand, M. Hemer, K. Joehnk, E. Jones, D. McKinnon, N. Margvelashvili, M. Mongin, P. Oke, F. Rizwi, B. Robson, S. Seaton, J. Skerratt, H. Tonin, K. Wild-Allen (2016). eReefs Marine Modelling: Final Report, Jan. 2016, CSIRO, Hobart, 497pp.

Executive Summary

1 Purpose and scope

Although the Great Barrier Reef is recognised as one of the best managed reef systems in the world, coral cover has declined over the last decades at rates similar to less well managed reefs, and research based management and policy is recognised as a pathway for mitigating this trend. Model development to guide management actions is considered a criterion for the effective integration of science and management. Integrated models spanning physical processes through to water quality and ecosystem response are expected to assist regulatory authorities with issues relating to reef management, and to serve as a tool to assist in the evaluation of effectiveness of various management strategies and actions.

In this context, the marine modelling component of eReefs was tasked to deliver numerical models capable of simulating and predicting the physical hydrodynamic state, sediment transport, water quality and basal ecology of the Great Barrier Reef lagoon and reef matrix. Together, these models represent a capability to simulate the transport and fate of waterborne material, of either oceanic or terrestrial origin, and its impact on Reef water quality.

The numerical models are built using CSIRO's Environmental Modelling Suite, and this report describes the application of that suite to the Great Barrier Reef, including details of regional 4 km and 1 km resolution models, and an automated re-locatable coastal ocean modelling system (RECOM) capable of resolving individual reefs, estuaries and embayments at resolutions of tens to hundreds of metres. For the regional models, the report describes their spatial application and the forcing applied to the model boundaries, as well as specific model developments necessary for their application to the Great Barrier Reef. Model calibration and validation against observations is presented and examples of model application to understand and characterize behavior of a number of bio-physical processes on the GBR are described. RECOM required new development to the Environmental Modelling Suite, and details of this are included along with three case studies demonstrating its use in reef and coastal environments.

Detailed in this report, and summarized in the Technical Summary, are highlights of the outputs of modelling products and an assessment of the model performance. The complete model outputs are available through the eReefs information system. Further details of the underlying mechanics of the Environmental Modelling Suite such as numerical methods, are detailed in other published works, which are listed in this report.

2 Overview of models

The major components of the eReefs marine models are a hydrodynamic model to predict the physical state of the system, a sediment transport model predicting the fate of suspended fine sediments and a biogeochemical model for water column and benthic production, water quality and nutrient cycling. Supporting these components are an optical model with spectral resolution, data assimilation systems, wave models and an offline transport model. Data assimilation is used for parameter estimation during the calibration procedure, to improve the state estimates of the model, and to gain insight into model uncertainty. Wave models

provide forcing for the resuspension of particulate matter from the sea floor. The transport model efficiently performs the transport of sediment and biogeochemical variables.

A nested suite of regional models is used; a regional 4 km resolution model is nested within a global general circulation model, and a 1 km resolution model is subsequently nested within the 4 km model. Both regional models extend along the Queensland coast from Papua New Guinea to the New South Wales border, and offshore to beyond the continental slope. The 4 km model encompasses some of the Western Coral Sea and the Queensland Plateau, whereas the 1 km model is limited to the shelf regions.

The hydrodynamic model relies on Bureau of Meteorology's numerical weather prediction models (ACCESS-R) to provide surface forcing including wind, atmospheric pressure, surface heat fluxes and rainfall. Freshwater inputs representing the major river systems along the Great Barrier Reef are also included via streamflow observations from the Queensland Government. Open ocean boundary information for the 4 km regional model is supplied from the Bureau of Meteorology's numerical Ocean Modelling Analysis and Prediction System (OceanMAPS) global ocean model, and the 1 km model receives information from the 4 km model. The eReefs hydrodynamic models provide outputs of sea level, currents, temperature, salinity and mixing characteristics. Outputs are saved offline and subsequently used to transport sediment and biogeochemical variables. The sediment and biogeochemical models operate in both the water column and sediment layers, with exchange of mass across the interface via settling, resuspension and mixing. Ecological processes represented in the models include the photosynthetic growth of 4 categories of phytoplankton and of seagrass, macroalgae, and coral zooxanthellae, secondary production by zooplankton and corals, gas exchanges of oxygen and carbon dioxide, and transformations of nitrogen, phosphorus and carbon in various forms. Open boundary and river input information for sediments and biogeochemistry is provided using statistical relationships between river flow and loads, and climatology.

The models operate in near real-time, such that current conditions may be estimated, and a hindcast archive of historic conditions exists back to September 2010 for the 4 km model and December 2014 for the 1 km model. The near real-time outputs are continuously appended to the archive, so that the hindcast grows over time and is always up-to-date. This hindcast archive is suitable for performing scenario analyses such as exploring the impacts of reductions in nutrient or sediment loads from Queensland catchments. This provides, for the first time, a comprehensive three-dimensional, time varying, view of the current and historical state of the Great Barrier Reef circulation and water quality, though understanding fine sediment dynamics and biogeochemistry.

Specific model development was required to capture important and unique processes within the Great Barrier Reef that are not captured by generic models. This included improvements to open boundary conditions and the treatment of river inflows, sub-grid scale reef parameterisations, surface nutrient fluxes, inclusion of biogeochemical functional groups including corals, seagrass and important cyanobacteria (e.g. *Trichodesmium*), and biogeochemical processes including carbon chemistry and spectrally-resolved optics.

The re-locatable model, RECOM, is an automated re-locatable modelling system capable of generating high resolution models of hydrodynamics, waves, sediment transport and biogeochemistry that are nested within the 4 km or 1 km regional models. This package is

designed for non-specialist users, whereby the user simply and intuitively interacts with the models via a graphical workflow interface.

3 Calibration and validation

The models contain numerous parameters, schemes and configurations that have been refined to optimize the model's capacity to match observations from the Great Barrier Reef. This requires a calibration / validation procedure, where first the model configuration is altered (either heuristically or using data assimilation techniques) so that the output optimally mirrors observations, then this configuration is validated against independent observations (i.e. observations not used in the calibration) to ensure that the model configuration is robust under different conditions. The independent observations may consist of withheld samples, or may cover a different time period. Key to successful calibration is the availability of suitable observations. These observations must span the variables the model is predicting and have adequate spatial and temporal coverage throughout the Great Barrier Reef. The report describes the observational data sets used in the calibration and validation process, which include Reef Rescue monitoring data, data from Australian Institute of Marine Science and CSIRO cruises, data from the Integrated Marine Observing System and satellite observations. Critically, for these observations to be considered adequate, the time and space scales of their sampling must resolve the features that the models are attempting to predict. Inadequate frequency of sampling can lead to serious aliasing of observational records when comparing to model output, and inadequate spatial coverage can lead to small mismatches in position of a feature translating to large quantitative errors.

Although a large amount of observations have been collected in the Great Barrier Reef, not all of these are suitable to constrain a model. For example, monthly samples are insufficient to constrain a model whose dynamics are influenced by diurnal, weather band frequency or episodic (e.g. flood, cyclone) events. Surface observations are inadequate to constrain a model where sub-surface dynamics dominate (e.g. sub-surface chlorophyll maximums, sediment transport). Some observations within the Great Barrier Reef are well suited to model calibration (e.g. inshore sea level), whereas some have insufficient spatial and temporal cover (e.g. nutrients). The availability of adequate observation directly impacts the quality of the model calibration able to be achieved, and consequently more certainty can be placed in some components of the models and regional areas than others. Generally, there is a decrease in observation suitability for calibration when moving from hydrodynamics, through sediment transport to biogeochemistry, and consequently the quality of calibration changes accordingly when moving through those components.

Comparison of model output to observations is performed qualitatively via visual comparison, and quantitatively using root mean square errors, mean absolute errors, correlation coefficients, bias and statistical based model skill assessment (e.g. Willmott's skill scores). The configuration that best optimizes model versus observation across all metrics and variables is chosen as the calibration configuration. The quantitative metrics convey the model skill and degree of confidence that may be placed in the model when applying them to their intended use.

The calibration / validation procedure reveals that the models do replicate broad scale patterns, are consistent with climatology, capture seasonal dynamics and the occurrence of intra-seasonal events, although the exact timing and location of these events may contain

uncertainly. This makes the models suitable for hindcast characterization and scenario analysis (e.g. projections of how Great Barrier Reef water quality will respond to altered environmental drivers). In combination with data assimilation (where sufficient real-time data are available), the models could also be used for short term forecasts.

4 Achievements

Relevant deliverables under the Collaboration Agreement and SEIF that are addressed within this report are:

Collaboration Agreement:

Dec 2013 Delivery of validated 4km and 1km Hydrodynamic model.
Dec 2015 Validated final version sediment and biogeochemical model delivered.
Jan 2016 Validated final version re-locatable nested Fine Scale/Estuary Modelling capability delivered.

SIEF:

Jan 2015 4.2 Validated final version of CSIRO EMS implementation of the 4km and 1 km GBR ocean prediction system (Hydrodynamics) available for routine implementation (e.g. CSIRO).
4.3 Validated final version sediment and biogeochemical model delivered and available for routine implementation.
4.5 Relocatable model applied to priority coastal and coral reef areas, including Fitzroy Estuary, Heron Island and Mackay.
4.6 Skill assessment of RECOM against optimised hydrodynamic-biogeochemical models of the Fitzroy Estuary and Heron Island lagoon.
4.7 Final version of Relocatable Coastal Ocean Model (RECOM) implemented and functionality demonstrable in a development environment, e.g. CSIRO.

These milestones have been achieved and evidence of their delivery is described in this report. The regional models are operating in near real-time, and outputs can be viewed online at:

<https://research.csiro.au/ereefs/ereefs-data-visualisation-portal/>

and

<http://www.emg.cmar.csiro.au/www/en/emg/projects/eReefs/Results.html>.

This includes snapshots and animations of key model variables, comparison of model to observations and forcing data used. The raw model data is available via THREDDS server:

<http://dapds00.nci.org.au/thredds/catalogs/fx3/catalog.html>

RECOM is functional and can be demonstrated in a CSIRO development computing environment. After consultation with stakeholders, a deployment strategy will be implemented after which RECOM will be publically accessible.

Currently, there have been 21 eReefs related papers published in peer-reviewed journals, and eReefs material has been presented at 27 international and national conferences, workshops and seminars. Since there remains a wealth of information residing in the eReefs archive yet to be explored, this list will undoubtedly grow. Many of these publications relate to state-of-the-art development that occurred during the eReefs project, and this development is a significant achievement in its own right. These enhancements notably include advances in data assimilation, open boundary conditions, transport models, optical models, carbon chemistry and inclusion of the impacts of *Trichodesmium* on nutrient budgets. These developments are transportable to other applications. RECOM was associated with significant development, and currently lies at the forefront of automated relocatable modelling systems; to our knowledge it is the only model of its kind capable of simulating hydrodynamics through biogeochemistry with its advanced level of automation.

5 Operational considerations

The eReefs marine models are suitable for, and currently performing in, near real-time operation. The infrastructure that supports the near real-time operation has now been functioning for multiple years and is considered robust. There is a commitment by CSIRO to continue to operate these models on an on-going basis, and provide outputs to the wider community at various levels ranging from snapshots and animations of key variables, value added products based on these key variables, web enabled exploration of the raw data and access to the raw data itself. Many of these model-based products and data access and integration tools are being developed through other eReefs projects. The on-going operation of the modelling suite and provision of data products will require resourcing, and the level of resourcing will be dependent on the uptake and demand for eReefs products. Currently the commitment is to make the eReefs outputs available and rectify any downtime in a reasonable timeframe within business hours (Mon-Fri, 9-5). Reasonable user requests will be facilitated along similar lines. If demand outpaces the ongoing resourcing levels, then there may be a requirement for additional investment in product delivery.

6 Conclusion and recommendations

The use of integrated models to assess the effectiveness of management strategies and guide actions is expected to assist Reef management and regulatory authorities with many of the current emergent issues facing the Great Barrier Reef.

Reef management challenges for which the eReefs modelling suite has potential application are numerous and include prediction of coral bleaching hotspots, impacts of ocean acidification on coral calcification, catchment impacts on reef health (sedimentation issues, eutrophication), crown of thorns starfish (COTS) infestations, hypoxia, management of dredging, shipping and port related activities, fisheries management, search and rescue, larval connectivity and prediction of impacts of floods or extreme weather events on marine systems. Since the modelling package operates routinely in near real-time, emergent events such as floods, dredge plumes, phytoplankton blooms, cyclones, vessel groundings, bleaching events etc. may be investigated and responded to in a timely manner. Maintaining a current

archive of the state of the Great Barrier Reef assures that any investigations of processes and dynamics remain relevant, and account for shifts in the state of the system.

The ultimate goal of major management initiatives such as Reef Plan and Reef Rescue is to protect the health of Great Barrier Reef ecosystems and the ecosystem services they support. These initiatives rely on a cause-effect chain linking land use and practices in catchments, to end of catchment flows and loads, to water quality in the Great Barrier Reef lagoon, to reef ecosystem health. These are complex systems, and there is inevitable uncertainty around all of these links. Quantitative links between end of catchment loads and reef performance measures are critical in order to set, e.g. end of catchment load targets, and to assess the relative benefits arising from load reductions in different catchments.

The modeling system developed under eReefs provides a capacity to predict impacts of catchment loads on water quality under acute flood event conditions, and chronic post-flood and dry season conditions. The combined water quality model provides a single integrated and consistent platform to predict changes in water quality in space and time in response to land use and load scenarios for any or all Great Barrier Reef catchments. Further, ecological response models can employ output from the water quality model to simulate, for example, coral cover, coral recruitment, habitat community composition, macroalgae and COTS as indicators of reef health.

There are a number of ways in which the eReefs modelling suite could be used to support management decisions. A standard use of models is to predict system responses under alternative management scenarios and use this to assist in planning actions. In this form, models link management actions to performance indicators. Models can also be used for diagnostic purposes; e.g., the model could be used to disentangle effects of interannual variability, or other pressures including climate change, from effects of actions in the catchment, and to explore the interactions among them. They can also be used to assess current compliance against set water quality targets. Models of this kind serve as an infrastructure platform for research as well as management. They provide an environment for evaluating new hypotheses about processes and system interactions and for designing field experiments and optimizing observing programs.

There is a commitment to continue the provision of eReefs marine modelling outputs to the wider community on an ongoing basis. These products are not an endpoint, but should be considered a tool in a manager's or researcher's toolkit that complements existing methodologies employed to gain system understanding (e.g. monitoring). They are also not static, but expected to adapt as new information becomes available to warrant enhancements. They will not solve all the Reef's problems, but if used appropriately will contribute to better solutions of reef management and fill gaps in system understanding. In a sense the difficult tasks are yet to come, whereby all information available, including eReefs products, are used in conjunction with expert's understanding of the Great Barrier Reef to deliver practical strategies that can improve reef health into the future.

Technical Summary

The eReefs Marine Modelling component has delivered a modelling suite capable of predicting the hydrodynamic, sediment transport and biogeochemical characteristics of the Great Barrier Reef (GBR). This is achieved through a nested suite of models, whereby a regional 4 km resolution model is nested within a global general circulation model, and a 1 km resolution model is subsequently nested within the 4 km model. These models provide outputs of sea level, currents, temperature, salinity, suspended sediment, primary and secondary production, nutrients and optical characteristics throughout the GBR domain. The models operate in near real-time, such that current conditions may be monitored, and a hindcast archive exists back to September 2010 for the 4 km model and December 2014 for the 1 km model. The archive is kept up-to-date by continuously appending the near real-time outputs. A Relocatable Coastal Ocean Model (RECOM) has been developed which is an automated re-locatable modelling system capable of generating high resolution models of hydrodynamics, waves, sediment transport and biogeochemistry (BGC) that are nested within the 4 km or 1 km regional models. This package is designed for non-specialist users, whereby the user simply and intuitively interacts with the models via a graphical workflow interface.

Hydrodynamic models at the 4 km and 1 km scale (GBR4 and GBR1 respectively) are operating routinely in near real-time within the CSIRO real-time framework (TRIKE). These model outputs are routinely posted on the web (<https://research.csiro.au/ereefs/models/model-outputs/>), and are publically available (<http://dapds00.nci.org.au/thredds/catalogs/fx3/catalog.html>). A five year archive currently exists of the 4 km output, which is appended using the routine near real-time output. The 1 km model began routine operation in December 2014. These models have been subject to calibration and validation, both in hindcast and near real-time, using available Reef Rescue monitoring data, data from Australian Institute of Marine Science and CSIRO cruises, data from the Integrated Marine Observing System and satellite observations. Skill assessment indicates that the models are performing well at the surface for temperature in terms of the annual and weatherband cycles. Surface salinity shows good agreement in the timing and magnitude of flow events. Biases exist in temperature and salinity at depth, which are speculated to be due to initial / boundary conditions. Diurnal and low frequency sea level correlate well with observations if a dual-relaxation open boundary scheme is used for boundary relaxation that accounts for the intrinsic temporal differences in tidal and low frequency motions. Average skill metrics are summarized in Table 5.1.3 and Table 5.2.2 of this report.

Algorithms for sub grid-scale parameterisation have been developed, based on existing bottom roughness parameterisation and a unique 'porous-plate' approach where kinetic energy is extracted from the system by vertical mixing to account for the impact of the reef matrix on flow. This is a function of the cross sectional area the reef occupies with respect to a model grid cell. The methodology of this reef parameterisation is incorporated into the hydrodynamic models.

The hydrodynamic model code has been re-configured to run in parallel on distributed memory architectures (as opposed to shared memory architectures which it can currently do). The methodology is based on master-slave data distribution, however, gather-scatter operations are performed in a slave-slave environment which introduces significant

efficiencies when compared to the traditional master-slave transfers. In a benchmarking exercise, the GBR 4 km model was shown to outperform an identical model simulated using the MOM4 ocean code. Additionally, the GBR 1 km model was shown to scale linearly up to 78 processors. This allows the models to be implemented in super-computing architectures.

Data assimilation (DA) is a method that is employed to merge the solution from a numerical model with available observational data to produce a 3-D time varying fields. The output from DA is considered to be the “best estimate” of the system state, where model uncertainty is reduced, and sparse observation data is dynamically interpolated using the numerical model. Within the context of eReefs, DA has been applied to both the marine hydrodynamic and biogeochemical (BGC) models. It has been used for both parameter estimation in the hydrodynamic model, and also state updating in the hydrodynamics and BGC.

Observations of temperature from remote sensing (Sea Surface Temperature), moorings and gliders, have been assimilated into the hydrodynamic model. Two approaches were used. The first assimilation approach was to constrain three parameters relating to the transmission, attenuation and bottom reflectance of short wave radiation. These parameters vary according to water clarity, bottom type and errors in surface heat fluxes. By including these variables in the data assimilation system, spatially varying fields were produced (see figures 4.3.20-22), that were subsequently used in the production run of the hydrodynamics. By estimating the spatially varying short wave radiation parameters, we reduced the bias of the hydrodynamic model by up to 3 degrees C, and reduced the RMS error to less than 1 degree C when compared to a withheld dataset.

The second approach used an efficient Ensemble Optimal Interpolation system for sequential updating of the model state (temperature) to assimilate observation from January 2011 – December 2014 in the hydrodynamic model, to create the first version of a high resolution reanalysis product for the GBR region. The average forecast error for temperature ranged between 0.4 and 0.9 degrees C, depending on observation density, typically related to cloud cover.

The assimilation system was also applied to the biogeochemistry, with observations from satellite remote sensing products being the only assimilated data. A simple ensemble optimal interpolation system was applied and the forecast error from this system was approximately half that of the control run. By applying a more advance ensemble Kalman filter system, there was a further reduction in forecast error, with the domain wide error reducing by a further 5-10 % when compared to the simple data assimilation system. It should be noted that recent BGC model developments and further improvements to the BGC DA scheme has led to the mean absolute prediction error dropping from 75% in earlier versions, to 25% in the latest system.

Wave models are required to provide accurate wave-enhanced bottom stress for the sediment transport model. Hindcasts for the wave models have been performed using both the WaveWatch III and SWAN models. As each of these models has certain advantages over the other, the aim is to identify the model most suitable for the GBR region, and capable of performing in an operational capacity. The WaveWatch III model has also been implemented in near real-time, and is capable of providing inputs to downstream models. Due to difficulties in obtaining the boundary information from the Bureau of Meteorology's (BoM) operational models required to force this model, the near real-time operation has been terminated. The BoM AUSWAVE wave products are used directly for downstream models, at coarser

resolution than the WWIII model. The SWAN model has also been applied to an estuarine environment (Fitzroy Estuary) for testing purposes, and subsequently included in the relocatable coastal model framework.

An offline transport model must be used to drive both the sediment transport and biogeochemistry (BGC), as these models are computationally too expensive when fully coupled to the hydrodynamic model. The Flux Form Semi-Lagrange Method (FFSL) used in the meteorology community has been implemented as the advection scheme in the transport model. The FFSL scheme conserves mass almost perfectly locally and can be run with longer time-steps to increase computational efficiency. The transport model was assessed against the 3D hydrodynamic model for a number of passive tracers and found to be suitable in terms of distribution of tracers, conservation characteristics and computational efficiency for driving the sediment and BGC libraries.

The suspended sediment model represents the resuspension and settling of fine sediments between the water column and 4 benthic layers of sediment. The model is initialised with the observed distribution of gravel, sand and mud on the seabed of the shelf region. Catchment sediments discharged into the GBR over the simulation period are represented in the model by two size classes of particles having varying settling velocities. The model tracks the distribution of these particles separately from the distribution of the historically accumulated sediment in the region. This arrangement underpins its capacity to discriminate between the local resuspension event and the input of sediments from catchments. The transport of modelled sediments is driven by simulated hydrodynamics and wave data. The sediment model supports biogeochemical model simulations and provides input to nested fine-resolution relocatable model RECOM. The sediment transport model produces a stable, realistic simulation, even when subject to extreme forcing events such as cyclone Yasi. The model is now routinely running in near real-time, using the transport model as a driver and WaveWatch III outputs as forcing fields.

The sediment transport model was calibrated in two stages. First, the model parameters (initial conditions and spatially varying bottom roughness) have been refined through the ensemble assimilation of 6 months of remote sensing data for total suspended solids (TSS). Ensemble of models, produced through the assimilation step, have been reduced to a single model, which was subsequently validated against time-series of the observed turbidity (i.e. data from coastal sensors and GBROOS shelf moorings). The validation of the 4-year run of the model revealed a long-term drift of the solution which was handled through the manual adjustment of the model parameters. The quality of the calibrated model varies across the GBR region and with time (as was expected). The distribution of the simulated suspended sediment on GBR, in general, is consistent with observations. The model tends to overestimate suspended sediment levels in northern Queensland and underestimate TSS levels in Torres Strait.

The sediment transport model is capable of predicting the broad patterns of suspended sediment in the GBR, and variability at tidal and seasonal time-scales, and is suitable for use in scenario analyses. Due to the inherently stochastic nature of the sediment processes on the shelf and due to resolution and process limitations of the model itself, there is uncertainty in forecasts of sediment concentrations at specific locations in space and time.

A number of preliminary scenarios have been simulated with the calibrated model. Numerical experiments highlight the role of very fine fraction of catchment sediments (representing

either tails of the sediment size-distribution or flocs of fine particles characterised with a low settling velocity) as a carrier of sediment signals propagating from catchments to the GBR region. Scenarios with varying loads of sediments from catchments illustrate spatial and temporal variability of changes of suspended sediment levels on GBR. The response of TSS to varying loads from catchments in these scenarios is expressed in terms of changes of the annual mean probability for TSS to exceed 2 mg/L. This threshold (2 mg/L) represents GBRMPA (2009) guideline trigger value for TSS effects on marine ecosystems in open coastal and midshelf waters of GBR.

Preliminary analysis of these simulations suggests a relatively short term-response of the GBR system to changes in catchment loads. Scenarios with a 4-year run of the model having elevated loads from catchments does not show an incremental, multi-year build-up of the excessive TSS levels in the region. Instead, the TSS response to the increased load from catchments is most pronounced during wet years (and, according to some scenarios, during the first dry year following wet years). During the subsequent dry years changes in catchments have a much smaller impact on the probability for TSS to exceed 2 mg/L.

The ecological processes represented in the biogeochemical model include the photosynthetic growth of 4 categories of phytoplankton and of seagrass, macroalgae, and coral zooxanthellae, secondary production by zooplankton and corals, gas exchanges of oxygen and carbon dioxide, and transformations of nitrogen, phosphorus and carbon in various forms. Key ecological processes that were developed specifically for GBR waters include a host-symbiont representation of coral dynamics, a multi-type seagrass model, equilibrium carbon chemistry calculations, *Trichodesmium* nitrogen fixation, and a spectral-resolved optical model for accurate representation of the in-water light field and water-leaving optical properties. The new processes for GBR waters have been developed in collaborations with experimental and observational scientists at AIMS, JCU, UQ and UTS and published in the peer-review literature to ensure the robustness of their formulation. A complete description of the optical and biogeochemical model is given in Appendix B.

The biogeochemical model is driven by the hydrodynamic model using an offline transport model that is computationally efficient and conserves mass. Initial biogeochemical model conditions and parameters were derived from climatologies, historical observations and literature values, with ocean boundary conditions scaled against density profiles for synchronisation of mesoscale forcing. Coastal nutrient and sediment loads were derived from SOURCE catchment model loads for 21 major river systems along the Queensland coast and atmospheric nutrients were deposited into the upper ocean with rain.

Results from a 4 year hindcast were compared with observations from a range of model platforms, sensors and analytical techniques to assess model skill. The model reproduced the observed nutrient climatology, the spatial gradients in remotely-sensed ocean colour and in situ water quality observations with sufficient skill for the purpose of a water quality (phytoplankton, nutrients, turbidity, oxygen) hindcast, near real time and scenario simulation in the GBR World Heritage Area. Of the quantities available for comparison with in situ observations, model skill was highest for carbon chemistry properties. Compared to the 14 AIMS Reef Rescue inshore sampling sites, pH had a root mean square (rms) error of +/- 0.03, while aragonite saturation had an rms error of +/- 0.23. Comparison with chlorophyll fluorescence from the Reef Rescue mooring sites with simulated chlorophyll a showed a bias of only -0.07 mg chl a m⁻³, and a rms error of 0.33 mg chl a m⁻³. A summary of skill metrics are available in Table 5.5.5, and a complete analysis in Appendix A.

The Relocatable Coastal Model (RECOM) is designed for non-expert modellers to generate high resolution models over limited area coastal or reef domains within the GBR, and produces hydrodynamic, sediment transport, wave and biogeochemical outputs. It uses initial and boundary conditions from the GBR1 or GBR4 regional models, and surface fluxes from ACCESS. Wave conditions are predicted using the SWAN model. RECOM has undergone extensive testing on arbitrary domains within the GBR, and three regions have been simulated and examined in detail to assess the accuracy of the RECOM outputs. Interaction with the RECOM software is via an intuitive and simple graphical workflow interface. The elements of the workflow include orthogonal curvilinear grid generation via a graphical 'point and click' interface, selection of parameter 'sets' for sediment transport and biogeochemistry to be applied to the models, and selection of the forcing products and time period for the simulation. Extensive run monitoring options are available for the user to monitor the progress of the models. RECOM is similar to BLUElink's re-locatable model (ROAM), with added functionality of general orthogonal grid generation and capability of simulating suspended sediments and BGC with minimal expert user interaction.

The three test cases to which RECOM was applied were the Fitzroy Estuary (for a freshwater impacted estuarine environment), Heron Island (for a reef environment) and the Whitsunday Islands (for a non-river impacted bay). Users were able to successfully generate RECOM output in these test cases that compared generally favourably to optimized models of the same region or observations. RECOM is able to produce pilot models that are capable of reproducing first order dynamics. To improve the realism and obtain a fully calibrated and validated state requires careful assessment against observations, and heuristic optimization by an experienced modeller familiar with the dynamics of the ocean and the numerical implementations that approximate them. RECOM has shown to be a perfect tool for non-specialists to generate a first view of the dynamics of a local region, and to effortlessly produce a solid basis for further model optimization for more experienced users. RECOM should not be considered as one final product, but one capable of evolution based on user feedback.

1. Introduction

The Great Barrier Reef (GBR) : http://www.reefed.edu.au/_data/assets/pdf_file/0009/18783/SDC2004120620Sept200420General20Reference.pdf) is a 2000 km long reef and lagoon complex. It is a UNESCO World Heritage Area covering 347,800 sq. km, sandwiched between the Australia's northeastern coastline and the Coral Sea. It includes an estimated 2800 fringing, patch and shelf reefs organized in a matrix filled by an immense lagoon of average depth ~35m. It supports \$AUS250 million of commercial, ships and tourism industries (Wachenfield et al. 1998). It is recognized that activities within catchments that drain in to GBR have adversely impacted the coastal water quality and marine ecosystem health (Brodie and Waterhouse, 2012).

A modelling framework which links the management of agricultural activities in catchments that drain into the GBR to water quality and ecological responses in receiving waters has been recommended as an approach to support the design and implementation of water quality improvement plans (Webster et al., 2008). Such a framework would link models of land use and contaminant supply to the transport of these contaminants down rivers and through estuaries and ultimately to the transport and transformation of this material in marine systems. The conceptual linkages between agricultural activities in catchments and receiving water quality targets are illustrated in Fig. 1.1.

The fate of material delivered to the marine environment can be simulated through the application of materials transport and transformation models (see Figure 1.1-2). Hydrodynamic models simulate the advection and mixing of water and as such are a necessary precursor to the development of water quality and ecological response models. Sediment transport models then predict the fate of suspended particulates in the water column and benthos, including transport and mixing processes, settling, resuspension and flocculation. These models require the use of wave models to supply accurate shear stress at the sea bed. Biogeochemical models then build on these to provide a picture of primary and secondary productivity, nutrient cycling and dissolved oxygen dynamics. The eReefs project will develop such a coupled system for the GBR that spans hydrodynamics through to biogeochemistry, and will form the basis of a predictive framework that can be applied generically in the GBR lagoon to support Water Quality Improvement Plan (WQIP) development and implementation (Webster et al., 2008).



Figure 1-1.1. Conceptual linkages between management action targets and targets/objectives for receiving waters water quality and ecosystem health (from Webster et al. 2008)

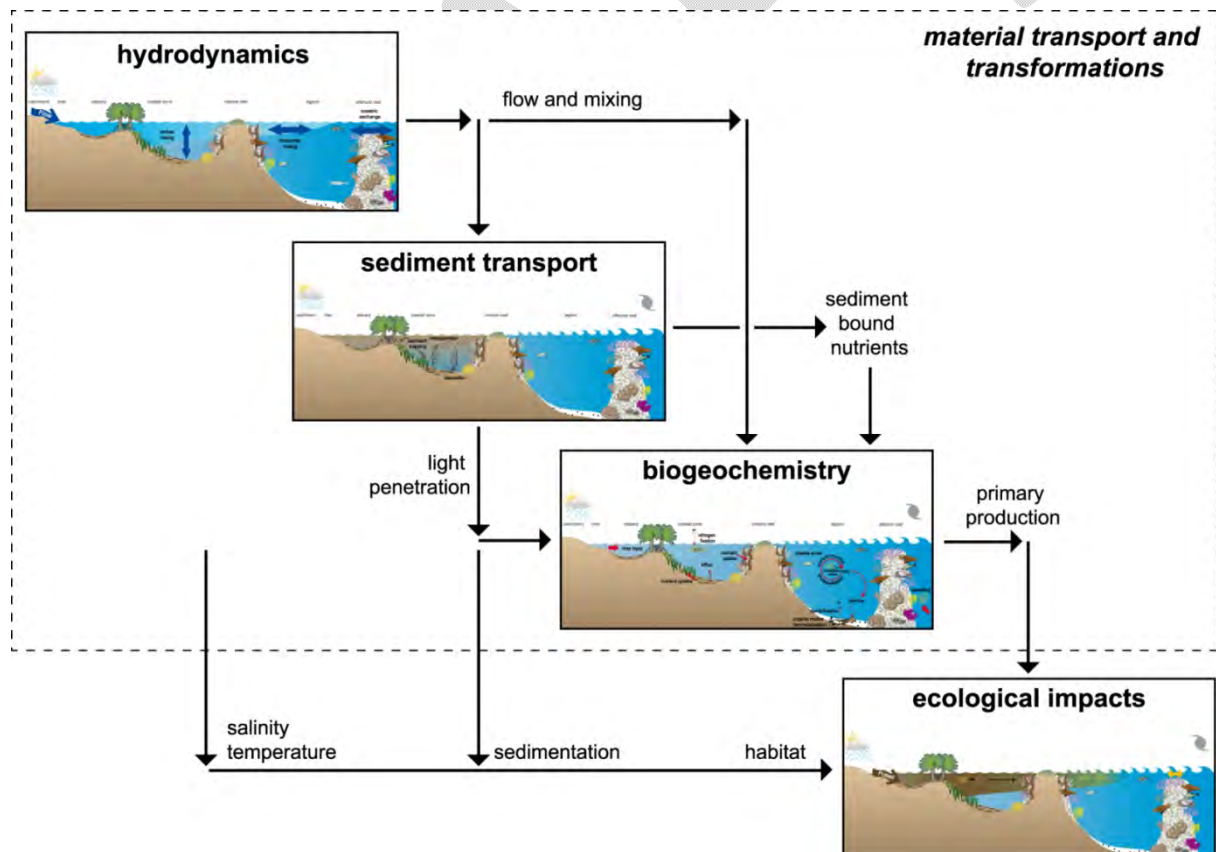


Figure 1.1-2. Primary components of a material transport and transformation models (inside box), and showing internal linkages between sub models and linkage to ecological impacts models (from Webster et al. 2008).

The models will need to address multiple spatial scales, ranging from whole of GBR (thousands of kilometres) to individual reefs and estuaries (hundreds of metres). This will require a flexible and nested approach to model resolution and domain. It's proposed that two classes of models will be developed:

- Whole-of-GBR models will deal with connectivity and interactions, from catchment to ocean, across the whole system. These models will likely be developed at several levels of resolution, to allow short-term nowcasts and forecasts, and long-term scenarios.
- Relocatable nested models will be developed to provide high resolution in local domains.

The success of eReefs lies in the ability of numerical models to deliver information that addresses the scientific issues surrounding the GBR lagoon and reef; i.e. delivery of nutrients from the catchment, processing of those nutrients by estuaries, eutrophication potential, sediment transport, hypoxia, reef acidification and coral bleaching. Most of these issues require coupled benthic-pelagic sediment transport and biogeochemical (BGC) models to deliver the required system understanding and information. Consequently, the successful simulation of these models, both operationally and in hindcast, is pivotal to the success of eReefs.

DRAFT

2. Background

2.1 Hydrodynamics

The general circulation of the Great Barrier Reef region is described by Burrage et al (1996). The South Equatorial Current flows westwards through the Coral Sea as a number of narrow current jets controlled by the complex plateaux, seamounts and ridge topography of this ocean basin, with the most significant of these jets occurring immediately north and south of the Queensland Plateau. On approaching the western boundary of the Coral Sea, these multiple jets are steered by the Australian continental shelf to form the southward flowing East Australian Current (EAC) and the northward flowing Hiri Current. The Hiri Current flows along the shelf edge of the northern GBR into the Gulf of Papua where it forms a semi-closed cyclonic eddy. Both these boundary currents are known to impact low frequency currents on the GBR shelf (Brinkman et al., 2002). In the central GBR, upwelling due to fluctuations in geostrophic currents or northeast monsoon winds transports cool water along the bottom of the central GBR shelf to the seaward edge of the GBR lagoon. This cool water does not create a surface signature. However, the cool water may reach the surface via upwelling due to internal or barotropic shelf edge tides, island wakes, topographically induced eddies or bottom Ekman pumping.

The southward flowing EAC is known to cause a shallowing of the thermocline along the shelf edge in the central and southern GBR, and movement of the thermocline in response to variability in the strength of the EAC is known to drive episodic upwelling and intrusions of cool water along the shelf edge of the southern and central GBR (Steinberg, 2007). Near the coast the temperature does not fluctuate in response to the tide. In shallow water near reef edges diurnal fluctuations of up to 4°C were observed by Griffin et al. (1987) and attributed to solar heating effects. Further offshore a tidal oscillation of up to 2°C was observed on a flood spring tide. Larger temperature oscillations are observed in deeper waters and are attributed to tidal pumping. The temperature lags the offshore current component by 90° (temperature minima occur at the end of the incoming tide). Griffin et al. (1987) show that a tidal current of 0.25 ms⁻¹ may induce a vertical displacement of 60m resulting in ~1.5°C temperature variation.

The circulation and thermal characteristics of Capricorn region at the southern end of the GBR have been studied by Griffin et al. (1987). The Capricorn Channel is associated with large tides of amplitude approaching 4 m at the coast. The tide is of semidiurnal nature in the north, progressing to equal diurnal and semidiurnal behaviour in the south near Lady Elliot Island. Flood tide directions have a strong alongshore component in the GBR lagoon, becoming stronger and later further north.

The thermocline also oscillates on longer timescales (6 – 10 days) on the shelf break and slope, but this non-tidal circulation is complex and highly variable. Generally, circulation off the shelf break is dominated by pulses of north-westward flow greater than 0.3 ms⁻¹, having a period of 6 – 10 days. This large flow is due to the cumulative effect of several baroclinic coastally trapped wave modes (Griffin and Middleton, 1986) and gives rise to a mean north to north-westward current predominantly parallel to the isobaths. The origin of these coastally trapped waves is further south beyond Fraser Island. Local wind stress contributes to circulation on the shelf, and to a lesser extent to mean flow on the shelf break. Griffin et al. (1987) postulated the presence of a large cyclonic eddy located at the southern mouth of the Capricorn Channel, generated by the EAC. This results in a north-westward backflow on the

shelf-break in the vicinity of Lady Musgrove Is. The appearance and disappearance of this eddy in response to EAC fluctuations may give rise to a long period (90 day) variation in the mean current on the shelf-break.

2.2 Sediment Transport

Discharge of sediments from catchments into the GBR Lagoon has increased many-fold over the last 150 years as a result of human activities (Furnas, 2003; Kroon et al., 2012). Most of these sediments are delivered to GBR during high flood events associated with tropical cyclones and monsoonal rainfall (Brodie and Furnas, 2001). Because of their size and geomorphology, dry catchments (Fitzroy and Burdekin) deliver the majority of sediment loads to the GBR coast (Brodie et al., 2013). River flows and sediment loads exhibit high variability over the range of time scales (Kuhnert et al., 2012; Darnell et al., 2012, Kroon et al., 2012) including diurnal, seasonal, annual and decadal scales.

Estuaries along the GBR coast are generally ranked as tidally dominated (Webster et al., 2008). Strong tidal currents in a constrained channel can maintain high levels of the suspended sediment in the mid-estuary region even during periods of low river flow. During extreme flood events a considerable amount of sediments can be deposited on the coastal floodplain, but this amount is not well quantified. Under moderate flood conditions a general consensus is that estuaries along the Australian GBR coast are mainly too small to have much impact on the magnitude of the fine sediment delivery to the lagoon (Neil et al., 2002). During non flood conditions these estuaries, generally, trap significant fraction of catchment sediment. Estimates of sediment loads to GBR are often based on measurements above the estuary, thus missing inputs and losses of sediment occurring many kilometres downstream from the measurement point.

Turbidity plumes from the major rivers may extend tenths and even hundreds of kilometres along the shelf, but tend to be constrained to within 20 km of the coasts by buoyancy and wind stress (Webster et al., 2008; Brodie et al., 2012). Most of the suspended sediment settle out of the flood plumes and deposit on the seabed within 10 km of the coast (Orpin et al., 1999; Lewis et al., 2014). A sedimentary pool created by these sediments can be partly buried into deeper sediments and partly resuspended by wind-driven waves and tides and then dispersed further by currents. Coastal currents, under the dominant southeast (SE) trade winds, tend to carry sediments northward along the coast. A fraction of the fine sediments can be ultimately trapped in northward facing embayments sheltered from the exposure to south-easterly swells by coastal features (e.g. Broad Sound, Bowling Green Bay, Princess Charlotte Bay) (Larcombe and Woolfe 1999; Williams, 2001). The amount of modern sediments trapped in these embayments is not well known. Recent measurements, for example, indicate that inorganic sediments delivered from the Burdekin River are trapped within 50 km from the mouth and very little of this sediment reaches north-west into the Bowling Green Bay and Cleveland Bay (Lewis et al., 2014). In Princess Charlotte Bay (Northern GBR) the terrestrial silt-clay component is dominated (more than 80%) by sediment derived from the coastal plain and input from local catchments (Olley et al., 2013).

Sediment processes on the GBR region have led to the development of a strongly sediment-partitioned shelf, with modern mud-rich sediments almost exclusively restricted to the inner and inner-middle shelf of 0 to 20 m depth (Neil et al., 2002). Further off-shore, at depths of

20 to 40m, a middle shelf zone is marked by a thin veneer of mixed terrigenous-carbonate sand ribbons and sand dunes. The passage of intermittent cyclones creates strong northward along-shelf currents, which cause erosion of the middle shelf seabed and transport of mobile bedload (Larcombe and Carter, 2004). At depths of 40 to 80 m, an outer shelf zone of reef-perimeter is dominated by carbonate sediment (Larcombe and Carter, 2004).

High natural variability and wide range of spatial and temporal scales of the sediment processes on GBR makes the inference of marine manifestations of the altered land-use practices in this region non-trivial to achieve. According to one school of thought, chronic turbidity at coral reefs due to suspension of fine sediments by tides and winds will not be significantly affected by changes in sediment inputs since the sedimentary pool in the Lagoon is already large (Larcombe and Woolfe, 1999). On the other hand, recent measurements suggest that the geological deposits together with newly imported materials additively determined water clarity inshore as well as mid-shelf (Wolanski et al., 2008; Fabricius et al., 2013; Schroeder et al., 2014; Fabricius et al., 2014). The new evidence shows significant correlation between catchment loads and turbidity on the shelf. The processes connecting catchment loads to the observed changes of turbidity across the GBR, however, are still not well understood. Transport of fine inorganic sediment and biogeochemical cycling of organic particulates have been considered recently as potential drivers of these changes (Lewis et al., 2014; Fabricius et al., 2014; see also section 5.5.7 of this report).

2.3 Biogeochemistry

Nutrient and phytoplankton dynamics across the whole GBR region spans the range from highly eutrophic estuarine systems to extremely oligotrophic offshore reefs. These systems are not distributed evenly by area or latitude with estuaries and coastal waters (<30 m depth) accounting for 30%, mid- and outer shelf waters 60% of the area and offshore reefs contributing just 10% of the area (Furnas & Mitchell 1986). The shelf is widest (~120km) in the south which supports higher levels of productivity (up to 1g C m⁻²) in inshore and offshore waters (Furnas et al., 2005).

Anthropogenic catchment loads enhance estuarine and inshore productivity particularly during the wet season and flood events. Nutrient rich plume waters support diatoms and larger phytoplankton growth modulated by high turbidity levels which can limit light available for photosynthesis. Coastal productivity is transported along shore (general northwards) and dispersed offshore by coastal currents and tidal mixing. This supports secondary productivity in the lagoon and inner reef including benthic deposit and filter feeders and reef communities. Inshore productivity is highest during the wet season (October - April) particularly in the central and northern GBR (Furnas et al., 2005).

On the outer reefs productivity is limited by very low nutrient supply. Typically the seasonal thermocline and associated nutricline intersects the shelf slope at ~100m which is below the depth of the outer shelf. New nutrients from offshore only arrive at the reef during episodic intrusions or upwelling events that are energetic enough to raise deep nutrient rich water onto the shelf. Episodic events have been observed throughout the year but are strongest in October - May (Furnas & Mitchell 1986; Andrews & Furnas 1986). At other times of the year primary production in the lagoon and outer shelf is maintained by efficient recycling of nutrients through the microbial loop. This phytoplankton community, consists of tiny pico-

and nano-plankton including photosynthetic autotrophs, heterotrophs and microzooplankton, cycles nutrients with growth rates of 0-2 doublings per day (Furnas 1991).

In addition to land and oceanic nutrient loads, the atmospheric contribution of nutrients to the GBR, in rain water and dust deposition, is comparable to oceanic fluxes (see Table 1 & Furnas & Mitchell 1996). Nitrogen fixation by reef organisms and blue-green microalgae *Trichodesmium* also occurs throughout the region although the patchy distribution and cryptic life history of N fixing organisms makes this flux difficult to constrain (Furnas & Mitchell 1996).

	Cairns (central-north GBR)		Tully (central-south GBR)	
	N	P	N	P
Sewerage	19	2.3	10	1.2
Rivers	157	6.9	350	15.4
Rainfall	84	2.2	110	2.9
<i>Trichodesmium</i>	140-6500		188-8700	
Reefal N-fixation	89		90	
Upwelling	52-96	11-20	83-145	17-30
Total	541-6945	22.4-31.4	831-9405	36.5-49.5

Table 1: Estimated annual inputs (Mmoles) of N and P to the Cairns (central-north GBR) and Tully (central-south GBR) regions from external sources (modified from Furnas & Mitchell 1996).

3. Modelling framework

The modelling framework adopted for this study involves nesting a regional hydrodynamic model within a global circulation model, in order to provide accurate forcing data along the boundary within the Coral Sea, where mesoscale oceanographic processes strongly affect exchange between the Coral Sea and the GBR Lagoon. The regional model (GBR4) covers the continental shelf from the NSW border to the mainland of Papua New Guinea, extending eastwards into the Coral Sea Territories a sufficient distance to avoid the topographical complexities of the Queensland and Marion plateaus. The regional model is intended to simulate the dominant oceanographic processes impacting on the GBR shelf, including the significant mesoscale features of the South Equatorial Current (SEC) and the current jets that result from the interactions of the SEC with the Queensland and Marion Plateaus. The average resolution of the regional model is ~4 km. Within this regional grid, a more finely resolved model (the shelf model) with resolution of ~1 km (GBR1) is nested to cover the continental shelf areas and the adjoining tract of the Coral Sea. Output from the regional model is used to force the boundaries of the shelf model.

Due to computational constraints it is not possible to run sediment transport and biogeochemistry directly coupled to the hydrodynamics model. A transport model is used to achieve the same objective; this model uses currents and mixing variables stored offline from the hydrodynamic model to advect and diffuse the sediment transport and biogeochemical variables. Since this model uses an unconditionally stable semi-Lagrangian advection scheme, the time-step can be significantly increased over that used in the hydrodynamic model, leading to orders of magnitude increases in runtime that allow long term simulations to be achieved.

Coastal locations or individual reefs are likely to be required to be modeled at high resolution (< 1km) to capture important small-scale processes and dynamics. A re-locatable coastal model (RECOM) is developed that can be deployed anywhere within the domain with minimal user input, making it useful for the development of site-specific coastal models by non-specialist users. Such a system exists in the BLUElink (<http://www.marine.csiro.au/BLUElink/>) project for hydrodynamics only (ROAM – Relocatable Ocean and Atmospheric Model, <http://www.emg.cmar.csiro.au/www/en/emg/projects/BLUElink--ROAM.html>). The concept of this system is extended to sediments and biogeochemistry, and allow for the construction of more complex curvilinear grids. RECOM will be two-way nested into the regional models, allowing feedback of the local dynamics to the larger scale and vice versa.

4. Methods

4.1 Whole of GBR Hydrodynamic Model

The hydrodynamic model SHOC (Sparse Hydrodynamic Ocean Code; Herzfeld et al., 2006, <http://www.emg.cmar.csiro.au/www/en/emg/software/EMS/hydrodynamics.html>) is employed for this study for both the regional and shelf model applications. SHOC is the hydrodynamic component of the broader Environmental Modelling Suite (EMS), which includes libraries for sediment transport, biogeochemistry (BGC), waves and tracer statistics (<http://www.emg.cmar.csiro.au/www/en/emg/software.html>). SHOC is a general purpose model (Herzfeld, 2006) based on the paper of Blumberg and Herring (1987), applicable on spatial scales ranging from estuaries to regional ocean domains. It is a three-dimensional finite-difference hydrodynamic model, based on the primitive equations. Outputs from the model include three-dimensional distributions of velocity, temperature, salinity, density, passive tracers, mixing coefficients and sea-level. Inputs required by the model include forcing due to wind, atmospheric pressure gradients, surface heat and water fluxes and open-boundary conditions such as tides and low frequency ocean currents (Figure 4.1). The model is based on the equations of momentum, continuity and conservation of heat and salt, employing the hydrostatic and Boussinesq assumptions. The equations of motion are discretised on a finite difference stencil corresponding to the Arakawa C grid.

The model uses a curvilinear orthogonal grid in the horizontal and a choice of fixed 'z' coordinates or terrain-following σ coordinates in the vertical. The 'z' vertical system allows for wetting and drying of surface cells, useful for modelling regions such as tidal flats where large areas are periodically dry. The current implementation of the model uses z-coordinates. The bottom topography is represented using partial cells. SHOC has a free surface and uses mode splitting to separate the two dimensional (2D) mode from the three dimensional (3D) mode. This allows fast moving gravity waves to be solved independently from the slower moving internal waves allowing the 2D and 3D modes to operate on different time-steps, resulting in a considerable contribution to computational efficiency. The model uses explicit time-stepping throughout except for the vertical diffusion scheme which is implicit. A Laplacian diffusion scheme is employed in the horizontal on geopotential surfaces. Smagorinsky mixing coefficients may be utilized in the horizontal. The ocean model can invoke several turbulence closure schemes, including k- ϵ , k- ω , Mellor-Yamada 2.0 & 2.5 and Csanady type parameterizations. A variety of advection schemes may be used on tracers and 1st or 2nd order can be used for momentum. The model also contains a suite of open boundary conditions, including radiation, extrapolation, sponge and direct data-forcing. A generous suite of diagnostics is included in the model.

The 'sparse' coordinate system (Herzfeld, 2006) employed by SHOC facilitates the use of highly complex curvilinear grids that allow resolution optimization. This sparse system allows the removal of dry land cells in the gridded domain, thus reducing the computational burden. It has been shown that runtime increases exponentially as wet cell ratios decrease using the sparse system (Herzfeld, 2006). This is an important efficiency method for the GBR models, especially for the 1 km model which is only 20% wet. The sparse system also presents several other advantages, including arbitrary domain decomposition for distributed processing, reduced file sizes for storage and compatibility with finite volume approaches.

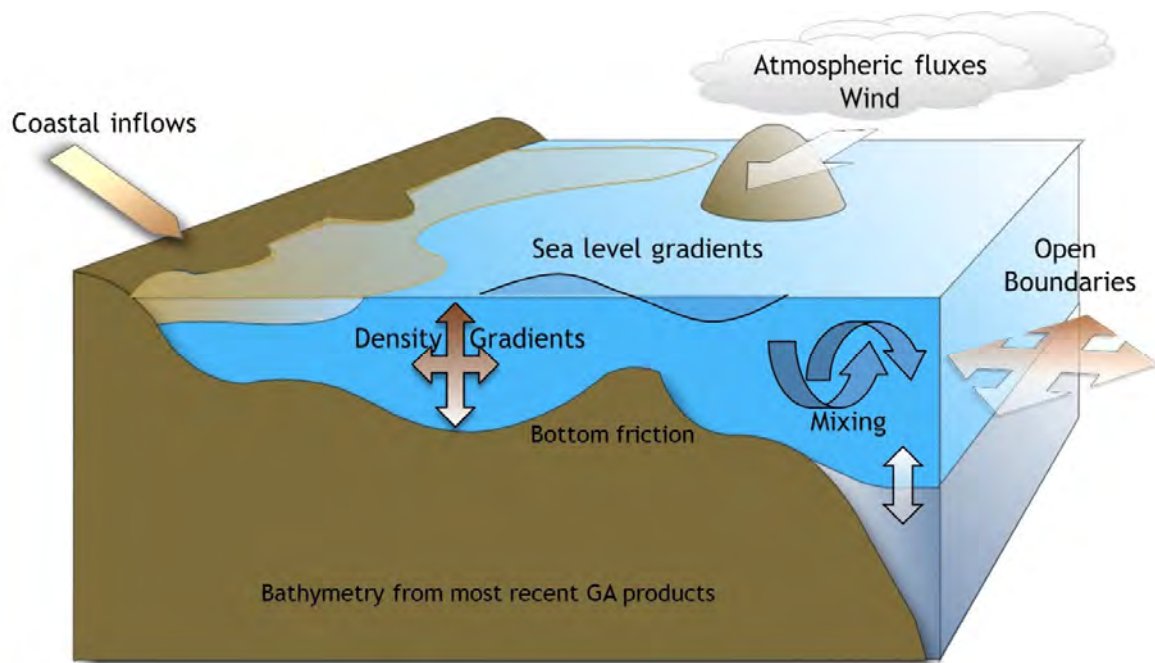


Figure 4.1.1. Schematic representation of major forcing inputs for the SHOC hydrodynamic model.

Over a 20 month period ending in June 2011 the project '2.5i.1 – Hydrodynamics of the whole of GBR scale' (delivered through collaboration between CSIRO and AIMS and co-funded by GBRMPA; <http://www.emg.cmar.csiro.au/www/en/emg/projects/GBR/Summary.html>) produced 4 km and 1 km resolution models for the whole of the GBR. Both these models use the Sparse Hydrodynamic Ocean Code (SHOC) as a code base. These models encompass the reef from Papua New Guinea to the NSW border, and are fit for purpose in the sense that they optimally resolve the GBR reef and lagoon whilst maintaining manageable run-times. The reef model of resolution < 1 km is the product of most importance to stakeholders, since the ability of the 4 km model to resolve the reefs is marginal. The primary role of the 4 km model is to act as a nesting vehicle between the BLUElink 10 km model and 1 km model, recognising that the reef model cannot be nested directly into the global model as open boundary condition (OBC) ratios should not ideally exceed 5:1. A secondary objective is the ability to directly couple to sediment transport and biogeochemistry if necessary, with acceptable runtimes, to perform longer scenario simulations. The current regional model is considered optimal in these regards and conforms to the Water Quality Improvement Plan outlined by Webster et al. (2008). The 4 km model has been currently running routinely in near real-time at CSIRO O&A for a ~5 years. This period encompasses a range of forcing conditions imposed by the seasonal cycle, including extreme conditions of flood and cyclones, and has remained stable and accurate. These models were extended to achieve eReef's objectives.

The grids to be used in eReefs are displayed in Figure 4.2; these are refinements of the grids used in the Hydrodynamics of the whole of GBR scale project. The 1km grid (GBR1) is extremely large, with size 510 x 2390 which delivers slightly more surface cells than the global

BLUElink model (OFAMv2). There are 48 vertical layers, with 1m resolution at the surface. Although the grid is large, only 50% of the surface cells and 22% of the full 3D domain is in fact wet. The 4km grid (GBR4) is less computationally demanding; size is 220 x 500 x 44 with 1m vertical resolution at the surface. It may be possible to perform longer hindcasts with this model with modest compute resources. Results of both models (temperature, salinity, sea level, currents) will be archived.

Both models employ orthogonal curvilinear grids over the domain. These grids offer the optimum economy in terms of resolution placement, grid orientation and removal of dry cells. A higher resolution can be achieved in the areas that matter most using the minimum number of cells whose alignment is oriented parallel and normal to the dominant flow directions. The GBR area of interest comprises a very large domain – to impose a constant grid size throughout risks unnecessarily increasing the number of surface cells and consequently runtime. Additionally, the 4 km and 1 km model have 68% and 22% wet cells in the domain respectively, which impacts strongly on run-time. Allowing the curvilinear grid to follow the coast not only naturally aligns the cells in the alongshore and cross-shelf direction (which assists stability and accuracy) but also decreases the number of land cells in the grid. A 'square' grid would possess much lower wet cell ratios, leading to much larger run-time implications.

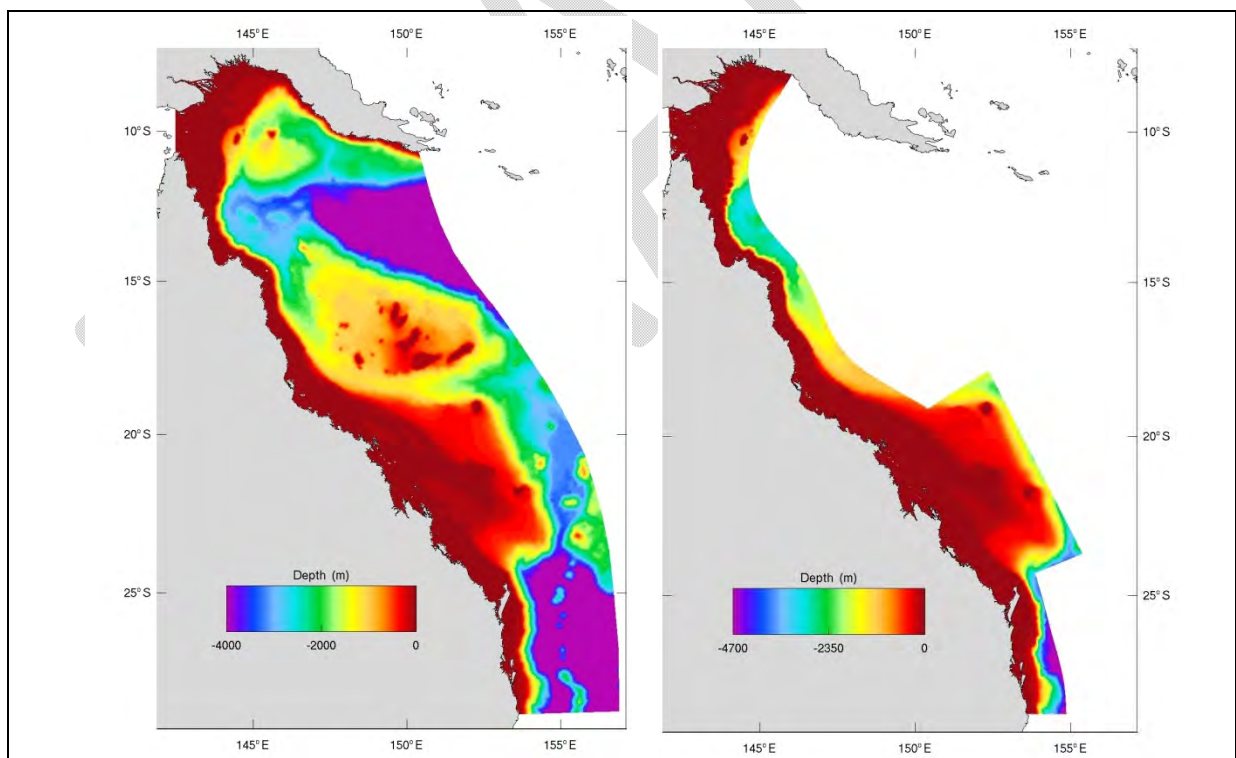


Figure 4.1.2. Model grid and bathymetry established for pilot 4km (GBR4; left) and 1km (GBR1; right) resolution model.

Bathymetry for the 1 km and 4 km models is sourced from the Digital Elevation Model of the GBR produced at 100 m spatial resolution (Beaman, 2010), <http://www.deepreef.org/>. In the

northern limits of the domain this is supplemented by the GA 2009 bathymetry (Geoscience Australia, 2009). Bathymetry from local estuaries may require supplementary data sourced from targeted field efforts.

The 4km model is forced with the global model OMAPS data (http://www.bom.gov.au/BLUElink/products/prod_oceanmaps.html) on the open boundaries using the method of Herzfeld and Andrewartha (2012). The tide is introduced through 22 constituents derived from the global CSR tide model of Cartwright and Ray (1990) using the implementation of Eanes and Bettadpur (1995). Currently the surface fluxes are obtained from the ACCESS meteorological model run operationally by BoM (<http://www.bom.gov.au/nwp/doc/access/NWPDData.shtml>). Surface fluxes comprise of momentum, heat and freshwater sources. The 1km model is forced on the open boundaries with outputs from the 4km model (1-way nesting). In the absence of observations or high resolution global model products, open boundary conditions for sediments and BGC may be derived from statistical regressions of nutrients to temperature profiles.

River flows input into the models are obtained from the DERM gauging network (http://www.derm.qld.gov.au/water/monitoring/current_data). Initially the rivers in Table 1 are included in the 1km and 4km models. The Fly river in Papua New Guinea is included due to its high discharge (consistent average over the year of $6,000 \text{ m}^3\text{s}^{-1}$, Harris et. al, 2003, Wolanski et. al, 2000) and high sediment loads; both natural and due to mining upstream. The flows and concentrations associated with these rivers (temperature and salinity) are input into the model as an open boundary condition (OBC). The flow is input directly as a parabolic velocity profile, with maximum flow at the surface and zero at some predefined pycnocline depth. Tracer concentrations in the river boundary cell are computed based on mass divergence, where it is assumed an infinite pool of water with prescribed concentrations (zero for salinity and measured temperature) exists upstream of the boundary cell.

Name	Wet / dry	Annual Volume (km ³)	Monthly Mean (ML)
Cape York Region			
Normanby River	Wet	4.95	8229
Wet Tropics Region			
Barron River	Wet	0.81	1777
Daintree River	Wet	1.26	2418
Mulgrave-Russell Rivers	Wet	3.64	2186
Johnstone River	Wet	4.67	2229
Tully River	Wet	3.29	8571
Herbert River	Wet	4.01	6884
Burdekin Region			
Haughton River	Dry	0.74	1149
Burdekin River	Dry	10.29	24,539
Don River	Dry	0.75	494
Mackay Whitsunday Region			
O'Connell River	Dry	1.54	683
Pioneer River	Dry	1.19	3586

Fitzroy Region			
Fitzroy River	Dry	6.08	14,708
Calliope	Dry	0.3	456
Boyne	Dry	0.29	-
Burnett Mary Region			
Burnett River	Dry	1.15	3248
Mary River	Dry	2.72	4031
Other			
Brisbane River	-	-	-
Caboolture River	-	-	-
Pine River	-	-	-
Logan River	-	-	-
Fly River	-	-	-

Table 4.1.1: Rivers included in the regional and shelf models, and the 2008-2009 wet season hindcast.

Atmospheric fluxes are computed using data supplied by ACCESS (wind, mean sea level pressure, cloud amount, air temperature and dew point temperature); see Herzfeld 2005, Chapter 9. These atmospheric variables are used in conjunction with the bulk scheme of Large and Pond, (1982) or (Kondo, 1975) to compute sensible and latent heat fluxes. Black body radiation using the model SST is applied to compute long wave radiation (Zillman, 1972) with a cloud cover correction included. Short wave radiation is computed using the sun's hour angle at the latitude of each model cell with a correction for cloud cover (Reed, 1977). Short wave radiation must be partitioned between the long wavelengths that are attenuated in the water column rapidly, and the shorter ones that penetrate to depth. This is accomplished via a transmission coefficient (with value = 0 to 1). Additionally, in shallow water, a bottom absorption coefficient (values = 0 to 1) is required to parameterise the amount of heat that is lost to the sea bed. In the absence of information on the thermal properties of the substrate, this parameter typically is treated as a calibratable parameter. Data assimilation is used to estimate short wave extinction, transmission and bottom absorption parameters (Section 4.3.6.2). The salt flux is defined as the difference between evaporation minus precipitation; precipitation was derived from ACCESS and evaporation was obtained from the latent heat flux supplied by the bulk method divided by the latent heat of evaporation.

Both the 1 km and 4 km models are currently routinely run in near real-time. Outputs can be viewed at (<http://www.emg.cmar.csiro.au/www/en/emg/projects/eReefs/Results.html>).

4.1.1 Bathymetry analysis

As mentioned above, the bathymetry for the 1 km and 4 km models is sourced from the Digital Elevation Model of the GBR (GBR100) produced at 100 m spatial resolution (Beaman, 2010), <http://www.deepreef.org/>. The resolution differences between the Beaman and the GBR4 bathymetries mean that ~1600 GBR100 points are included in a GBR4 grid cell, and these points will span a range of depths. The largest differences between the GBR4 depths at each cell and the shallowest and deepest GBR100 depths found within that cell are displayed in Fig. 4.1.3. These figures indicate which locations are subject to a large degree of depth variability within the 4x4 km GBR4 cell.

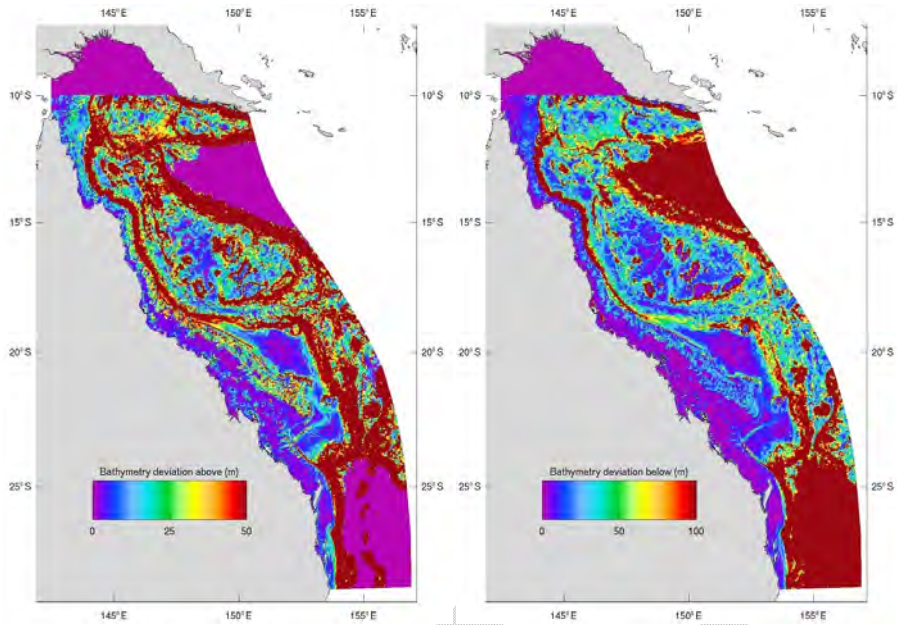


Figure 4.1.3. Maximum differences between GBR4 bathymetry and the shallowest (left) and deepest (right) depths in the GBR100 database.

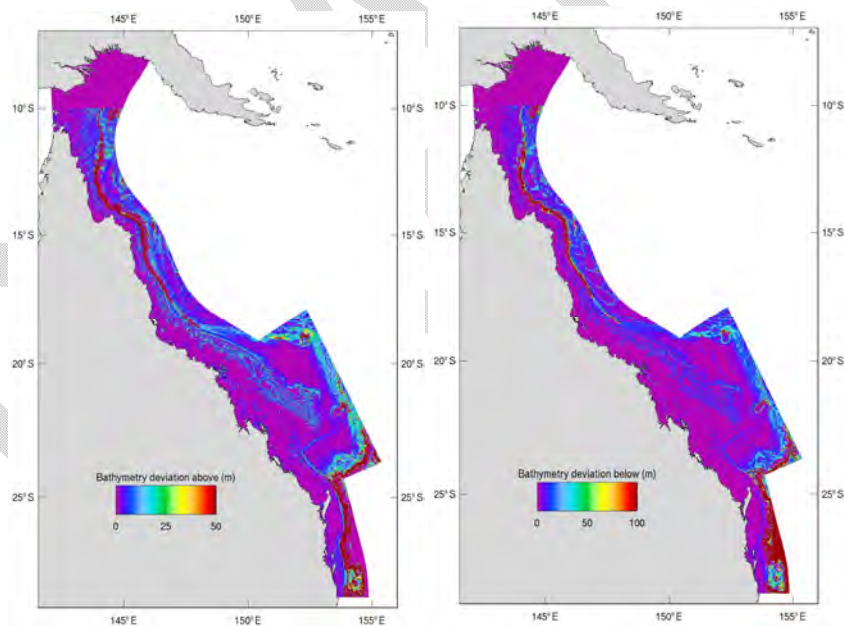
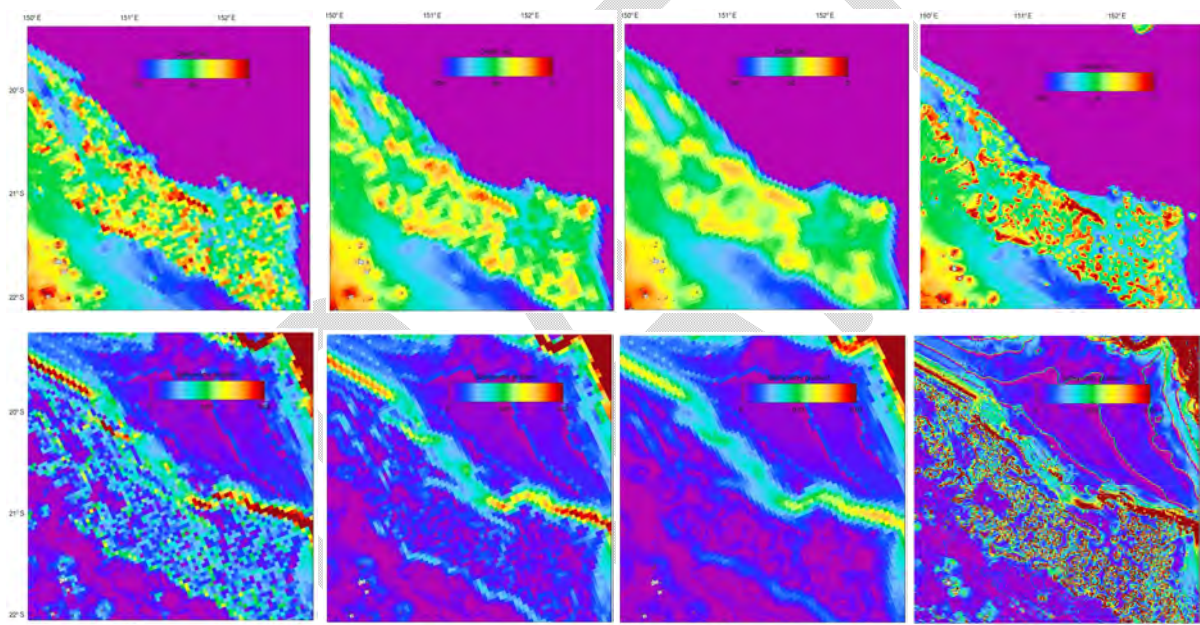


Figure 4.1.4. Maximum differences between GBR1 bathymetry and the shallowest (left) and deepest (right) depths in the GBR100 database.

Over the GBR lagoon and shelf, the largest variability unsurprisingly occurs at the shelf edge, however, the reef matrix also shows a large degree of bathymetric variability. In some cases (e.g. within the Capricorn Bunker group) the actual bathymetry as recorded in GBR100 is over 50m shallower than that used in GBR4, i.e. the reef matrix is poorly resolved in the GBR4 model. This has implications on the ability of the reef to steer circulation (see Section 5.2.1) and on the heat budget from differential heating effects. An equivalent bathymetry analysis is presented for the GBR1 grid in Fig. 4.1.4; here bathymetry deviations over the reef are less

than half those seen in the GBR4 grid, and the GBR1 grid provides a far superior representation of the reef matrix. If the model bathymetry is smoothed (which generally aids model stability), then the situation is compounded. Fig. 4.1.5 shows the GBR4 bathymetry subject to 1 and 3 smoothing passes. The depth and bathymetric gradient rapidly deteriorate when smoothing is applied, such that after 3 passes the reef matrix does not really exist at all; smooth undulations are seen to exist over the reef, associated with negligible bathymetry gradient. Any bathymetric smoothing beyond 1 pass is unlikely to result in a realistic impact on the hydrodynamics by the reef matrix. For reference, Fig. 4.1.5 (d) shows the GBR1 depth and gradient, which clearly shows the benefits of decreased grid size in resolving the reef structure; at this resolution lagoons associated with individual reefs are visible. Section 4.2.1 shows that the best way overcome poor reef representation is to increase resolution (e.g. using GBR1 – model outputs are qualitatively assessed in Section 5.2.1). If this is not possible, then sub-gridscale parameterizations can be used to represent the effects of the reef on the hydrodynamics (Section 4.2.1).



(a) No smoothing (b) 1 smoothing pass (c) 3 smoothing passes (d) GBR1 no smoothing
 Figure 4.1.5. GBR4 bathymetry (a-c) and GBR1 (d) in the Capricorn Bunker group subject to smoothing; depth (top row) and gradient (bottom row).

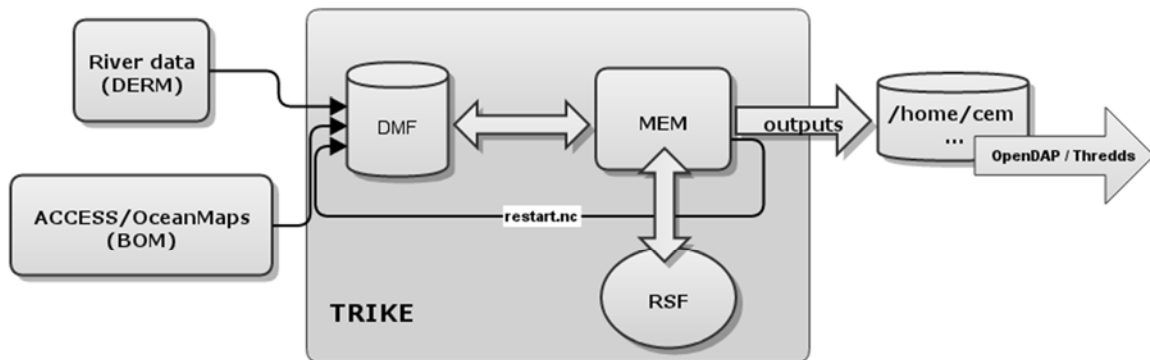
4.1.2 TRIKE

The near real-time framework that the models are implemented and execute within is TRIKE (the scientific version of ROAM developed within BLUElink). This system is mature, documented, supported and has proven capability in run specification, run coordination, data management and model execution management.

The framework itself is installed and customised on the local desktop machine **bruny**. The actual computations are done on the CSIRO high performance cluster **burnet**. These compute nodes are easily reconfigured to point to a different cluster should the need arise without disrupting the integrity or the external view of the output data.

The 3 basic components of TRIKE are as follows (Fig 4.1.6):

- **DMF** – Data Management Framework. This routinely collects and registers the various data streams (including model output for dependant runs) as forcing/input data.
- **MEM** – Memory Execution Manager. This manages the actual model runs by querying the DMF for the forcing data and farming out the model execution to the compute node. A single instance of this is able to handle multiple model runs.
- **RSF** – Run Specification Framework. This is the GUI through which users interact with TRIKE (Fig. 4.1.7); it allows for setting up of model runs shows its progress. Many different RSF may connect to the same MEM.



Definitions:

DMF - Data Management Framework. Downloads all forcing files and keeps track of them in a database. It also keeps track of some output files, eg. restart.nc
MEM - Model Execution Manager. Manages the run as specified
RSF - Run Specification Framework. This is the GUI through which we interact with Trike

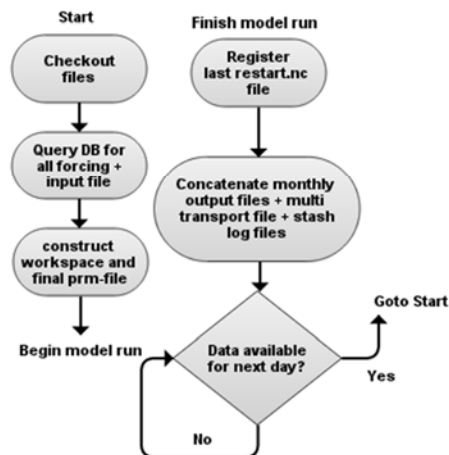


Figure 4.1.6. Components of TRIKE

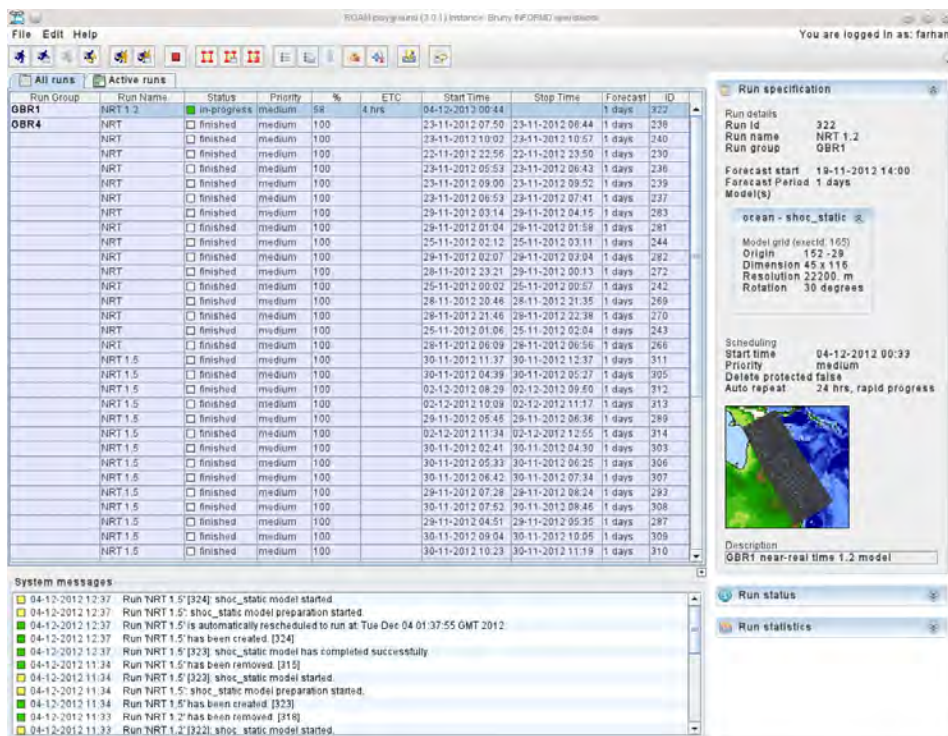


Figure 4.1.7. Screen snapshot of the TRIKE graphical user interface.

A subversion repository for the configuration files has been set up at:

<https://svnserv.csiro.au/svn/CEM/projects/eReefs/model/>

This contains all of the SHOC parameter files (prm) needed to run the GBR4 and GBR1 models. At every model execution by TRIKE, these files are updated in the workspace so any changes by the user are automatically transferred to the next run. These include, but are not limited to, changes in the output netCDF file, new time-series, mixing scheme, parameter coefficients etc. A parameter file revision number is propagated through to the output files as well as various run logs. There is also an ID number associated which is updated for significant changes.

The following wiki page keeps an ongoing log of the model updates:

<https://wiki.csiro.au/display/ceM/GBR4+Trike+Updates>

The specific data stream registered with TRIKE are:

- **OceanMaps v2.1**, ensemble 00 from BoM for ocean boundary.
 - Daily mean sea level (scaled by -0.25 to provide a datum relative to msl), salinity, temperature and velocity.
- **ACCESS-A** surface model output from BoM for atmospheric data.
 - Air temperature, precipitation (converted to daily from accumulated), wind, cloud, dew point and surface pressure.
- River data from Qld. Department of Natural Resources.
 - Stream discharge and water temperature for 25 rivers,

- o Daily ftp setup.

GBR4 model output is currently being archived locally in Hobart and is available CSIRO wide via OpenDAP at http://wave.hba.marine.csiro.au:8080/opendap/ModelOutput/near-real_time/contents.html.

TRIKE's modular design allows for implementation of small components that work together to build larger systems. The DMF (data management framework) that hosts the global data is a separate entity to the one that hosts the near real time models. This greatly simplifies management of these separate components and allows for independent testing before they are inserted into the bigger system. The re-locatable modelling system (RECOM) uses both of the abovementioned hosts to build up the complete set of forcing datasets needed to execute the finer scale coastal model (Fig. 4.1.8). It is a separate host that is decoupled from the others.

These systems are currently file based when exchanging data but may be configured for other protocols such as OpenDAP/WCS and even WMS in the case of data visualisation. The workflow allows for partial specification and persistence so that users can go back and modify any previously defined runs.

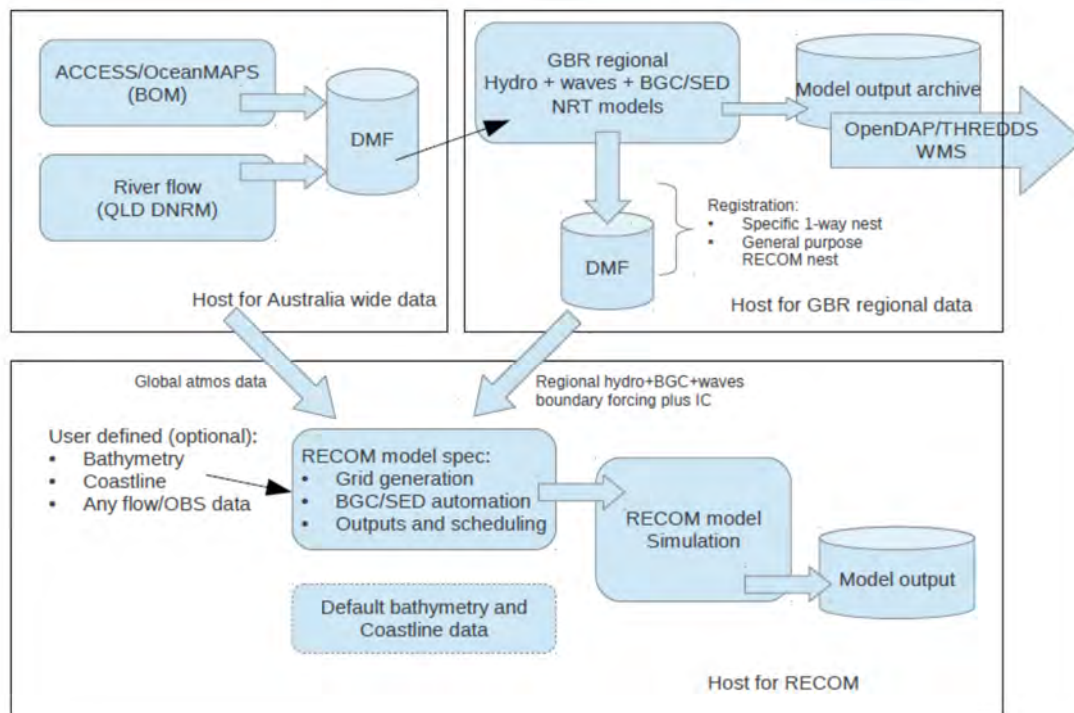


Figure 4.1.8. Modular configuration of TRIKE hosting Global, static and RECOM DMFs.

4.1.3 River inflow

The method of input of river flows into models is a subject of international attention. Estuaries process water properties along their length, so what enters the estuary at the head is not equivalent to what exists at the mouth. Tidal mixing and entrainment along the length of the salt wedge act to dilute properties entering at the head of estuary. Any tracer deposited at the mouth within the salt wedge undergoes advection upstream and mixing within the estuary before transport downstream, such that resultant surface concentrations at the

mouth differ to those if the estuary were absent. Although water properties at the estuary mouth differ from those at the head, it is typically the location of the latter that observations are made. This poses a problem for inclusion of freshwater sources in regional models too coarse to adequately resolve the estuaries. Typically the water properties at the head are input at the coast in these regional models in what is termed a simple inlet, which turns out to be a pretty poor approximation. The situation is worse for other quantities, e.g. suspended sediments where sediment is pumped up-estuary in many tropical environments, so that even the direction of the sediment flux at the coast may be incorrect.

There are basically two methods used to introduce a freshwater flux at the coast. Both use a simple inlet, which is defined by Garvine (2001) as 'a rectangular breach in the coastal wall with uniform inflow water properties, including density and discharge velocity'. Garvine (2001) chose to impose a flow field constant in time and space (i.e. depth independent) at the inlet boundary, in conjunction with prescribed water properties; we refer to this type of input as a *flow input*. The alternative is to input a volume flux of zero salinity water directly into one or more layers of the model (via the continuity equation), with no associated velocity profile. We refer to this input method as a *point source input*. This method was used by Schiller and Kourafalou (2010), where they included an additional term in the barotropic pressure calculation to account for the pressure exerted from the mass of freshwater input by the river. This extra term may not be necessary with a point source if the river volume is added to the divergence term when updating sea level. Mass fluxes of tracers must also accompany the volume input for inclusion in tracer mass divergence when updating tracers. The point source input method directly accounts for neither the baroclinic contribution due to density change or momentum input by the river's inertia.

There is typically also a numerical response to the estuarine input, regardless of the method of input. Garvine (2001) classifies three types of buoyant plume responses resulting from inputting fresh water into a simple inlet at the coast. Firstly, the plume turns under the influence of Coriolis and propagates downstream from the simple inlet (downstream is left of the inlet in the Southern Hemisphere, right in the Northern Hemisphere). There is little flux of fresh water upstream of the inlet and a steady state is achieved; these are termed type 1 plumes. Secondly, a continuously growing upstream intrusion forms, where water circulates in an anticyclonic gyre before returning downstream to form a coastal current. The front of the gyre propagates upstream to produce a non-steady distribution of fresh water. These are classified as type 2. For type 3 plumes, a large anticyclonic bulge forms that grows offshore with time. The downstream coastal current is weak. Most real river discharges are found to produce type 1 plumes, with few examples of type 2 or 3, whereas most model applications produce plumes of type 2 or 3.

Garvine (2001) attributes the development of type 2 and 3 plumes in numerical models to the simple inlet itself, and Yankovsky (2000) further attributes the response to the type of boundary condition imposed in the simple inlet. The blocking of up-estuarine baroclinic flow at the bottom (i.e. salt wedge propagation) by the simple inlet creates a cyclonic vortex on the upstream edge of the plume to result in an initial left turn for the flow (Northern Hemisphere) and consequently an upstream intrusion. Yankovsky (2000) found that modifying the boundary condition in the inlet made plumes behave more like type 1. The boundary was modified such that vertically integrated inflow remained the same but the vertical structure was allowed to be modified by the interior velocity. Garvine (2001) showed via an analytical model that the upstream propagation of type 2 intrusions is reduced by using

a shallower coastal wall, reduced vertical diffusivity and increased vertical viscosity. Using a channel having an angle to the coast of less than 90° was also found to reduce the occurrence of type 2 plumes. Type 2 and 3 plumes exist in the absence of any other forcing (tides, wind), however, the introduction of an ambient flow of ~0.05 ms⁻¹ results in type 1 plume behavior. Using a point source type of flow, Schiller and Kourafalou (2010) demonstrated that a spectrum of solutions could be obtained by varying the depth over which the freshwater was distributed, the vertical mixing in the inlet or the degree of lateral spreading applied to the freshwater input, with deeper penetration of the input (up to 40% of water depth) resulting in type 1-like plumes.

Garvine (2001) states 'an inlet flow field that better mimics that observed at the mouths of estuaries leads to reduction of intrusion'; motivated by this an alternative inlet boundary condition is developed. Both the point source and flow input methods must have a predefined depth prescribed over which to distribute the inflow flux, and such a depth may not be always known. The skill of the system response to the input depth may not consistently correlate with any measurable quantities, hence the input may consequently need to be optimized using a calibration procedure where the depth is heuristically 'tuned' by comparing the model response to observation. Such a procedure is not always desirable (e.g. if the domain contains many interacting rivers) and an alternative boundary formulation is presented that aims to contain no predefined parameters. This approach aims to address the brackish nature of the flow at the mouth and the landward flow in the salt wedge, and consists of three tasks:

1. Estimate a depth of the salt wedge at the mouth using an analytic expression,
2. Modify the flow profile to account for baroclinic flow,
3. Modify tracer concentrations to account for landward transport of tracer.

Keulegan (1966) provides an analytic expression that relates the depth of the salt wedge at an estuary mouth to the inflow velocity and mode 1 internal wave speed:

$$H_{ck} = H \left(1 - \frac{1}{2^{2/3}} \left[\frac{2v_r}{v_\Delta} \right]^{2/3} \right) \quad 4.1$$

where H_{ck} is the depth of the salt wedge at the estuary mouth, v_r is the river velocity, and $v_\Delta = \sqrt{\frac{\Delta\rho}{\rho} gH}$ is the internal wave speed at the mouth, with $\Delta\rho$ the density difference between top and bottom, ρ the mean density and g the acceleration due to gravity.

If additional 'ghost' cells are appended to the boundary cell, the density at these locations can also be computed via the equation of state. This then allows the baroclinic contribution to velocity to be computed at the boundary face;

$$v_{BC}(t, z) = \frac{g}{h\rho} \int_z^\eta \frac{\partial\rho}{\partial x} dz \quad 4.2$$

If the velocity profile at time n is assumed to be a parabolic velocity profile whose vertical integral equals the river flow, $v_{OBC}(z)$, then the total velocity at time $n+1$ is:

$$v^{n+1}(t, z) = v_{OBC}(z) + \Delta t v_{BC}(t, z) \quad 4.3$$

This is additively scaled so that the total flow is equal to the river flow. The salinity in the 'ghost' cells is then updated using a mass balance and upstream advection algorithm to account for concentration change due to advection. This has the effect of making the ghost cell salinity more saline if flow is landward in the boundary cell (e.g. near the sea floor within the salt wedge), and less saline near the surface where flow is into the domain and thus bringing in fresh water. It can be seen that a feedback mechanism exists between the salinity of the ghost cell, and the flow direction as computed through the baroclinic contribution, Eq. 4.3.

To demonstrate the functionality of the various river inputs methods a simple test case of Yankovsky (2000) is replicated using a point-source (PSS), a flow input with salinity concentration prescribed at the river boundary (TRCONC) and the implantation described above (DYNAMIC). Following previous studies, a test case is designed to emulate the input of a river into a quiescent water body using a simple inlet. Solutions are compared to a baseline case where the river is resolved to beyond the upstream limit of salt wedge propagation. The domain is an open channel of 2.5 x 1.25 km resolution and no forcing other than an impulsive flow event having mean velocity of 0.1 ms⁻¹. The simple inlet is located on the southern boundary halfway along the channel.

Salinity and flow field at the end of the simulation (30 days) are displayed in Fig. 4.1.9 for the baseline case. The surface salinity solution shows a type 1 plume response, where a bulge forms at the inlet with little upstream intrusion. Anticyclonic circulation exists in the bulge, with flow joining a downstream coastal current. This response is consistent with previously published studies of this nature.

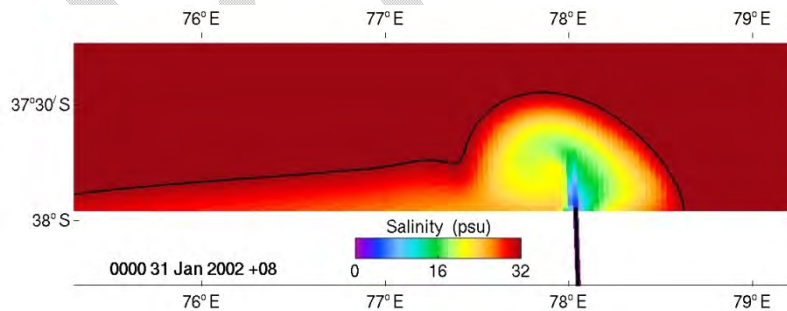
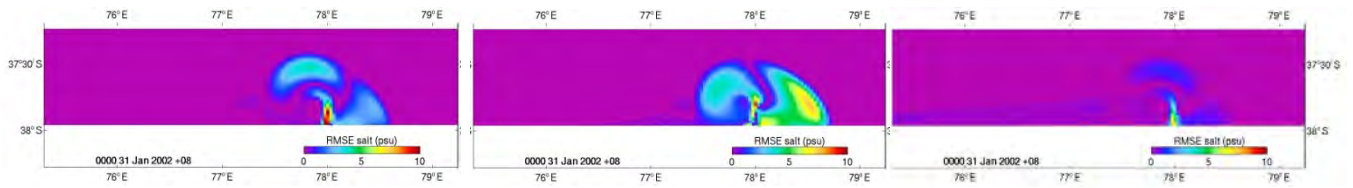


Fig. 4.1.9. Surface salinity solution at 30 days for the baseline test case. The contour is at 31.65 psu (95% of ambient salinity).

Skill is assessed using the RMSE of the various input methods relative to the baseline; solutions using PSS, TRCONC and DYNAMIC are displayed in Fig. 4.1.10. The TRCONC and PSS method input the tracer in the top 1m of the water column; solutions are sensitive to this depth distribution and a spectrum of plume responses may be achieved by varying this input depth. The PSS and TRCONC solutions in Fig. 4.1.10 may be consequently improved, but this involves a difficult heuristic tuning exercise. Overall, the DYNAMIC method exhibits the highest skill, even after optimising the input depth for the PSS and TRCONC methods. The PSS method consistently performs the worst. This observation holds across a variety of test cases with differing resolution and flow regimes.



TRCONC (a) PSS (b) DYNAMIC (c)

Figure 4.1.10. Surface salinity at 30 days for the impulsive flow test.

The circulation dynamics at the estuary mouth is a baroclinic phenomenon, whereas the application of a point source invokes a barotropic response. Consequently, this input method is prone to type 2 and 3 plumes, and results in solutions with lower skill compared to other input methods. Furthermore, the input depth and mixing in the inlet must be optimised to achieve acceptable skill, and this can be unintuitive, where the depth does not correlate with any physical characteristics to the system (e.g. pycnocline depth). For these reasons, the point source should be avoided if possible. The flow input must also be optimised, but input depths close to the pycnocline depth appear to provide adequate responses. The dynamic method requires no tuning, and consistently provides the best skill in test applications.

In the context of the GBR models, the input of zero salinity into simple inlets at the coast results in the lagoon becoming too fresh (see Section 5.1.10). The DYNAMIC method inputs brackish water at the coast leading to more accurate solutions, and is consequently used in the GBR4 and GBR1 applications. Alternatively, in the absence of sophisticated techniques such as the dynamic method, a flow dependent salinity may be imposed on input methods, however, this relies on long term salinity data for each estuary mouth which unavailable. Implementation of this approach is therefore impractical. An example regression of flow vs salinity was performed for the Fitzroy River for January to April 2005; the regression included a lag of 4 days to correlate highest flow at the head of estuary with lowest salinity at the mouth. The regression is displayed in Fig. 4.1.11 and mathematically expressed as:

$$salt = 36 \exp(-0.014 \sqrt{flow}) \quad 4.1$$

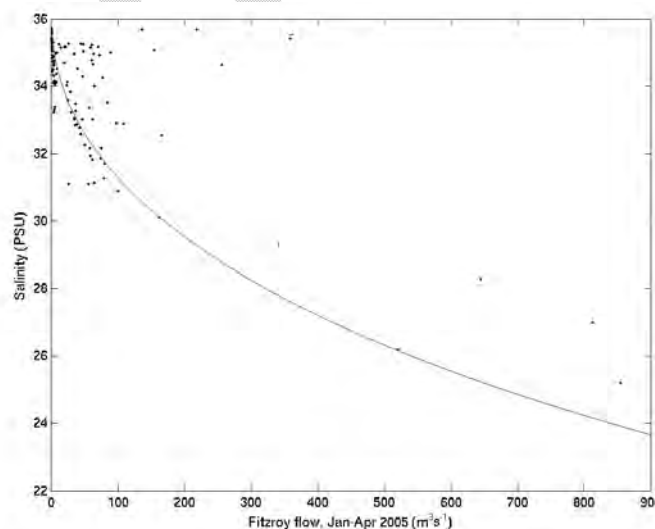


Figure 4.1.11. Regression of flow vs salinity for the Fitzroy, Jan-Apr 2005

A manuscript describing the DYNAMIC flow input method has been published in Ocean Modelling; Herzfeld (2015), including an assessment of how the method performs when applied to the Fitzroy Estuary.

4.1.4 Dual relaxation

The open boundary condition of Herzfeld and Andrewartha (2012) is a Dirichlet based condition where 3D velocities from an external model are directly applied to the open boundaries of the downscaled model. Barotropic velocity open boundary conditions are the depth average of these 3D velocities. The elevation is left unconstrained, and can therefore perfectly respond to outward propagating signals; it is this aspect of the open boundary condition that reduces the impact of over-specification error. However, since volume fluxes through boundary sections invariably differ between external and downscaled models (due to bathymetry differences and interpolation error), the downscaled model is often prone to basin filling or emptying over time. To overcome this, a local flux adjustment is applied, where normal barotropic velocities are adjusted every time-step so that the volume divergence in the boundary cell achieves some target elevation (supplied from the external model, and augmented with the tidal signal). The normal barotropic velocity is relaxed toward the adjusted velocity with a pre-defined time-scale. If this is the 2D time-step, then the target elevation is achieved exactly every time-step, and the boundary behaves as a (reflective) clamped condition. Herzfeld and Andrewartha (2012) noted that if a timescale of $\tau_f = h_1 / \sqrt{gD_B}$ is used, then the local flux adjustment takes the form of the Flather radiation condition (Flather, 1976), and this time-scale can be considered a 'default' timescale that best optimizes volume conservation and area averaged kinetic energy in the domain (Herzfeld and Andrewartha, 2012). However, this time-scale is too long to accurately reproduce the tidal amplitude and phase characteristics in many domains.

To overcome the conflict in time-scales required to resolve short (tidal) and longer (weather-band frequency) motions, a dual boundary relaxation method is developed. Assume that the normal barotropic velocity through the open boundary face is equal to the sum of a high and low frequency component, $V_B = V_{BT} + V_{BL}$. The continuity equation can be written in a form where a flux through one cell face is similarly split into contributions from high and low frequency depth averaged velocities, e.g. for a western boundary;

$$\frac{\eta^{t+\Delta t} - \eta^t}{\Delta t_{2D}} = -\nabla D U = -[F_{i+1} - (F_T + F_L) + F_{j+1} - F_j] / h_1 h_2 = \frac{F_T + F_L}{A} - \frac{\Delta F}{A} \quad 4.2$$

where $U = \frac{1}{H + \eta} \int_{-H}^{\eta} u dz$ is the depth average of velocity u , $\eta^{t+\Delta t}$ and η^t are the elevations at the forward and current time-step respectively (using Euler forward time discretization), Δt_{2D} is the 2D time-step, $D = H + \eta^t$ is total depth, h_1 and h_2 are the grid spacing in the axis directions, e_1 and e_2 , respectively F_T is the tidal volume flux through cell face i , F_L is the low frequency

volume flux through cell face i , F_{i+1} , F_j and F_{j+1} are volume fluxes through cell faces $i+1$, j and $j+1$ respectively, $\Delta F = F_{i+1} + F_{j+1} - F_j$ and $A = h_1 h_2$.

Eq. 2.1 is then set up in two fractional steps (Kowalik and Murty, 1993, p64);

$$\frac{1}{2} \frac{\eta' - \eta^t}{\Delta t_{2D} / 2} = \frac{\eta' - \eta^t}{\Delta t_{2D}} = \frac{F_T}{A} - \frac{\Delta F}{2A} \quad 4.3$$

$$\frac{1}{2} \frac{\eta^{t+\Delta t} - \eta'}{\Delta t_{2D} / 2} = \frac{\eta^{t+\Delta t} - \eta'}{\Delta t_{2D}} = \frac{F_L}{A} - \frac{\Delta F}{2A} \quad 4.4$$

where η' is an intermediate elevation. Then Eq. 4.2 = 4.3 + 4.4. Assume that target tidal and low frequency elevations are supplied, η_T and η_L respectively. Following Herzfeld and Andrewartha (2012) Appendix A, first set the flux required to achieve the elevation due to the tide (η_T) using Eq. 4.3;

$$F_T = \frac{A}{\Delta t_{2D}} (\eta_T - \eta') + \frac{\Delta F}{2} \quad 4.5$$

The depth averaged velocity required to achieve this flux is;

$$V_T = \frac{F_T}{h_2 D_B} \quad 4.6$$

The velocity on the boundary is then relaxed towards V_T using a time-scale of τ_T according to (Eq. A.3 in Herzfeld and Andrewartha, 2012):

$$V_{BT}' = V_B - \frac{\Delta t_{2D}}{\tau_T} (V_B - V_T) \quad 4.7$$

The flux through the boundary cell, $F_{BT} = V_{BT}' h_2 D_B$, is computed followed by a new elevation in the boundary cell using Eq. 4.3;

$$\eta' = \eta^t - \frac{\Delta t_{2D}}{A} \left(\frac{\Delta F}{2} - F_{BT} \right) \quad 4.8$$

The flux required to achieve the low frequency elevation (η_L) is computed using Eq. 4.4:

$$F_L = \frac{A}{\Delta t_{2D}} ((\eta_L + \eta_T) - \eta') + \frac{\Delta F}{2} \quad 4.9$$

The depth averaged velocity required to achieve this flux is;

$$V_L = \frac{F_L}{h_2 D'} \quad 4.10$$

where $D_B' = \eta' - H$. The boundary velocity is then updated by relaxing toward this low frequency component using a relaxation time-scale of τ_L ;

$$V'_{BL} = V'_{BT} - \frac{\Delta t_{2D}}{\tau_L} (V'_{BT} - V_L) \quad 4.11$$

We then set $V'_B = V'_{BT} + V'_{BL}$ and $F'_T + F'_L = D_B h_2 V'_{BT} + D'_B h V'_{BL}$ for use in Eq. 4.2.

A simple test case was developed to assess the performance of the dual relaxation method. The model used to test the open boundary is described in Herzfeld (2006). The test domain consisted of a river emptying into a bay of 20m depth with one offshore boundary subject to a 1 m semi-diurnal tide (Southern Hemisphere). Freshwater is input at the head of the river at a rate of $100 \text{ m}^3\text{s}^{-1}$, and the river depth increases from 5 m at the head to 20 m at the mouth. A cyclonic wind stress is also applied with the centre of the system positioned near the offshore boundary and maximum wind stress $\sim 0.1 \text{ Nm}^{-2}$ over the bay. This creates a steady state low frequency response in the bay. Resolution is 1 km and 10 'z' layers are used with 0.5 m resolution at the surface and 5 m resolution near the bottom. The 3D time step is 140 s and the 2D step is 7 s. The solution after 30 days of simulation, when a steady state is achieved, is illustrated in Fig. 4.1.12, showing a sea level depression and associated cyclonic gyre due to the wind stress, and elevated sea level along the northern rim of the bay as the freshwater flow is deflected to the left at the mouth and follows a clockwise trajectory around the northern bay.

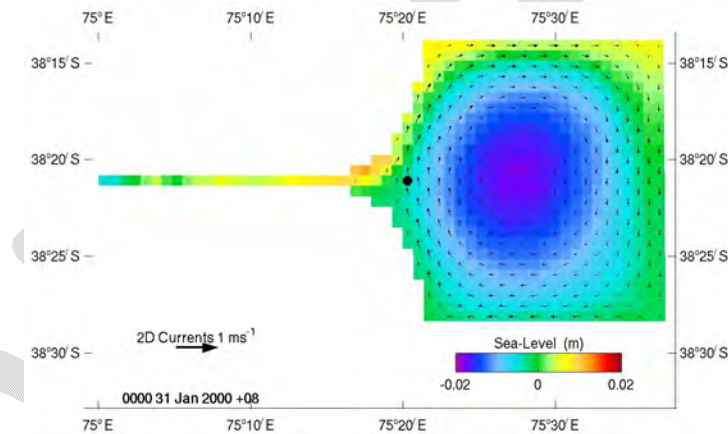


Figure 4.1.12. Sea level and surface currents after 30 days in the test domain. The black dot signifies the locations that tidal time series metrics were computed.

A baseline case representing low frequency circulation was generated, where the tide was not imposed and passive Flather radiation conditions were applied at the open boundary. Velocity and sea level on the boundary were saved to file to be used in the Dirichlet condition with the tidal signal superimposed for various test cases. In this case the simulations with tide added have interior forcing consistent with the low frequency boundary forcing and boundary specification error should be at a minimum; i.e. this represents a 'best case' downscaling scenario. In this context, when relaxing with a single time-scale, hard relaxation is anticipated to provide the better solution. The simulations compared are summarised in Table 4.1.5.

Table 4.1.5 Summary of test experiments.

Run	Tide	OBC	Relax method	Relax time (tide/low)
BASE	No	Flather	-	-
HARD	Yes	Dirichlet	single	7 s
DEFAULT	Yes	Dirichlet	single	default
2d/2d	Yes	Dirichlet	dual	7s / 7s
2d/def	Yes	Dirichlet	dual	7s / def
def/def	Yes	Dirichlet	dual	def / def

The tidal solutions were compared at a location in the domain interior (at the location of the black dot in Fig. 4.1.12). In this case the hard relaxation with single relaxation time-scale (HARD) was considered the base case to which tidal comparisons were made. Skill metrics are presented in Table 4.1.6. The elevation over a high tide cycle and elevation difference for the whole simulation is illustrated in Fig. 4.1.13. The low frequency response was assessed by computing the RMSE between the sea level derived from BASE and the mean sea level at the simulation end from the various tests; these results are displayed in Figs 4.1.14 to 4.1.17.

Table 4.1.6. Skill metrics of the tidal component in the model interior.

	skill	RMSE	CC	MAE	Bias
DEFAULT	0.9436	0.3163	0.8991	0.2829	-0.0089
2d/2d	1.0000	0.0019	1.0000	0.0014	0.0004
2d/def	0.9997	0.0243	0.9999	0.0230	0.0229
def/def	0.9936	0.1142	0.9878	0.1014	0.0178

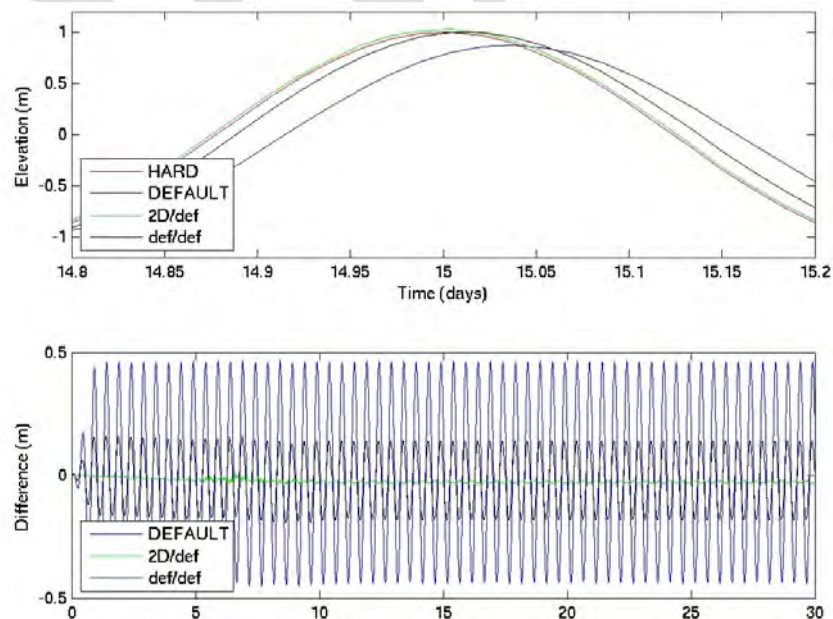


Figure 4.1.13. Elevation for the tests over a high tide cycle (top panel) and difference over the entire simulation (bottom panel).

Table 4.1.6 shows that the 2d/2d case provides solutions almost identical to the HARD case, i.e. using short relaxation in the dual formulation reduces to the hard relaxation single case. This is supported by inserting a relaxation timescale that achieves the target exactly in Eq. 4.11 and working backwards to recover the single relaxation equation. The DEFAULT case shows significant phase shift and reduction in amplitude (Fig. 4.1.13) which translates into the worst skill metrics of the tests. Of the dual relaxation methods, relaxing hard to the tide and using the default for the low frequency produces the best skill, followed by the dual method with default relaxation for both time-scales.

Low frequency RMSE for the HARD case (Fig. 4.1.14) is better than that of the DEFAULT case (Fig. 4.1.15) as speculated above, due to the compatibility of interior and boundary forcing leading to the lack of over-specification error and the need for a non-reflective boundary to transmit transient sea level perturbations. Both these cases show elevated error near the offshore open boundary where the OBCs have the greatest impact. Both dual relaxation methods (Figs. 4.1.16 and 4.1.17) show a superior low frequency response to the single relaxation methods. Of these the 2d/def case is the better, indicating that the tide may contribute to the low frequency circulation and hence a better representation of the tide feeds through to better low frequency. The def/def error is greatest near the open boundary, where this effect is least likely to be swamped by the interior forcing.

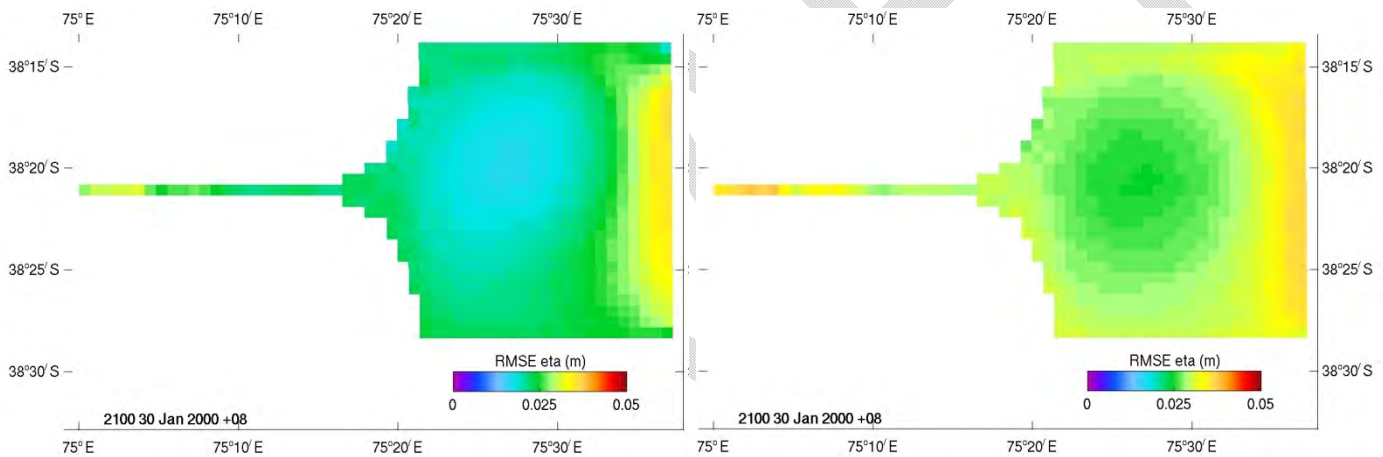


Figure 4.1.14. RMSE for the HARD test case. Figure 4.1.15. RMSE for the DEFAULT test case.

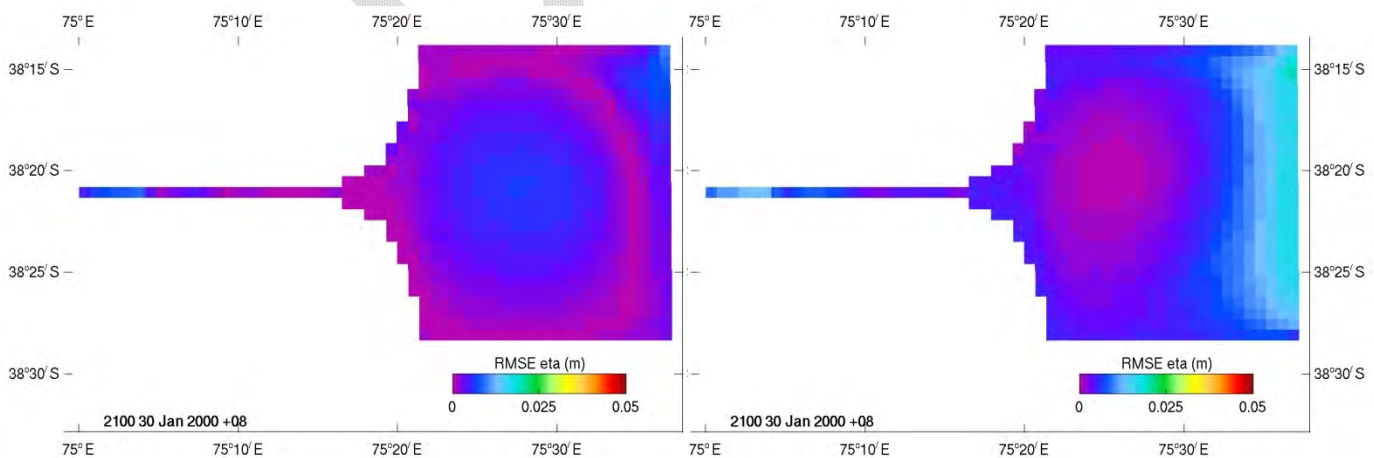


Figure 4.1.16. RMSE for the 2d/def test case. Figure 4.1.17. RMSE for the def/def test case.

These tests demonstrate that the dual relaxation method significantly improves both tidal and low frequency responses compared to a single relaxation method in a steady state solution where boundary forcing is highly compatible with the interior forcing. In this case using short relaxation for the tidal component and default relaxation for the low frequency resulted in the highest skill. Consequently these boundary conditions are used in the GBR models, with the expectation that the tidal component will improve in the interior whilst retaining the favourable low frequency response. Results are further presented in Section 5.1.7.

A manuscript describing the dual relaxation method has been submitted to Ocean Modelling and is under review.

4.2 Further develop HD model

4.2.1 Sub-grid scale development

4.2.1.1 Background

The GBR presents an extreme example where processes at various spatial scales interact and provide strong feedback from, for example, reef-scale processes to meso-scale circulation. Large reef complexes steer the prevailing currents toward areas of low reef density, and flow through the reef matrix produces wakes and tidal jets which in-turn deflect the mesoscale circulation. The strength of the tidal jets and wakes, and their interaction with the mesoscale circulation are modulated by the spring-neap cycle (e.g. Andrews & Furnas, 1986, Burrage et al., 2003, Luick et al., 2007 and Monismith, 2007).

The hydrodynamic models developed and applied as part of the eReefs project have horizontal grid resolutions approximately 4 km and 1km. At these resolutions, many of the features of the reef matrix and bathymetry associated with the coral reef, together with their influence on the momentum balances and the broader scale circulation, are unresolved by the model grids.

The current parameterisation study is intended to identify and evaluate methods to include relevant sub-grid scale features that enable some resolution of process occurring at scales smaller than can be resolved by a particular model grid resolution. Methods are tested and evaluated for incorporation into SHOC allowing the effects coral reefs on large scale ocean dynamics to be represented in the best way possible for both horizontal and vertical scales and computational efficiency.

4.2.1.2 Methods

In evaluating potential approaches for sub-grid scale parameterisation, the Delft3D suite (Deltares, 2011; herein forth Delft3D) was elected as numerical modelling tool to investigate the effects of the horizontal grid resolution, the seabed bottom friction, and permeability of the coral reefs on the dynamics of larger-scale circulation. Delft3D was chosen for the evaluation because it contained a number of features that were a potential solution to the sub-grid problem (e.g., by adding terms to the momentum equation to account for local

energy sources or losses, as quadratic or linear parameterisations). The method adopted for evaluation was to perform an ensemble of numerical simulations using different parameterisation approaches on consistent model grids to enable cross-comparison between the results

The model domain established for this study covered only a region that present challenges to the representation of coral reefs, and included both small and large coral reefs, as well as different shapes and spatial density (Fig. 4.2.1, top panel).

The numerical modelling system was conceived to provide the same boundary conditions for the individual models established to evaluate the various parameterizations imposed for the coral reefs. To achieve this, a 'regional-scale' outer numerical model with 4km spatial resolution was established within which to nest other models, with increased spatial resolution, up to 500m. Considering that the numerical model will be forced by tides only, this methodology ensures the nested models, no matter what their spatial resolution, will have the same oscillations of the water level at their boundaries and will be isolated from the boundary effects from the outer area. The described numerical grid system with the 'regional-scale' outer grid and the nested grids is shown on the bottom panel of Fig. 4.2.1.

DRAFT

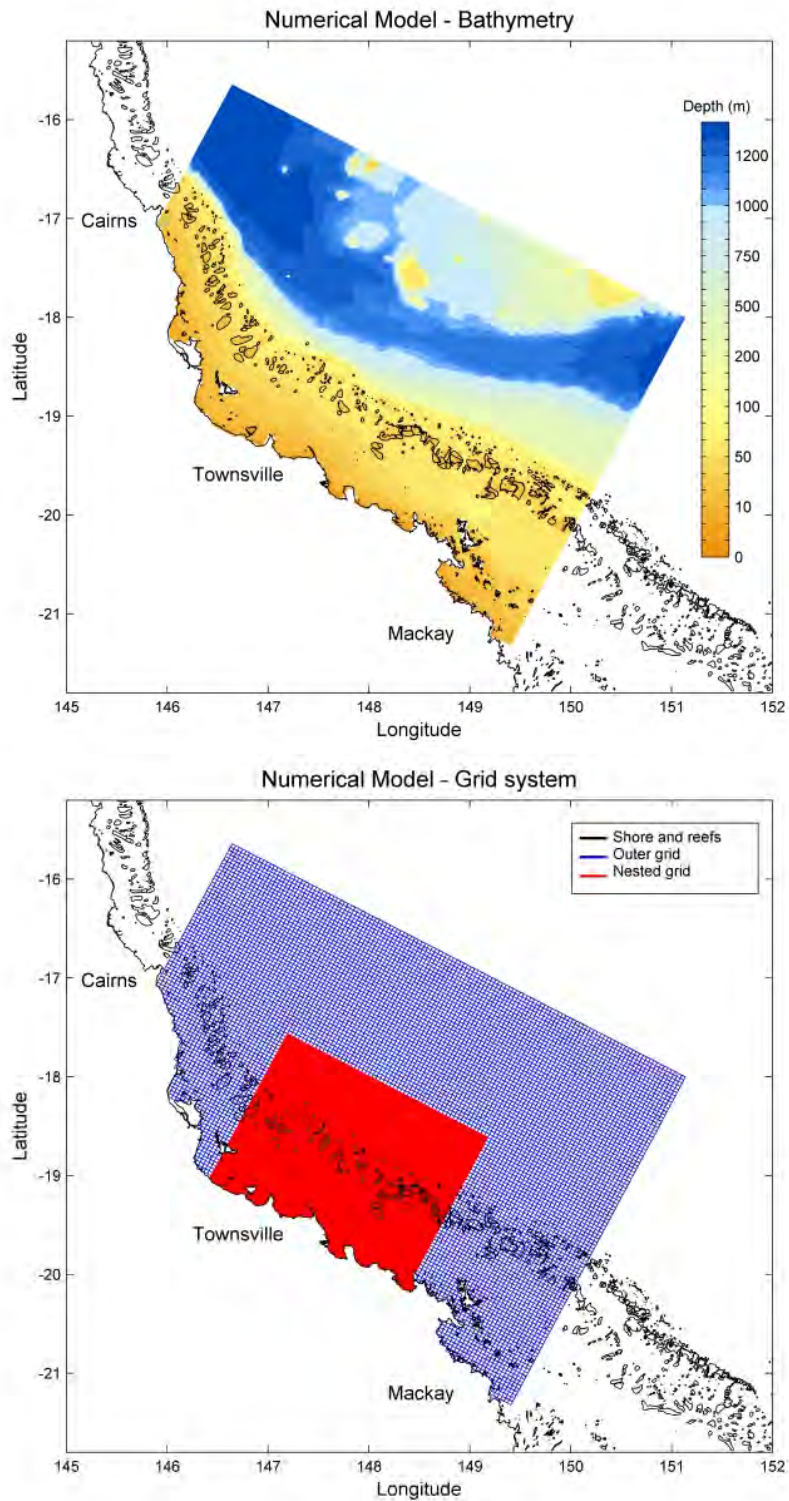


Figure 4.2.1. Map showing the modelled domain with respective bathymetry (in meters, top panel). Reef and coastal outlines are shown as black features along the coast. In the bottom panel is shown the numerical grid system used in this study.

Fig. 4.2.2 presents the horizontal discretization for a specific region in the modelled domain. This figure illustrates the importance of spatial resolution in representing the complexity and diversity of reef size, shape and density.

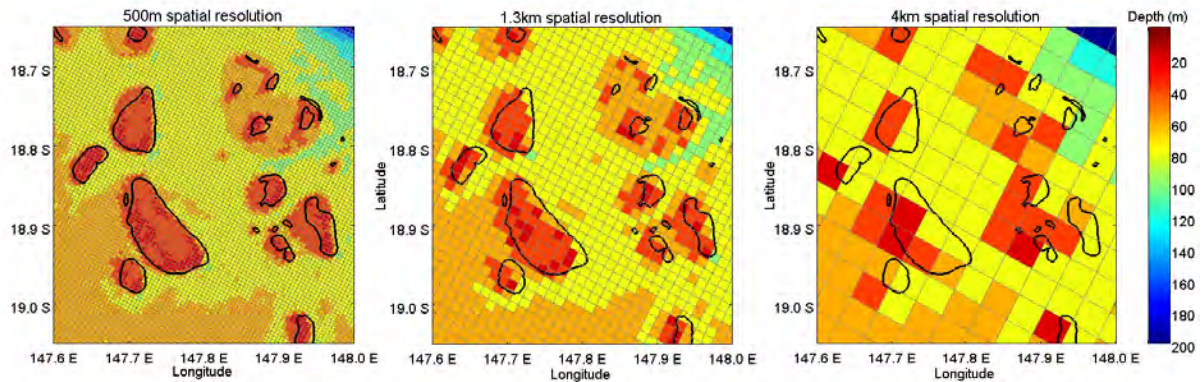


Figure 4.2.2. Left panel: horizontal representation of coral reefs in the nested grid with 500m spatial grid resolution. Centre panel: the same as left panel for 1.3km resolution. Right panel: the same as left panel for 4km resolution. Colour shows model representation of bathymetry and actual reef outlines are shown as black lines.

Due to its higher spatial detail and therefore a better representation of coral reefs, the numerical model that used the numerical grid with 500m spatial resolution is hereafter named as a reference run. And for simplicity, 1.3km resolution is named as 1km resolution. A non-hydrostatic approach to vertical pressure distribution was adopted to account for potentially large vertical accelerations due to the abruptly changing bottom topography of coral reefs included.

Coral Reefs Parameterization.

Rosman and Hench (2011) reported that coral reefs have been parameterized in numerical modelling using drag coefficient (C_d) or roughness length scales (z_0), and these coefficients can span over two orders of magnitude. They indicate the need for a more sophisticated modelling that includes a vertical structure over the reefs. Many models have been calibrated and validated for partial GBR. However, few attempts have been done using 3D simulations. Reasons for that can be found in many studies (e.g. Andutta et al., 2011; Luick et al., 2007; Brinkman et al., 2002).

Both horizontal and vertical parameterisations have been employed to attempt to capture the 3D influence of coral reefs on circulation dynamics (references above). The first approach uses a modified drag coefficient, identified following a review of the literature. Reidenbach et al. (2006a,b) presented a comprehensive study of the implication of coral reefs on boundary layer, wave effects, flow structure in the Gulf of Aqaba (Red Sea). Their findings identified increased drag at reef sites being 3–5 times larger than at sites characterized by sand bed roughness only. Although Reidenbach's studies were made in a gulf protected from waves, the factor used by him is significantly smaller than that used in Andutta et al. (2011) for the GBR (factor = 100). Huthoff and Augustijn (2006) investigated the vegetation roughness in open channels to evaluate the water level dependence on vegetation. They

performed field measurements and laboratories experiments (with homogeneously distributed cylinders) considering a two layer system. They observed many correlations among the flow in the upper layer, in the vegetation layer, the depth averaged velocity and ratio between the separation of cylinders and their height. Therefore, one of their conclusions pointed out that it is important to describe idealized vegetation resistance in as few possible parameters and, sometimes, when the region presents itself with complicated vegetation resistance models, the standard roughness height methods (e.g. Nikuradse or Strickler roughness heights) could be used. Numerical experiments with modified drag coefficient were considered in this study. Such experiments were named as “reef rough” (rgh). Below we presented how this modification of the drag coefficient was included in the model in relation to the standard coefficient (std). This parameterisation used an increased drag factor applied for regions covered by coral reefs.

By definition, the bottom friction coefficient (C_f) is related to Chèzy roughness (C) by

$$C_f = x \cdot \frac{g}{C^2} \quad \text{Eq. 4.2.1}$$

Where g is the acceleration due gravity and x , the factor used to modify the bottom drag coefficient (different value for coral reefs locations and one elsewhere).

The Chèzy coefficient, as proportional to the water depth (H) and bed material is computed as:

$$C = \frac{\sqrt[6]{H}}{n} \quad \text{Eq. 4.2.2}$$

Where n is Manning’s roughness (0.026-0.035 for coarse sand). An intermediate value for the Manning’s roughness (equal to 0.03) was used.

The second approach is based on reef porosity (permeability) and it is applied on the vertical axis. The technique known as the porous plate can be applied in both directions of propagation of hydrodynamic flow and also has the ability to cover specific vertical layers or the entire water column. The conceptual parameterization used here was developed by Farraday & Charlton (1983) for the design of bridges. It is based on the obstruction in the flow imposed by an obstacle with small dimension compared to the fluid (grid cell) to which it opposes. Emphasizing the choice of this vertical parameterization is the fact that porous plate is partially transparent and enables the exchange of mass and momentum between both sides, with an anticipated hydrodynamic behaviour similar to coral reefs. With a porous plate, the energy loss is a function of quadratic friction. However, it is worthy to note the energy loss is not vertically constant through the water column and is considered independent from that lost by bottom friction. Secondly, the implementation of the porous plate as a representation of coral reefs is based on the flow resistance due to the blockage of the flow by the coral reefs (Eq. 4.2.3). An additional term related to the energy loss (Eq. 4.2.4) in the i -direction, for a coral reef positioned along j -direction (perpendicular to the flow direction) is considered in the momentum equation. Where required, this concept is applied for each vertical layer independently.

The absence of coefficient of porosity for species present in the GBR required the use of porosity coefficients from species from other locations. In addition, the porosity of the coral reefs reflects their biological condition. Through field measurements from species along the California coast, Crane & Burke (2007) obtained coefficient of porosity of 45% for living corals and 33% for dead corals.

For the current region of interest, an average percentage of living corals around 20% is obtained from linear projection based on Sweatman et al. (2011). It is important to note that Sweatman's study presents a more detailed spatial distribution of the situation of corals in the GBR, which can be used to estimate a coral reefs parameterization with uneven spatial distribution.

However, this study has not considered the spatial variation of the biological condition of the corals in the region of interest. Thus, a weighted combination of above values indicates a coefficient of average porosity around 35% for the numerical domain.

At this point it is important to mention that the values used in this study can be modified to suit other environments.

$$c_{loss-i} = \frac{C_{drag} \cdot \Delta_{block-j}}{2 \cdot \Delta_{tot-j}} \cdot \left(\frac{\Delta_{tot-j}}{\Delta_{eff-j}} \right)^2 \quad \text{Eq. 4.2.3}$$

$$M_i = -\frac{c_{loss-i}}{\Delta_i} \cdot u_i \cdot \sqrt{u_i^2 + u_j^2} \quad \text{Eq. 4.2.4}$$

Where,

C_{loss-i}	Energy loss coefficient in direction (i)
C_{drag}	Drag coefficient (for the coral reefs = 1.5, Favier (2003) in Huthoff and Augustijn, 2006)
Δ_{tot}	Total cross sectional area (depending of grid resolution, either horizontal and vertical)
Δ_{block}	Sectional area blocked (in the presence of coral reefs, 65% of Δ_{total})
Δ_{eff}	Effective wet cross sectional area (in the presence of coral reefs, 35% of Δ_{total})
M_i	Addition quadratic friction term in the momentum equation due the presence of porous plate (here, coral reefs with 35% porosity)
Δ_i	Spatial resolution of cell grid in direction (i)

For the current settings, where each parameter (and their used values) is described above, they imply a constant C_{loss} equals to 2.653 (dimensionless).

The following figure shows a graphical representation of coral reefs parameterization. On the left panel are highlighted the cells subjected to horizontal parameterization (standard and/or modified) while the right panel shows the cells subjected to vertical parameterization (porous plate).

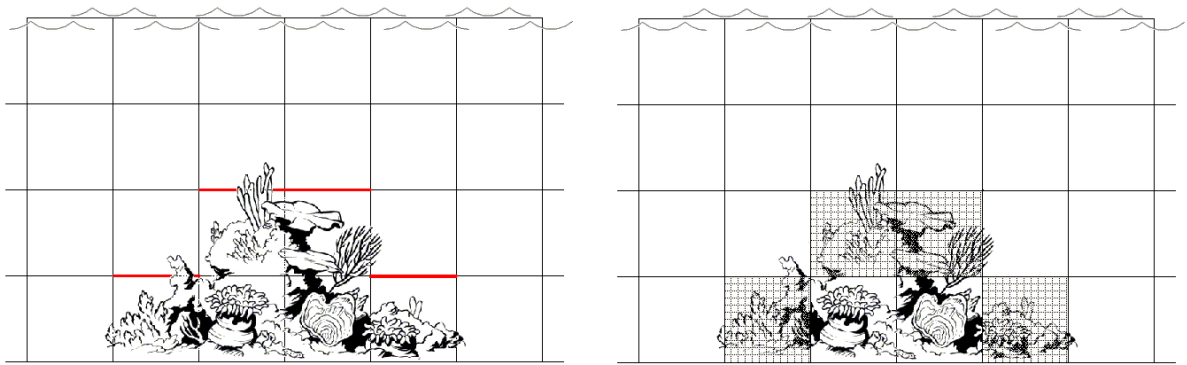


Figure 4.2.3. Schematic representation of both possibilities for parameterization of coral reefs. In red on the left panel are shown the cells subject to horizontal parameterization and the right panel show analogous subject to the vertical parameterization.

4.2.1.3 Results

The numerical experiments were run for 65 days and the analysis considered a spring-neap tidal cycle. The following table (Table 4.2.1) shows the nomenclature used to associate the parameterization of coral reefs with its reference in the presentation and analysis of results.

Table 4.2.1. Nomenclature and associated coral reef parameterizations used in the numerical experiments.

<i>Nomenclature</i>	<i>Coral reefs parameterization</i>
<i>std</i>	<i>no parameterization</i>
<i>rgh</i>	<i>modified roughness (horizontal)</i>
<i>pp</i>	<i>porous plate (vertical)</i>

In addition, the spatial resolution of each of the simulations is denoted with the suffix nomenclature corresponding to respective spatial resolution. For example, *std_pp_4km* refers to the experiment with the bottom friction proportional to the water depth (*std*) with coral reefs parameterized as porous plate (*pp*) to the 4km grid resolution.

The following figure shows the intensity of flooding flow (through vectors fields) for all considered spatial resolutions, for both surface and bottom, for the standard (*std*) parameterization for the bottom friction. Those figures were intended to highlight the importance of spatial resolution in the horizontal representation of coral reefs (as previously suggested on Figure 4.2.2). Figure 4.2.4 shows, on the upper panels, the vector field of velocity as result of numerical modelling for the surface and the lower panels, the analogous for the bottom layer. The colour representation for the intensity of vectors is the same and it is presented in m/s.

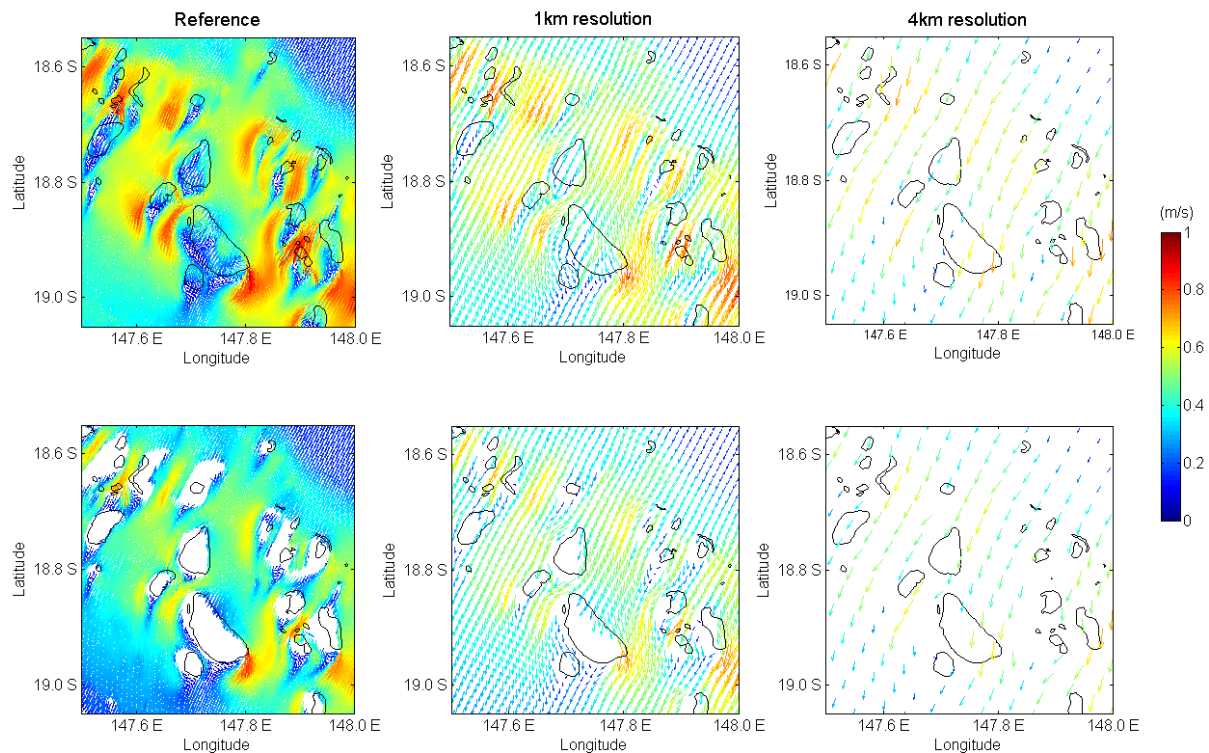


Figure 4.2.4. Detail of the vector field of velocity (m/s) for tidal flooding as result of numerical modeling for the GBR region, for standard (std) roughness parameterization. Upper panels present the results for the surface and lower panels for the bottom layer.

Sensitivity tests were performed to determine the best factor to be used to multiply the drag coefficient over the regions where coral reefs are present; the “rgh” runs (see Table 4.2.1). As the vertical discretization of the model was set as 5m (z coordinate), some coral reef regions had from one to three layers above the seabed, and such tests were important to achieve the best factor able to produce a consistent hydrodynamic circulation. The values used for the factor were: 2, 10, 50 and 100, and the results are not shown here. In general, a factor of 2 presented no significant changes on the hydrodynamics of those regions. Moreover, a factor of 2 has not shown significant increase in the vertical shear when compared with the same points for the runs where no reef parameterization was applied (std). On the other hand, factors of 50 and 100 showed a significative and quasi-homogeneous vertical blockage of circulation, and a more than expected reduction of hydrodynamic flow. That said, using a factor of 10 performed well for both the vertical shear and the reduction of the horizontal velocity near the bottom. The modified (rgh) parameterisation used a factor 10 over the std to the coral reefs sites.

Figure 4.2.5 shows a comparison of the vector field of velocity due to different spatial resolution using a modified seabed roughness parameterisation (rgh). The modified parameterisation was applied only for the 1km and 4km spatial resolution simulations and the left most panels show the reference run; i.e. the closer the 1km and 4km models appear compared to the reference, the better the applied reef parameterisation method is working.

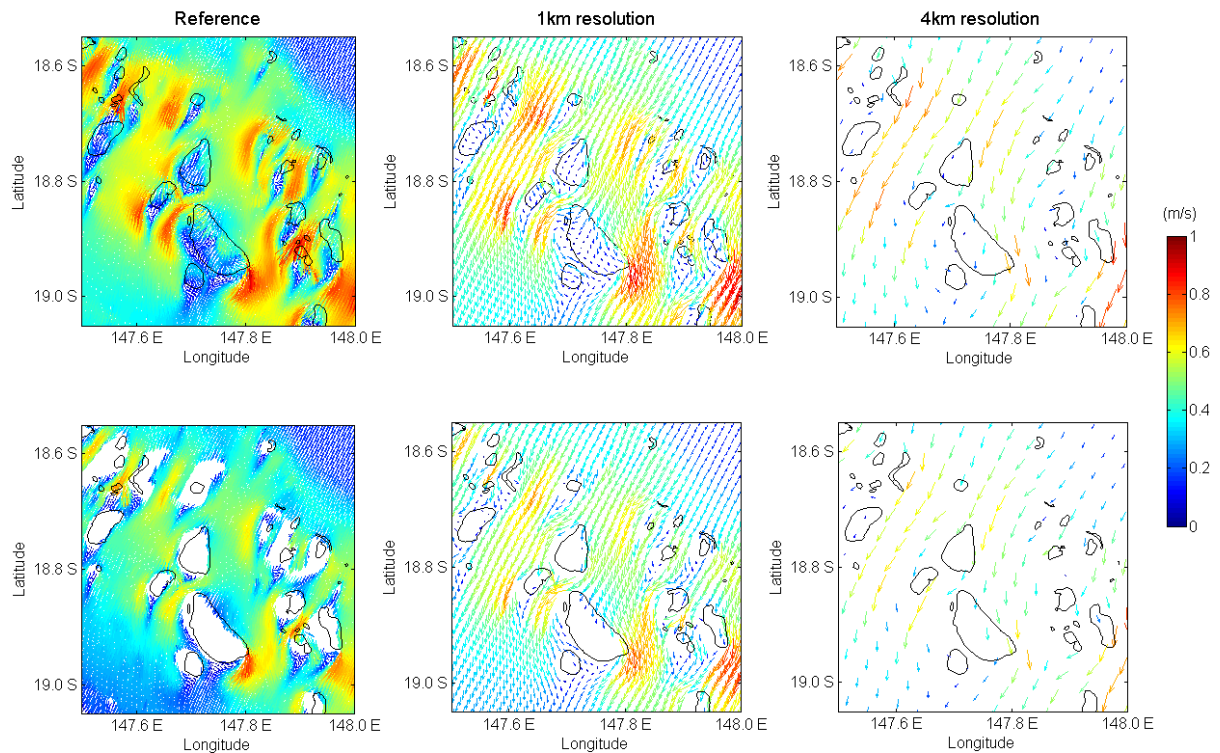


Figure 4.2.5. Detail of the vector field of velocity (m/s) for tidal flooding as result of numerical modeling for the GBR region, for modified (rgh) roughness parameterization. A factor 10 was used over the coral reefs sites in the parameterisation of seabed roughness. Upper panels present the results for the surface and lower panels for the bottom layer.

The previous figures show that the horizontal spatial resolutions play an important role in the representation of coral reefs in numerical model. The representation of the vector field of surface currents do not show significant differences regarding the magnitude and direction of horizontal current vectors (upper panels of previous figures). On the other hand, the highest spatial resolution is obviously better able to represent the bathymetric features (the left panels of Figure 4.2.4 and Figure 4.2.5). However, in this example coral reefs are represented as obstacles changing velocity direction and not as a volumetric entity able to percolate the water.

For a closer inspection and cross comparison of the results from numerical simulations, four points were selected (Figure 4.2.6). These points were selected based on different locations where different spatial resolution or reef parameterization schemes used for the numerical experiments is likely to produce a difference to the hydrodynamic circulation. These points comprise a location near a narrow channel formed by a set of coral reefs and also include one coral reef itself. An additional point away from reefs was chosen to evaluate the influence of refined grid resolution.

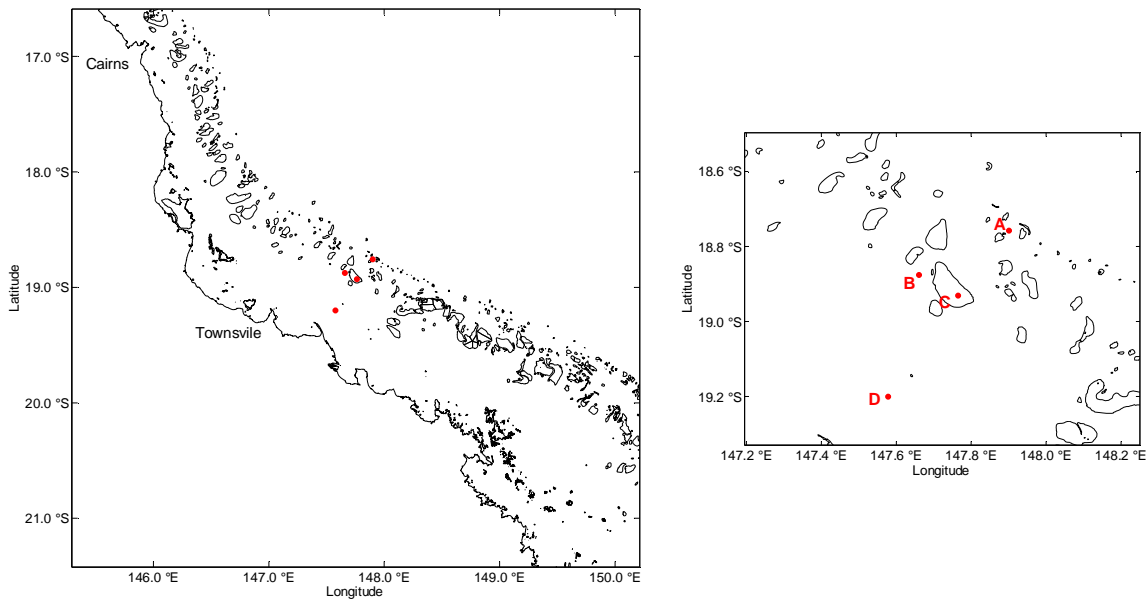


Figure 4.2.6. Selected points for cross comparison between the results of numerical simulations with spatial resolution of 500m, 4km and 1km and with or without the parameterization of coral reefs on the vertical axis. Left panel: overview of the region. Right panel: Spatial detail of the location of the selected points.

The following figure shows the time series of kinetic energy (KE) output from the numerical model for the points presented on Figure 4.2.6. All plots refer to the standard parameterisation for seabed roughness.

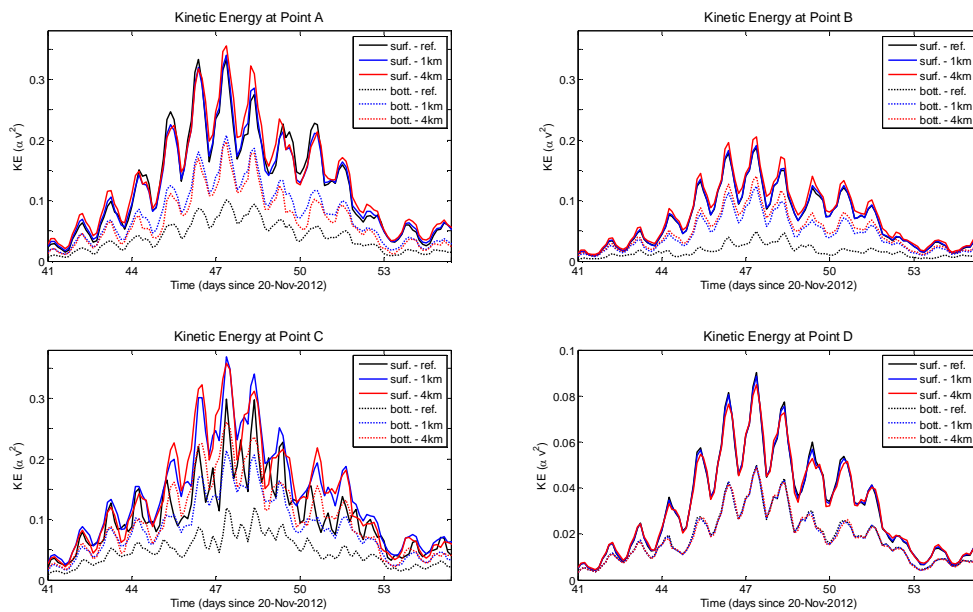


Figure 4.2.7. Time series of the kinetic energy (KE) as result of the numerical simulations with spatial resolution of 4km and 1km using the standard parameterization for seabed roughness. Spatial positioning of points is shown on Figure 6.

The analysis of time series of KE confirms the observations made from the plots of the vectors field currents: the importance of horizontal spatial resolution in the representation of such features. The results for points A and B show the energetic variation due to the different spatial resolutions, with relation to the distance to other reef and topographic features (see Figure 4.2.2 as reference). Despite small distances between the features around them and the points themselves, the times series of KE for points A and B did not show significant differences for the kinetic energy in the surface layer and, near the bottom, they presented themselves more energetic than the reference run. This vertical kinetic energy shear can potentially be related to the bathymetric resolution, since for these points the grid with higher resolution (reference) had a larger number of vertical layers than other two. Point D is far away from any features and, as expected, shows coherence between the results of numerical experiments independent of the spatial resolution used. Time series of KE for point C demonstrate the need for better representation of coral reefs to get a better coherence between the results when it requires a change in the horizontal spatial resolution.

Based on the assumptions made on previous section, the porous plate parameterization was imposed on the vertical axis to the grid points where coral reefs exist on the numerical modeling domain. For the GBR it was set a porosity of 35% by volume. The results of this coral reef parameterization as computed by the numerical model for the Point C are displayed below.

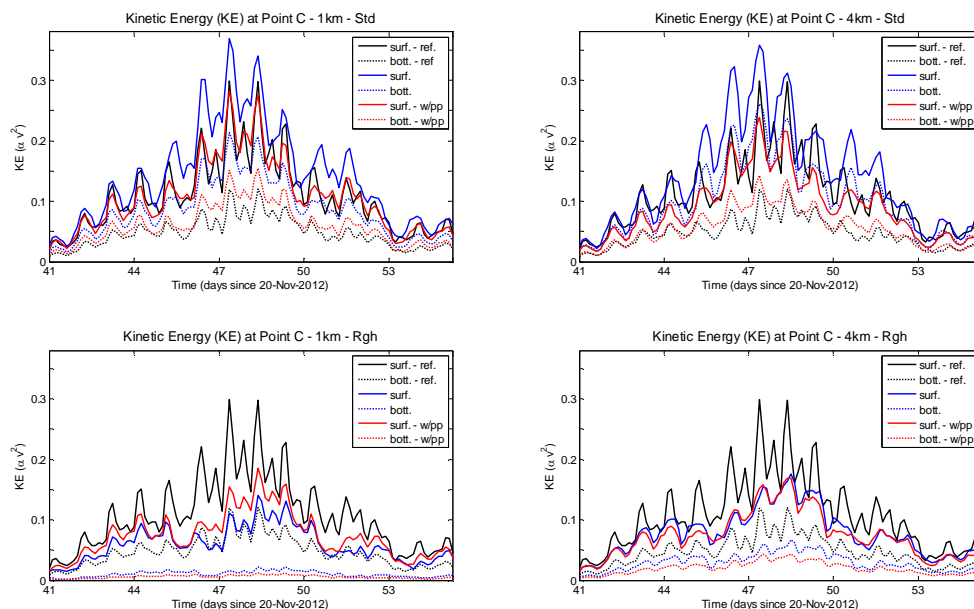


Figure 4.2.8. Time series of kinetic energy as computed by the numerical model for the Point C (see Figure 6) for surface and bottom layers, for both seabed roughness parameterization and with (w/pp) and without a vertical parameterization of coral reefs as porous plate.

From the figure above some observations can be made only by visual inspection. The panels on top row (std) show when the vertical parameterisation is applied (porous plate – w/pp), the time series of KE with pp approaches the time series of KE representing the numerical simulation of reference. This behaviour is observed for both spatial resolutions and depths. On the other hand, the bottom row (rgh) presents a mixed behavior, showing a slight improvement when pp is applied to the 1km resolution (low left panel) and a worsening when it is applied to the 4km counterpart (low right panel).

In this context, the percentage variation of KE was calculated for each of the numerical experiments taking 500m spatial resolution defined as reference. These results (Fig. 4.2.9) show a way to quantify the influence of parameterization in the results obtained by numerical simulations. The ideal result would be no variation, indicated by a horizontal line. Positive values correspond to the case where the numerical simulation overestimates the kinetic energy while negative values indicate the opposite. Results are graphically showed on Fig. 4.2.9 while their respective mean values computed over the entire period are summarised in Table 4.2.2.

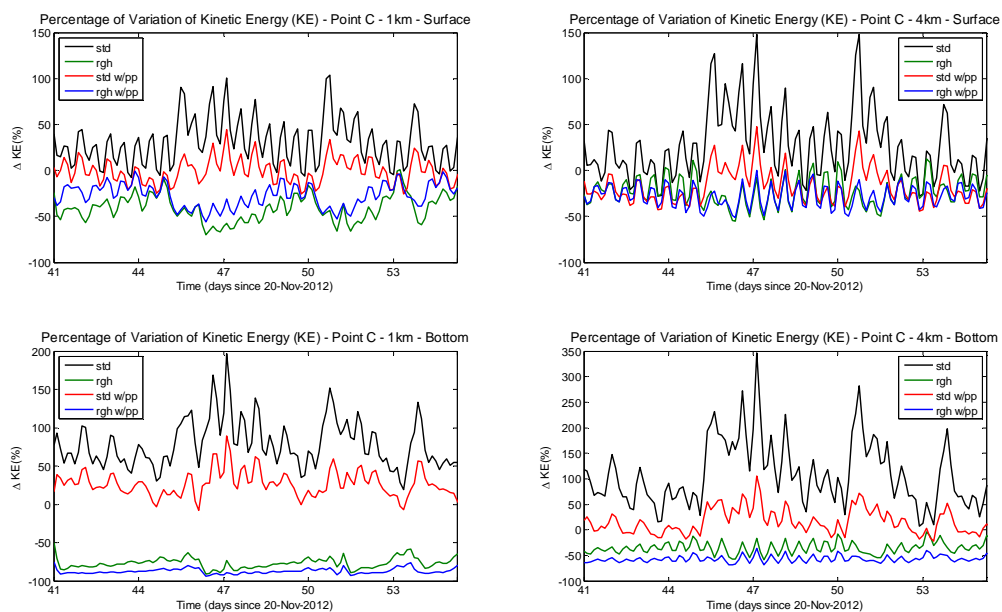


Figure 4.2.9. Time series of percentage variation of kinetic energy (KE) for the Point C using 500m spatial resolution as reference.

Table 4.2.2. Mean values (%) of the time series of variation of kinetic energy (KE) computed for Point C over the entire period for all time series showed on Figure 9.

Mean values (%) of variation of kinetic energy over the simulated period

Configuration	Surface	Bottom
<i>std 1km</i>	30	76
<i>std 4km</i>	26	105
<i>std w/pp 1km</i>	-1	25
<i>std w/pp 4km</i>	-18	15
<i>rgl 1km</i>	-37	-76
<i>rgl 4km</i>	-22	-35
<i>rgl w/pp 1km</i>	-26	-87
<i>rgl w/pp 4km</i>	-28	-57

The results presented above (Fig. 4.2.9 and Table 4.2.2) indicate that the use of porous plate coupled with standard horizontal seabed roughness (*std w/pp* – red lines in all panels – Fig. 4.2.9; third and fourth rows – Table 4.2.2) provides the best results for the parametric representation of coral reefs. Among all the experiments considered, the results in this configuration had the lowest percentages deviation from mean calculated over the period.

Previous work showed through aerial photos and field work that barotropic systems are able to have vertical flow (upwelling-downwelling) and stable eddies influenced by tidal forces (Wolanski et al., 1996; Wolanski et al., 1984a, b). Such small scale processes are important to coral reef ecology (e.g. resuspension of seabed sediment, coral larvae displacement among others). Therefore it is necessary that such hydrodynamics are represented in numerical models implemented in the GBR.

In this context, the following figures present simultaneous snapshots of two properties hydrodynamically relevant in this environment. The first presents the vertical velocity along a transect running through two coral reefs separated by a narrow channel, and the second present the vorticity near the same region.

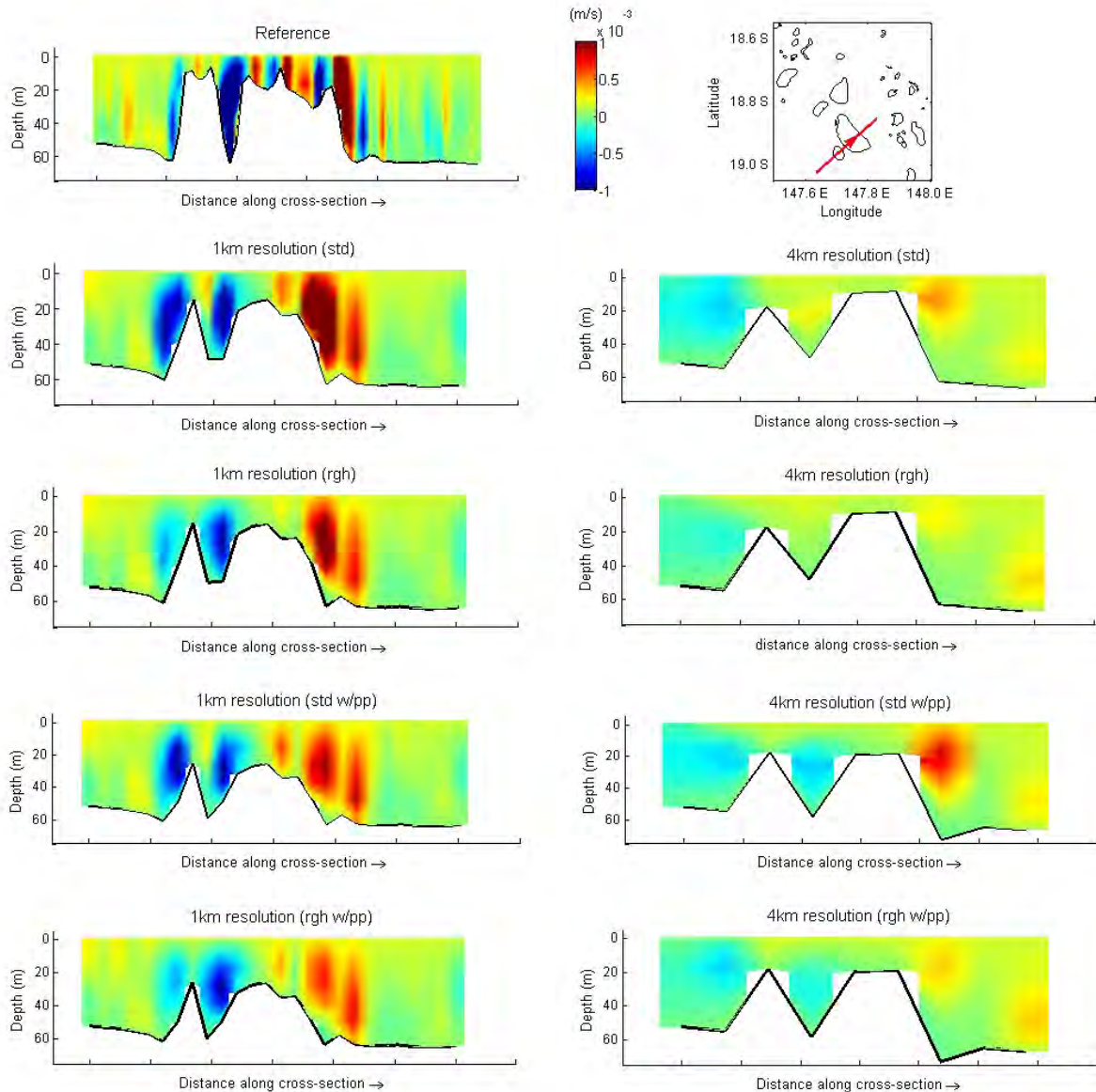


Figure 4.2.10. Snapshot of vertical velocity (m/s) along the cross section shown on top right corner. Negative values mean downward water movement and positive values, the opposite.

Results of numerical experiments do not reproduce quantitatively the property shown in the reference simulation. When the porous plates are not considered (second and third row), the 1 km resolution is able to better represent the vertical velocity along the section with its upward and downward movements when compared with the 4km run (both compared with the reference run – uppermost left panel).

When the porous plates are considered, the numerical experiments for both resolutions present an improvement in the representation of the vertical velocity when compared with the reference simulation. For the 1km resolution (third and fourth row - left hand side), we can observe a better definition of the regions in which the vertical velocity changes direction. For the 4km case (third and fourth row - right hand side), the vertical velocity shows the downward movement in the region of the central channel of the section (the central trough in the two lower panels on the right hand side). The use of porous plates improved the

definition of regions with different vertical velocities for simulations at 1km resolution, but for the 4km resolution, the use of porous plates provided improved representation of the vertical velocity components in regions.

However, for both spatial resolutions when compared the horizontal parameterization for coral reefs, or not (rgh and std, respectively), one can observe that the intensity of vertical velocity is better represented with no parameterisation of bottom roughness (std).

The following figure shows the mid-water vorticity as result of numerical modelling.

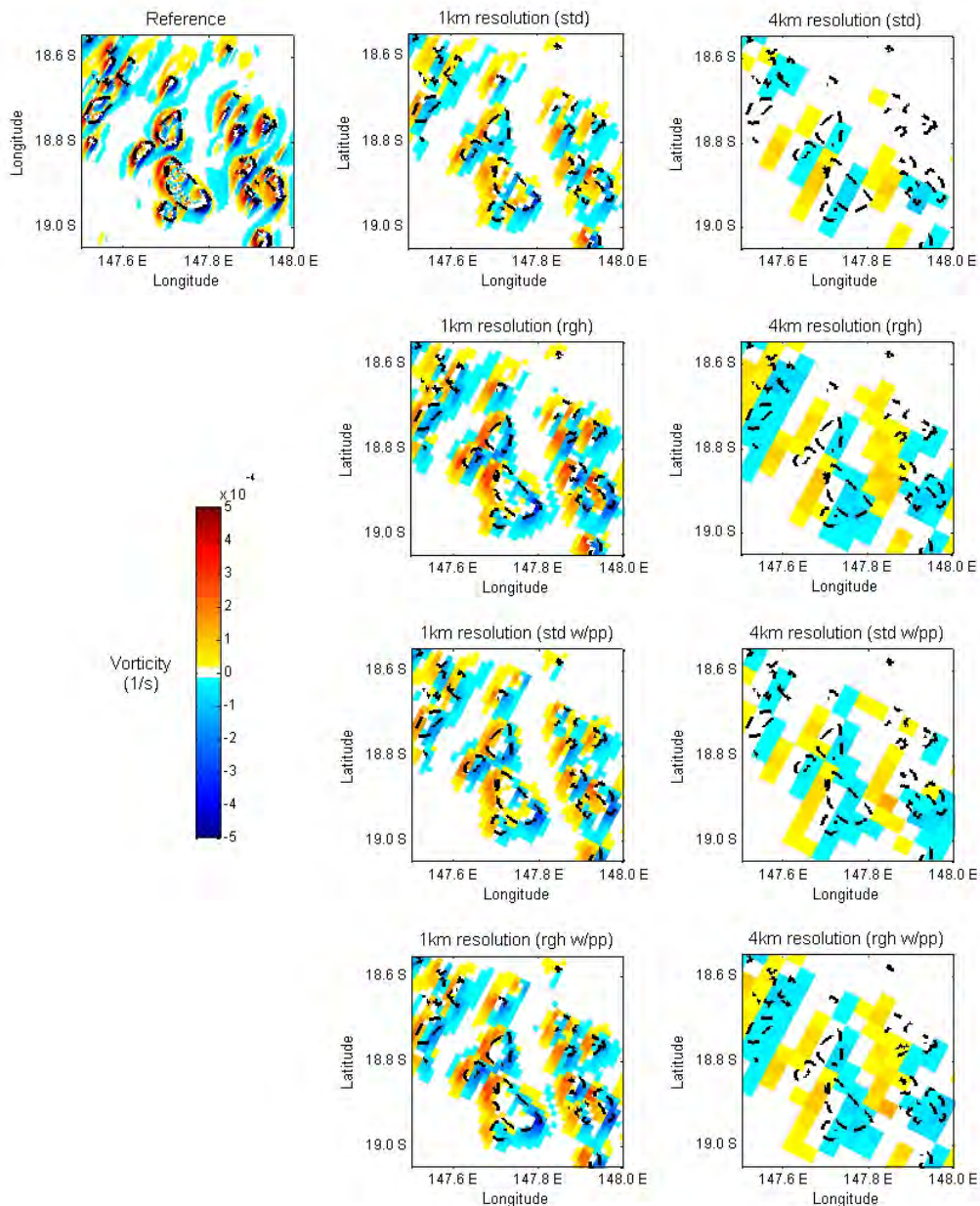


Figure 4.2.11. Snapshot of mid-water vorticity (1/s) as result of numerical modeling. Regions with negative values mean clockwise water displacement and regions with positive values, the opposite. Coral reefs are represented as dashed lines.

The resolution of 1km (left panels) is able to better represent numerically the property in question than the results reported for the resolution of 4km (right panels). Considerations

with regards to the combination of horizontal and vertical parameterization for the coral reefs are made below.

When compared to the reference run (uppermost left panel), the horizontal parameterization has imposed a spatial disturbance on the vorticity field – second row panels (rgh) against uppermost panels (std). This observation has a dubious interpretation, since the rgh parameterization improves the representation at some points but not at others. This is more evident for the coarser resolution.

However, the use of porous plates as vertical parameterization for coral reefs improves the quantitative comparison for the resolution of 1km and brings a better spatial definition of the vorticity field for the 4km resolution (third and fourth rows).

4.2.1.4 Comments

This study was conducted in order to assess previously developed parameterizations of coral reefs in numerical models and propose a new parameterization scheme. While previous methodologies were based on 2D models and focused the parameterization of the coral reefs through seabed roughness, the new method uses a 3D hydrodynamic model and suggests a vertical parameterization. In the later, the coral reef parameterization is based on the concept of porous plate, which is able to percolate water.

We performed numerical experiments with three horizontal resolutions for the numerical grid. The numerical simulation with highest resolution was used as reference, while simulations using grids with lower spatial resolution were used with existing methodologies for coral reefs parameterization as well as with the new proposed method.

There were numerical simulations using the standard seabed roughness parameterization and a modified roughness based the presence of coral reefs for a horizontal coral reef parameterization. The modified scheme used the control parameterization with a factor 10 applied to the drag coefficient. An inovative vertical coral reef parameterization called the the porous plate was set in combination with the horizontal parameterisation. The idea is to use a vertical parameterization which is able to reduce the kinetic energy where it is imposed and, at same time, it makes the grid point able to percolate water.

Both quantitative analyses (kinetic energy) and qualitative analysis (vertical velocity and vorticity) show that the standard seabed roughness acting together with the vertical parameterization of coral reefs through porous plate is able to achieve the proposed objectives: to reduce the kinetic energy and percolate while maintaining a vertical and spatial structure of water circulation. In summary, porous plate seems to be an appropriate methodology for coral reef parameterization to be used in numerical modelling.

4.2.2 SHOC Performance development

4.2.2.1 Overview

The 4 km and especially the 1 km GBR models require distributed processing to execute owing to their computational demands and resultant low run-time ratios (models days : one day real-time). Obviously it is desirable to have these models run as fast as possible. The issue of runtime is related in equal importance to scalability, load balance, wet cell ratio, IO and functionality invoked. Considering the low wet cell ratio in these domains, it is anticipated runtime bottlenecks will be wet cell ratio and load balance related. IO is anticipated to also be an issue due to the higher frequency of input/output required to resolve the tidal cycle. Initial profiling indicates that the 4 km GBR domain runtime plateaus after ~48 processors (Figure 4.2.13). Further profiling will need to be undertaken to identify and rectify these bottlenecks. An assessment of the distributed SHOC code was undertaken relative to an implementation of GFDL's Modular Ocean Model (MOM4) model for the GBR 4km domain.

On the CSIRO computer 'burnet', with nearly identical setups of the eReef's GBR4km configuration, SHOC's quickest run time ratio (days the model integration progresses per real day) was 216:1 on 60 processors, with MOM4's best result being 158:1 on 72 processors. On the BoM computer 'solar', with GBR4 configurations similar to the anticipated final implementations, SHOC and MOM4 achieved run time ratios of 82:1 and 22:1 respectively. Further code development, particular in the application of surface and boundary forcing, are likely to improve both model speeds on solar.

SHOC is able to operate in distributed processing mode using both shared, and more recently, distributed memory. The latter version is in prototype stage and is anticipated to be shortly integrated into the core branch. This version uses more sophisticated slave-slave message passing (Fig. 4.2.12) than the master-slave distribution commonly used in most distributed processing models (e.g. MOM and ROMS). While master-slave requires information from the slaves to be passed to the master in the gather operation followed by the scatter of these data from master to slaves, the slave-slave transfers do not require the gather operation and directly scatter information from slaves to slaves. By removing the overhead associated with gathering data to the master, efficiency is greatly improved. Additionally, SHOC employs the 'sparse' internal organisation of data, which among other factors, removes all dry cells (both land cells and cells beneath the sea bed). This type of system has been shown to increase runtime exponentially as the wet:dry cell ratio decreases. This makes SHOC more efficient compared to conventional models using Cartesian representation as the percentage of wet cells in the domain shrinks. MOM4 can allow layout maps to be produced where null processors are placed over land, but this can only coarsely block out land computations and does not address processing of land cells beneath the sea bed. The sparse system also allows arbitrary domain decomposition so that load balance can be individually tailored to each domain taking into account geometry, bathymetry and volume of data to be exchanged. SHOC supports both striping and rectangular blocking domain decomposition in both directions as default options (MOM4 allows regular blocking only). This allows the issue of load balance to be finely optimised in SHOC, which can lead to gains in efficiency of around 20%.

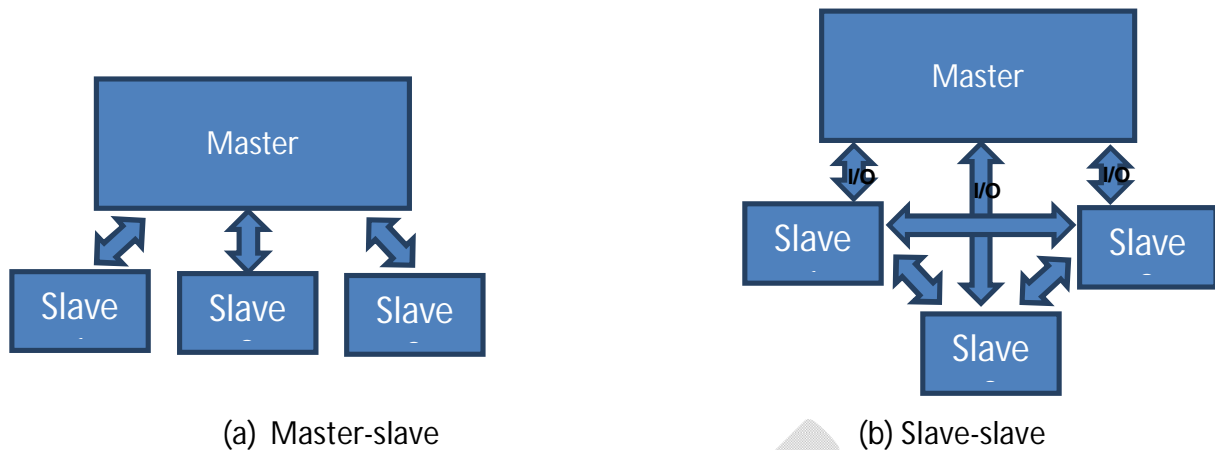


Figure 4.2.12. Data transfer methods for distributed processing.

4.2.2.2 4km Models

In order to compare the performance of MOM and SHOC, a test domain that is configured as closely as possible for each respective model is required. The domain was chosen to be the GBR 4km domain, and functionality was invoked in each model so as to render the configuration as comparable as possible. This included the same time steps, grid structure (albeit Arakawa C vs. B grids), vertical discretization, turbulence closure scheme (k-ε) using the same stability functions (Schumann & Gerz), same horizontal viscosity (constant Laplacian), minimal output dumps (1 dump at initialisation), same number of tracers, similar monotonic, positive definite advection schemes, upstream advection open boundary conditions for tracers, no tidal forcing, no river discharge, comparable non-reflective active open boundary conditions and surface flux forcing. There do remain, however, some differences between the models. SHOC interpolates surface and boundary forcing spatially and temporally inline, whereas MOM4 requires pre-processing onto curvilinear grids for these data. Similarly, post-processing of output is required to visualize MOM data since output is generated for each partition and must be stitched together into a single file at the simulation end. This file contains no geographic data required to map curvilinear grids onto a geographic projection, and must be further post-processed to combine geographic data in a `grid_spec` file into the output file. SHOC output is visualization-ready. The Dirichlet open boundaries used in SHOC require a larger volume of data to be read from file than the radiation conditions used in MOM4 (2x3-D velocity arrays + 1 sea level array as opposed to one sea level array). Surface heat fluxes are computed using the bulk method in SHOC based on standard meteorological measurements, whereas the surface fluxes were read directly into MOM4. These factors generally dictate that SHOC requires more computational effort during the simulations than MOM4 for this test configuration. The GBR4km model has 46% wet cells, and 34% of dry cells lie beneath the sea bed, hence wet cell ratio issues are not likely to factor highly with this implementation.

Both models were run on the HPCCC computer ‘burnet’ using a range of processors, and resultant runtime recorded. Runtime for SHOC was obtained from the real-time diagnostics produced by this model (`diag.txt`) and was computed for MOM4 from the runtime average statistics output in `fms.out` at the program’s termination, where initialisation computational costs were excluded from the runtime (i.e. the runtime reflects the integration computational effort) and pre and post-processing excluded for MOM4. Results are displayed in Fig. 4.2.13.

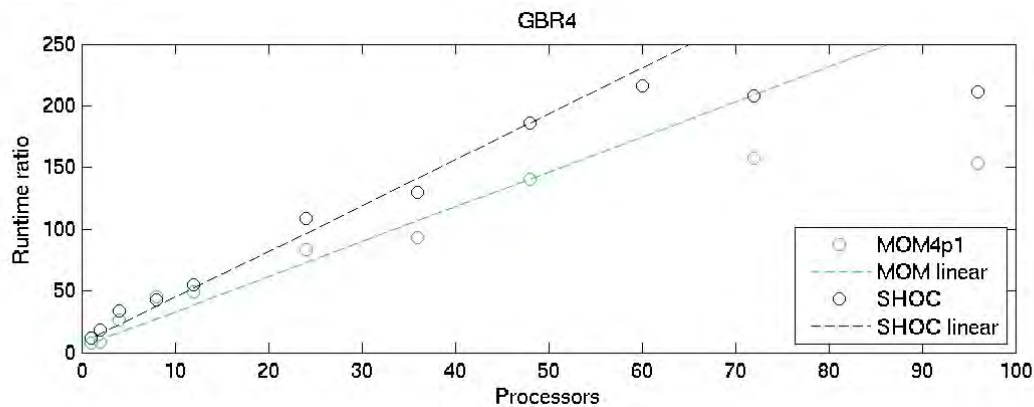


Figure 4.2.13. Runtime ratios as a function of processors for equivalent SHOC and MOM versions of the GBR 4km grid run on burnet.

It is seen that SHOC performs more efficiently than MOM4 on this domain, achieving a maximum runtime of 216:1 on 60 processors, with MOM4 achieving 158:1 on 72 processors. Both models scale linearly to around 48 processors, after which they begin to plateau; i.e. there is little benefit gained from increasing processor numbers beyond ~48. This test does not demonstrate the maximum speed achievable by these models, rather, the relative speeds under a certain configuration (out-of-the-box implementations with no compiler or load balancing optimisation).

Pre and post-processing costs for MOM4 are not insignificant. The transport mode in SHOC can be used to re-format data into a form compatible with MOM4 input onto the curvilinear grid. SHOC simulations interpolate boundary data every time-step, and at this frequency the transport mode processes the open boundary data onto the GBR 4km grid at a rate of 10:1. Pre-processing at hourly intervals (which is considered the bare minimum for open boundary input) runs at ~350:1. A 10 minute interval is considered a reasonable frequency to maintain model stability and accuracy, and this is processed at a rate of ~65:1. Pre-processing the surface forcing data using the transport mode in SHOC runs at ~860:1 for hourly output (which is sufficient to resolve the diurnal cycle). Post-processing 5 variables of output data (T, S, u, v, eta) for the whole 3D grid costs about 4s/dump using the program mppnccombine.c. A further ~2s/dump is required to re-format with geographic information included. In total, ~2.5 minutes are required to post-process a day's worth of data at hourly intervals. The transport files required for running sediment transport and biogeochemistry in SHOC's transport mode require 7 variables (T, S, u, v, w, Kz, eta) at hourly intervals, hence a minimum of ~3.3min/day is required for post-processing output. Therefore, it is estimated a total of 2.5 hours / day are required to process data in MOM4 using these methods to a standard equivalent to SHOC's inline methods.

The models were again benchmarked on the BoM machine 'solar'. The models used for these tests were individually optimised during a calibration process subsequent to the benchmarking described above, hence configurations and associated functionality invoked had diverged such that direct model runtime inter-comparison is not meaningful. It is anticipated that further calibration will contribute towards model configurations diverging further. Nevertheless, this test does benchmark the resources BoM are anticipated to require if these models are to be run operationally. The architecture of solar differs to that of burnet in that solar has less memory per node and slightly lower cpu speed/cache resulting in overall

poorer performance than burnet when used with models of this nature. SHOC was installed on solar without compiler optimisation or load balancing optimisation. Model runs were performed on 72 processors only, with SHOC achieving a total runtime of 82:1 and MOM4 of 22:1. This indicates that SHOC requires >3x less compute resources than MOM4 when run on solar. These runtimes include initialisation costs, of which generating the multi-processing partitions and file initialisation can be significant. Note that the MOM4 runtime reflects both pre-processing of forcing data and model integration time (3 hours and 17 minutes respectively), and its runtime would improve if pre-processing could be parallelised. Only open boundary forcing is parallelised on SHOC; surface forcing is not and could also be optimised in this regard. The configuration of MOM4 uses a nudging OBC that requires the input of more data than SHOC's Dirichlet OBC. Both models interpolate OBC data at high frequency (every time-step for SHOC), hence the computational burden is great. The integration-only component of MOM4 yields a runtime of 254:1, and that of SHOC 117:1, however, the SHOC runtime still includes forcing data interpolation which cannot be easily separated from the overall runtime without a full profile. Additionally, SHOC computes the open boundary tidal signal inline (every time-step), whereas MOM4 pre-processed this component into the forcing data. Load balancing without optimisation is also poor on SHOC, with the fastest partition running ~7 times faster than the slowest (MOM4 always achieves perfect load balance without optimisation). Differences such as these demonstrate the difficulty in comparing efficiency with divergent model configurations, and direct comparisons should be based on the tests conducted on burnet described above where models were configured as similar as possible. Model output for a 72 hour forecast on solar is ~600Mb for both models. The runtime of both these models is deemed to be not significant for operational modelling, and should not be an impediment to implementation for either model.

4.2.2.3 1km Models

The GBR1km model is an extremely large computational domain, with 510 x 2389 x 44 cells in total. The wet cell ratio is 24% of total cells, and 52% of dry cells lying beneath the sea bed. Wet cell ratio is likely to become a factor in determining runtime for this model. The size of the GBR1km model is comparable to some of the global models simulated. A MOM4 version of the 1km model does not exist, so here we examine the runtime of the SHOC implementation in isolation to assess scalability and estimate resources required to run it operationally on solar. Model speedup on burnet is plotted in Figure 4.2.9; this demonstrates that the model scales linearly up to 72 processors, achieving a runtime of ~21:1 with 72 processors. Since the domain is comparable to global models, similar computational resources are required to achieve good runtimes; this result is consistent with the notion that many 100s of processors would be required to achieve runtimes in excess of 100:1. Since the 1km domain contains many more cells than the 4km model, the ratio of cells comprising partition interfaces to that of cells within a partition remains lower as the number of partitions increases, i.e. the runtime is expected to plateau much later than with the 4km model. This appears to be the case in Fig. 4.2.14, where no indication of Amdahl's Law coming into effect is observed up to 72 processors.

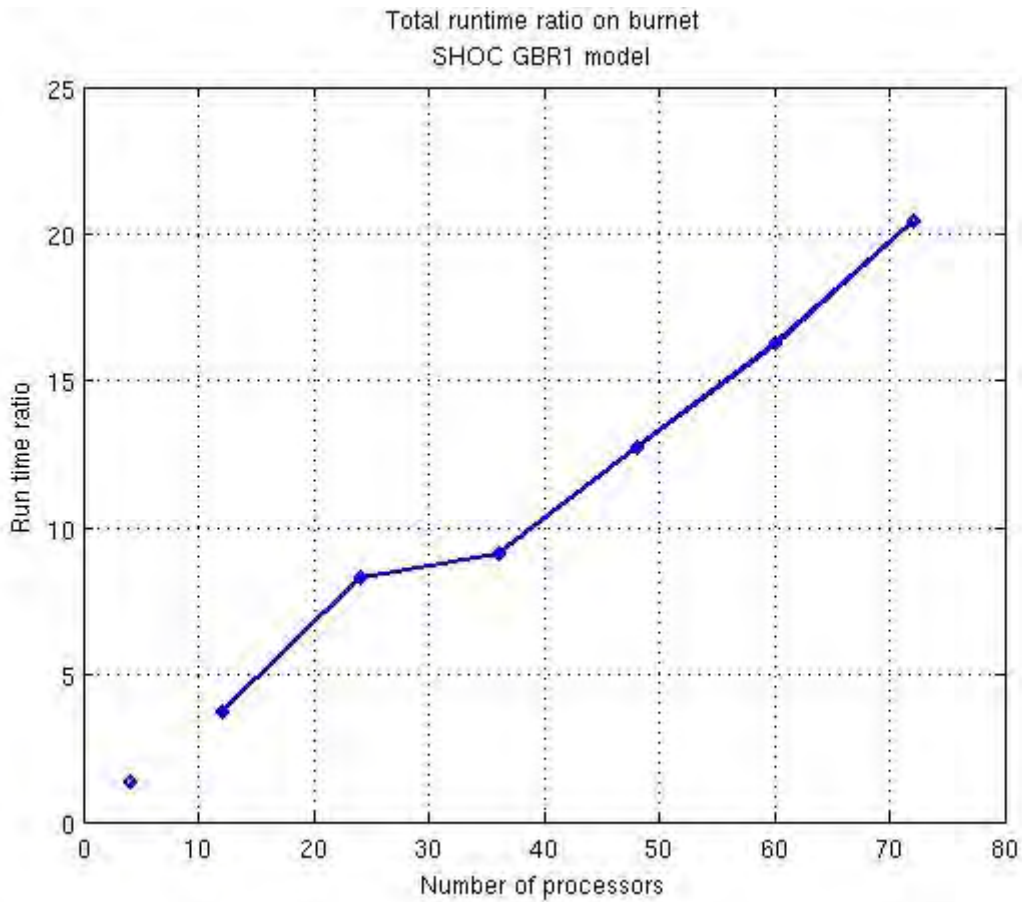


Figure 4.2.14. Runtime ratio for the SHOC GBR 1km model on burnet.

The 1km model was unable to be run on solar, as each node of this machine only contained 24Gb of memory which was insufficient for the 1km model in its current configuration. With further development it would be possible to reduce this memory requirement for each partition, however, there will still need to be at least one node with at least 48Gb to house the master. Note that burnet has half of its nodes with 48Gb and half with 96Gb of memory, which is sufficient to run the GBR 1km model. Therefore, a computer with greater memory capacity is required if the GBR 1 km model is to be run operationally at BoM.

4.3 Data assimilation

4.3.1 Introduction

The overall goal of the Data assimilation (DA) system is to reduce model error and provide some insight (and quantification) of model uncertainty by constraining the output of a numerical model with observations. DA into the eReefs models have progressed along two parallel fronts. Assimilation into these models presents a number of challenges as run time ratios are low, and observations within the domain are relatively sparse. Compounding these facts, are a variety of sources of model error and uncertainty.

Phase I of eReefs saw a focus on algorithm development, data discovery and the implementation of the GBR4 hydrodynamic model (4 km resolution model) in a distributed computing environment. Phase II further developed the DA algorithms to produce a 4 year reanalysis of the hydrodynamic state, and also extend the the algorithms for use in the biogeochemistry. This section is structured in the following manner:

- The DA methodology and approaches are introduced in Section 4.3.2;
- Available observations are discussed in Section 4.3.3;
- Sources of model error and uncertainty are discussed in Section 4.3.4;
- Effects of uncertainty and model error are explored in Section 4.3.5;
- Two approaches to DA are presented and preliminary results are discussed in Section 4.3.6; and
- A summary is then given in Section 4.3.7.

4.3.2 Hydrodynamic DA Methodology

Two alternative DA approaches have been implemented:

- A coastal Ensemble Optimal Interpolation (EnOI) approach similar to that detailed in Jones (2012) and Oke (2008; 2013); and
- An ensemble approach using an augmented Ensemble Kalman Filter (EnKF) with localization for joint parameter-state estimation (Jones et al., In Preparation).

The EnOI approach requires a 'long' control run (free run) of the model, with no DA. From this control run a number of different anomaly fields have been constructed. Depending on the characteristic errors in the model and the observing system, various errors can be represented and corrected using different windows of averaging. Different combinations of 'short' and 'long' averages of model outputs have been trialled to form three different sets of anomaly fields.

The ultimate goal of a coastal DA system is to reduce errors in the model solution by correcting the cause, not just the symptoms. Unlike the chaotic behaviour in global models associated with meso-scale eddies, for example, friction in the coastal domain acts to dampen these meso-scale structures. Due to the high grid resolutions and complex topography, there are some very fine scale chaotic structures that appear in coastal models. Therefore due to there being some deep areas of the domain (i.e. in the NE portion of the grid), there are numerous chaotic behaviours that occur on a variety of scales. Given the sparse nature of the observing system detailed above, it is unlikely that the current system will be able to constrain

the small-scale chaotic behaviour. However, as we have reasoned in Section 4.3.4, other sources of error can be targeted by the assimilation system.

4.3.3 Hydrodynamic Observations

In a model domain (GBR4) that spans an area bounded by the NSW border in the south, Papua New Guinea (PNG) in north, the coast to the west and the shelf break and deep ocean to the east, observations tend to be sparse in space and largely clustered around near shore and reef sites in areas used for specific process studies. Typically these in-situ observations comprise of time series of temperature, salinity and pressure at various depths. Supplementing the in-situ data, is Satellite Remote Sensing (SRS) data retrieved from IMOS.

Within the region there are approximately 130 in-situ observational locations (i.e. locations that have a unique latitude, longitude and depth). This data has been drawn from the AIMS data repository and supplemented with the GBROOS and FAIMS data from IMOS. From Fig. 4.3.1, it is clear that these sites are clustered closely around reef and coastal locations. To supplement the in-situ data, SRS data from IMOS has also been compiled and are shown in Fig. 4.3.1. If a histogram of observation vs. depth is created (Fig. 4.3.1) it is clear that the SRS data offers a very valuable spatially resolved data set. Below the surface layer (<2m), it is clear that there is very poor spatial coverage in the eReefs GBR4 domain. Further supplementary data set that could be included are Argo, XBT, SOOP and animal tags.

However, as in any system, data is required to be withheld from the assimilation system to validate the model. Therefore, we are presently withholding the Argo, XBT, SOOP and Animal Tag data for these purposes. Furthermore, these data sets (with the exception of Argo) are not available in near real time, and are therefore not available for assimilation into operational models. However, if a reanalysis is performed, all data can be ingested by the DA system if required.

To date we have focused on assimilating temperature data only. The present goal has been to use the assimilation system for not only state estimation, but also parameter estimation (discussed in Section 4.3.5 and Section 4.3.6). Other observations that are available for assimilation include in-situ salinity (moorings, glider and GBROOS infrastructure) and along track satellite altimetry. The DA system is presently setup to ingest salinity data. However, some work needs to take place to bring coastal altimetry into the system.

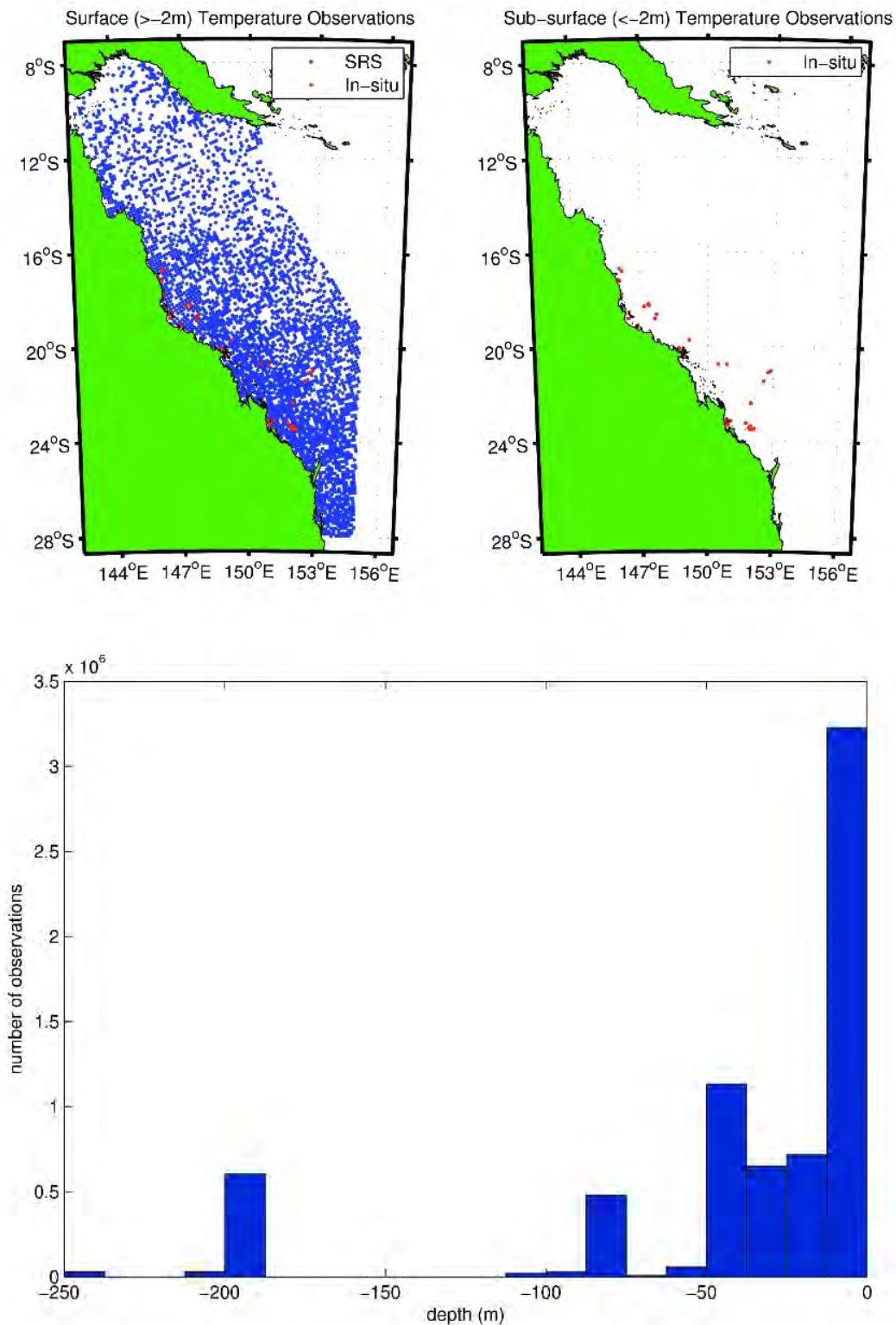


Figure 4.3.1. Map displaying the spatial distribution of Satellite Remote Sensing (SRS), SST and in-situ temperature observations to a depth of 2m (upper left). In-situ temperature observations below 2m depth (upper right). Histogram of the number of observations vs. depth for 2011 (lower).

4.3.4 Hydrodynamic model error and uncertainty

Errors and uncertainties in coastal ocean models can enter in the following ways:

- Model forcing and boundary conditions (e.g. open ocean boundary conditions, head of estuary forcing, surface forcing, bathymetry);
- Initial conditions (e.g. initial distributions and values of the model state variables); and
- Internal process parameterizations (e.g. mixing/turbulence, uncertainty in process parameters etc).

Coastal hydrodynamic models require prescribed forcing at the sea surface, open ocean and head of estuary boundaries. In most instances there is a deep nested complexity, in that these prescribed forcing's are often the output of complex numerical models with their own inherent uncertainty. For this reason, one can think of there being a series of "nested" uncertainties, whereby the uncertainty associated with the output for one model is considered the uncertainty associated with the "input" of the next level model.

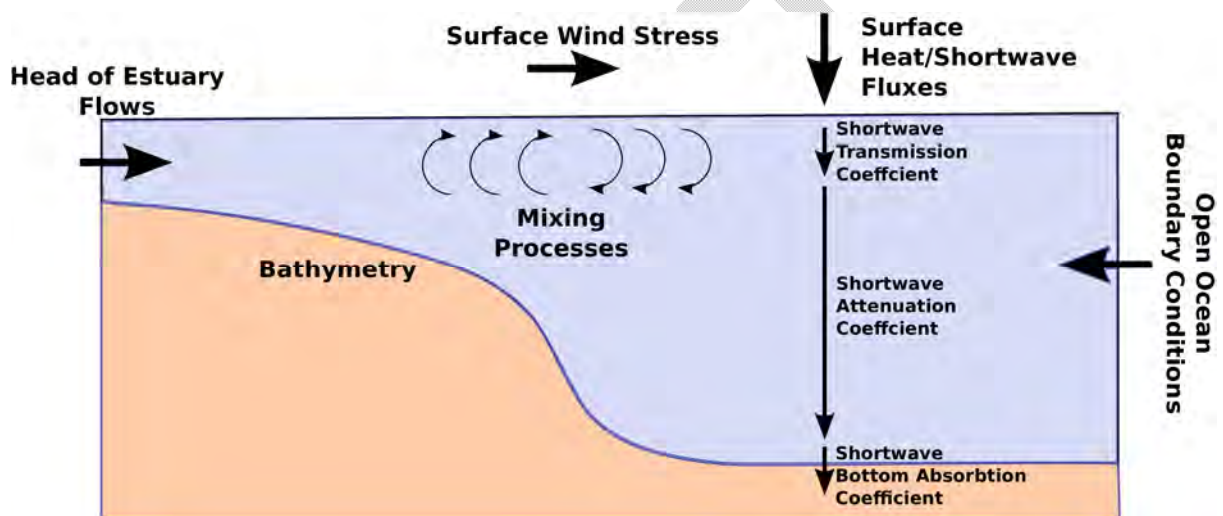


Figure 4.3.2. Conceptual diagram of the sources of error and uncertainty in the hydrodynamic model.

The open ocean boundary conditions for the GBR4 model are taken from an Ocean General Circulation Model (OGCM), in this case BLUElink (Section 4.1). Again so far as the coastal hydrodynamic model is concerned the location of the uncertainty is in the prescribed boundary conditions, which is considered an "input". Similarly, head of estuary river flows and loads are often taken from catchment models.

In instances where the Navier-Stokes equations behave chaotically, it is assumed that a substantial proportion of the model error stems from initial conditions. This essentially arises due to very small perturbations in the model growing, causing model solutions to diverge. Unlike OGCM's, coastal hydrodynamic models are subjected to shallow water effects, whereby friction tends to dampen out mesoscale chaotic behaviour. Instead, we see chaotic behaviour emerge at much shorter length scales as grid resolution increases. Such features include upwelling and river plume filaments, sub-mesoscale coherent vortices, lee eddies in the wake of headlands and various other topographically induced turbulent/chaotic processes.

Within all process based environmental models, real world complex processes are represented by simplified process models. Errors may arise due to solving the governing

equations on a grid, and therefore sub-grid scale processes need to be accounted for, e.g. mixing and turbulence. It may also be too computationally expensive to model the process without approximations. An example of this is the interaction between shortwave radiation and the optical properties of waters.

To understand the effect of these errors, perturbations can be made to model (or forcing fields etc), that represents the appropriate sources of error. The perturbations must represent the dominant source(s) of error within a system. As mentioned above, in Ocean General Circulation Models (e.g. BLUElink), the dominant sources of errors are due to chaotic circulation related to the spatial and temporal errors associated with mesoscale eddies, and chaotic behaviour in the coastal domain occurs on much shorter time and length scales. For a data assimilation system to correct for these errors, the observing system must be capable of resolving such features. With the exception of some high-resolution satellite sea-surface temperature (SST) products (e.g. AVHRR) and coastal high-frequency radar, it is unlikely that the sub-surface properties of the GBR will ever be resolved by observational platforms at the sub-mesoscale with sufficient resolution to constrain a high-resolution data-assimilating model. The underlying reason for implementing a DA system is to reduce and quantify the effects of model error in model simulation (either forecast, nowcast or hindcast mode).

Fig. 4.3.3 displays the coverage of in-situ temperature and salinity loggers within the GBR lagoon. If data is required in near real time, there are fewer than 5 sites across the entire model domain that provide in-situ measurements. Acknowledging these limitations, errors with coherent long spatio-temporal errors, can be resolved. Therefore the initial perturbation experiments conducted under eReefs that are described here focus on two common sources of error in coastal models:

1. Bias in the initial conditions, and the resulting effects of boundary forcing; and,
2. Errors arising from unresolved processes that alter the internal light field of the model, and penetration of short-wave radiation (SWR).

There are three parameters (SWR transmission = R_t , SWR attenuation = R_a and SWR bottom absorption = R_b ; see Section 5.1.9) that control the absorption of short-wave radiation in the water column. These three parameters need to be tuned for specific applications and depend on water mass optical properties and substrate type. Given that water mass optical properties in coastal environments change due to biogeochemical processes and riverine discharge, R_t and R_a , will vary in time and space. However, as benthic processes are often slow, R_b could be considered constant in time, but variable in space. Presently, these parameters are all treated as spatio-temporally invariant, which may be a major source of error in coastal regions.

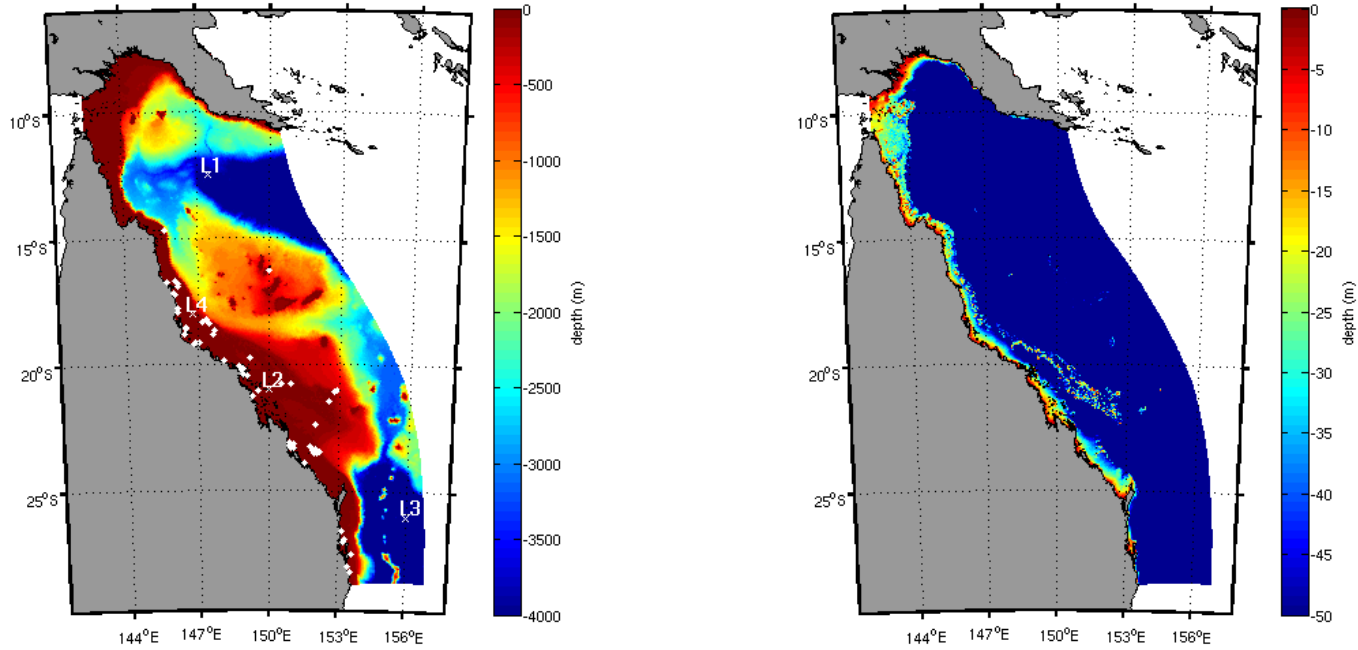


Figure 4.3.3: The bathymetry of the eReefs domain with in-situ observational platforms and location 1-4 (L1-L4) that will be used to characterise model behaviour in the left panel, and in the right panel, the bathymetry has been truncated at -50m to enhance the shallow offshore reef matrix.

4.3.5 Hydrodynamic model perturbations

Bias in the temperature and salinity field can enter coastal models from a number of sources and its effects on coastal dynamics can be unclear "a-priori". Given that the model may respond non-linearly to perturbations, a series of numerical experiments have been run to quantify the model response.

The effects of these two sources of error are investigated using ensemble methods (with no data-assimilation), using a 30-member ensemble. The background states for these experiments were created by spinning up the GBR4 model for 15 months (1/9/2009 - 1/1/2011, from initial conditions derived from the analysis field of the latest BLUElink ReANalysis (BRAN; Oke et al. 2013) on the 1/9/2009, interpolated onto the GBR4 grid. After the 15 month spin up of GBR4, the full state is saved on the 1/1/2011, is represented as:

$$\mathbf{w}_0 = [\mathbf{u}, \mathbf{v}, \eta, \mathbf{T}, \mathbf{S}]^T \quad 4.3.1$$

Where \mathbf{w} is the state vector, \mathbf{u} and \mathbf{v} are the 3D velocity fields, η is the sea-surface elevation and \mathbf{T} and \mathbf{S} are the 3D fields of temperature and salinity respectively. The superscript T denotes the vector transpose. The subscript $_0$ denotes initial time. To investigate the effects of parameter uncertainty and bias in the initial conditions an experiment was run, whereby perturbations were made to the short wave radiation (SWR) parameters (R_t , R_a and R_b) and the state vector \mathbf{w} by adding a spatial uniform offset to the temperature and salinity field, representing large scale biases that may be present at initialization.

4.3.5.1 Perturbations to the SWR Parameters

Perturbations were made to the SWR parameters (R_t , R_a and R_b). For example, in the default settings of SHOC, R_t is set to 0.2 and is spatio-temporally invariant. Given that these parameters are uncertain and “a-priori”, we may only have limited information about them. They could be sampled from some probability distribution. For this experiment, we place the following distributions over the SWR parameters (R_t , R_a and R_b):

$$\begin{aligned} R_t &\sim \text{uniform}[0,1], \\ R_a &\sim \text{uniform}[0,1] \\ R_b &\sim \text{uniform}[0,1] \end{aligned} \quad 4.3.2$$

We then set θ to be the parameter vector, where $\theta = \{R_t, R_a, R_b\}$.

4.3.5.2 Perturbations representing bias in the initial conditions

Spatially uniform increments are added to \mathbf{T} and \mathbf{S} in the state vector \mathbf{w}_0 . An N member ensemble of \mathbf{T} and \mathbf{S} perturbations are generated by:

$$\begin{aligned} \mathbf{T}_{0,n} &= \mathbf{T}_0 + \zeta_{T,n} \quad n=1 \dots N \\ \mathbf{S}_{0,n} &= \mathbf{S}_0 + \zeta_{S,n} \quad n=1 \dots N \end{aligned} \quad 4.3.3$$

where n is the ensemble member, $\zeta_{T,n}$ is the bias offset that is drawn from $\zeta_{T,n} \sim \text{Gau}(0,2)$ and $\zeta_{S,n} \sim \text{Gau}(0,0.5)$ and N is the total number of ensemble members (90 in this case). The full state vector for each ensemble member is then reconstructed and augmented by the parameter perturbations:

$$\mathbf{w}_{0,n} = [\mathbf{u}, \mathbf{v}, \eta, \mathbf{T}_n, \mathbf{S}_n, \theta_n]^T \quad 4.3.4$$

4.3.5.3 Perturbation Experiment Results

The summary statistics for the ensemble (Fig. 4.3.4) provide some insight into the spatial variation in the effects of bias in initial conditions. The ensemble Sea Surface Height (SSH), is elevated in the offshore central section of the GBR. This aligns with the inflow from the Coral Sea and well described by Brinkman, (2002) and Ganachaud, (2007). The depressed Sea Surface Height (SSH) in the deep central north basin, combined with elevated SSH in coastal regions south of Papua New Guinea, drives the transient South Papua (or Hiri) current. This draws water through Torres Strait and from the northern GBR lagoon. The southern inshore region of the GBR shows a marked decrease in SSH with a strong cross-shore gradient.

The standard deviation of SSH in the ensemble was relatively low, and peaked at 0.03m in the south-eastern corner of the domain. It should be noted that this peak in the standard deviation is closely aligned with the region where the East Australian Current (EAC) accelerates southwards along the northern NSW coast line. A recent paper by O’Kane et al., (2011), demonstrate that the predictability and growing error modes are directly related with perturbation made to the temperature field at the base of the mixed layer. These results suggest that the temperature field in the central and southern GBR contributes to setting the cross-shore SSH and therefore may modulate the strength of the EAC in the southern GBR.

The mean SST varies strongly in an alongshore manner with a magnitude of up to 4°C. The eastern boundary of the model domain, bounded by 10°S and 17°S, show the effects of the inflowing Coral Sea waters. This region also has the lowest standard deviation in SST, suggesting this region is strongly forced by the eastern open ocean boundary. The fringing offshore reefs between 19°S and 21°S, show a marked decrease in mean SST when compared with the surrounding waters. This suggests there is strong tidal pumping (Wolanski et al., 2002) with an injection of cool deep water into the surface layers.

The shallow inshore waters have the highest SST standard deviation. Given the initial perturbations to the ensemble were +/- 2°C, the effects of altering the SWR parameters combined with the transition from wet to dry season, show this shallow inshore area has large temperature variations. To fully examine the relative effects of radiative cooling compared to variations in SWR parameters, a detailed examination of the time varying SST anomalies (SSTA) are presented in the discussion.

The mean and standard deviation for the Sea Surface Salinity (SSS) highlight the effect that coastal rivers have on the salinity budget. This is especially apparent on the southern coastline of PNG, where the Fly River has substantial freshwater discharge. Beyond the influence of river plumes, the standard deviation of SSS, is below 0.2 PSU.

Four sites (L1 - L4) that are representative of various regions within the model were chosen to investigate the behaviour of the ensemble in the two experiments. Sites L2 and L4 are in the near shore region within the GBR lagoon complex. L1 is in the deep offshore waters outside of the northern GBR, while L3 is on the southern offshore waters of the GBR. Time-series plots of the ensemble trajectories are plotted for temperature and salinity at a number of depths at each of these locations (Fig. 4.3.5 – 4.3.8). The initial perturbations span +/-2°C and +/-1 PSU. The ensemble of perturbed states are then integrated forward in time. The model response to these perturbations are location and depth specific. Fig. 4.3.9 and 4.3.10 illustrate the change in ensemble range over the length of the simulation.

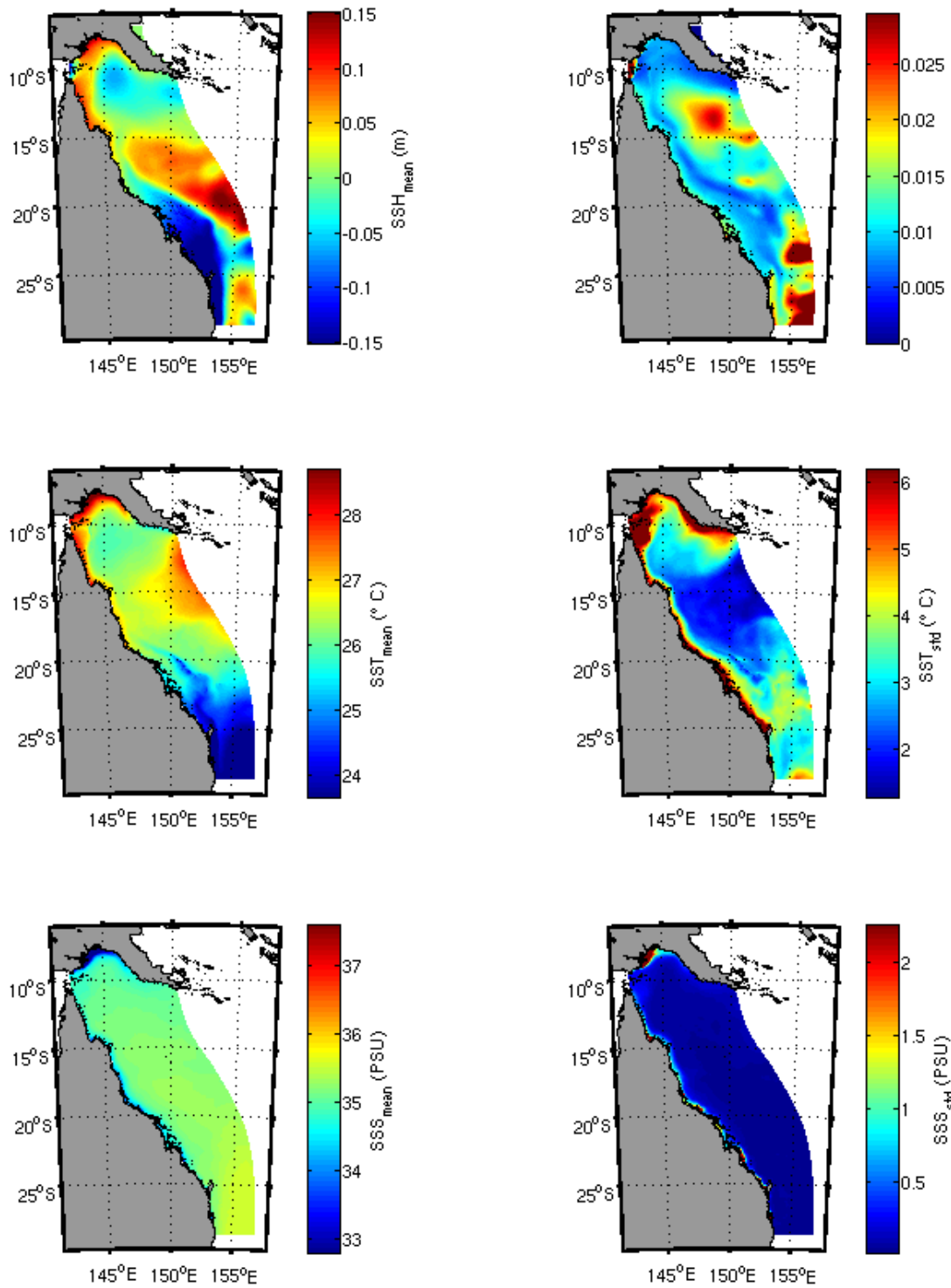


Figure 4.3.4. Temporal mean (left) and standard deviation (right) for the modelled sea-surface height, sea-surface temperature and sea-surface salinity for the period 1/3/2011 to the 31/5/2011.

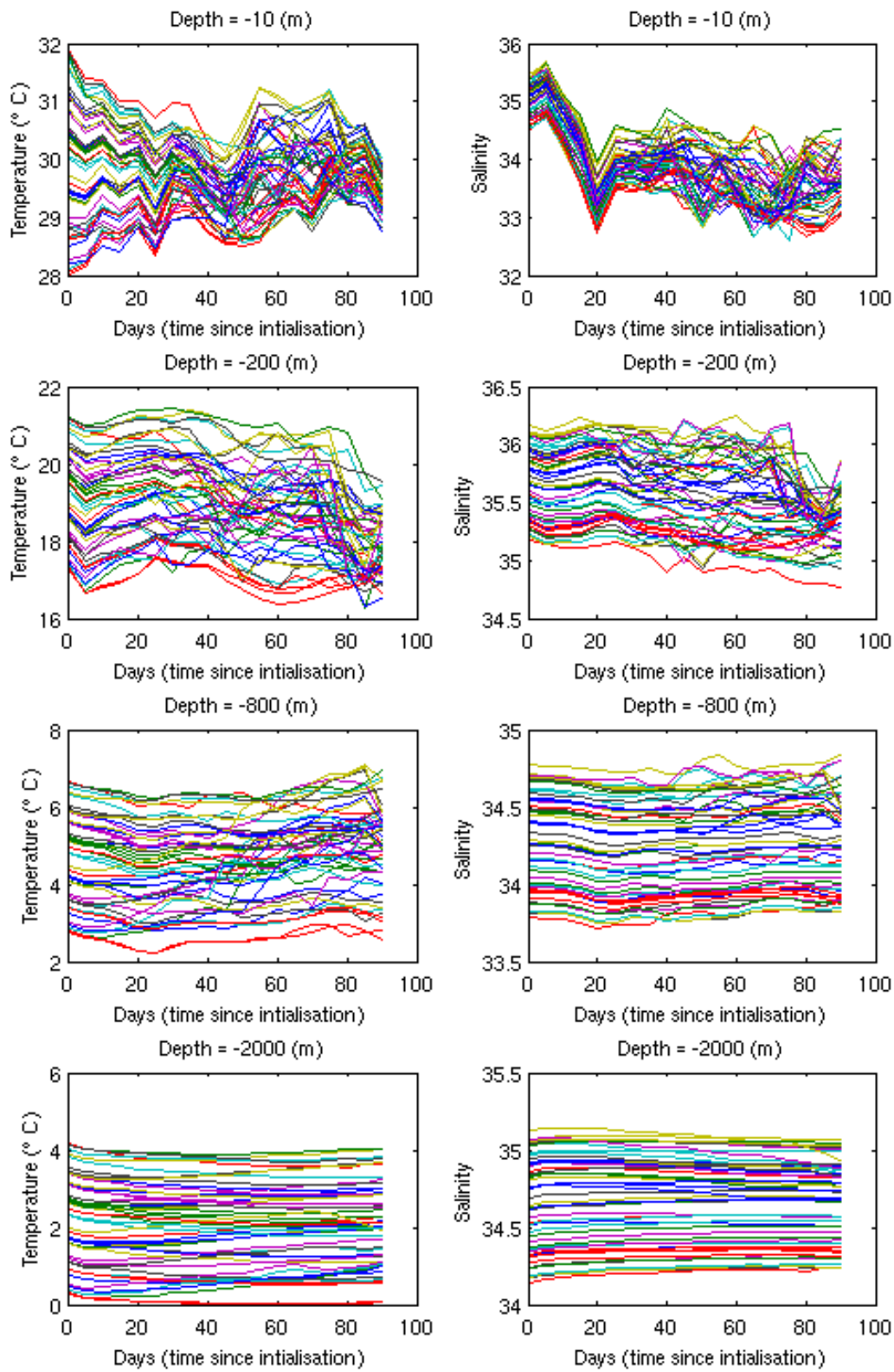


Figure 4.3.5. Time-series plots of each ensemble member at L1 (see Fig. 4.3.3).

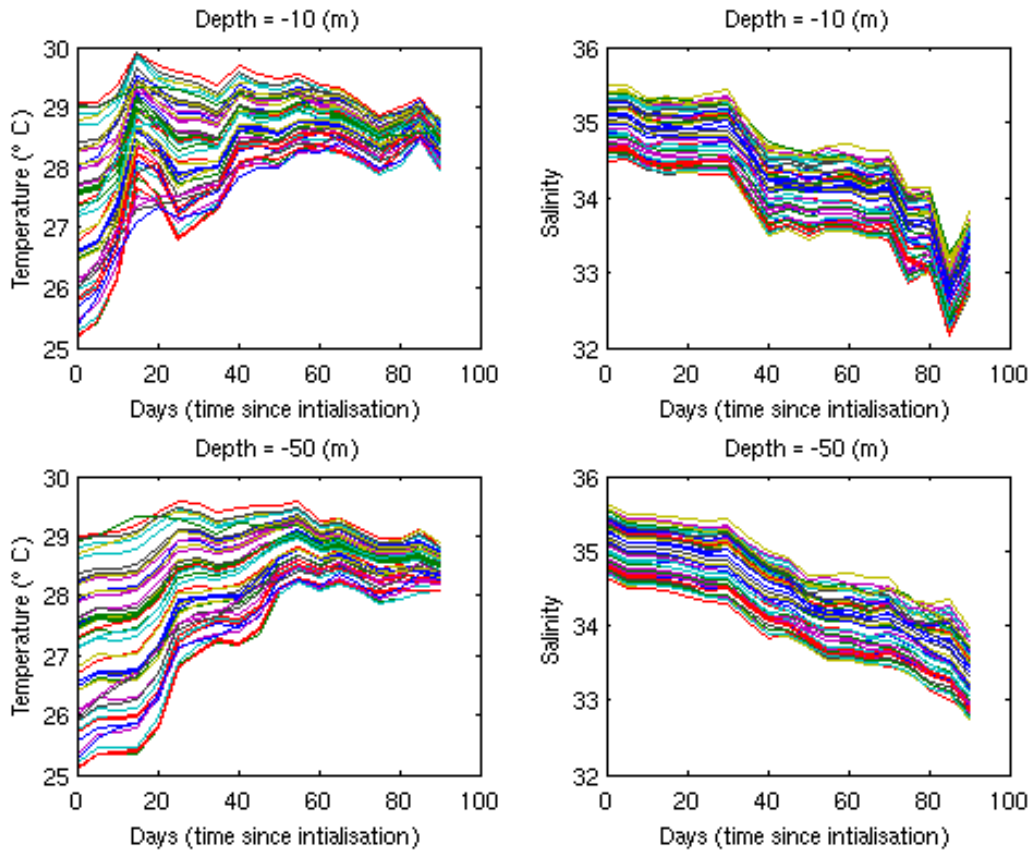


Figure 4.3.6. Time-series plots of each ensemble member at L2 (see Fig. 4.3.3).

The behaviour of the ensemble at L1 (Fig. 4.3.5) can be interpreted by looking at whether individual ensemble members maintain parallel trajectories; and whether the ensemble spread (range) contracts or expands. These behaviours are also investigated at sites L2-L4. The ensemble temperature range at 10m depth at L1 contracts with time. After day 25, ensemble trajectories appear to stop behaving in a parallel manner and begin to cross paths. The ensemble temperature range does not contract at depth, with the initial spread of 4°C maintained. At 200 and 800m, trajectories diverge at 25 days. However, at 2000m, almost all trajectories remain parallel. The initial 1 PSU salinity perturbation range at 10m grows over the simulation period to a 2 PSU range. The trajectories again start to cross at 25 days, and look to become chaotic after day 30. The growth of the perturbation range does not occur at depth.

The ensemble behaviour at the two shallow sites (L2 and L4, Figs. 4.3.6 and 4.3.8) show very similar behaviour. The temperature range decreases to between 25-50% of the initial perturbation range over the 90 day simulation. This is seen in both the 10m and 50m time series. Fig. 4.3.9 summarizes the contraction of the ensemble and shows the contraction asymptotes after 50 days. The ensemble spread is maintained by the variation in the SWR parameters. The salinity time series of the ensemble is different to that of the temperature time series. The temperature trajectories maintain a relatively parallel behaviour, and do not diverge. The spread of the salinity variable is maintained throughout the simulation at L2, however, there is a substantial increase in the ensemble range at L4 in the surface layer, while the deeper time series spread remains unchanged.

The final deep water site, L3, is located in the south eastern region of the domain, in the centre of the southwards flowing EAC. The initial ensemble spread rapidly collapsed to a range of only 0.3°C by day 20 in the surface layer. In the deeper layers, the ensemble maintained a spread close to the initial values (Fig. 4.3.7). The salinity perturbation took approximately 35 days to collapse onto a very narrow range of only 0.1 PSU. The behaviour at 200m was similar, however, below 200m the ensemble maintained the initial spread. At all depths there was a divergence of trajectories.

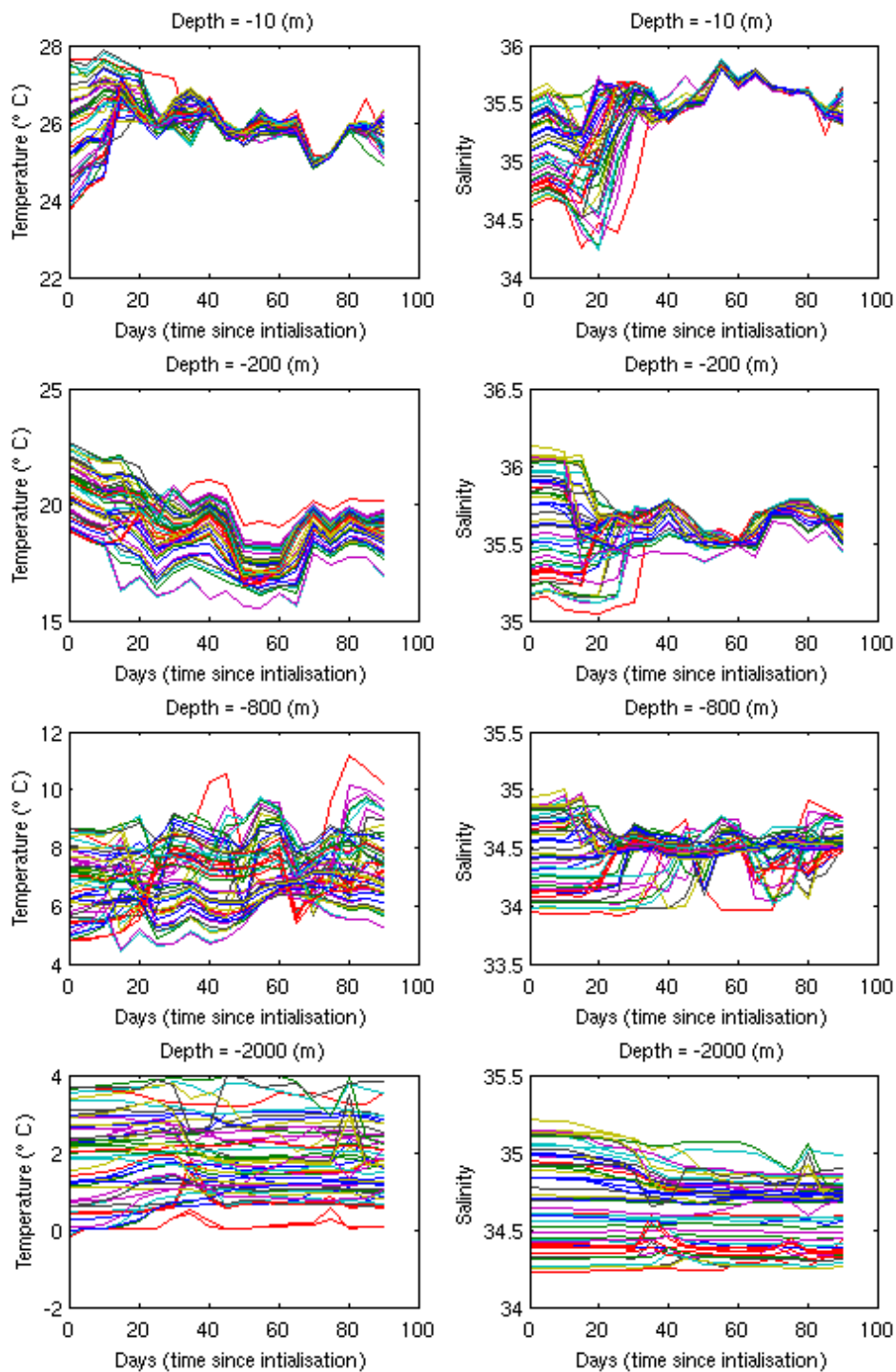


Figure 4.3.7: Time-series plots of each ensemble member at L3 (see Fig. 4.3.3).

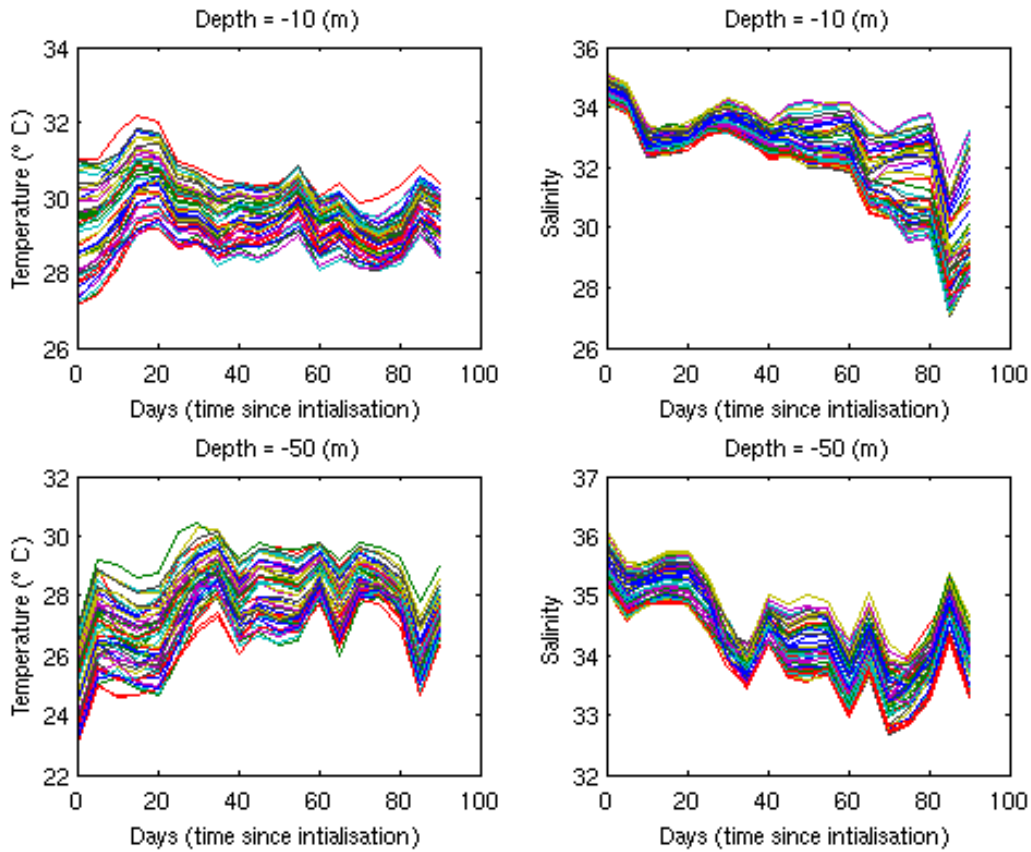


Figure 4.3.8: Time-series plots of each ensemble member at L4 (see Fig. 4.3.3).

A comparison between the ensemble members of the GBR4 model, and temperature observations in an inshore region (Fig. 4.3.10), show that the model is able to represent the observed temporal variability seen at both diurnal time scales (heating and cooling over day-night cycle), and also longer period variability associated with the passage of weather systems. The initial ensemble spread generally spans the observations, however, after 20 days there appears to be a warm bias in the model that persists through the remaining simulation time. This bias cannot be attributed to bias in the initial conditions, or uncertainty in the SWR parameters. It is most likely related to processes that determine the surface heat fluxes.

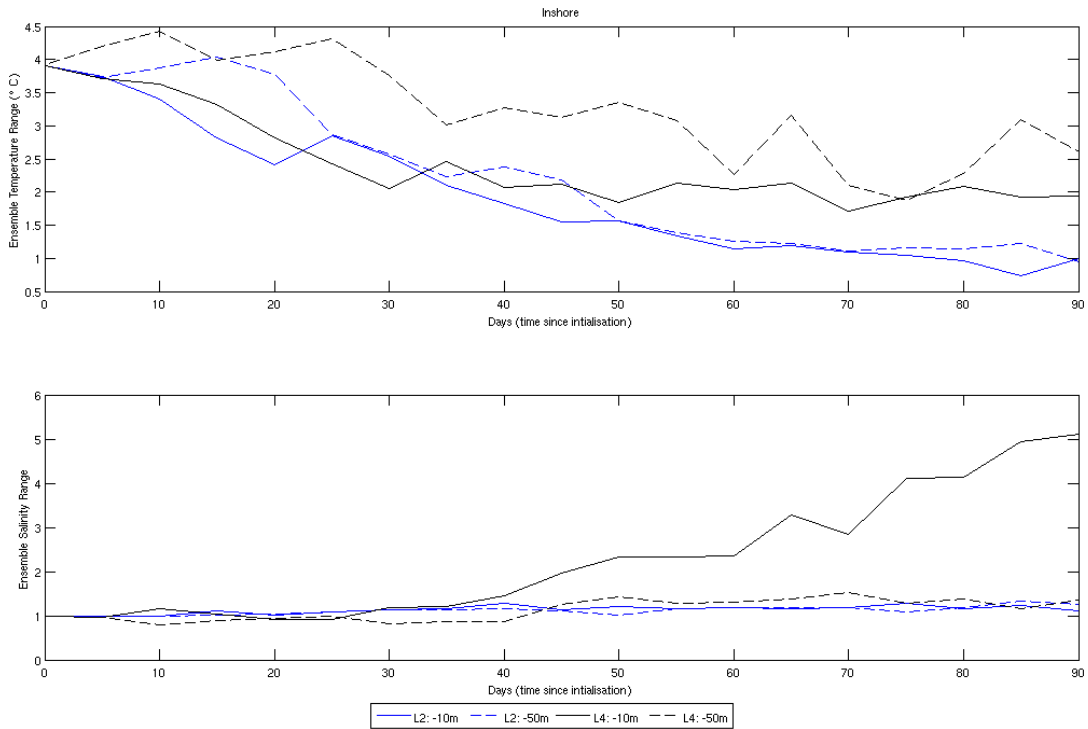


Figure 4.3.9: The ensemble range in temperature (top) and salinity (bottom) at L2 and L4 (the shallow sites) at each depth point.

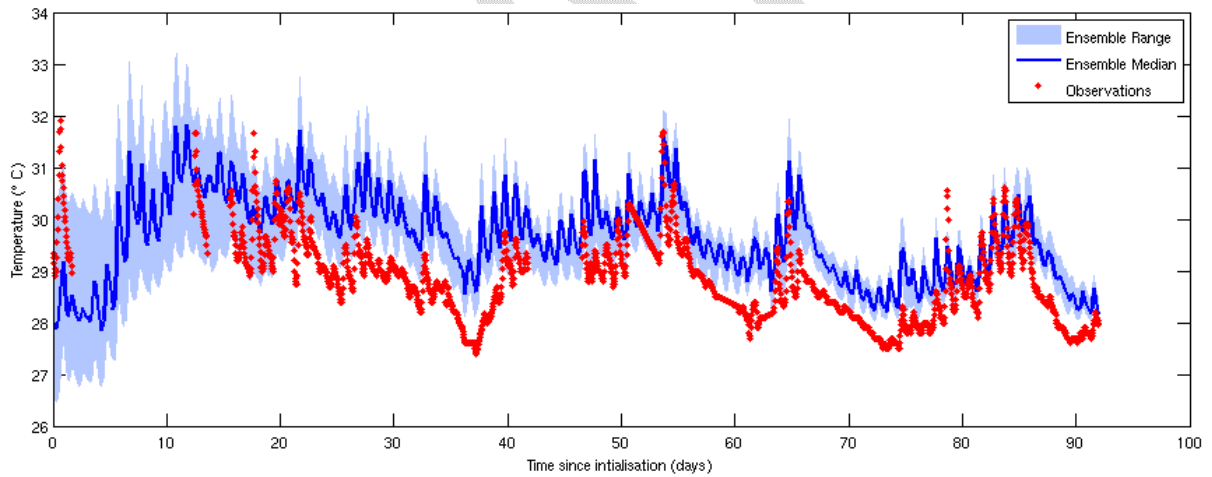


Figure 4.3.10. Time-series plot of the ensemble median & range, and observed temperature at the Townsville waverider buoy.

Ultimately the errors and uncertainties in the SWR parameters and the initial conditions, do not only affect the time series of T and S. Fig. 4.3.11 shows the resulting impact of these errors and uncertainties on the sea surface elevation (η) field. The η anomaly (η') is calculated by:

$$\eta'_{t,n} = \eta_{t,n} - 1/N \sum_{n=1}^N \eta_{t,n} \quad n=1 \dots N \quad 4.3.5$$

where the subscript t denotes the time, subscript n denotes the ensemble members with an ensemble size of N members. It is not unexpected that perturbations made to the initial conditions of the T field also manifest themselves in the η field. At the deep water sites of L1

and L3, the bias in the initial conditions results in an ensemble range of up to 0.6 m. At the shallower inshore sites, the ensemble range is reduced, but still results in a range of up to 0.2 m. There is a low frequency modulation of the range that appears to exist at weatherband time scales.

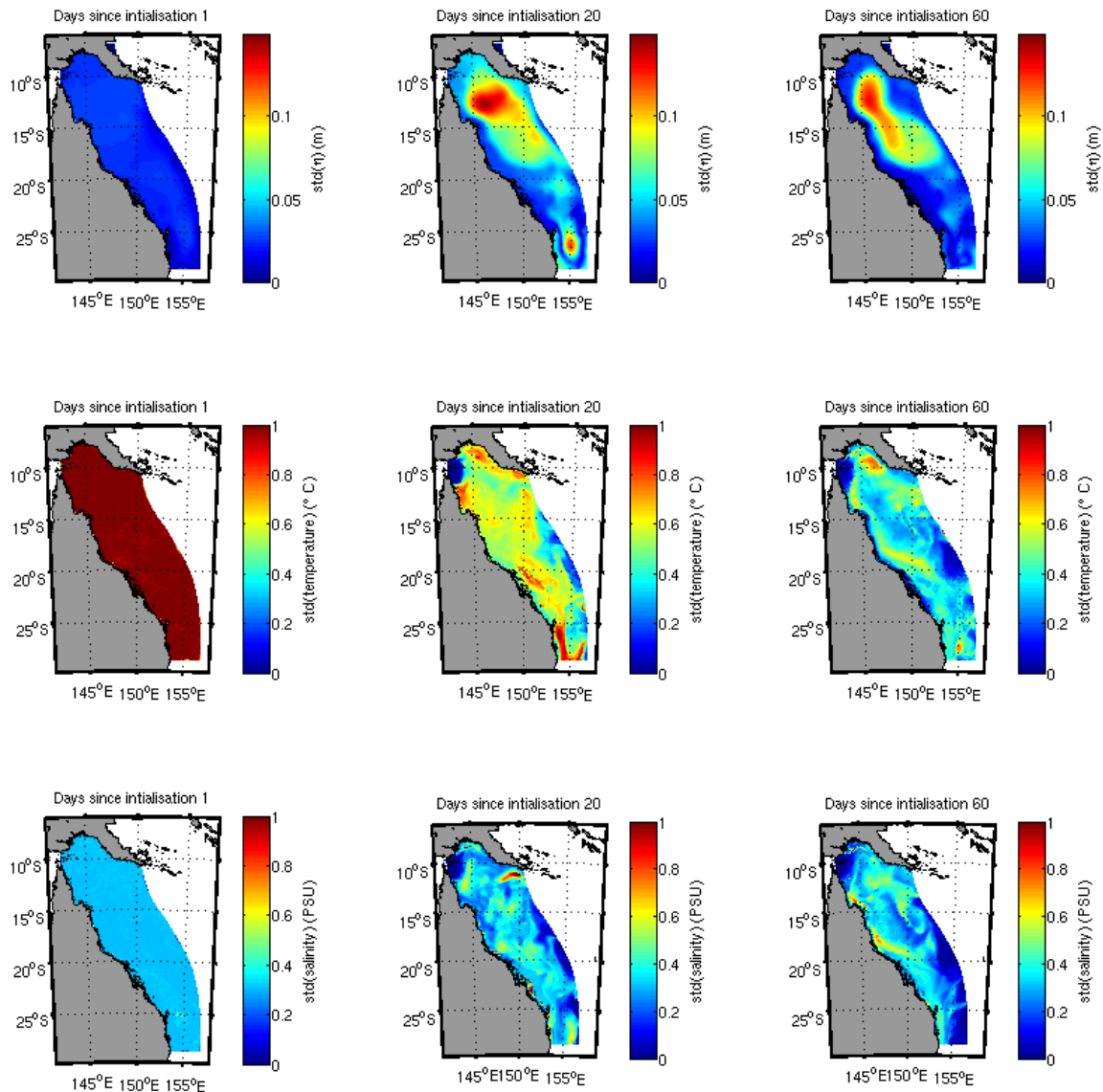


Figure 4.3.11. The evolution of the surface variance for temperature, salinity and η , at days 1, 20 and 60.

4.3.5.4 Discussion

A time series plot of the ensemble ranges at L1-L4 (Figures 4.3.5 and 4.3.8) reveal very different behaviours in offshore compared to inshore sites, as well as for salinity compared with temperature. The ensemble range for temperature at the inshore sites appears to asymptote after 60 - 70 days in both the surface and deeper layers. This behaviour is linked the well mixed nature of the water column at these inshore sites. The asymptotic behaviour towards a range > 0 , is due to the perturbation made to the SWR parameters, the magnitude of the range after 60 - 70 days has the same magnitude as that range reported in experiment

1. This asymptotic decline in ensemble range for temperature in the inshore region is driven by the water column and atmosphere needing to reach a quasi-stable equilibrium whereby through the interaction of the heat fluxes, where the spread is then maintained by the variance in the SWR parameters.

The specific ensemble behaviour at the offshore sites is largely determined by their proximity to the open ocean boundary of the GBR4 grid. Site L1 lies well within the model domain, whereas L4 is in an area in the southern section of the domain, which is strongly influence by an adjacent open ocean boundary. The surface layers at L1 and L3 show a similar behaviour to the inshore site, in that the surface heat fluxes and SWR parameters cause a reduction in the ensemble range. This is compounded at L3, where the ensemble almost collapses onto a single solution at day 70, which is driven by the external OceanMAPS (Ocean Modelling Analysis and Prediction System; Brassington et al. 2007) boundary forcing. The ensemble range at L1 in the deeper layers, is amplified initially, then converges back towards the initial ensemble range. The deeper layers at L1 and L3 maintain their range, as these layers are respond to timescales much longer than the 90 day simulation used in this study.

Salinity in the coastal inshore zone is largely controlled by the balance between precipitation-evaporation, and also the effects of freshwater input from rivers. All locations except the surface layer at L4 maintain the initial ensemble range. The surface layer at L4 is the exception. This site is affected by a nearby river. Given the perturbations to the initial conditions and SWR parameters, we see an amplification of the ensemble spread. There is a substantial decrease in salinity over the 90 day simulation. There is a subtle interaction between the perturbed density structure that alters the sea surface height anomaly, in turn this contributes to substantially modifying the plume dynamics.

Surface variance fields for η , T and S after 1, 20 and 60 days from initialization (Fig. 4.3.12) give some insight into the dynamics that cause spatial patterns in the variance fields (see also the animations in the supplementary material). After 1 day, the variance of the initial perturbations is largely preserved. However, after 10 days, in areas subjected to flushing by the open ocean boundaries, the ensemble variance has almost collapsed to zero. Of significant interest, is the formation of two high variance structures in the sea surface elevation field (top centre). The first structure is in the deep water to the south of Papua New Guinea, and the second is near the southern boundary of the model. The northern structure has significant implications for the NGCC and the NOC, as variability in areas with strong gradients in SSH will modulate the strength of these coastal jets. Similarly, the southern area of high variance will determine the strength and location of the southward flowing EAC. The variance in the SSH field was entirely determined by perturbations to the SWR parameters and initial conditions of temperature and salinity. Therefore, if any model of the GBR region is to have any skill in predicting the location and magnitude of these coastal jets, the model needs to adequately represent the 3D baroclinic structure, with as little bias as possible.

By Day 60, the southern region of high SSH variability has substantially diminished, however the northern area of high variability has elongated along the offshore side of the shelf break, extending well north into the Gulf of Papua. The implications for of the SSH variability filed is seen in the surface variability fields for T and S. In areas where there is a high gradient in the SSH variability, the T and S variance is preserved or amplified. Furthermore, the variability in the density structure (not shown) has significant implications on the trajectory of river plumes in the near shore zone. This is demonstrated by the amplification of the salinity field near the

Fly River, Herbert, Tully and Fitzroy Rivers. There is also a significant signal in the variability of the T and S fields in areas of upwelling along the southern coastline of PNG.

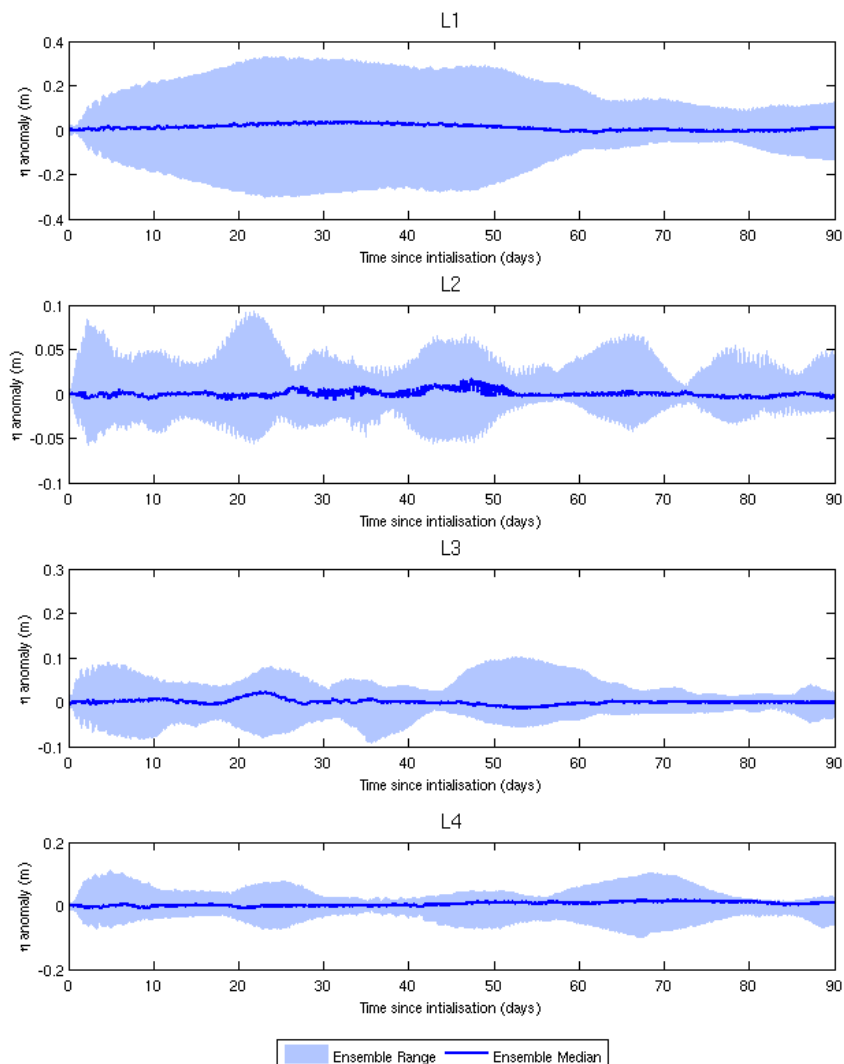


Figure 4.3.12: A time-series of the ensemble median and range for η , at L1- L4.

The implications of the ensemble behaviour directly affect the predictability of the GBR region. The inshore region behaves fairly linearly with respect to perturbations in initial conditions and parameters. The exception to this generalization is in the vicinity of river plumes, as evidenced by increase in salinity range seen in the surface layer at L4 (Fig. 4.3.9). Therefore, any DA system needs to account for these two distinct regions. To this end, the DA system will need to account for errors not only in the initial conditions, but also the boundary conditions, surface forcing and uncertainties in the model parameters. Furthermore, given that the trajectories remain relatively parallel for durations less than 10 days from initialization, the assimilation cycle and observation window used could be as long as 15-20 days. As it is also likely that biases appear over long spatial scales, and remain coherent, hence a relatively sparse observing system should be able to correct for these errors.

4.3.5.5 Conclusions

The ensemble responds strongly to surface fluxes in the well mixed inshore region and in the surface layers offshore. In areas strongly forced by the open ocean boundaries, the ensemble

experiences a near collapse at time scales approximately equal to flushing times from the boundary. The variation in the SWR parameters causes the ensemble to asymptotes towards a temperature value that allows the water column to reach a steady state equilibrium with the surface forcing. The inshore region is strongly damped by friction and does not exhibit any strong non-linear chaotic behaviour. On the other hand, offshore deep water sites display nonlinear and possibly chaotic behaviour beyond 25-30 days from initialization. Perturbations to the model state and parameters resulted in non-linear error growth in the salinity field in areas affected by river plumes and upwelling. In other areas, the ensemble maintained the initial perturbation range. The fact that bias still enters the model on time periods of greater than 30 days, suggests that there are other sources of model errors that are unaccounted for. The likely candidates are the sensible and latent heat fluxes. Similarly, errors are able to enter through the open ocean boundaries.

4.3.6 DA Algorithms applied to GBR4 hydrodynamics

4.3.6.1 EnOI for state estimation

Algorithm description

For pure state estimation, an Ensemble Optimal Interpolation (EnOI) approach that is described in Jones et al., (2012) and Oke et al., (2008, 2013) has been adopted. As before, if the state is denoted by:

$$\mathbf{w} = [\mathbf{u}, \mathbf{v}, \eta, \mathbf{T}, \mathbf{S}, \boldsymbol{\theta}]^T \quad 4.3.6$$

then the EnOI algorithm updates the state vector according to:

$$\mathbf{w}^a = \mathbf{w}^f + \mathbf{K}(\mathbf{w}^o - \mathbf{H}\mathbf{w}^f) \quad 4.3.7$$

where the superscript ^a, ^f and ^o denote the analysis, background and observations. \mathbf{K} is the Kalman gain matrix and \mathbf{H} is an observation operator that relates the model state to the observations. The Kalman gain matrix is given by:

$$\mathbf{K} = \mathbf{P}\mathbf{H}^T(\mathbf{H}\mathbf{P}\mathbf{H}^T + \mathbf{R})^{-1} \quad 4.3.8$$

\mathbf{R} is the observation error covariance matrix, which we assume to be diagonal, \mathbf{P} is the background error covariance matrix which is given by:

$$\mathbf{P} = \mathbf{A}\mathbf{A}^T/(N-1) \quad 4.3.9$$

Where \mathbf{A} is a static ensemble of anomaly fields and N is the ensemble size. There is some discretion as to the method used to calculate the anomalies. As discussed in Jones et al., (2012) the “short” time-scale used to construct the anomaly fields should represent the forecast errors, while precluding the effects of tides, while the longer time-scale, should be approximately equal to the time over which the errors enter the model.

Results

To assess correlation structure captured in \mathbf{A} , the footprints of the Heron Island mooring and Stradbroke island moorings were constructed (Figs. 4.3.13 and 4.3.14 respectively). Furthermore, the effect of the localisation function was also investigated. Localisation was supplied using an isotropic Gaussian function with a characteristic de-correlation length scale of 1.2 degrees latitude. As can be seen in Figs. 4.3.13 and 4.3.14, there exists realistic

longshore correlation structures, with a much shorter cross-shore de-correlation scale. It appears that there are significant amounts of spurious long range correlations, which support the use of the localisation functions.

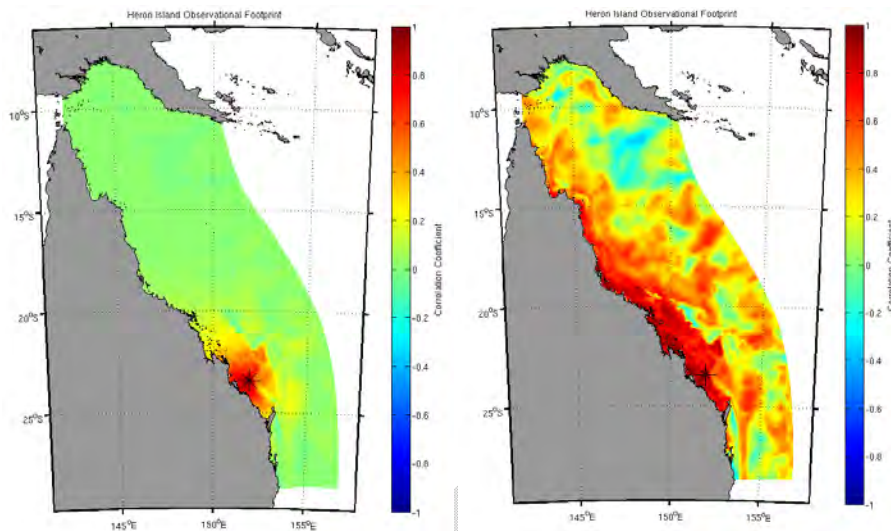


Figure 4.3.13. The observational footprint (spatial correlation structure) for the Heron Island mooring (denoted with an *) with localisation (left) and without localisation (right).

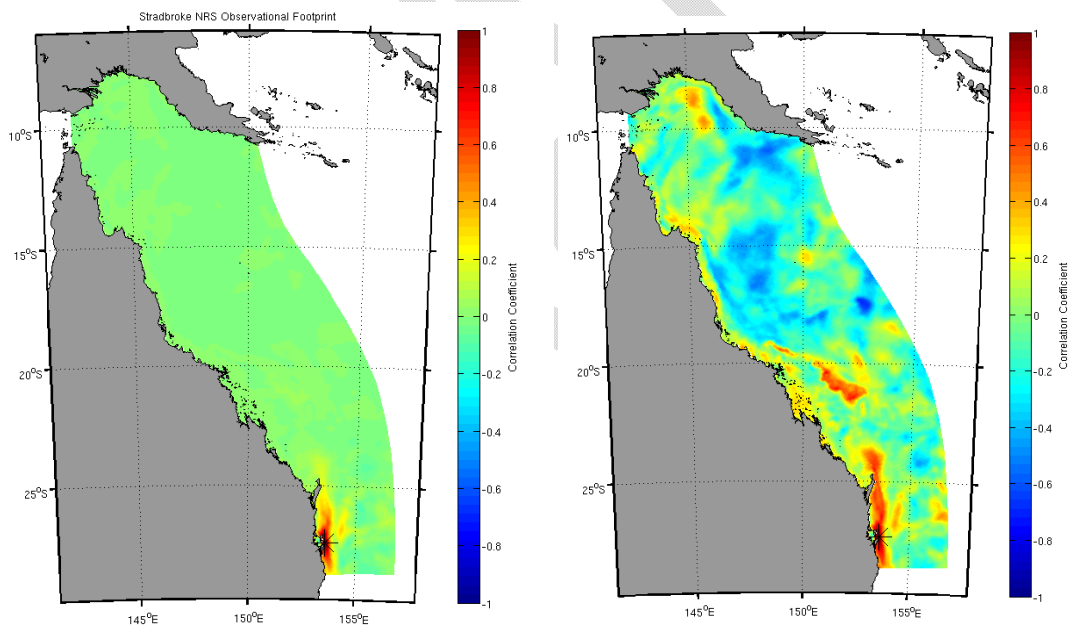


Figure 4.3.14. The observational footprint (spatial correlation structure) for the Stradbroke Island mooring (denoted with an *) with localisation (left) and without localisation (right).

In this phase of eReefs, the EnOI system has undergone a short pilot test, whereby the system was tested through 15 analysis cycles. The system was configured to produce an analysis field $\mathbf{w}^a(t)$ from the previous forecast cycle $\mathbf{w}^f(t)$. The model was then restarted at $t-6$ hrs and relaxed towards $\mathbf{w}^a(t)$ using adaptive linear relaxation. The state vector of the relaxed field is then denoted as $\mathbf{w}^{a*}(t)$. A 24hr forecast is made is $\mathbf{w}^{a*}(t)$ as the initial conditions. The analysis cycle is then repeated.

A pilot test of the GBR4 EnOI has proceeded with using 15 analysis cycles starting on the 4th of March 2011. A comparison between observations and the forecast field for temperature (T^f), is shown in Fig. 4.3.15. As can be seen in the comparison between the forecast and observations, there is generally reasonable agreement between the forecast model and the observations. It is clear that there does exist some small scale spatial variability within the observations, which in many cases is captured by the forecast.

When these observations are assimilated and analysis fields are constructed, the model is then relaxed towards the analysis fields (Fig. 4.3.16). There is an improvement in the agreement between the relaxed field (T^{a*}) and observations, with many more of the small-medium scale features captured in this field. This is especially evident in the southern region of the domain where the EAC is focussed to the east and south of Fraser Island. Furthermore, the Hiri Current system is also improved in the relaxed fields.

The difference between the relaxed field (T^{a*}) and the forecast field (T^f) gives an indication of where temperature is gained or lost. The innovations ($w^o - Hw^f$) are overlaid to give an indication of model/observation mismatch. As can be seen, there is a large coherent gain in temperature in the central, eastern and southern portions of the domain. There is good agreement between the increments and innovations, without the appearance of over-fitting.

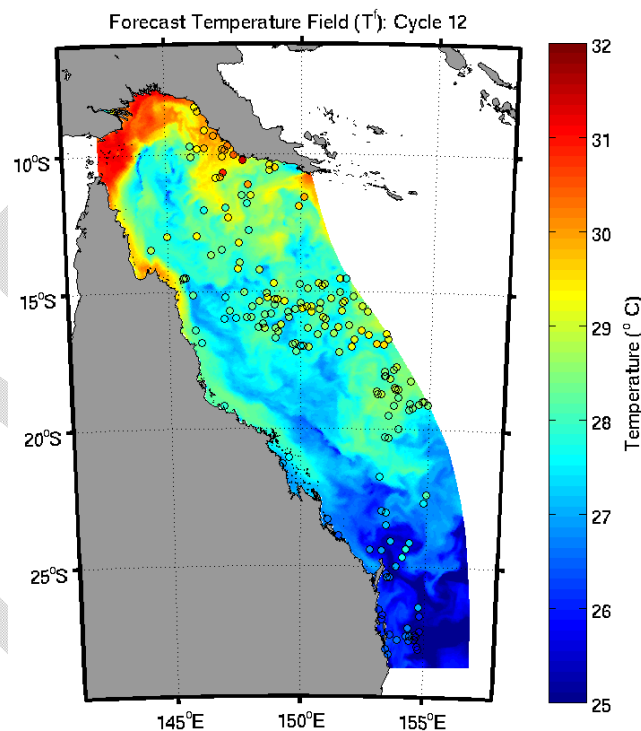


Figure 4.3.15. A comparison between the forecast field for surface temperature (T^f), and observations (coloured circles) for analysis cycle 15.

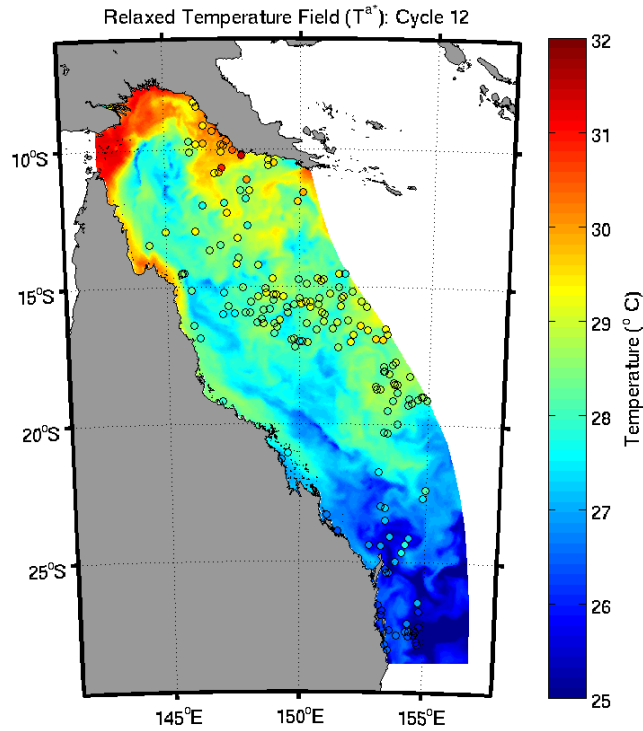


Figure 4.3.16. A comparison between the surface temperature field (T^{a*}) that has been relaxed towards the analysis field (T^a), and observations (coloured circles) for analysis cycle 15.

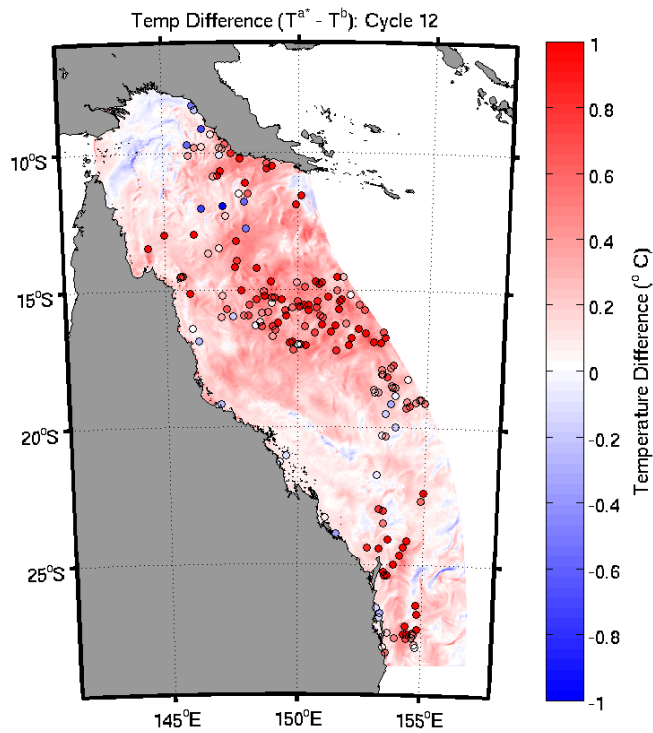


Figure 4.3.17. A comparison between the $T^{a*} - T^b$, and innovations between the observations and forecast field (coloured circles) for analysis cycle 15.

The mean increment across all assimilation cycles can give an indication of the presence of bias (Fig. 4.3.18). If the system is regularly adding or subtracting heat from the model, this gives an indication that there are errors entering the system through either the forcing term, and/or internal model parameterisations. The mean increment for temperature in the surface layer ranges between +0.1 and +0.6°C. This pattern is repeated, though at a lesser magnitude at -13m. However, it does not appear that this spatially coherent bias is present at -120m. This result indicates that there is a process that is causing the surface layer to be too cool and enters over relatively short time scales. As previously mentioned, the SWR parameters are uncertain and expected to vary spatially across the domain.

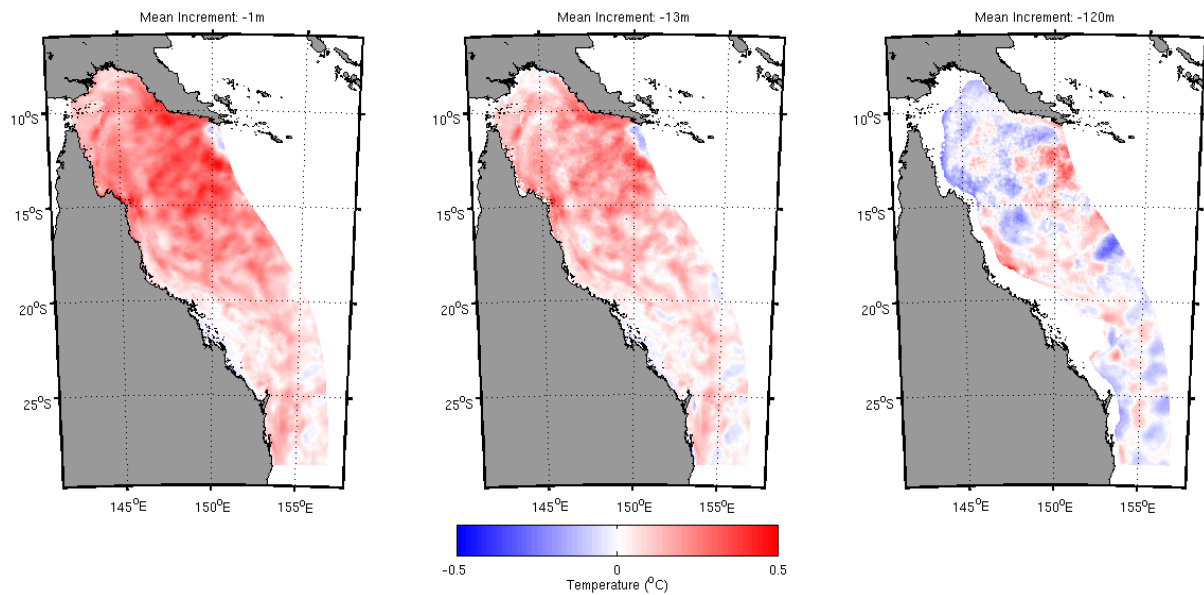


Figure 4.3.18. The mean increment added to the background field during the 15 analysis cycles for the surface (left), -13m (centre) and -120m (right).

To assess the overall performance of the DA scheme, a time-series of RMSD between observations and the forecast, analysis, relaxed and persistence fields are given in Fig. 4.3.19. The RMSD of the forecast field typically ranges between 0.6 and 1.0°C. The relaxed fields improve on the forecast fields by reducing the RMSD by between 0.2 and 0.4°C. However, as is usually the case over short assimilation cycles, the persistence ($T^a(t-1) - T^{obs}$) fields beat the forecast by between 0.1 and 0.2°C. It should be noted that typical observation errors are of the order 0.5°C, and therefore both the forecast and relaxed fields are performing remarkably well when compared with observations.

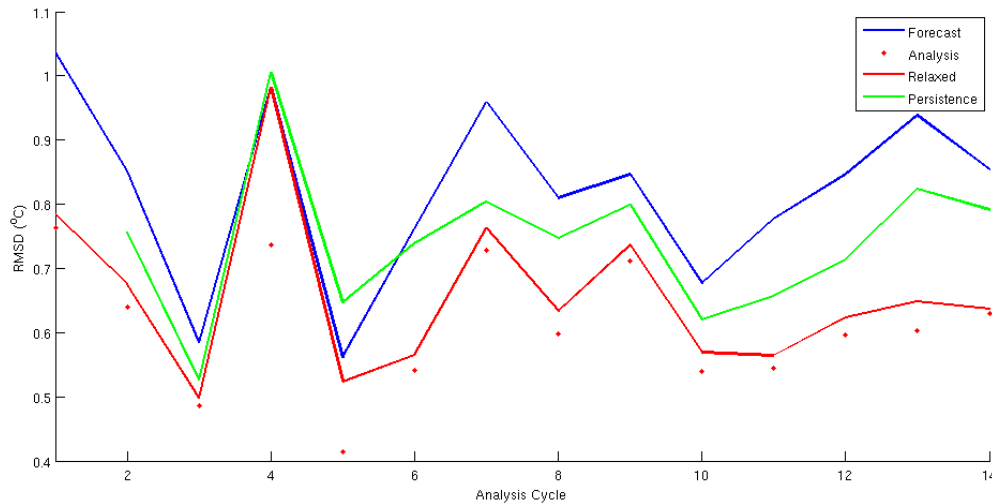


Figure 4.3.19. A time series of the root mean square difference (RMSD) between the observations and the forecast, analysis, relaxed and persistence fields.

It is well known that persistent biases in the forecast fields lead to sub-optimal results in an assimilation system. Given that the mean increment presented in Fig. 4.3.18 is in the order of 0.5°C and the ensemble range caused by perturbations in the SWR parameters is typically 1°C in the surface layer (Fig. 4.3.5 – Figure 4.3.8), this suggests that the model solution and also the performance of the assimilation scheme would benefit from joint state and parameter estimation. If the biases are neglected, the assimilation scheme cannot be expected to result in optimal analysis fields.

4.3.6.2 EnKF for joint state and parameter estimation

As mentioned in Section 4.3.4, internal model parametrization can have a significant impact on the model solution, and more importantly be the source of bias. A key example of this is the parameters that control the distribution of short-wave energy throughout the water column. Depending on the parameter set chosen, the water column can reside in one of two stable domains; (1) well mixed by buoyancy forcing (i.e. heating at the bottom, causing an overturning of the water column, or (2) stratified by heating in the surface. There should exist some form of correlation (linear or otherwise) between the short-wave parameters (R_t , R_a and R_b), and the temperature structure. This is clearly evident from Figs. 4.3.5-8. In shallow areas that behave in a quasi-linear manner, an augmented Kalman Filter may be able to quantitatively estimate these parameters.

The EnOI update equation given in Eq. 4.3.6 – 4.3.9 are a special case of the more general Ensemble Kalman Filter Equation (Evensen, 2009). As expressed in equation 4.3.6, the state vector can be augmented with parameters, and updated sequentially through time. In the case of EnOI, using a static background error covariance matrix, it is not possible to update θ , unless there is a prescribed spatial statistical model that can be used for a prior over θ . In this instance we have chosen to adopt the Deterministic EnKF of Sakov and Oke (2008) and augment the state vector with θ . Data from in situ temperature loggers, moorings and GHRSSST were assimilated every 5 days, with a window 4 hrs wide centred on the analysis time. The assimilation period spanned 1st April 2011 – 30th June 2011. At this stage, we do not

nudge the model towards w^a , we only update θ . The ensemble mean θ at the end of the assimilating run is then used in a subsequent long hindcast of the hydrodynamic model. State updating has been avoided to provide self consistent trajectories for the BGC model. It is this long run, with updated parameters that is then compared to GHRSSST observations in Figs, 4.3.23 – 4.3.24.

Fig. 4.3.20 – 4.3.22 present the ensemble mean for R_t , R_a and R_b respectively. As can be seen, there is a strong cross shore gradient in all parameters, with the shallow lagoon system having lower R_t and high R_a than the offshore water. Similarly, R_b is approximately 0.45 inshore, however in deep offshore waters that are not influenced by this parameter, R_b takes on the prior mean value.

Parameter values for R_a and R_t have a physical interpretation, in that the water quality within the lagoon system and inshore GBR waters are strongly influenced by freshwater injected into the system by river discharge. The hydrodynamic model does not explicitly account for the differing optical properties of the inshore region of freshwater influence. Therefore, the shortwave parameters need to account for the optical difference of the regions and the subsequent impact on heat distribution in the water column.

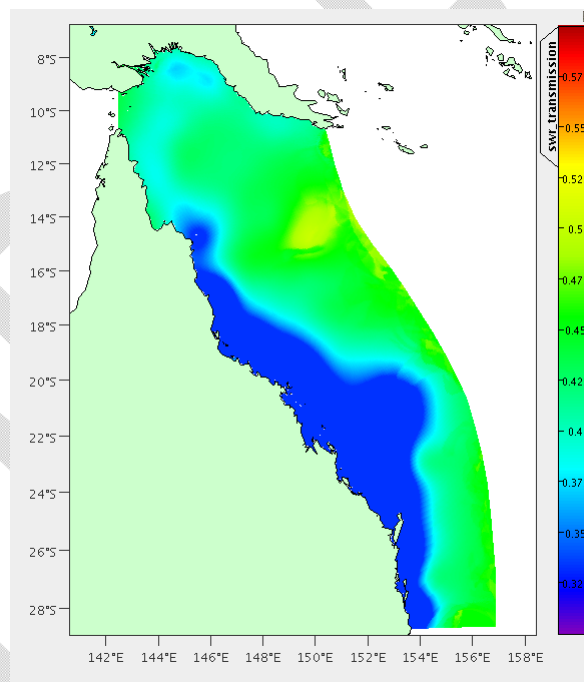


Figure 4.3.20. The ensemble mean for R_t

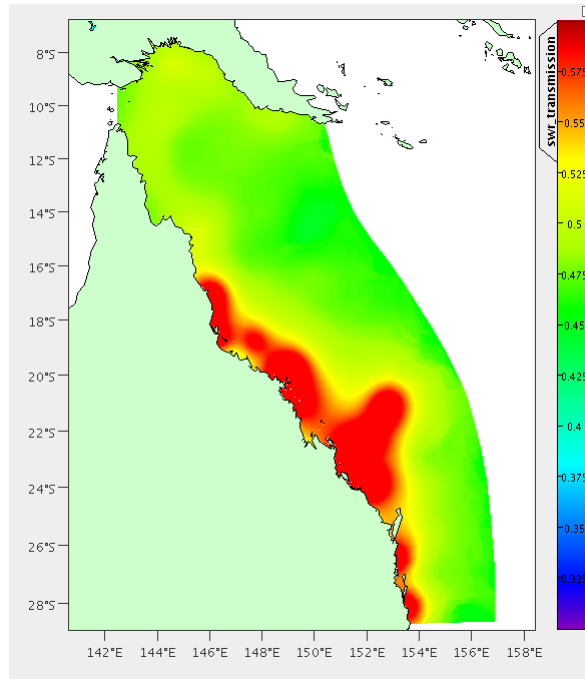


Figure 4.3.21. The Ensemble mean for R_a .

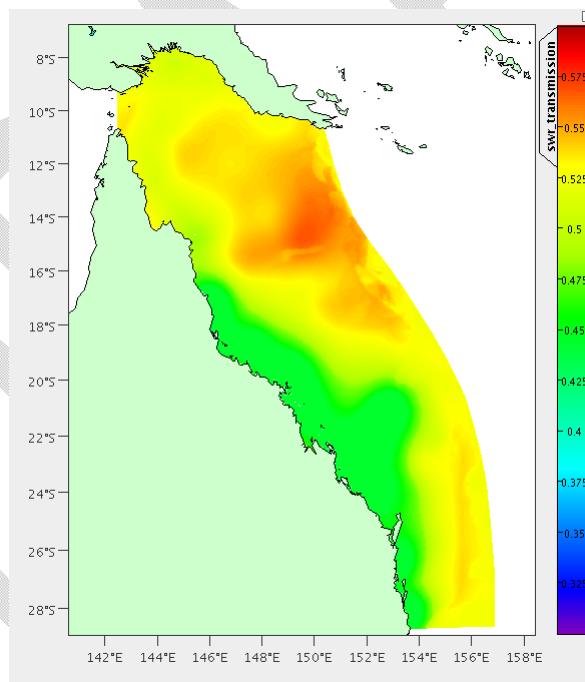


Figure 4.3.22. The ensemble mean for bottom absorption R_b

A quantitative comparison using a 2D histogram between the control run without assimilation (Fig. 4.3.23) and the run with the modified SWR parameters (Fig. 4.3.24), shows the run with parameter estimation has removed substantial bias in the comparison with GHR SST data. This is most notable in Fig. 4.3.25, which shows the difference between Figs. 4.3.23 and 4.3.24. Areas of blue denote combination where mass has been subtracted, while red areas denote combination where mass has been added. Clearly the parameter estimation routine has shifted mass towards the 1:1 line in Fig. 4.3.25.

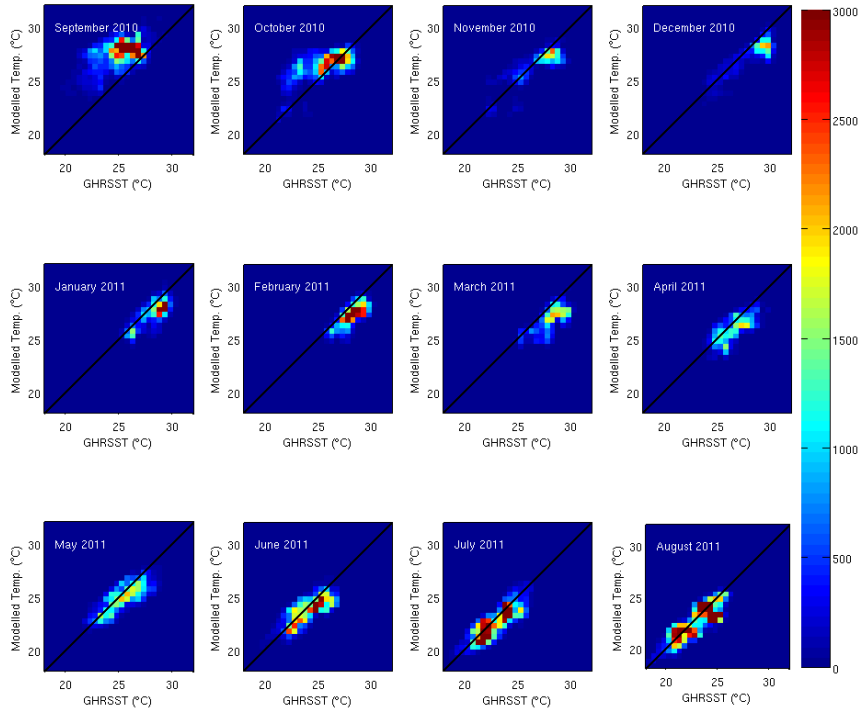


Figure 4.3.23. A 2D histogram displaying the mass of GHRSSST observations vs. predicted SST for the control run with no parameter estimation.

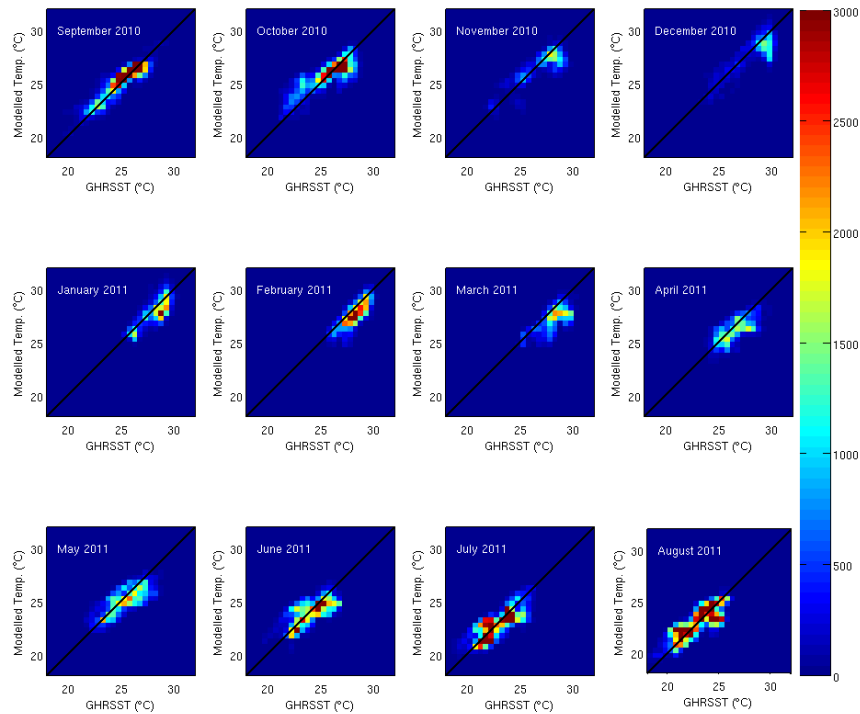


Figure 4.3.24. A 2D histogram displaying the mass of GHRSSST observations vs. predicted SST for the assimilating run.

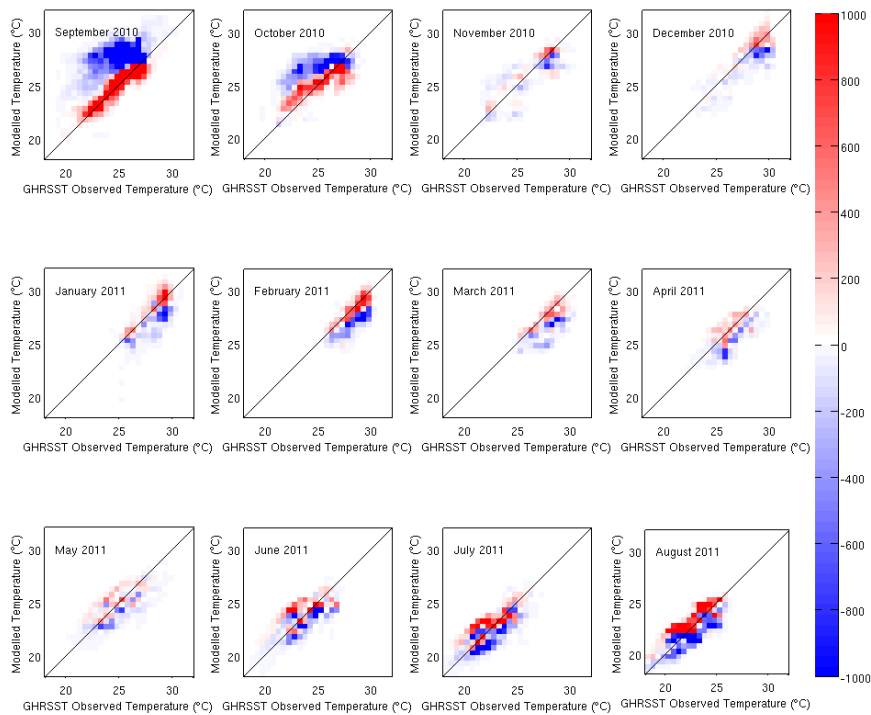


Figure 4.3.25. The difference between the 2D histogram of the control run (Fig. 4.3.23) and the assimilating run (Fig. 4.3.24).

Therefore, using a combination of SST data and in-situ temperature profiles, the augmented EnKF system can infer the time invariant, but spatially dependent short wave radiation parameters (attenuation, transmission and bottom absorption). Furthermore, we have demonstrated that the model is sensitive to these parameters and if naively tuned can lead to substantial bias in shallow coastal regions.

4.3.7 Data Assimilation Pilot Summary

Two DA schemes were tested and deemed suitable for use on the GBR4 grid. The EnOI scheme has been trialled over a short period and has shown to substantially improve the temperature fields of the GBR4 model. There is evidence of bias in the model forecasts due to the mean increments ranging from 0.2 – 0.5°C in the surface layers. Therefore, a joint state-parameter estimation scheme should yield improved results. Furthermore, acknowledging that GBR4 will be used to force a BGC model, we have also implemented an EnKF scheme that performs parameter estimation alone. This has been undertaken to avoid shocks to the system during the analysis step. Shock must be avoided as it is well known that these deleterious effects on the BGC models. Also, when GBR4 is used for scenario runs, state updating is not an option. Both schemes are able to perform state estimation, with the latter tailored to the spatial estimation of parameters. There is a clear goal to try and use the DA system to reduce the error entering the model from BC's and internal model parameterizations. We see this as an important step forward, as sequential updating of the state in hydrodynamic models has been shown to degrade the solutions to embedded BGC models. However, we are yet to demonstrate this in the GBR domain. The running of a full EnKF scheme on the GBR4 domain would require computing power that is currently unavailable to eReefs project, therefore for a long multi-year reanalysis, the EnOI system is the only feasible approach.

4.3.8 GBR4 Hydrodynamic model 4 year reanalysis

The EnOI system was run from January 2011 until December 2014 and assimilating a combination of temperature data from moorings (AIMS and GBROOS/IMOS), gliders (CSIRO and IMOS) and SST (GHRSSST L3S from IMOS). This product is the first version of a reanalysis undertaken for the GBR4 grid.

Construction of new model anomaly fields:

A key step in implementing the simple Ensemble Optimal Interpolation (EnOI) is the generation of a representative field of background anomalies that are used in the static background error covariance matrix. During Phase 1, a short model run (1 year) was used to generate these fields. There is now a realistic 4-year simulation that we have used to generate a new set of background fields for use in the DA.

State Estimation

The EnOI system has been run on the hydrodynamics and is presently completed September 2010 to January 2014. The archive is continually increasing as this system catches up to behind real time. This reanalysis is being run at the NCI where compute resources allow assimilation of the full range of observations. Once the reanalysis has caught up to real time, it will continue to be appended to in real-time using the DA in the TRIKE infrastructure run locally. The local compute architecture is not sufficient to ingest the full observational dataset, hence will be run using a truncated dataset that will result in an assimilated product of lesser skill. If, in the future, a reanalysis is required using the full observations, then this will be required to be re-run at the NCI under a separate project.

Reanalysis Results:

The reanalysis has been assessed using two sets of independent observations, firstly those from a withheld set comprising of data from the Queensland wave rider network, and secondly we use the forecast errors (before assimilation takes place).

Data from the Queensland wave rider buoys were withheld from the reanalysis system for validation purposes. Time series of the reanalysis and control runs at each of these sites can be found in Figures 4.3.26– 4.3.32 below. Both the control and reanalysis products capture the seasonal cycle, however, the control run is biased in some regions by up to 2 degrees C. In most cases, the reanalysis products have a lower Root Mean Square Difference (RMSD) between the model and observations, by between 0.2 and 0.5 degrees C. The reanalysis RMSD is typically between 0.4 and 0.6 degrees C, which is comparable to the diagonal of the observation error covariance matrix applied to the SST observations that are assimilated.

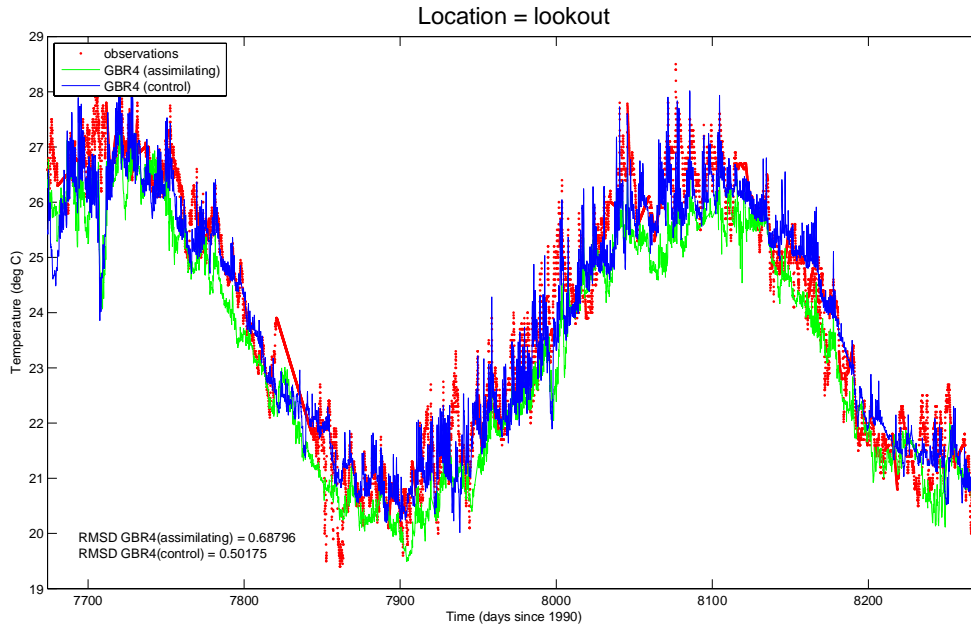


Figure 4.3.26: time series of the observations (red dots), assimilating model (green) and control run of the model (blue) for the Point Lookout waverider.

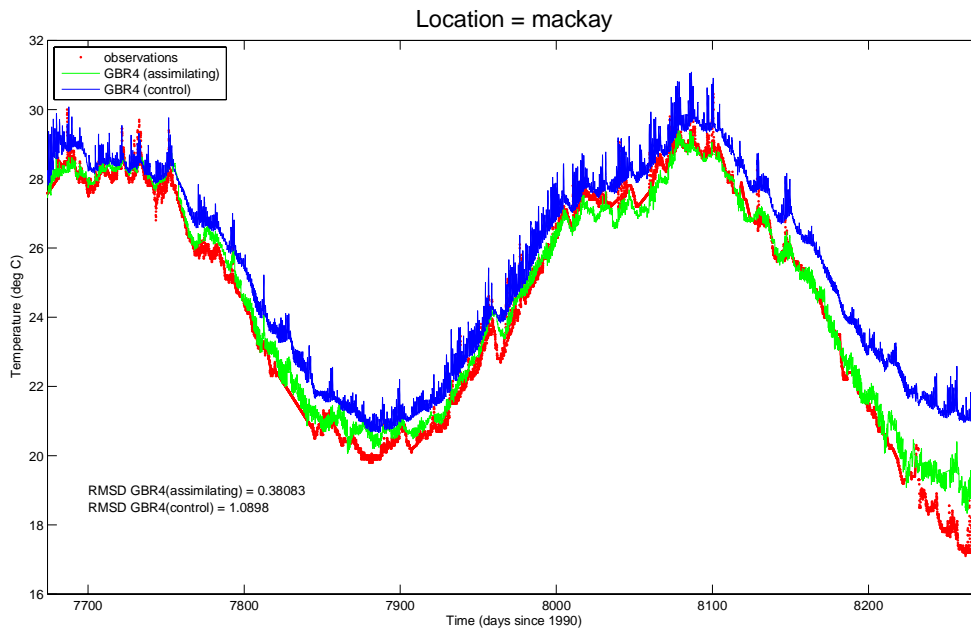


Figure 4.3.27: time series of the observations (red dots), assimilating model (green) and control run of the model (blue) for Mackay waverider.

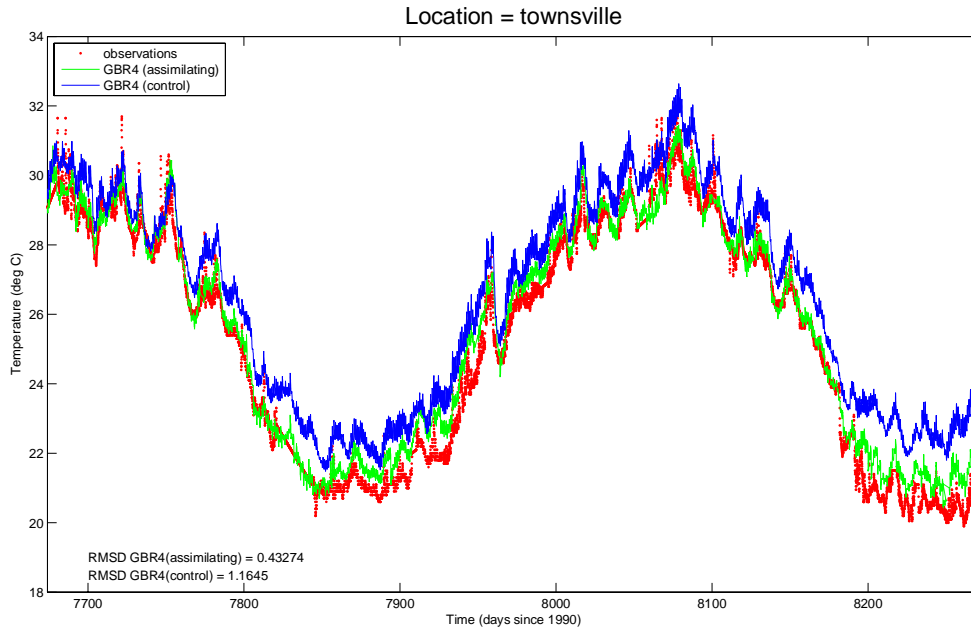


Figure 4.3.28: time series of the observations (red dots), assimilating model (green) and control run of the model (blue) for the Townsville waverider.

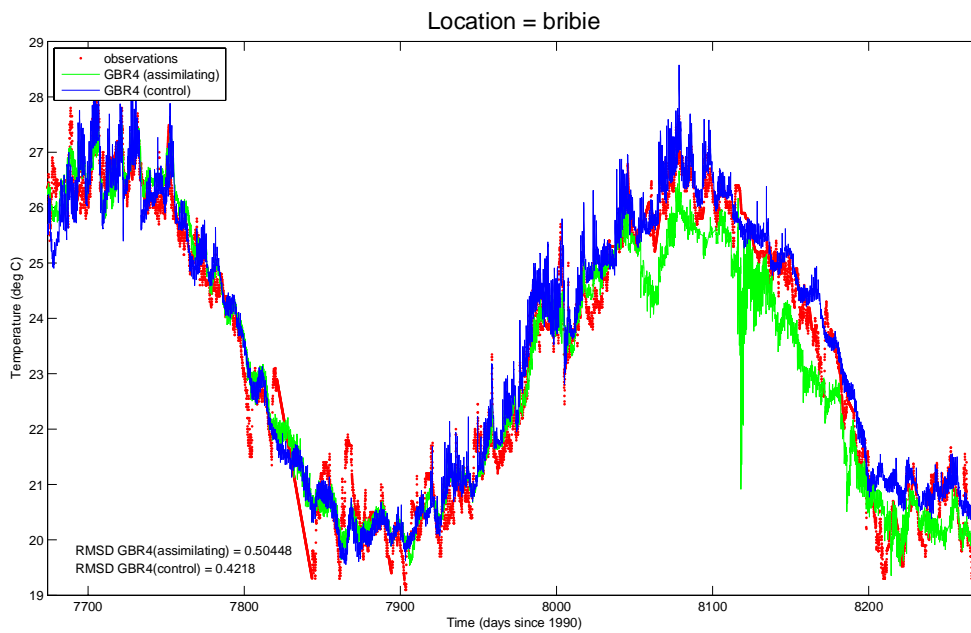


Figure 4.3.29: time series of the observations (red dots), assimilating model (green) and control run of the model (blue) for the Bribie Island waverider.

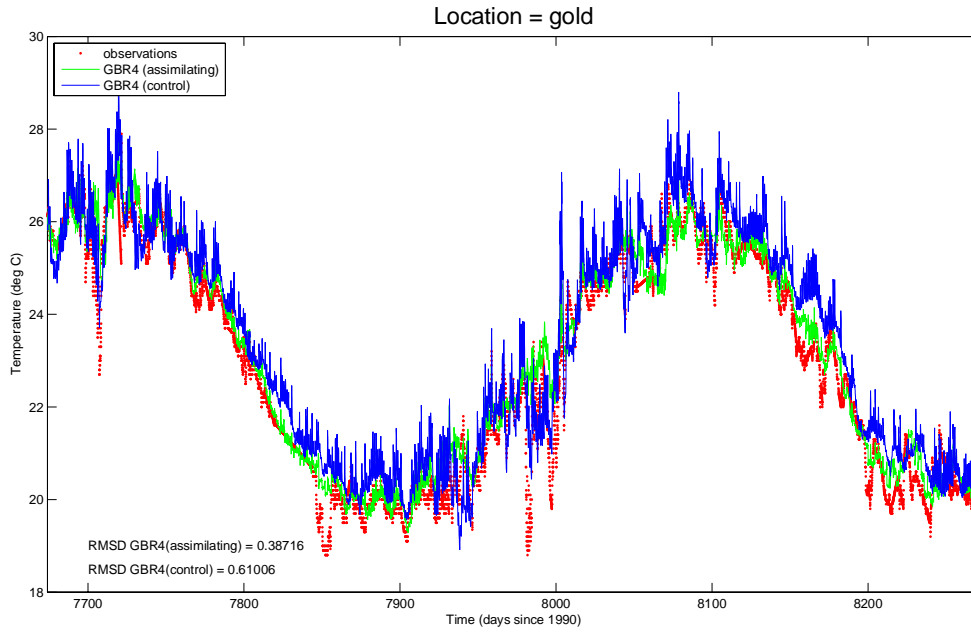


Figure 4.3.30: time series of the observations (red dots), assimilating model (green) and control run of the model (blue) for the Gold Coast waverider.

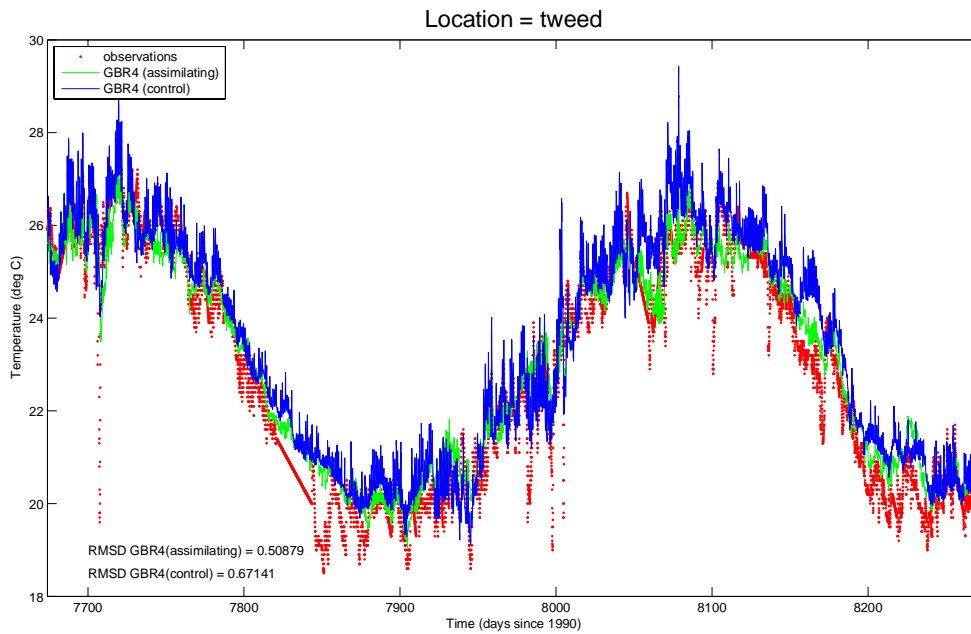


Figure 4.3.31: time series of the observations (red dots), assimilating model (green) and control run of the model (blue) for the Tweed Heads waverider.

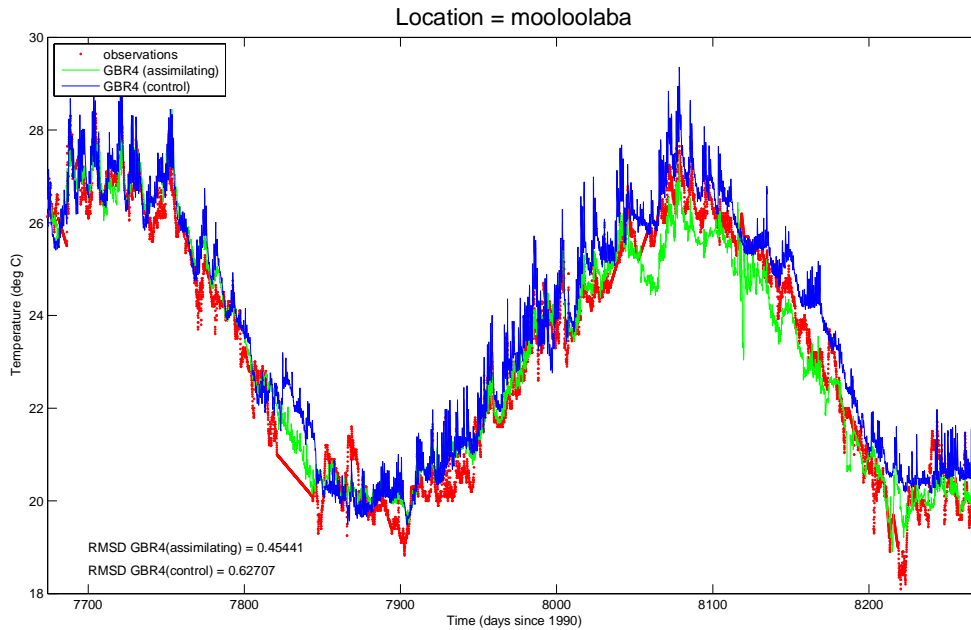


Figure 4.3.32: time series of the observations (red dots), assimilating model (green) and control run of the model (blue) for the Mooloolaba waverider.

A time series of the domain wide forecast error and analysis error suggests that the temporal variability of the error is at a minimum in the dry season, which is related to the number of observations available for assimilation. During the dry season there is less cloud cover, which allows for a great spatial area to be constrained by the assimilation system. During the wet season when cloud obscured a large portion of the domain, some regions may go many days with very few SST observations. This allows for a substantial increase in forecast error, ultimately resulting in the system having an RMSD of up to 1°C at times.

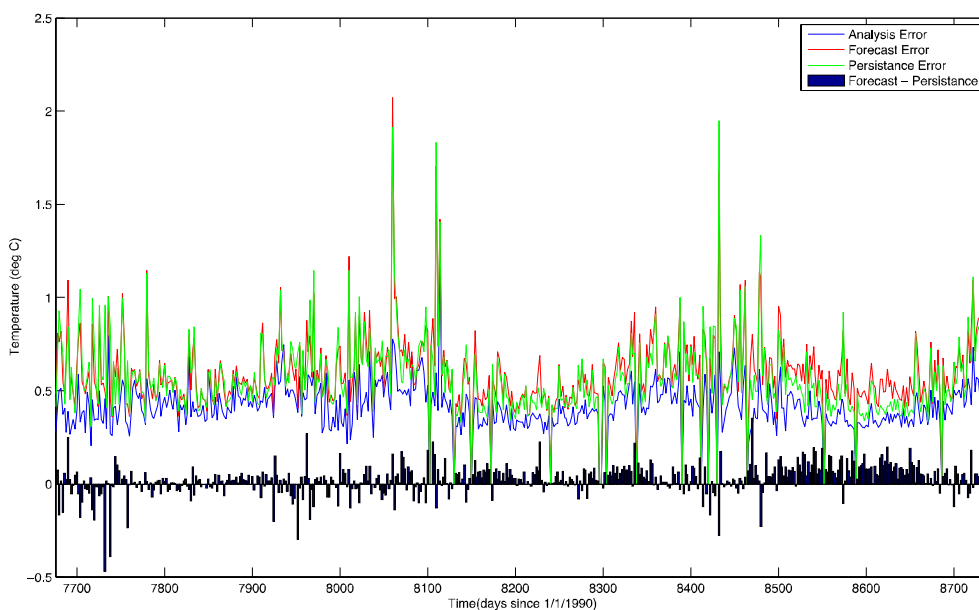


Figure 4.3.33: A times series of the analysis error (blue), forecast error (red) and persisting the analysis field forwards 1 cycle (green). The Forecast – Persistence is then given by the bar graph.

Model Bias

The EnOI system was run using two model configurations for the first 3 months of 2011 to investigate the effects of using spatially variable parameters within the reanalysis system. Experiments were undertaken using 1.) Spatially constant shortwave parameters and 2.) those derived from the augmented EnKF from Section 4.3.6.2 above. The increments added to the background state vector at each assimilation step can give insight into the existence of persistent model bias. If the increments are positive (negative), it suggests that during the forecast step, bias is able to creep in by making the model too cool (warm). By taking the temporal average of the increment field over January 2011 – March 2011 (inclusive), the spatially uniform parameters result in a solution that is biased towards being too warm (Fig. 4.3.34, top panel, see Section 4.3.6.1). By using the spatially varying parameters from the augmented EnKF, the bias is substantially reduced (Fig. 4.3.34, low panel), to less than 0.2 degrees C. Given that it is the optical characteristics that determine the distribution of short-wave energy, it is likely that unresolved processes contribute to this bias.

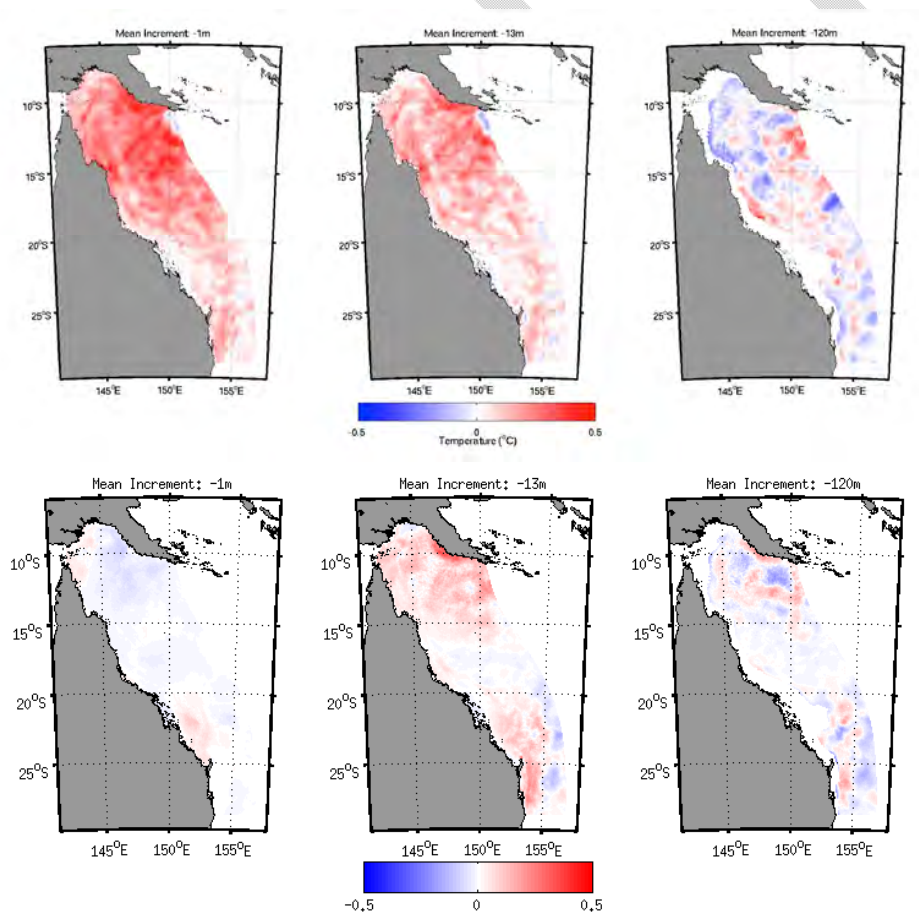


Figure 4.3.34. The mean increments for 1/1/11 – 1/4/11 applied to the forecast fields in the Ensemble Optimal Interpolation DA system. The top panel is the mean increments using spatially uniform short-wave parameters. The lower panel is the mean increments using the spatially varying parameters shown in Fig. 4.3.26.

4.3.9 BGC Data Assimilation

The BGC DA progressed on three fronts. At best this is a proof of concept, and to draw substantive conclusions a more thorough assessment against in-situ BGC observations is required. However, the results are very promising, and the assimilation of satellite remote sensing data is able to reduce errors associated with some biogeochemical variables. Two approaches have been tested, that are very similar to those used in the hydrodynamics. Firstly, an EnOI system using static background error covariances is used. Secondly, an EnKF with perturbed initial conditions, parameters (small and large zooplankton mortality rates), and head of estuary loads (NH₄, NO₃, DIP and Fine Sediments). The former method (EnOI) is computationally efficient, whereas the EnKF system is expensive and sensitive to ensemble collapse.

In this study, four data assimilation experiments were undertaken. In each case remotely sensed products were assimilated and compared against withheld mooring data for the purposes of system assessment. The three EnOI experiment undertaken were set up to assess the suitability of remote sensing products for assimilation, while the fourth experiment was used to test the advantage gained from using a more complex and expensive assimilation system (the EnKF). The details of the experiments are:

EnOI1: We assume that the MODIS OC3 derived Chl-a product is equivalent to the modeled total Chl-a concentration in the surface layer of the model. In this experiment we expect a “difference in kind” or more commonly known as a representation error to be present, as we know that MODIS OC3 chl-a concentration in the coastal zone is severely error prone to contamination by other optically active constituents. Nonetheless there are many studies that try and compare modeled Chl-a with MODIS OC3, and it is still widely used.

EnOI2: We assume that observed MODIS OC3 derived Chl-a is equivalent to the simulated OC3 from the BGC model. The expectation is that the model error arising from the misplacement of BGC features is the dominant source of error, rather than representation error. We use the in water optical model (see Section 4.7.4.1) to simulate the model derived OC3 Chl-a.

EnOI3: We assume that observed reflectance at 443, 488 and 555 nm are directly equivalent to modeled reflectances at the same wavelengths. Again, the expectation is that model error dominates, rather than errors associated with difference in kind.

EnKF1: This experiment is similar to EnOI3, except that an EnKF system is used with 36 dynamic ensemble members with perturbed initial conditions, head of estuary nutrient and sediment loads and zooplankton mortality parameters. This experiment is computationally expensive and was run to explore the possible advantages of a dynamic background ensemble.

4.3.9.1 BGC Spatial Covariance's

Every DA techniques uses some form of statistical model to spread the information from an observation to other unobserved variables and locations in the model domain. The two main ensemble methods (EnOI and EnKF) rely on the model to create these spatial (cross-) covariance's. The EnOI method uses a long integration of the model to build up an ensemble of anomaly fields that represent the main modes of model error. The EnKF method uses an ensemble of models with each member being subjected to a unique perturbation representative of the main source of model error. Both techniques rely on a stable and semi-

realistic model implementation; this requirement is common to both the BGC and hydrodynamics.

It is difficult to assess the model generated spatial covariance against those naturally occurring. Recent work by Jones et al., (2015) use MODIS OC3 Chl-a anomalies to investigate “observed” covariances for all the IMOS NRS sites. While there are known problems with MODIS OC3 Chl-a in coastal regions, recent work by Baird et al., (2014) has allowed us to simulate the OC3 Chl-a. The comparison between MODIS OC3 and modeled OC3 covariances at the Yongala NRS (Fig. 4.3.35), displays good agreement within 60km of the mooring site. However, more broadly, the long-shore correlation patterns are very similar between the two products. Based on the similarities between the products, this provides a reasonable level of confidence that the modeled anomaly fields are suitable for assimilation purposes in the EnOI system.

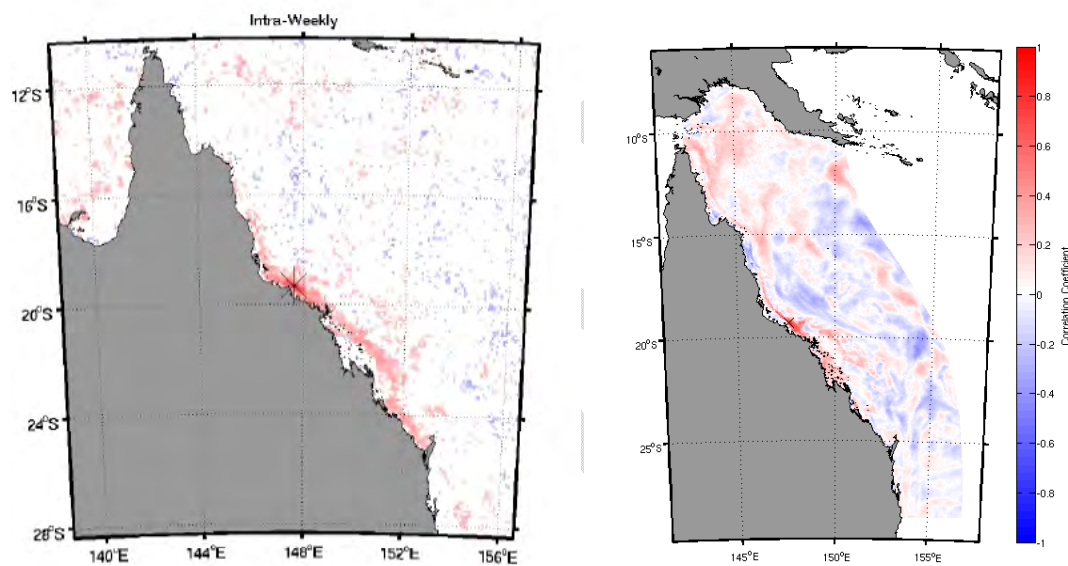


Figure 4.3.35. The spatial covariance field for Chl-a derived from (left) MODIS OC3 and (right) the modeled OC3.

4.3.9.2 Observing System Design Strategies

The anomaly fields used for EnOI described above are multivariate and can be used to assess the footprint and ability of a regional observing system to constrain model variables. Within the eReefs domain, the in-situ observing system is relatively sparse. The moorings within the central GBR typically observed the lagoon and fringing reefs with a correlation coefficient of 0.75 or higher (Fig. 4.3.36). However, the region to the north of 15°S, is very poorly observed with in-situ moorings (Fig. 4.3.36). The area to the south of 20°S, is also patchy with large gaps near Broad Sound (Fig. 4.3.36).

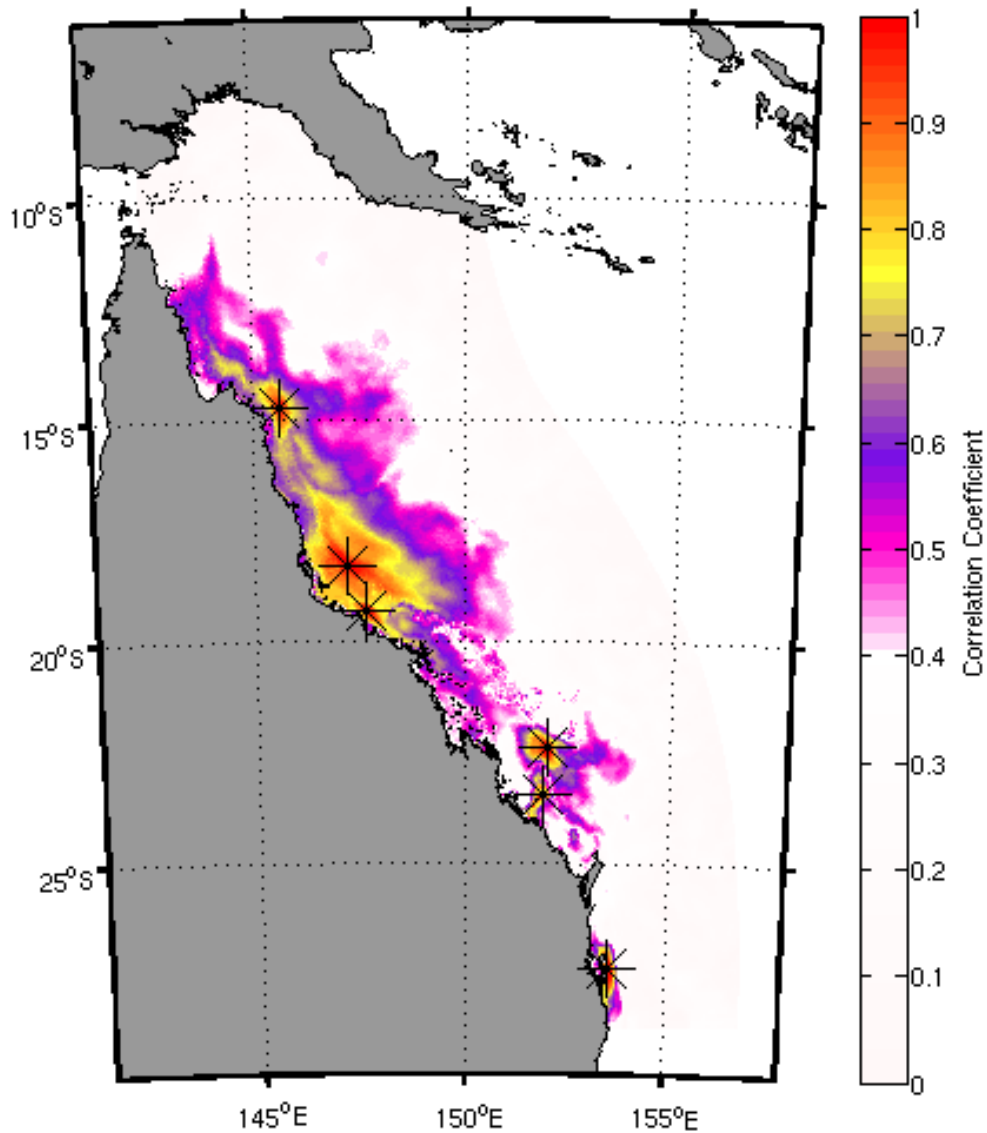


Figure 4.3.36. The maximum absolute correlation (Chl-a) of the Great Barrier Reef Observing System moorings that have (or had) water quality meters.

The multivariate composition of the anomaly fields used in EnOI allows for an observed variable (e.g. Chl-a) to spread information (project) onto an unobserved variable (e.g. Phytoplankton Nitrogen concentration). With the inclusion of an optical model, the cross correlation between optical variables and BGC state variables can be included in the assimilation scheme.

An example of this effect is the cross-correlation between the reflectance at 488nm and modeled dissolved inorganic nutrients (Fig. 4.3.37, left). Given an observation at the bandwidth at Yongala, there is a strong positive correlation immediately to the WNW of the observation site, but a strong negative correlation along the fringing reefs and to the SE. Additionally, there is a correlation of between 0.4 – 0.6 for much of the deeper western Coral Sea. The cross-correlation between the reflectance at 531nm and Small Phytoplankton Nitrogen is limited to a region close to Yongala (within 20km) but there are some weak long-range negative correlations with the fringing reefs to the north (Fig. 4.3.37, right).

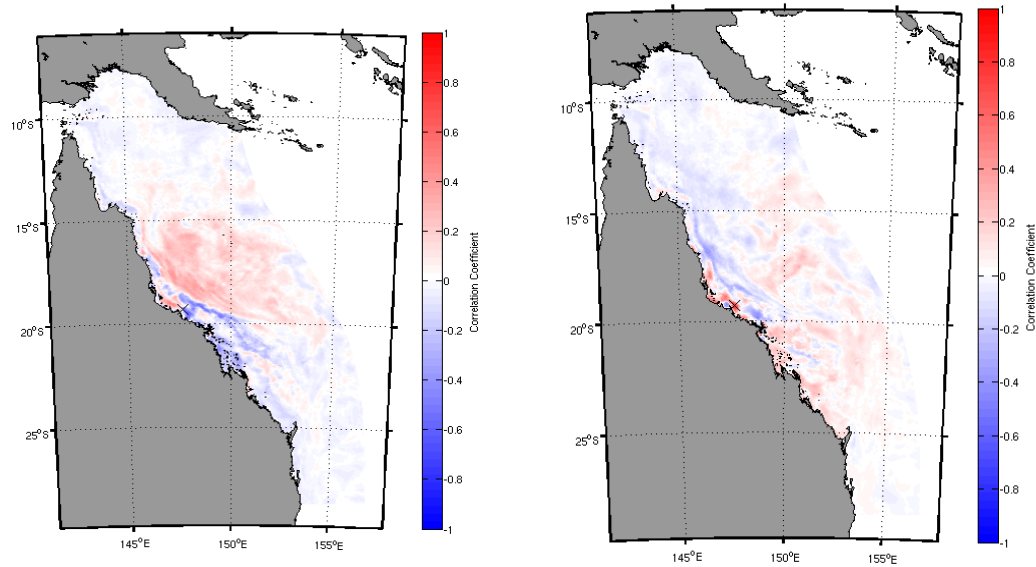


Figure 4.3.37. (Left) Modelled reflectance (488nm) at Yongala cross-correlated with modelled dissolved inorganic nitrogen (nutrients). (Right) Modelled reflectance (531 nm) at Yongala cross-correlated with modelled small phytoplankton nitrogen

There have been few studies to date that try coupled DA whereby observations of hydrodynamic and BGC variables are assimilated simultaneously. However, due to the eReefs models including optical active constituents introduced through the catchment models, there may be an opportunity to constrain salinity using MODIS reflectances. Preliminary results suggest that the modelled reflectance at 443nm projects strongly onto salinity at Yongala (Fig. 4.3.38). This observation constrains not only the signal at Yongala but also surrounding lagoon waters within a 100 km radius.

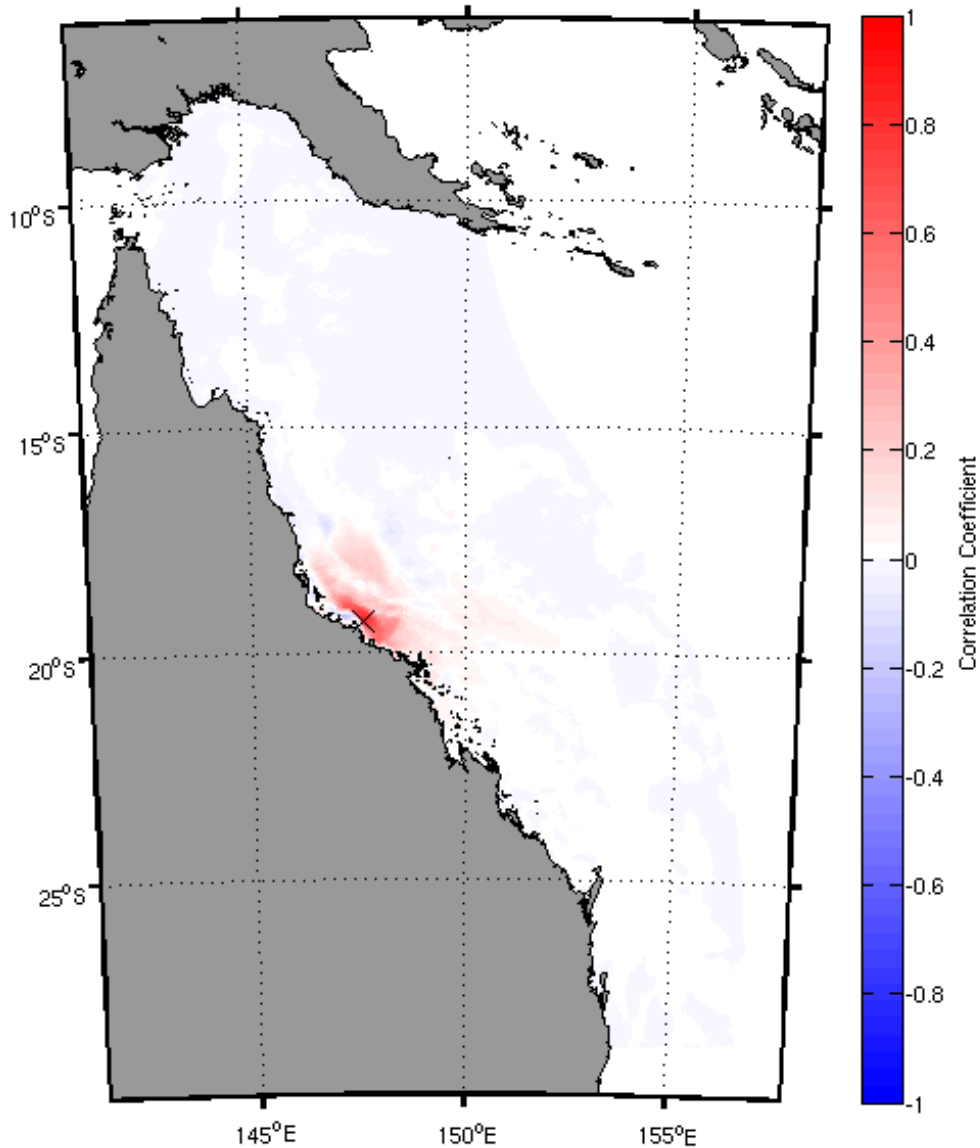


Figure 4.3.38: Modelled reflectance (443nm) at Yongala cross-correlated with salinity.

4.3.9.3 BGC DA: EnOI

In the series of panels below 4.3.39-41, the forecast fields for reflectance at 443 nm and 488nm are shown, when a subset of observations are assimilated, the analysis fields in the lower panels of each figure result. A validation set of withheld observations are plotted over the top in each panel. Where there is an obvious colour difference, there is a difference in magnitude between the observed and modelled reflectance. If the colours are the same, then the error is small. Both the 443 and 488 forecast fields over predict the inshore reflectance, resulting in a large cross-shelf gradient. When reflectance observations are assimilated, the cross-shelf reflectance gradient is reduced and the model prediction is substantially improved.

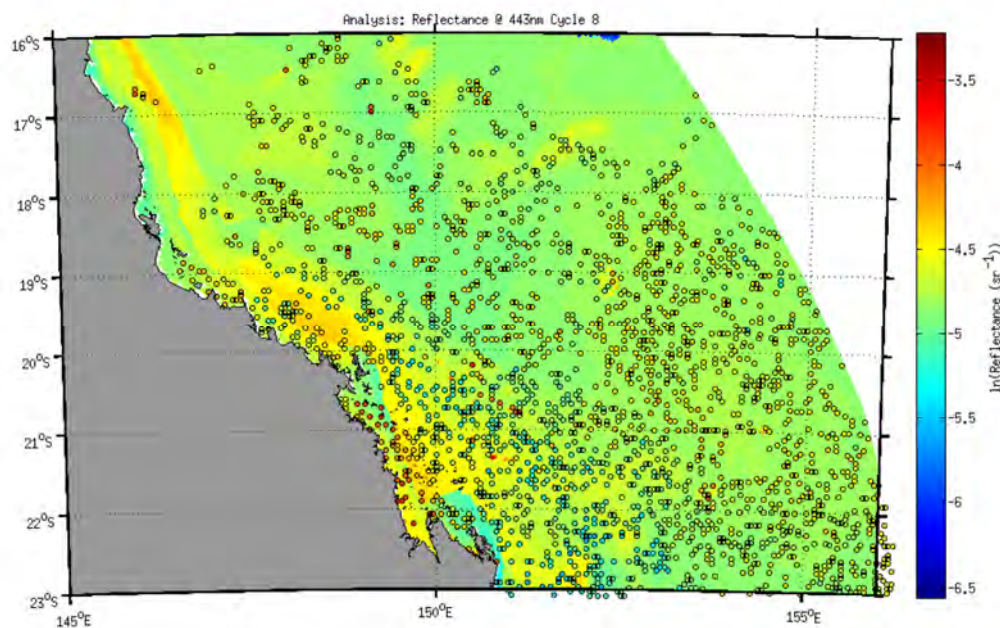
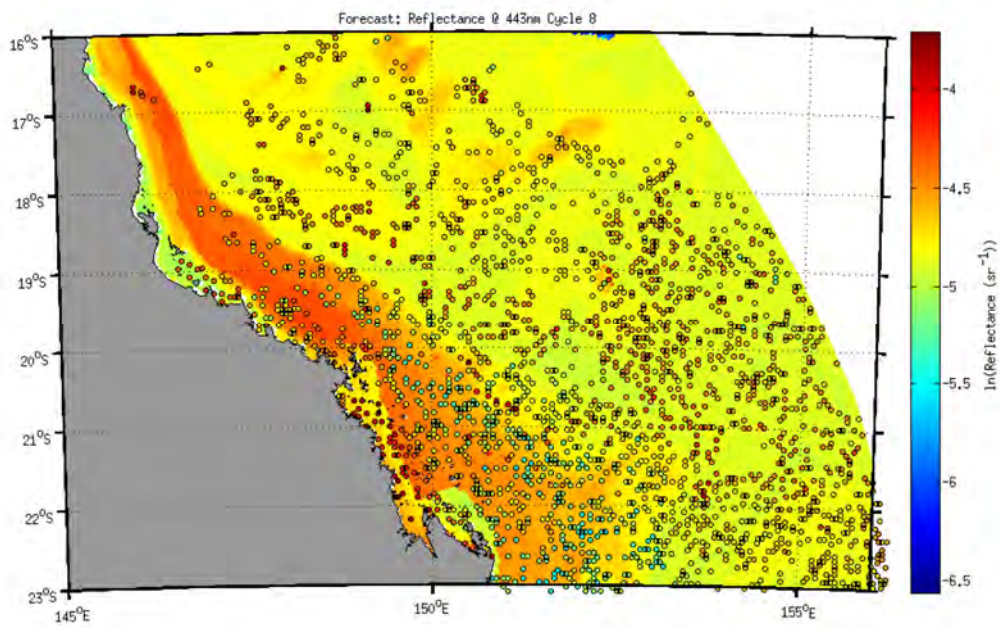


Figure 4.3.39. the forecast reflectance at 443 nm (top) and the analysis field for 443nm (bottom) with observation overlaid in the colored circles.

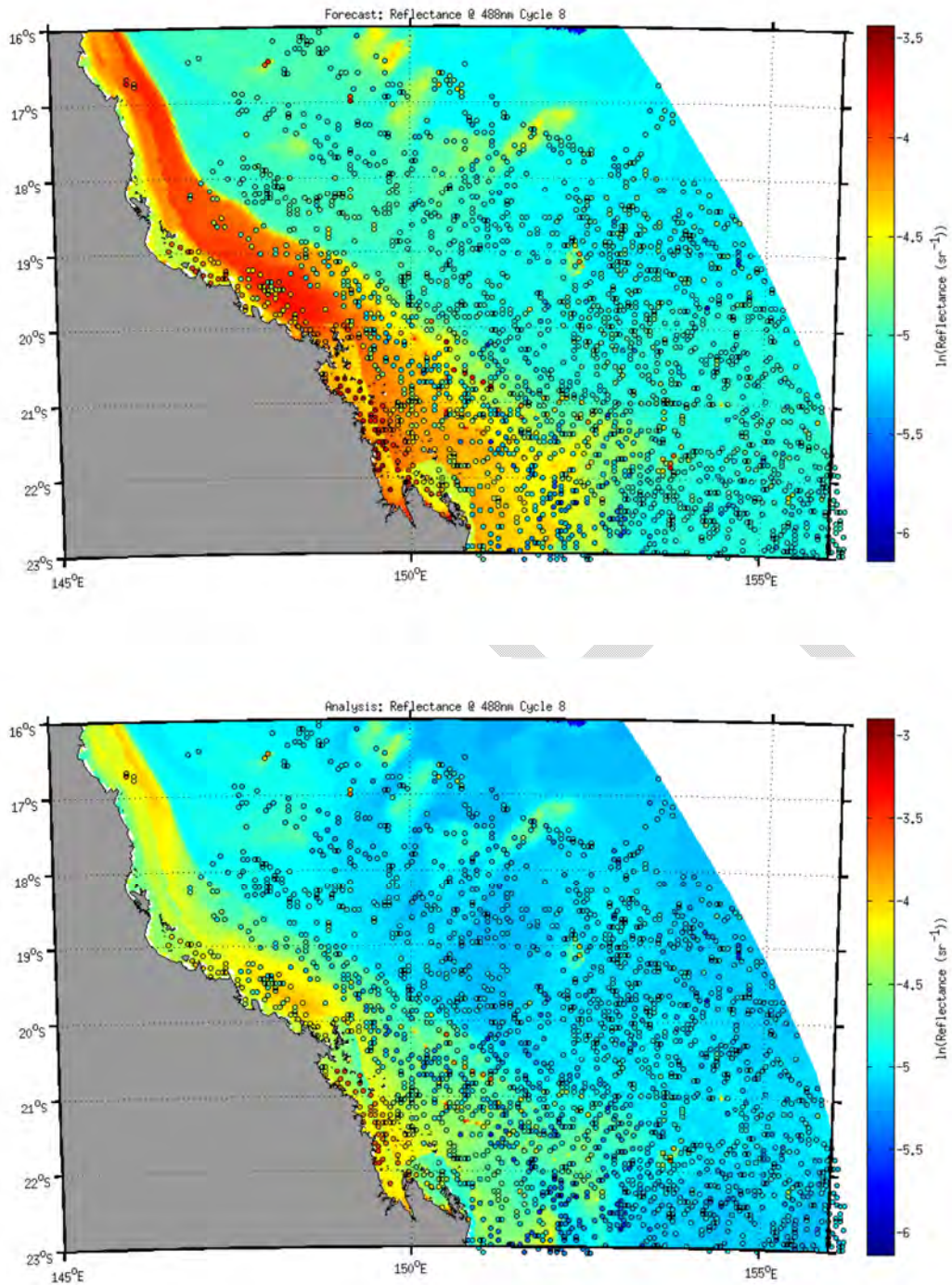


Figure 4.3.40. the forecast reflectance at 443 nm (top) and the analysis field for 443nm (bottom) with observation overlaid in the colored circles.

The result of assimilating observation at 443, 488 and 555 nm (not shown), results in an addition of Phytoplankton biomass in the vicinity of the Fitzroy River plume, while biomass is removed to the southeast of the plume. This suggests that the model did not correctly simulate the location and magnitude of the phytoplankton plume that occurs on the periphery of the Fitzroy River plume.

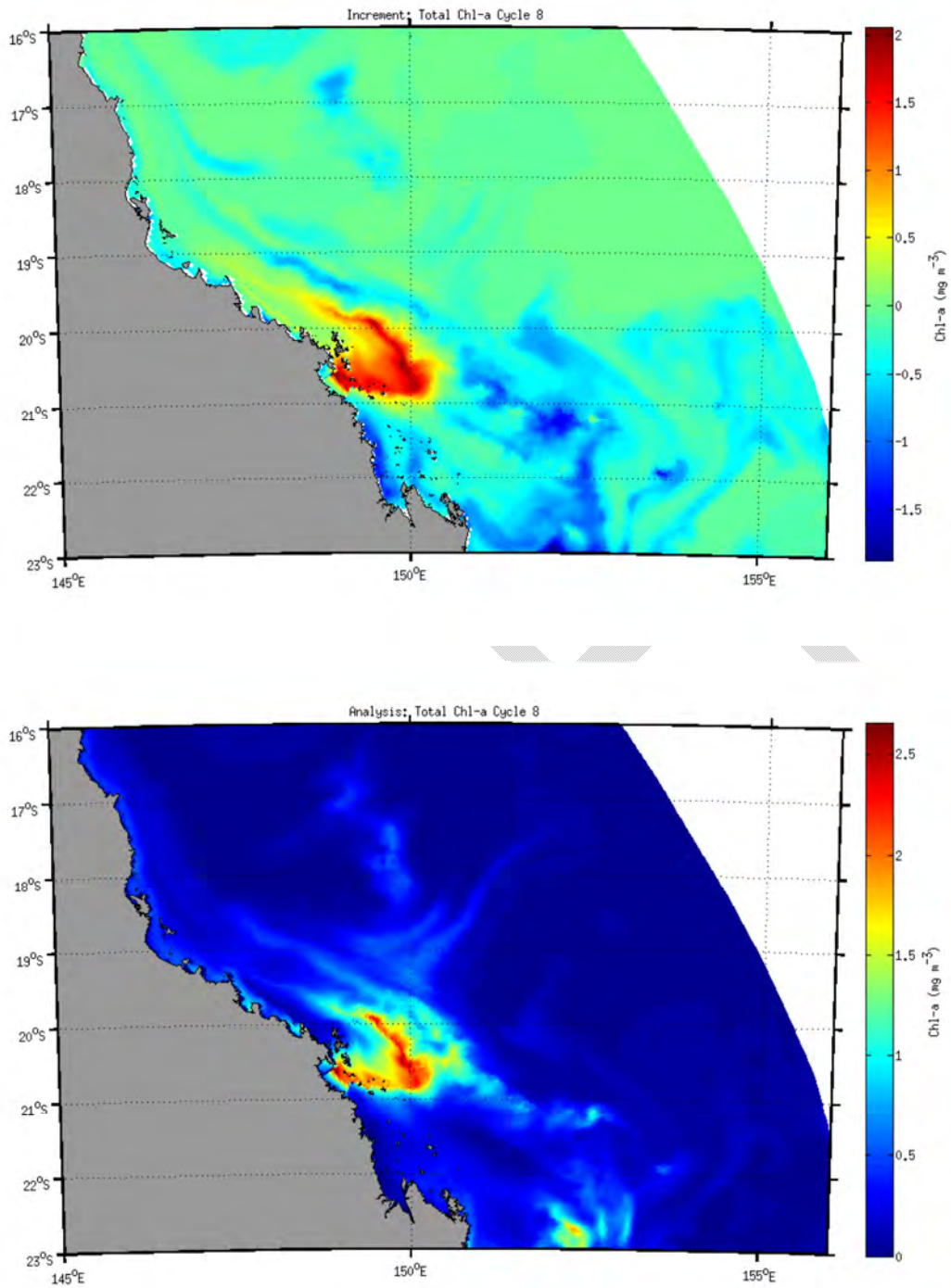


Figure 4.3.41. Increment (top) and analysis field (bottom) for total modelled chlorophyll-a derived from the assimilation of reflectance data shown in figure 4.3.32-33.

4.3.9.4 BGC DA: Discussion

The comparison of the correlation fields that are used in the EnOI and EnKF BGC DA system suggest that the correlation fields change in time as a function of the system dynamics. The implication of this is that while the EnOI system captures the climatological (long term) covariance's, there does exist a temporal variability that cannot be captured. The time-

varying covariance's derived from the EnKF system, reflect the changing dynamics of the system. An example of the difference between the EnOI and EnKF covariance's is demonstrated in Figure 4.3.42. The Heron Island region is at times affected by inshore water masses, and at other times, the East Australian Current impinges on the reef system bringing Coral Sea water into the vicinity of the Island. Figure 4.3.42 (right) is taken from cycle 8 of the EnKF system and shows an offshore water mass affecting the observation site. This is clearly not seen in the EnOI covariance structure depicted in Figure 4.3.42 (left). EnOI solution will therefore be sub-optimal, as it will spread information incorrectly at these times. However, EnKF system is far more expensive to run and also suffers from ensemble collapse.

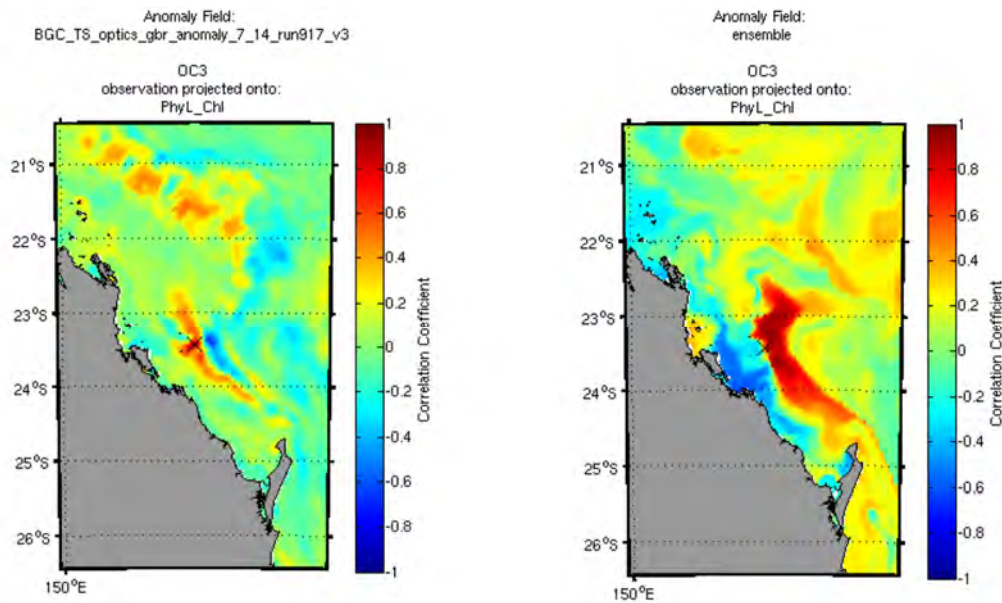


Figure 4.3.42: The spatial correlation map for a measurement taking in the surface layer at the Heron Island South mooring location. The Ensemble OI field (left) is static, whilst that derived from the EnKF system (right) will vary in time.

A comparison between the EnOI system and EnKF system using independent observation from the GBROOS Lizard shelf, Myrmidon and One Tree Island are shown in Figure 4.3.43. It should be pointed out that the control of the BGC model (run 917) is shown and has been subsequently improved substantially. The same configuration was used in each of these assimilation experiments. The control run captured the increase in phytoplankton at Lizard Island, but under predicted the magnitude. The assimilation system that naively assumes that remotely sensed Chl-a equals modelled Chl-a perform very poorly, and substantially over estimated the Chl-a concentration at all three mooring locations. The three experiments that used the EMS optical model to reduce the effects of representation error substantially improve the assimilation solution compared with that where modelled Chl-a was naively assumed to be equivalent to MODIS OC3 Chl-a.

The forecast errors for the four assimilation experiments are compared against those of the control run (BGC run 917). It should again be pointed out that the BGC results report in section 4.5 are those from a later optimised version of the BGC model. However, for the purposes of demonstrating the utility of the BGC DA system, run 917 was sufficient. The forecast errors are reported for shallow regions (depth < 200m) and then the whole of domain, which for which the forecast error is dominated by class 1 waters.

The control run has a Mean Absolute Percentage Error (MAPE) of 109% and 165% in the shallow of whole of domain respectively. The assimilation of MODIS OC3 Chl-a in experiment EnOI1 reduced the error in shallow water to a MAPE of 90.7% (Table 4.3.1), and in deep water the error was reduced substantially to 102%. There was only marginal improvement by introducing the EMS optical model to reduce the representation error (EnOI2). The optical model however, enable the assimilation of 3 bands of MODIS reflectance's (EnOI3), where the MAPE drop to 80% in shallow water and 93% in the whole of domain. The greatest gain was achieved by using the EnKF system where errors in the shallow regions were reduced by 30% and by 70% domain wide. In interpreting these results, the EnOI system is heavily reliant on a realistic background error covariance. Given that the BGC model has evolved substantially since run 917, more accurate background covariances would be expected from the most recent implementation of the BGC model.

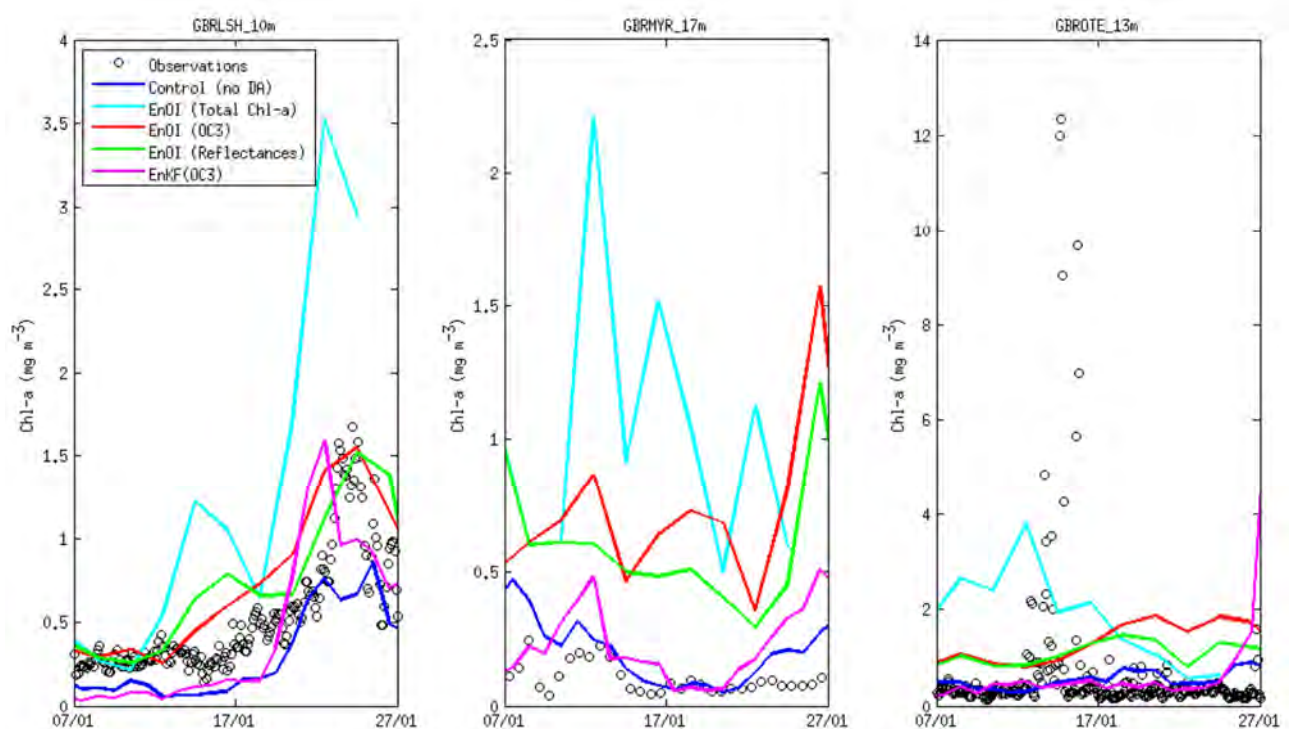


Figure 4.3.43: Time series of observed Chl-a (open circles), and results for the assimilation experiments at the Lizard Shelf mooring (left), Myrmidon Reef (centre) and One Tree Island (right).

Table 4.3.1: Comparison of the results obtained from 4 assimilation experiments.

Experiment	Shallow < 200m depth		Whole of Domain	
	MAPE %	RMSD (mg Chl m ⁻³)	MAPE %	RMSD (mg Chl m ⁻³)
Control (No Assimilation)	108.5%	1.520	165.0%	0.842
EnOI1 (Total Chl)	90.7%	1.254	102.3%	0.681
EnOI2 (OC3)	90.1%	1.253	92.7%	0.681
EnOI3 (R443,R488,R555)	81.9%	1.191	92.6%	0.659
EnKF1 – (R443,R488,R555)	76.1%	1.058	88.3%	0.522

4.3.9.5 BGC DA Summary:

Four BGC assimilation systems have been tested and evaluated against in-situ observations. Additionally, forecast error statistics have been used to assess the system performance against remote sensing data. The EnOI system using MODIS reflectances appears promising, however, this has only been a proof of concept and further testing is required to make definitive statements. It should also be noted that the BGC DA system is heavily reliant on a BGC model that adequately captures the correlation structure between the variables that are observed/assimilated and those state variables that are updated by the linear correlation structure implicit to the DA system. Taking into account these statements, the configuration used in EnOI3 (using MODIS reflectance's) is pragmatically the most likely system to be deployed for nowcast/forecasting in the BGC region.

4.4 GBR-wide Wave Model

4.4.1 Introduction

Sediment transport is an essential component of nutrient cycles in many aquatic systems. Accurate simulation of sediment resuspension and transport is essential for successful prediction of changes in water quality and aquatic habitats. This has repeatedly proven to be a problematic component of modelling efforts (Robson et al., 2008). Often, turbulence and resuspension is dominated by the effects of wind-induced waves. It has also been shown that global climate change has a significant effect on wave climate (Young et al., 2011). Although several models exist to describe the impact of wind-induced wave dynamics and wave-current interactions on sediment resuspension and transport, examples of their integration into complete hydrodynamic models are rare. Currently we are aware of four other initiatives to describe wave dynamics in the Great Barrier Reef Lagoon:

- AMC-UTAS (Lou Mason): WAM-GBR for simulation of cyclones (Hardy et al., 2000).
- Swinburne University/NOAA EMC (van der Westhuysen, Babanin, Zieger): Wavewatch III development for near-shore waters for the simulation of cyclone effects.
- JCU (Jaffres): Wavewatch III simulations in the GBR (Jaffrés et al., 2011).
- BOM: 0.1 degree wave model (AUSWAVE) as part of Australian regional forecast effort.

The first three wave modelling efforts focus mainly on event simulations (i.e., cyclones). None of these models has the aim of integrating 3D hydrodynamic modelling. WAMGBR is designed to model wave characteristics for non-cyclonic and tropical cyclone waves in the geographically complex environment of the Great Barrier Reef. Recent simulations of wave heights for the 2011 cyclone Yasi are able to include the shading effects of the reef matrix (Lou Mason, pers. comm.). However, the validation of this and other models is hindered by the sparse data availability of wave measurements. The operational model of wave dynamics maintained by the Bureau of Meteorology is based on WAVEWATCH III (Tolman, 2009). However, the resolution of AUSWAVE (BOM 2010) on its finest grid is only 0.125 deg or about 13 km.

The suitability of models for integration into eReefs was limited to two candidates, SWAN and Wavewatch III. While SWAN has the advantage to be already used by the Coastal Environmental Modelling Team, is already implemented in TRIKE, includes shallow water physics, and is an implicit scheme, Wavewatch III is possibly easier to implement/nested into the operational BOM AUSWAVE wave forecast system, and it already includes a sub-grid reef parameterization. The approach which has been pursued has been to utilise WaveWatch III across the regional 'GBR4' domain, using spectral boundary forcing from a global implementation of the WaveWatch III model. The intention is that nested 'estuary-scale' domains will be implemented using SWAN with boundary forcing taken from the regional implementation of WaveWatch III, although this has not yet been implemented.

A hydrodynamic model two-way coupled with a wave model has the benefit of directly simulating the role of surface current and water level effects on the wave characteristics, and the input of waves on the circulation through the radiation stress forced wave-driven currents, and the possible additional production of turbulence by waves. Within eReefs task 3A.3, a one-way coupled system has been implemented, where surface current and water level fields from SHOC/EMS (Herzfeld & Waring 2008) simulations are used as additional

forcing for the surface wave model, altering wave refraction through the effects of variable water depth and currents. The output of the hydrodynamic model, and the hydrodynamic forced wave model is fed back to SHOC allowing for further simulations using its sediment transport and resuspension sub-models and enables the user to, e.g., quantify wave-induced versus tidal induced resuspension.

4.4.2 WaveWatch III implementation

Recent versions (since version 3.14) of WaveWatch III (Tolman, 2009) have included source terms for shallow water physics, including wetting and drying effects. This, along with the reef-parameterisation scheme which involves sub-grid scale blocking from surfacing reefs, and that WaveWatch III is the model currently implemented by the National Meteorological Operational Centre at the Bureau of Meteorology resulted in WaveWatch III being considered the more appropriate model to apply across the regional GBR4 domain.

The major disadvantage of WaveWatch III, relative to SWAN, for the GBR application is the explicit time-step requiring application of the CFL condition to ensure model stability. SWAN uses an implicit time-stepping scheme, which enables longer time steps to be used, consequently reducing computation time. Computational restraints were not deemed a concern, allowing application of WaveWatch III. Triad wave-wave physics parameterised within SWAN, but not in WaveWatch III were considered of secondary importance relative to advantages offered by WaveWatch.

Currently, this model is running without integrating surface current output from SHOC due to numerical issues, and only takes simulated water levels into account. However, it is capable of defining reef obstructions. Simulations to test the effect of the reef matrix on the generated wave fields have been completed.

The initial test of GBR WaveWatch model was to carry out a wave hindcast on the GBR4 grid. The aim is to provide the sediment transport model with wave parameters for wave driven resuspension mechanisms.

Three hindcast simulations have been carried out (Table 4.4.1), each spanning the period Sep 2010 to June 2012. Wavewatch III (v4.11) is implemented using Ardhuin et al. (2010) source term physics, on the GBR4 model grid with forcing as specified. The wave spectra is discretised with 29 logarithmically spaced frequency bins from 0.035 Hz to 0.5047 Hz and 24 directional bins (15 degree resolution). Version 4.11 of WaveWatch III is an alpha version pre-release of the model from NOAA (the code developers). The currently supported version of WaveWatch III (v3.14) does not support curvilinear grids, and this application has provided a suitable testing bed for use of the new version of the model.

Open boundary forcing for each of the hindcast runs is derived from a 1 degree resolution global implementation of WaveWatch III (v4.08), forced with surface winds derived from the NCEP Climate Forecast System Reanalysis (Saha et al., 2010), implementing the source term physics of Ardhuin et al. (2010).

Example output is displayed in Fig. 4.4.1, showing snapshot output from the GBR4 wave model, and Fig. 4.4.2 shows a time-series plot of significant wave height and peak wave period over the TC Yasi period.

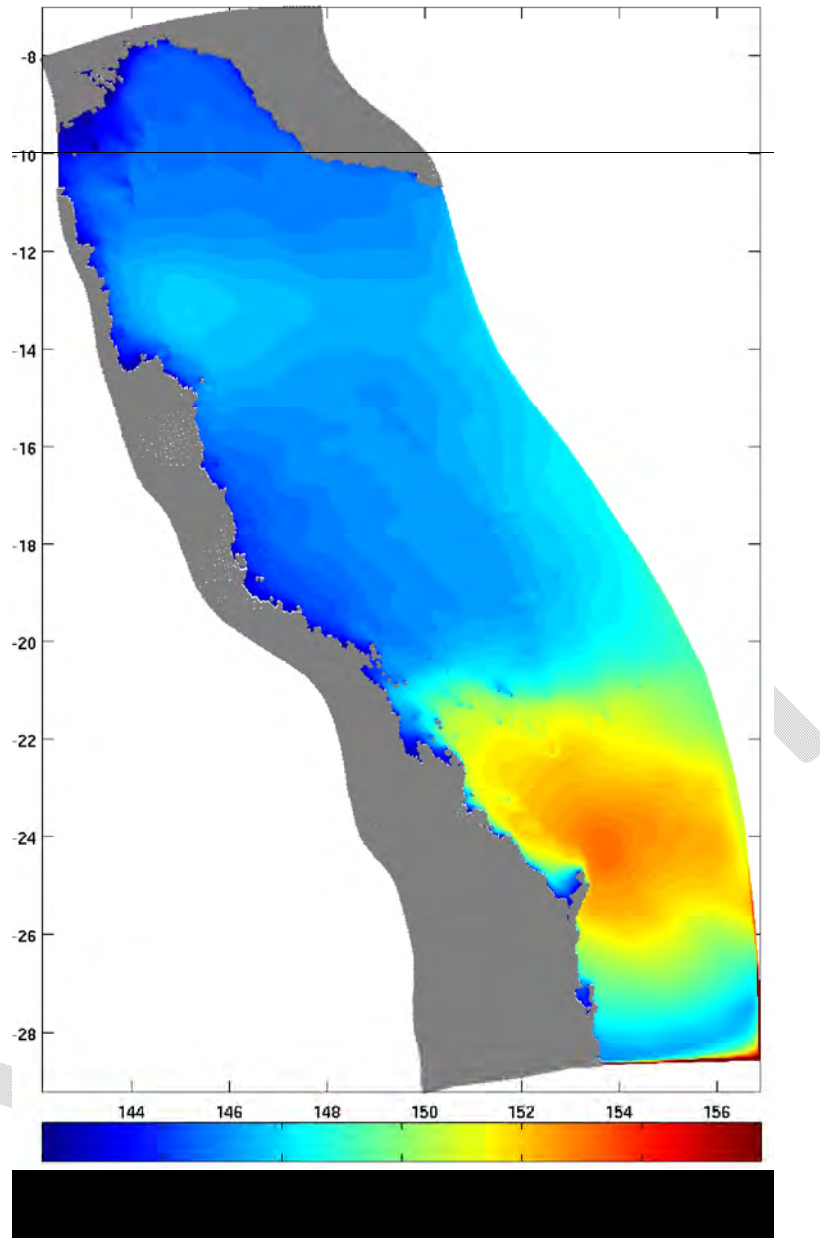


Figure 4.4.1. 16 Feb 2011 Snapshot of significant wave height from the GBR WAVE WaveWatch III implementation.

Table 4.4.1. Description of hindcast runs

Hindcast	Forcing
GBRrun005	ACCESS surface winds
GBRrun006	ACCESS surface winds + SHOC run20 water level
GBRrun007	ACCESS surface winds + SHOC run20 water level + surface currents

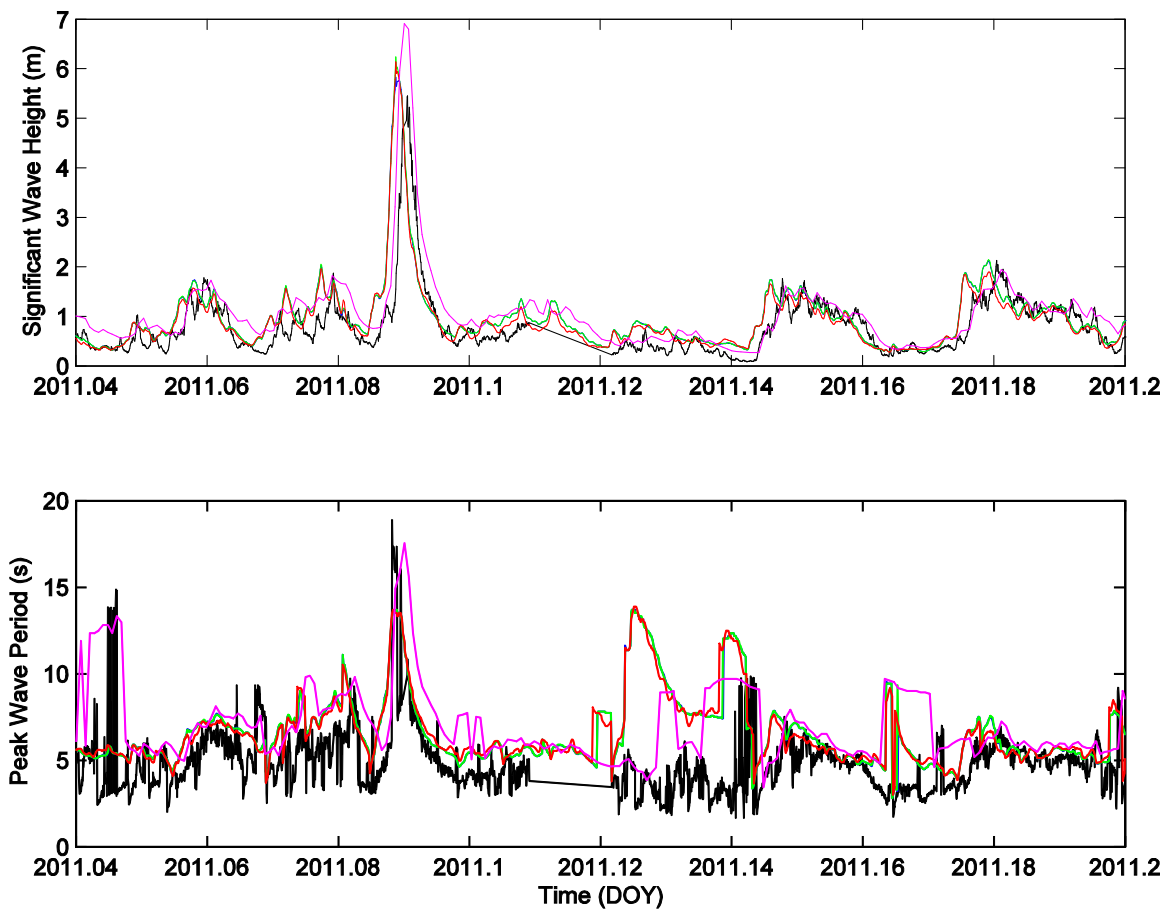


Figure 4.4.2. Time-series of significant wave height (upper) and peak wave period (lower) for the period of Jan-Feb, 2011 at the Townsville waverider buoy, during the passage of cyclone Yasi. Black curve denotes observed conditions; Blue/Green/Red/Magenta curves denote GBRrun005/Run006/GBRrun007/CAWCR hindcast respectively.

The Centre for Australian Weather and Climate Modelling (CAWCM) partnership between CSIRO and the Bureau of Meteorology) have recently completed a 31-year global wind-wave hindcast - hereafter the CAWCR hindcast (Durrant et al., 2013). The CAWCR hindcast was run on a 0.4 x 0.4 degree global grid with a series of nested grids of 10 arcminutes down to 4 arcminutes in the Western Pacific and Australian regions. The GBR4 grid spans the 4' and 10' grids (Fig. 4.4.3). All CAWCR grids were forced with the NCEP Climate Forecast System Reanalysis (CFSR) surface winds at 0.3 degree spatial and hourly temporal resolution. Model settings otherwise are consistent with the eReefs hindcast runs defined above. We use the CAWCR hindcast as a reference dataset to assess the performance of the eReefs wave hindcast runs.

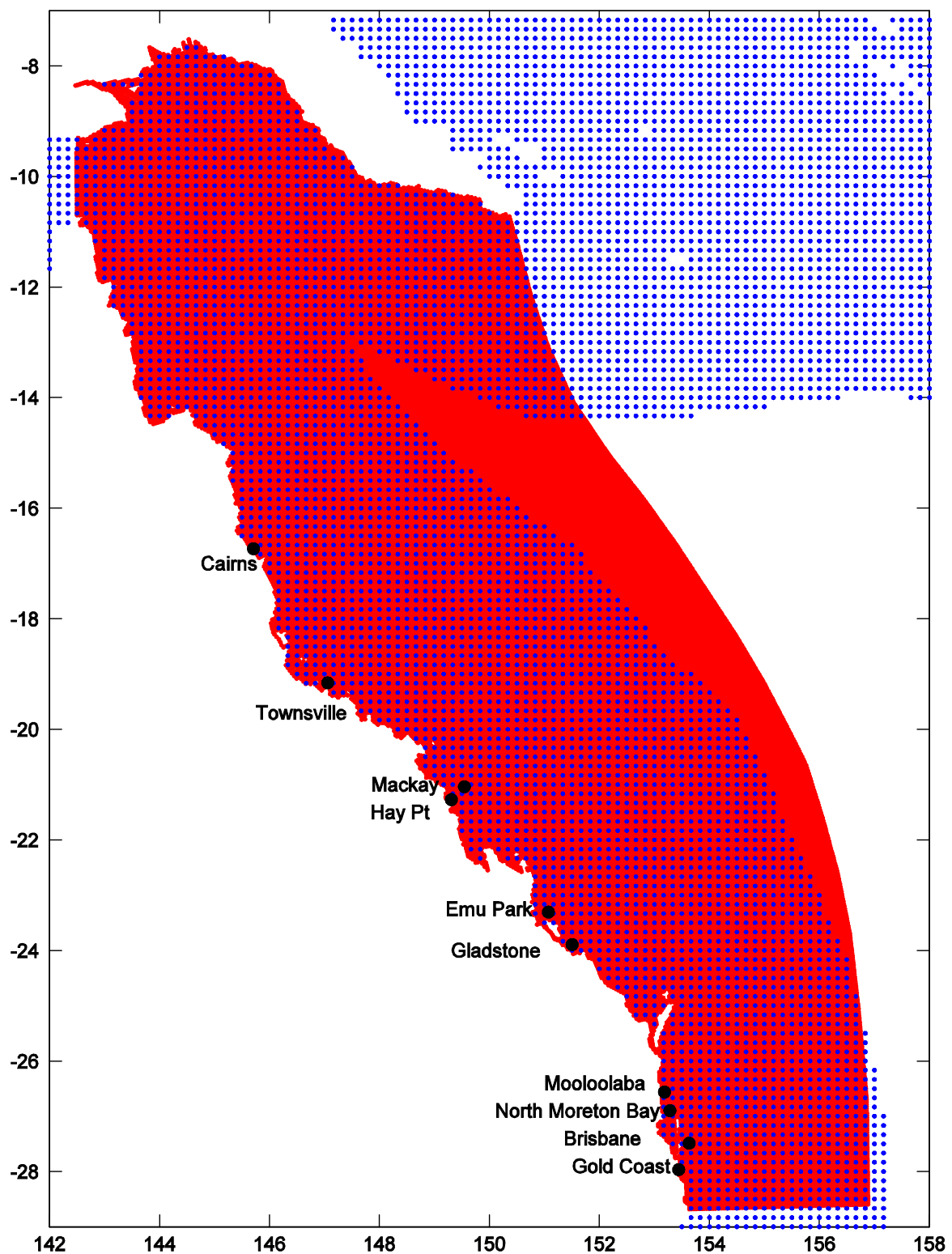


Figure 4.4.3. Model domain covered by the WaveWatch III implementation. The red area indicates the extent of the GBR4 grid. The blue dots represent the extent of the 10' archived data from the CAWCR wave hindcast. The 4' archived data spans approximately one half the width seen of the 10' grid. Black circles indicate the location of Old EPA waverider buoys at which verification of the wave model has been carried out.

Validation

Queensland Department of Environment and Heritage Protection wave buoy data has been obtained for the period January 2010 through to July 2013 for 10 locations which are situated within the GBR4 domain (Table 4.4.2).

Table 4.4.2. Site details of Old DEH wave buoys used for model verification

Site	Latitude	Longitude	Depth
Brisbane	27°29.285'S	153° 37.931'E	76m
Cairns	16°44.060'S	145° 42.600'E	9m
Emu Park	23°18.380'S	151° 04.380'E	18m
Gladstone	23°53.670'S	151° 30.220'E	13m
Gold Coast	27°57.950'S	153° 26.570'E	18m
Hay Point	21°16.276'S	149° 18.572'E	10m
Mackay	21°02.375'S	149° 32.750'E	28m
Mooloolaba	26°33.814'S	153° 10.961'E	33m
North Moreton Bay	26° 53.932'S	153° 16.892' E	35m
Townsville	19°09.583'S	147° 03.457'E	15m

Regression statistics between in-situ buoy and model data over the period of the hindcasts were used to determine skill of the wave model (Table 4.4.3). Four model datasets were considered – the three eReefs hindcasts, to determine merit (if any) of water level and surface current forcing. It is worth noting that the addition of surface current forcing leads to an overhead of computational time (resources) of approximately 25%. Ignoring the effects of currents enables conservation of the variance (energy) of a wave package. This is not the case if currents are considered due to the work done by the current on the mean momentum transfer of waves (Longuet-Higgins and Stewart, 1961). In this case, wave action is conserved. Regression statistics are compared with those obtained for the CAWCR hindcast, as a benchmark.

Fig. 4.4.4 and 4.4.5 display quantile-quantile plots and probability distribution functions for significant wave height respectively, summarising the performance of the models to represent wave height. Some key conclusions are drawn from the eReefs modelling are:

The CAWCR hindcast tends to outperform the eReefs hindcasts at the buoy locations. Only at Emu Park do the eReefs hindcasts (runs005-7) display a better fit to observations than the CAWCR hindcast. A notable difference between the CAWCR hindcast and the eReefs runs is

the quality of swell waves generated outside the GBR4 domain. Away from the shelf region, the CAWCR hindcast has a resolution of 0.4 degrees. Outside the GBR4 domain, waves used to force the eReefs hindcasts at the open boundaries are generated by a 1 degree resolution global model. Another key difference is the application of curvilinear grids for the eReefs hindcasts. The eReefs hindcasts are the first application of the curvilinear capability of WaveWatch III, and the relative influence of the grid choice on model outputs has not been tested. Given model physics and settings are otherwise equivalent, these are the most likely sources of difference between the runs.

The addition of water level forcing is insignificant at the buoy locations. The shallowest buoy at which comparisons were made is 9 m. The effects of variable water level can be expected to be insignificant in these depths. Larger effects may be observed in shallower cells, however at the 4 km scale, any benefit is likely minimal.

The addition of surface current forcing has minimal influence on model performance at buoy locations. Run007, with surface current forcing, displays minor differences to run005 and run006. At some locations (e.g., Cairns, Emu Park) current forcing leads to slight improvement, whereas at other locations run007 displays poorer performance in reproducing observed wave heights. These differences are minor. While observed peak wave periods are not well represented by any model, the addition of current forcing does result in minor improvements. For the computational overhead introduced with addition of current forcing, the benefit to the GBR4 simulation is minimal.

The GBR4 wave model hindcasts poorly resolve large storm and extreme wave heights. Coarse resolution winds forcing waves outside the domain which influence the magnitude of boundary forced waves will account for a considerable portion of this, but model winds over the domain may also be worthy of greater attention.

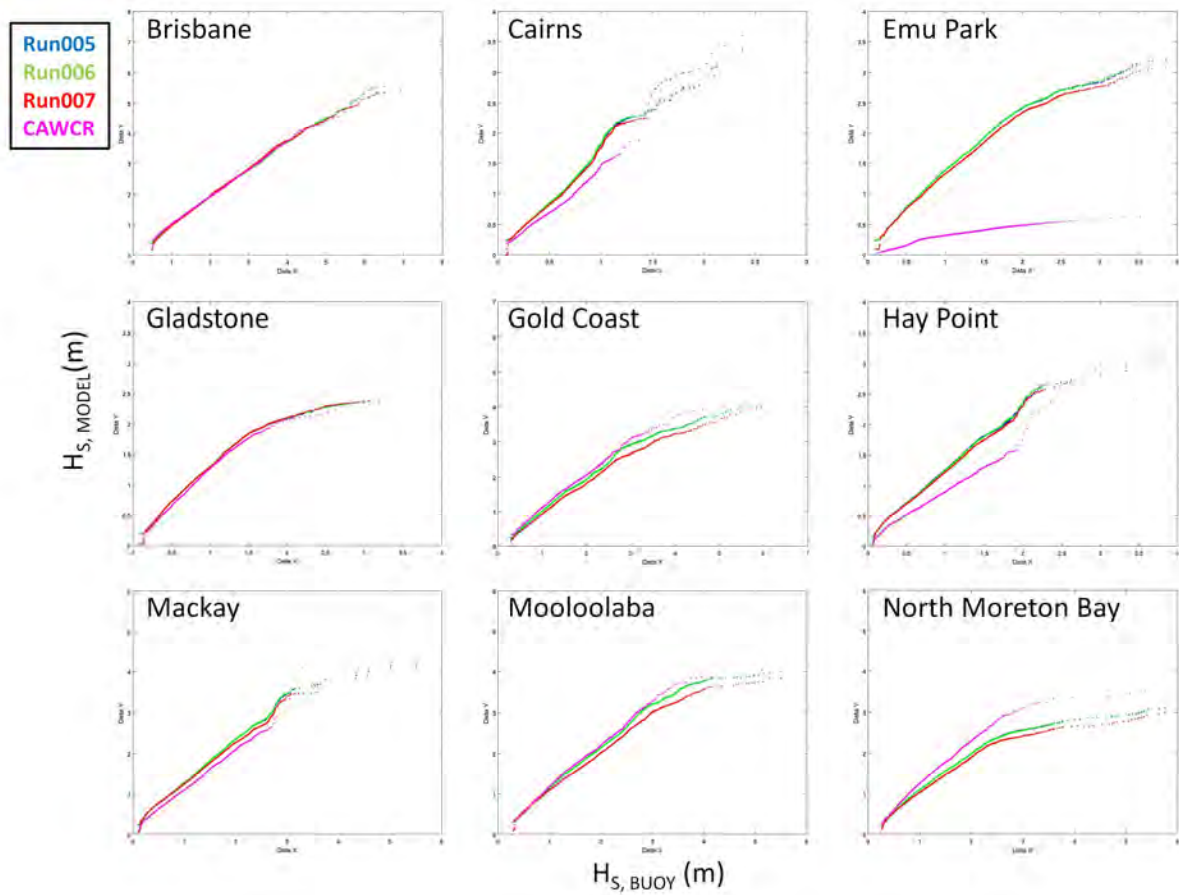


Figure 4.4.4. Quantile-quantile plots of significant wave height between hindcast datasets and in-situ buoy records. Blue/Green/Red/Magenta curves denote GBRrun005/GBRrun006/GBRrun007/CAWCR hindcast respectively.

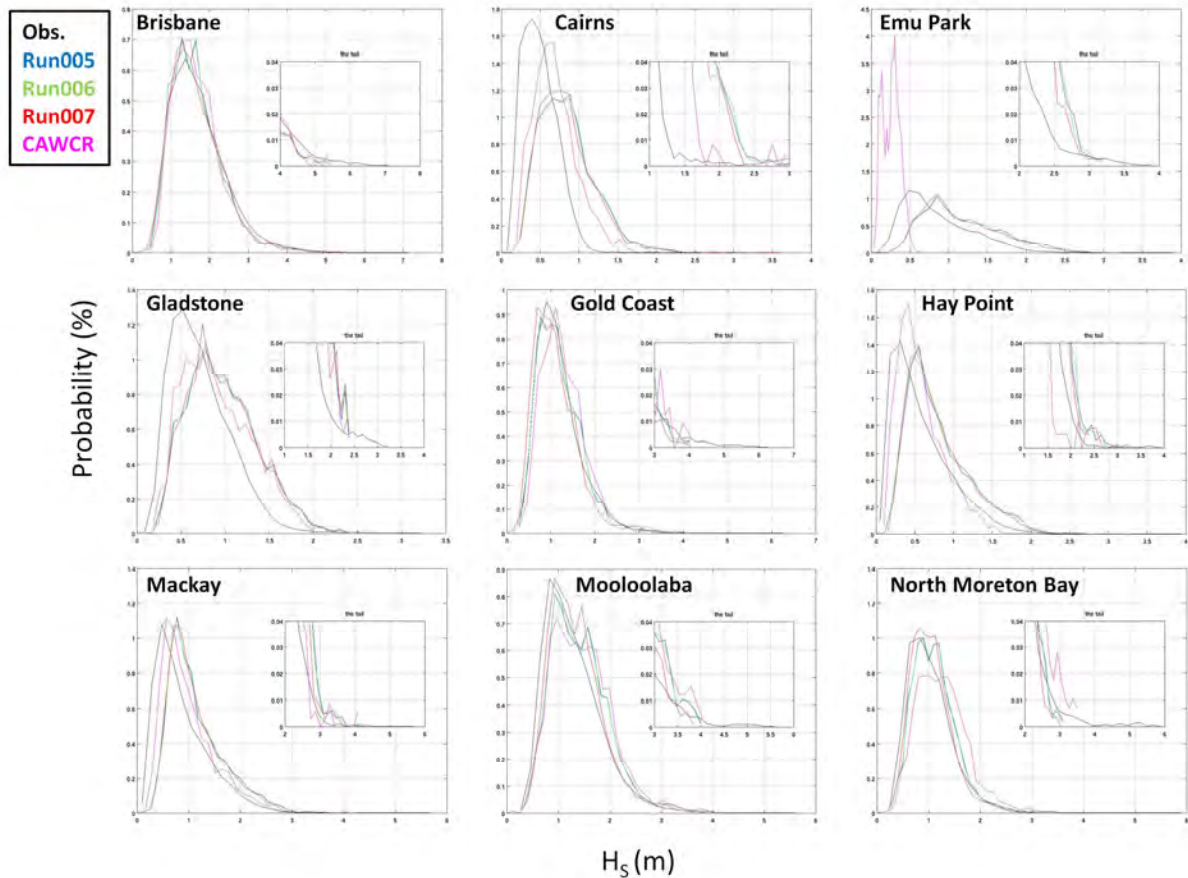


Figure 4.4.5. Probability Distribution Function plots of significant wave height for hindcast datasets and in-situ buoy records. Inner sub-plots represent the upper-tail of the distribution. Blue/Green/Red/Magenta curves denote GBRrun005/GBRrun006/GBRrun007/CAWCR hindcast respectively.

Real-time implementation

The WaveWatch III implementation on the GBR4 grid is being run in near-real time (NRT) within the TRIKE framework. The model is forced with ACCESS surface winds and spectral open boundary conditions derived from the operational WaveWatch III models operated by the Bureau of Meteorology National Meteorological Operations Centre (NMOC - AUSWAVE).

The boundary points of the GBR4 grid are defined in the NMOC AUSWAVE implementation and spectral boundary files are archived from operational runs of AUSWAVE at 6 hourly intervals. Four files are created daily at 00Z, 06Z, 12Z and 18Z, which each include 48hr forecasts with hourly varying spectra. The Boundary spectra files are transferred daily to CSIRO from the NMOC, with the 00Z archive, an analysis run, used to force the NRT GBR4 wave model.

The current implementation of WaveWatch III on the GBR4 grid shows no benefit of forcing with water level or currents from the hydrodynamic model, with only the cost of increased computation added. Thus, at this time the wave model is wind and open boundary forced only. The non-improvement of the wave model with current forcing might be improved through future ongoing model tuning and development. Until such time, the NRT wave model

is run independently of the hydrodynamic model, with results used to feed the sediment model.

The NRT GBR4 wave model has been in operation since August 2013. Queensland in-situ buoy data have only been made available to June 2013. No verification of the NRT wave model has been carried out to date.

NMOC requested that a fee be associated with the delivery of boundary condition data for the real-time WWIII model, which eReefs was unwilling to support. Consequently the real-time model was discontinued and the eReefs real-time system uses the BoM AUSWAVE system for its real-time wave archive. Since this product does not cover the timeframe of the entire eReefs archive (November 2010 onwards) various products were assembled to create a continuous wave record. This is as follows:

1. 01/10/2010 → 30/06/2012 : GBR4 WWIII model described above using BoM boundary forcing
2. 01/07/2012 → 30/04/2013 : BoM AUSWAVE Australia model
3. 01/05/2013 → present : BoM AUSWAVE Regional model

The latter two products do not include the bottom stresses required for resuspension; the WAVES library in EMS is used to generate this field. Therefore, a consistent set of parameters is available for the entire hindcast, notwithstanding that the bottom stress is available from dataset 1 above.

4.4.3 SWAN implementation

GBR4 grid

Similar to the WaveWatch III implementation above, the SWAN wave model has been implemented on the GBR4 grid. However, this model is wind forced only with no forcing at the open boundaries defined. Given the large amount of wave energy received from the open boundaries, this provides for a poor test of the SWAN model in comparison to WaveWatch III for simulating waves in the GBR region. Given the greater progress of the WaveWatch III implementation on the GBR4 grid, SWAN efforts have focussed on the smaller scale applications. With ongoing work, the WaveWatch III GBR4 model (GBR WAVE in Fig. 4.4.6 below) could be developed such that spectral boundary files were defined to provide forcing for relocatable nested SWAN models (SWAN estuary in Fig. 4.4.6).

Relocatable Estuary Model

To integrate the wave modelling also into the relocatable estuary model, a local, estuary model was nested in a larger regional model. As test example we used the well-studied Fitzroy Estuary and Keppel Bay. SHOC/EMS has been previously applied to this system without a wave model, but results for suspended sediments have been unsatisfactory (Margvelashvili et al., 2006, in prep.).

The SHOC-SWAN coupled model is a 1-way approach. Both programs run independently over the whole computational period and exchange information via output files containing the necessary information. Both programs run in serial, not in parallel. Such an approach is easier to implement and maintain than, e.g., switching between programs after a prescribed time interval, or directly integrating the SWAN source code into the SHOC source code. It also

allows for instant exchange of new versions made available by Deltares for SWAN, which otherwise would not be possible or only after adapting the source code.

With respect to a relocatable estuary model, nesting of the local simulation (estuary) within a larger regional grid (GBR1 or GBR4) is used to generate reliable boundary conditions for currents, water level etc., as well as waves on the open ocean boundaries of the local model. The nesting itself is again done as a 1-way coupled model running in serial for SHOC and SWAN simulations, where the computational grids used in SHOC and SWAN are identical.

The model structure of the loosely coupled model is depicted in Fig. 4.4.6 as a flow chart. The regional model is to be supplied with the appropriate boundary conditions for water currents, water elevation, temperature, etc. for the hydrodynamic model and spectral wave information for the wave model. On the regional grid, SHOC is simulated passing data of surface currents and water elevation to the wave model. In eReefs these data are currently archived for the last three years. A local model is nested into the regional model, again running the hydrodynamic model first or reading its output from the archive and thereafter running the local wave model. The latter is using hydrodynamic input from the local model and spectral wave information on its boundary from the regional wave model. The wave model then passes back information on wave data (significant wave height and period, orbital bottom velocity) to the SHOC/EMS system, which then can be used to run the sediment transport and biogeochemistry sub-models. Here the orbital bottom velocity is directly linked (via an allometric relation depending on sediment composition) to sediment resuspension. Underlying the whole system are gridded meteorological forcing data from the Bureau of Meteorology (ACCESS). Thin arrows in this flow chart signify flow of data in the sub-models themselves, which do not need further processing, while thick arrows include a data transformation step between models.

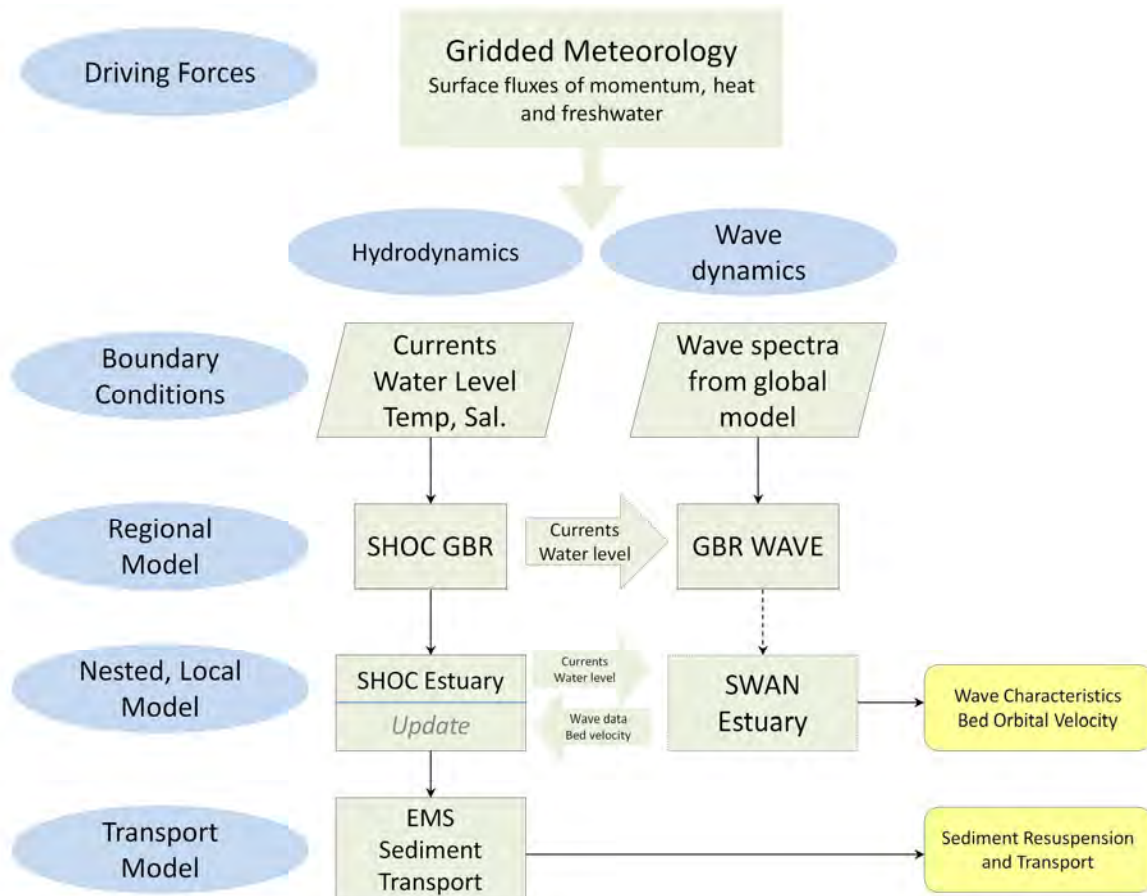


Figure 4.4.6. Flow diagram for the 1-way coupled hydrodynamic and wave models. The shaded area denotes an additional step of the sediment transport sub-component.

The nested, coupled model was exemplified on the Fitzroy Estuary/Keppel Bay, where hydrodynamic modelling using SHOC was done in previous years (e.g., Herzfeld et al. 2006) providing basic information on bathymetry and a first choice in parameter settings. Meteorological data were chosen for the summer of 2009 with a strong storm system passing the region. The model run was accomplished as shown in the flow diagram of Fig. 4.4.6. First SHOC was run to simulate water currents and elevation in the GBR lagoon, which serve as input for the regional wave model. The GBR4 simulation using the regional SWAN model (Fig. 4.4.7) shows a snapshot of the driving meteorology, here the easterly wind velocity, over the computational grid of the GBR and the significant wave heights calculated by SWAN. The correlation between large significant wave heights and the strong wind field in the southern part of the domain are obvious.

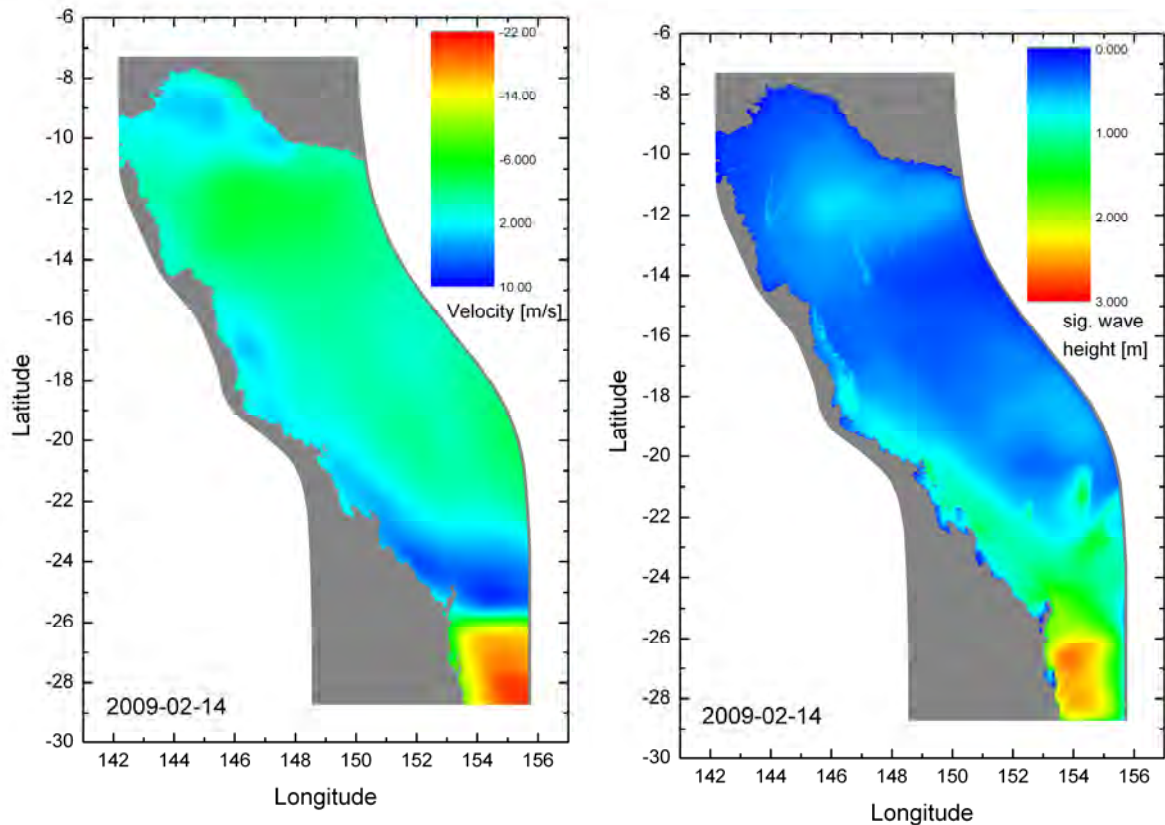


Figure 4.4.7. Magnitude of the easterly wind component over the GBR computational area (left), and simulated significant wave height. This SWAN model contains no forcing at the open boundaries.

Based on this regional GBR4 simulation, the local (Fitzroy Estuary) model was run – again first SHOC and thereafter SWAN, using output of the local SHOC model and the wave spectra on its boundary from the regional GBR4 wave simulation. Spectral boundary files generated by regional SWAN, or likewise the regional WaveWatch III model, are used to drive the relocatable nested SWAN model. Fig. 4.4.8 shows the results for bottom orbital velocity and significant wave heights simulated for Keppel Bay. Overall, the model generated quite high values for significant wave heights associated with strong bottom orbital wave motion across the bay. Only in the shadow of the islands and the estuary arms wave action was less dominant. A very pronounced increase in bottom velocity can be seen along the northern tip of Curtis Island.

It should be noted that discrepancies in bathymetry between the older regional 4 km grid and the local estuary are evident. Such discrepancies lead to a certain mismatch in the significant wave heights. This discrepancy will be overcome using the newer GBR4 grid based on the JCU bathymetries.

The nested wave model is easily relocatable between estuaries and does not need extra adaptations for boundary conditions since SWAN interpolates field data from coarse model output to boundary grid points of the nested grid. In Phase II the local wave model will be incorporated into the TRIKE framework to run within RECOM (Section 4.7), forced with

boundary data from the regional WWIII model, and hydrodynamic data from the hydrodynamic component of RECOM.

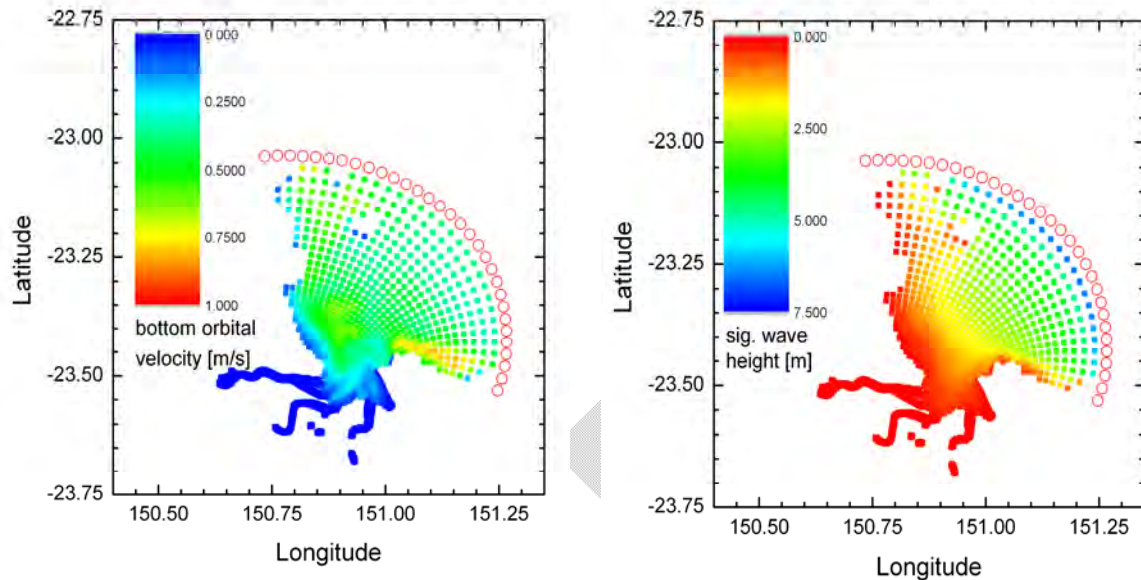


Fig. 4.4.8: Bottom orbital velocity (left) and significant wave height (right) calculated by the nested simulation of the SWAN model.

4.4.4 Recommendations

An eReefs wave model hindcast has now been implemented on the GBR4 grid, and is providing a dataset to support ongoing development of the sediment modelling component of eReefs. A 4km scale wave model is also operating routinely in near real-time within the TRIKE framework. The hindcast model has undergone initial validation, but it is expected that the model could improve representation of the wave field with further tuning with surface current forcing. The three factors which require focussed attention to improve the model simulations are assessing sensitivity to different current forcing datasets (hydrodynamic modelling parameterisations), tuning the obstruction grids (which represent the reef matrix in the wave model), and determining which wave source term package is best suited to the GBR regional sub-domain (current choice is based on tuning for global simulations). After this development, it would be anticipated that hydrodynamic forcing of the wave model would improve wave model skill. Once achieved, the NRT model would benefit from current and water-level forcing.

The predominant wave modelling effort on the GBR4 domain has been with WaveWatch III. This choice was partially made on the basis that the model will be more easily operationalised by the NMOC who already use WaveWatch III. Development of WaveWatch III to archive boundary forcing for relocatable nested sub-domains which are defined at any point in time would support the development of the SWAN estuary implementation which has also been carried out within eReefs. To archive all spectral data from the WaveWatch III model to provide boundary forcing for any sub-domain would require large data storage solutions. The

preferred approach is to define nested sub-domains, and output boundary forcing from the NRT model as defined. This would introduce the limitation of not having optimal, or consistent, boundary forcing for any sub-domain hindcast.

DRAFT

Table 4.4.2: Wave model error regression statistics for significant wave height, Hs. Comparison of model hindcasts relative to Qld waverider buoy data for period September 2009 to June 2012.

		N	RMSE (m)	BIAS (m)	R	SI
Brisbane	Run005	15336	0.52	-0.12	0.75	0.38
	Run006	15336	0.52	-0.12	0.75	0.38
	Run007	14863	0.57	-0.13	0.71	0.41
	CAWCR_hc	15336	0.36	-0.11	0.89	0.25
Cairns	Run005	15336	0.48	0.39	0.63	0.41
	Run006	15336	0.48	0.39	0.63	0.42
	Run007	14863	0.46	0.37	0.62	0.40
	CAWCR_hc	15336	0.32	0.24	0.67	0.32
Emu Park	Run005	15336	0.43	0.31	0.81	0.32
	Run006	15336	0.43	0.31	0.81	0.32
	Run007	14863	0.40	0.27	0.80	0.32
	CAWCR_hc	15336	0.70	-0.61	0.82	0.38
Gladstone	Run005	15336	0.35	0.23	0.76	0.30
	Run006	15336	0.35	0.23	0.76	0.30
	Run007	14863	0.35	0.23	0.76	0.30
	CAWCR_hc	15336	0.26	0.18	0.89	0.22
Gold Coast	Run005	15336	0.35	-0.04	0.79	0.31
	Run006	15336	0.35	-0.05	0.79	0.31
	Run007	14863	0.39	-0.14	0.75	0.33
	CAWCR_hc	15336	0.22	0.06	0.92	0.20
Hay Point	Run005	15336	0.33	0.21	0.79	0.33
	Run006	15336	0.33	0.21	0.80	0.33
	Run007	14863	0.32	0.19	0.79	0.33
	CAWCR_hc	15336	0.19	-0.02	0.86	0.25
Mackay	Run005	15336	0.40	0.21	0.80	0.35
	Run006	15336	0.40	0.21	0.80	0.35
	Run007	14863	0.39	0.18	0.79	0.36
	CAWCR_hc	15336	0.24	0.05	0.89	0.25
Mooloolaba	Run005	15336	0.38	0.09	0.78	0.32
	Run006	15336	0.38	0.09	0.78	0.32
	Run007	14863	0.39	0.01	0.73	0.34
	CAWCR_hc	15336	0.25	0.13	0.93	0.19
NMWB	Run005	15336	0.31	0.04	0.74	0.29
	Run006	15336	0.31	0.04	0.74	0.29
	Run007	14863	0.32	-0.02	0.69	0.31
	CAWCR_hc	15336	0.28	0.19	0.91	0.20
Townsville	Run005	15336	0.36	0.23	0.79	0.33
	Run006	15336	0.36	0.24	0.79	0.34
	Run007	14863	0.34	0.20	0.77	0.33
	CAWCR_hc	15336	0.37	0.30	0.90	0.27

Table 4.4.3: Wave model error regression statistics for peak wave period, T_p . Comparison of model hindcasts relative to Qld waverider buoy data for period September 2009 to June 2012.

		N	RMSE (s)	BIAS (s)	R	SI
Brisbane	Run005	15336	2.33	-0.74	0.42	0.71
	Run006	15336	2.33	-0.74	0.42	0.71
	Run007	14863	2.28	-0.97	0.40	0.67
	CAWCR_hc	15336	1.85	-0.49	0.58	0.58
Cairns	Run005	15336	4.15	3.15	0.09	1.21
	Run006	15336	4.15	3.16	0.09	1.21
	Run007	14863	3.97	3.02	0.12	1.15
	CAWCR_hc	15336	4.09	3.17	0.12	1.16
Emu Park	Run005	15336	2.44	0.95	0.46	0.87
	Run006	15336	2.44	0.94	0.46	0.87
	Run007	14863	2.44	0.88	0.43	0.88
	CAWCR_hc	15336	3.12	-0.40	0.48	1.19
Gladstone	Run005	15336	2.30	0.33	0.48	0.84
	Run006	15336	2.30	0.32	0.48	0.84
	Run007	14863	2.29	0.26	0.46	0.84
	CAWCR_hc	15336	2.07	0.33	0.58	0.76
Gold Coast	Run005	15336	2.54	-0.79	0.47	0.78
	Run006	15336	2.54	-0.78	0.47	0.78
	Run007	14863	2.52	-0.75	0.43	0.78
	CAWCR_hc	15336	1.96	-0.55	0.63	0.61
Hay Point	Run005	15336	3.13	1.44	0.30	1.21
	Run006	15336	3.12	1.43	0.30	1.21
	Run007	14863	3.00	1.27	0.30	1.18
	CAWCR_hc	15336	2.92	1.44	0.38	1.11
Mackay	Run005	15336	2.50	0.89	0.38	0.92
	Run006	15336	2.49	0.87	0.38	0.92
	Run007	14863	2.46	0.71	0.35	0.92
	CAWCR_hc	15336	2.21	0.28	0.45	0.86
Mooloolaba	Run005	15336	2.22	-0.46	0.47	0.72
	Run006	15336	2.22	-0.46	0.47	0.72
	Run007	14863	2.11	-0.21	0.45	0.70
	CAWCR_hc	15336	1.84	-0.18	0.61	0.61
NMWB	Run005	15336	2.40	-0.19	0.44	0.82
	Run006	15336	2.40	-0.19	0.44	0.82
	Run007	14863	2.35	0.04	0.42	0.80
	CAWCR_hc	15336	1.96	0.12	0.60	0.67
Townsville	Run005	15336	3.20	2.37	0.19	0.98
	Run006	15336	3.20	2.37	0.19	0.98
	Run007	14863	3.19	2.38	0.19	0.97
	CAWCR_hc	15336	2.99	2.23	0.23	0.91

4.5 *Transport model*

4.5.1 *Background*

Within the Environmental Modelling Suite (EMS), the term ‘transport model’ denotes the use of (typically) hourly-averaged velocity fields from the hydrodynamic model, together with hourly snapshots of surface elevation, temperature, salinity, diffusion and short-wave radiation fields, to drive the downstream sediment transport and biogeochemical (BGC) models. The development of the transport model means that the BGC model (for example) can be run offline without the necessity of re-running the hydrodynamics each time, thus saving computation time. Within the transport model, advection of the biogeochemical tracers is treated using a semi-Lagrangian scheme, which allows relatively long (i.e. 1 hour) time steps to be used without incurring stability problems in the BGC model. In this way, the tracer-intensive BGC model can be run at acceptable computational cost. Without the use of the semi-Lagrangian advection scheme, the shorter time steps required to maintain numerical stability with Eulerian advection schemes would make BGC model runtimes impractical (e.g. slower than real time). Thus the use of a semi-Lagrangian advection scheme is currently unavoidable to perform high-resolution BGC simulations.

A shortcoming of semi-Lagrangian advection schemes, however, is that they are fundamentally non-conservative i.e. mass on both local and domain-wide scales is not conserved over an integration period. Clearly, conservation of mass is an important criterion to both the BGC and sediment transport modelling efforts. Over the past few years, the CEM team has expended considerable effort attempting to improve the conservation performance of the transport model. Algorithms have been developed to impose mass conservation on a global (domain-wide) and local (grid cell) scales (global and local fills respectively). These approaches follow methods of posteriori restoration of mass (e.g. Priestly, 1993), also referred to as global filling (Rood, 1987). Although these algorithms have improved the conservation properties of the transport model, they have not fundamentally solved the non-conservation problem. For the eReefs project, two key challenges have therefore been undertaken:

- (i) To configure the transport model in its current form to provide the best performances relative to the 1 km and 4 km hydrodynamic models, to facilitate development of the sediment transport and BGC models.
- (ii) To improve the performance of the transport model by upgrading the advection scheme to a fundamentally conservative one, while retaining the capability to use long time steps.

The first objective was achieved during the first year of eReefs (see Section 4.5.2). During the second year of the project, we have focussed on the second objective (see Section 4.5.3).

4.5.2 *Semi-Lagrangian transport model*

Although the semi-Lagrangian advection scheme is intrinsically non-conservative, it does retain utility in that it is truly unconditionally stable, monotonic, positive definite and execution time scales well with increasing tracers. For these reasons it is often used as a precursor to the FFSL. In this section we assess the performance of the transport model

against solutions derived from the hydrodynamic model (considered here the baseline solution).

4.5.2.1 Tools and methods for ongoing evaluation of transport model.

Skill assessment of the transport model is addressed by developing MATLAB scripts to quantitatively compare predictions of passive tracer distributions from the transport model with equivalent predictions obtained by including one or two passive tracers in the hydrodynamic model simulations. Four skill/error metrics are being calculated: the root-mean-square error (RMSE), the mean absolute error (MAE), model bias, and a model skill metric (d_2) described by Willmott et al. (1985). These metrics have so far been applied to surface layer tracer concentrations. The total mass of tracer within the model domain is also being used to evaluate the transport model performance, in particular its conservation performance.

4.5.2.2 Preliminary transport model based on pilot HD model.

The semi-Lagrangian advection scheme was tested to identify the best performing mass-preserving algorithm (global or local fill). Some effort has been expended on improving the input of tracer through the river boundary in the transport model, to provide the best reproduction of the hydrodynamic model simulations. Because the advection schemes for the two models are different, the input of tracer through the river boundaries is treated differently, and total flux of tracer at a particular source may be different. In the hydrodynamic model, tracer flux is calculated as a product of the river flow and tracer concentration. In the transport model, the tracer flux is not calculated per se; rather, the strength of the flow determines the length of the Lagrangian trajectory, which in turn specifies the upstream distance from where the updated tracer concentrations are derived. Since the gradient of tracer concentration is unknown in the river boundaries, the Lagrangian method creates some uncertainty in the flux of tracer into the boundary cell, particularly during low flow conditions, and it is not evident that the correct flux of tracer into the model domain is being specified. Thus the mass of tracer entering the domain through the river boundaries is uncertain, which obviously creates difficulties when comparing modelled concentrations between the transport and hydrodynamic models. For this reason the river inputs in the transport model are entered as point source mass fluxes, where mass is directly added to a pre-defined depth range at a water column.

4.5.2.3 Evaluate transport against HD for 4 km model.

A year-long simulation, from September 2010 – September 2011, with two passive tracers released in both the hydrodynamic model and the transport model, has been used to test the metrics and scripts. In Fig. 4.5.1, four plots show the four metrics calculated for the surface layer concentrations of a passive tracer over the year-long simulation. The passive tracer was set initially to low concentrations throughout the model domain, and was supplied through the riverine boundaries at concentrations of $\sim 190 \text{ mg m}^{-3}$. No influx of tracer is specified through the open boundaries. Hence errors are low, and the model skill high, in the bulk of the domain where little change in tracer concentration has occurred. Close inshore, however, where the tracer sources are located, there is much greater variability in the model performance. Predicted surface layer tracers from both models at the end of the simulation (i.e. on 01 September 2011) are shown in Fig. 4.5.2. The transport model captures qualitatively the distribution of the tracer field, with elevated concentrations close inshore,

particularly around the mouth of the Fly River. However, quantitatively there are discrepancies between the transport model and hydrodynamic model predictions. The concentrations around the mouth of the Fly River are significantly under-predicted (bias < -1.0). Along the mainland coast, bias may be positive or negative. For example, concentrations along the strip of coast to the north-west of Fraser Island are significantly over-predicted by the transport model. This is believed to be a result of the boundary condition in the transport model, which for the Mary River is discharging too much tracer (compared to the HD model). In contrast, further north (between Townsville and Mackay), tracer input from the O'Connell River is under-predicted relative to the HD model. Further effort needs to be spent on improving the riverine flux of tracer in the transport model such that the comparison of tracer distributions can be properly assessed.

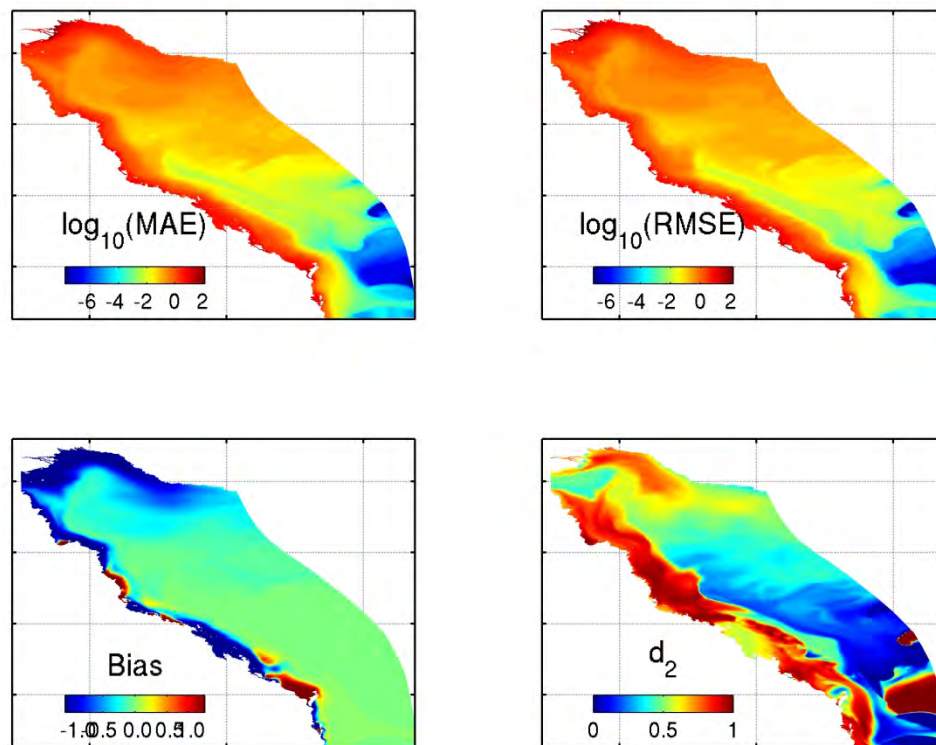


Figure 4.5.1. Maps of skill metrics calculated for surface layer concentrations of a passive tracer (DIN) over year-long simulations by the hydrodynamic and transport models.

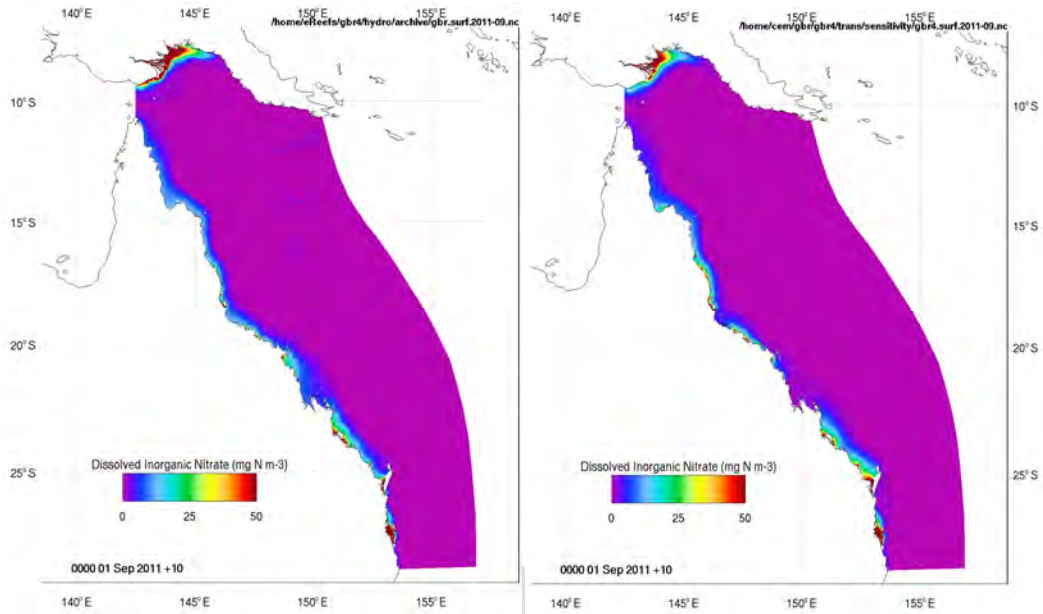


Figure 4.5.2. Maps of predicted surface layer concentrations of DIN on 01 September 2011 at the end of the year long simulation. Hydrodynamic model output is on the left, transport model predictions on the right.

In addition to metrics calculated at individual locations over a time series, the RMSE, MAE and bias metrics have all been applied spatially, giving domain-wide metrics that vary over time (Figure 4.5.3). The metrics shown in Figure 4.5.3 have been calculated for the surface layer tracer concentrations, and show that over the whole domain, the transport model has a negative bias of typically -0.5. The mean average error is about 1.0, whereas the RMSE is about 5.0. The larger RMSE relative to the MAE indicates that a relatively small number of points have large errors, which dominate the RMSE calculation. This is expected since over a large portion of the domain errors are small, with large discrepancies between the transport and HD models confined to the coastal zone.

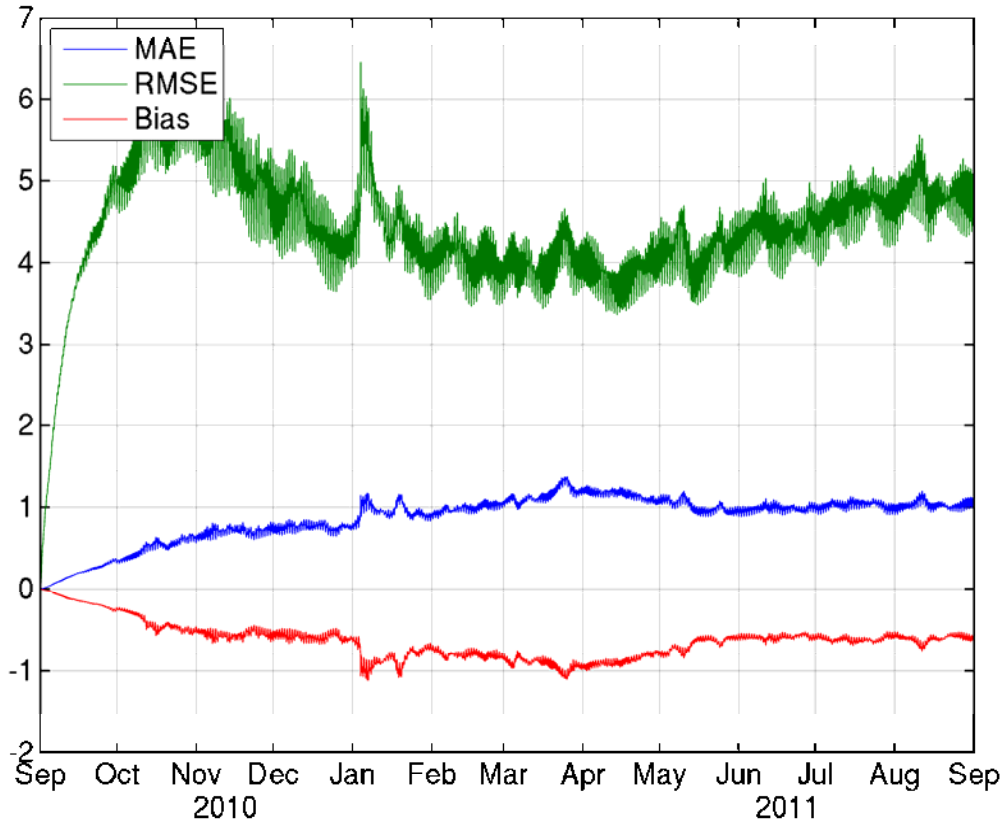


Figure 4.5.3. Domain-wide metrics for the surface layer tracer concentrations

The global mass of tracer in the model domain is also a critical indicator of the performance of the transport model. Clearly, for a passive tracer, the global mass needs to be conserved (subject to losses through the open boundaries). We have run a month-long simulation with the hydrodynamic model with two passive tracers implemented; the total tracer mass in the domain was calculated every hour and saved to file. The simulation was then repeated with the transport model, using different mass-preserving schemes, with hourly values of total tracer saved to file. A number of mass-preserving schemes have been developed, based on conserving mass globally or locally. Examples of a few of the simulations are shown in Figure 4.5.4.

The global schemes appear, superficially, to perform better than the local schemes i.e. they provide a better approximation of the hydrodynamic model time series. However, as noted above, it is not evident at present that the source of tracer to the GBR domain in the transport model is correctly modelled. Thus the uncertainty in the tracer source needs to be reduced before the appropriate mass-preserving scheme can be identified.

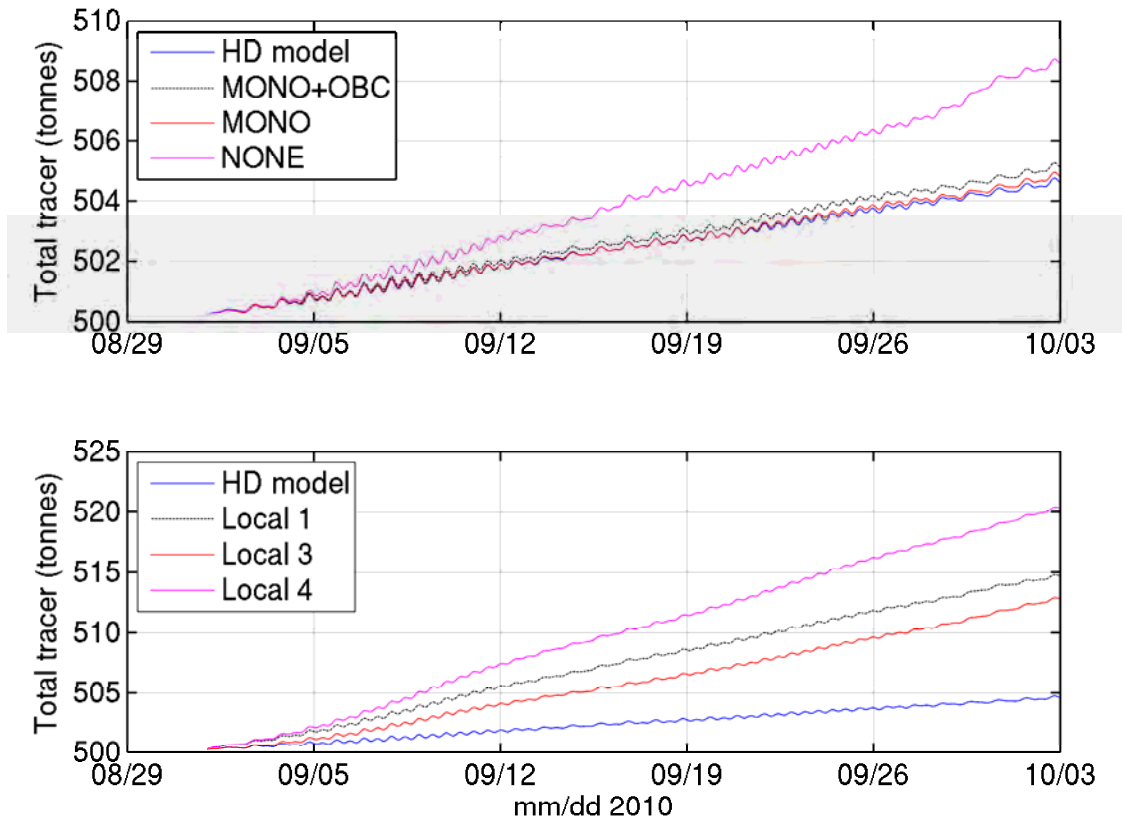


Figure 4.5.4. Global mass of passive tracer in the GBR4 model domain, as calculated during a simulation of September 2010 using different mass-preserving schemes. The target mass is provided by the hydrodynamic (HD) model simulation (blue). In the top panel, the tracer mass in a simulation without any mass-preserving scheme is shown (NONE), together with two applications of the monotonic global fill (MONO) with and without an open boundary adjustment (OBC). In the lower panel, three variants of the local fill schemes are shown.

4.5.3 FFSL transport model.

The combination of mass conservation with the ability to use long time steps has been developed in tracer advection algorithms by the atmospheric modelling community. To the best of our knowledge, these schemes have not been adopted by the ocean modelling community, and there appears to be little awareness of them. Two particular schemes of interest are the flux-form semi-Lagrangian (FFSL) method of Lin and Rood (1996, 1997), and the COSMIC scheme of Leonard et al. (1996). In their general approach these two methods, coincidentally published in the same year, are very similar. According to the authors, the FFSL scheme is fundamentally conservative, and produces noise-free solutions without additional diffusion (Lin and Rood, 1996), whilst allowing time steps that exceed the Courant number limitation that restricts hydrodynamic models. Both published schemes are developed and described for regular grids (i.e. constant Δx). We have adapted and implemented both the Lin & Rood (1996) FFSL scheme and the Leonard et al. (1996) COSMIC scheme for curvilinear ocean grids (i.e. variable Δx). We describe the algorithm below, and present some comparisons of tracer advection for the transport model compared to the full hydrodynamic model. The scheme of Leonard et al. (1996) is currently used in the GBR models.

The semi-Lagrangian approach to advection for a tracer ϕ solves the equation:

$$\frac{D\phi}{Dt} \equiv \frac{\partial\phi}{\partial t} + \bar{u} \cdot \nabla \phi = 0 \quad (4.5.1)$$

A typical semi-Lagrangian advection scheme operates by starting from each grid cell centre and tracing backwards along a streamline a distance $L = u\Delta t$ to get to the head of the streamline. The tracer value at the bottom of the streamline (i.e. the starting point at the grid cell centre) at time step $n+1$ is given by the tracer value at the head of the streamline at time step n . In other words, the model operates in a Lagrangian frame of reference, tracing the advection of parcels of water rather than using finite differences or other traditional modelling approaches to solve for advection. Trajectories can be traced back relatively long distances, allowing long time steps to be used by the model. (Lagrangian schemes are unconditionally stable; however, their accuracy depends on how “well” the estimated trajectory matches the real trajectory: as the time step increases, accuracy typically declines). However, because mass flux divergence equation is not solved, there is no mechanism in the Lagrangian approach to ensure that the total mass of tracer integrated across the model domain is the same at time step $n+1$ is the same as it was at time step n . When using curvilinear grids, where the grid spacing varies, it is certain that mass will not be conserved using this approach. And, in fact, the interpolation necessary to obtain the tracer value at the head of the streamline makes Lagrangian advection schemes non-conservative on all types of model grid, rendering the scheme fundamentally non-conservative.

In contrast, the FFSL and COSMIC schemes apply Lagrangian techniques to the mass flux terms on the faces of each grid cell. To achieve this, tracer concentrations on the *cell face* are derived by tracing backwards along trajectories that begin at the face. As with the traditional Lagrangian approach, relatively long time steps can be used to obtain upstream values, provided a good approximation of the real trajectory is made. (Note, however, that the FFSL and COSMIC schemes are *not* unconditionally stable; the stability constraint will be described later). The updated tracer concentration at the cell centre is then determined by solving the mass flux divergence in the usual way. In this way, because mass flux divergences are solved at each cell, mass is automatically conserved at the local and domain-wide scales.

We seek to solve the transport equation for a tracer ϕ conservatively with the ability to use long ($C_r \gg 1$) time steps, where $C_r = \max(u_1\Delta t/h_1, u_2\Delta t/h_2, w\Delta t/\Delta z)$ is the Courant number. From the hydrodynamic model, the cell dimensions ($h_1, h_2, \Delta z$), sea surface elevation $\eta^{n_{i,j}}$, and time-averaged volume fluxes $(u_1h_2h_3)^{n_{i\pm 1/2,j}}$ and $(u_2h_1h_3)^{n_{i,j\pm 1/2}}$ are known at each time step (superscript n) and grid location (i,j) on a staggered *curvilinear* Arakawa ‘C’ grid where h_1 and h_2 are *not* constant.

The three-dimensional transport equation for a tracer ϕ can be written:

$$\frac{\partial\phi}{\partial t} + \nabla \cdot (\bar{u}\phi) = 0 \quad (4.5.2)$$

where \bar{u} is the three-dimensional velocity vector. Implementing a flux-form solution on a curvilinear grid leads to:

$$\frac{\partial(h_3\phi)_{i,j}}{\partial t} + \frac{1}{(h_1h_2)_{i,j}} \left[\frac{\partial(uh_2h_3\phi)}{\partial\xi_1} + \frac{\partial(vh_1h_3\phi)}{\partial\xi_2} \right] + \frac{\partial(wh_3\phi)}{\partial z} = 0 \quad h_3 = \begin{cases} \Delta z + \eta & k = nk \\ \Delta z & k < nk \end{cases} \quad (4.5.3)$$

Following Lin & Rood (1996), the updated tracer concentration Φ^{n+1} is given by:

$$\phi_{i,j}^{n+1} = \frac{1}{h_3^{n+1}} \left\{ (h_3\phi)_{i,j}^n - F \left[\phi^n + \frac{1}{2} g(\phi^n) \right] - G \left[\phi^n + \frac{1}{2} f(\phi^n) \right] - H \left[\phi^n \right] \right\} \quad (4.5.4)$$

where

$$\begin{aligned} F[\theta] &= \frac{1}{(h_1h_2)_{i,j}} [X_{i+\frac{1}{2}} - X_{i-\frac{1}{2}}] = \frac{1}{(h_1h_2)_{i,j}} [\Delta t(u_1h_2h_3\theta)_{i+\frac{1}{2}} - \Delta t(u_1h_2h_3\theta)_{i-\frac{1}{2}}] \\ G[\theta] &= \frac{1}{(h_1h_2)_{i,j}} [Y_{j+\frac{1}{2}} - Y_{j-\frac{1}{2}}] = \frac{1}{(h_1h_2)_{i,j}} [\Delta t(u_2h_1h_3\theta)_{j+\frac{1}{2}} - \Delta t(u_2h_1h_3\theta)_{j-\frac{1}{2}}] \\ H[\theta] &= Z_{k+\frac{1}{2}} - Z_{k-\frac{1}{2}} = \Delta t[(w\theta)_{k+\frac{1}{2}} - (w\theta)_{k-\frac{1}{2}}] \\ f(\theta) &= \left(\frac{u_1\Delta t}{h_1} \right)_{i,j} [\theta_{i+\frac{1}{2}} - \theta_{i-\frac{1}{2}}] \\ g(\theta) &= \left(\frac{u_2\Delta t}{h_2} \right)_{i,j} [\theta_{j+\frac{1}{2}} - \theta_{j-\frac{1}{2}}] \end{aligned} \quad (4.5.5)$$

and

$$\begin{aligned} u_{1i,j} &= \frac{u_{1i+\frac{1}{2},j} + u_{1i-\frac{1}{2},j}}{2} \\ u_{2i,j} &= \frac{u_{2i,j+\frac{1}{2}} + u_{2i,j-\frac{1}{2}}}{2} \end{aligned} \quad (4.5.6)$$

The terms F[] and G[] denote the horizontal mass flux divergences in each direction, and H[] denotes the vertical divergence. The terms g(φ) and f(φ) are transverse advection terms that are required to improve accuracy and maintain numerical stability with the longer time step Δt that may be used. The terms X, Y and Z are the mass fluxes at cell faces in the horizontal and vertical directions.

In the FFSL scheme, the vertical transport is treated independently of the horizontal transport (in the sense that the transverse terms associated with vertical advection are ignored). In this case, two additional 3D tracers must be declared for each modelled tracer in order to calculate the transverse terms. For the fully 3D COSMIC scheme of Leonard et al. (1996), the transverse terms are calculated in all three dimensions, leading to the calculation of an additional six tracers for each modelled tracer. Thus the FFSL scheme has the potential to be significantly quicker than the COSMIC scheme, but the COSMIC scheme is likely to be more stable numerically.

In order to allow long time steps, the flux terms must be broken into integer and fractional components relative to the local grid spacing. On curvilinear grids, the integer component is determined in the ξ_1 direction at face $i-1/2$ by finding $K_{i-1/2}$ such that:

$$L_{i-1/2}^x = u_{i-1/2} \cdot \Delta t = \begin{cases} \sum_{k=1}^{K_{i-1/2}} h_{i-k} + \delta x_{i-1/2} = \Delta x_{i-1/2} + \delta x_{i-1/2}, & L_{i-1/2}^x > 0 \\ -\sum_{k=1}^{-K_{i-1/2}} h_{i-1+k} - \delta x_{i-1/2} = -(\Delta x_{i-1/2} + \delta x_{i-1/2}), & L_{i-1/2}^x < 0 \end{cases} \quad (4.5.7)$$

where $K_{i-1/2}$ is an integer value, with the same sign as $L_{i-1/2}$, chosen so that:

$$\begin{aligned} 0 < \delta x_{i-1/2} < h_{i-K_{i-1/2}-1} & \quad K_{i-1/2} > 0 \\ 0 < \delta x_{i-1/2} < h_{i+K_{i-1/2}+1} & \quad K_{i-1/2} < 0 \end{aligned} \quad (4.5.8)$$

Because the grid spacing is not uniform in curvilinear grids, the integer component of the trajectory is derived by tracing back along the trajectory and subtracting successive values of h_1 from $L_{i-1/2}$ until the remainder of the trajectory is less than the next value of h_1 . The fractional component of the flux term is then expressed as the ratio of the remainder of the trajectory δx and h_1 at the head of the trajectory, e.g.:

$$c_{i-1/2}^x = \frac{\delta x_{i-1/2}}{h_{i-K_{i-1/2}+1}^x} \quad (4.5.9)$$

Values of K and c must be determined for both the cell faces and the cell centre in both ξ_1 and ξ_2 directions.

The integer flux at a left-hand face, $i-1/2$, is computed by e.g.

$$I_{i-1/2}(\theta) = \begin{cases} \sum_{k=1}^{K_{i-1/2}} \theta_{i-k}^n, & K_{i-1/2} \geq 1 \\ 0, & K_{i-1/2} = 0 \\ -\sum_{k=1}^{-K_{i-1/2}} \theta_{i-1+k}^n, & K_{i-1/2} \leq -1 \end{cases} \quad (4.5.10)$$

The transverse operators, $f(\phi^n)$ and $g(\phi^n)$, can be written as:

$$\begin{aligned}
f_{i,j} &= (\phi_{I,j}^n - \phi_{i,j}^n) + |c_{i,j}^x| (\phi_{I^*,j}^n - \phi_{i,j}^n) \\
g_{i,j} &= (\phi_{i,J}^n - \phi_{i,j}^n) + |c_{i,j}^y| (\phi_{i,J^*}^n - \phi_{i,j}^n)
\end{aligned}
\tag{4.5.11}$$

Where the indices I and J are given by

$$\begin{aligned}
I &= i - K_{i,j}^x; J = j - K_{i,j}^y \\
I^* &= I - \text{SIGN}(1, K_{i,j}^x); J^* = J - \text{SIGN}(1, K_{i,j}^y)
\end{aligned}
\tag{4.5.12}$$

The FFSL algorithm operates as follows. To solve the tracer flux in the x-direction, define a temporary tracer, $\phi_{i,j}^g$, such that:

$$\begin{aligned}
\phi_{i,j}^g &= (\phi)_{i,j}^n + \frac{1}{2} g_{i,j} \\
&= \frac{1}{2} [\phi_{i,J}^n + \phi_{i,j}^n + |c_{i,j}^y| (\phi_{i,J^*}^n - \phi_{i,j}^n)]
\end{aligned}
\tag{4.5.13}$$

Define $\Phi' = (h_1 \phi^g)_{i,j}^n$. Then, the mass flux across the left-hand face of the cell (i,j) is given by:

$$X_{i-\frac{1}{2},j} = (h_2 h_3)_{i-\frac{1}{2},j} I_{i-\frac{1}{2},j} (\Phi') + c_{i-\frac{1}{2},j}^x (h_2 h_3) \{\Phi'_{I,j}\}
\tag{4.5.14}$$

where the Van Leer scheme is used to obtain the tracer value at the face in the fractional component of the equation, and the indices

$$I = \text{INT}(i - C_{i-\frac{1}{2},j}^x)
\tag{4.5.15}$$

The terms $X_{i+\frac{1}{2}}, Y_{j-\frac{1}{2}}, Y_{j+\frac{1}{2}}, Z_{k-\frac{1}{2}}, Z_{k+\frac{1}{2}}$, are calculated similarly. From these terms, the updated tracer concentration at the cell centre can be derived.

From a hydrodynamic model simulation, hourly-averaged values of the volume fluxes, e.g. $U_{i-\frac{1}{2}} = (u_1 h_2 h_3)_{i-\frac{1}{2}}$, and velocities at cell faces, and instantaneous values of the sea surface height (η), temperature and salinity are archived. It is necessary to archive both the velocity fluxes and velocities because the former are required for the flux calculations described above, and the latter are used to determine the trajectory distances.

4.5.3.1 Numerical Stability

Unlike semi-Lagrangian advection schemes, the FFSL (and COSMIC) scheme described above is not unconditionally stable, but is subject to the Lipschitz condition:

$$\max \left(\frac{\Delta t \Delta u_1}{h_1}, \frac{\Delta t \Delta u_2}{h_2}, \frac{\Delta t \Delta w}{\Delta z} \right) \leq 1
\tag{4.5.16}$$

where Δu_1 is the difference between the velocities on the upstream and downstream faces of a cell i.e.

$$\Delta u_{1i,j} = \left| u_{1i+1/2,j} - u_{1i-1/2,j} \right| \quad (4.5.17)$$

The time step is set by calculating the values of $\Delta u_1/h_1$, $\Delta u_2/h_2$ and $\Delta w/\Delta z$ across the grid at each time step, and ensuring the above condition is met.

The Lipschitz condition is typically much less restrictive than the usual Courant number condition. However, the Lipschitz number is a strong function of the grid spacing (h_1), and will become more restrictive for higher resolution grids.

4.5.3.2 Model Tests

The transport model has been tested in a test estuary, both closed and with an open boundary, and using the GBR4 model. A selection of the test results are presented here. In both sets of tests, we have looked at two aspects of advection of a passive tracer:

- (i) Does the transport model advection scheme produce similar tracer distributions to those simulated by the full hydrodynamic model?
- (ii) Is tracer mass conserved by the transport model?

To illustrate the results of these tests, we present below images of tracer distributions from the full hydrodynamic model alongside comparable distributions from the transport model, and we present time series of tracer mass calculated by both models.

The first test was performed in a closed estuary basin. The basin had a depth of 20 m, shoaling along the estuary at the western domain to 5 m depth at the head. The horizontal grid spacing in both directions was 1000 m. In the vertical, 20 layers were used with a minimum thickness of 0.5 m in the upper 10 layers, increasing to a maximum of 5 m thickness. River flow into the estuary was $1000 \text{ m}^3\text{s}^{-1}$, discharging at the head of the estuary. No wind forcing were simulated. Coriolis acceleration was imposed equivalent to the value at 38°S . The initial tracer concentration throughout the domain was zero. A point source of passive tracer was discharged in the centre of the basin, at a rate of $1000 \text{ mg}\cdot\text{s}^{-1}$. Since there is no open boundary, no tracer should be lost from the domain. The simulation ran for 10 days. Modelled surface tracer distributions at the end of the 10 day period, from the full hydrodynamic model and the two transport model methods, are shown in Fig. 4.5.5. Clearly, the FFSL scheme compares very well with the full hydrodynamic model, with closely matching peak concentrations at the discharge point and very similar concentrations throughout the tracer plume as it is swept around the closed basin. By contrast, the distribution obtained using the semi-Lagrange advection scheme (with a monotonic global fill adjustment) is much more diffusive (a known facet of the semi-Lagrange scheme), with noticeably lower peak concentrations around the discharge location. For this test case, all three schemes conserve mass well (Fig 4.5.5 bottom panel).

The second set of tests was performed in an identical estuary basin, except that the eastern boundary was open. All conditions were as described above, except that tidal forcing was applied at the eastern boundary. The specified tide had an amplitude of 1 m and a period of 12 hours. River flow into the estuary was $1000 \text{ m}^3\text{s}^{-1}$, discharged at the head of the estuary. Again, the initial tracer concentration throughout the domain was zero, and a point source of passive tracer was discharged in the centre of the basin, at a rate of $1000 \text{ mg}\cdot\text{s}^{-1}$. At the open eastern boundary, a no-gradient condition was used during outflow and an oceanic tracer value of zero was used during inflow. The simulation ran for 10 days. Modelled surface tracer distributions at the end of the 10 day period, from the full hydrodynamic model and the two transport model methods, are shown in Fig. 4.5.6. Again, the FFSL scheme compares very well with the full hydrodynamic model, with closely matching peak concentrations at the discharge point and very similar concentrations throughout the tracer plume as it is swept along the northern perimeter of the estuary basin. Since the estuary is open, tracer is lost from the model domain when the plume reaches the open eastern boundary. The south-east quadrant of the domain remains almost entirely free of tracer. As in the previous test, the distribution obtained using the semi-Lagrange advection scheme (with a monotonic global fill and open boundary adjustment) is much more diffusive, with noticeably lower peak concentrations around the discharge location. For this test case, mass conservation by the full hydrodynamic model and the FFSL transport model were identical, with mass lost from the domain from 7 January onwards (Fig 4.5.6 bottom panel). By contrast, the semi-Lagrange scheme showed a higher tracer mass in the estuary basin, indicating either that less mass exited the domain, or that tracer was spuriously generated over the latter part of the simulation.

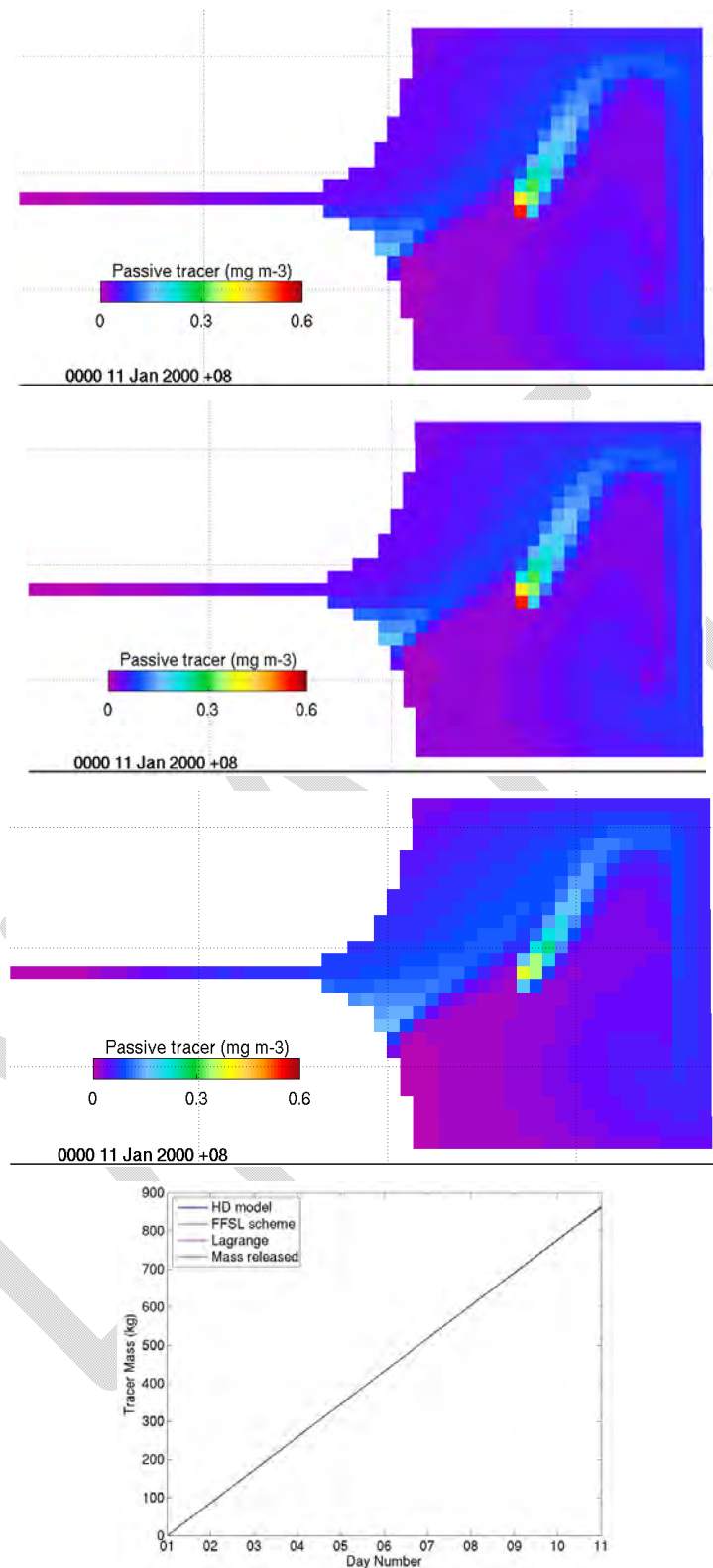


Figure 4.5.5. Tracer distributions after 10 days of discharge in a closed estuary, predicted by the full hydrodynamic model (top panel), the transport model with FFSL advection (second panel), and the transport model with the semi-Lagrange advection scheme (third panel). The total tracer mass in the model domain over the integration is shown in the bottom panel for each scheme; note the loss of mass through the open boundary after 6 days.

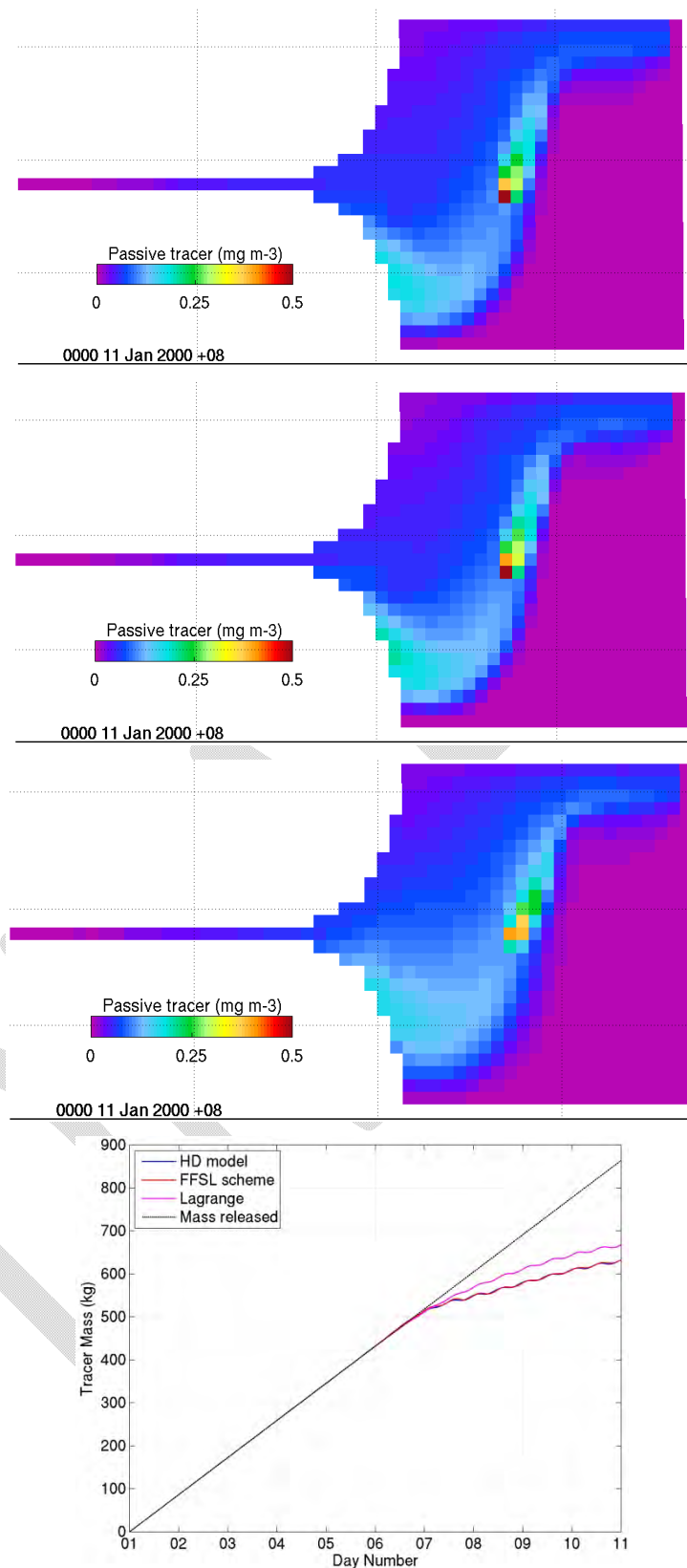


Figure 4.5.6. Tracer distributions after 10 days of discharge in an open estuary, predicted by the full hydrodynamic model (top panel), the transport model with FFSL advection (second panel), and the transport model with the Lagrange advection scheme (third panel). The total tracer mass in the model domain over the integration is shown in the bottom panel for each scheme; note the loss of mass through the open boundary after 00:00 on Day 7.

In the GBR4 model domain, tests were conducted with the release of two tracers for a simulation period of one month over September 2010 and January 2011. The model configuration for these tests matched the best hydrodynamic model configuration described elsewhere (Section 5.1.1) in this report. In short, tides and low frequency velocity and sea level forcing for September 2010 were applied along the open boundaries. Freshwater input was supplied via 22 rivers along the Queensland and Papua New Guinea coasts. Wind and atmospheric forcing were taken from the BoM ACCESS product. These tests, therefore, assess the transport model under real model forcing conditions.

The first test tracer, nominally called Dissolved Nitrate (DIN) was initialized over the entire domain with a value of one. Along each open boundary, external values of DIN were specified as zero, as were riverine concentrations. The test therefore simulates the flushing of a uniformly distributed tracer from the GBR domain by “clean” river and ocean waters. Initial distributions of the second passive tracer were set to zero. This tracer was released at four discrete sources in the domain, at a discharge rate of 1000 mg.s^{-1} at each source. Modelled surface tracer distributions at the end of the month long simulation, from the hydrodynamic and transport models are shown below.

The GBR4 results repeat those of the test estuary results. The DIN tracer distribution from the FFSL advection scheme closely matches that of the full hydrodynamic model (Fig. 4.5.7). The oceanic water, with a tracer concentration of zero, penetrates into the GBR domain in elongated filaments, driven by the large scale ocean circulation. Mixing between the ambient GBR water and the intruding boundary water leads to zones of intermediate tracer concentrations. In the very near-shore region river water, also with tracer concentrations of zero, mixes with the coastal water. In the intermediate region between coast and offshore boundaries, water properties are not modified in the time available (30 days) by either the river or open boundary water, and the tracer concentration remains steady at one.

Close inspection of the tracer distributions resulting from the Lagrangian scheme (Fig. 4.5.7) show much greater effective diffusion, an inherent trait of Lagrangian schemes. The filaments of high tracer concentrations are diluted, and the central body of undisturbed water (tracer concentration of one) is noticeably reduced. For example, the filament of high tracer concentration near the eastern boundary of the domain, from $20 - 23^\circ\text{S}$, has a peak value of about 0.8 in the semi-Lagrangian scheme distribution, compared to 0.94 in both the HD model and the FFSL results.

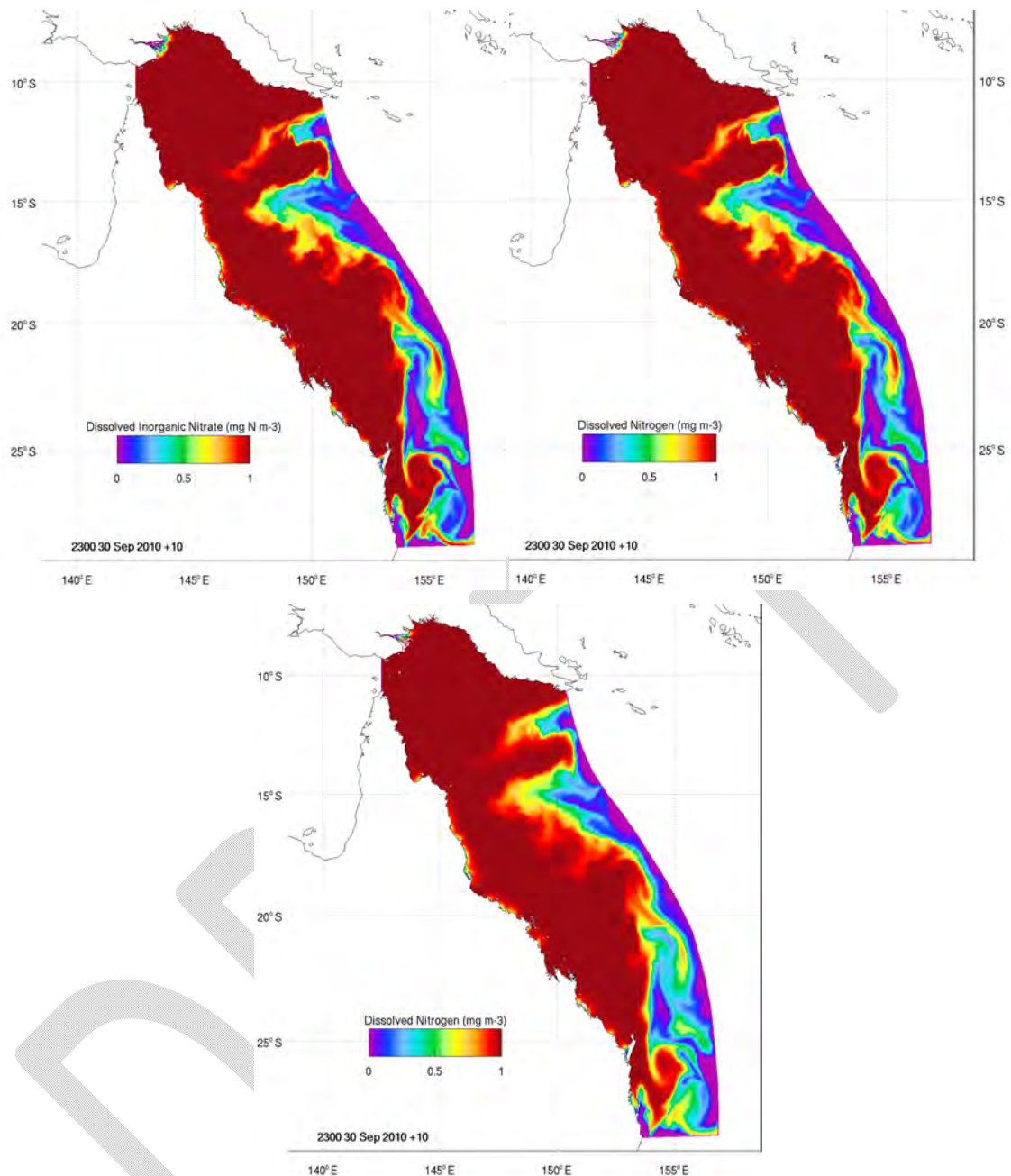


Figure 4.5.7. Distributions of a tracer (nominally called Dissolved Inorganic Nitrate) after 30 days simulation by the full hydrodynamic model (top left panel), the transport model with FFSL advection (top right panel) and the transport model with semi-Lagrange advection (bottom panel).

The four point sources of the second tracer can be located in Fig. 4.5.8, which indicates the extent of the tracer plumes after 30 days simulation on the scale of the whole GBR. Magnified snapshots of the tracer plumes after 30 days discharge are shown in Fig. 4.5.9. The FFSL scheme again provides a better, less diffusive, representation of the HD model advection than the semi-Lagrange scheme. The plumes are more clearly defined, whereas there is considerably more smearing of the plumes with the semi-Lagrangian scheme.

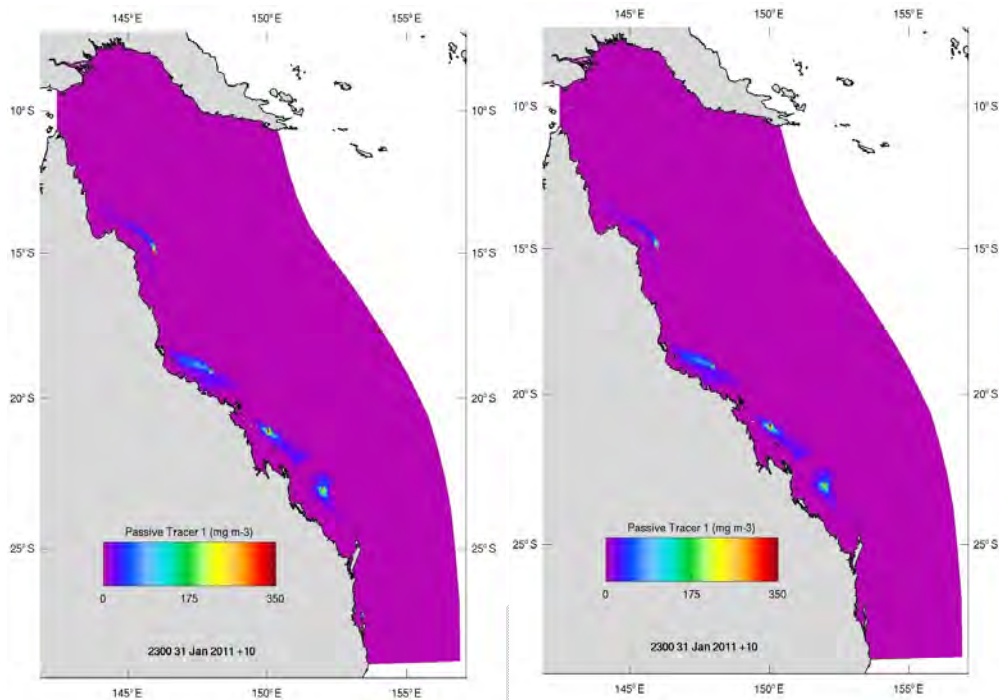


Figure 4.5.8. Surface distributions of passive tracer after 30 days simulation by the full hydrodynamic model (left panel) and the transport model with FFSL advection (right panel). The tracer plumes are shown in more detail in Figure 4.5.9.

The total mass of tracer in the domain is conserved by all schemes (Fig. 4.5.10). The semi-Lagrange scheme was run with the monotonic global filling and open boundary adjustment switches in order to force mass conservation. The effect of these corrections, however, is to increase the effective diffusion of the already diffusive semi-Lagrange scheme, as is evident from the modelled tracer distributions. The semi-Lagrange scheme was also run with no global filling; in this case the drift in total mass is clearly seen in Fig. 4.5.10.

Finally the FFSL scheme was tested to comply with the constancy condition, which states that an initially homogeneous scalar should remain identically equal to that initial constant value everywhere throughout a simulation. The distribution of a unit tracer after 30 days of simulation is displayed in Fig. 4.5.11, from which it is seen the initial value has not deviated to within machine precision.

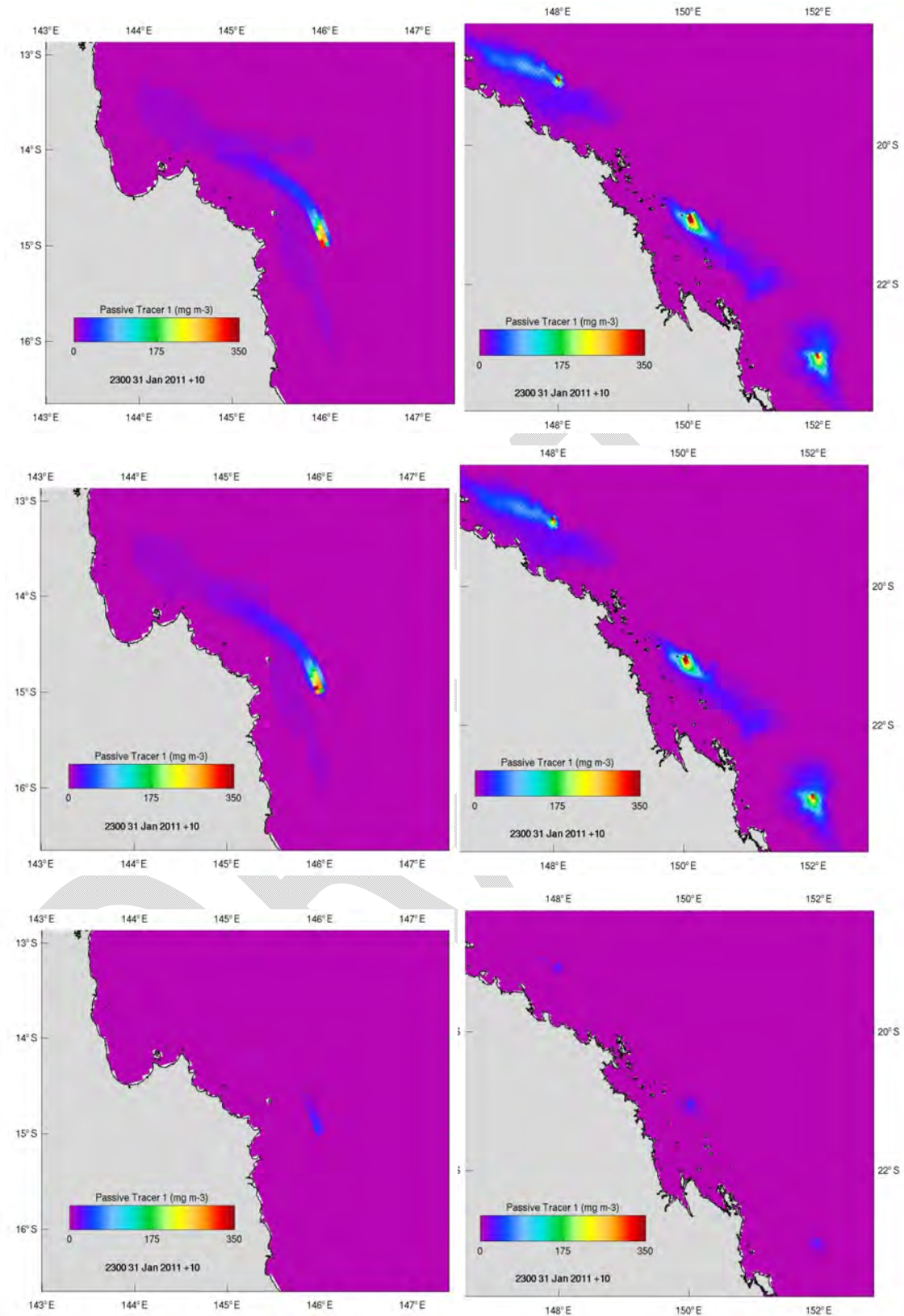


Figure 4.5.9. Close-ups of the surface distributions of passive tracer after 30 days simulation by the full hydrodynamic model (top panels), the transport model with FFSL advection (middle panels) and the transport model with semi-Lagrangian advection (bottom panels). The northern plume is in the left panels, while the southern three plumes are on the right.

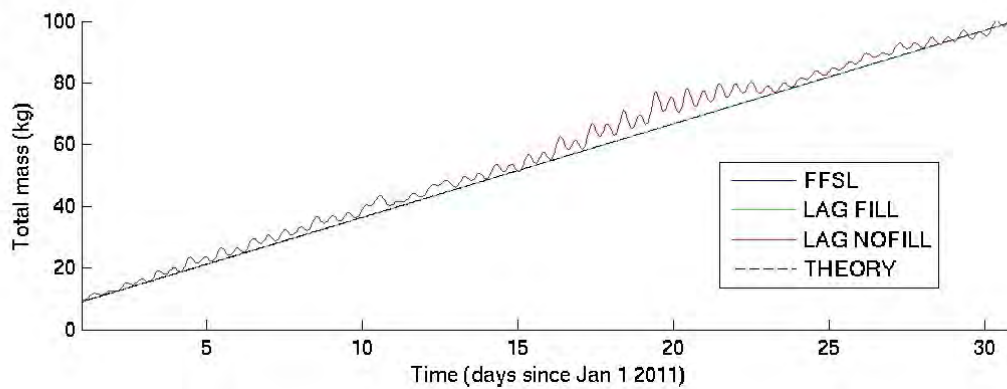


Figure 4.5.10. Total mass of the passive tracer, integrated over the whole GBR4 domain, for the test simulations. The mass of tracer released is also shown for comparison.

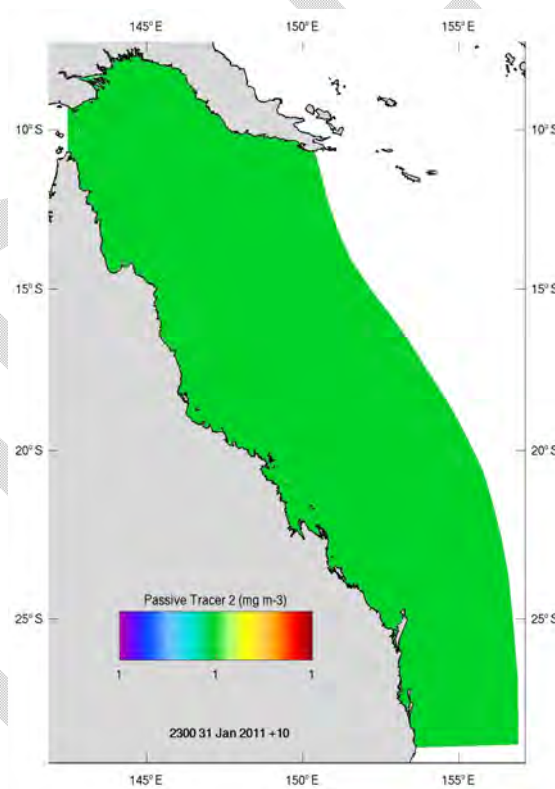


Figure 4.5.11. Constancy condition test using the FFSL scheme.

4.5.3.3 Efficiency

The results shown here demonstrate the accuracy and conservation properties of the FFSL advection scheme. However, it is also essential that the transport model with the FFSL scheme

runs efficiently. The transport model is used to simulate advection in the sediment transport and biogeochemical models described elsewhere. These models use many tracers to simulate sediment transport and biogeochemical processes, many of which are subject to advection and diffusion. The semi-Lagrangian transport model is typically several orders of magnitude faster than the full hydrodynamic model when run with a small number of tracers, as in these tests cases. Furthermore, this scheme becomes more efficient as tracer numbers are increased, as the streamline origin only needs to be located once, whereupon an interpolation onto this origin only is required for every extra tracer. The FFSL scheme needs to be of comparable efficiency, and to scale up efficiently from a few to many tracers.

The model speeds for the test runs described above are presented in Table 4.5.1. The model speed is defined as the ratio of the time taken (walltime) to complete a simulation to the length of the simulation itself. So, if a model simulation of one month (30 days) takes one day to complete, the model speed is given as 30:1. The model speed is also machine-dependent, and the speed of the full hydrodynamic (HD) model full is also dependent on the number of processors (cores) used. In all the tests, the transport model was run on the same machine as the equivalent HD model run. The number of cores used in the HD model simulation is given in the table. The table shows that for these simulations, with typically 2 -3 tracers, the FFSL is comparable or quicker than the semi-Lagrange scheme. In limited experiments undertaken so far, we have found that the COSMIC scheme is 15% slower than the FFSL scheme. The semi-Lagrange scheme is slowed by the necessity to implement the global filling and open boundary adjustments to ensure global mass conservation. These results demonstrate that the transport model using the FFSL and COSMIC schemes is comparable in speed to the semi-Lagrangian advection scheme, and an order of magnitude quicker than the hydrodynamic model. The challenge remaining is to determine how well the FFSL and COSMIC schemes scale up to large numbers of tracers, and distributed processing may be required to achieve target runtimes (e.g. solving each tracer on separate processors).

Table 4.5.1. Comparative model speeds of the transport model with the FFSL advection scheme, the transport model with the traditional semi-Lagrange advection scheme and the full hydrodynamic (HD) model. The comparison is very machine-dependent; in all tests, the transport model simulations were run on the same machine as the HD model, with the same number of passive tracers. The number of processors (cores) used by the HD model is shown; in all cases, the transport model used one core.

Test Case	No. Cores	Model Speed (Time ratio)		
		HD model	FFSL Scheme	Lagrange scheme
Closed Estuary	1	5300:1	72000:1	57600:1
Open Estuary	1	5877:1	66461:1	61714:1
GBR4	12	34:1	367:1	319:1

4.6 Sediment transport model

The sediment transport model adds a multilayer sediment bed to the hydrodynamic model grid and simulates sinking, deposition and resuspension of multiple size-classes of suspended sediment (Margvelashvili et al., 2008). The model solves advection-diffusion equations of the mass conservation of suspended and bottom sediments and is particularly suitable for representing fine sediment dynamics, including resuspension and transport of biogeochemical particles. Sediment particles settle on the seabed due to the gravity force and resuspend into the water column whenever the bottom shear stresses, exerted by waves and currents, exceed the critical shear stress of erosion. The resuspension and deposition fluxes are parameterised with the Ariathurai and Krone (1976) formula. Estimates of the bottom shear stress, required by this formula, are derived through the Grant and Madsen boundary layer model (Madsen, 1994). Bottom roughness is scaled by ripple dimensions (Grant and Madsen, 1982) which are considered the model input parameters and must be specified through observations or calibration study.

Sediments in benthic layers undergo vertical mixing due to bioturbation, represented by local diffusion. The corresponding diffusion coefficient is scaled with the sediment depth so that the bioturbation of sediments ceases to operate at the bottom of the biologically active layer. The resistance of sediments to resuspension increases with the sediment depth and there is no direct exchange of particles in horizontal directions within the benthic sediments.

The numerical grid for sediment variables in the water column coincides with the numerical grid for the hydrodynamic model. Within the bottom sediments, the model utilises a time-varying sediment-thickness-adapted grid, with the top active sediment layer having constant thickness, and the thickness of deeper layers varying with time to accommodate the deposited sediment. Horizontal resolution within sediments follows the resolution of the water column grid.

The sediment transport model can be fully coupled to the hydrodynamic model implying that both models run in parallel and have the same time step. Another option is to simulate sediment transport in off-line mode. In this case currents and diffusion coefficients saved from the hydrodynamic model run provide inputs into the stand-alone sediment transport model. The simulation time-step is much larger than that of the coupled model and there is no feedback from the sediment processes to the hydrodynamics, i.e. the impact of sediments on flow, density and turbulence are not simulated. This decoupling of the sediment and hydrodynamic models provides substantial benefits in computational efficiency.

4.6.1 Initial conditions

The sediment transport model was initialised with the observed distribution of gravel, sand and mud fractions of benthic sediments acquired from Geoscience Australia MARine Sediment (MARS) database. The corresponding sampling sites and the distribution of the interpolated data are illustrated in Fig. 4.6.1. The model simulates transport of only fine-sediments represented by mud (plus transport of sediments from catchments, discussed in the next paragraph). Heavier particles (gravel and sand, which during the resuspension event tend to accumulate within a thin near-bottom layer typically not resolved by the 3D model grid), were kept immobilised with the benthic sediments.

Apart from the mud, which is initially allocated with the modelling domain and represents historically accumulated sediments, the model also simulates resuspension, deposition and transport of fine sediments delivered from catchments *during the simulation period*. Initial concentration of these catchment-sediments is set to zero throughout the modelling domain.

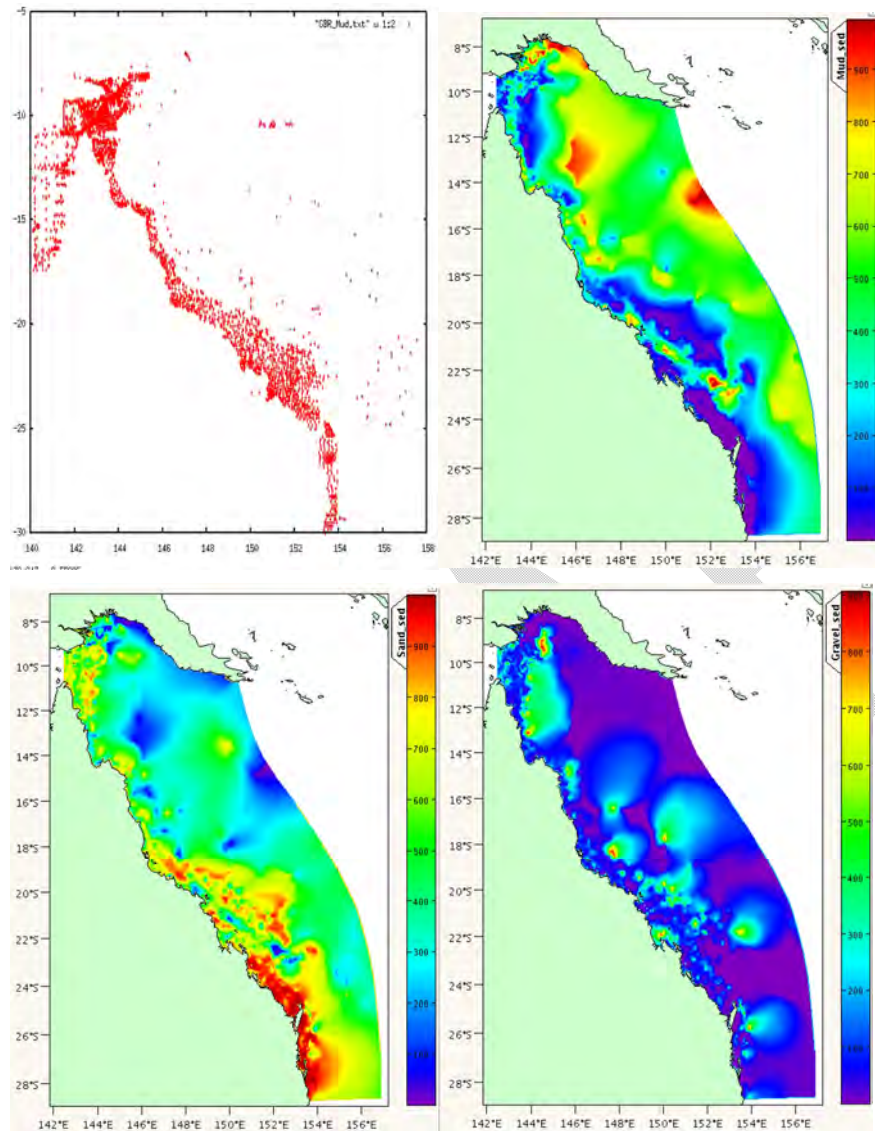


Figure 4.6.1. Sampling sites (top left) and interpolated maps of mud (top right), sand (bottom left) and gravel distribution in benthic sediment (data from GA MARS database; units kg m⁻³).

4.6.2 Forcing

The sediment transport model was driven by hourly mean velocities and diffusion coefficients as produced by the 4km hydrodynamic model. The sediment model is coupled to the transport model, where advection is performed using offline flow fields in the Flux Form semi-Lagrange scheme (Section 4.5.3) to evolve the concentration fields forward in time.

The wave data (RMS of near bottom orbital velocity, wave direction and period) were obtained from the shelf-scale WaveWatch III (WWIII) model nested into the global-scale WWIII model (Section 4.5). Spatial resolution of the wave-model is about 4km across the region and the data are generated with an hourly time-step.

4.6.3 Catchment loads

According to the sediment transport model, sediments delivered from catchments into the GBR region over the 4-year simulation period are represented by two classes of particles – “fine-sediment” and “dust”. Physical characteristics of “fine-sediment” (e.g. settling velocity, critical shear stress of resuspension, etc.) are exactly the same as that of the mud (i.e. fine sediments accumulated in the region over the course of its history). This class represents the bulk mass of fine particles delivered from catchments. The settling velocity of this fraction is set to 17 m/day. The corresponding loads are obtained either through the simulation of the catchment model (Waters et al., 2014) or have been inferred from the literature data (Furnas, 2003). For the latter approach, a certain concentration of the suspended sediment is assigned to each river considered in this model. This concentration is constant throughout the simulation period so that the sediment load is scaled only by changes in the river flow (Fig. 4.6.2). Fig. 4.6.3 illustrates comparison between annually mean loads based on these estimates against literature data.

Alternatively, estimates of catchment loads of fine sediments are based on simulations by catchment model (Waters et al 2014). Daily estimates of sediment loads from the Queensland catchment models for the 22 rivers included in the 4km model grid were available for the GBR region during the last three months of the eReef project. The catchment model estimates GBR average annual loads of sediments, pesticides and nutrients for each of the 35 catchments draining to the GBR as part of the Paddock to reef program (http://www.reefplan.qld.gov.au/measuring-success/paddock-to-reef/catchment-loads/#_monitoring). For loads outside the GBR region estimates of these loads, based on literature data (Furnas, 2003) were used to provide an input into the model.

Another class of catchment-sediments (“dust”) represents very fine fraction of sediments (tails of the sediment size distribution) delivered from catchments. Recent studies highlighted the role of such particles in influencing turbidity levels on GBR (Lewis et al., 2015). These particles may stimulate the development of highly mobile organic-rich flocs which can travel over the much longer distances compared to the bulk mass of the fine sediment delivered from catchments. In a high-energy environment the process of flocculation is likely to be a dynamic process where disruption of larger flocs is balanced by aggregation of smaller flocs and individual particles. The knowledge of physical properties and transport characteristics of such a mixture of clay-sized particulates and their flocs is very limited. According to (Amos et al., 2004) during the flood event in the Burdekin River the clay-sized minerals comprise from 10 to 70 % out of the total mass of TSS. Data from another study also suggest significant content of clay-sized particles in TSS on the inner-shelf under non-flood conditions (Browne et al., 2012). Given this uncertainty, in our study we conduct a number of numerical experiments with the mass-fraction of the catchment “dust” varying from 0, to 3, 10 and 20 % of the total mass of “fine-sediment” delivered from catchment. The settling velocity of these particles is set to 1 m/day, characteristic to the settling velocity of the organic particulates.

Further description and analysis of catchment loads is available in the biogeochemistry section of this report. By the time of writing this report an error has been discovered in a script processing sediment loads from the Burdekin catchments for a subset of simulated scenarios. This translated into zero loads of heavier fraction of fine-sediment from Burdekin for the first 2 years of simulation in these scenarios (i.e sediment loads were represented only by “dust” fraction sediment). This error is expected to have a localised impact on TSS in the vicinity of the river mouth and will be addressed in the future.

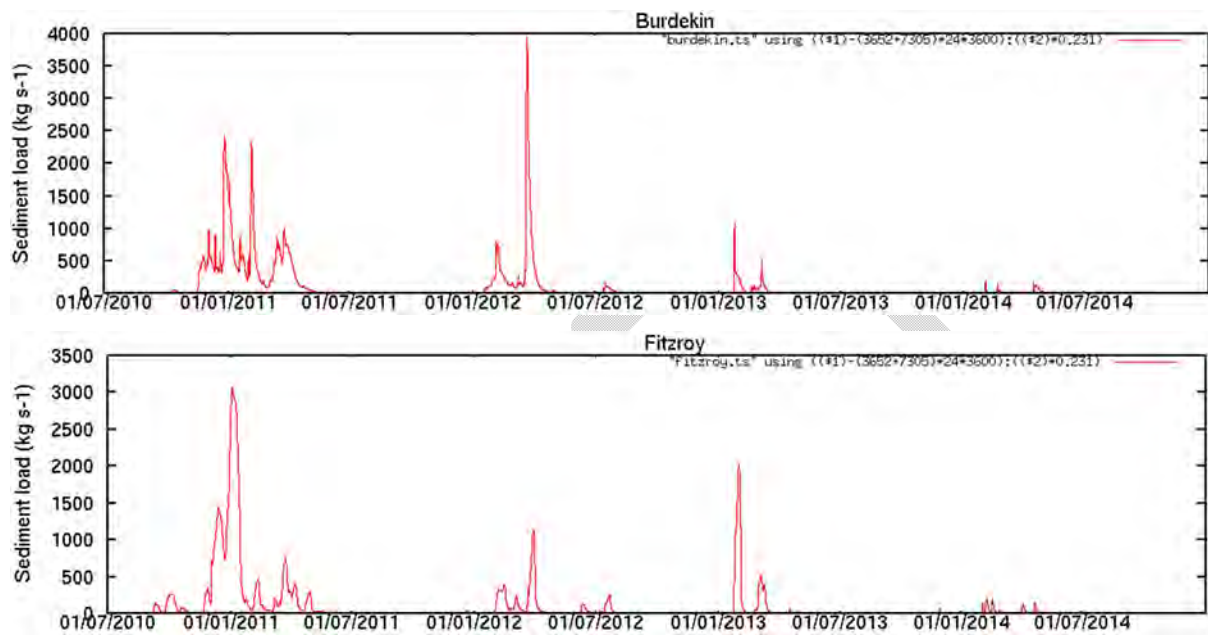


Figure 4.6.2. Sediment loads from Burdekin and Fitzroy catchments as used in simulations.

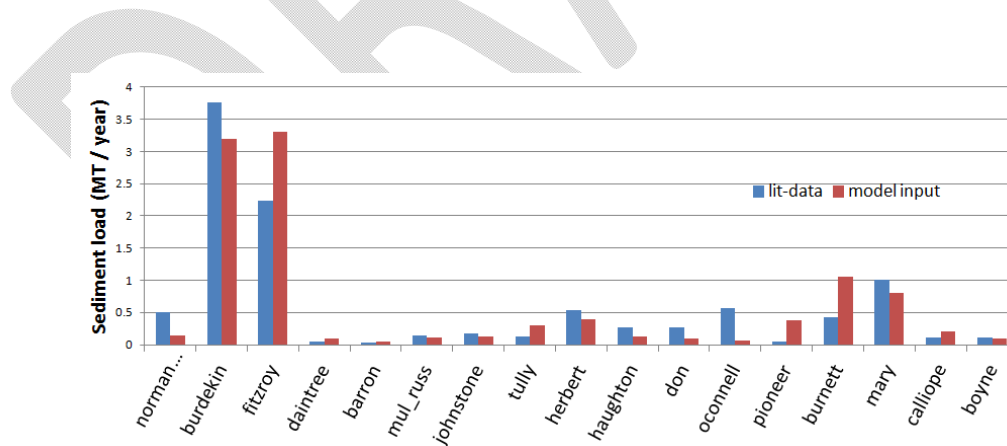


Figure 4.6.3. Estimated annual loads of sediment from catchments vs. literature data (Furnas, 2003).

4.6.4 Calibration strategy

One of the key challenges facing the development of the sediment transport model in the GBR region is the task of constraining the model uncertainty with observations. The model is based on semi-empirical site-specific relationships that must fine-tuned to fit the model to

observations. This task is particularly challenging in the GBR region because of the scale and variability of the heterogeneous coastal and shelf environments. The problem is further exacerbated by typically poor quality of observations. Field-samples are scattered in space and time and represent single-point data rather than variables integrated over the grid-cell area. Time series of turbidity tend to provide good temporal coverage of the signal at specific locations but give poor spatial coverage of the domain. Remote sensing products offer higher resolution of the surface layer, but may not have sufficient coverage in time and in depth. Different sets of data have their own uncertainty which often is not known upfront and in some cases might be comparable to or even exceed the uncertainty of the model.

The strategy to calibrate the sediment transport model of the GBR region, adopted in this study, is as follows. First, the model is constrained with the remote sensing data. Because of the large volumes of such data, manual tuning of the model to observations in this case is not feasible. Instead the remote-sensing data are assimilated through the data-assimilation software eDICE (short description to follow in the next paragraph) which was enhanced during the course of this project to meet eReefs specific requirements (i.e. added capacity to handle spatially varying parameters). eDICE produces ensemble of the data-assimilating models which are then integrated through time and across members of the ensemble to produce initial conditions and parameters for a single sediment transport model. This single model is validated against time-series of turbidity and refined further when needed. One of the reasons for the validation and refinement of the model following the data-assimilation step is a sparse temporal coverage of the remote sensing data which is likely to translate into missed resuspension events. Additionally, the time period of the data-assimilation was limited to 6 months (because of the computational constraints involved in running ensemble of models). Subsequent multi-year free-run of the improved model revealed a long-term drift of the solution thus requiring further manual interventions to adjust parameters of the model. The reason for collapsing ensemble of models into a single model is computational constraints of the operational modelling system integrating hydrodynamics, sediment transport and complex multivariate biogeochemical models.

Ensemble assimilation of the remote sensing data has been carried out by eDICE - an emulation and data assimilation software developed in recent years at CSIRO and tested in a number of coastal applications (Margvelashvili et al., 2013; Herzfeld et al., 2012). eDICE assimilates observations sequentially with time over the predefined sequence of time-windows. For each time-window it builds an emulator; a fast and cheap surrogate of the complex model. This emulator is then used as a substitute of the complex model to assimilate observations. To build an emulator, eDICE runs ensemble of models and takes snapshots of the ensemble states at specific time points. Simulated fields are decomposed into the set of basis-functions via Singular value Decomposition (SVD). Gaussian Process Modelling (GPM) is then applied to propagate decomposition coefficients of the SVD forward in time. GPM and SVD together comprise an emulator of the model which can be used to assimilate observations. More detailed description of eDICE is available in (Margvelashvili and Campbell, 2012; Margvelashvili et al., 2015). During the course of the eReefs project, eDICE has been further refined and updated to fit e-reefs sediment-model data-assimilation requirements. The refined version of the code is being documented into the eDICE User Manual.

4.7 Biogeochemical Model

4.7.1 Introduction

The CSIRO O&A coastal biogeochemical model has evolved through a series of case studies (Fig. 4.7.1) including the Port Phillip Bay Environmental Study (Harris et al 1996; Murray & Parslow 1997), the National Land and Water Audit Estuaries Theme, the Gippsland Lakes Environmental Study (Parslow, et al., 2001), the Derwent Estuary ERA (Parslow et al., 2001), and the Ord-Bonaparte Study (Parslow et al., 2003). Each study addressed specific environments and ecological questions resulting in the development, implementation and testing of a diverse range of model components. In these previous studies the biogeochemical model was linked to a box model which represented physical transport with relatively low vertical and horizontal resolution (Walker, 1997).

In more recent studies the biogeochemical model has been restructured in modular form, with a software core linked to a central library of ecological processes. With this structure the code has been fully incorporated into the CMAR Environmental Modelling Suite (EMS) and dynamically linked/coupled to a high resolution 3D hydrodynamic model SHOC (Herzfeld et al., 2005) and a multilayer sediment model (MECOSED, Margvelashvili 2003). The biogeochemical model has been directly coupled to a 3-D hydrodynamic model at continental shelf scales in the North-West Shelf Environmental Study (Condie et al., 2009), the Strategic Research Fund for the Marine Environment study off WA (Koslow et al., 2006), and in estuarine applications in the Huon Estuary and D'Entrecasteaux Channel (Wild-Allen et al., 2005), the Fitzroy Estuary (Douglas et al., 2005; Wild-Allen et al., 2005), and the Derwent Estuary (Wild-Allen et al., 2013).

The ecological model code is processed in columns equating to the model grid. Biogeochemical dissolved tracers are advected and diffused in an identical fashion to physical tracers such as temperature and salinity and ecological particulate tracers sink and are resuspended by the same formulation as sediment particles. At each ecological time step, non-conservative ecological rate processes such as growth, nutrient uptake, grazing and mortality are integrated within the ecological module which returns updated tracer concentrations to the hydrodynamic model via an interface routine.

COASTAL ENVIRONMENTAL MODELLING TEAM

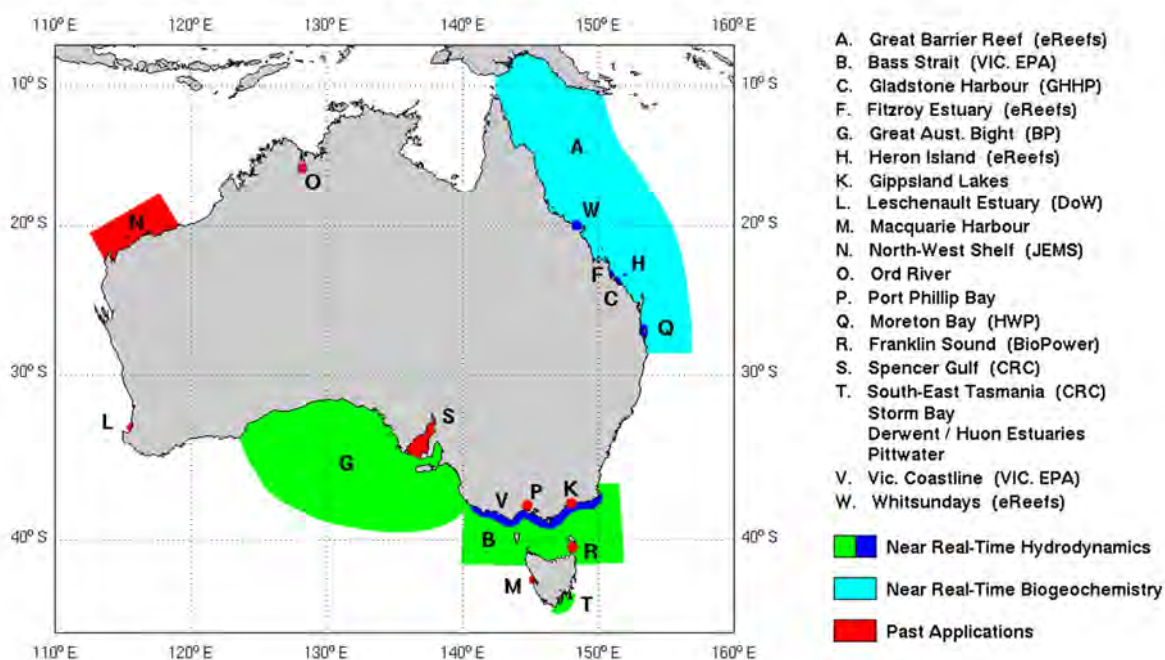


Figure 4.7.1. Integrated biogeochemical modelling studies completed by CSIRO in Australia

Most recently the biogeochemical model has been coupled to a transport model (Section 4.4) to facilitate simulation of biogeochemical dynamics over fine-scale and computationally large model grids (Wild-Allen, 2008). With this formulation, velocity fields from the hydrodynamic model are saved to file at high spatial and temporal resolution and are subsequently used to force a transport model which advects and disperses biogeochemical and sediment model tracers throughout the model domain. The principal advantage of this formulation is that it is computationally efficient allowing the biogeochemical model to be solved over much finer scales than previously possible.

4.7.2 Model description

The ecological model water column is organised in 3 'zones': pelagic, epibenthic and sediment. Depending on the grid formulation the pelagic zone may have one or several layers of similar or varying thickness. The epibenthic zone overlaps with the lowest pelagic layer and shares the same dissolved and suspended particulate material fields. The sediment is modelled in multiple layers with a thin layer of easily resuspendable material overlying thicker layers of consolidated sediment.

Dissolved nutrients are advected and diffused throughout the model domain in an identical fashion to temperature and salinity while particulate substances sink and are resuspended in the same way as sediment particles. For each layer and grid location the time evolution of each model substance (Y) is the sum of conservative advection, diffusion and sinking processes (ωY) and non-conservative biogeochemical rate processes (βY):

$$\partial Y / \partial t = -\phi Y + \beta Y \quad 4.7.1$$

where $\phi Y = (\mathbf{u}\Delta Y + \Delta_H A_H \Delta Y) - (\partial/\partial z)K_z(\partial Y/\partial z) + (\partial \mathbf{w}_s Y/\partial z)$

and $\Delta = (\partial/\partial x) + (\partial/\partial y) + (\partial/\partial z)$; $\Delta_H = (\partial/\partial x) + (\partial/\partial y)$

[Here \mathbf{u} is the velocity vector; A_H and K_z are the horizontal and vertical diffusion coefficients and \mathbf{w}_s is the settling velocity.]

Non-conservative biogeochemical processes are organized into pelagic processes of phytoplankton and zooplankton growth and mortality, detritus remineralisation and fluxes of dissolved oxygen, nitrogen and phosphorus; epibenthic processes of growth and mortality of macroalgae and seagrass, and sediment based processes of phytoplankton mortality, microphytobenthos growth, detrital remineralisation and fluxes of dissolved substances.

The standard biogeochemical model (Fig. 4.7.2) includes four groups of microalgae (small and large phytoplankton, dinoflagellates and microphytobenthos) and two macrophytes (seagrass and macroalgae) which grow at a 24 hour mean rate determined by access to dissolved nutrients (nitrogen and phosphate) and photosynthetically active radiation (PAR) (Baird, 1999). Autotrophs are assumed to take up ammonium and nitrate with equal preference, and phosphate and dissolved inorganic carbon are taken up by phytoplankton at the Redfield ratio (106C:16N:1P) and by macrophytes at the Atkinson ratio (550C:30N:1P). Ambient PAR is calculated from incident surface 24 hour mean PAR attenuated by seawater, coloured dissolved organic substances (estimated from an inverse linear relationship with salinity), and organic and inorganic particles. Chlorophyll is calculated from a nitrogen to chlorophyll ratio of 7 mgN/mgChl.

Micro- and meso-zooplankton graze on small and large phytoplankton respectively, at rates determined by swimming speed and particle encounter rate (Baird, 1999). Half of grazed material is released as dissolved and particulate carbon, nitrogen and phosphate, with the remainder forming detritus. Additional detritus accumulates by mortality. Detritus and dissolved organic substances are remineralised into inorganic carbon, nitrogen and phosphate with labile detritus transformed most rapidly (days), refractory detritus slower (months) and dissolved organic material transformed over the longest timescales (years). The evolution (by photosynthesis) and utilization (by respiration and remineralisation) of dissolved oxygen is also included in the model, and depending on prevailing concentrations facilitates or inhibits the oxidation of ammonia to nitrate and its subsequent denitrification to dinitrogen gas which is then lost from the system. Further details of the biogeochemical model, including model equations and parameter values, are included in (Wild-Allen et al., 2005).

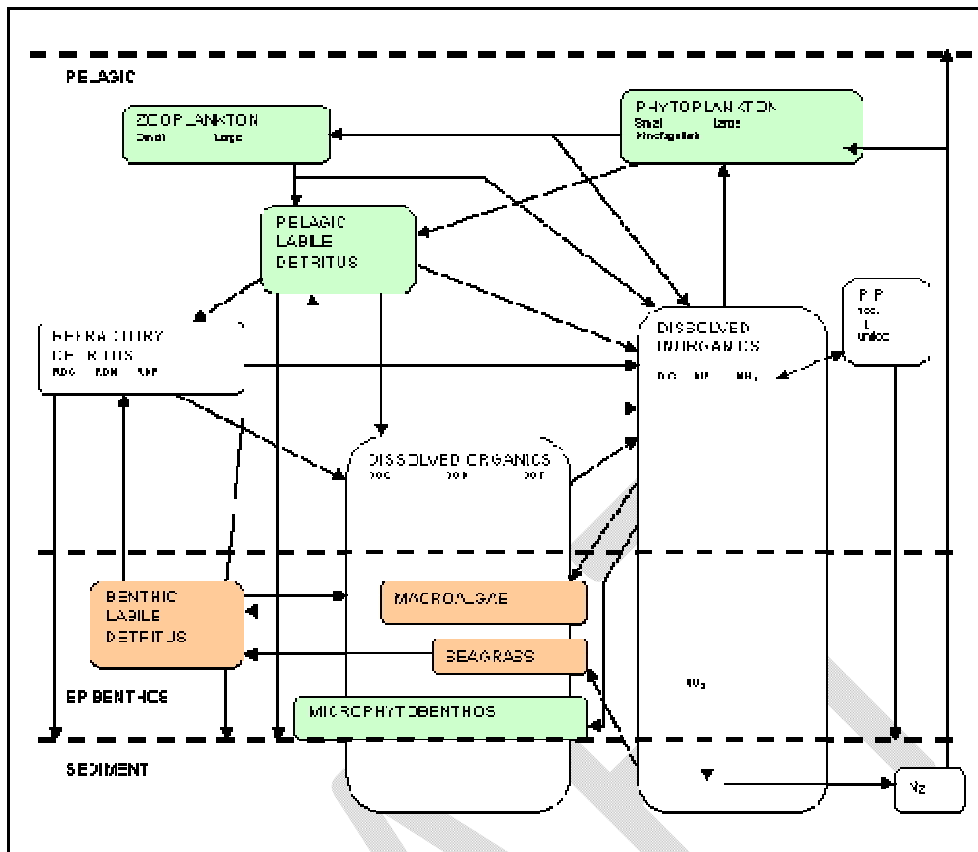


Figure 4.7.2. Schematic diagram of the standard EMS biogeochemical model compartments, links and vertical layers. Green compartments have fixed nutrient content at Redfield ratio (106C:16N:1P); brown compartments are fixed at Atkinson ratio (550C:30N:1P).

4.7.3 Biogeochemical cycling in the GBR

4.7.3.1 Background

In the GBR and Coral Sea pelagic photosynthesis is dominated by nanoplankton (10-2 μm) and picoplankton (<2 μm) which comprise >50% of the chlorophyll standing crop with little spatial and temporal variability (Furnas and Mitchell 1986 & 1987). Phytoplankton production is tightly coupled with microzooplankton grazing and efficient recycling through the microbial loop. Some seasonality occurs in the typically diatom dominated microplankton (>10 μm), associated with enhanced seasonal nutrient supply to the shelf in summer.

During the wet season (December – March) increased coastal and river runoff delivers elevated nutrients and sediment loads to the coastal waters (Furnas et al., 2005). These nutrients are efficiently taken up by diatoms which grow rapidly and escape grazing control allowing blooms to form (>2 $\mu\text{g/l}$). These brief increases in productivity support secondary production and the original nutrients are subsequently recycled through pelagic and benthic foodwebs including reef systems. In addition to coastal nutrient supply episodic intrusions of deep nutrient rich water through the reef matrix and onto the shelf can occur between Oct-April (Furnas and Mitchell, 1996). These intrusions have been estimated to exchange up to 1/3 of the shelf water mass and supply 30 and 75% of shelf P and N respectively (Furnas and Mitchell 1996). In addition to coastal and intrusive supply of nutrients to the shelf, Aeolian

input of nitrate and phosphate via rainfall and dust deposition supplies an estimated 3 and 100 Mmoles of P and N per year respectively (Furnas and Mitchell 1996).

In several studies surface pelagic productivity has been identified as nitrogen limited (Furnas and Mitchell 1986 & 1987; Furnas et al., 2005). High light availability and clear oligotrophic waters allow active photosynthesis to depths >100m, which on the outer shelf are conducive to the formation of deep chlorophyll maxima (80 – 120m) at or just above the seasonal nutricline/pycnocline. As much of the shelf is <70m deep, given suitable substrate there is adequate light available for microphytobenthos, macroalgae and seagrass growth.

In addition to phytoplankton that uptake P and N from the water column, the nitrogen fixing phytoplankton *Trichodesmium* sp. is found throughout the tropics including the GBR shelf. Growth of *Trichodesmium* is understood to be constrained by access to both P and iron in addition to light and the species often aggregates into conspicuous surface slicks (looks like sawdust) that may be detectable from space (depending on the spatial and spectral resolution of the instrument).

4.7.3.2 Conceptual model

The Great Barrier Reef shelf ecosystem is presumed to be an open system. Energy, carbon and nutrients enter and leave the shelf system via a number of pathways and are actively recycled within the system (Fig. 4.7.3). Figs. 4.7.4a and 4.7.4b present conceptual models of nitrogen (N) and phosphorus (P) pools and cycling within waters and sediments of the NE Australian continental shelf (from Furnas et al., 2011). These models have guided our thinking about the structure and function of planktonic and benthic (soft sediment) communities in the GBR. A number of these pools and fluxes have been measured or constrained in regional-scale budgets (e.g. Alongi and McKinnon, 2005; Furnas et al., 2011), but not tested in dynamic frameworks.

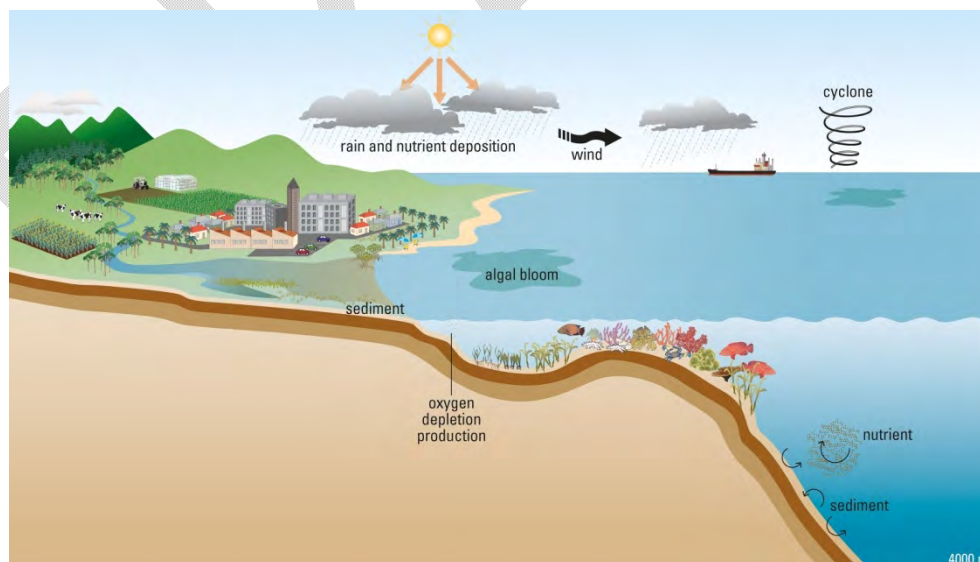


Figure 4.7.3. Conceptual model of the Great Barrier Reef shelf ecosystem

4.7.3.3 Terrestrial inputs of N and P to shelf waters

Considerable effort has been put into estimating terrestrial runoff of sediment and nutrients (N,P) into the GBR over the last two decades. These efforts have come together in the last decade (e.g. Furnas, 2003; Prosser et al, 2001; Brodie et al., 2004). As new data sets,

information and modelling approaches have become available, estimates of terrestrial runoff of sediment and nutrients have been progressively upgraded (e.g. Kroon et al., 2012). The estimation process has been approached in a number of ways, including empirical estimates, statistical models and spatial modelling, but most modern estimates now fall within a 2 to 5-fold range.

Furnas (2003) estimated riverine sediment and nutrient (N,P) inputs to the GBR from estimates of volume averaged wet season loads of N and P derived from intensive sampling in a number of wet- and dry-catchment rivers (Table 4.7.1). All GBR rivers exhibit strong seasonal (wet-dry) flow differences and are strongly event-driven. As a result, none exhibit clear flow-concentration relationships. Accordingly, volume-averaged wet season export coefficients (tonnes of N or P per km³ of discharge ~ µg L⁻¹) were derived for wet- and dry-catchment river types. These can be applied to higher frequency (daily) discharge data to estimate inputs to the shelf.

Table 4.7.1. Volume-averaged wet season export coefficients for nutrients from wet- and dry-catchment rivers. From Furnas (2003).

	Wet Catchment Rivers	Dry Catchment Rivers
	Tonnes Km ⁻³	Tonnes Km ⁻³
DIN (mostly nitrate)	171	197
DON	80	139
PN	145	503
DIP (mostly phosphate)	4.2	26
DOP	5.8	9
PP	32	130
Total N	396	840
Total P	42	165

These values, and the entire AIMS water quality data set, have been supplied to the Biogeochemical modelling team.

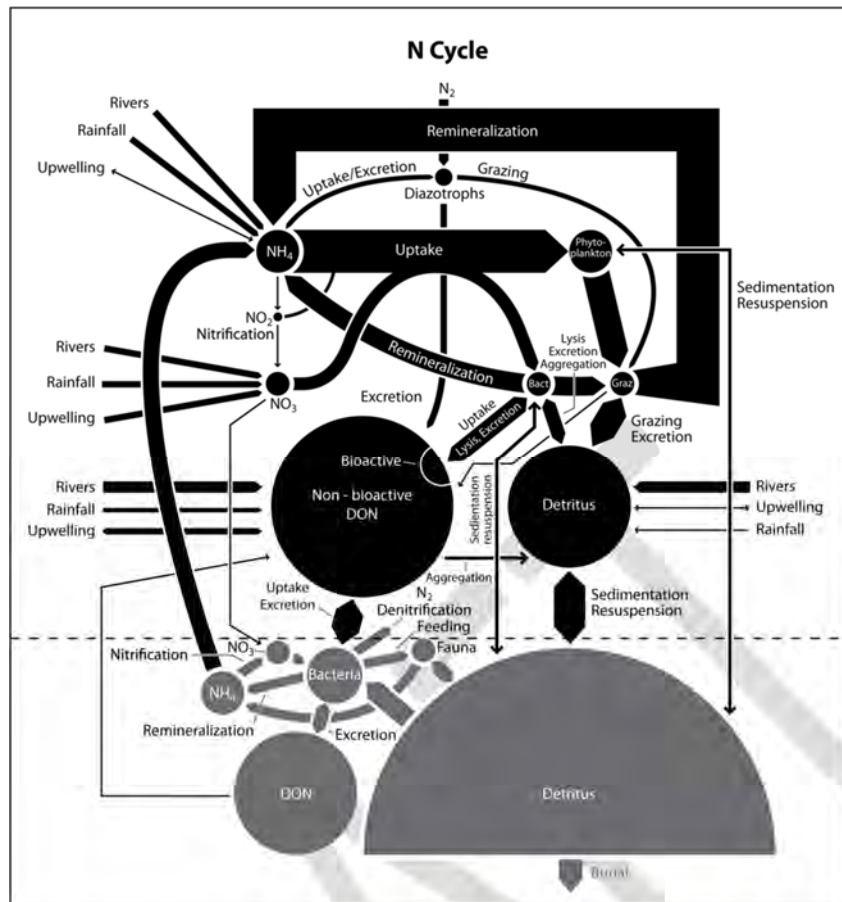


Figure 4.7.4a. A conceptual model of nitrogen pools and fluxes in waters and sediments (including reefs) of the Great Barrier Reef shelf system. Pool sizes and flux arrow widths are roughly scaled to the inferred magnitude of respective pools and fluxes. From Furnas et al., 2011.

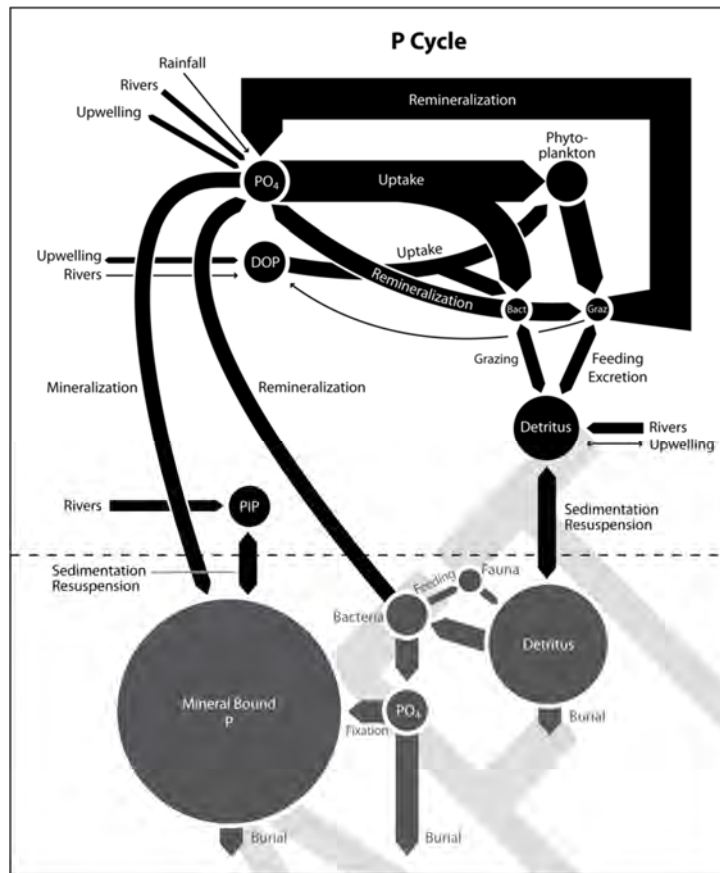


Figure 4.7.4b. A conceptual model of phosphorus pools and fluxes in waters and sediments (including reefs) of the Great Barrier Reef shelf system. Pool sizes and flux arrow widths are roughly scaled to the inferred magnitude of respective pools and fluxes. From Furnas et al., 2011.

4.7.3.4 Nutrient input via rainfall

Between 100 and 400 km³ of rain falls onto the GBR shelf every year (450 – 1,800 mm averaged over area). The nutrients in this rainfall represent a small, but significant input to the system. Based on a large number of shipboard and coastal collections of rainwater within the GBR region, estimates of nutrient levels in rainfall are listed in Table 4.7.2.

Table 4.7.2. Median nutrient concentrations (µM/yr) in coastal and marine rain collected in the GBR region (Furnas unpubl.)

	NO ₂ + NO ₃	NH ₄	Total N	PO ₄	Total P	Si
Median	0.72	2.1	5.9	0.04	0.08	0.04
Minimum	0.08	0.2	0.0	0.00	0.00	0.0
Maximum	12.3	23.2	25.5	4.7	10.1	5.5
N	173	173	123	173	127	165

4.7.3.5 Nutrient input via upwelling

Nutrient-enriched sub-surface waters from the Coral Sea episodically intrude onto the GBR shelf and, in some locations, can be a significant source of external nutrients to the system. These events have been detected at sites along the length of the GBR (11-24 °S). The intruded or upwelled water is a mixture between low-nutrient Coral Sea Surface waters and cooler Sub-tropical Lower Water (SLW) with higher nutrients, which forms a distinct high-salinity layer in the upper thermocline. SLW forms in the SW Pacific Ocean to the east of the Coral Sea and extends westward as a distinct water mass to the GBR along its entire length. The bottom of the low-nutrient surface mixed layer is normally deeper than the shelf-break depth (50-80 m) along the outer GBR, but on occasion, a number of mechanisms can cause shoaling of the thermocline above the shelf-break.

Two activities were undertaken during 2012 to better estimate the contribution that upwelling makes to the nutrient dynamics of the GBR system. These were not formally conducted under eReefs, but were conducted by eReef partners and have contributed to the understanding of GBR processes that eReefs ultimately aims to portray, hence a description of the outcomes of these activities is included below.

As part of the AIMS-funded 'Coral Sea Connections' (CSC) project, temperature-salinity loggers (Seabird SBE37) were deployed near the bottom at six sites (Fig. 4.7.5) along the GBR shelf-break (nominally at 100 m) between 11° and 21 °S. Previous work in the central GBR has clearly shown that downward short-term excursions of near-bottom water temperature are a good marker for the intrusion of cool thermocline water onto the normally well-mixed shelf, and that estimates of the SLW content of that water (with associated nutrients) can be estimated from the temperature-salinity characteristics of intruded water. The first logger was deployed (Elusive Reef – 21° S) in April 2012 and recovered in June 2014. Table 4.7.3 and Fig. 4.7.5 give the locations of the six loggers. The two southernmost loggers and the Jewell Reef logger are deployed on the shelf outside of the barrier reef as previous observations indicate that mixing through a dense reef matrix destroys the intruded water signal.

Table 4.7.3. Locations of shelf-edge temperature-salinity loggers

Location	Deployed	Recovered	Latitude	Longitude
Mantis Reef	May 2012	Jun 2014	12.232°S	143.872°E
Hicks Reef (Lizard Island)	May 2012	Jun 2014	14.429°S	145.443°E
Grafton Passage	May 2012	Jun 2014	16.624°S	146.260°E
Palm Passage	May 2012	lost	18.173°S	147.116°E
Hydrographers Passage	Aug 2012	Jun 2014	20.047°S	150.537°E
Elusive Reef	April 2012	Oct 2014	20.942°S	151.854°E

Decadal time series of upwelling activity have previously been measured in the central (17°S, partial record in Furnas & Mitchell 1999) and southern GBR (20°S). The current observation program will produce time series greater than 1 year along virtually the full length of the GBR, to estimate the seasonality and latitudinal extent of upwelling events along the shelf-break, and the potential role of shelf waves in upwelling processes (Fig. 4.7.6). An imperfect back-

up for the Palm Passage instrument record (due to instrument depth differences) will be obtained from the IMOS instruments deployed near the entrance to Palm Passage.

In parallel with this activity, an analysis of AIMS historical nutrient data collected along the outer margin of the GBR and in the far-western Coral Sea was undertaken to better define temperature nutrient relationships in this region which can be used to better parameterize model nutrient distributions along the seaward boundary of the GBR (Figs. 4.7.7 – 4.7.9).

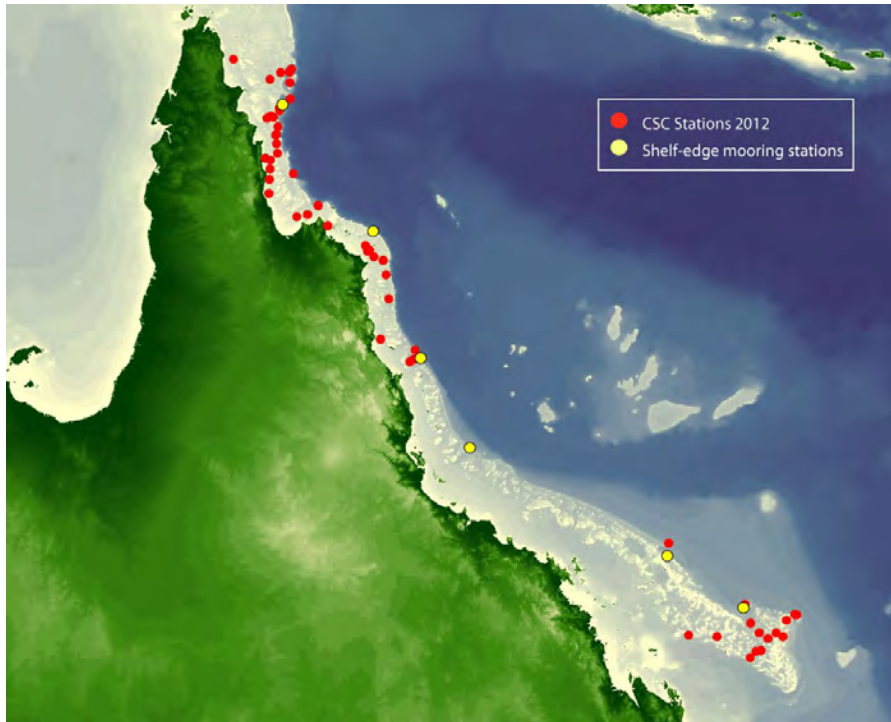


Figure 4.7.5. Locations of hydrographic stations sampled during 2012 as part of the Coral Sea Connections project and locations of shelf-edge temperature-salinity loggers.

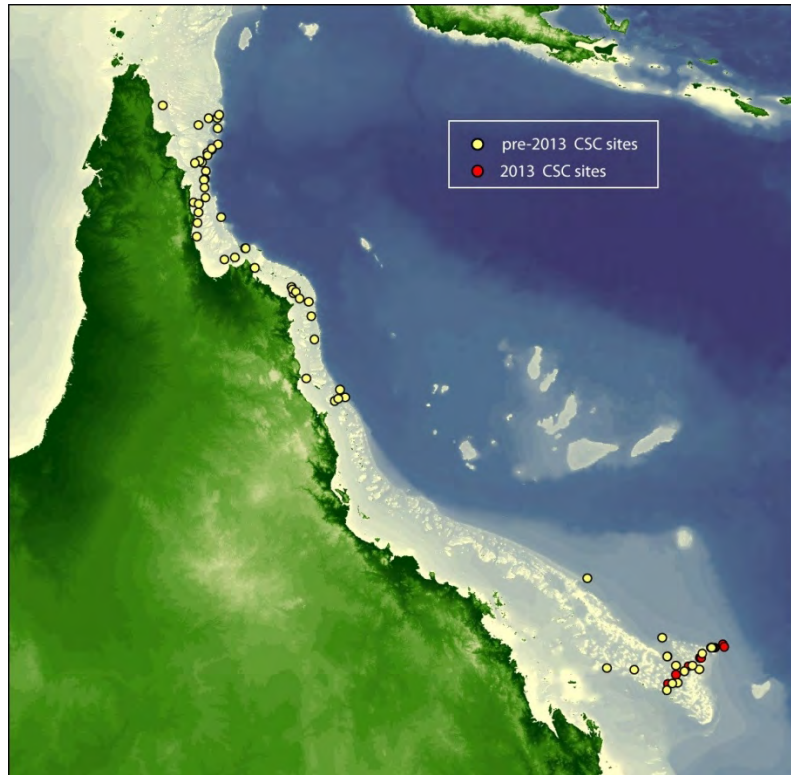


Figure 4.7.6. Locations of stations sampled during 2011-13 for investigations of GBR shelf-ocean interactions. Red symbols indicate stations sampled in 2013.

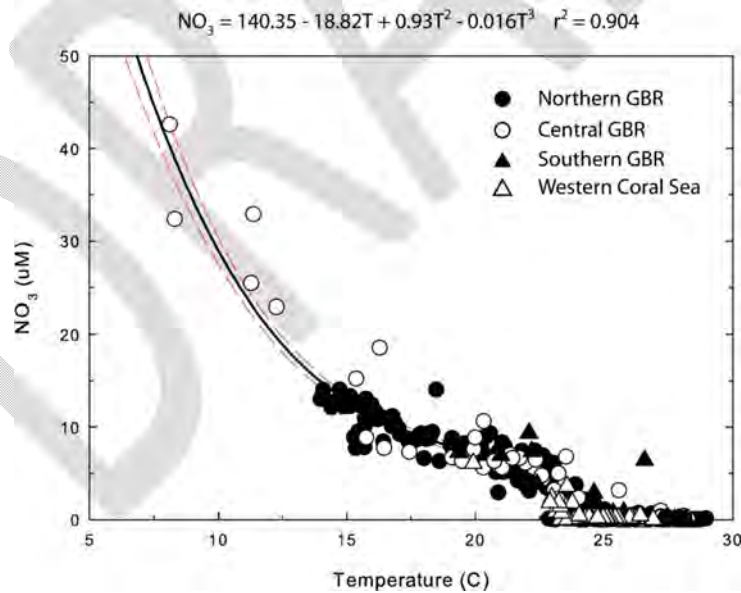


Figure 4.7.7. Observed relationship between nitrate concentrations and water temperature at stations over the continental slope (depth > 80 m) bordering the GBR and in the Queensland Trough. Data were collected on a large number of cruises between 1979 and 2009. The polynomial regression shown only applies to samples with a temperature < 25 °C. Samples warmer than 25 °C were in the surface mixed layer where nitrate is almost always depleted to very low levels. The 95% confidence limits for the regression are shown in red. The core of the Sub-tropical Lower Water layer has a temperature usually falling between 21.5 and 22.5 °C.

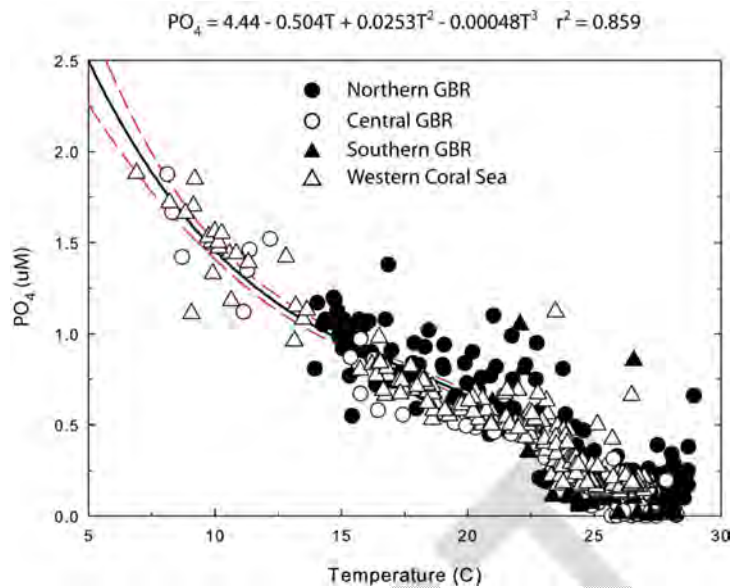


Figure 4.7.8. Observed relationship between phosphate concentrations and water temperature at stations over the continental slope (depth > 80 m) bordering the GBR and the Queensland Trough. Data were collected on a large number of cruises between 1979 and 2009. The polynomial regression shown only applies to samples with a temperature < 25 °C. Samples warmer than 25 °C were in the surface mixed layer where phosphate is almost always depleted to very low, but usually detectable levels. The 95% confidence limits for the regression are shown in red. The core of the Sub-tropical Lower Water layer has a temperature usually falling between 21.5 and 22.5 °C.

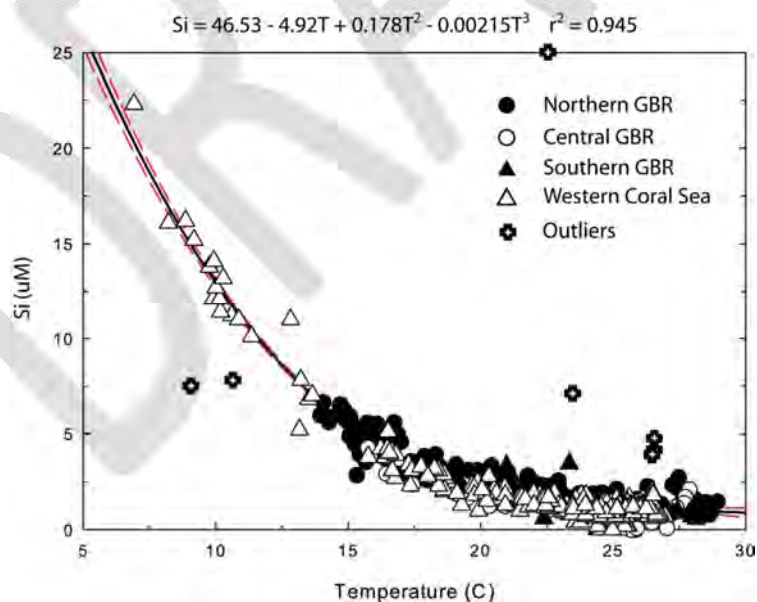


Figure 4.7.9. Observed relationship between silicate concentrations and water temperature at stations over the continental slope (depth > 80 m) bordering the GBR and the Queensland Trough. Data were collected on a large number of cruises between 1979 and 2009. The polynomial regression shown only applies to samples with a temperature < 25 °C. Samples warmer than 25 °C were in the surface mixed layer where silicate was almost always detectable. The 95% confidence limits for the regression are shown in red. A number of

outlier points were not used in computing the regression. The core of the Sub-tropical Lower Water layer has a temperature usually falling between 21.5 and 22.5 °C.

4.7.3.6 Cross shelf-break exchange of organic and inorganic nutrients

A considerable amount of cross shelf-break mixing also takes place along the seaward margin of the GBR with constant mixing of water masses between the GBR and the adjacent Coral Sea. This exchange is primarily driven by cross-shelf tidal currents (Andrews and Bode, 1988), the north-south infiltration of surface waters from the boundary currents flowing along and through the outer margin of the reef matrix (e.g. Brinkman et al., 2001) and to a much lesser extent, upwelling of thermocline waters from the Coral Sea (Furnas and Mitchell, 1996).

While the lateral gradients of nutrient concentration at the shelf-break are small (10^{-1} to 10^{-2} μM), the volumes of water exchanged are large (10^2 - 10^3 km^3 per tidal cycle; residual drift ≈ 0.5 Sv $\approx 10^2$ km^3 per day). While tidal currents move the largest volumes of water, the largest net fluxes through the system are from the residual drifts associated with pressure gradients of the boundary currents. For these large volumes, small differences in concentration can give rise to large net fluxes (e.g. 1 $\mu\text{mol DIN L}^{-1}$ in 1 $\text{km}^3 = 14$ t N). Over an annual cycle, persistent differences in concentration of just 0.01 $\mu\text{mol L}^{-1}$ and a net exchanged water volume of 1×10^2 km^3 per day would produce net fluxes (\pm) on the order of 4×10^3 , 5×10^3 , 1×10^4 and 1×10^4 tonnes of C, N, P and Si, respectively. These quantities are large relative to other known external nutrient sources such as rainfall, upwelling and terrestrial runoff (e.g. Furnas et al., 2005). Knowledge of these fluxes is necessary to constrain and close shelf-scale nutrient budgets for the GBR.

As part of the CSC project, the existing AIMS holding of cross shelf-break data for a range of measured nitrogen and phosphorus species (DON, PN, DOP, PP) is currently being analysed to better parameterize cross-shelf gradients, and ultimately fluxes.

The CSC project also includes an effort to re-sample all important N and P species (DIN, DON, PN, DIP, DOP, PP) in the water column across the shelf-break margin of the GBR to expand the current small amount of stations and transects where all important nutrient species were measured. While a substantial number of stations have been occupied in this transitional zone to date, most do not include sampling and measurement of the full range of important N and P species necessary for closing nutrient budgets, particularly in the far-northern and far-southern GBR. To date, 98 additional stations have been occupied and most include water sampling for this purpose.

The sampling program to measure cross shelf-break differences in nutrient stocks will conclude in June 2014 when shelf-break temperature loggers are recovered from six sites between 11 and 23°S. Fig. 4.7.10 presents a summary of results obtained to date on cross shelf-break differences in surface mixed-layer concentrations of a number of carbon and nutrient species. The sampling was concentrated in both the far-northern (11-15°S) and southern (22°S) GBR, areas which have previously received little coverage with regard to outer-shelf and offshore nutrient levels. The individual box and whisker plots show ranges of depth-weighted mean water column (shelf) or surface mixed-layer (0-60 m) concentrations in outer-shelf and adjoining deeper off-shelf waters. Statistical comparisons within this restricted data set indicate that while small differences in mean concentrations do occur, there are no statistically significant concentration differences between shelf and offshore

stations for any of the nutrient species tested. Additional data is needed to resolve whether these small differences are potentially seasonal or persistent, and the sources of observed variability. In one case (DOC), differences in concentrations for one cruise are quite large, primarily due to samples collected in the lee of shelf-break barrier reefs. Again, additional samples are needed to resolve whether this is a one-off (e.g. analytical issue) or a recurrent (seasonal) feature.

Analysis of historical nutrient data sets for the western Coral Sea and GBR shelf-edge zone (Figs. 4.7.7, 4.7.8, 4.7.9) has shown that there are temporally and regionally stable temperature-nutrient relationships for the major inorganic nutrient species (NO_3^- , PO_4^{3-} , Si). These relationships can be used to construct sub-thermocline nutrient fields from temperature profiles and to estimate quantities of nutrients in thermocline-sourced intruded water masses on the shelf. The current sampling program also includes dissolved inorganic carbon (DIC) and a full range of dissolved organic, and particulate nutrient species (DON, DOP, DOC, PN, PP, PC) which have not been sampled, or only infrequently sampled in previous work in this area (Fig 4.7.11). As in previous analyses, the major inorganic nutrient species (DIC, NO_3^- , PO_4^{3-} , Si) exhibit strong linear temperature-dependent relationships within the thermocline. The organic nutrient species, however, exhibit a varied range of temperature nutrient relationships related to the formation and biological consumption of these species in the water column. These relationships will be used to account for all major forms of C, N and P in upwelling nutrient budgets.

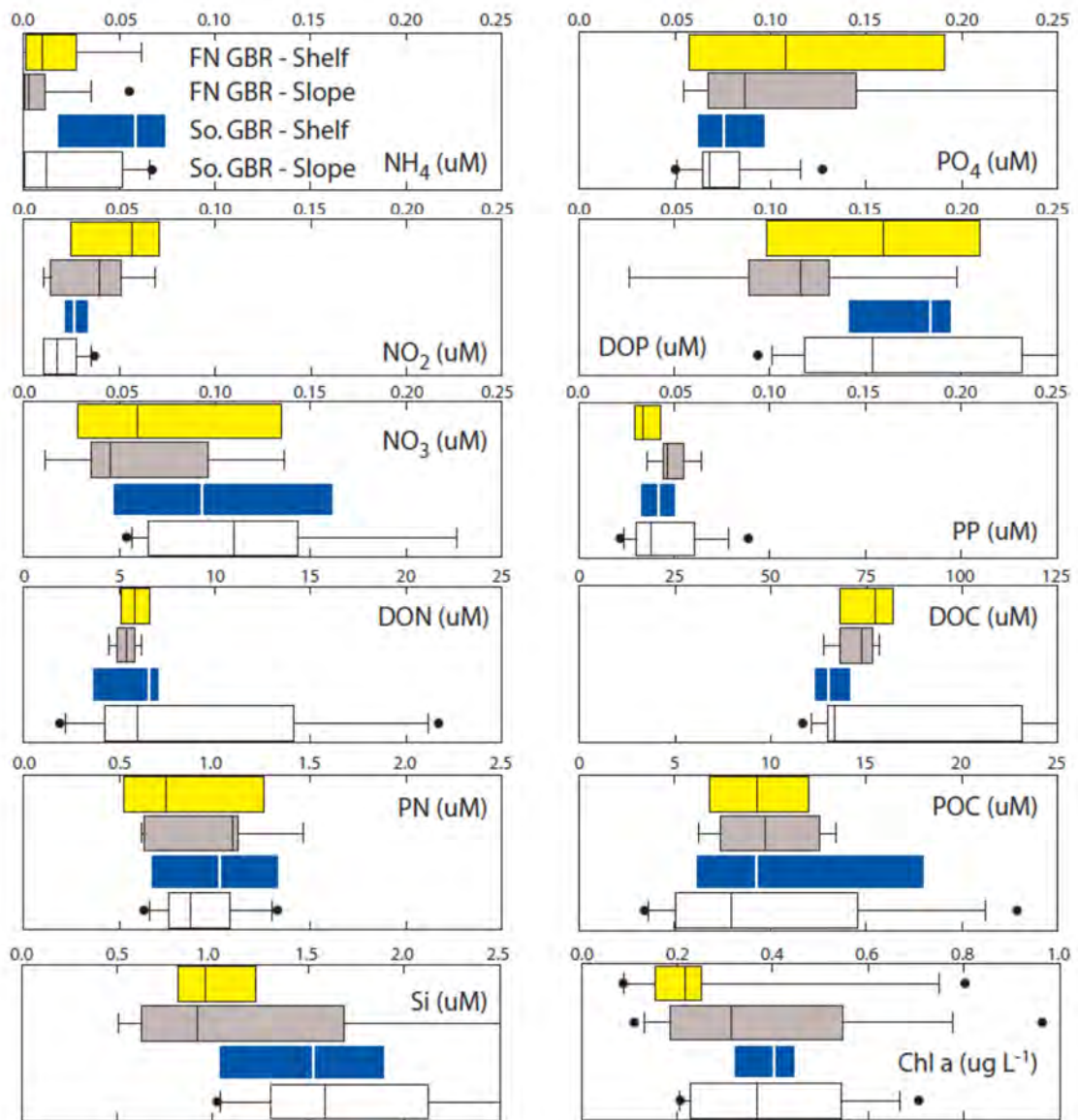


Figure 4.7.10. Differences between concentrations of important nitrogen, phosphorus, carbon, silicate and chlorophyll pools in the surface mixed layer (0 – 60 m) at outer-shelf and slope stations in the far-northern (11-15°S) and southern (23°S) GBR. Solid bars indicate the 25th to 75th percentile range and whiskers the 10 to 90th percentile range, with values outside this range as individual dots. The median (50th percentile) is also shown by a vertical bar.

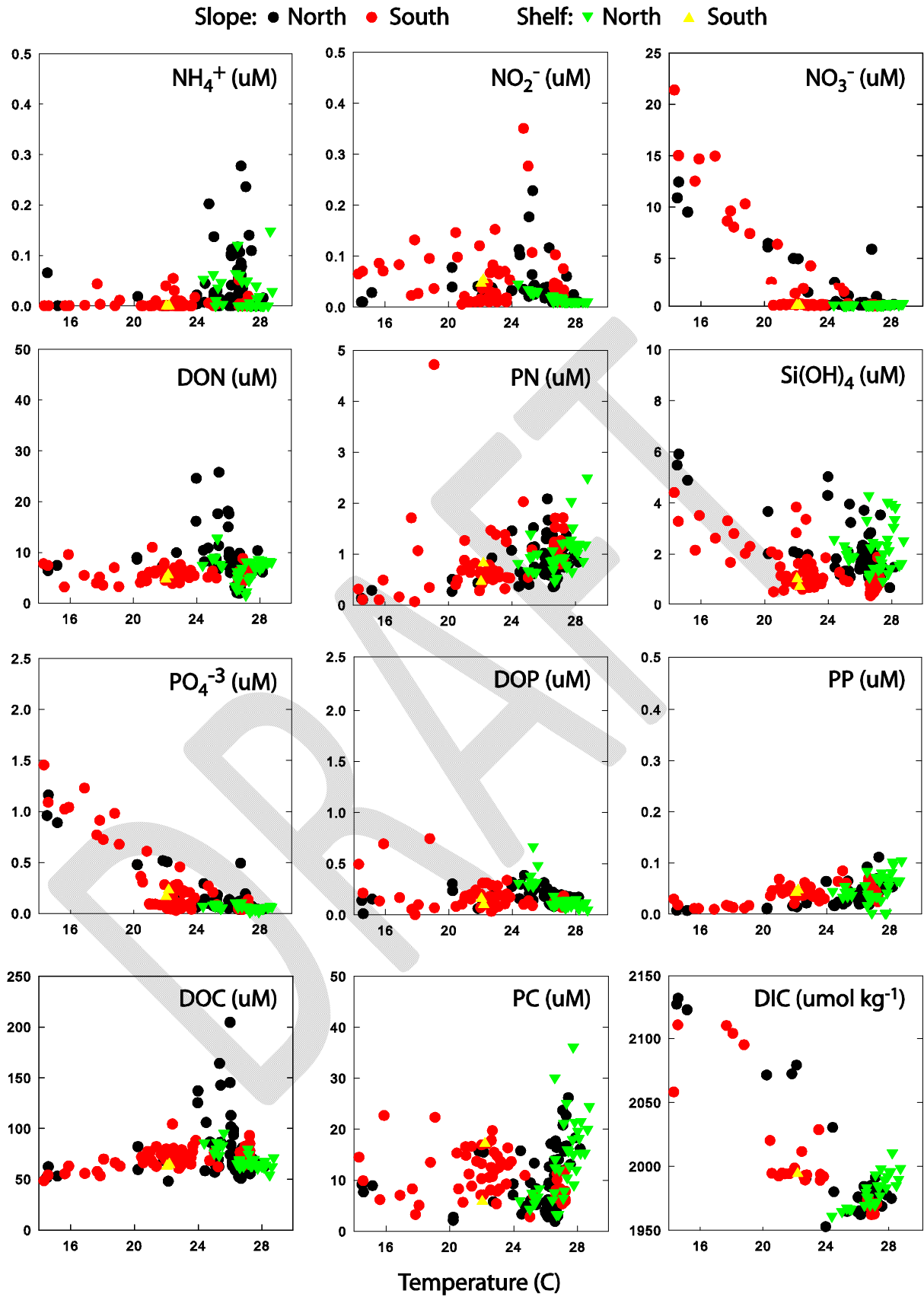


Figure 4.7.11. Nutrient-temperature relationships for important nitrogen, phosphorus, silicate and carbon species at shelf-edge and deeper slope stations sampled during 2011-2012.

4.7.3.7 Pelagic plankton communities

In parallel with the nutrient sampling at the shelf-break, at a limited number of stations, water samples were preserved for phytoplankton community analysis by flow cytometry and microscopy. Picoplankton (cells < 2 µm) were counted by flow cytometry on a number of cruises; however, results were limited due to technical issues with the cytometer (Fig. 4.7.12). Picoplankton counts from a number of other stations to the general area from earlier cruises exist and are considered representative of the modelling domain. In general, outer-shelf and slope phytoplankton communities are dominated by *Prochlorococcus*, with similar, or smaller amounts of *Synechococcus* spp. (Crosbie and Furnas, 1999, 2001). Ratios of cell numbers of the dominant cyanobacterial genera, *Synechococcus* and *Prochlorococcus* in Coral Sea and shelf-edge samples are typically < 1, while ratios in inshore waters with higher levels of nutrient input are > 1. Under extreme runoff conditions (e.g. March 1998), Syn/Pro ratios may be > 10. In water samples examined to date using microscopy, numbers of larger phytoplankton (diatoms, dinoflagellates) are very low in surface waters (generally < 10⁴ cells L⁻¹), consistent with the preponderant distribution of chlorophyll in the < 2 µm size fraction.

Estimates of nitrogen-fixation within the whole GBR system are currently not well constrained (Furnas et al., 1995; Bell et al., 1999). N-fixation by cyanobacteria occurs in both benthic habitats (coral reefs, sediments) and in the plankton (*Trichodesmium* and free-living bacteria). Current measurements of N-fixation by bacteria in inter-reefal sediments suggest rates in this habitat are fairly low (Furnas et al., 2011). Estimates of N-fixation in reef communities are largely based on a widespread extrapolation of rates measured at a small number of sites (Larkum et al., 1988). There are very few direct measurements of water column N-fixation by *Trichodesmium* (Bell and Fu, 2005) or free-living bacteria (Montoya et al., 2004) in or near the GBR.

While there is considerable experimental data regarding N-fixation by *Trichodesmium* (e.g. Capone et al., 2008), so that it is readily possible to estimate biomass-specific N-fixation by *Trichodesmium*, there are very few extant measurements of *Trichodesmium* abundance in GBR waters (Marshall, 1933; Revelante et al., 1982; Bell et al., 1999) to extrapolate this data. To remedy this, stations occupied as part of AIMS biological oceanographic research and Reef Plan Marine water quality monitoring now include sampling for *Trichodesmium* colonies. Because of their large size and distinctive pigments, even individual *Trichodesmium* filaments (trichomes) and colonies are readily identifiable and counted under low magnification. These data will be used to expand the current temporally and spatially limited data sets on *Trichodesmium* abundance in the GBR.

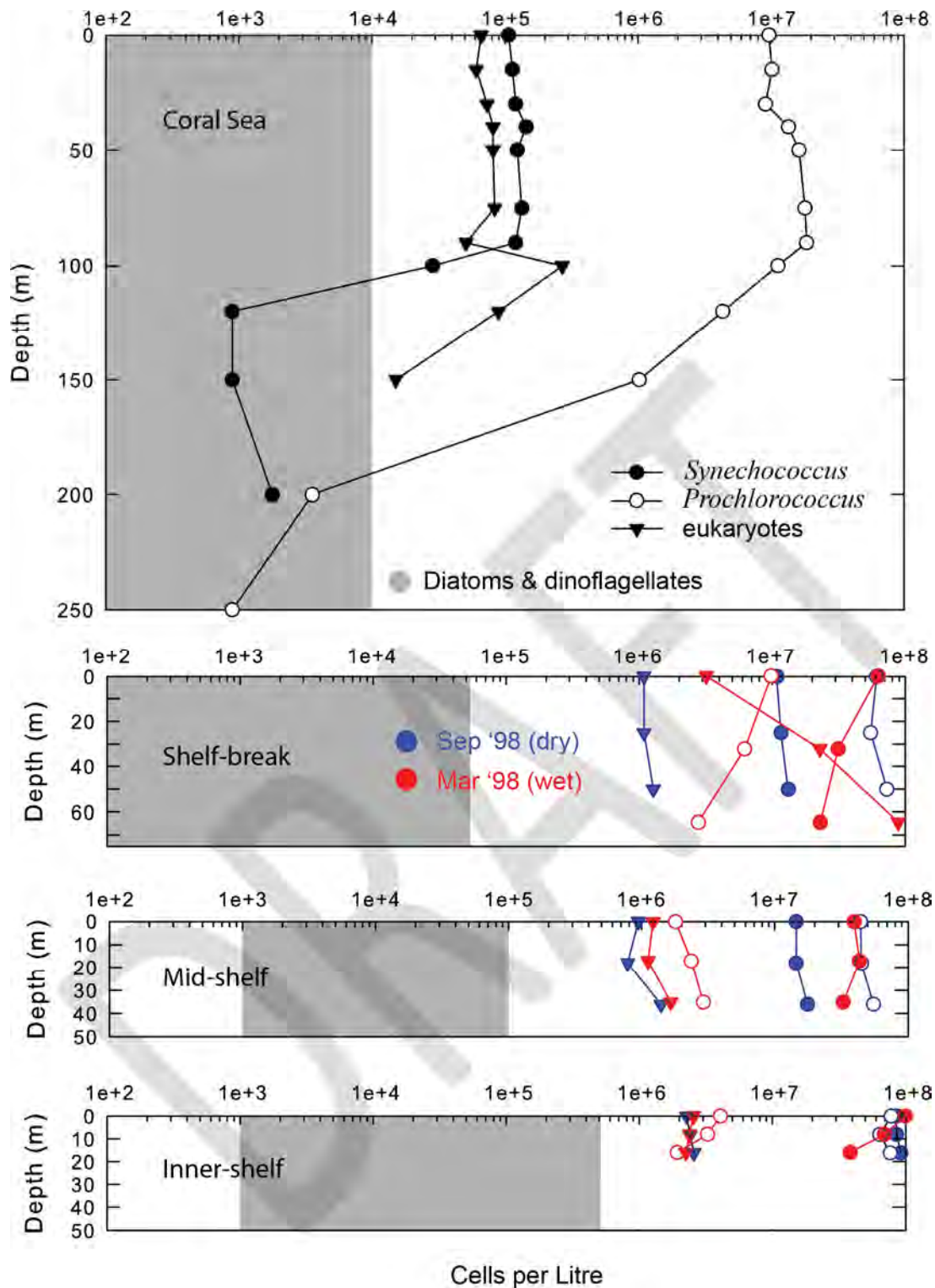


Figure 4.7.12. Vertical profiles of flow cytometric counts of small phytoplankton at a representative oceanic Coral Sea station (October 1999) and off Cairns under late-dry season (September 1998) and late-wet season after strong runoff into the GBR lagoon (March 1998). The grey shaded area indicates the predominant abundance range for microscopic counts of diatoms and dinoflagellates to date in GBR waters.

4.7.3.8 Zooplankton collection

Collections were taken of water column plankton populations in shelf and deeper offshore waters. At shelf stations, replicate vertical net tows were taken with a flow-metre equipped ring net (73 μm mesh) through the water column (Fig. 4.7.13). In addition, replicate oblique tows were taken with a bongo net (100-350 μm mesh). At deep, offshore sites (>150 m), depth-stratified oblique tows were taken with a Hydrobios Multinet. This net has five (5) individual nets which can be set to open and close at pre-determined depths. Depth strata sampled were determined dependent on local vertical hydrographic structure. The contents of catches from individual net tows were either filtered onto pre-weighed mesh disks to determine biomass (dry wt), analysed for chemical composition (C, N) or split, with portions saved for community structure and taxonomic analysis, and the remainder used for physiological measurements.

For cruises subsequent to August 2012, plankton samples were collected with a purpose-built bongo net that size-fractionates the sample in situ to partition the zooplankton community into size ranges of interest (McKinnon et al. 2005). One side of the bongo net was fitted with a WP-2 net of 350 μm plankton mesh, and the other side with a 150 μm plankton net of 34cm diameter nested inside a 73 μm net of 50cm diameter. Therefore, this bongo net array allowed us to collect zooplankton samples fractionated into the >350 μm , >150 μm and 73-150 μm size ranges. Hydrobios electronic flowmeters were mounted off-centre in the mouths of the 150 μm and 350 μm nets (Gehring & Aron, 1974).

Each net sample was split into three portions: half was transferred into cryovials and frozen in liquid nitrogen for subsequent enzymatic assays, one quarter which was preserved in formaldehyde for analysis of community composition, and one quarter filtered on to a pre-weighed disk of 73 μm mesh and frozen. The frozen mesh was subsequently dried (65 $^{\circ}$) and re-weighed to estimate zooplankton community biomass as dry weight. The dried plankton was subsequently ground and analysed for C and N content on a Shimadzu CN analyser. Biomass in the 73-150, >150 and >350 μm size ranges was calculated directly from the samples taken from the respective nets, and the total biomass >73 μm was then calculated by summing the samples collected from the 73 and 150 μm nets.

4.7.3.9 Zooplankton community composition

The 73-150 μm size fraction is dominated by the nauplii and early copepodites of copepods, together with juvenile larvaceans and chaetognaths and meroplankton. The >150 μm size fraction captures all late stage and adult copepods, which comprise ~80% of the mesozooplankton by number. The >350 μm size fraction captures the largest copepods, decapod and peracarid crustaceans, and large gelatinous zooplankton such as ctenophores and siphonophores. The 73-150 μm and >150 μm size fractions are dominated by suspension feeders likely to be important as grazers of phytoplankton primary producers, whereas the >350 μm fraction is dominated by carnivorous zooplankton.

A review paper on the zooplankton community composition of the Great Barrier Reef is in preparation. This paper combines data from the Coral Sea Connections work with all previous AIMS zooplankton projects. The sampling locations are shown in (Fig. 4.7.14).



Figure 4.7.13. Size-fractionating bongo net. The net on the left comprises a 150 μ m mesh net nested within a 73 μ m mesh net; the net on the right is a 355 μ m mesh net. An instrument package sits between the two nets, and includes a Laser Optical Plankton Counter (LOPC) and CTD unit.

4.7.3.10 Zooplankton biomass

Overall, the average >73 μ m biomass was 21 mg DW m⁻³ (as sum of the 73-150 and >150 μ m size fractions; Table 4.7.4). All size fractions comprised between 22-27% C and 5-7% N, with a C:N ratio ~4. By comparison, Harris et al. (2000) report the dry weight of small zooplankton is 14.8-42.8 %C, and 1.8-5.6 %N, and the average C:N ratio of copepods, the most common component of GBR zooplankton samples, is 5.16. We conclude that our measurements of biomass are consistent with the samples including mostly organic material, putatively zooplankton.

Table 4.7.4. Mean values of zooplankton dry weight (DW), Carbon and Nitrogen (all as mg m⁻³) aggregated over all stations in each of the 3 size fractions sampled by the bongo net, with their ratios by weight.

<i>Mesh</i>	<i>DW</i>	<i>C</i>	<i>N</i>	<i>C:DW</i>	<i>N:DW</i>	<i>C:N</i>
73- 150μm	7.62	1.65	0.36	0.217	0.047	4.601
>150μm	13.06	3.48	0.88	0.267	0.067	3.957
>350μm	8.99	2.31	0.58	0.257	0.065	3.968

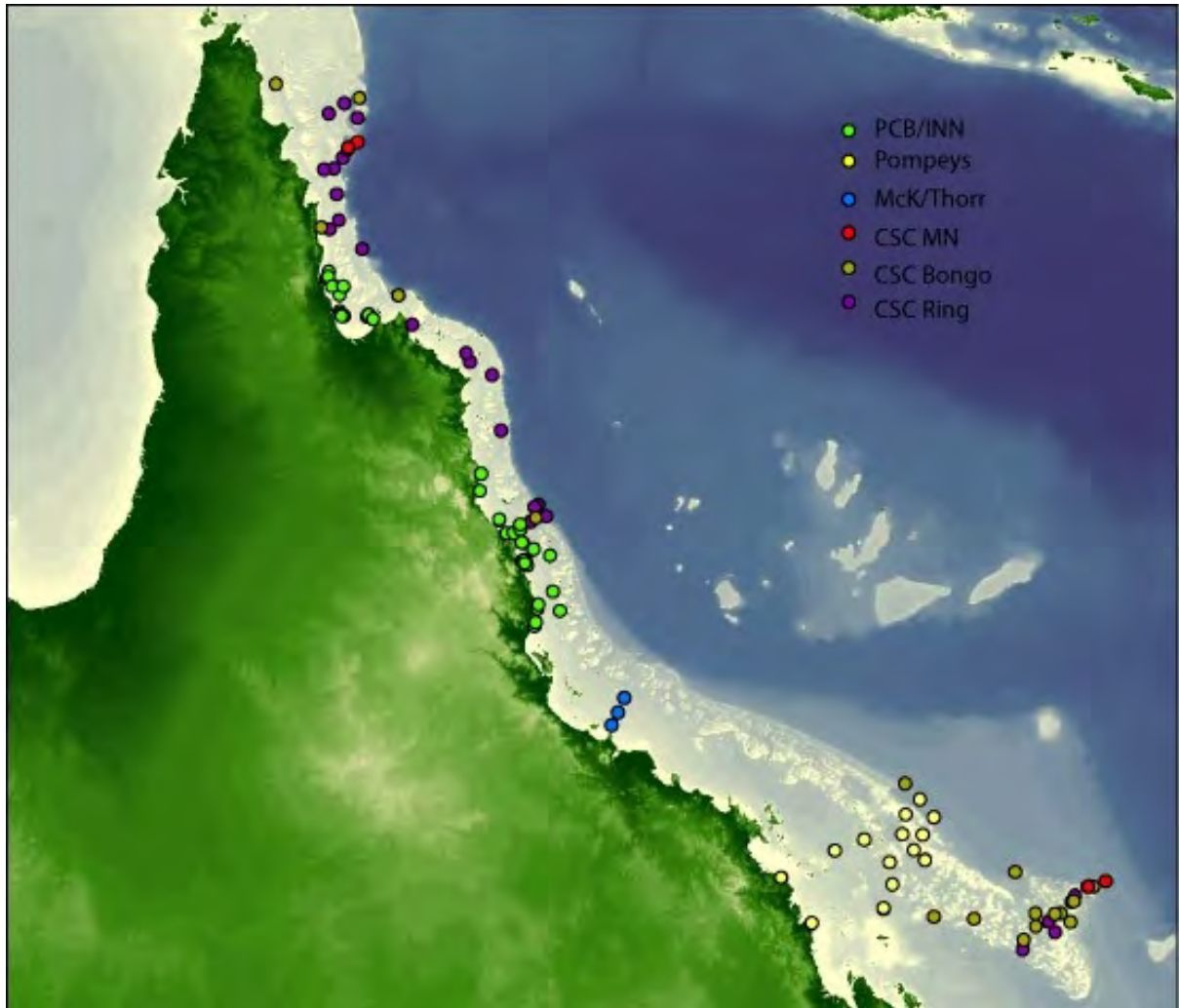


Figure 4.7.14. Coverage of zooplankton samples available for the GBR. PCB/INN are the samples of ((McKinnon et al. 2005)), Pompeys those of ((Alongi et al. 2015)), and McK/Thorr those of ((McKinnon and Thorrold 1993)). The CSC samples are divided into those taken by Multinet (MN), Bongo net and Ring net.

Box plots of the biomass data (Fig. 4.7.15) highlight that biomass is lower in the August-September period, which is consistent with the pattern shown by total zooplankton abundance (McKinnon and Thorrold 1993). Overall, 37% of the biomass is in the 73-150 μ m fraction, 20% in the 150-350 μ m fraction, and 43% is >350 μ m (Table 4.7.4).

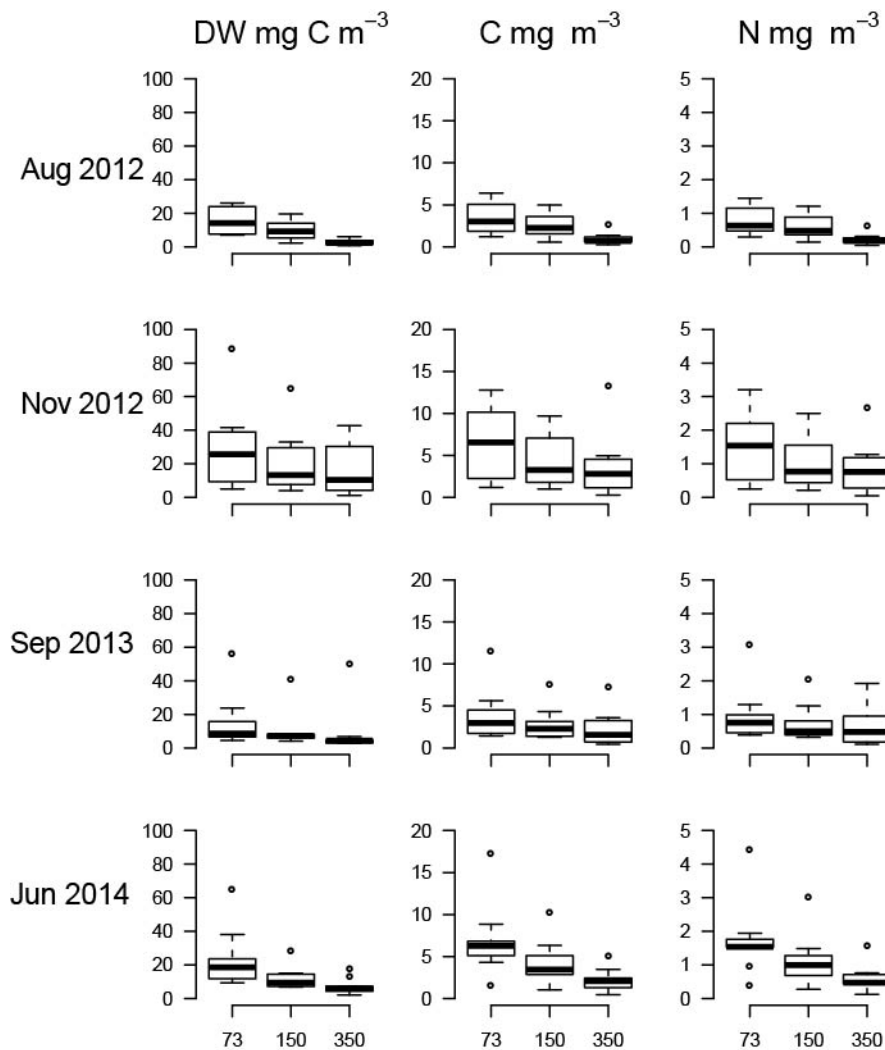


Figure 4.7.15. Zooplankton biomass in 3 size fractions (>73µm, >150µm, >350µm) aggregated over all stations shown in units of mg dry weight (DW), carbon (C) and nitrogen (N).

4.7.3.11 Zooplankton grazing

Most phytoplankton production on the GBR occurs in the picoplankton size class – i.e. cells <2µm in size. These cells are too small to be grazed directly by mesozooplankton grazers, except for mucous net feeders such as pelagic tunicates (larvaceans and salps) and pteropod molluscs. Most of the grazing on picoplankton is by microzooplankton (heterotrophic nanoflagellates, heterotrophic dinoflagellates, ciliates and copepod nauplii).

To model zooplankton grazing, we recommend two strategies.

1. For grazing on picoplankton, Calbet & Landry (2004) present a global synthesis of the impact of microzooplankton grazers, and find that 67% of phytoplankton daily growth is accounted for by this size fraction of grazers. Since there is only modest variation of this number between studies and the experiments are difficult to conduct, we suggest applying the literature value.

- The remaining phytoplankton production is accounted for by mesozooplankton grazing and by sedimentation/flocculation into marine snow.

To parameterize the mesozooplankton component, the CSC project has been making measurements of mesozooplankton biomass in 3 size fractions. At each of the stations occupied during CSC cruises (Fig 4.7.16), we have zooplankton biomass measurements in the following size fractions: 73-150 μm , 150-355 μm , and >355 μm . At present these data are only available as dry weight, but we are in the process of analysing the samples for elemental composition, and will be able to express biomass in units of nitrogen. In addition to the bongo samples, at deeper stations on the edge of the Coral Sea we have collected depth-stratified samples with a Hydrobios multinet. These samples are only in the >100 μm size fraction.

Aliquots of the samples have also been preserved in formalin for community analysis, and a further aliquot frozen in liquid Nitrogen for enzymatic analysis. These analyses are progressing, but our intention is to measure the activity of the enzymes AARS and ETS in the whole zooplankton community within each size fraction. AARS activity can be used to calculate growth rate, and ETS can be used to calculate respiration. Then, according to the simple formula:

$$I = G + R + E \text{ (Ikeda \& Omori, 1984),}$$

where I = ingestion, G =growth, R = respiration and E = excretion, we will be well-placed to model mesozooplankton grazing rates for inclusion into the eReefs model. Under normal circumstances, $E \ll R$, so G and R are the only sizeable terms.

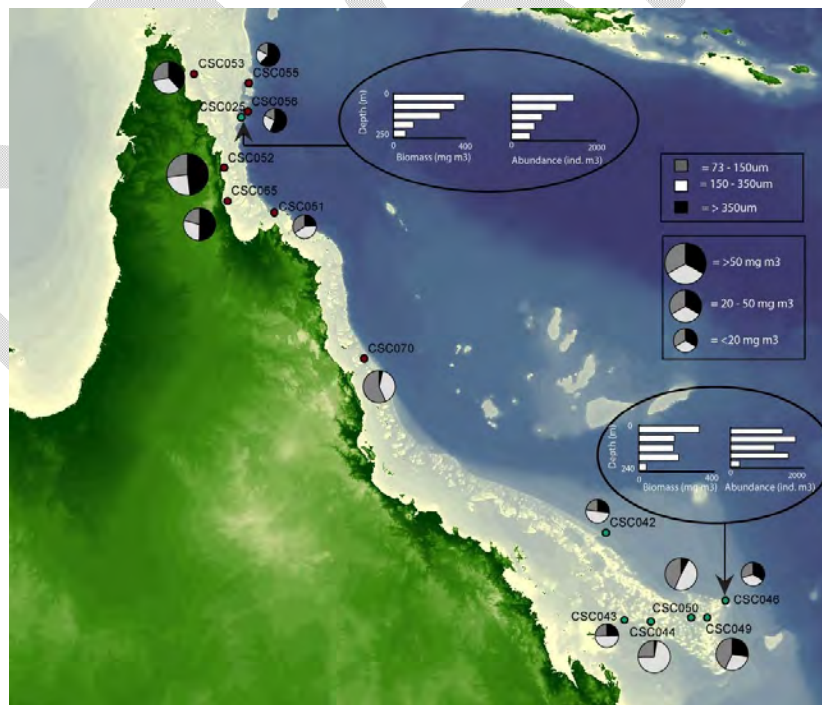


Figure 4.7.16. Location of stations where zooplankton samples have been taken to parameterize grazing rates. Vertical bars are depth strata of >100 μm zooplankton sampled by multinet; pies are biomass charts of total zooplankton biomass in three size fractions as sampled by the bongo net.

4.7.3.12 Zooplankton growth and respiration

Aminoacyl-tRNA synthetases (AARS) catalyze the first step of protein synthesis and their activity is significantly related to somatic growth in freshwater and marine crustaceans. The activity of AARS can be used as an index of copepod somatic growth (Yebra and Hernández-León 2004). AARS activity was measured using the method of Yebra & Hernández-León (2004), and was corrected for the in-situ temperature with an activation energy of 10.5 kcal mol⁻¹ (Guerra 2006).

The electron transport system (ETS) is nearly ubiquitous in mitochondrial membranes, and can be used as an indicator of organic matter remineralisation, as it consists of a complex chain of cytochromes, flavo proteins and metabolic ions that transport electrons from catabolised foodstuffs to oxygen. ETS activity is correlated to in vivo respiration, so that ETS activity can be used as an estimate of mesozooplankton respiration rate. The ETS activity was assayed using the method of Packard (1971), as modified by Gómez et al. (1996). ETS activity was corrected for the in-situ temperature at each depth using the Arrhenius equation with an activation energy of 15 kcal mol⁻¹, as given by Packard et al. (1975).

The community respiration rates (R; mg C m⁻² h⁻¹) were assessed from specific ETS activities (ml O₂ mg prot⁻¹ h⁻¹) and integrated biomass (mg protein m⁻²), assuming a respiratory quotient of 0.97 (Omori & Ikeda 1984) and a theoretical R : ETS ratio of 0.5 (Hernández-León & Gómez 1996; Ikeda et al. 2000). We assessed the community potential ingestion (I; mg C m⁻² h⁻¹) from respiration rates (R), assuming an assimilation and a gross growth efficiency of 70 and 30%, respectively, and applying the equation proposed by Ikeda & Motoda (1978):

$$I = 0.75 R / (70 - 30) - 2.5 R.$$

The results of the enzymatic analyses have been analysed, and laboratory experiments confirm literature values of the relationship between ETS activity and respiration rate (McKinnon et al., 2015). We can make the following observations, based on box plots of the data (Figure . 4.7.17):

- AARS activity in the 73-150 fraction was marginally higher during the Nov 12 and Sept 2013 cruises, but there was no convincing difference in the other size fractions
- ETS activity was lower in all size fractions in the Aug 2012 cruise, with the Sep 2013 cruise showing higher rates than other cruises in the >150 and >350 size fractions.
- Overall, there are no consistent temporal differences in the activities of these two enzyme systems.

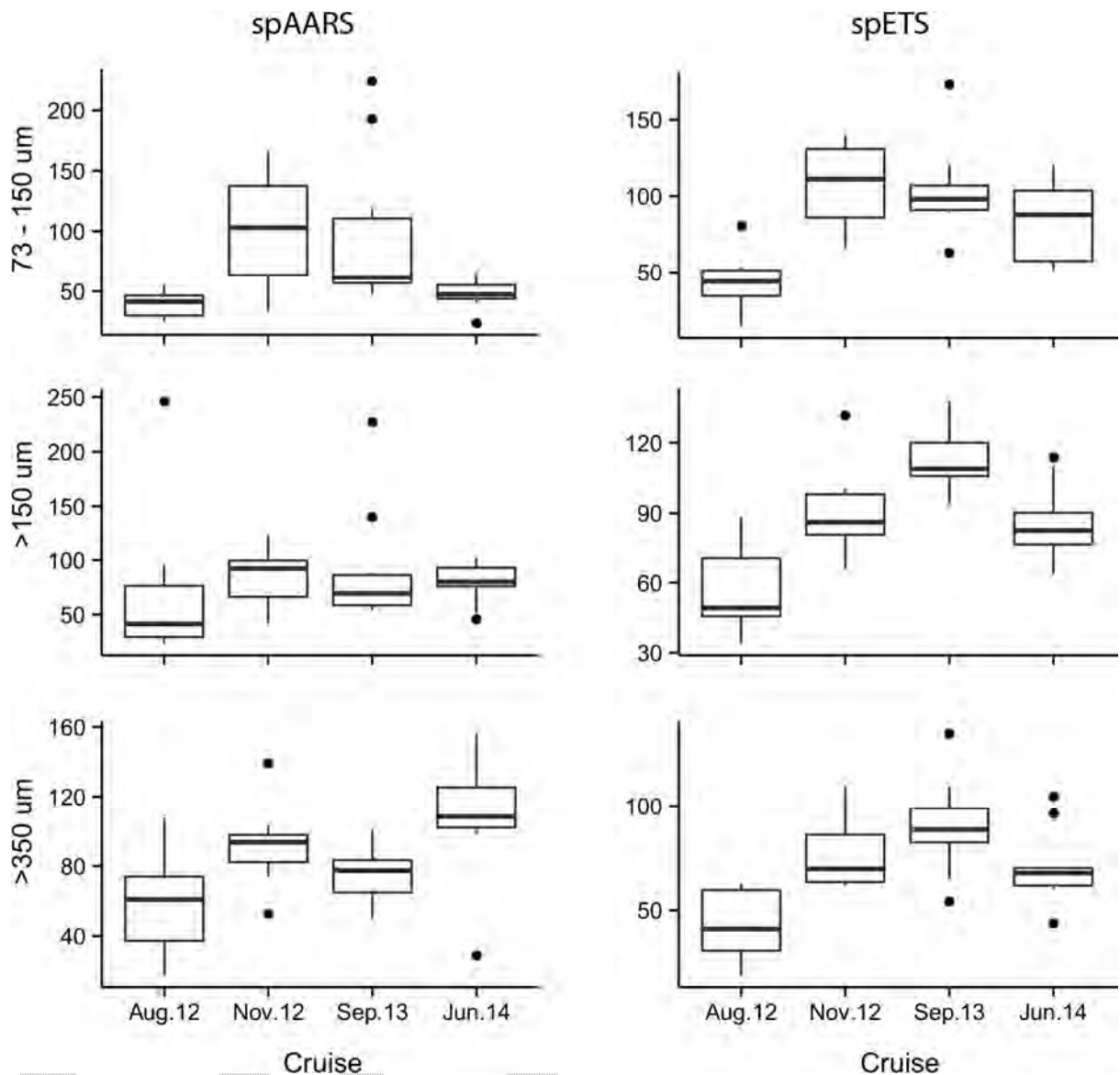


Figure 4.7.17: spAARS activity (nmol PPI mg protein⁻¹ hr⁻¹) and spETS activity (μL O₂ mg protein⁻¹ hr⁻¹) in 3 size fractions (73-150μm, >150μm and >350μm) on each cruise (McKinnon et al., 2015).

Based on the equation of Herrera et al. (2012), the mean growth rates based on AARS are 0.69 for the 73-150μm fraction, 0.77 for the >150μm fraction, and 0.78 for the >350μm fraction. Considering only the >150μm fraction, and applying the growth rate of 0.77 to a >150μm biomass of 0.88 mgN m⁻³ (Table 4.7.4), yields a secondary production rate of 0.68 mgN m⁻³ d⁻¹. Assuming an average water column depth of 35m, this equals an area-specific secondary production rate of 24mg N m⁻² d⁻¹. Taking a growth efficiency of 33% (Harris et al 2000), this is equivalent to a grazing rate of 71mg N m⁻² d⁻¹. Taking an average primary production rate of 730 mgC m⁻² d⁻¹ (McKinnon et al. 2013), equivalent to 111 mgN m⁻² d⁻¹ assuming a Redfield ratio of 6.6C:1N, then the theoretical maximum grazing rate, based on the AARS data, is ~64% of the average primary production rate.

Calculation of mesozooplankton respiration rates from the ETS data result in mean (aggregated over all stations) rates of 5.2, 16.5 and 8.0 $\mu\text{mol O}_2 \text{ m}^{-3} \text{ d}^{-1}$ in the 73-150 μm , >150 μm and >350 μm size fractions respectively. Assuming an average water depth of 35m and applying the equations of Ikeda & Motoda (1978), i.e. that Ingestion I = 0.75 R/(70 - 30) - 2.5 R, we calculate the grazing rates of the >150 μm size fractions as 1.7 mg C $\text{m}^{-3} \text{ d}^{-1}$.

It is important to recognize that the AARS data represent the upper limit of the zooplankton production rate, and that the grazing rates calculated on this basis are unrealistically high (e.g. 64% of average primary production by the >150 μm fraction alone). Nevertheless it is suggestive of food-limitation of zooplankton growth on the GBR, as has been suggested in our earlier work. The measurements of respiration (as measured with the ETS assay) are actual rates, rather than a theoretical upper limit. However, the grazing rates calculated on this basis still seem very high, which prompted us to embark on an experimental program to confirm the empirical relationship between ETS activity and respiration rate.

What proportion of primary production do our estimates of grazing rates represent? Unfortunately, for our GBR samples there were no direct measurements of primary production on these cruises. However, we can assume a mean value of 730 mg C $\text{m}^{-2} \text{ d}^{-1}$ (McKinnon et al., 2013) resulting in a mean volume-specific primary production of 21 mg C $\text{m}^{-3} \text{ d}^{-1}$ assuming an average water depth of 35 m, in which case it appears that trophic transfer from primary producers to >150 μm zooplankton has an efficiency of about 6%, and that >150 μm zooplankton consume ~8% of primary production.

4.7.3.13 Application to eReefs zooplankton model

The eReefs model partitions phytoplankton and zooplankton into 2 size classes. It is reasonable to assume that microzooplankton consume ~60% of phytoplankton primary production (Schmoker et al. 2013). If this was true of the GBR, then our estimate of mesozooplankton grazing based on the ETS data accounts for the balance, but leaves nothing for other loss processes such as sedimentation. However, mesozooplankton are primarily grazers of microzooplankton, so taking into account the effect of trophic interactions our calculations may not be unrealistic.

4.7.4 Biogeochemical model process enhancement

The eReefs marine modelling system is implemented at scales from turbid estuaries (especially in RECOM applications) to the open ocean, and involving ecosystems dominated in different regions by plankton, seagrass and corals. Further model outputs are being assessed against observations ranging from remote-sensing to in situ sampling, and from chemical concentrations to habitat mapping. To represent these process, and match with these observations, has required significant process model enhancements that are central to eReefs biogeochemical model.

Model enhancements that have been undertaken as part of this project are:

1. Inclusion of a spectrally-resolved optical model that determines inherent optical properties (IOPs) from the state of optically-active constituents and produces apparent optical properties (AOPs) such as downwelling PAR, simulated remote-sensing reflectance (Baird et al., 2016a). Associated with this enhancement were the

modelling variable carbon to chlorophyll ratios by inclusion of a chlorophyll synthesis processes (Baird et al., 2013).

2. Implementation of an additional nitrogen-fixing plankton type representative of *Trichodesmium* (Robson et al., 2013).
3. Preferential uptake of ammonia over nitrate in all autotrophs.
4. Addition of equilibrium carbon chemistry calculations including precipitation (calcification) and dissolution of calcium carbonate and alkalinity dynamics (Mongin et al., 2014, 2016).
5. Improved representation of air-sea fluxes of carbon dioxide and oxygen, and an improved representation of anoxic chemistry.
6. Improved process representation for seagrass, in particular of uptake of nutrients from multiple sediment layers (Baird et al., 2016b).
7. Improved macroalgae model with diffusion-limited nutrient uptake.
8. Addition of coral animal and zooxanthellae dynamics (Gustafsson et al., 2013).
9. Parameterization of sub-grid scale reef substrate type and function.
10. Atmospheric deposition of nutrients in rain.
11. Inclusion of zooplankton carnivory.

A schematic summary of the complete model with these process enhancements and their interactions is shown in Fig. 4.7.18. Where references appear in the above list, the new formulations have been published in the peer-review literature. For the other enhancements, and for a complete description of the biogeochemical and optical models, see Appendix B.

Process model enhancements are described in more detail in the following sections.

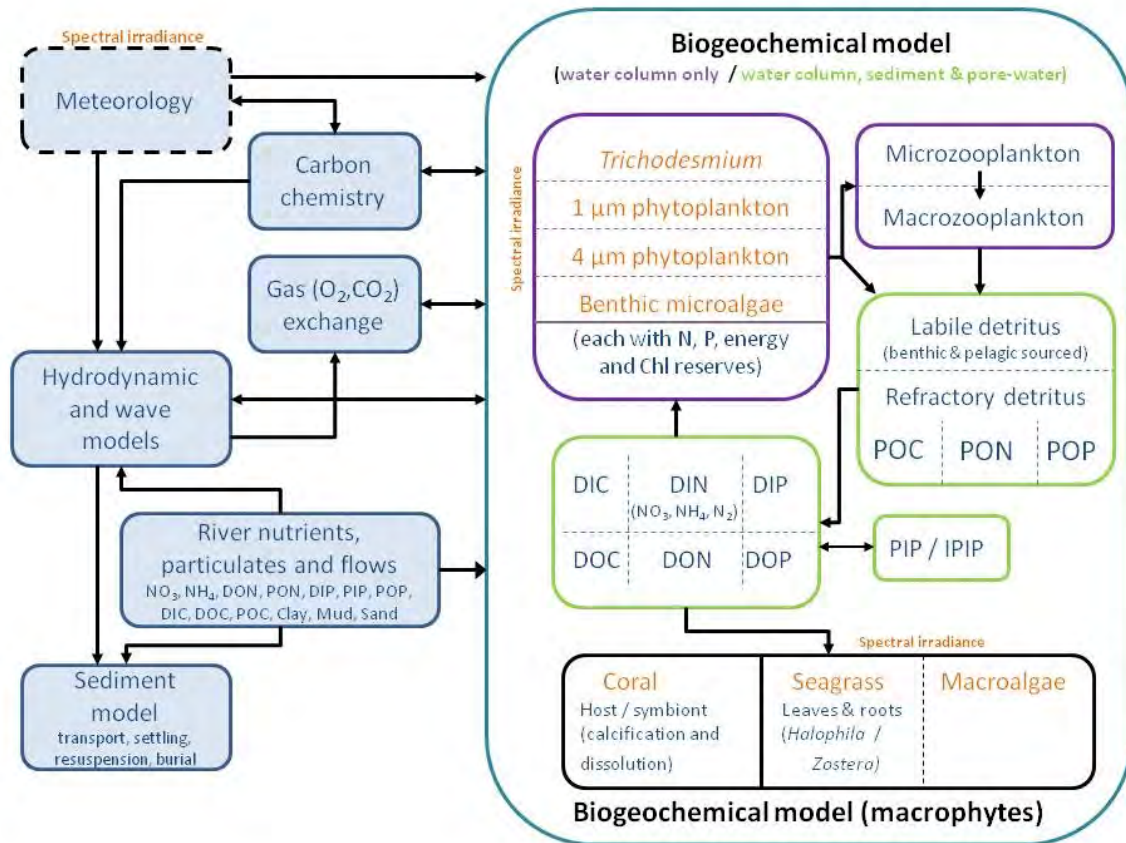


Figure 4.7.18. Schematic summary of EMS model for eReefs

4.7.4.1 Spectral irradiance, variable C:Chla and diurnal autotrophic growth

The previous light model within the EMS suite (used until mid-2012) was designed for a shallow water column with microalgae and benthic plants that grow using daily-averaged growth rates. Given this simple formulation, some physical processes that are standard in many optical models, were not included in EMS. For example, while the light at the top of the water column included the effect of zenith angle, the light was assumed to propagate vertically through the water column. Furthermore, the effect of absorption and scattering were combined to calculate a vertical attenuation coefficient.

In recent years new observations have made the above limitations too restrictive. In particular:

1. In-situ observations of spectrally-resolved absorption and scattering properties. Scientists are now routinely using ac9 and acs absorption meters, and HS-6 backscatter instruments. With these instruments the absorption and scattering properties can be determined independently, and should be resolved separately in the model.
2. In-situ spectrally-resolved radiometers, such as deployed from ships (Satlantic) and on autonomous gliders and AUVs provide spectrally-resolved irradiance. This is best compared to a spectrally-resolved optical model.

3. Through IMOS, there are now significantly more fluorometers deployed on moorings, gliders and at National Reference Stations. These provide an estimate of chlorophyll, but not microalgal biomass, as predicted by the present EMS model. Therefore a variable C:Chl ratio should be developed for each of the microalgal types in the model.
4. High intensity fluorometers (such as the Fast Repetition Rate fluorometer, FRRf, and the Pulse Amplitude Modulated fluorometer, PAM), combined with HPLC pigment analysis, are revealing properties of the photophysiology that have not be easily quantified previously. Can these be incorporated into an aquatic ecosystem model?

For eReefs the EMS code has been augmented with a spectrally-resolved optical model, variable C:Chla dynamics and diurnal autotroph growth to improve our ecosystem model prediction and model assessment.

Photo-physiology and variable C:Chla

A number of novel photo-physiological model parameterisations were investigated for single-cell microalgae models. These included models of photoadaptation (using variable chlorophyll content), photoprotection (using a dynamic xanthophyll cycle) and cell fluorescence.

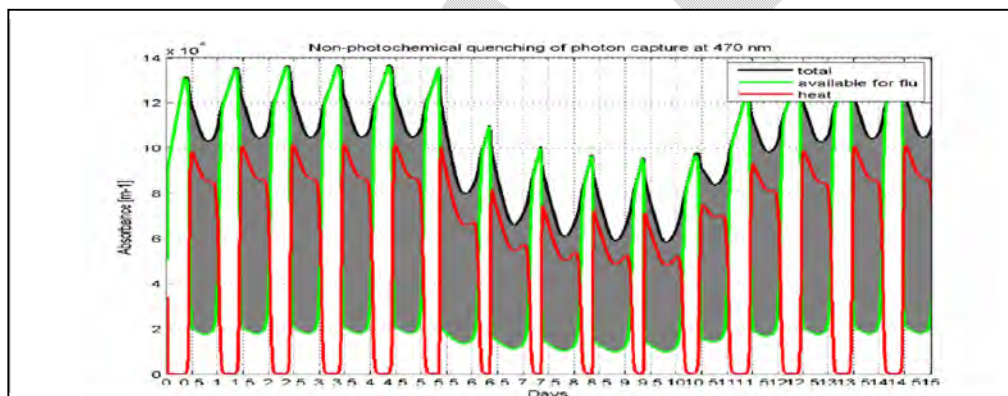


Figure 4.7.19. Non-photochemical quenching (NPQ). The absorbance by all pigments (black), absorbance by chlorophyll and xanthophylls in the non-photoprotective state leading to photosynthesis (green) and absorbance by xanthophylls leading to heat dissipation. NPQ is the difference between the total and the absorbance leading to photosynthesis (represented by the height of the grey area).

The laboratory experiments of Anning et al. (2000) were used to assess the photo-physiological models. Fig. 4.7.19 shows the sink of energy from absorption due to non-photochemical processes as captured by the photo-physiological model during high light (days 0 – 5, 10-15) and low light (days 5-10). The sink of heat occurs with increasing activity of the photoprotective pigments (Baird et al., 2013).

The photoadaptation model was identified as the most likely to result in improved model performance, as it improves both the accuracy of light absorption calculations and produces a water column chlorophyll concentration against which observations can be directly checked. The photo-physiology model for photoadaptation was therefore implemented in the

eReefs biogeochemical model providing a dynamically variable C:Chl_a ratio for phytoplankton (Fig. 4.7.20).

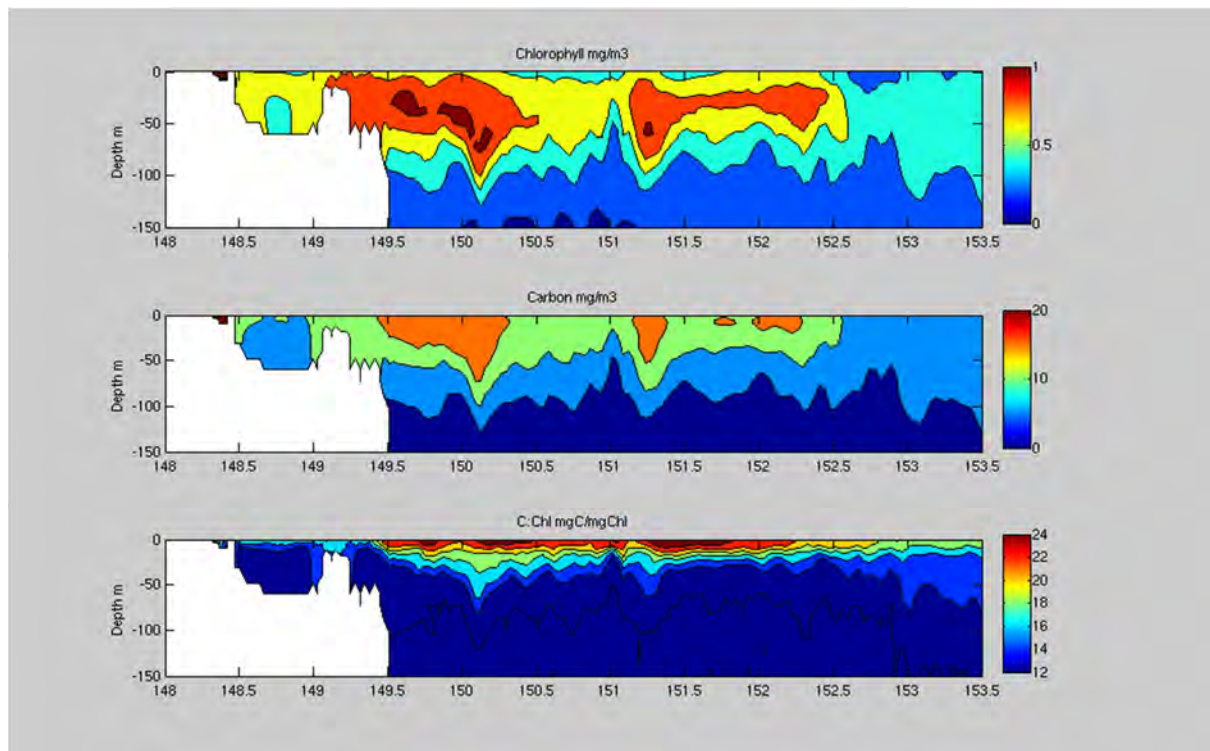


Figure 4.7.20. Cross section along 19.6 °S from west (left) to east (right) showing the simulated distribution of total phytoplankton chlorophyll, carbon and the dynamically varying C:Chl ratio on the 18th October 2012.

Spectrally-resolved light and diurnal autotrophic growth model

The spectrally-resolved optical model with diurnal autotrophic growth has been coded as an option in EMS by including processes with “_spectral” in their filename, and by addition of appropriate biological parameters, initial and boundary conditions. The revised model includes:

1. Implementation of a spectrally-resolved light field, with flexible choice of wavebands for the simulation.
2. Development of model code for an optical parameter library, presently populated with temperate and tropical properties.
3. Vertical attenuation calculations have been improved to consider zenith angle within the water column, and absorption and scattering of non-phytoplankton components.
4. Phytoplankton (small and large), *Trichodesmium* and microphytobenthos components now have a variable carbon:chlorophyll ratio and the addition of internal quotas of phosphorus as a means of calculating growth rate.

5. Phytoplankton (small and large), *Trichodesmium* and microphytobenthos components absorb a spectrally-resolved light field in the water column, and also on the sediment for microphytobenthos.
6. The spectrally-resolved light field at the bottom of the water column is integrated into a PAR light field above the epibenthos and sediment.
7. Autotrophs in the model absorb light for photosynthesis, growth and respiration during the day and utilise stored energy pools overnight.
8. The numerical approximation of the microalgae absorption cross section, and its derivative (which is used to determine rates of chlorophyll synthesis), has been improved to avoid numerical issues at low absorption values.
9. A diagnostic file (spectral.txt) is now produced at the beginning of the simulation that summarises the optical model implementation and the details of the numerical integration (i.e. details of the spectral resolution and waveband intervals).

Further details of the spectrally resolved model are included in the user guide to the EMS ecology code (CSIRO Coastal Environmental Modelling Team, 2015), and Baird et al. (2016a). Representative results are shown in Figs. 4.7.21 and 4.7.22.

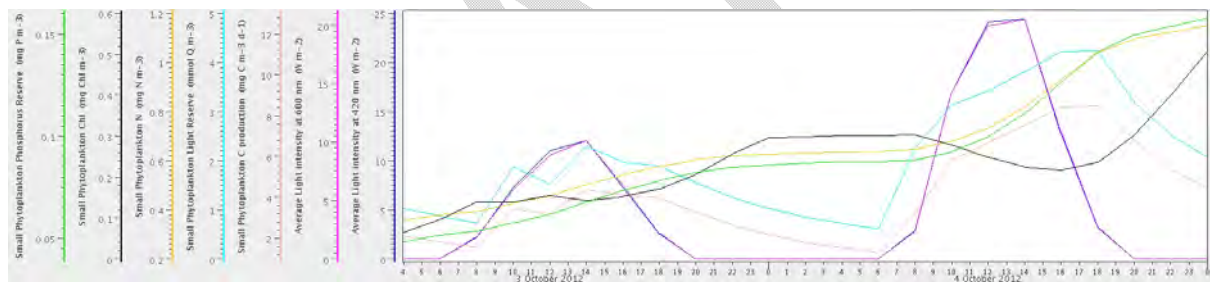


Figure 4.7.21. Diurnal cycle of light in the surface layer at 600 nm (pink) and 420 nm (blue). Small phytoplankton light reserve (cyan) and C production (pink) peak in late afternoon. Nutrient reserve (green) and biomass (yellow) increase during the day and the first half of the night, until depleting light reserves slow growth. Chlorophyll (black) is synthesised most rapidly under low light, during the first part of the night and diminishes due to dilution during the day.

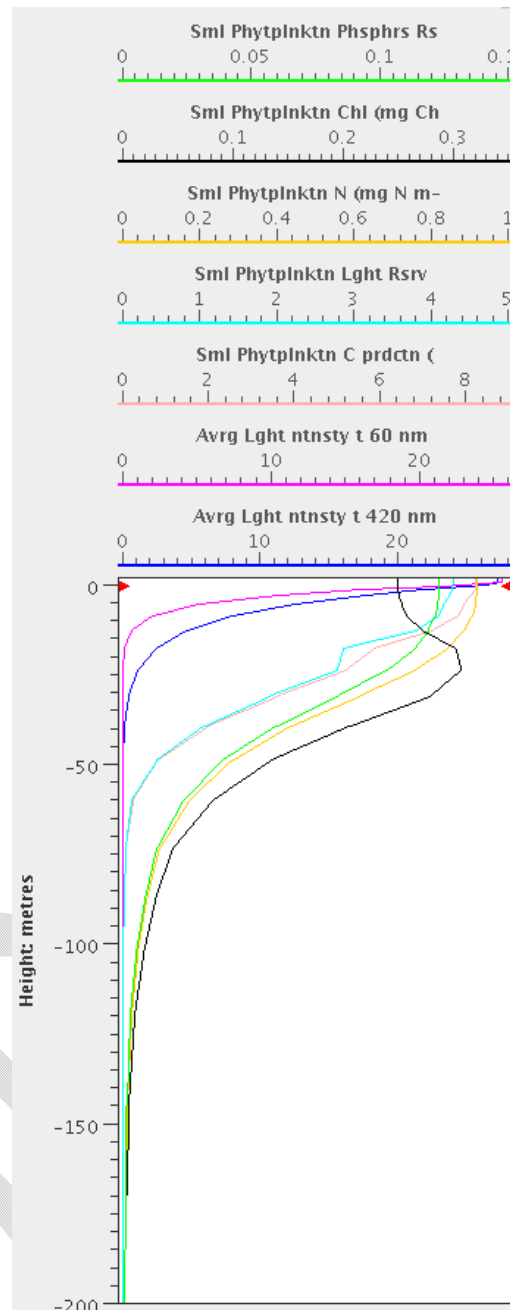


Figure 4.7.22. Profile of light at 600 nm (pink) and 420 nm (blue) and small phytoplankton biomass (yellow), nutrient reserve (green), light reserve (cyan), C production (pink) and chlorophyll content (black). Note peak in pigment at depth, whilst biomass and productivity are greatest in the surface layer.

Development of Matlab diagnostic software

The output of the full spectrally-resolved light model cannot be stored due to its size (number of water column cells x number of wavelengths). To overcome this, a Matlab routine has been developed that recreates the apparent optical properties (i.e. scalar irradiance) for a subset of the model domain (e.g. at a particular time, on a vertical slice etc.) from the inherent optical

properties (see Fig. 4.7.23). An advantage of this routine is that model can be run with one set of wavelengths (i.e. 300, 400, ... 700 nm), but the output analysed at another set (i.e. the MODIS satellite bands, acs wavelengths etc.). The Matlab routine also provides a valuable independent check of the calculations within EMS. This routine is now used in the near real time implementation to calculate remote-sensing reflectance, among other products, during the simulation.

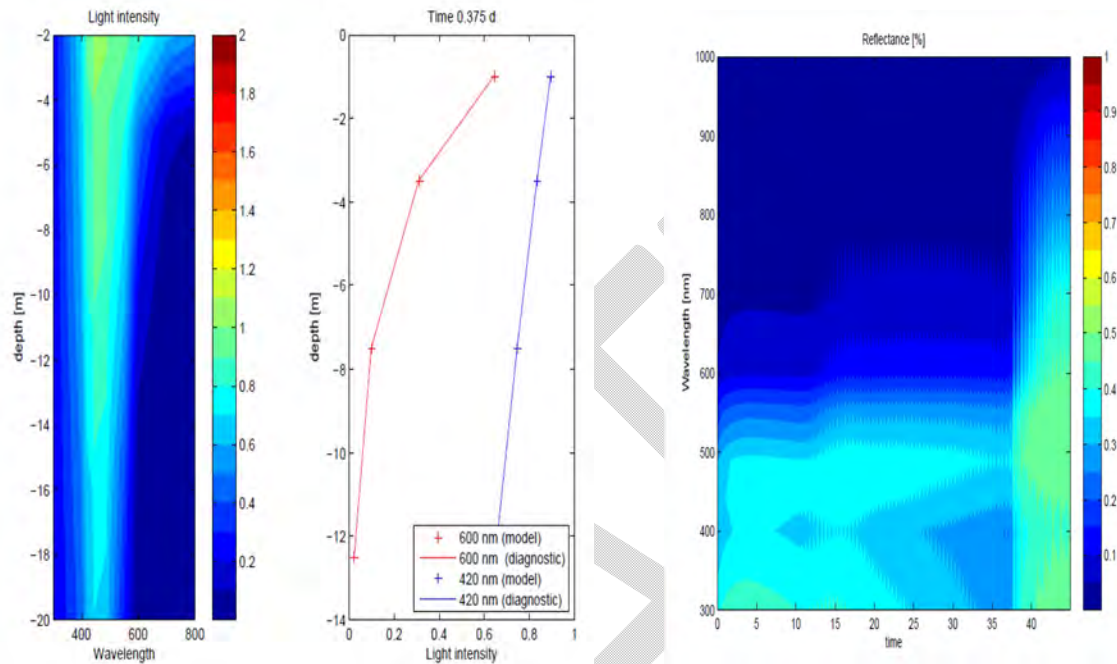


Figure 4.7.23. Images from the diagnostic Matlab routine. Left; spectrally-resolved light field recalculated from inherent optical properties at arbitrary wavelengths. Centre; validation of the optical model through calculations within the EMS code (+) and in the diagnostic routine (lines) at two wavelengths. Right; calculation of surface reflectance from inherent optical properties using the diagnostic routine.

Comparison of model and observed surface reflectance

The spectrally-resolved optical model calculates remote-sensing reflectance (ratio of outgoing irradiance at a solid angle to incoming irradiance) at any required wavelength, which can be directly compared to observed values. Since the optical model now produces remote-sensing reflectance at any wavelength, it is now possible to use satellite algorithms such as OC3 to directly compare model and observed properties. A particularly interesting such satellite product is true colour (Baird et al., 2016a).

True colour images are often used in the geophysical sciences to provide a broad spatial view of phenomenon such as cyclones, droughts or river plumes. Their strength lies in the human experience of the natural colours that allows three 'layers' of information (red, green and blue), and the interaction of these information streams, to be contained within one image. Spectacular satellite true colour images of, for example, the Great Barrier Reef (GBR), simultaneously depict reef, sand and mud substrates, sediment-laden river plumes and

phytoplankton blooms (Schroeder et al., 2012). Further, the advection of suspended spatially-variable coloured constituents reveals highly-resolved flow patterns. For these reasons and more, true colour imagery has become a valued communication tool within both the geosciences and wider community.

"Simulated true colour" is calculated from combining simulated remote-sensing reflectance at the red, green and blue wavelengths. Thus simulated true colour is a product of the physical-optical-sediment-biological model alone, independent of any remote observations.

True colour images use intensity in the red, green and blue wavebands. We have chosen to calculate simulated remote-sensing reflectance at 645, 555 and 470 nm for the production of simulated true colour images, and also to facilitate comparison with wavebands 1, 2 and 4 used on the MODIS (Moderate Resolution Imaging Spectroradiometer, NASA) sensors. We have also adopted the processing techniques used to produce MODIS true colour images (Gumley et al., 2010): true colour image brightness (on a scale of black = 0, white = 1) is adjusted by linearly mapping surface reflectance at each of the three wavelengths to a brightness that approaches 1 in the brightest of the three bands. Additionally, a piece-wise linear scaling is used to brighten dark components. Thus, simulated true colour is determined from combining simulated (not observed) surface reflectance at 645, 555 and 470 nm using the techniques developed for processing observed true colour.

Fig. 4.7.24 shows the simulated true colour before, during, and after the impact of Tropical Cyclone Yasi on the GBR. The coastal waters in the middle of the images show enhance scattering, a result of the combination of resuspension of sediment and river discharge.

Apart from revealing multiple phenomenon in one image, simulated true colour images are likely to play an important role in understanding biogeochemical responses on the GBR. Firstly simulated true colour can be used to estimate plume extents during cloudy periods (often coincident with the most devastating run-off events) using the same techniques presently applied to satellite remotely-sensed true colour images (Schroeder et al., 2012).

Secondly, the biogeochemical modelling system assimilates ocean colour data directly into the model to estimate biogeochemical parameters. As the optical model calculates spectrally-resolved remote-sensing reflectance, the assimilation routines will quantify model state error by the difference in remote-sensing reflectance at each observed band. Present biogeochemical assimilation techniques typically match simulated in situ chlorophyll with error-prone remotely-sensed ocean colour algorithms such as OC3. In our approach, by comparing simulated and observed surface reflectance directly, the intermediate, error-prone step involving a chlorophyll algorithm is excluded. In short, we are now able to compare simulated apples and observed apples. This waveband-specific assimilation approach is likely to be sensitive to the accuracy of the simulated colour. Simulated true colour provides a stringent test of the faithfulness of the simulated colour representation, thus providing confidence in the assimilation processes.

In summary, simulated true colour is a novel, potentially powerful tool for the visualisation and analysis of ocean models, and may have similar utility in the atmospheric and terrestrial sciences. Many geosciences models already have sophisticated spectrally-resolved optical sub-models, so with little additional development these models could be visualised using beautiful true colour images.

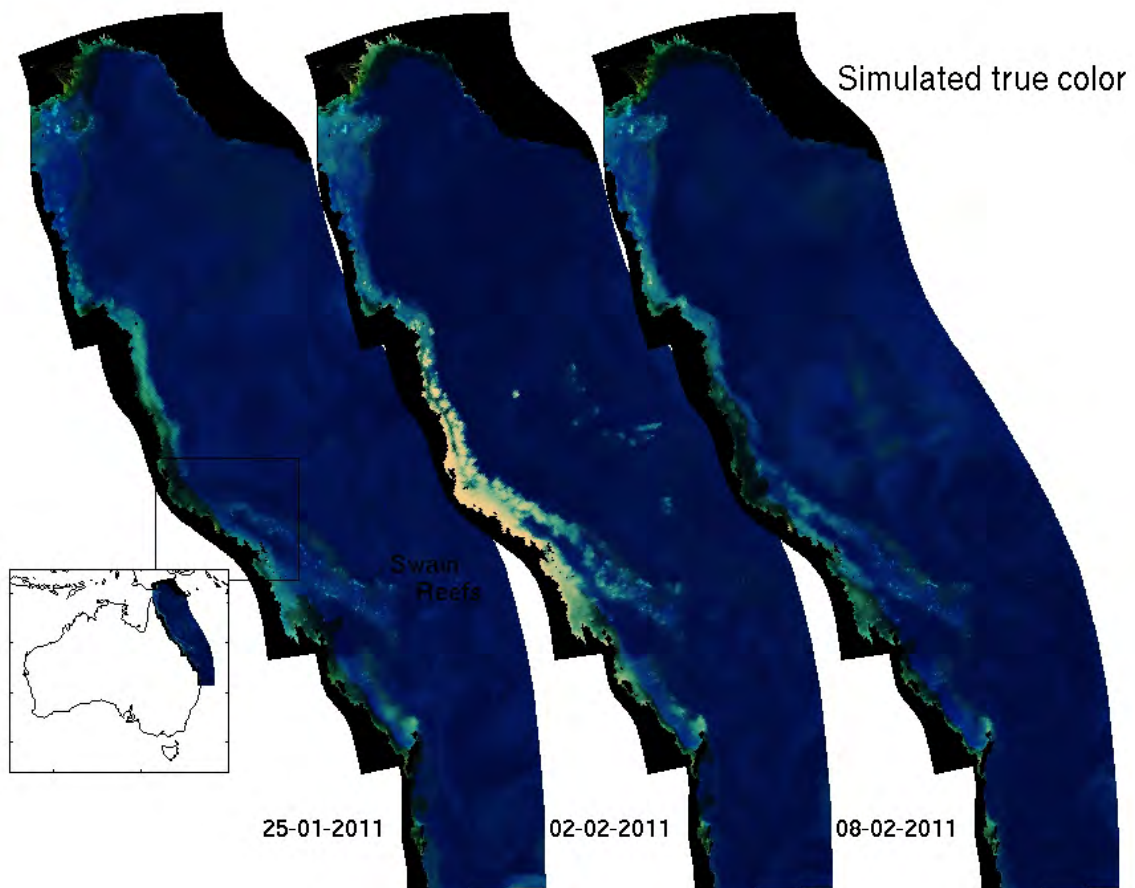


Figure 4.7.24. True colour from the simulated remote-sensing reflectance at 645, 555 and 470 nm of the coupled physical-optical-sediment-biological eReefs model on the 1, 2 and 10 Feb 2011 on the GBR, off Australia's northeast coast. Black is land with Papua New Guinea located at the top of the image, and the bottom of the image extending to 29 S. Yellow, dark green and green-blue hues result from scattering and absorption being dominated, in first optical depth, by river sediment, CDOM and phytoplankton, respectively.

4.7.4.2 N fixing phytoplankton functional group *Trichodesmium*

Nitrogen fixation by *Trichodesmium* is believed to form a substantial component of the nitrogen budget of the Great Barrier Reef Lagoon (GBRL), though this contribution is difficult to quantify. It may also be important in driving the redistribution of phosphorus in the water column.

Trichodesmium are notoriously difficult to measure accurately in the field (Chang, 2000) and difficult to culture in the laboratory. Satellite estimates are possible when surface blooms form, but may give rapidly varying results when *Trichodesmium* leave the surface due to increased mixing or diel variations in buoyancy. Because the availability of nitrogen to drive primary production may depend in large part upon the production and transport of *Trichodesmium*, it nonetheless is important to model this cyanobacterial species. As part of the improvements to the EMS biogeochemical model undertaken for eReefs, we have developed a new model for *Trichodesmium* that simulates the key physiological processes

that are known to affect this cyanobacterium. While keeping to a minimum number of additional parameters required, the model includes:

1. Preferential uptake of ammonium over nitrate, reflecting the slightly lower energetic cost of ammonium uptake.
2. Fixation of atmospheric nitrogen when both ammonium and nitrate are limited, with an energetic cost that reduces chlorophyll production capacity and reduces the maximum growth rate when nitrogen fixation is required.
3. Variable intracellular chlorophyll:C:N:P ratios.
4. Variable cell buoyancy that is a function of accumulation and depletion of intracellular carbohydrate stores.
5. Light absorption that depends on the spectral quality of irradiance.
6. Collapse of large populations due to viral lysis.

The model is fully described in a peer-reviewed conference paper that has been published in the proceedings of [MODSIM 2013](#) (Robson et al., 2013).

A number of additional factors have been identified as potentially important, but are not included in model because they would require considerable additional complexity that may not be supported by the available data. In further testing and development, we will consider carefully whether the model needs to be revised to include:

1. Iron limitation of nitrogenase production.
2. Variable pigmentation.
3. The physics of floating surface scums.
4. Variable colony size and morphology.
5. Direct effects of turbulence on colony sustainability.

Given the very limited available *Trichodesmium* data, priority will be given to using the model to explore the potential magnitude of the contribution of *Trichodesmium* to the nitrogen budget of the Great Barrier Reef Lagoon, and working with the remote sensing team to determine the suitability of satellite observations for identification and quantification of *Trichodesmium*.

4.7.4.3 Preferential ammonia uptake.

With the increasing measurement of ammonia in aquatic sciences, the modelling of preferential uptake of ammonia over nitrate has been included in the model. The model contains two forms of dissolved inorganic nitrogen (DIN), dissolved ammonia (NH₄) and dissolved nitrate (NO₃) (Fig. 4.7.18). The rate of uptake of DIN by photosynthetic organisms is assumed to be a function of DIN concentration, among other factors. In the revised model, the ammonia component of the DIN pool is assumed to be taken up first, followed by nitrate, with the caveat that the uptake of ammonia cannot exceed the diffusion limit of ammonia uptake. The molecular diffusion coefficients for ammonia and nitrate are $19.8 \times 10^{-10} \text{ m}^2 \text{ s}^{-1}$ and $19.0 \times 10^{-10} \text{ m}^2 \text{ s}^{-1}$ respectively (Li and Gregory 1974).

Interestingly, by using the diffusion-limit to calculate ammonia preference, we avoid introducing new, uncertain, parameters that most biogeochemical models contain, while at the same time representing the processes that is most likely determining the preference itself.

4.7.4.4 Carbon chemistry reef processes

We have implemented carbon chemistry equilibrium calculations in order to calculate coral calcification rates, seawater pH, air-sea fluxes of carbon dioxide and aragonite saturation, among other phenomena, as described in Mongin et al. (2014, 2016)

This parameterization of reef biogeochemical processes has been successfully applied to an isolated reef system (Mongin and Baird, 2014) and generalised across the whole GBR region (Mongin et al., 2016).

Results showing alkalinity and aragonite saturation state (measure of coral reef ability to calcify) in the GBR4 model are shown in Figs. 4.7.25 and 4.7.26. Because the carbon system is strongly physically-forced through temperature changes, river inputs, circulation and air-fluxes, the model has obtained excellent skill in predicting carbon chemistry quantities (Mongin et al., 2016).

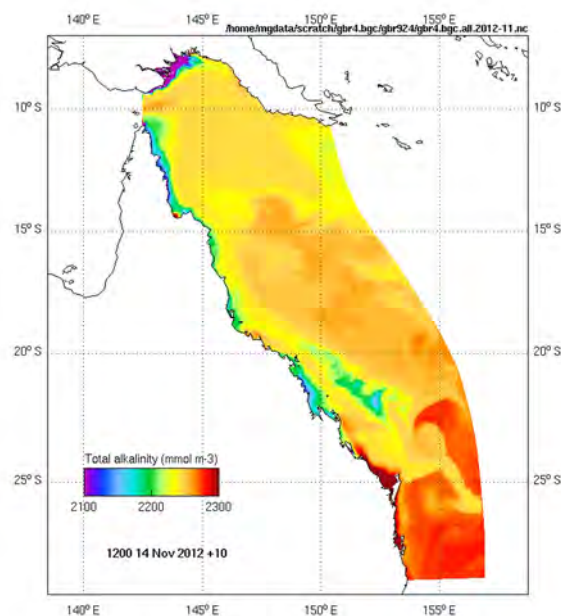


Figure 4.7.25. Snapshot of surface alkalinity on 14th Nov 2012 from the GBR4-924 simulation.

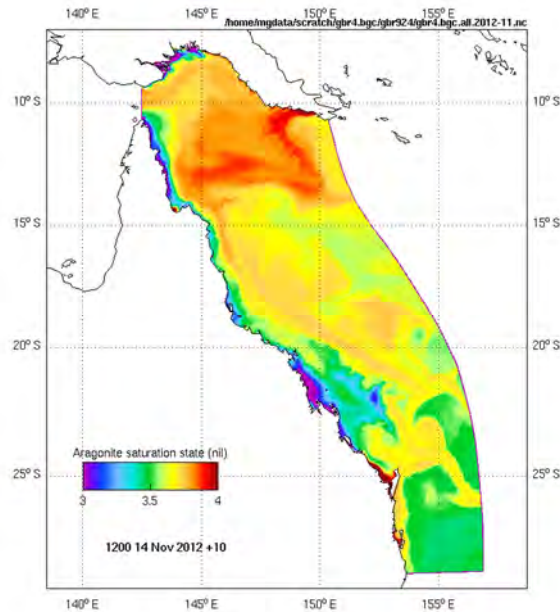


Figure 4.7.26. Snapshot of surface aragonite saturation on 14th Nov 2012 from the GBR4-924 simulation .

4.7.4.5 Air-sea gas exchange

Air-sea gas exchange at the sea surface has been modified to vary with wind speed. Exchange is calculated using a cubic relationship between wind speed (Wanninkhof et al., 1999), the saturation state of the gas and the Schmidt number of the gas (Wanninkhof et al., 1992). For oxygen, saturation state is determined as a function of temperature and salinity following (Weiss, 1970), while the saturation state of carbon dioxide is derived using the carbon chemistry equations summarized above.

This improved representation of air-sea exchange improved the calculation of oxygen concentration, but it became clear that low oxygen dynamics was poorly resolved in earlier versions of the model. Thus we introduced a tracer chemical oxygen demand (COD). COD represents the oxygen demand of reduced chemical species such as hydrogen sulphide in the sediments, without explicitly represent the complex chemical reactions that these reduced species undertake. Introduction of COD also allows an oxygen balance to be undertaken, a significant new consistency check for the model equations.

4.7.4.6 Seagrass

Seagrass are a critical component of GBR ecosystem, and their representation has been significantly improved to better represent of seagrass carbon capture and ecological function (Baird et al., 2016b). In the GBR region a number of tropical species are found including both seed bearing and forms with vegetative reproduction (Fig. 4.7.27).

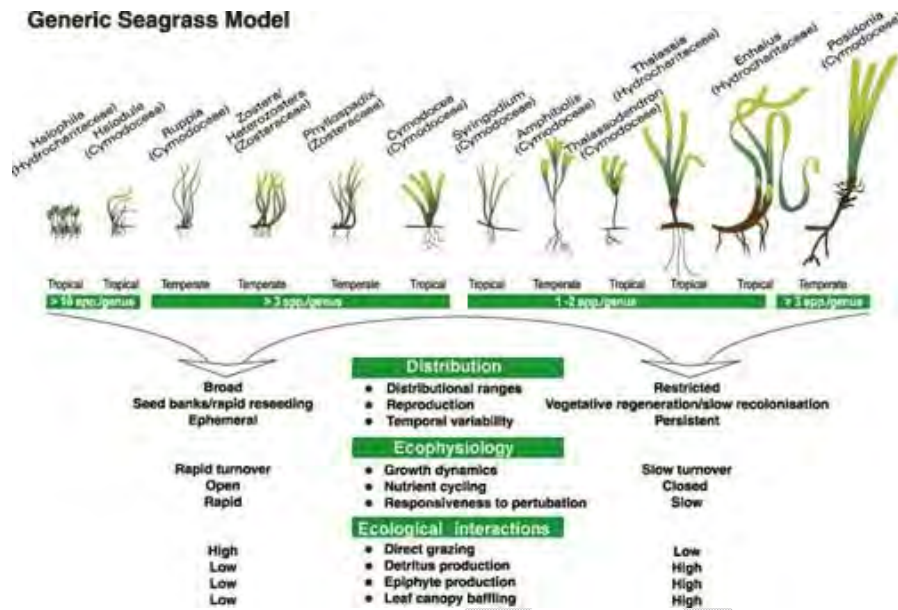


Figure 4.7.27. Range of tropical and temperate seagrass forms (Butler 1999)

The enhanced model now includes:

1. Two seagrass types, representing *Halophila* and *Zostera*.
2. Calculation of relationship between bottom cover and biomass using $1 - \exp(-\Omega B)$, a theoretically-derived equation shown to be accurate (Baird et al., 2016b).
3. Separate state variables for above and below ground biomass.
4. Absorption calculations using a spectrally-resolved light field.
5. Nutrient uptake from multiple layers of sediment.
6. Translocation of C, N, and P between above and below ground biomass.
7. A seed bank to allow re-population of areas.
8. Use of species-specific observations of minimum light requirement (MLR) to parameterise respiration.

The seagrass model (Baird et al., 2016b) is now one of the most sophisticated and well justified models described in the literature, having been developed in a collaboration with modellers from UQ, physiologists from UTS and observational scientists from JCU.

4.7.4.7 Macroalgae

Macroalgae in the standard EMS model are simulated in a relatively simple form (Wild-Allen et al., 2010) to represent epiphytic species that compete with seagrass for light and nutrients. Given elevated water column nutrient concentrations these epiphytic macroalgae will increase in biomass, shade and overgrow seagrass cover.

In the GBR various forms of macroalgae occur, however the most significant cover by area is probably that of turf algae overgrowing reef substrate (Fig. 4.7.28). In addition to a change

in the macroalgae the eReefs model is representing, other enhancements mentioned above also required new parameterisations for macroalgae.

Thus the macroalgae model has been re-written for eReefs and now includes the following traits:

1. Bottom coverage and light absorption represented using the form $1 - \exp(-\Omega B)$ used for seagrass (Baird et al., 2016b).
2. Spectrally-resolved absorption cross-section based on leaf measurements.
3. Diffusion limitation of nutrient uptake, being a function of bottom shear stress (i.e. turbulence).
4. Preferential ammonia uptake (see above).

This new form is most appropriate for the simulation of fine turf algae on the broad scale macroalgae on the GBR.



Figure 4.7.28. GBR macroalgae among reef: turtle grass (left) and turf algae (right).

4.7.4.8 Coral

A simplified version of the host-symbiont coral model (Gustafsson, et al., 2013) has been implemented in the EMS code. In the model the coral host consumes water column zooplankton, phytoplankton, organic N and the symbiont (zooxanthellae). Symbiont grows similar to water column microalgae with cells containing reserves of energy, nitrogen, phosphorus, as well as a variable C:Chl content.

The coral model has been trialled in a configuration of the eReef model on Heron Island (Mongin and Baird 2014). The model shows reasonable rates of water column uptake of dissolved and particulate matter (see Fig. 4.7.29), and spatially-resolved changes in biomass of both symbiont and host biomass (Fig. 4.7.30).

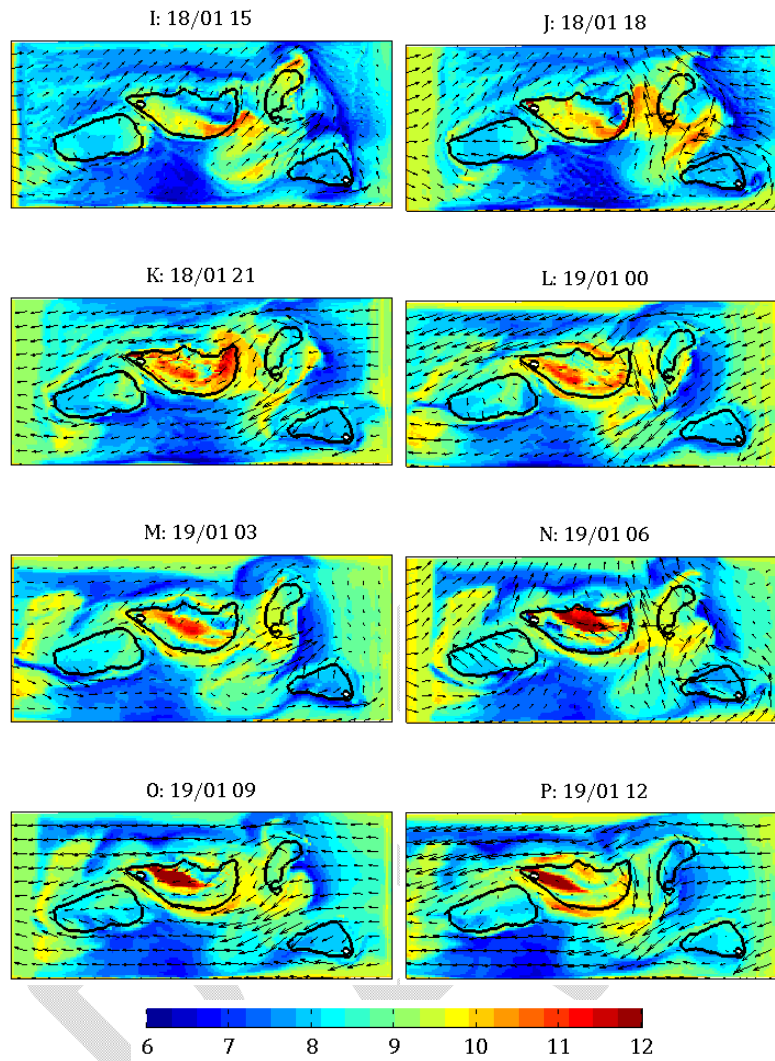


Figure 4.7.29. Results from the application of the host-symbiont coral model on a 167 m resolution configuration of the Heron Island. Panels show PON at the surface of the water column in unit mg N m^{-3} during a low wind period when residence time of Heron is at a maximum. The title of each panel states the time point letter as well as the date and time of day. The contours mark where the water depth is 5 m.

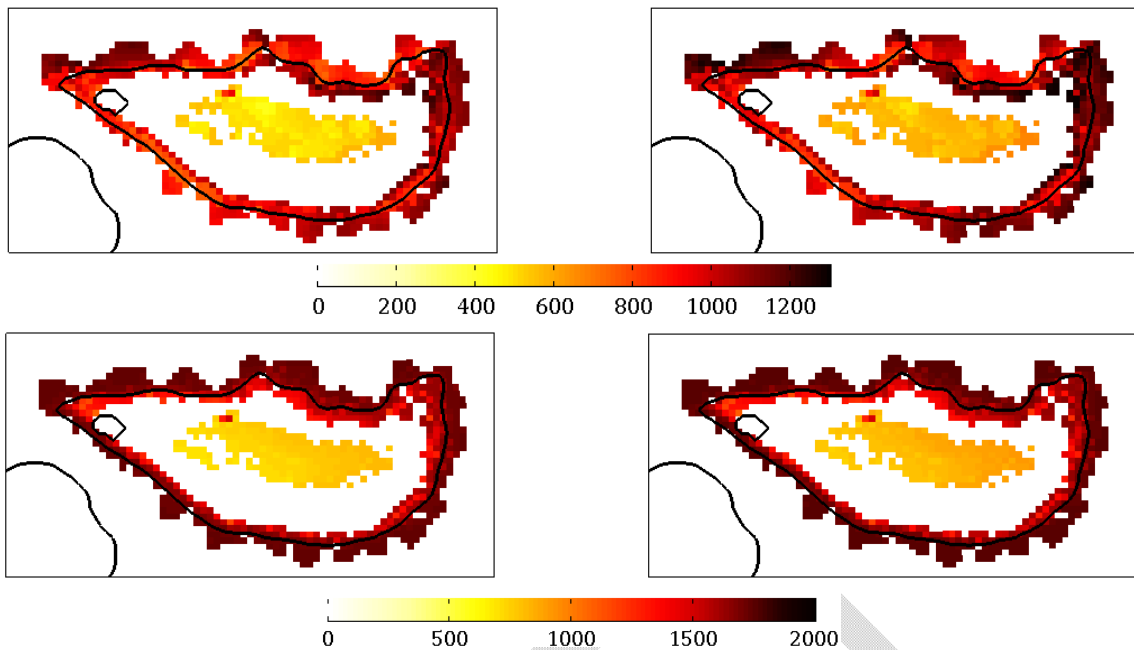


Figure 4.7.30. Mean biomass of coral host and symbiont population for two simulations with a short residence time (left) and a long residence time (right), biomass in mg N m^{-2} .

4.7.4.9 Reef substrate type and function

Dense reef communities do not persist over an entire reef platform, but are usually present on the reef slope and crest where nutrients are resupplied from the open ocean during the rising tide. On the reef flat, downstream of the dense coral communities, sand with microphytobenthos are predominant. Thus the dense communities exist for a few hundred metres inshore of the reef rim.

As our model equations for coral processes are based on dense coral communities, when a grid cell dimension is greater than a few hundred metres, the coral reef rates must be reduced to account for the fractional cover of coral. In order that the scaling can be seamlessly applied across the regional grids (4 km and 1 km) and in RECOM, we use a geometric derivation to determine the fraction (Fig. 4.7.31).

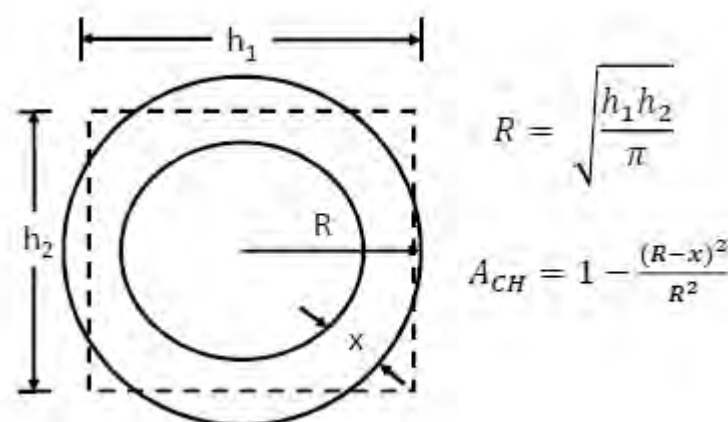


Figure 4.7.31. Schematic showing the geometric calculation of the sub-grid parameterisation of the effective projected area fraction of corals, ACH. Nominal width of dense coral

communities, $x = 200$ m, grid cell dimensions h_1 and h_2 are 4000 m for the 4 km grid, and R is the equivalent circular radius of the grid cell. For the 4 km and 1 km grids, ACH is 0.10 and 0.36 respectively. For the RECOM configurations ACH varies from cell to cell.

4.7.4.10 Atmospheric deposition of nutrients in rain

Up to 2 meters of rain falls every year onto the central GBR shelf (16-18°S) (Furnas et al, 1995) and up to 11 meters of rain may fall at coastal sites in the wet tropics (Hausler, 1991). Most rain comes between January and March. Furnas et al., (1995, unpubl.) collected and sampled 173 rainwater samples at sea in the GBR and at coastal sites near Townsville. They found most levels of inorganic nutrient concentrations were low (Table 4.7.2). However, there were a small number of samples that had high levels of ammonium and nitrate. Ammonium was the principal inorganic nitrogen species deposited in rainfall.

Duce et al., (2008) in a review in *Science* estimated that atmospheric anthropogenic fixed nitrogen entering the ocean could account for up to a third of the oceans external (non-recycled) nitrogen supply. In the region of the GBR and Coral Sea their estimates were approximately $200 \text{ mg N m}^{-2} \text{ yr}^{-1}$ of which 70 mg was DON and 140 mg DIN. Of the DIN overall 10% was NO_x and 90% ammonia.

Model development has been undertaken to allow input of surface fluxes of generic tracers. In eReefs we have implemented atmospheric deposition by adding ammonia as a surface flux over the ocean region ($140 \text{ mg m}^{-2} \text{ yr}^{-1}$). Surface fluxes can be input as tracer attributes for individual tracers, and are applied as a surface boundary condition in the vertical mixing algorithm. Since this algorithm is implicit, the input of nutrient via a surface flux and the mixing of the nutrient throughout the water column occur simultaneously.

An alternative method of atmospheric deposition is addition of nutrients relative to real time rainfall (see hydrodynamic section). However, the addition of nutrients via surface flux was used as a large proportion of the model grid encompasses the Coral Sea which receives rainfall from the east during the wet season with low nutrient content. There are also limited historical rainfall nutrient data sets over the entire region with many site locations situated close to the lagoon and coast. Future developments may include more flexible parameterization of rainfall which would permit higher nutrient values close to the coast (e.g. $2.0 \text{ }\mu\text{M}$ ammonia) and lower nutrient values for rainfall in the Coral Sea (e.g. $0.2 \text{ }\mu\text{M}$ ammonia).

4.7.4.11 Zooplankton carnivory.

An additional processes of large zooplankton consuming small zooplankton (in addition to grazing on large phytoplankton, *Trichodesmium* and microphytobenthos) was included. This improved the model performance and is similar to that used in other shelf and open sea models (Fasham et al., 1993). As the model food web of 4 phytoplankton types and 2 zooplankton types is an abstraction of the more complex reality, it is difficult to use observations with any certainty to determine which links should occur in the model. But the improved model performance (for chlorophyll concentration) is seen as an indication that including zooplankton carnivory improves the lower trophic level foodweb interactions.

It is worth noting that as the representation of grazing includes the calculation of clearance rates based on swimming speeds, zooplankton radius and a maximum growth rate, all of

which were already defined in the model for the process of large zooplankton grazing on phytoplankton, no new parameters were required for this formulation. Thus model uncertainty was not increased by defining any new, uncertain parameter values.

4.7.5 Whole of GBR biogeochemical model simulations

Components of the eReefs biogeochemical model have been tested across a number of model grids including a test estuary configuration, a Heron Island fine resolution model grid, a 20km, and a 4km resolution whole of GBR model grid and a 1km resolution GBR and Queensland shelf model grid. On the 4km model grid pilot BGC model simulations have been achieved in hindcast and near real-time modes, with results displayed live on the EMG web page at <http://www.emg.cmar.csiro.au/www/en/emg/projects/eReefs/Results.html>.

At the whole of GBR scale, the BGC model is simulated in a transport mode using the Flux Form semi-Lagrangian scheme (Section 4.5.3). This allows the hydrodynamic and wave models to be run independently whilst the sediment and biogeochemical models are driven by the transport model from archived files of currents, diffusion coefficients, temperature, salinity and short wave radiation. The simulation time-step is 1 hour and there is no feedback from the sediment and BGC process models to the hydrodynamics.

4.7.5.1 Coarse resolution fast test model

The multi-grid capability in the transport model was used to transpose the transport variables for the 4km grid on a coarser 20km grid (Fig 4.7.35). This coarser resolution decreases the number of cells in the model domain, thus increasing runtime to ~700:1 for BGC and sediment simulations. Multiple runs can be performed in the time it takes a single run to finish at 4km resolution. The coarse resolution, however, introduces error, particularly around the reef matrix and coastal geographic complexities. The trade-off between speed and accuracy allowed an approximate calibration to be achieved using this model (e.g. Fig. 4.7.36) which was then transferred to the slower 4km model for subsequent fine tuning.

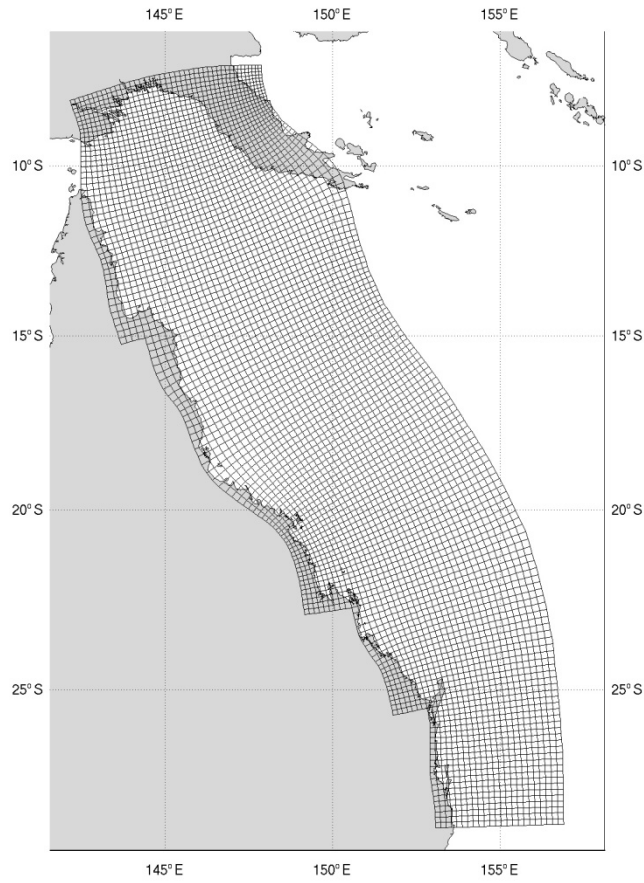


Figure 4.7.35. Grid configuration for the 20km model.

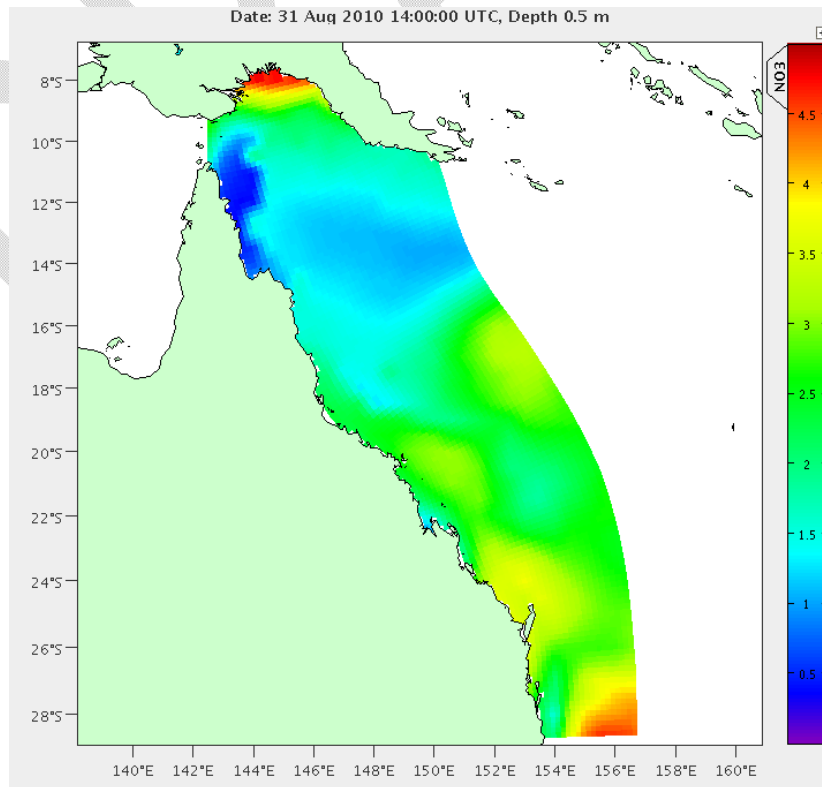


Figure 4.7.36. Surface dissolved inorganic nitrogen on the 20km model grid.

4.7.5.2 4km Hind-cast and near real time model

The biogeochemical and sediment model is run in transport mode on the same 4 km grid as the hydrodynamic model with a runtime ratio of ~70:1 on 16 processors. A hind cast biogeochemical simulation was run from September 1st 2010 until June 1st 2012 to confirm numerical stability of the full biogeochemical process library (i.e. the model can proceed through the simulation period with no abnormal termination). More recent simulations have extended the hind-cast period to December 2015. The model has the standard EMS capability activated plus the new processes for spectrally resolved optics, variable C:Chl ratio, autotroph diurnal growth, carbon chemistry, air-sea gas exchange, coral photosynthesis, reef substrate and seagrass growth. The full list of processes included in the model is shown in Table 4.7.5, and model parameters and boundary conditions are summarized in Appendix A.

Table 4.7.5. Biogeochemical processes implemented in the eReefs model.

water column	epibenthos	sediment
microphytobenthos spectral	macroalgae spectral growth	microphytobenthos spectral growth
phytoplankton spectral growth (small)	seagrass spectral growth <i>Zostera</i>	microphytobenthos spectral mortality
phytoplankton spectral growth (large)	seagrass spectral growth <i>Halophila</i>	phytoplankton spectral mortality (small)
<i>Trichodesmium</i> mortality	mass balance	phytoplankton spectral mortality (large)
<i>Trichodesmium</i> growth	light spectral	zooplankton mortality (small)
phytoplankton spectral mortality (small)	diffusion	zooplankton mortality (large)
phytoplankton spectral mortality (large)		<i>Trichodesmium</i> mortality
zooplankton mortality (small)		nitrification denitrification
zooplankton mortality (large)		phosphorus adsorption
zooplankton large carnivore spectral growth		mass balance
zooplankton small spectral growth		
nitrification		
p adsorption		
carbon chemistry		
gas exchange		
mass balance		
light spectral		

An equivalent version of the model was implemented to run in near real-time using the automated TRIKE scheduling system from December 2014. A pilot version of the biogeochemical model 1km grid has been running since January 2015 with live display of a selection of model results on the group website at <http://www.emg.cmar.csiro.au/www/en/emg/projects/eReefs/Results.html>.

4.7.5.3 Initial Conditions

We use the CARS Ocean Atlas to initialise the 3D fields of DIP, NO₃ (e.g. Fig. 4.7.37) and Oxygen. Generalised empirical relationships for nutrient profiles are scaled on the model density profile specifying top and bottom water columns values from CARS ocean atlas. Surface NO₃ is initialised as 0 mg m⁻³. In deeper waters nutrient concentrations increase from 0 to 500 m depth and then remain constant down to the ocean floor (4000 m depth, 500 mg m⁻³ ~ 40 mmol m⁻³). DIC and Alkalinity are calculated from linear regression from GLODAP data (use DIC/ALK temperature salinity regression curves and apply them using to the GBR4 simulated temperature salinity (Key et al., 2004; Lenton et al., 2015). Oxygen is initialised using temperature and salinity regression from CARS.

The initial conditions for most other tracers were not spatially resolved, since observations for the outer reef and Coral Sea are limited temporally and spatially. Organic matter concentration was calculated using the relationship between net primary production and steady state organic content in the ocean (Hansell et al 2009, see detail in EMS user guide). Plankton concentrations in the sediment (Table 4.7.6) were initialised to low value except for microphytobenthos (Heil, et al., 2004). Concentrations of most other tracers in the sediment matched the bottom water column concentration, except for detrital tracers that were scaled against the distribution of mud (Table 4.7.6). Table 4.7.7 shows the initial conditions for epibenthic macroalgae, seagrass and coral

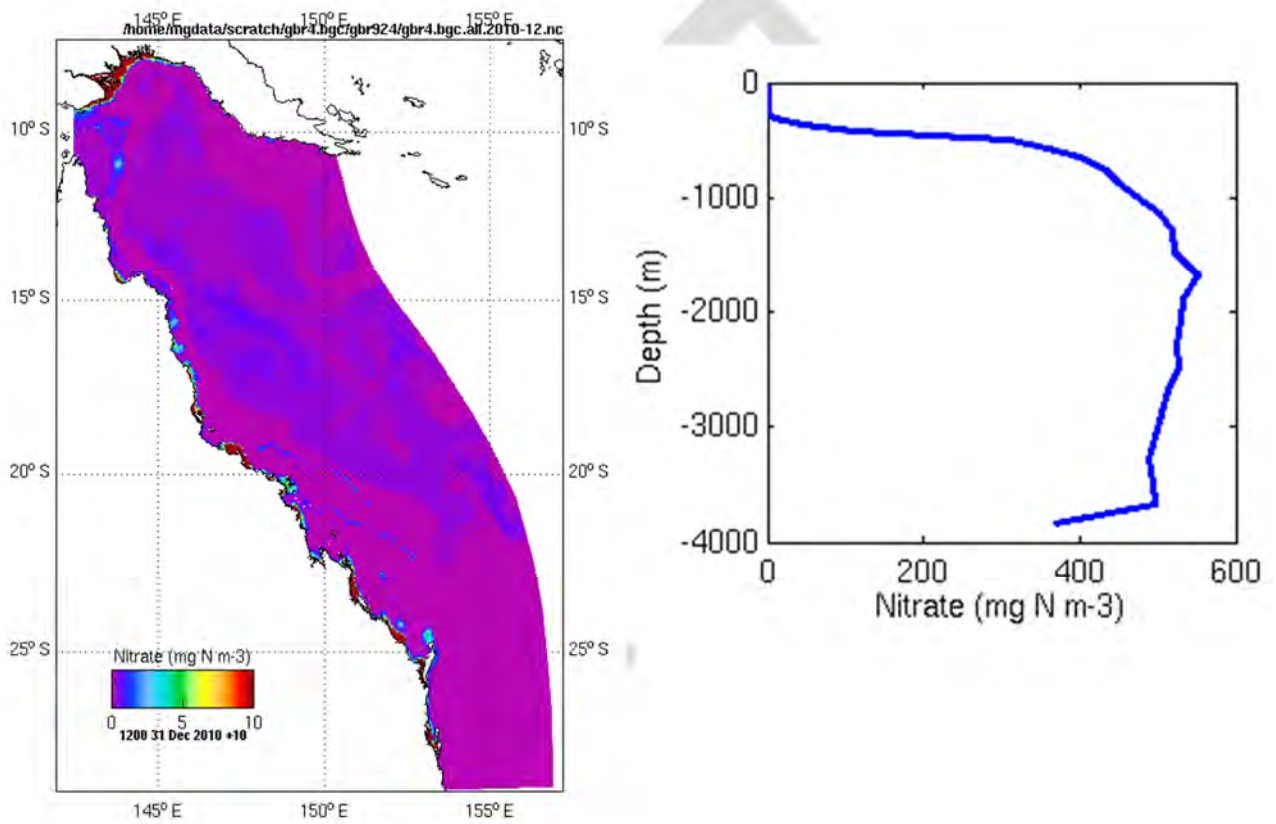


Figure 4.7.37. Initial surface distribution and vertical profile of NO₃

Table 4.7.6. Initial conditions for dissolved organic and inorganic nutrients, carbon, alkalinity, plankton and oxygen across the model domain for detrital sediment and water column values.

	Water Column value	Sediment value	Units	Origin / script	Reference
NH4	0.2	200	mg N m ⁻³	Default Fill in value	EMS user guide
NO3	Ocean atlas CARS (below 500 m). Fitted on the model density profile (from 0 to 500 m) 0 at surface	500	mg N m ⁻³	Default Fill in value (sed), SHOC (wc)	CARS EMS user guide
DIC	Based on Salinity relationship	Bottom of the water column	mg C m ⁻³	Pre-processing script	Lenton et al, 2015
alk	Based on Salinity relationship	Bottom of the water column		Pre-processing script	Lenton et al, 2015
DIP	Ocean atlas CARS (below 500 m). Fitted on the model density profile (from 0 to 500 m) 0 at surface	Assumes a DIN/DIP ratio of 5 mg N/mg P	mg P m ⁻³	Default Fill in value (sed), SHOC option (wc)	CARS EMS user guide
DORC	536 (surface), 350 (100m). Steady state value from primary production	5300	mg C m ⁻³	Pre-processing script	Hansel et al 2009. Gladstone Harbor observations (pers.comm.: Alongi, AIMS)
DORN	94 (surface), 60 (1000 m) Redfield from DOC.	938	mg N m ⁻³	Pre-processing script	Redfield
DORP	13 (surface), 9 (1000 m) Redfield from DOC	129 Redfield from DOC	mg P m ⁻³	Pre-processing script	Redfield
O2	6200 (surface), 5700 (500m) CARS O2 saturation values fitted to model T & S profiles.	65	mg O m ⁻³	Pre-processing script + Default Fill in value (sed)	CARS
DetBI_N	0	0	mg N m ⁻³	Default Fill in value	
DetPI_N	25 Steady state from primary production	800 Gladstone Harbor observations	mg N m ⁻³	Pre-processing script	Hansel et al 2009. Dan Alongi -Harbor
PhyL_I	1.654 (0 below 500 m)	0	mmol photon m ⁻³	Default Fill in value Pre-processing script	EMS user guide
PhyL_N	0.7 (0 below 500 m)	0	mg N m ⁻³	Default Fill in value Pre-processing script	EMS user guide
PhyL_NR	0.35 (0 below 500 m)	0	mg N m ⁻³	Default Fill in value Pre-processing script	EMS user guide
PhyL_PR	0.048 (0 below 500 m)	0	mg P m ⁻³	.tran default Fill + Matlab script	EMS user guide
PhyL_ChI	0.1 (0 below 500 m)	0	mg Chl m ⁻³	Default Fill in value Pre-processing script	EMS user guide
Zool_N	0.7 (0 below 500 m)	0	mg N m ⁻³	Default Fill in value Pre-processing script	EMS user guide
MPB_I	0	797.22 (0 if depth > 100 m)	mmol photon m ⁻³	Default Fill in value Pre-processing script	EMS user guide
MPB_N	0	337.5 (0 if depth 100 m)	mg N m ⁻³	Default Fill in value Pre-processing script	EMS user guide
MPB_NR	0	169 (0 if depth 100 m)	mg N m ⁻³	Default Fill in value Pre-processing script	EMS user guide
MPB_PR	0	23.32 (0 if depth 100 m)	mg P m ⁻³	.Default Fill in value Pre-processing script	EMS user guide

Table 4.7.7. Initial conditions for epibenthic macroalgae, seagrass and coral [units are mg/m² unless otherwise stated].

	Benthic value	Unit	Origin	Reference
CH_N	0.5 (scaled by the reef percentage cover). This assume a surface area at 66 %. Location based on observations	mg N m ⁻²	Pre-processing script	Location from Beaman, 2012. Value from EMS user guide
CS_N	10 (scaled by the reef percentage cover), steady state	mg N m ⁻²	Pre-processing script	Location from Beaman, 2012 Value from EMS user guide
CS_ChI	4.8 (scaled by the reef percentage cover), steady state	mg ChI m ⁻²	Pre-processing script	Location from Beaman, 2012 Value from EMS user guide
SG_N	0.66 Assumes a surface area at 66%. Location based on observations	mg N m ⁻²	Pre-processing script	Location from McKenzie, LJ et al. (2014) Value from EMS user guide
SG_N_root	0.5	mg N m ⁻²	Pre-processing script	EMS user guide
Ma_N	0.25 (0 below 100m). This assume a surface area at 22 % cover	mg N m ⁻²	Pre-processing script	EMS user guide
SGH_N	0.047 Everywhere	mg N m ⁻²	Default Fill in value	EMS user guide
SGH_N_root	0.0228 Everywhere	mg N m ⁻²	Default Fill in value	EMS user guide

Data from the Great Barrier Reef and Coral Sea Geomorphic Features (a JCU e-atlas product) were used to calculate the percentage of the grid cells in the model (at 4 and 20 km scales) occupied by coral reef (with the geographic definition of a coral reef Cay, Island, Mainland, Reef, Rock and Sand features taken from GBRMPA definitions). The percentage coral reef ecosystem cover on the 4km and 20km model grids is shown in Fig. 4.7.38. Percentage cover is used in the coral reef carbon model, in the sediment model and could be used in the sub-grid scale parameters for the hydrodynamic model. Initial concentrations of coral and symbiont were scaled against percent cover assuming a surface area of 20 % (see EMS user guide for details about surface area definition for benthic organisms). Macroalgae were initialised on the euphotic shelf (0-100m) with uniform concentration to obtain 66 % surface area. Seagrass were initialised using a composite of coastal seagrass meadow observations from McKenzie (2014) assuming 63 % surface area.

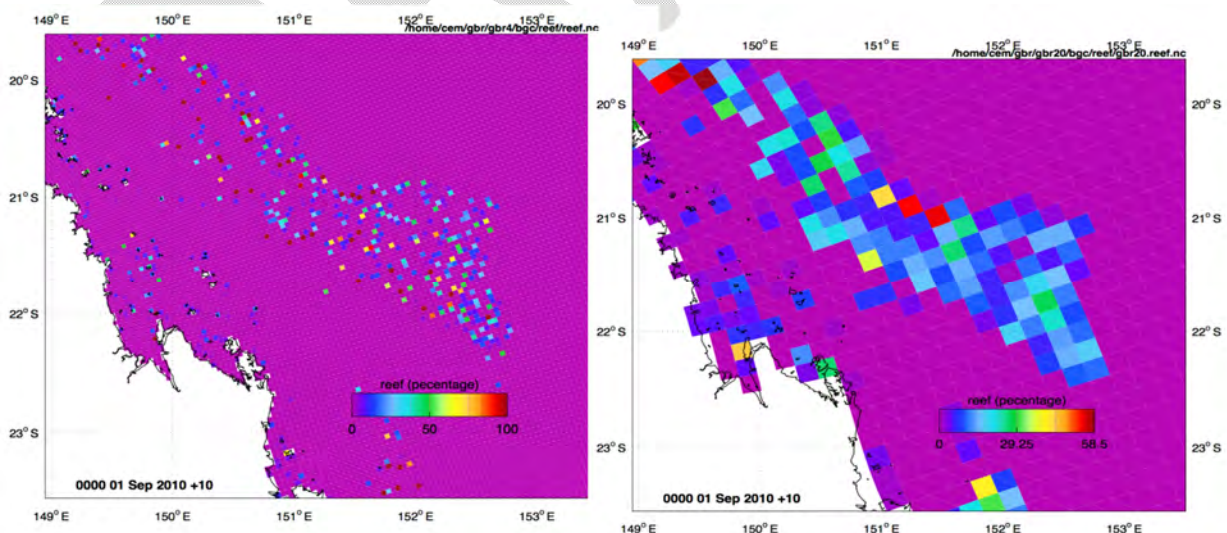


Figure 4.7.38. Percentage cover of model grid cell occupied by coral reef system; 4 km scale (left) and 20 km scale (right).

4.7.5.4 Marine Boundary Conditions

The eReefs BGC and sediment model has 3 open ocean boundaries. Initial simulations trialled climatology's and empirical nutrient-temperature relationships at the open ocean boundaries. These data were specified as an upstream condition such that water flowed out of the model with simulated concentrations of tracers, but entered the model with prescribed values. In all cases prescribed boundaries were insufficient to propagate accurate tracer concentrations into the model resulting in plumes of unrealistic nutrient concentration and associated bands of stimulated phytoplankton and zooplankton productivity.

Given the unconstrained nature of the very long eastern open boundary a statistical no-gradient condition (STATIS) was trialled with some success. This boundary condition estimates the concentration of incoming tracer from a statistical representation of the water in the immediately vicinity of the boundary. The statistic is set at the 20th percentile concentration over a range near the boundary where the normal velocity changes by 10% of its boundary value. As the STATIS condition can be applied across all tracers simultaneously there is no significant mis-match in relative concentrations and the model remains in quasi-steady state close to the boundary. An exception to this is seen in some months at the southern boundary during periods of consistent northward flow. Under these conditions relic low concentrations may be propagated into the model for some distance isolating the evolving water mass from the boundary and limiting its influence on the inflowing water mass.

During multi-year model simulations the nutrient concentrations in the interior of the model can be steadily eroded resulting in unrealistically low nutrient concentrations in offshore waters, and an under-estimation in the flux of nutrients onto the shelf. To avoid this situation we apply the initial density scaled CARS nutrient profiles at the open boundaries (Table 4.7.6) together with an upstream boundary condition.

4.7.5.5 River Boundary Conditions

There are 22 rivers included with nutrient inputs in the GBR4 model (Fig 4.7.39 and Fig 4.7.40a and b). The Fly River in Papua New Guinea is also included due to the high volume of water discharged from this river (consistent average over the year of 6,000 cumecs; Harris et al., 2004, Wolanski et al., 2008) and high sediment loads both from natural sources and due to upstream mining.

Nutrients in the coastal shelf break are usually low due to predominantly oligotrophic surface waters entering the shallow shelf break rather than the deeper nutrient rich water layers. The only strong evidence of eutrophication is in the river plumes (Brodie et al., 2013) where there are high primary production rates due to high levels of suspended nutrients and solids. There are high rates of production in the surface despite low levels of chlorophyll, so it is possible to have high productivity at low plankton biomass.

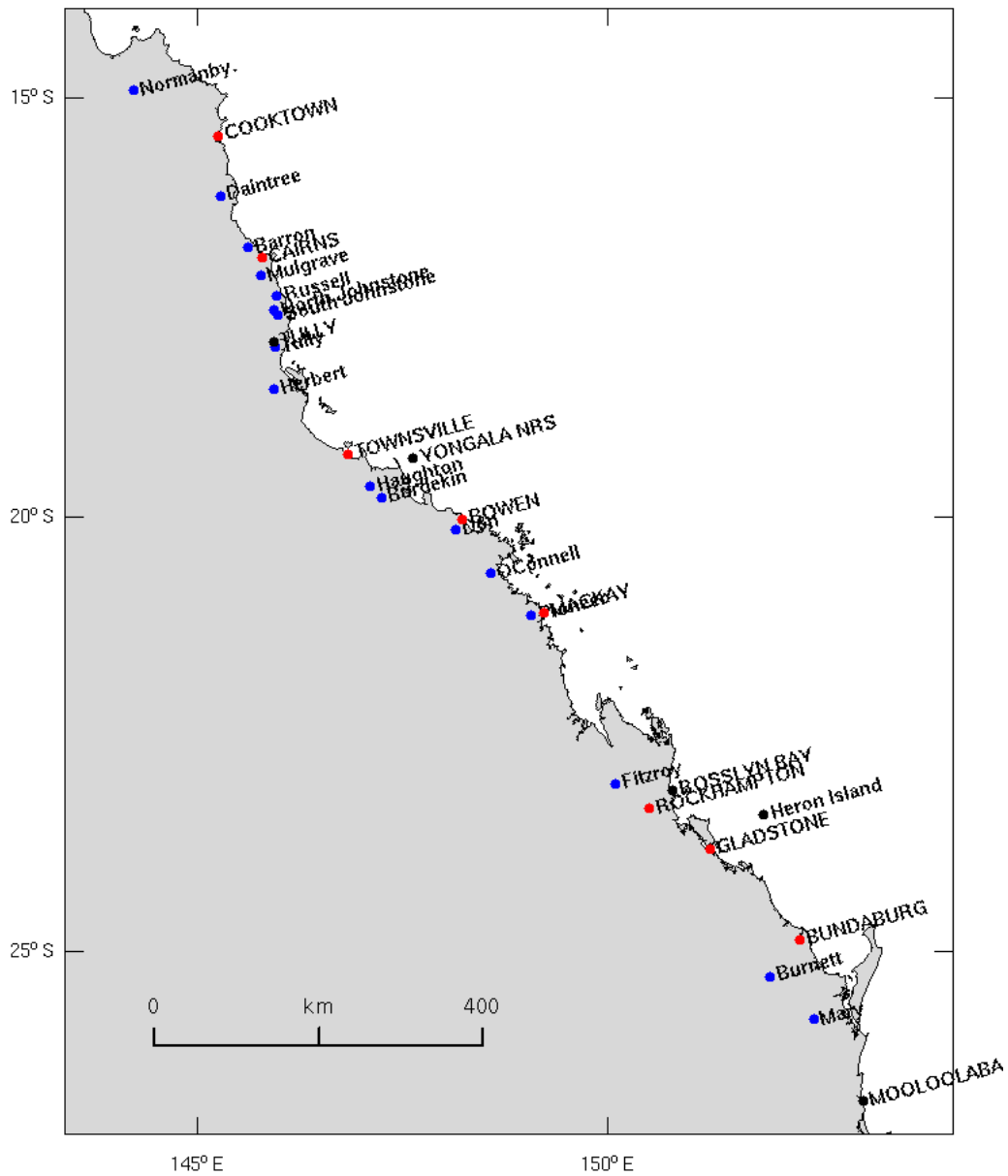


Figure 4.7.39. Rivers (blue dot) with nutrient input in the eReefs model. Red dots represent towns. The Fly River in PNG and Moreton Bay inputs are not shown.

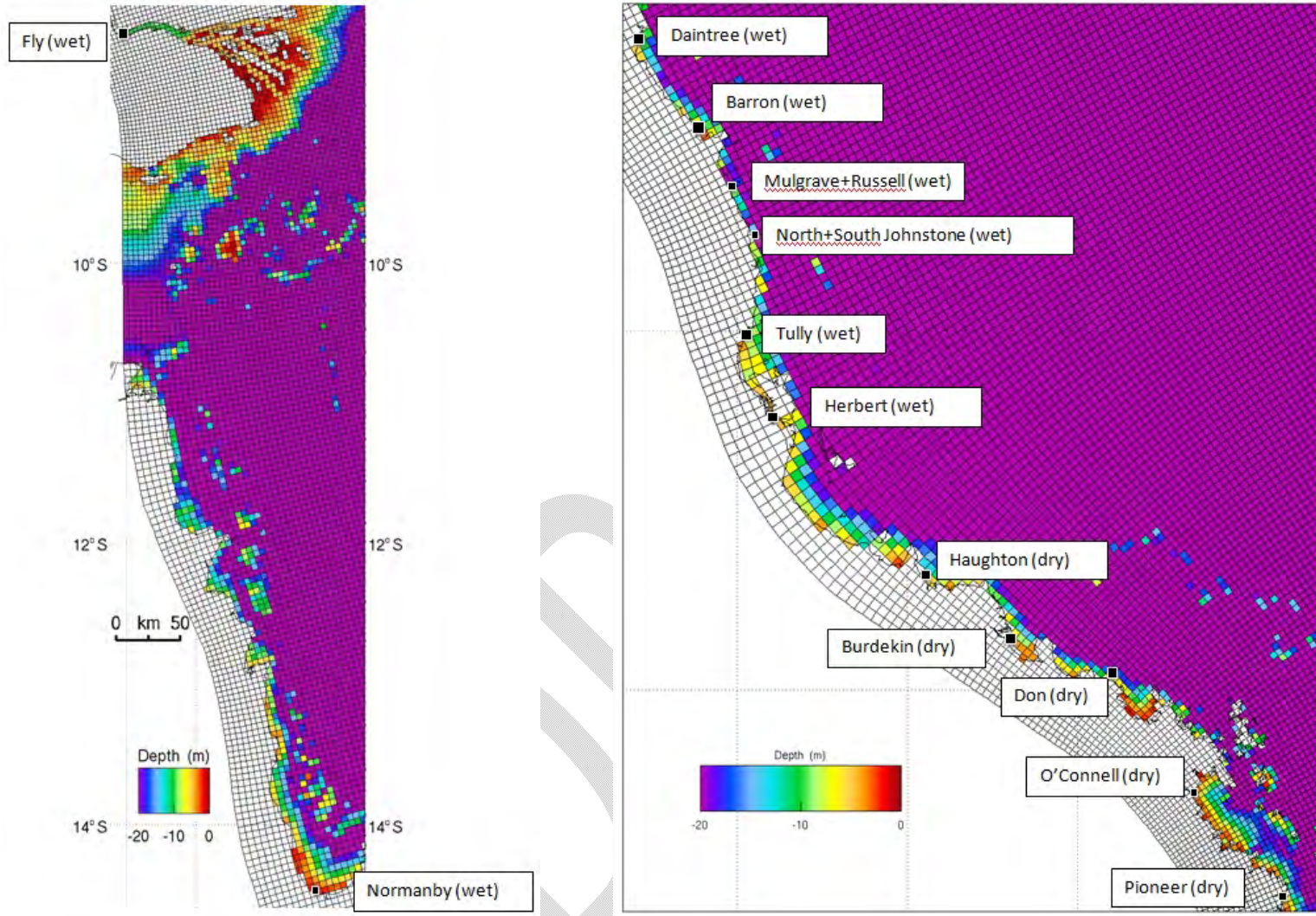


Figure 4.7.40a. GBR4 model showing the near-shore bathymetry of the model and the grid cell entry point of the rivers and their categorisation into wet or dry according to gauged flow linear load (GFL) relationships used in the near real time within the model domain.

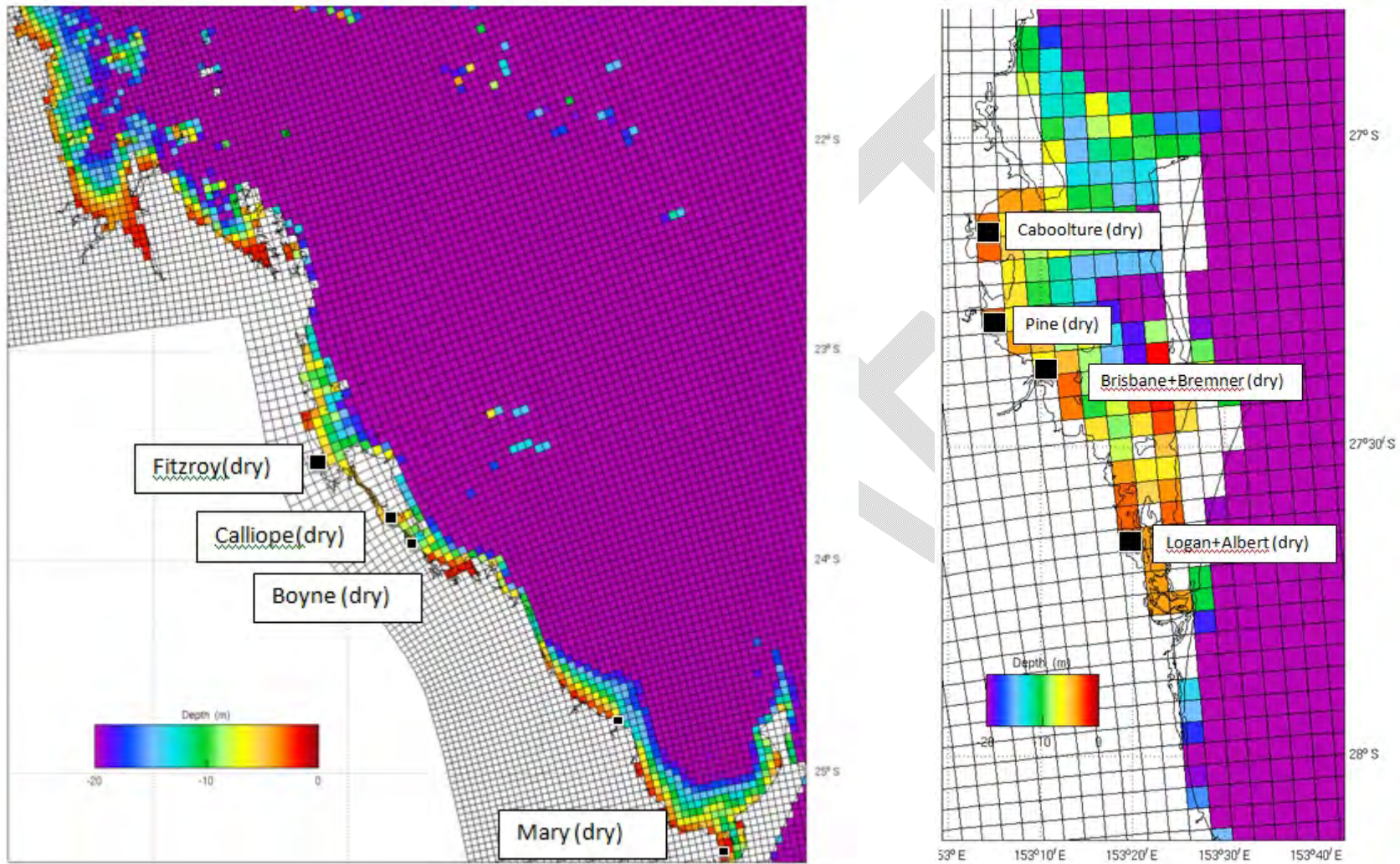


Figure 4.7.40b. GBR4 model showing the near-shore bathymetry of the model and the grid cell entry point of the rivers and their categorisation into wet or dry according to gauged flow linear load (GFL) relationships used in the near real time model.

Two methods of incorporating the rivers into the coastal model were used.

1. Gauged flows with linear load (GFL): This uses linear flow to load with increased loads for some GBR rivers: see BGC Appendix A p 33 for rivers.
2. Gauged flows with catchment model loads (GFCM): This uses the concentration of loads from the QLD catchment model with the gauged flow of the rivers (see BGC Appendix A p 33).

Gauged flows with catchment model loads (GFCM)

An updated catchment model (Waters et al 2015) was run for the coastal hindcast model from September 2010 to June 2014. Daily estimates of sediment loads for the 22 rivers within the GBR4 region became available for use in the coastal model in September 2015. The catchment model estimates GBR average annual loads of sediments, pesticides and nutrients for each of the 35 catchments draining to the GBR as part of the Paddock to Reef program (http://www.reefplan.qld.gov.au/measuring-success/paddock-to-reef/catchment-loads/#_monitoring). For the GBR4 grid we include loads and flows for the 22 major rivers in the GBR region. The catchment model contained flows and loads for 35 catchments which may be used in future hindcasts of the GBR coastal model.

Gauged flow with linear load relationship (GFL) and modified GFL (mGFL)

Gauged flows with linear load (GFL) were used for rivers outside the GBR region (Logan+Albert, Caboolture, Brisbane+Bremer and Fly) and for all rivers in the near real time model. Previous estimates of these loads, based on literature data (Furnas, 2003, Herzfeld et al 2014) were used to inform the model of river loads (see below). For this latter approach, a concentration of the suspended sediment and nutrient was assigned to each out of the 4 remaining river systems considered in this model simulation. The concentration is constant throughout the year so that the nutrient and sediment loads are scaled only by changes in the river flow (see Figure 4.7.44 and BGC Appendix A p 33).

We also use the modified GFL relationship (mGFL) for all rivers for the coastal NRT model as it is not possible to run the catchment model in near real time for the coastal model. The modification to the loads was based on the lack of gauging at some of the river sites (Steven et al 2014) and the position of the gauging station (which can be up many km up river). We compare these loads to the monitored loads, (Wallace et al 2014,2013, Turner et al 2013, Garzon-Garcia et al 2015) (see Figure 4.7.44 and BGC Appendix A p 33).

For the near real time model the GFL algorithmic relationships are used to account for nutrient and sediment inputs from rivers into the model. Nutrient concentrations are relatively constant within each river, thus providing a realistic initial set of loads. In the model we characterise each river as being a wet or dry river (Table 4.7.7) based on the research of Furnas et al, (2003) which divides the estimated annual exports of N and P from rivers categorised in terms of wet or dry in relation to annual freshwater discharge (Table 4.7.8). Based on the catchment work of Steven et al 2014 we then adapted some of the ungauged rivers to increase some of their loads (Table 4.7.9).

Table 4.7.7. Queensland rivers included in the biogeochemical model and categorised into wet or dry rivers (based on Furnas et al 2003, see also Fig. 4.7.10 and Fig. 4.7.40a, b for grid cell entry point)

Wet	Dry	Fly
Tully	Pioneer	Fly
Normanby	Pine	
Mulgrave+Russell	O'Connell	
Johnstone	Mary	
Herbert	Logan+Albert	
Daintree	Haughton	
Barron	Fitzroy	
	Don	
	Calliope	
	Caboolture	
	Burnett	
	Burdekin	
	Brisbane+Bremer	
	Boyne	

Table 4.7.8. Estimated annual exports of important forms of N and P from wet catchment and dry catchments in relation to annual freshwater discharge (from Furnas 2003) tonnes per km cubed.

Nutrient input into rivers	WET measured: South Johnston, Tully, Herbert Rivers	DRY measured: Burdekin Fitzroy
Dissolved inorganic Nitrogen (DIN)	171	197
Dissolved inorganic Phosphorus (DIP)	4.2	25.8
Dissolved Organic Nitrogen (DON)	80	139
Dissolved Organic Phosphorus (DOP)	5.8	8.9
Particulate Nitrate (PN)	145	503
Particulate Phosphate (PP)	32	130
N:P ratio	20.8	11.3
Total Nitrogen (TN)	396	839
Additional rivers where nutrients were not measured but categorised (as in Furnas 2003) and used as input into model	Mulgrave, Barron, Russell, Lockhart, Normanby, Daintree, Fly (PNG) (not in model but also wet: Mossman, Murray, Endeavour, Stewart, Olive-Pascoe)	Haughton, Don, O'Connell, Burnett, Mary, Pioneer (other rivers are dry but not included)

Table 4.7.9. Queensland rivers included in the GBR4 biogeochemical model simulations showing the percent of river that is ungauged (from Steven et al 2014) and the respective percentage increase in river loads for nutrients and TSS in the eReef coastal model for the modified gauged flow with linear load relationship (mGFL) catchment algorithms for the near real time model.

Primary rivers within the GBR	GBR rivers included in coastal model	Percent of river ungauged	% increase in river loads for nutrients and TSS in coastal model
Pioneer	yes	8	50
Johnstone	yes	41	50
Calliope	yes	42	50
Mulgrave-Russell	yes	52	50
Daintree	yes	61	50
Normanby	yes	67	50
O'Connell	yes	70	50
Don	yes	84	50
Tully	yes	12	20
Herbert	yes	13	20
Mary	yes	19	20
Haughton	yes	32	20
Barron River	yes	11	0
Boyne	yes	12	0
Burdekin	yes	0	0
Burnett	yes	2	0
Fitzroy	yes	5	0

The particulate load from the rivers for the GFL is split between labile (30%) and refractory (70 %) for all wet and dry rivers. This may be altered in the future. Table 4.7.10 shows numerical averages of discharge-weighted fine sediment for wet and dry rivers.

Partitioning is as follows for all rivers:

Wet rivers

$$\text{DetR}_N = 0.7 * 145 = 101.5 \text{ mg m}^{-3}$$

$$\text{DetR}_C = 0.7 * 145 * 6.6 = 669.9 \text{ mg m}^{-3}$$

$$\text{DOR}_C = 80 * 6.6 = 528 \text{ mg m}^{-3}$$

$$\text{DetR}_P = 0.7 * 32 = 22.4 \text{ mg m}^{-3}$$

$$\text{DetPI}_N = 0.3 * 145 = 43.5 \text{ mg m}^{-3}$$

Fine sediments: Normanby 0.066 kg m⁻³. Daintree, Mulgrave, Russell, Herbert: 0.053 kg m⁻³. Barron: 0.15 kg m⁻³. Johnstone: 0.061 kg m⁻³. Tully: 0.031 kg m⁻³.

Dry rivers

$$\text{DetR}_N = 0.7 * 503 = 352.1 \text{ mg m}^{-3}$$

$$\text{DetR}_C = 0.7 * 503 * 6.6 = 2323 \text{ mg m}^{-3}$$

$$\text{DOR}_C = 139 * 6.6 = 917.4 \text{ mg m}^{-3}$$

$$\text{DetR}_P = 0.7 * 130 = 91 \text{ mg m}^{-3}$$

$$\text{DetPI}_N = 0.3 * 503 = 150.9 \text{ mg m}^{-3}$$

Fine sediments: Fitzroy, Haughton, Burdekin, Don, O'Connell, Pioneer, Burnett 0.231 kg m⁻³

Table 4.7.10 Numerical averages (± 1 Std. Deviation) of discharge-weighted fine sediment concentration in g m^{-3} and slopes of origin-forced regressions of wet-season fine sediment export on concurrent wet season freshwater discharges from some GBR catchment river systems [p values are for fit to linear regression].

River	N	Mean discharge-weighted load (g m^{-3})	Slope (Mt/Km^3)	r^2	p
Normanby	6	0.084 \pm 0.041	0.066	0.553	0.090
Barron	6	0.132 \pm 0.095	0.150	0.725	0.031
Russell	1	0.021			
N. Johnstone	6	0.040 \pm 0.025	0.061	0.956	<0.001
Tully	6	0.028 \pm 0.011	0.031	0.874	0.006
Herbert	5	0.066 \pm 0.016	0.056	0.793	0.043
All WET	30*	0.069 \pm 0.059	0.052	0.659	<0.001
<i>Burdekin</i>	7	<i>0.759\pm0.601</i>	<i>n.s.</i>	<i>n.s.</i>	<i>n.s.</i>
<i>Fitzroy</i>	8	<i>0.363\pm0.191</i>	<i>0.231</i>	<i>0.499</i>	<i>0.050</i>

Exact partitioning of the rivers in terms of the model is shown in Table 4.7.11 which shows the relationships of nutrients and sediment for all parameters used for river input into the model. The Fly River has been made a special subdivision from the wet and dry rivers due to its extremely high river flow and high levels of detritus.

Annual loads for each river in model simulation 924 for GFL are presented in Figs. 4.7.41 – 4.7.43. The values in 4.7.43 compare well with the 10 year average estimates by Furnas et al, (2003). This comparison demonstrates that using the modified nutrient concentration (constant with time) and river flow as shown in Table 4.7.11 is suitable to simulate nutrient (and sediment) loads in the near real time model. It is clear from the figures that three rivers (Fitzroy, Burnett and Burdekin) are responsible for the majority of nutrient input in the GBR region, and this is consistent with the observations (Brodie et al 2013). These nutrient and sediment loads could be combined with the model output to perform detailed nutrient budgets of these areas.

The catchment model loads and flows for the current simulation (model run 926 Dec 2015)) were compared against the coastal model using gauged flows and catchment concentrations going into the coastal model over the 4 year period. There is less than a 1% difference in the model simulation loads and the catchment model loads (Figure 4.7.44) over the 4 year simulation.

Table 4.7.11. River nutrients entering into the model if using GLL. # The particulate load from the rivers is split between labile (30%) and refractory (70%) for all rivers with partitioning based on the Wet and Dry river relationships described in the text *Relationships based on Furnas et al 2003. \$Relationships based on Robson et al. (2014). @N:Chl ratio of 7 from Wild-Allen et al., (2010). +1060/16 energy content (max cell density at redfield ratio) Division by 2 so the reserves are half full (≤ 1) ^Tilbrook et al. pers comm.

	units	Wet Rivers	Dry rivers	Fly River
%FineSed	kgm ⁻³	0.066	0.231	0.066
Mud	kgm ⁻³	0	0	0
Sand	kgm ⁻³	0	0	0
%NO3	mgm ⁻³	171	197	197
%NH4	mgm ⁻³	0.1	0.1	0.1
%DIP	mgm ⁻³	4.2	25.8	25.8
\$PIP	mgm ⁻³	4.2*54.5719	25.8*54.5719	25.8*54.5719
\$PIPI	mgm ⁻³	0	0	0
%DOR_N	mgm ⁻³	80	139	469.69
%DOR_P	mgm ⁻³	5.8	8.9	29.24
%DOR_C	mgm ⁻³	528	917.4	3100
#DetR_N	mgm ⁻³	101.5	352.1	352.1
#DetR_P	mgm ⁻³	22.4	91	91
#DetR_C	mgm ⁻³	669.9	2323	2323
#DetPL_N (Labile Detrital Planktonic N)	mgm ⁻³	43.5	150.9	150.9
#DetBL_N (Benthic Labile Detrital N)	mgm ⁻³	0	0	0
^alkalinity	mmol m ⁻³	900	900	900
^DIC	mgm ⁻³	900.0*12.01/1.16	900.0*12.01/1.16	13400
Oxygen	mgm ⁻³	0.9*8234.0	0.9*8234.0	3290
@PhyS_N	mgm ⁻³	1*7	1*7	1*7
@PhyL_N	mgm ⁻³	1*7	1*7	1*7
@PhyS_NR (Phyto N reserve)	mgm ⁻³	1*7/2	1*7/2	1*7/2
@PhyL_NR (Phyto N reserve)	mgm ⁻³	1*7/2	1*7/2	1*7/2
@PhyS_PR (Phyto P reserve)	mgm ⁻³	1*7/2/16*32/14	1*7/2/16*32/14	1*7/2/16*32/14
@PhyL_PR (Phyto P reserve)	mgm ⁻³	1*7/2/16*32/14	1*7/2/16*32/14	1*7/2/16*32/14
@+PhyS_I (Phyto energy reserve)	mmol photon m ⁻³	1*7/2/14*1060/16	1*7/2/14*1060/16	1*7/2/14*1060/16
@+PhyL_I (Phyto energy reserve)	mmol photon m ⁻³	1*7/2/14*1060/16	1*7/2/14*1060/16	1*7/2/14*1060/16
PhyS_ChI	mgm ⁻³	1	1	1
PhyL_ChI	mgm ⁻³	1	1	1
@ZooS_N	mgm ⁻³	1.0*7.0	1.0*7.0	1.0*7.0

@ZooL_N	mgm ⁻³	1.0*7.0	1.0*7.0	1.0*7.0
---------	-------------------	---------	---------	---------

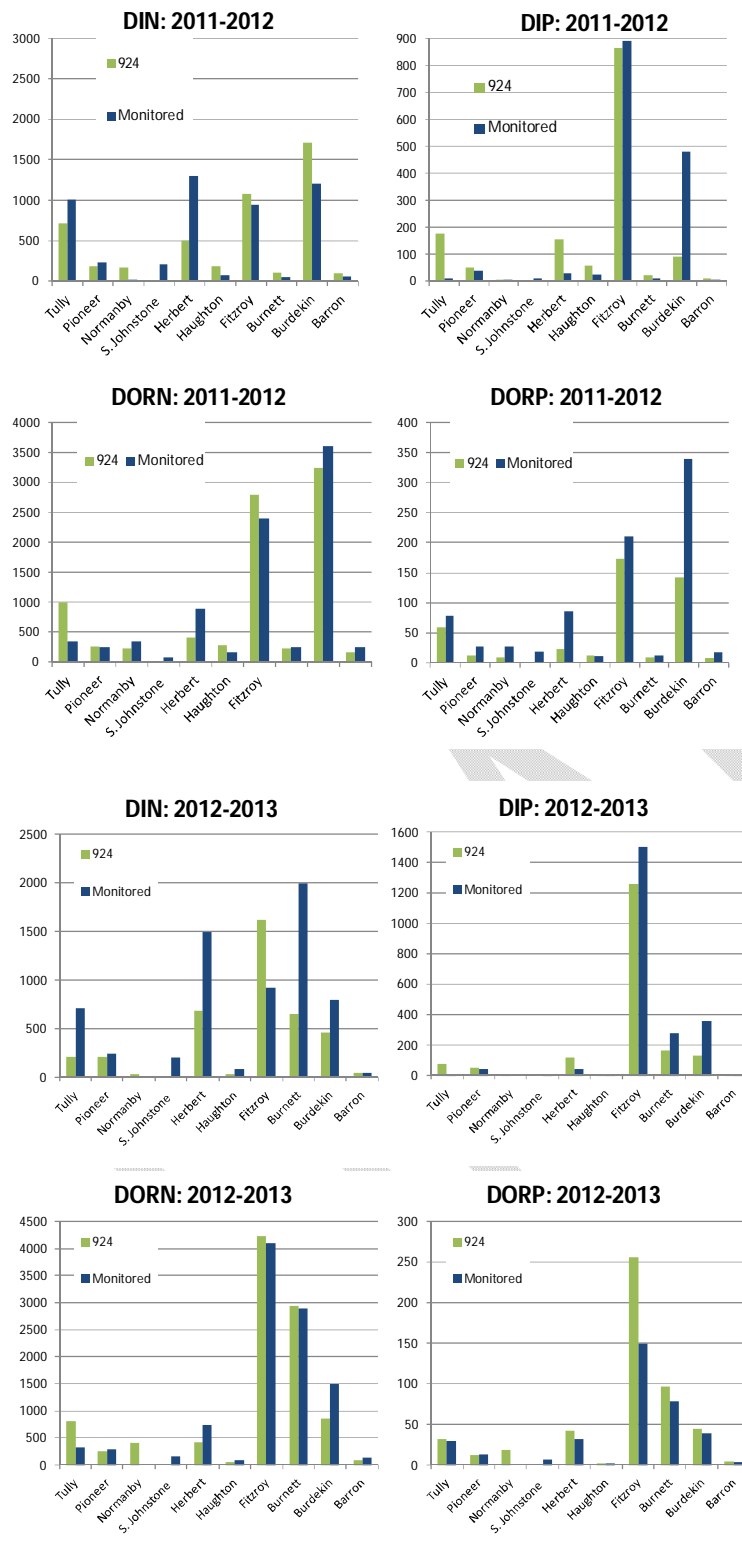


Table 4.7.41. River nutrients (tonnes per year) entering into the model for catchment model concentrations and gauged river flows (run 924) and monitored loads (from <http://www.reefplan.qld.gov.au/measuring-success/paddock-to-reef/assets/2011-2012-gbr-catchment-loads-report.pdf> and <http://www.reefplan.qld.gov.au/measuring-success/paddock-to-reef/assets/2012-2013-gbr-catchment-loads-technical-report.pdf>).

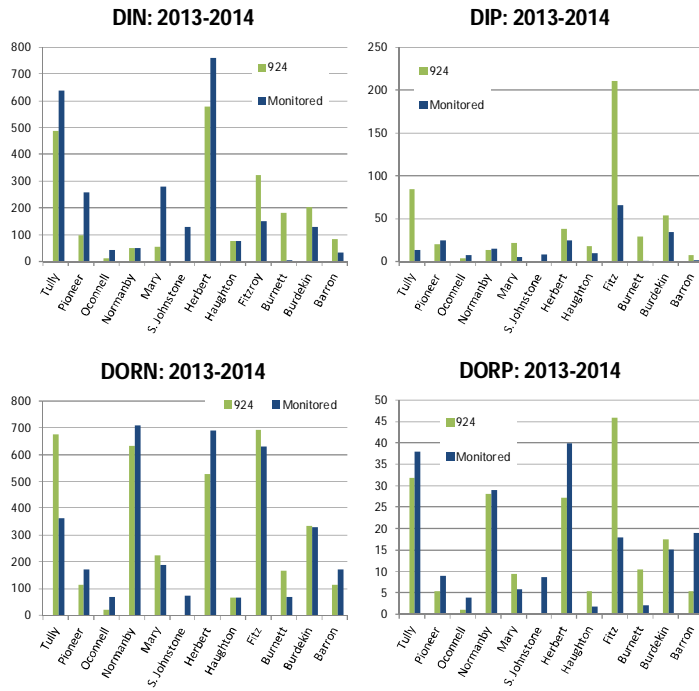


Table 4.7.42. River nutrients (tonnes per year) entering into the model for catchment model concentrations and gauged river flows (run 924) and monitored loads (from <http://www.reefplan.qld.gov.au/measuring-success/paddock-to-reef/assets/2013-2014-gbr-catchment-loads-report.pdf>).

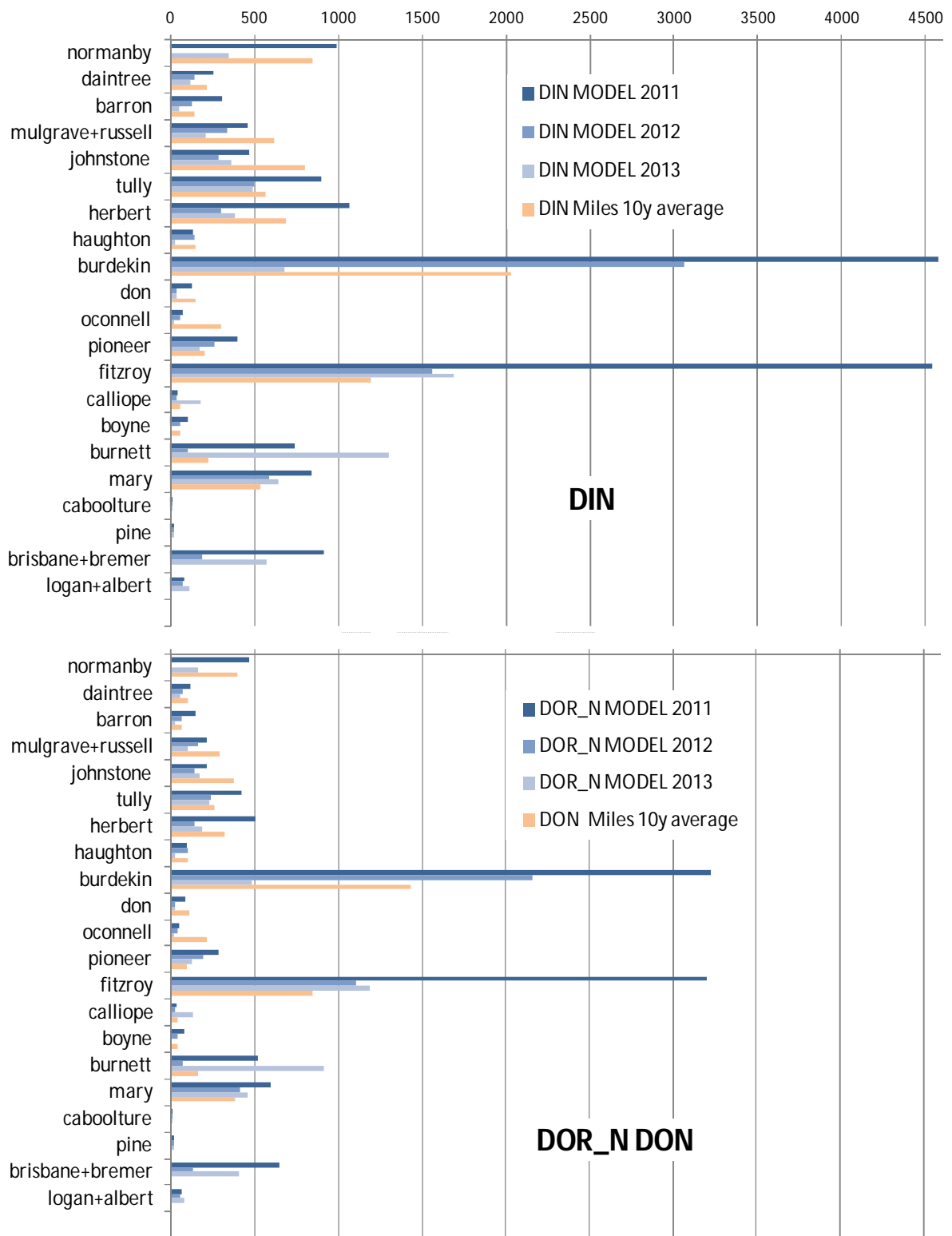


Figure 4.7.43. River loads into the model for DIN and DOR_N/DON in 2011, 2012 and 2013 compared with 10 year average loads (Furnas 2003). The rivers are listed from northern to southern most latitudes. (Fly river not shown). Loads are based on relationships for wet and dry rivers (see Table 4.7.13).

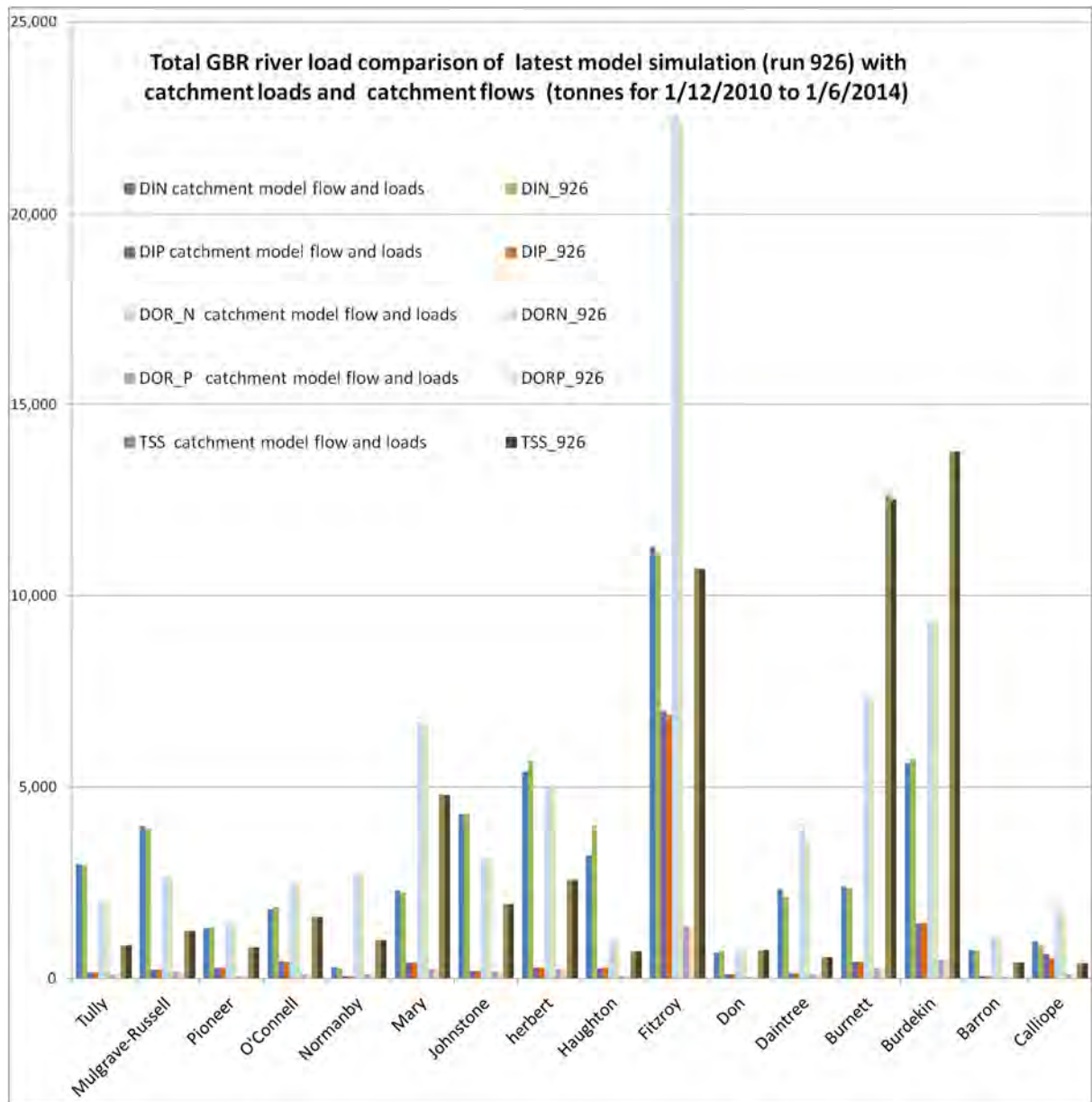


Figure 4.7.44. Total GBR river load comparison of latest model simulation (run 926) with catchment loads and catchment flows (tonnes for 1/12/2010 to 1/6/2014).

4.7.5.6 Incident surface irradiance

The transport model is forced with surface hourly short wave radiation (swr) from the 4km model, which varies with latitude and cloud cover. Spectrally resolved light throughout the water column is calculated from incident surface radiation, attenuated by optically active substances in the water column. An example of mean surface radiation is shown in Fig. 4.7.45; radiation is highly variable across GBR due to spatial variability in cloud cover.

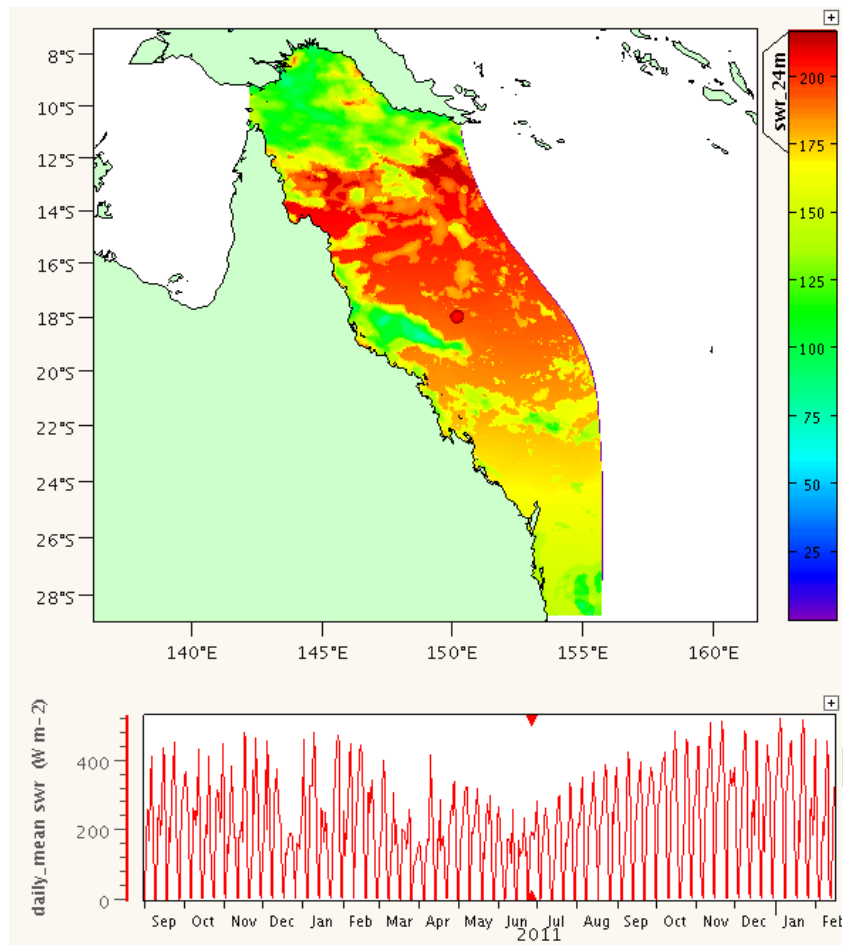


Figure 4.7.45. Snapshot of 24 hour mean surface short wave radiation (top) and time series of 24 hour mean surface short wave radiation in the centre of the GBR region (bottom).

4.7.5.7 Regional Analysis

The visualisation and analysis of the results of the ecological model is a non-trivial task given the size and resolution of the GBR model domain and the number of ecological parameters. The time and space scales of processes captured by the model and observed data differ, and averaging must be applied to model/observations to render them compatible for comparison. For this reason one of the methods of assessment and summarising the results of the biogeochemical model will be undertaken using regional analysis. We have divided the GBR model domain into similar regions to those used by GBRMPA in the paddock to reef integrated program (Fig. 4.7.46), and have included the area used by Furnas et al (1995) in their analysis of the budget of the Central Great Barrier Reef Shelf (regions 1 and 2). Within these regions the state variables (model and observations) can be averaged in space and time. The division of the model grid into regions thus allows us to statistically compare model and observations within a region and results between regions. We also have the ability to compute the exchange of tracers between these regions to develop regional budgets. At present there are 15 regions (Fig. 4.7.46). In bespoke analyses of the model data, the regions can be modified to suit the needs and requirements of partners and stakeholders.

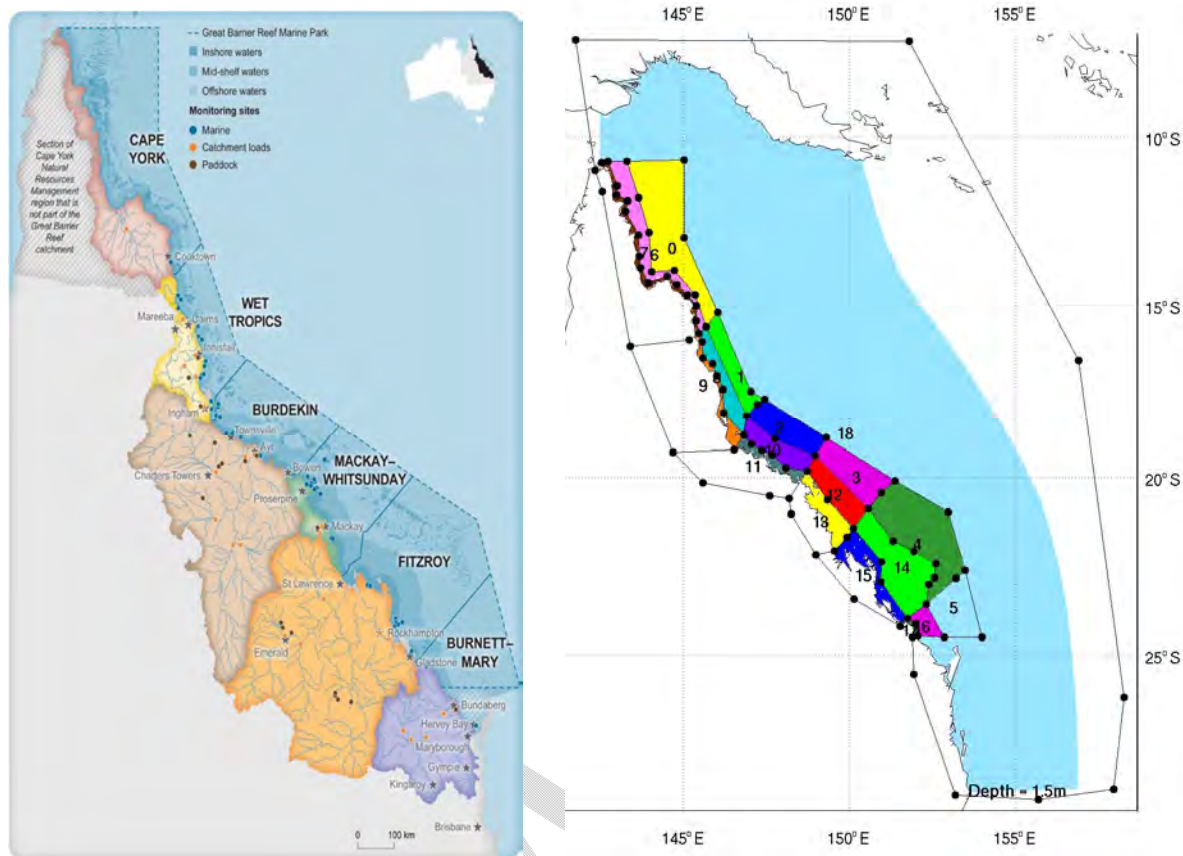


Figure 4.7.46. Regional classification from “Paddock to reef integrated program” and regions available for use in the model that correspond to the GBR NRM regions.

4.7.5.8 Ensembles runs for eReefs GBR4 BGC model.

Using the NCI computing facilities, we ran ensembles of 30 members of the GBR4 BGC model testing different combinations of model parameters. These included:

- Phytoplankton (large and small), detritus sinking rates,
- Mortality of zooplankton,
- Zooplankton swimming velocities,
- Detritus remineralization rate,
- Small phytoplankton size and allometric relationship to determine small phytoplankton maximum growth rate, sinking, small zooplankton growth rate.

Initial results show that the model is mostly sensitive to large phytoplankton sinking velocity and small zooplankton mortality. This information can therefore be used to target calibration parameterisations, both in terms of the sensitive parameters requiring perturbation and the values of those parameters (e.g. ensemble means, potentially varying spatially and temporally).

Experiment 1: Swimming velocity of large zooplankton varies between 10 - 1000 $\mu\text{m s}^{-1}$

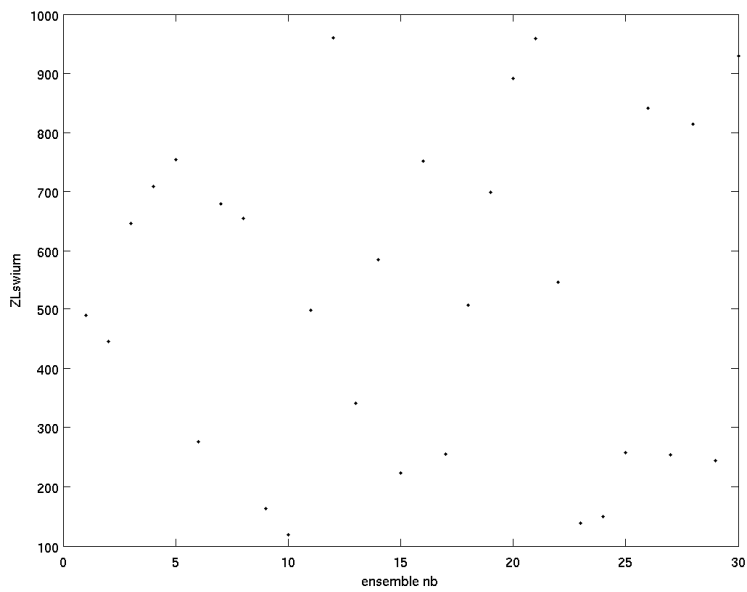


Figure 4.7.47: Ensemble of large zooplankton Swimming velocity used in experiment 1.

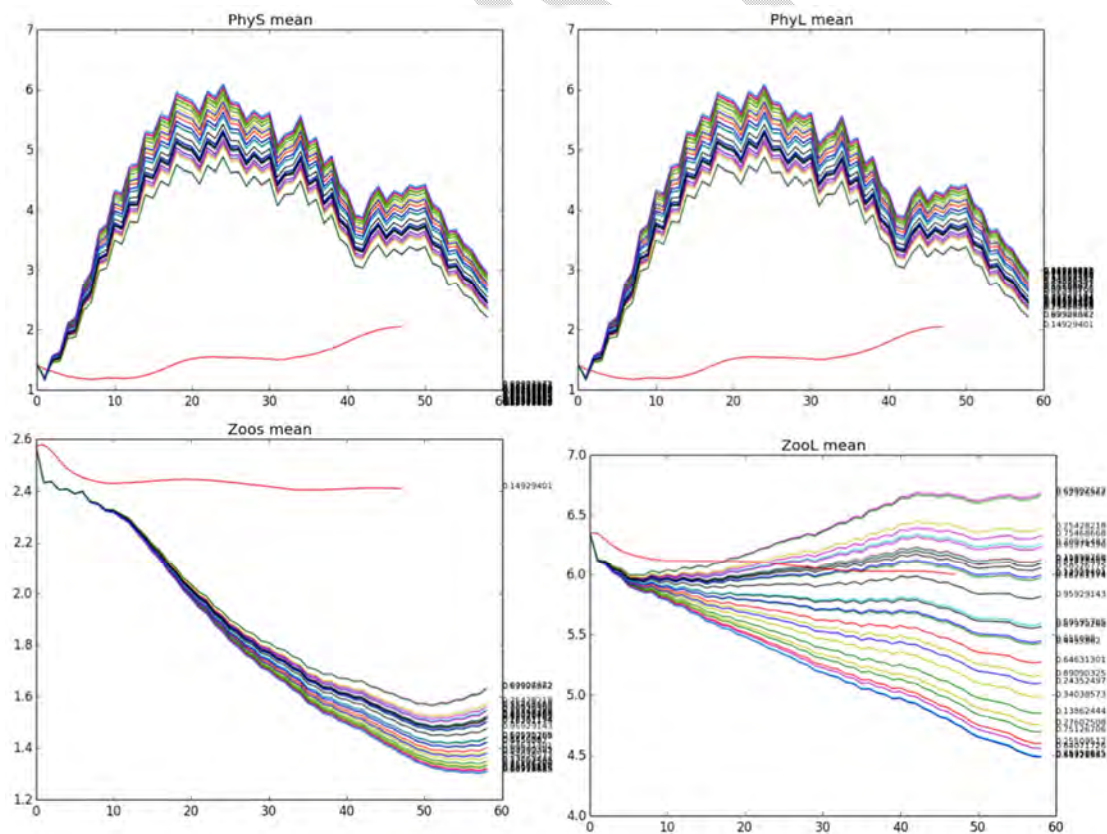


Figure 5.7.48. Results from experiment 1, mean concentration over time (in days) of small large phytoplankton and zooplankton over the entire model domain (surface only).

Experiment 2 : Phytoplankton size and allometric relationship.

Small phytoplankton radius : 0.25, 0.5, 1, and 2 micro m, large Small phytoplankton radius 1, 2, 4, 8 micro m. Phytoplankton size also used to calculate volume & mass for growth and grazing pressure.

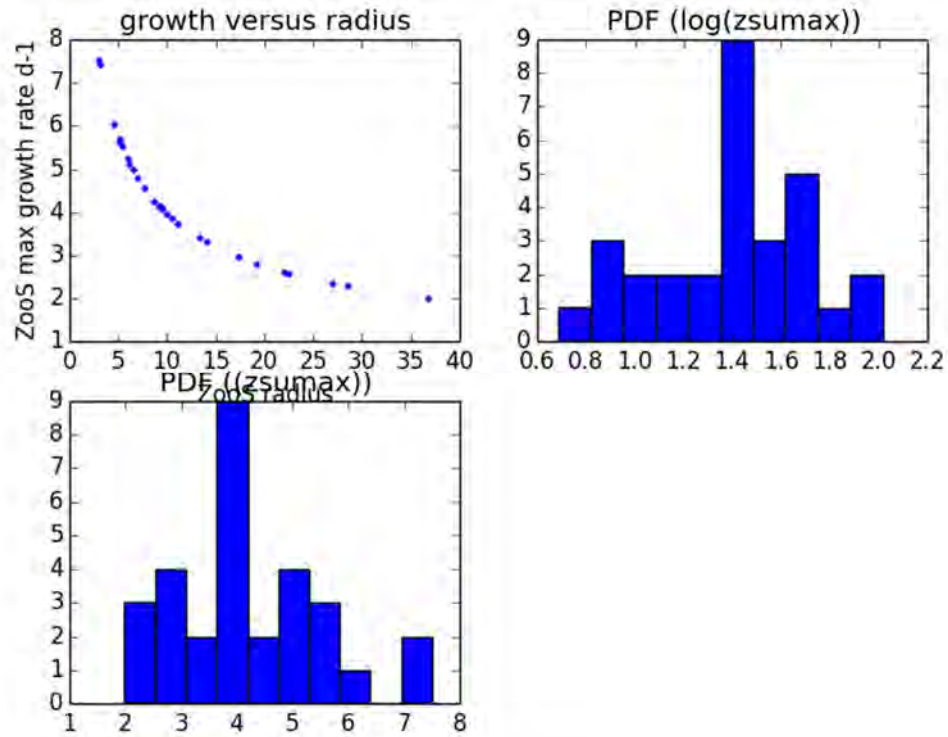


Figure 4.7.49. Allometric relationship used in the experiment 2.

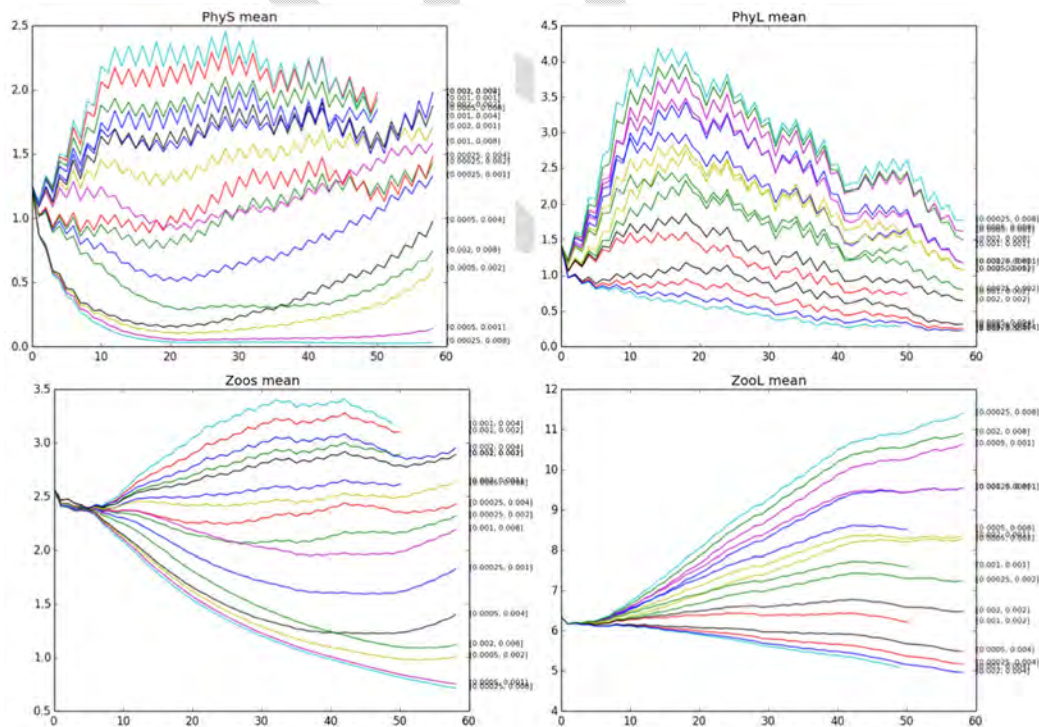


Figure 4.7.50. Results from experiment 2, mean concentration over time (in days) of small large phytoplankton and zooplankton over the entire model domain (surface only).

Experiment 3: Detritus remineralization rate (0.05 to 0.35 d^{-1})

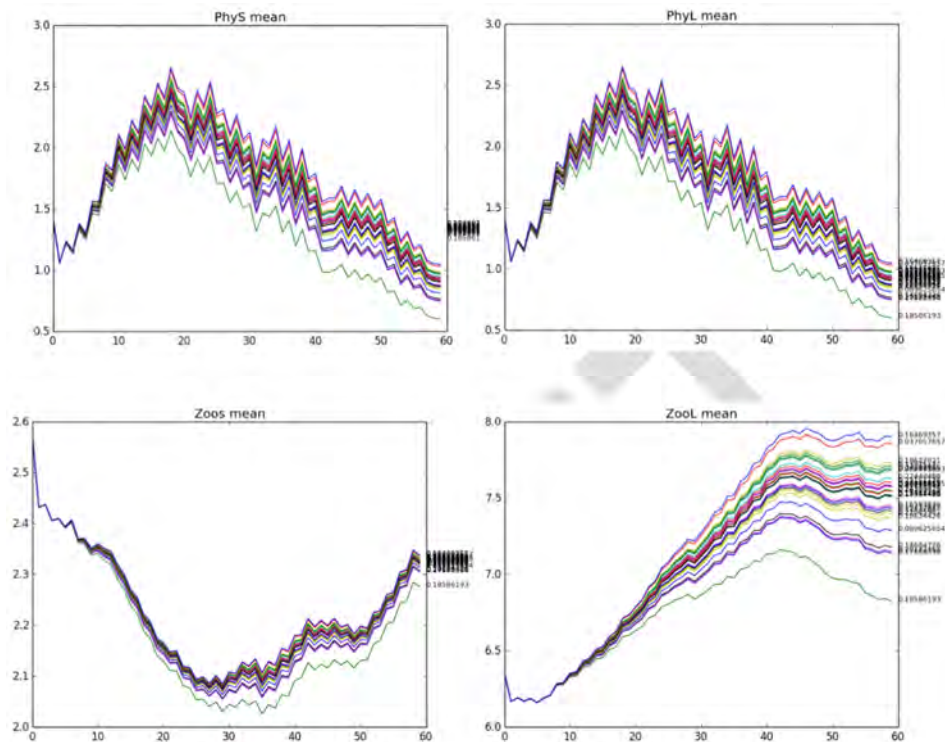


Figure 4.7.51. Results from experiment 3, mean concentration over time (in days) of small large phytoplankton and zooplankton over the entire model domain (surface only).

Experiment 4: Sinking rate of phytoplankton.

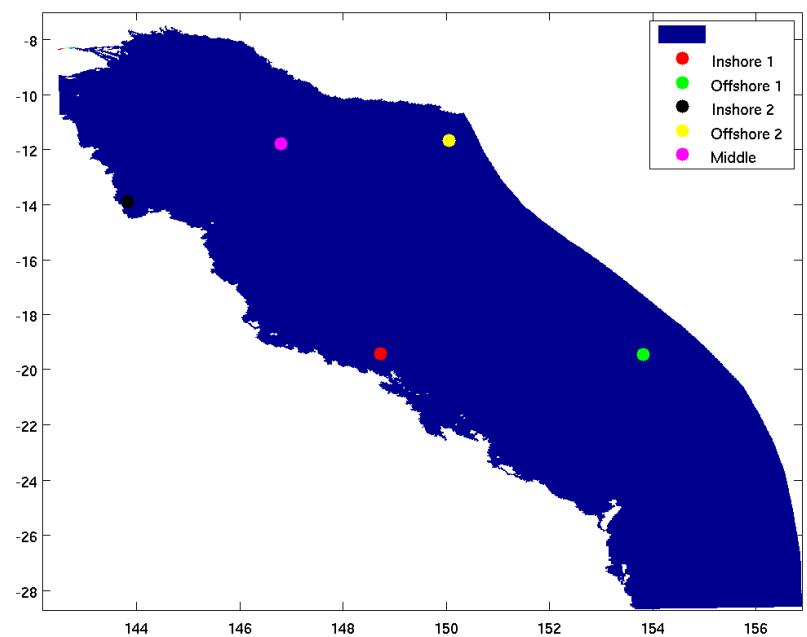


Figure 4.7.52. Location of the time series where the model result are presented.

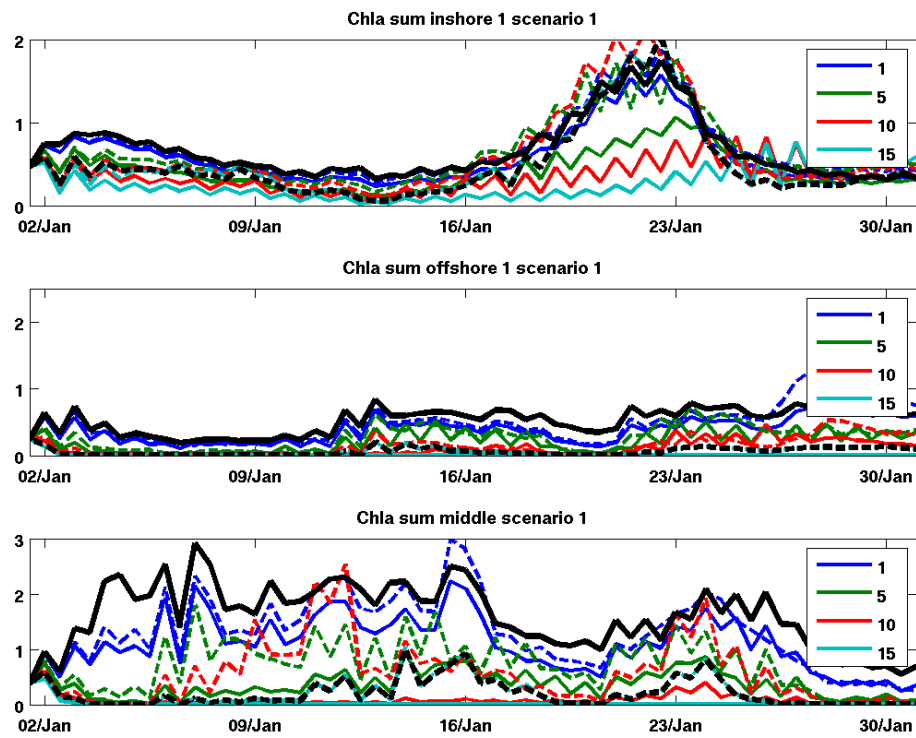


Figure 4.7.53. Time series of total Chlorophyll for different sinking rates of phytoplankton and zooplankton (legends show sinking rate of small phytoplankton, large phytoplankton sinks at double the rate and zooplankton either sink at the same rate (dashed lines) or not (plain lines)).

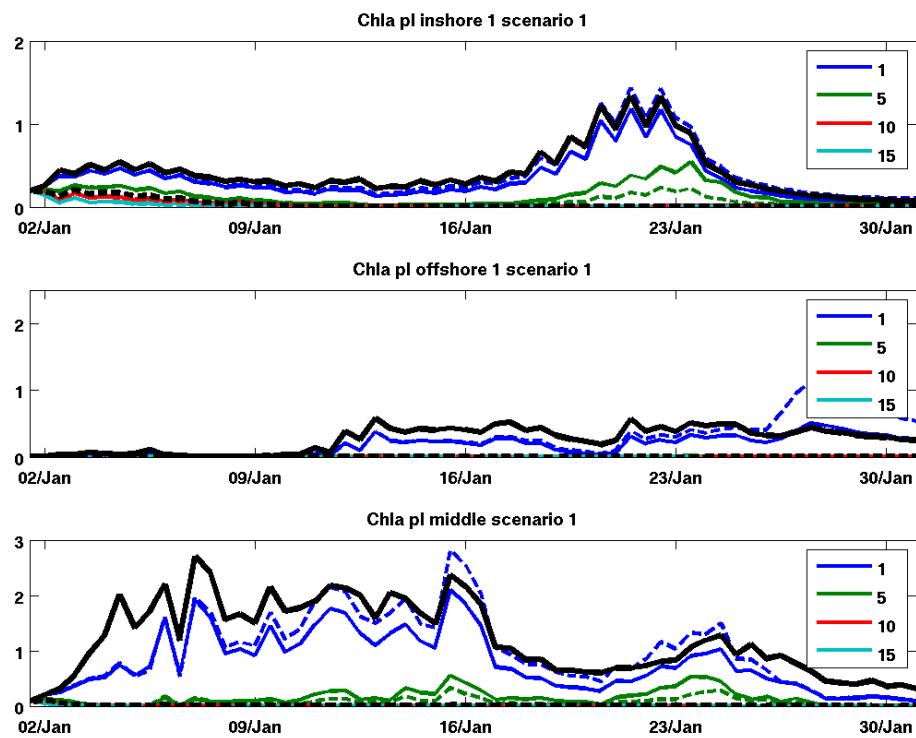


Figure 4.7.54. Time series of large phytoplankton Chlorophyll for different sinking rates of phytoplankton and zooplankton (legends show sinking rate of small phytoplankton).

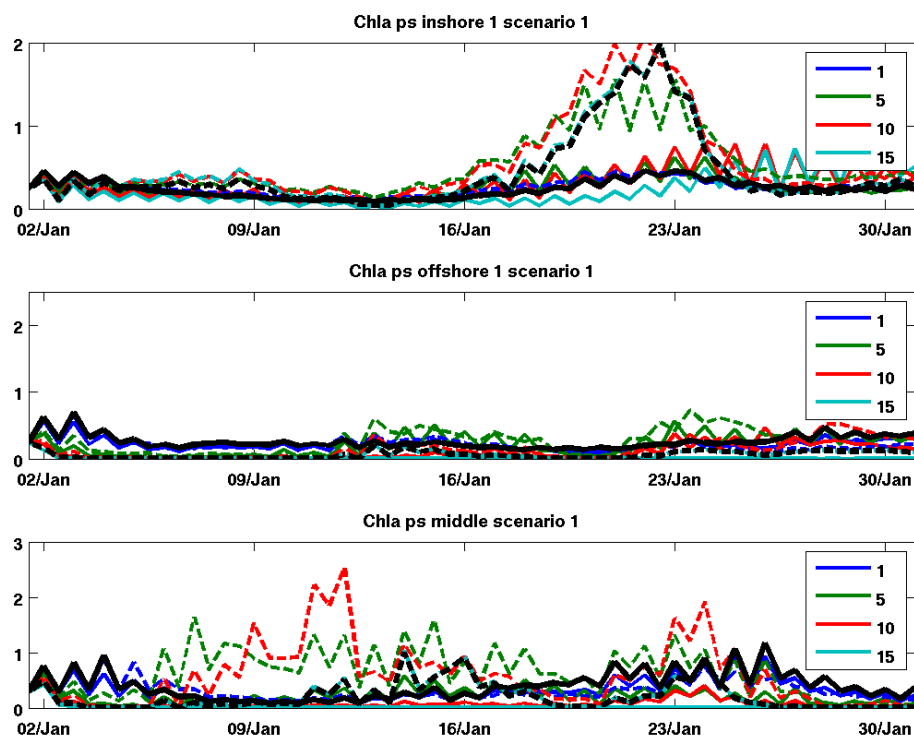


Figure 4.7.55. Time series of small phytoplankton Chlorophyll for different sinking rates of phytoplankton and zooplankton (legends show sinking rate of small phytoplankton, large phytoplankton sinks at double the rate and zooplankton either sink at the same rate (dashed lines) or not (plain lines)).

4.7.6 1km near real time BGC Model

A 1km Queensland shelf model augmented with sediments and biogeochemistry was implemented in near real time based on the 1km hydrodynamic model, GBR1 (Section 4.1) and utilising the Flux Form semi-Lagrange transport model for the advection of tracers (Section 4.5.3). Model BGC processes and parameters are identical to the optimised 4km BGC model.

The model was initialised in December 2014 using results from the 4km sediment and biogeochemical model results interpolated onto the 1km grid. The model is 'nested' in the 4km near real time BGC model and forced along the ocean boundary with an upstream condition for all BGC pelagic tracers. River forcing employs the GFL algorithmic relationships to account for nutrient and sediment inputs into the model (see Section 4.7.5.5).

Due to the fine spatial resolution of the model grid and numerous sediment and BGC tracers the model runs very slowly with a model to real time ratio of ~10:1. To date this has precluded hindcast and scenario simulation. Results from the 1km near real time model are a down-scaled hypothesis of the validated 4km model.

4.8 Develop and test relocatable coastal model platform

4.8.1 Motivation

The rivers flowing into the Great Barrier Reef Lagoon (GBRL) from the Queensland coast are a vital component of the system as a whole, contributing freshwater, sediments and nutrients to the system (Kroon et al. 2012).

While the 1km and 4km grids of the eReefs models make it possible to simulate the GBR lagoon as a whole, it is often desirable to simulate estuaries and near-shore areas on a finer resolution. Reasons include:

1. There is evidence that physical and biogeochemical processes in the estuaries and coastal receiving waters of these rivers substantially modify the timing and magnitude of sediment and nutrient loads delivered to GBR lagoon waters (Davies and Eyre 2005; Ford et al. 2005; Margvelashvili et al. 2006; Robson et al. 2006; Ryan et al. 2007; Robson and Brando 2008). More detailed representation of processes in these areas allows more accurate calculation of loads reaching the reefs.
2. Flood plumes create sharp physical and chemical gradients on small spatial scales (Eyre and Balls 1999), which a 1 km grid cannot adequately represent.
3. Water quality in estuaries is in itself of interest to coastal managers (e.g. Connell et al. 1981; Trott and Alongi 2000; Dunn et al. 2007). A 1 km grid does not allow estuarine channels to be included in the GBR-scale model.

To provide capability to model areas of particular interest in a flexible and robust way, we are developing a relocatable coastal model (RECOM). This model aims to:

- Allow a modeller or sophisticated model user to quickly and easily select a geographical area of interest and define a new model grid for this area at an appropriate resolution,
- Automatically set parameter values and initial conditions appropriate to the estuary and the available observational data (a labour-intensive and time-consuming task with existing tools),
- Run the same hydrodynamic, sediment and biogeochemical models on this new model grid as are used in the four kilometre grid GBRL model,
- Dynamically couple the fine-scale and large-scale models so that boundary conditions are handled appropriately and the models mesh smoothly,
- Visualise the results of the integrated fine-scale and large-scale results together.

Development of the relocatable coastal model lies at the cutting edge of modelling methodology. We have built on the work performed in BLUElink to extend the capability of TRIKE to generate complex curvilinear grids for coastal environments and register dedicated data streams (e.g. river flow). The sediment transport and BGC, driven by the transport model, will also be included in TRIKE. The estuary models are 1-way coupled to the 1 km or 4 km GBR model; in the future this is anticipated to be extended to 2-way coupling. The foundations of the 2-way coupling has been developed in this project and comprises an innovative autonomous coupling relying on push-pull data transfer rather than existing overarching orchestration methodologies such as AGRIF (Debreu et al. 2008). The autonomous approach will allow a plug-and-play approach to including or omitting relocatable estuaries within the system. The transport model will be required to be extended to multi-grids, or assume an unstructured nature.

4.8.2 Framework

There now exists three separate software platforms (ROAM, TRIKE, RECOM) that can perform automated relocatable model deployment, however, these three platforms have distinct differences. ROAM and TRIKE can initiate downscaled simulations globally to resolutions of ~2km, and are nested within the global OceanMAPS model. ROAM is used by Royal Australian Navy personnel, whereas TRIKE is the research version that is available to CSIRO scientists and contains enhancements under development. TRIKE can also operate in a static capacity (i.e. on purpose built custom grids rather than in re-locatable mode with the associated instability constraint invoked) to power near real-time implementations (e.g. GBR4 and GBR1). RECOM can only operate within the GBR4 domain for the period that the output archive exists. RECOM is reliant on registering GBR4 (or GBR1) output for open boundary forcing and initialisation (hydrodynamic, sediment and BGC), and therefore must obtain approval to access output from these models before it can operate (i.e. the supply of GBR4 data can dictate when and where RECOM is deployed). RECOM also delivers sediment transport and BGC outputs. The data registered with RECOM for downscaling currently is:

- Regional sets of 12 minute temperature, salinity, sea level and 3D velocities,
- Regional water column BGC and sediment transport prognostic variables.

This involves the archive of a large amount of data, but allows downscaled models to be deployed anywhere within the GBR4 domain. It is envisaged that in future a downscaled implementation using RECOM will request data from the regional models at the required open boundary geographic locations, and this will be supplied at high frequency to RECOM in point-array format (i.e. only at the open boundary locations).

ROAM and TRIKE are relocatable, automated frameworks for hydrodynamics only. The extension of TRIKE to sediments and biogeochemistry involves the specification of the tracers required for those processes, specification of attributes for those tracers (settling rates, densities etc.), global parameters (parameters that are process dependent) and for biogeochemistry the processes that define the type of model to be used. In typical case study approaches to building a model, these elements are defined either in the main parameter file or associated dedicated process or parameter files. For an automated implementation of these models, the respective components must be self-configuring, and TRIKE must be able to bootstrap itself from nothing using minimal user input. The case study approach to parameter and process prescription is not adequate in this context, since TRIKE is a run and data management system, not a run configuration system. This latter task falls to the individual models that TRIKE invokes; i.e. sediment and biogeochemistry must be self-configuring. As mentioned, hydrodynamics already possesses this functionality, developed under BLUElink. Automation of the tracer prescription, tracer attribute definition, global parameter specification and BGC process specification are discussed below. Note that once these elements have been defined, they must then be populated with values that will result in realistic simulations. This is the basis of a 'universal parameterisation' that is also discussed. The flow of control that TRIKE manages is illustrated in Fig. 4.8.1, and flows sequentially through hydrodynamics to sediments and BGC driven by the transport model using flow fields stored offline from the hydrodynamic model.

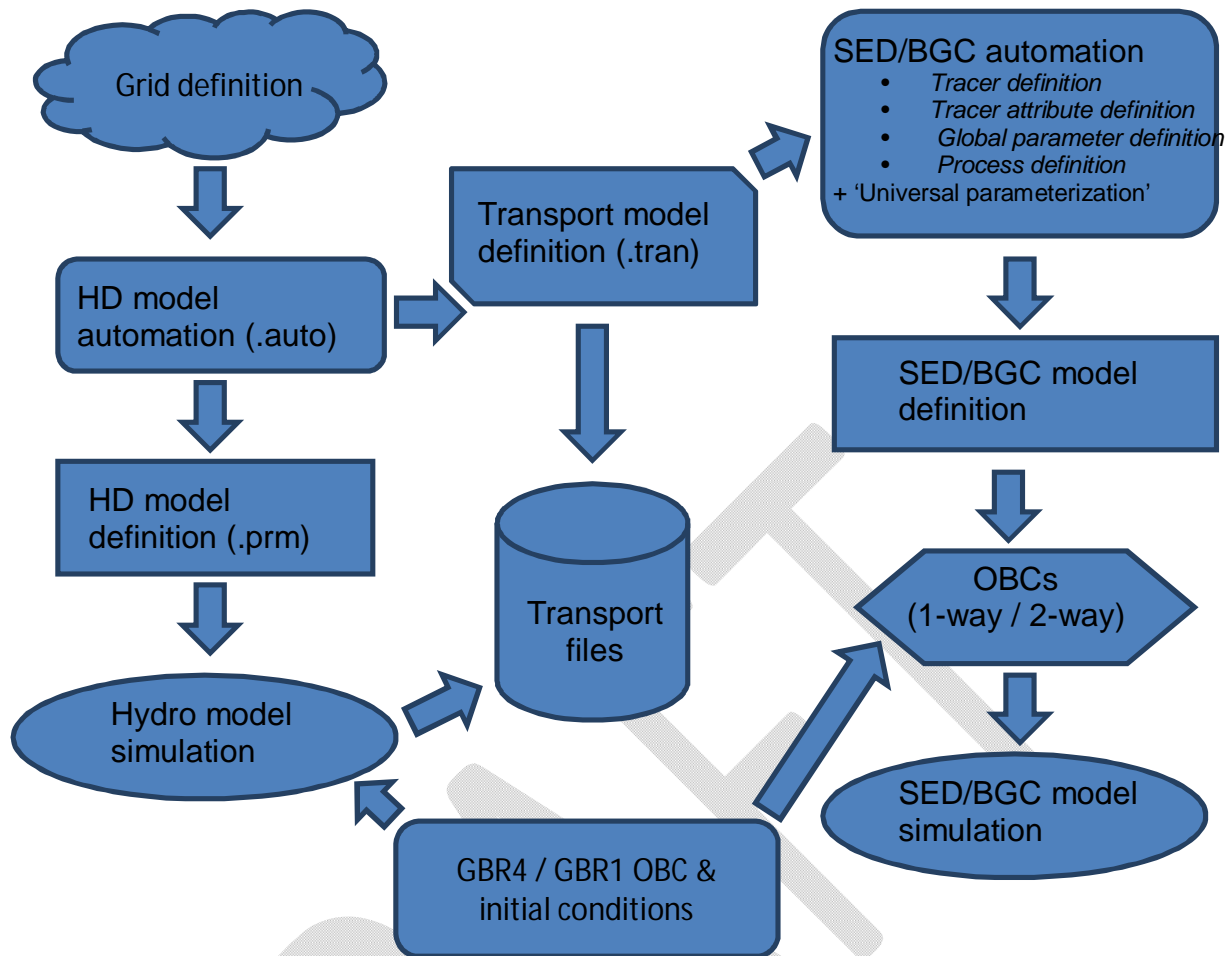


Figure 4.8.1. Flow of control in RECOM.

Once grid and simulation period definitions are specified in TRIKE for a simulation, the RECOM runner bundles these along with any forcing files created from a data extraction process (OBC and initial conditions from the regional models, atmospheric forcing data) into an auto (.auto) file. SHOC is then executed in 3 steps with the following options:

1. -rg to generate the hydrodynamic parameter (.prm) file, BGC & Sediments transport (.tran) file as well as the initial condition netCDF file,
2. -p to run the hydrodynamic model generating the transport netCDF files,
3. -t to run the BGC and sediment model using the output from step 2.

During step 3 the sediment and BGC automation is invoked, where a full process, tracer and parameter definition applicable to the run is invoked. These definitions are described in more detail below. At the completion of the model run all output and log files are archived and made available to the user at an ftp site.

Note that RECOM is a framework for the automated deployment of hydrodynamic, sediment transport and BGC models, and required sound forcing data to be realistic. Some of the required data streams (e.g. bathymetry, terrestrial inputs) are required to be registered with TRIKE to enable the model to access them. At this stage it is the user's responsibility to source these application specific datasets, since no universal database exists from which TRIKE can extract these data.

4.8.3 Tracer definition

The tracers that sediment transport and BGC require to perform a simulation are required to be defined by EMS rather than the user. To achieve this, a superset of all possible tracer names must be maintained internally (i.e. hardwired) by EMS, and a subset of these chosen to conform to the requirements of a particular simulation. This superset of tracer names can be expanded as desired; if this occurs then associated tracer attributes for the additional tracer (discussed in the next sub-section) must also be generated. Note that for BGC, the number of additional prognostic tracers can be greater than 50. For sediment transport, the user must specify which sediment classes they wish to simulate (e.g. mud, sand, gravel), and EMS constructs these tracers along with several mandatory diagnostic tracers (e.g. TSS, bottom stress). For BGC, the tracer list is constructed by interrogating the process specification and constructing a list of tracers that are required to integrate the defined processes. The identified tracers are then automatically constructed and included within the EMS tracer list.

4.8.4 Tracer attribute prescription

A tracer information data structure exists in EMS that defines all the attributes associated with a particular tracer. This includes the tracer name, units, type of tracer (water column, sediment, epibenthos), valid ranges, default fill value, advection and diffusion status. Additional tracer data structures have been introduced specific to sediment transport and biogeochemistry that contain information specific to those modules. This includes settling rates, particle size and density, resuspension and deposition status, cohesion and flocculation status, adsorption rates and the type of open boundary condition that tracer requires. When the tracer list has been defined, these private tracer attributes are then associated with each sediment or BGC tracer. The method of defining the tracer attribute values in the automated context is via hardwired sets of values in the EMS code. The hardwired sets of attributes can be accessed via a single keyword from the parameter file. Currently there exist two sets of attributes to choose from, but the number of sets can be expanded as required, e.g. to specify different types of systems (tropical, sub-tropical, macro-tidal, micro-tidal etc.). Usage of the tracer attribute specification is described in Section 15 and 16 of the SHOC User's Manual (Herzfeld, 2012).

4.8.5 Global parameter specification

Global parameters refer to parameters that are attached to processes as opposed to a tracer. This may be a growth rate for phytoplankton or a critical shear stress for sediments. The method of defining global parameter values in the automated context can either be via hardwired sets of values in the EMS code, specification in an external parameter file or dynamically based on the available information relating to the system to be simulated (e.g. bathymetry, latitude etc.). The framework for this latter method has been implemented, however, the dynamic 'rules' that lead to global parameter definition have yet to be constructed. The hardwired sets of global parameters can be accessed via a single keyword from the parameter file. Currently there exist two sets of global parameters to choose from for both sediment transport and BGC, but the number of sets can be expanded as required. Note this framework only facilitates the accommodation of the global parameters; the prescription of the actual values is another task that falls under the 'universal parameterisation'.

4.8.6 BGC process definition

The type of BGC model used in the simulation is controlled by the processes invoked from the process library. This may result in, for example, a simple pelagic NPZD model, a complex multi-group coupled benthic-pelagic model or a spectrally resolved radiative model. The type of model classified will define the tracers that are required to exist in order for that model to operate. These tracers are automatically generated by interrogating the process list *a priori*. The method of defining the BGC processes can either be via hardwired process descriptions in the EMS code, specification in an external parameter file or dynamically. Again, the framework for this latter method has been implemented, with no 'rules' governing the process description implemented. The hardwired sets of process descriptions can be accessed via a single keyword from the parameter file. Currently there exist two lists of processes to choose from ('default' and 'estuary'), and these can be expanded as required.

In order to simplify specification of processes to run, we have developed a 'default' process set for the EMS biogeochemical model. Though it is still possible to manually specify the set of processes to be run, this is no longer required. In most applications of RECOM, the default GBR parameter set will be used. This sets up RECOM to use a structure consistent with that of the GBR4 model and automatically populates the model with the required tracer variables.

The default process set for estuaries is slightly simplified and currently omits carbon chemistry, *Trichodesmium*, spectral light, coral, gas exchange detailed optical calculations. Included in the default 'estuary' process set are:

In the water column:

- tfactor (calculates temperature adjustments of process rates)
- viscosity (calculates viscosity)
- moldiff (calculates molecular diffusion rates)
- remineralization (calculates breakdown rates of organic materials)
- phytoplankton_growth_wc(small) (growth of small phytoplankton)
- phytoplankton_growth_wc(large) (growth of large phytoplankton)
- zooplankton_large_grow_wc (growth and mortality of large zooplankton, including grazing and predation)
- zooplankton_small_grow_wc (growth of small zooplankton, including grazing)
- nitrification_wc (nitrification)
- values_common (sets values of common coefficients)
- light_wc (simple optical calculations)

In the epibenthos:

- macroalgae_grow_epi (growth of macroalgae)
- macroalgae_mortality_epi (mortality of macroalgae)
- seagrass_grow_epi (growth of seagrasses)
- seagrass_mortality_epi (mortality of seagrasses)
- values_common_epi (specification of common coefficients)
- light_epi (calculates optical conditions in the epibenthos)
- diffusion_epi (calculates diffusion rates across the epibenthos)

In the sediments:

- tfactor (calculates temperature adjustments of process rates)
- viscosity (calculates viscosity)
- moldiff (calculates molecular diffusion)

phytoplankton_mortality_sed(small) (mortality of small phytoplankton while in the sediments)
phytoplankton_mortality_sed(large) (mortality of large phytoplankton while in the sediments)
nitrification_denitrification_sed (nitrification and denitrification rates)
p_adsorption_sed (phosphorus adsorption and desorption)
values_common (sets values of common coefficients)
light_sed (calculates optical conditions at the sediment surface)

4.8.7 BGC 'Universal' parameterisations

4.8.7.1 The need for a better approach to parameter specification

The ecology module of EMS includes over 110 parameters, defining biological properties and chemical process rates in the model. Because of the complexity of non-linear interactions and the high computational demands of coupled hydrodynamic-biogeochemical and hydrodynamic-ecological models, setting values for these parameters has traditionally been a very labour-intensive task, requiring a high degree of expertise. A typical workflow for the biogeochemical modeller has been:

1. Identify a physiologically or chemically realistic range for calibration of each parameter and initial condition, based on an understanding of the process represented and the structure of the relevant sub-model. The modeller is often able to draw on information compiled for previous modelling studies, such as Murray and Parslow (1997) and Murray et al. (2000), but must check that these ranges are still valid in light of interactions with new processes included in the model and new scientific information.
2. Assign initial (pre-calibration) values to each parameter, often taking a value in the middle of the physiologically realistic range or a value which was found suitable in a previous model application.
3. Implement a pilot model and conduct a sensitivity analysis to identify the parameters that have the greatest influence on the model results with respect to the outputs of most interest in the current study.
4. Find information in the literature or conduct new studies to provide more information regarding the likely actual values of these parameters, drawing on: a) process studies in the system to which the model is being applied; b) process studies in other, similar systems; and c) laboratory studies.
5. Run the model many times using different combinations of possible values of sensitive parameters to find a set that results in the best possible match to the data (i.e. calibration).

This is labour-intensive process that relies on a high level of modeller skill and has therefore been a significant barrier to implementing models for new locations.

A second problem with this traditional approach is that, due to the complexity of the workflow and the number of parameters involved, the connection between model parameter values and the observational evidence base is often weak and usually poorly documented.

Automated calibration is possible if the computational demands of the model are not too high and sufficient observational data are available. The most sophisticated automated calibration approaches require the modeller to specify a “prior distribution” for each parameter that is to be calibrated. A prior distribution indicates the anticipated likelihood that the parameter value will fall within each part of the range of possible values.

It is important for RECOM to have:

- a) reasonable default parameter values, supported by the available evidence and likely to result in plausible results when RECOM is applied naively to a new system; and
- b) evidence-based parameter priors that will support data assimilation and probabilistic modelling approaches in future.

To provide both reasonable default values and parameter priors, we have established the evidence-based parameter library. This library will be used both to specify default parameter values for RECOM and to facilitate calibration of the whole-GBR-scale biogeochemical models (GBR4 and GBR1).

4.8.7.2 The evidence-based parameter library

There have been several previous attempts to collate and tabulate parameter values from across the literature. Some of these efforts have been broadly focused on the most commonly used parameters in aquatic ecosystem models (e.g. Bowie et al., 1985) while others have more comprehensively reviewed the literature for a narrower range of parameters relating to a particular component of an aquatic ecosystem (e.g. Hansen, 1997). These sources have been, and remain, a very valuable resource for modellers.

In developing the evidence-based parameter library, we are building on this legacy by:

Bringing together parameter values from a wide range of sources, including past review papers as well as individual peer-reviewed experimental and observational research papers and observational values reported by research partners in both eReefs and the coastal carbon cluster.

Presenting these data in the form of prior probability distributions for each parameter, showing not only the mean and range of observed parameter values, but also the distribution of observations within that range.

Providing, through web services, both the raw data and the tools needed to make standard calculations required to produce the prior distributions, so that the eReefs team and other researchers can easily modify the assumptions that we have made (for example, in selecting relevant species or converting measured rates to expected rates at a common reference temperature).

Developing an open, crowd-sourced community parameter database to enhance collaboration between teams using different models and facilitate regular updates to parameter priors as new observational information becomes available.

Default parameter values for RECOM are taken from the mean values of distributions fitted to the collected observational data for each parameter after appropriate filtering to select the values most relevant to Great Barrier Reef waters.

For each parameter included in the library, we have conducted a literature review, drawing on previous reviews where appropriate, but also checking the original sources and bringing in new data from more recent studies. We have included only parameter estimates derived from peer-reviewed experimental or observational studies, not parameter values derived from calibration of models.

Where rates and responses have been measured under a range of temperatures, these have been converted to a common reference temperature using the Q10 equation used in the eReefs biogeochemical models.

In some cases, the development of the parameter library has dramatically changed the parameter values being used in the eReefs models, while in other cases, it has confirmed that the values used in the pilot version are likely to be correct (see examples in Fig. 4.8.2).

Observational data and fitted distributions for several other EMS parameters are shown in the figures and tables that follow. From each distribution, the mean value is used to define the default RECOM parameter value.

DRAFT

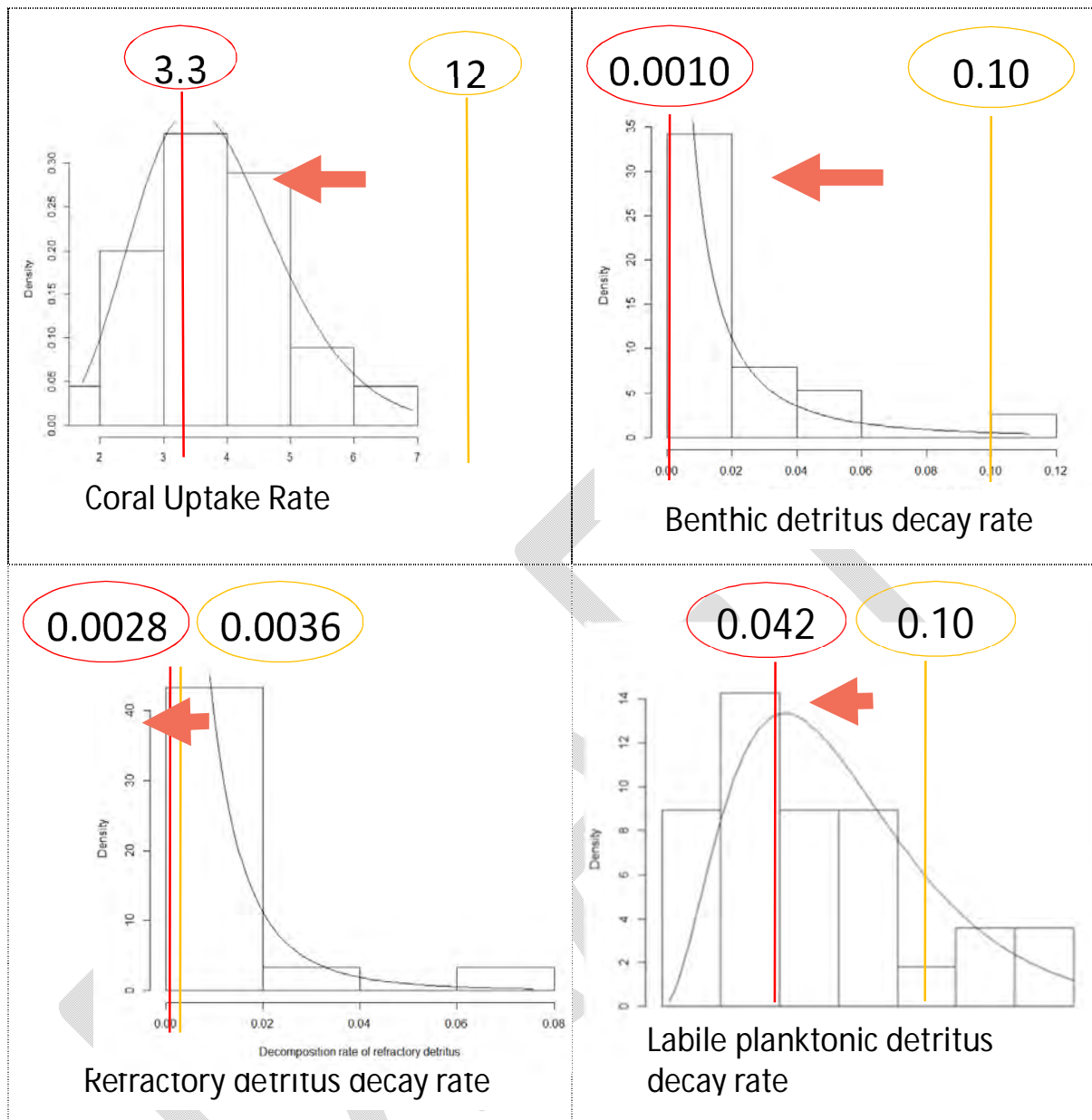


Figure 4.8.2. Four EMS parameters, showing probability distributions fitted to the observational data found in the literature (black histograms and fitted curves), parameter values used in the pilot eReefs model (yellow) and most likely values derived from the parameter library (red).

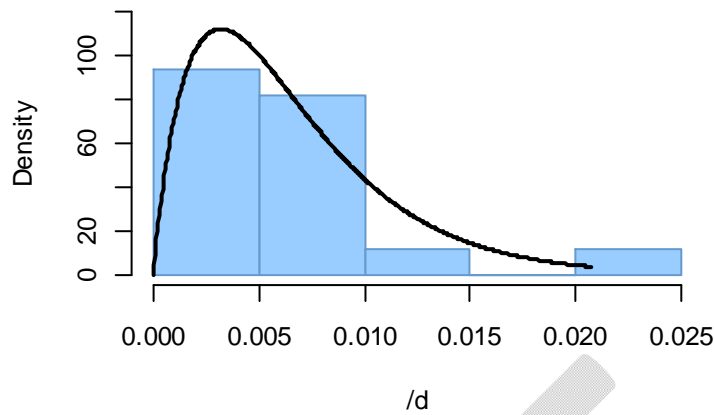


Figure 4.8.3. Decomposition rate of terrestrial detritus

Table 4.8.1. Decomposition rate of all terrestrial detritus components ($/d$) adjusted to 20C using the Q10 formulation, assuming $Q_{10} = 2$.

distribution	mean	shape	rate	5th %-ile	50th %-ile	95th %-ile	n
gamma	0.00653	1.96	300	0.00113	0.00546	0.0156	17

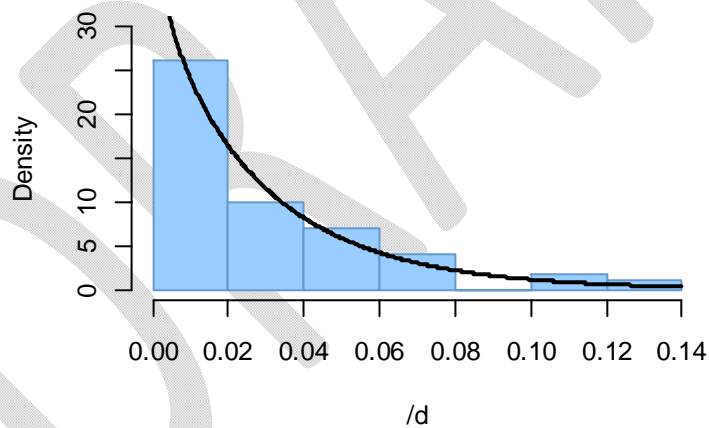


Figure 4.8.4. Decomposition rate of algal detritus

Table 3.8.2. Decomposition rate of algal detritus ($/d$) adjusted to 20C using the Q10 formulation, assuming $Q_{10} = 2$.

distribution	mean	shape	rate	5th %-ile	50th %-ile	95th %-ile	n
gamma	0.0288	0.899	31.2	0.00111	0.0191	0.0896	86

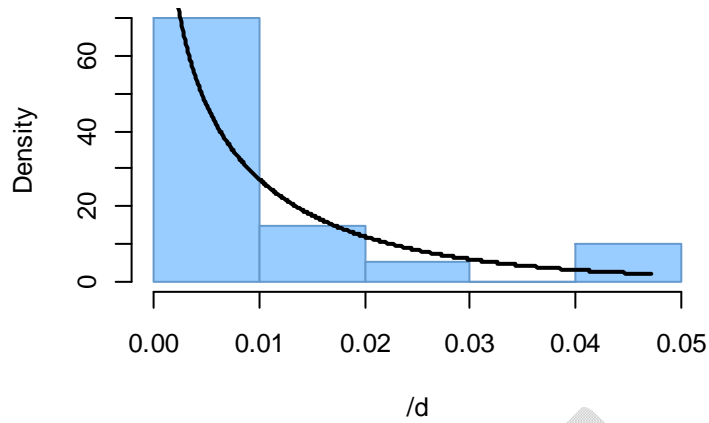


Figure 4.8.5. Decomposition rate of seagrass detritus

Table 4.8.3. Decomposition rate of seagrass detritus ($/d$) adjusted to 20C using the Q10 formulation, assuming $Q10 = 2$.

distribution	mean	shape	rate	5th %-ile	50th %-ile	95th %-ile	n
gamma	0.0109	0.609	55.8	0.000109	0.0058	0.0391	20

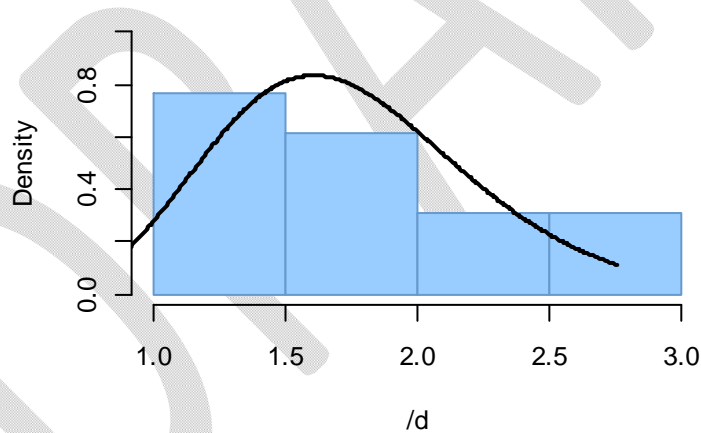


Figure 4.8.6. Maximum growth rate of small zooplankton

Table 4.8.4. Maximum growth rate of small zooplankton ($/d$) adjusted to 20C using the Q10 formulation, assuming $Q10 = 2$.

distribution	mean	shape	rate	5th %-ile	50th %-ile	95th %-ile	n
gamma	1.75	12.4	7.12	1.02	1.7	2.63	13

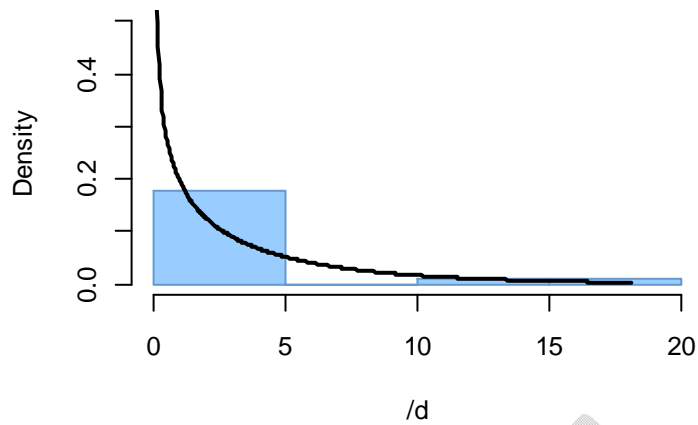


Figure 4.8.7. Respiration rate of small zooplankton

Table 4.8.5. Respiration rate of small zooplankton (/d) adjusted to 20C using the Q10 formulation, assuming $Q_{10} = 2$.

distribution	mean	shape	rate	5th %-ile	50th %-ile	95th %-ile	n
gamma	3.44	0.601	0.174	0.0326	1.81	12.4	17

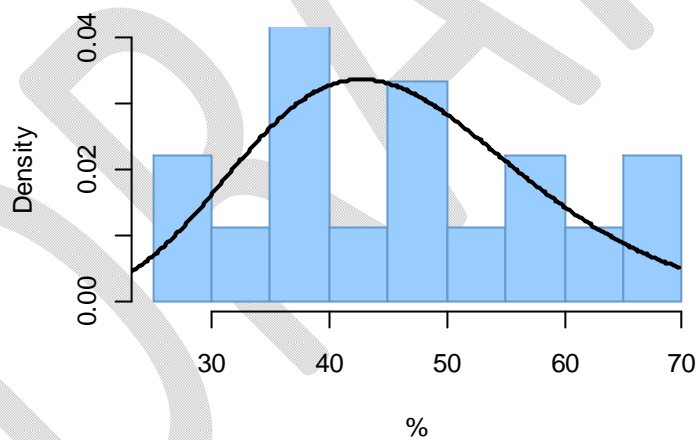


Figure 4.8.8. Growth efficiency of small zooplankton

Table 4.8.6. Growth efficiency of small zooplankton (%) adjusted to 20C using the Q10 formulation, assuming $Q_{10} = 2$.

distribution	mean	shape	rate	5th %-ile	50th %-ile	95th %-ile	n
gamma	45.9	14.2	0.309	27.9	44.9	67.7	18

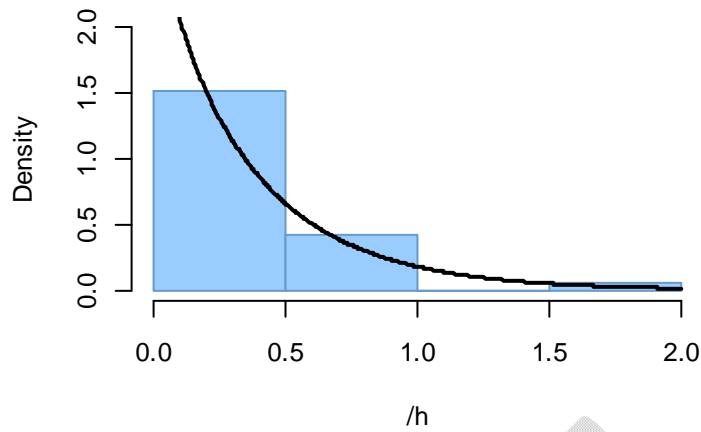


Figure 4.8.9. Maximum ingestion rate of small zooplankton

Table 4.8.7. Maximum ingestion rate of small zooplankton (/h) adjusted to 20C using the Q10 formulation, assuming Q10 = 2.

distribution	mean	shape	rate	5th %-ile	50th %-ile	95th %-ile	n
gamma	0.365	0.91	2.5	0.0146	0.243	1.13	33

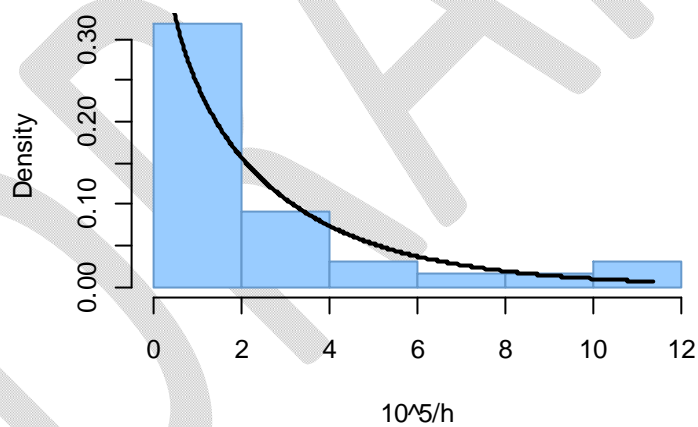


Figure 4.8.10. Maximum clearance rate of small zooplankton

Table 4.8.8. Maximum clearance rate of small zooplankton ($10^5/h$) adjusted to 20C using the Q10 formulation, assuming Q10 = 2.

distribution	mean	shape	rate	5th %-ile	50th %-ile	95th %-ile	n
gamma	2.6	0.801	0.308	0.0715	1.63	8.44	33

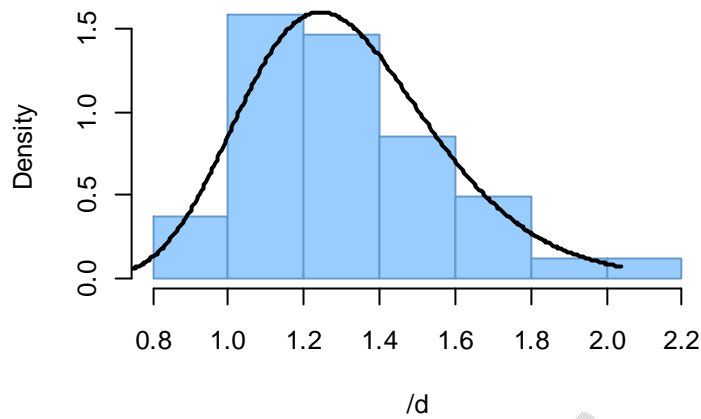


Figure 4.8.11. Maximum growth rate of large zooplankton

Table 4.8.9. Maximum growth rate of large zooplankton ($/d$) adjusted to 20C using the Q10 formulation, assuming $Q_{10} = 2$.

distribution	meanlog	sdlog	5th %-ile	50th %-ile	95th %-ile	n
gamma	0.257	0.196	0.936	1.29	1.78	41

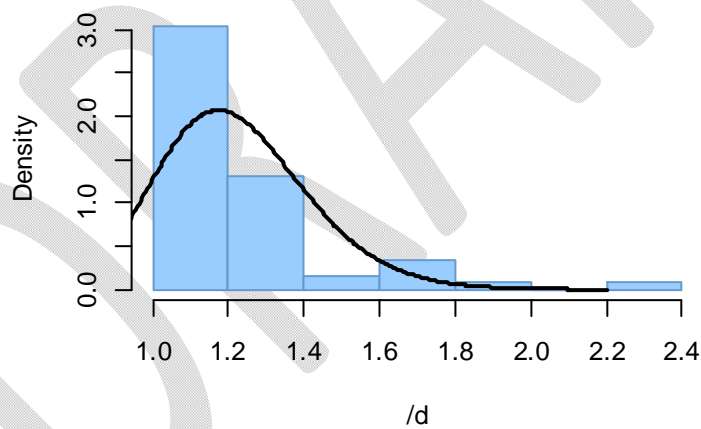


Figure 4.8.12. Respiration rate of large zooplankton

Table 4.8.10. Respiration rate of large zooplankton ($/d$) adjusted to 20C using the Q10 formulation, assuming $Q_{10} = 2$.

distribution	meanlog	sdlog	5th %-ile	50th %-ile	95th %-ile	n
gamma	0.186	0.162	0.923	1.2	1.57	61

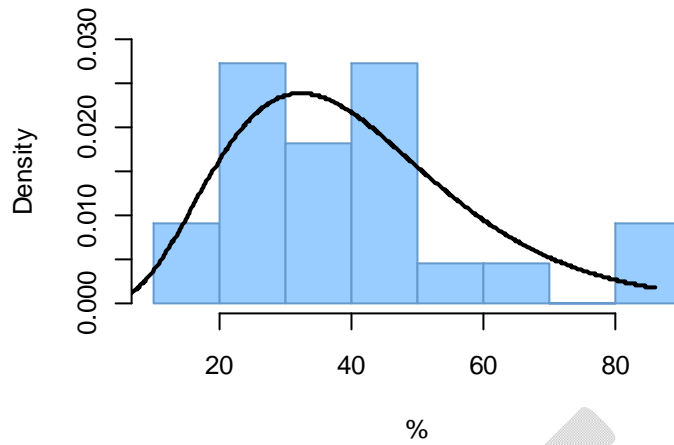


Figure 4.8.13. Growth efficiency of large zooplankton

Table 4.8.11. Growth efficiency of large zooplankton (%) adjusted to 20C using the Q10 formulation, assuming Q10 = 2.

distribution	mean	shape	rate	5th %-ile	50th %-ile	95th %-ile	n
gamma	40.6	4.92	0.121	15.8	37.9	74.6	22

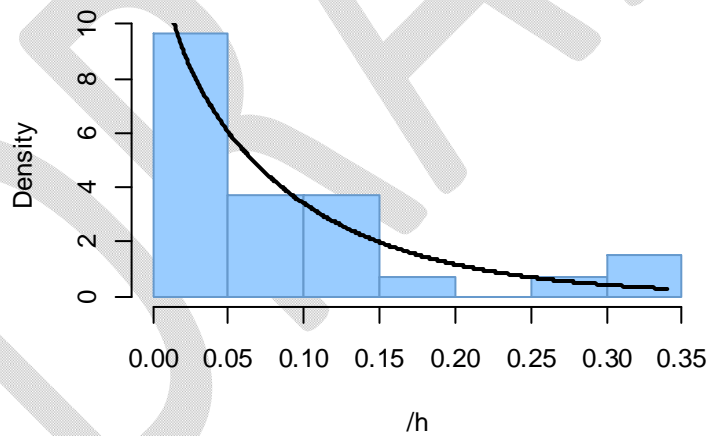


Figure 4.8.14. Maximum ingestion rate of large zooplankton

Table 4.8.12. Maximum ingestion rate of large zooplankton (/h) adjusted to 20C using the Q10 formulation, assuming Q10 = 2.

distribution	mean	shape	rate	5th %-ile	50th %-ile	95th %-ile	n
gamma	0.0899	0.883	9.82	0.0033	0.0591	0.281	27

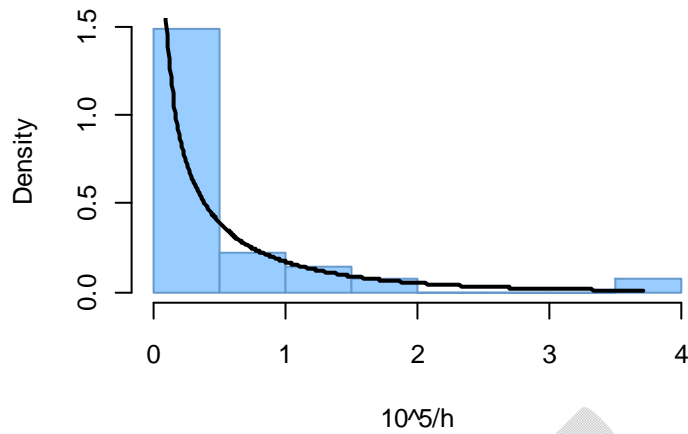


Figure 4.8.15. Maximum clearance rate of large zooplankton

Table 4.8.13. Maximum clearance rate of large zooplankton ($10^5/h$) adjusted to 20C using the Q10 formulation, assuming $Q10 = 2$.

distribution	mean	shape	rate	5th %-ile	50th %-ile	95th %-ile	n
gamma	0.465	0.364	0.783	0.000249	0.15	2	27

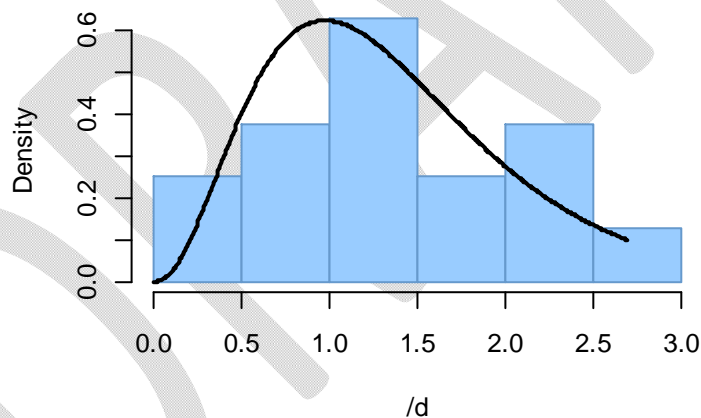


Figure 4.8.16. Maximum growth rate of cyanophytes

Table 4.8.14. Maximum growth rate of cyanophytes ($/d$) adjusted to 20C using the Q10 formulation, assuming $Q10 = 2$.

distribution	mean	shape	rate	5th %-ile	50th %-ile	95th %-ile	n
gamma	1.37	3.47	2.53	0.421	1.24	2.76	16

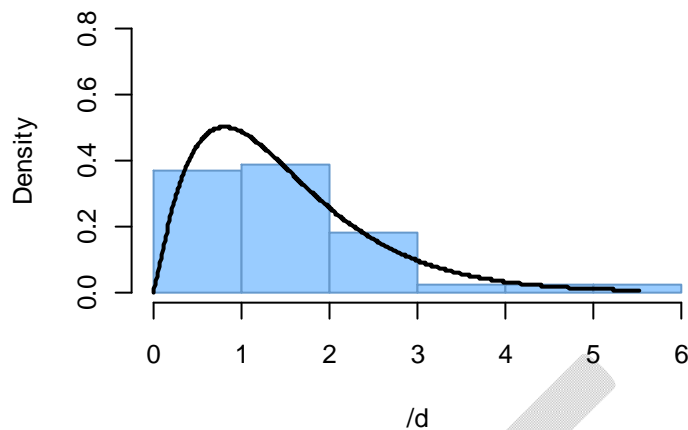


Figure 4.8.17. Maximum growth rate of large phytoplankton

Table 4.8.15. Maximum growth rate of large phytoplankton (/d) adjusted to 20C using the Q10 formulation, assuming Q10 = 2.

distribution	mean	shape	rate	5th %-ile	50th %-ile	95th %-ile	n
gamma	1.49	2.2	1.47	0.297	1.27	3.43	49

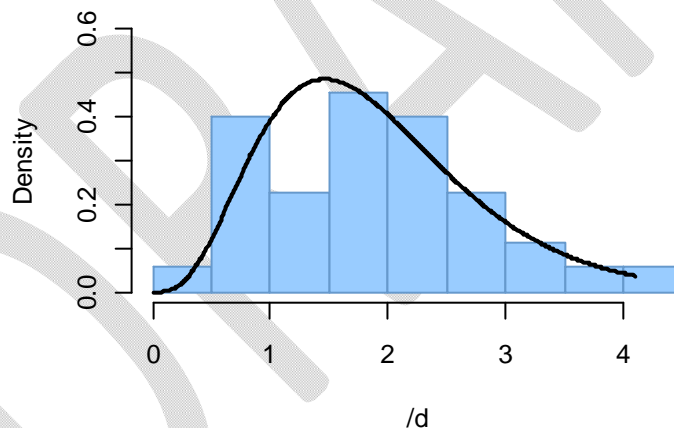


Figure 4.8.18. Maximum growth rate of small phytoplankton

Table 4.8.16. Maximum growth rate of small phytoplankton (/d) adjusted to 20C using the Q10 formulation, assuming Q10 = 2.

distribution	mean	shape	rate	5th %-ile	50th %-ile	95th %-ile	n
gamma	1.9	4.33	2.28	0.685	1.76	3.61	35

4.8.7.3 Data assimilation and uncertainty estimation

While the very computationally intensive nature of the full eReefs models prohibits multiple model runs, the smaller spatial domains for which the RECOM is intended, combined with the speed improvements allowed by running EMS in transport mode, make ensemble runs possible.

When the RECOM is applied to an estuary or coastal area, future developments may allow an ensemble of model runs to be generated. For each run, a value for each parameter that has not been fixed may be generated at random from its probability density function. This will generate a range of model outputs that will show the most likely result but will also provide a time- and space-varying estimate of uncertainty due to parameterisation.

Where sufficient monitoring data are available, the RECOM may also be able to select the combination of parameter values that best fits the observational data, according to a user-specified weighting function. Following the method of Jones et al. (2012), this could provide a more accurate simulation and allow more confident scenario predictions.

4.8.7.4 RECOM BGC options

RECOM currently supports two options for the process definition, but only one choice is available for tracer attributes and parameterisations. In the absence of alternative rationale, these definitions were influenced by existing Fitzroy Estuary and Heron Island case studies, as well as the 'universal' parameterisation described above. Further options may be included when it can be demonstrated that such alternatives can produce outputs that are more accurate than those generated using the regional parameterisations. The process definition in the regional models consists of a comprehensive process representation that has the capacity to respond dynamically to forcing or perturbations. Combined with the 'universal' parameterisation, this allows realistic biogeochemical responses at both regional and local scales. Until local scale specific processes or parameterisations are developed and demonstrated to possess higher skill, the regional GBR configuration is deemed suitable for RECOM.

The options available from the drop-down menus in the RECOM workflow configuration specification are:

BIOFNAME	gbr4
ECO_VARS_ATTS	standard
PROCESSFNAME	gbr4 optics_only

The *gbr4* and *standard* parameter and tracer attribute specification are the same as those used in the GBR4 regional model. The process definitions available are:

gbr4: The biogeochemical model considers four groups of microalgae (small and large phytoplankton, microphytobenthos and *Trichodesmium*), three macrophytes types (seagrass types corresponding to *Zostera* and *Halophila*, and macroalgae) and coral communities. Photosynthetic growth is determined by concentrations of dissolved nutrients (nitrogen and phosphate) and photosynthetically active radiation. Autotrophs take up dissolved ammonium, nitrate, phosphate and inorganic carbon. Microalgae incorporate carbon (C), nitrogen (N) and phosphorus (P) at the Redfield ratio (106C:16N:1P) while macrophytes do so at the Atkinson ratio (550C:30N:1P). Microalgae contain two pigments (chlorophyll *a* and an

accessory pigment), and have variable carbon:pigment ratios determined using a photoadaptation model.

Micro- and meso-zooplankton graze on small and large phytoplankton respectively, at rates determined by particle encounter rates and maximum ingestion rates. Additionally large zooplankton consume small zooplankton. Of the grazed material that is not incorporated into zooplankton biomass, half is released as dissolved and particulate carbon, nitrogen and phosphate, with the remainder forming detritus. Additional detritus accumulates by mortality. Detritus and dissolved organic substances are remineralised into inorganic carbon, nitrogen and phosphate with labile detritus transformed most rapidly (days), refractory detritus slower (months) and dissolved organic material transformed over the longest timescales (years). The production (by photosynthesis) and consumption (by respiration and remineralisation) of dissolved oxygen is also included in the model and depending on prevailing concentrations, facilitates or inhibits the oxidation of ammonia to nitrate and its subsequent denitrification to di-nitrogen gas which is then lost from the system.

Additional water column chemistry calculations are undertaken to solve for the equilibrium carbon chemistry ion concentrations necessary to undertake ocean acidification (OA) studies, and to consider sea-air fluxes of oxygen and carbon dioxide. The adsorption and desorption of phosphorus onto inorganic particles as a function of the oxic state of the water is also considered.

In the sediment porewaters, similar remineralisation processes occur as found in the water column. Additionally, nitrogen is denitrified and lost as N_2 gas while phosphorus can become adsorbed onto inorganic particles, and become permanently immobilised in sediments.

optics_only: This option calculates the inherent optical properties (IOPs) and apparent (AOPs) considering only suspended sediment and clear water scattering and absorption, and absorption due to CDOM. No ecological transformations occur. This option is to be used when a sediment - optics model is required.

4.8.8 Sediment model parameterisation

The presence of reefs is implicitly acknowledged in the sediment transport model through the altered hydrodynamic and wave forcing data which drive sediment transport. Apart from that the sediment transport model has also been updated to make it capable of handling spatial variability of other key parameters of the model such as ripple characteristics, settling velocity, bioturbation coefficients, diffusion across benthic and pelagic layers, critical shear stress, and thickness of the bioturbated layer. The user has the choice to either specify constant values of the parameter or to provide its spatial distribution over the region if such information is available. We believe such enhancement will improve the versatility of the code and its efficiency, particularly during large-scale coastal applications characterised by significant variability of the sedimentary settings.

The RECOM sediment parameterisation provides a choice of four different configurations, viz. *estuary*, *standard*, *shelf*, or *basic*. Each of these configurations is characterised by a particular sediment model parameterisation. The user can select one of these configurations during the

initialisation step of the RECOM (from the SED_VAR_ATTS drop-down list of the menu). The key reason for introducing these configurations is to allow the user to select quickly the parameterisation most appropriate for a particular application. Further adjustment of the model would require tuning of individual parameters of the model (including distribution of the initial concentration of sediments). To fulfil this task the modelling application must be downloaded to the local machine.

The *standard* configuration is based on the same settings as the GBR 4x4 km model except that bottom roughness in RECOM is uniform across the region while in the whole GBR model the roughness varies across the shelf. For consistent comparison between the large-scale GBR models and RECOM, the latter should be enhanced to enable handling of the spatially varying bottom roughness (to be interpolated from the large-scale GBR model). This may be a future development of RECOM if required.

The estuarine configuration of parameters (*estuary*) has roughness twice the roughness of the *standard* configuration, implying higher rates of the resuspension and, subsequently, more turbid environment.

The configuration *shelf* has roughness smaller than the roughness of the *standard* model. Simulations based on these setting tend to produces less turbid environment compared to the standard run.

Finally, the configuration *basic* provides simplified description of the sediment processes on the shelf. The corresponding scenario assumes no bioturbation in sediments, no flocculation, and no diffusion across water-sediments interface. Sediment exchange between pelagic and benthic layers in this scenario is driven only by resuspension and deposition of particles. These simulations tend to produce less turbid environment compared to the *standard* model.

Figs. 4.8.17 and 4.8.18 illustrate these configurations by showing suspended sediment concentrations in Keppel Bay simulated by RECOM for varying sets of parameters.

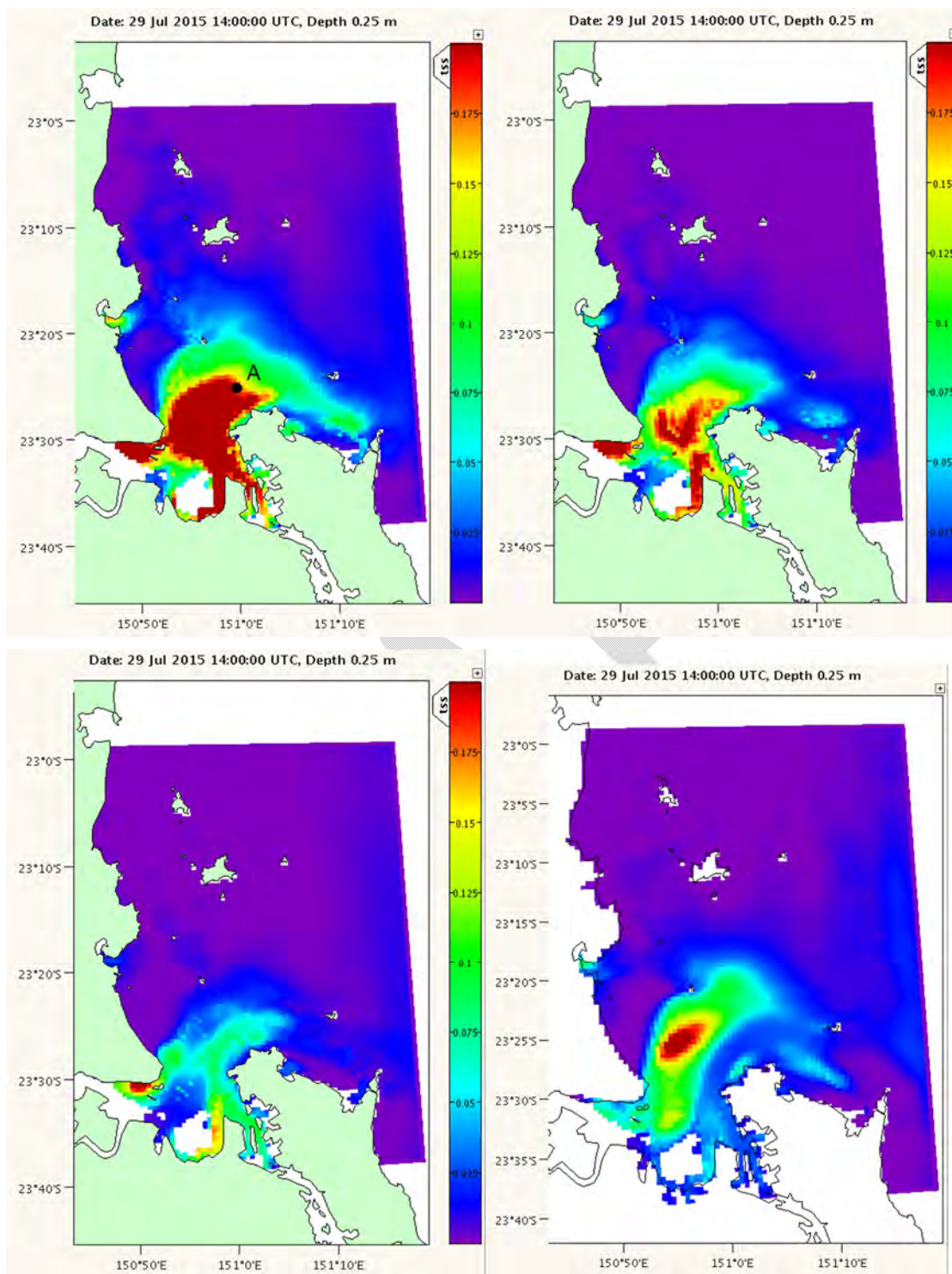


Figure 4.8.17. Snapshots of surface TSS simulated with RECOM for varying sets of parameters (kg m⁻³). *Estuary* set of parameters (top left), *standard* (top right), *shelf* (bottom left), and *basic* (bottom right).

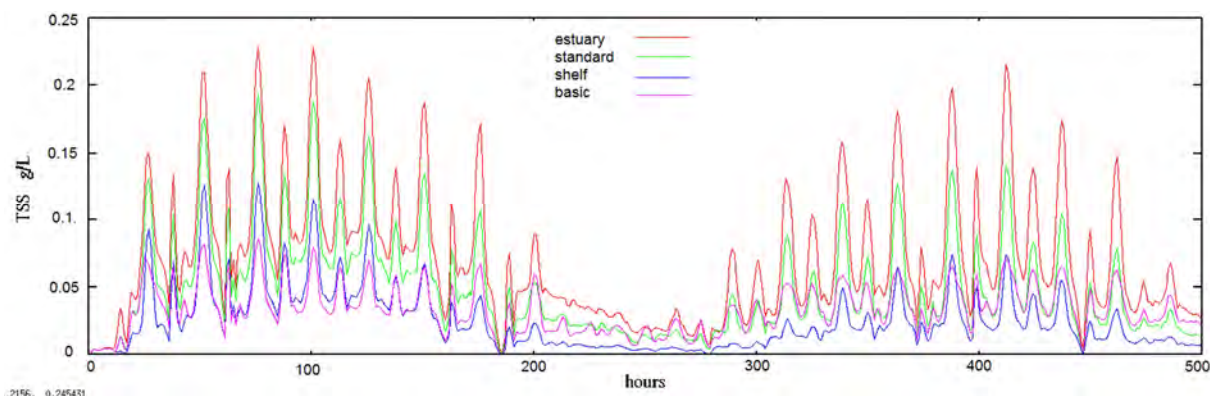


Figure 4.8.18. Simulated time-series of TSS in Keppel Bay (site A) for varying sets of parameters (see location map in Fig. 4.8.17).

4.8.9 Testing of temporal inflow boundary requirements

A second component of the work to refine inflow river concentrations has been an effort to better understand requirements for the temporal resolution of these boundary conditions; in particular, to test the assumption that sediment and nutrient inputs must vary on a daily or sub-daily time-step.

As a test case, flows, sediment and nutrient loads from the Fitzroy River during the 2007-2008 wet season were used in combination with a low-resolution test estuary grid. The 2007-2008 wet season was chosen because it included two major flow events with rainfall concentrated in different sub-catchments, so that markedly varying sediment and nutrient concentrations and flow-load relationships were observed over the course of a two-month period.

Three model runs were considered, using slightly different inflow boundary conditions.

Run 1 used the best available estimates (Packett, pers. comm.) of *daily* concentrations of suspended fine sediments, particulate nitrogen, particulate phosphorus, dissolved organic and dissolved inorganic nitrogen and phosphorus.

Run 2 used concentrations that changed *monthly*, to achieve the same monthly total sediment and nutrient loads as in run 1.

Run 3 used *constant* concentrations during the flow event (EMCs) and during low-flow conditions (DWCs) to achieve the same total sediment and nutrient loads over the course of the simulation.

A comparison of results showed remarkably little difference between the three simulations (e.g. Fig. 4.8.19), supporting the contention that monthly or event mean river loads are sufficient to drive the marine model. Analysis of total primary and secondary productivity in the test estuary also revealed little difference (approximately 3% difference) between the three simulations. Analysis of estimated total nitrogen, sediment and phosphorus exported to the ocean showed a difference of up to 22% between the three test cases, but this difference is within the bounds of uncertainty.

One note of caution is that in this test case, the two distinct flow events occurred in distinct months (February and March), which may exaggerate the similarity between the three runs.

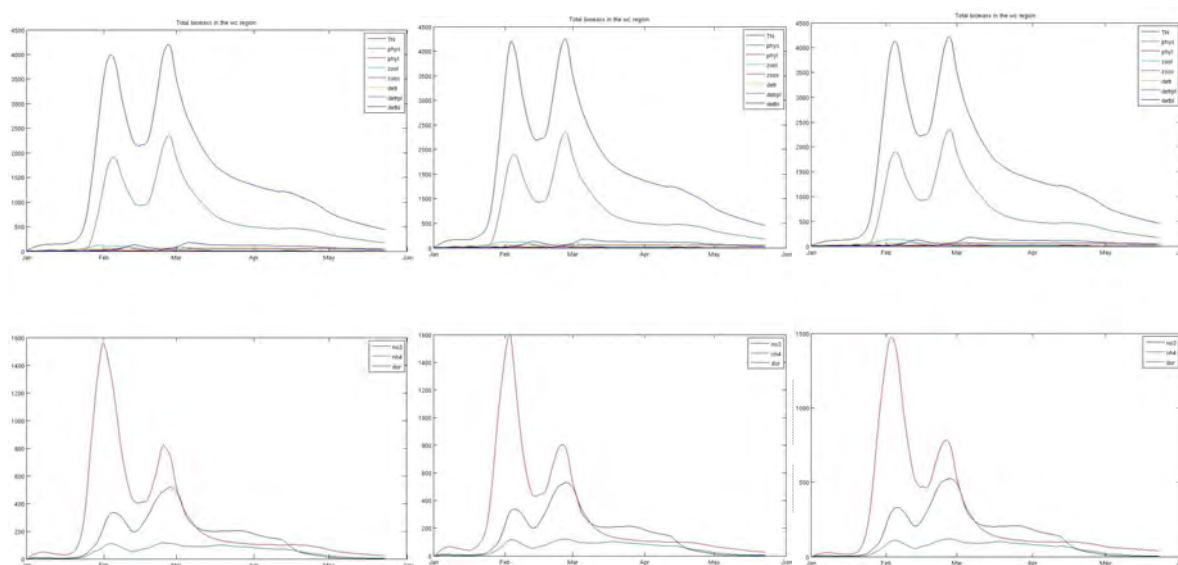


Figure 4.8.19. Comparison of variations over the duration of the simulation in total mass of several water-column variables in the test estuary: run 1 (left), Run 2 (middle), run 3 (right).

4.8.10 Grid generation

The generation of complex curvilinear grid typically used to represent estuarine geographies requires specialist software. This software serves two purposes, firstly to interactively define the grid specification through a graphical user interface (GUI), and secondly generate the curvilinear grid based on the information rendered on the GUI (see Section 14.3, SHOC User's Manual). This latter software (GRIDGEN, <http://code.google.com/p/GRIDGEN-c/>) takes a set of geographic waypoints and outputs an orthogonal curvilinear grid satisfying those waypoints. This is a non-interactive process based on terse text-file input and outputs, and currently is driven by a graphical front-end written in matlab (PLUM). PLUM enables users to place waypoints and visualise the output grid on a map, as well as make adjustments to the output (deleting points, adding lines, etc). However, PLUM being written in matlab raises issues around its portability, maintainability and the ability to easily create an attractive user interface that conforms to modern expectations and conventions. Consequently, PLUM is being re-written to a Java based package that will be web-enabled and compatible with both BLUElink and MARVL initiatives (i.e. the ROAM interface will have access to a wider variety of grids). Modernising the GUI will ease implementation, thus making it more accessible to the wider community without requiring extensive training or difficult installation (or a matlab licence). The interface software not only generates the curvilinear grid, but also performs the land masking, bathymetry generation and editing of grid, mask and bathymetry. Bathymetry is loaded from a number of databases; the most relevant to eReefs is that of Beaman (2010). The selected bathymetry may be interpolated onto the grid using nearest neighbour, linear, average, Sibsonian / non-Sibsonian natural neighbours, inverse distance or weighted area interpolation schemes. In addition to the creation of general orthogonal curvilinear grids, the grid generation is capable of producing geographic rectangular and polar type grids.

4.8.11.1 Webplum

The improved grid generation interface will be implemented as a browser-based application; this has the advantage that new users do not need to install software, and bug-fixes and updates are delivered instantly. To access the interface the user first loads the website in their browser. This contains an interactive map (in the style of Google Maps) on which they can place and edit their waypoints. When satisfied they can submit this for execution, whereupon the server formats the input for GRIDGEN and generates the grid. Once complete, the grid is displayed on the map in the user's browser, and if required may be edited until ready for download.

The basic workflow of Webplum grid creation goes something like this:

1. Define the Grid
2. Mask out areas of interest
3. Interpolate bathymetry values
4. Prepare results for use RECOM

4.8.11.2 Defining a Curvilinear Grid:

On the client side (via the browser), the user defines a set of points used to create the boundary of the grid through the use of a Google Maps style interface (Openlayers). These points are allocated attributes (Interior, Exterior, etc) as defined by the gridding executable (GRIDGEN). Once a valid set of points and attributes are created, they are sent to the server where they are converted to an ascii file and passed to the command line executable GRIDGEN. The output of this process is converted into a set of cells ($n * y$) in and persisted in GeoDjango which is subsequently uploaded to a GeoServer catalogue. After this, the server responds back to the client with the WMS endpoint for the new GeoServer layer, and it is displayed on the client using OpenLayers. This process can be repeated until the user is satisfied with the grids shape. The grids (as with the entire workflow) are saved for the user to recall and re-commence work at a later stage. A visual depiction of this step of workflow is shown in Fig. 4.8.20, and an example of the final rendered grid in Fig. 4.8.21. A similar process is followed for each of the remaining main steps in the workflow described below.

4.8.11.3 Masking the Grid:

Once the grid shape is defined, the user can move onto the next stage of the process which is to clip out irrelevant cells. The user has two choices at the stage, clip against a predefined coast line, or to manually click on cells and mark them as masked.

The process of auto clipping sends a request to the server where a PostGIS query reports all cells that fall inside a default coastline polygon. These cells are then marked 'masked', and the client is notified to redraw the cells. Note that GeoServer does not need to be modified again as it is only the cell attributes in the database that are changed. A re-render will use these new attributes automatically consumed by GeoServer and the WMS service. The manual clipping process allows selection of multiple cells which can be marked as masked or not. Upon hitting the save button all the modified cells are sent to the server to be updated, and the grid is re-rendered on the client. An example of a masked grid is shown in Fig. 4.8.22. Masked cells may then be edited, such that land may be made wet or vice versa (Fig. 4.8.23).

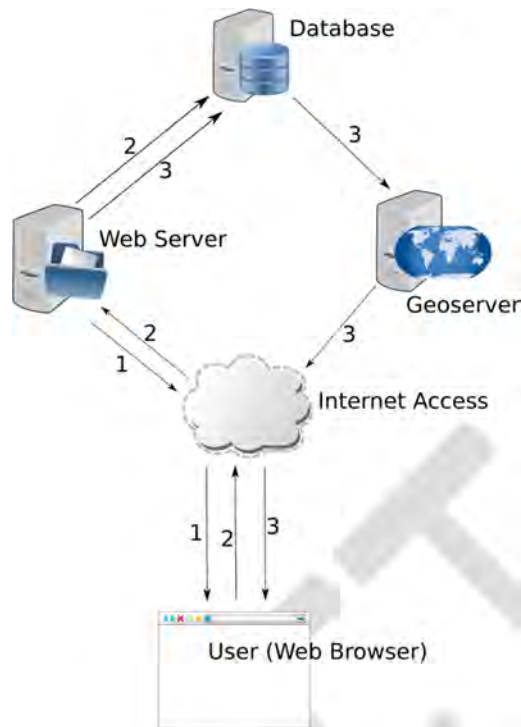


Figure 4.8.20. Graphical illustration of the grid generation workflow. The user loads the site on their browser (1). When the user submits their points, the server saves them to the database and formats an input file for GRIDGEN, then invoking it (2). When GRIDGEN finishes, the server parses the output file and stores it in the database. It then creates a layer in GeoServer, which will supply the rendering on the map in the user's browser (3).

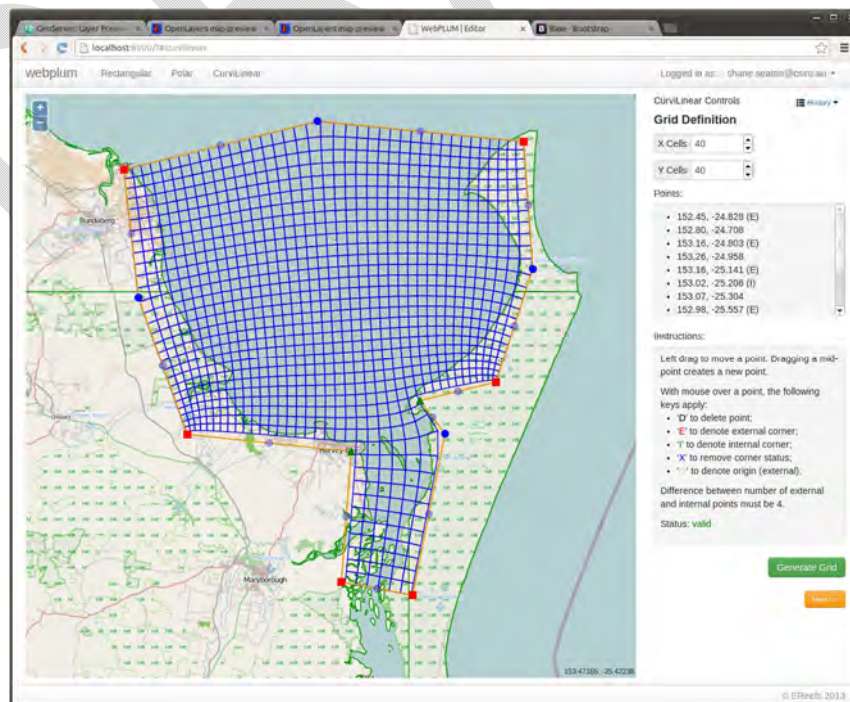


Figure 4.8.21. Illustration of a rendered grid in Webplum.

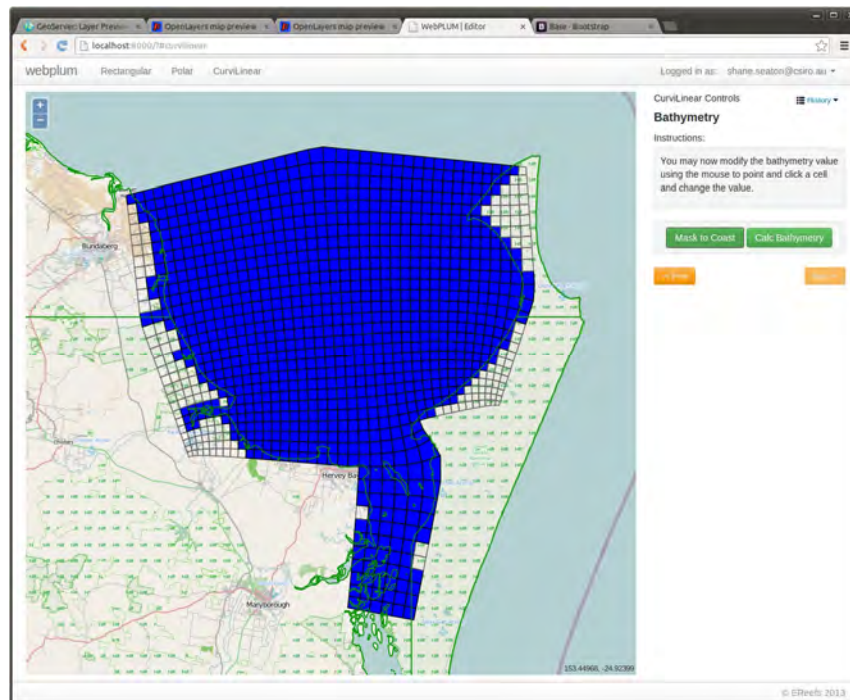


Figure 4.8.22. Illustration of masking a generated grid into land and water cells.

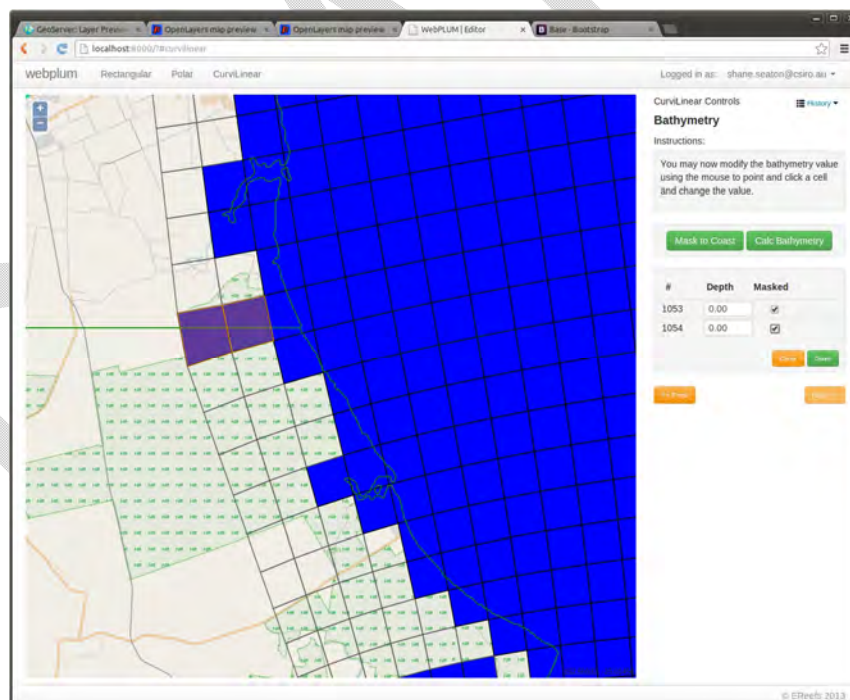


Figure 4.8.23. Illustration of mask editing, where wet cells are masked to land cells.

4.8.11.4 Interpolating Bathymetry:

Clicking the 'calculate bathymetry' button will send a request to the server to regenerate all bathymetry values for the non-masked cells. Once the server request happens, the cells are output into two text files, the cell definitions as defined by GRIDGEN (tmp.grd), and a masking file constructed from the cell attributes (tmp.msk).

Currently the bathymetry data is provided through a single netCDF file representing depth for the oceanic region. This file is too large to use with the bathymetry interpolation routine (GRIDBATHY), so a bounding box for the cells is calculated and used to produce a subset of the full netCDF file. This smaller file is then converted into an ascii representation usable by GRIDBATHY (tmp.bty).

Finally, these files are passed to GRIDBATHY with the following options:

```
gridbathy -a 1 -b tmp.bty -g tmp.grd -i CO -n 3 -m tmp.msk
```

Output is parsed and the new cell depths assigned to the appropriate cells. Again, GeoServer is not modified as only the cell attributes are changed. An example of the bathymetry interpolated onto the grid is provided in Fig. 4.8.24.

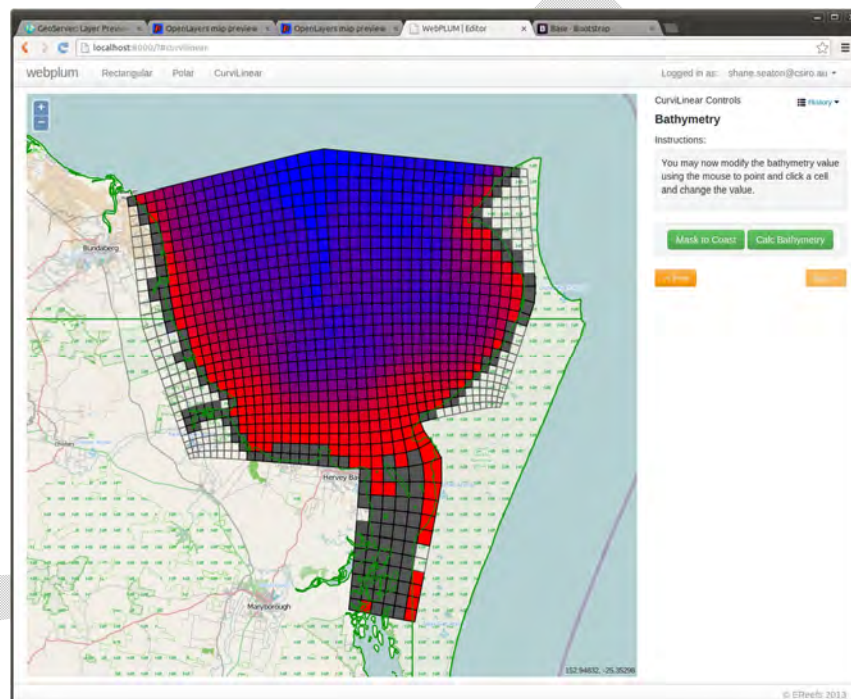


Figure 4.8.24. Example of bathymetry interpolated onto the grid.

The colour scheme used by the GeoServer WMS layer is an SLD (Style Layer Description) using variable substitution. This allows us to send through the min/max of the data (deepest/shallowest) and produce a colour scale to fit. In the future, this can also be used to allow the user to set their own min/max and associated colours.

Much like the masking, the bathymetry values can be manually edited via the web interface by click on cells and manually typing in the new values (Fig. 4.8.25). Future versions should provide more sophisticated ways of editing values by hand, either by specifying group modifications (increase all by 10%, decrease by 1m), or by allowing selection of cell via a bounding polygon.

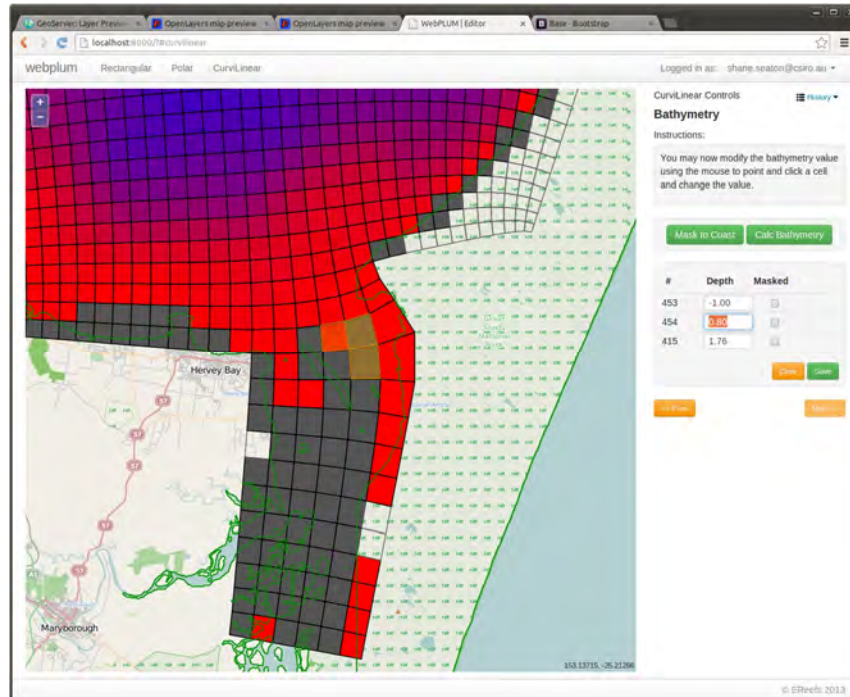


Figure 4.8.25. Example of edited bathymetry.

4.8.11.5. Output.

Webplum offers many download formats of the data it produces. For example, the following URL provides the final interpolated bathymetry in ascii format:

<http://webplum.csiro.au/webplum/grids/output/?id=11&dataset=bathy&format=asc>

Other dataset options available are:

- points : the original user grid points specification
- grid : single density grid points
- ddgrid : double density grid points
- mask : mask values of cell centres

An output format "shoc-bathy" is currently being developed that will generate the grid points and bathymetry data (including OUTSIDE/LAND masks) into a single file that can be directly inserted into a SHOC parameter file.

Webplum is also constructed using similar technologies (Django/Backbone) as the wizard style interface that is WebMarvl. As the WebMarvl interface is essentially a sequence of backbone views, integration of the Webplum backbone views should be a relatively straight forward process.

4.8.11.6 Technologies Used in the Development of Webplum

Client Side

- HTML, CSS (Less), Javascript
- Backbone
- Stickit
- Marrionette

- Openlayers
- Bootstrap

Server Side

- GeoDjango & Postgres/PostGIS
- GeoServer
- NCO Tools
- GRIDGEN, GRIDBATHY

4.8.11 ROBUST settings

RECOM is an automated system with little scope for user defined parameterisations. Within this context, there exists a balance between the accuracy of the model solutions and the robustness of a configuration with regards to model stability. Accuracy and robustness are generally mutually exclusive, and specific model parameterisation can be considered to lie on a robustness-accuracy spectrum (Herzfeld, 2009). RECOM included a set of ten predefined parameterisations that can be chosen using a 'robustness dial', where the higher the dial is set, the more robust and stable the hydrodynamic model will be at the expense of accuracy. This usually means that more friction is used to control instability, which has the effect of smearing fine structure from the solutions. The robustness settings are:

ROBUST=1:

- The model starts from rest,
- The k- ϵ mixing scheme is used,
- Smagorinsky horizontal diffusion is used with a constant of 0.1,
- The ULTIMATE QUICKEST tracer advection is used,
- No active alerts (i.e. constraint, Herzfeld, 2006b),
- Flux adjusted open boundaries using the default timescale,
- 1 bathymetry smoothing pass.

ROBUST=2: Same as ROBUST 1 above, constant viscosity, maximum bathymetric gradient = 0.05.

ROBUST=3: Same as ROBUST 1, active alerts, sponge zones on the boundary 8 cells wide ramping to 5 times the interior value, Van Leer tracer advection.

ROBUST=4: Same as ROBUST 3, constant viscosity.

ROBUST=5: Same as ROBUST 3, Mellor-Yamada 2.0 vertical mixing.

ROBUST=6: Same as ROBUST 5, starts using OceanMAPS velocity fields.

ROBUST=7: Same as ROBUST 5 with hard T/S ramp relaxation.

ROBUST=8: Same as ROBUST 7 with constant viscosity.

ROBUST=9: Same as ROBUST 6 with constant horizontal viscosity.

ROBUST=5: Same as ROBUST 5 with constant horizontal viscosity.

4.8.12 Two-way nesting

A coastal model requires information on its open boundaries (terrestrial and oceanic) for a successful simulation, and this is typically achieved by nesting within a larger scale regional model, where the larger scale model provides the information the coastal model needs without feedback (1-way nesting). This is the current approach in RECOM, however, 1-way approach has its limitations, especially in estuarine situations where the regional model rarely resolves the estuary upstream to beyond the tidal limit where fresh water can be input (i.e. input of water with salinity of zero). Usually this fresh water is input at the estuary mouth in the regional model, where in reality this water is brackish. For nutrient loads the situation is far worse, since estuaries are responsible for major processing of nutrients and what goes in at the head of the estuary is very different to what comes out at the mouth. Simply prescribing the concentrations applicable to the head at the location of the mouth is simply a bad approximation. A solution is to 2-way nest the coastal model into the regional model, so that terrestrial concentrations are delivered above the tidal limit in the highly resolved coastal model, and supplied as boundary conditions to the regional model at the location of the mouth. The regional model, in turn, supplies the oceanic open boundary information to the coastal model.

Tools exist to facilitate two-way nesting (e.g. AGRIF, Debreu et. al., 2008), however, these systems are complex and require some training and modification of the source code to implement. AGRIF acts as a coupler that controls the data transfer (via pointers), re-gridding and time synchronisation. It is our view that these coupler approaches are more complicated than is necessary, and a methodology that uses a push-pull data exchange for re-gridding and time synchronization and exploits existing OBC infrastructure in the code can accomplish two-way nesting in a far simpler manner. This approach is autonomous in the sense that each grid requires no knowledge of the other's attributes, and requires no over-arching coupler orchestration and code modification to implement. The added advantage of capitalizing on the non-reflective properties of certain OBCs minimizes specification issues at the dynamic interface which increases accuracy and stability. Currently we use the two way nesting with the open boundary condition of Herzfeld and Andrewartha (2012). Comparison of this implementation with conventional direct forcing is illustrated in Fig. 4.8.26, where NVOE and NVIE refer to the OBC stagger described in Herzfeld (2009). The autonomous approach will allow a 'plug-and-play' approach to including or omitting relocatable estuaries within the system, i.e. a new estuarine grid may be 'plugged in' to the regional model with no major reconfiguration of the system. This approach also allows a regional grid to 'plug out' an estuarine model if the model fails, and revert the open boundary to 1-way forced.

Most regional ocean codes, including SHOC, perform re-gridding of variables on output (i.e. variables can be dumped at specified latitude and longitude), on input (variables are interpolated onto the grid inline) or both. Therefore, re-gridding in two-way nesting may be performed by existing I/O routines in the code. Synchronisation in time must also exist, so that the coarse resolution model (regional model) will wait at the end of a time-step for the fine resolution model to catch up before supplying boundary data for the next time-step (an overview of two-way nesting can be found in Debreu and Blayo, 2008 and Debreu et al, 2012). In the autonomous nesting approach this is accomplished by sending a packet of information to a predetermined location in memory with a time stamp, t_{dump} , of when (in model time, t) that data was dumped (at intervals of Δt_{dump}) and a synchronisation time increment (Δt_{sync}) for which the data can be used. If the model time becomes greater than the $t_{dump} + \Delta t_{sync}$,

then the model will wait until a new packet of data arrives at the memory location. This simple synchronisation allows a great deal of control over the time refinement of the data exchange (see Fig. 4.8.27). It does, however, require some modification to the data input routines to enable the model to wait. These routines are contained in a generic library, hence are essentially model independent and accessible to any modelling platform. Additionally, these models are efficient, using data caching and buffering to perform temporal inline linear interpolation.

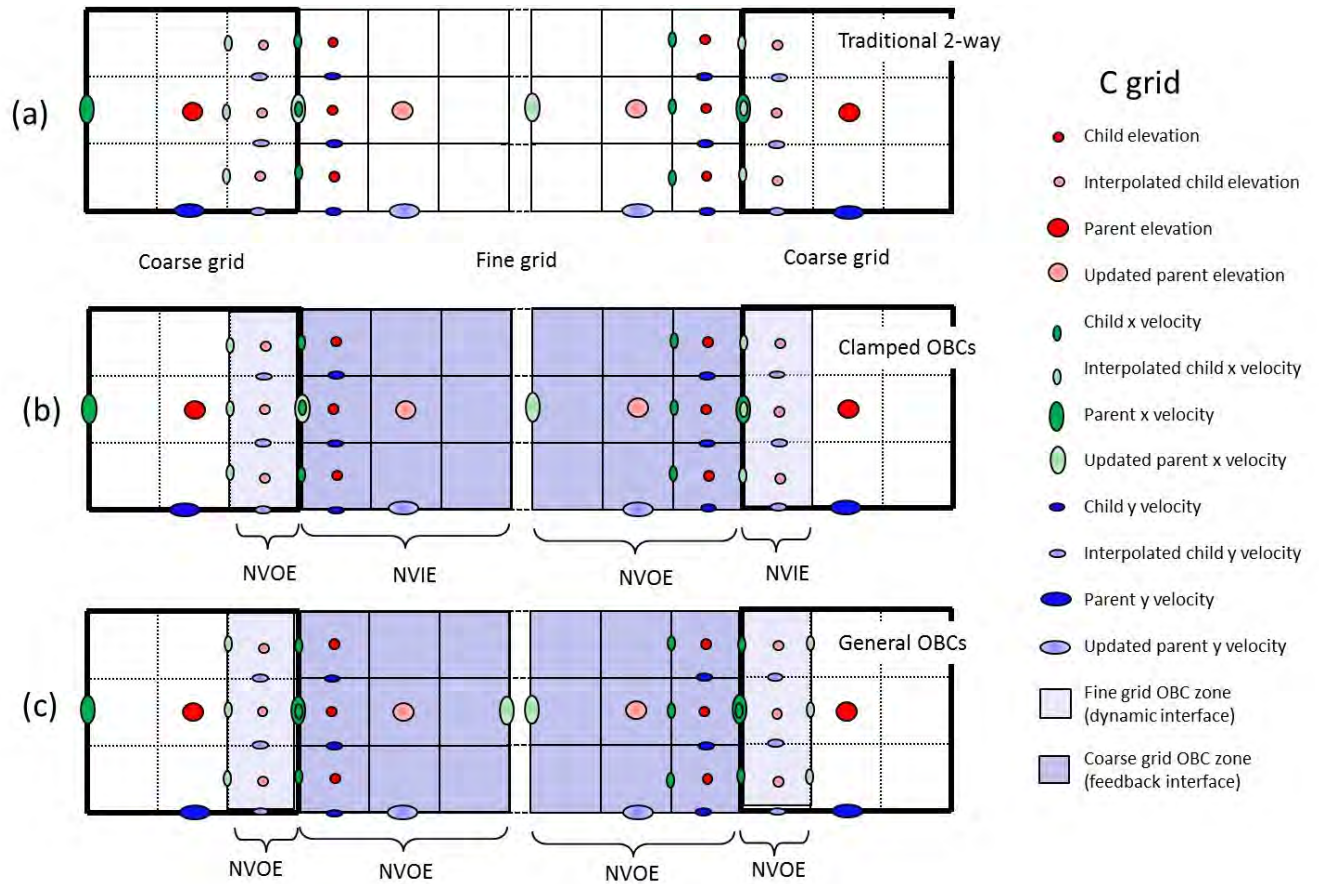


Figure 4.8.26. Open boundary configurations and implementation.

A manuscript describing the Fitzroy Estuary 2-way nested configuration and the nesting methodology is to be submitted to Ocean Modelling. The efficiency of data transfer will be improved in future using OpenMP protocols, and will be considered as the standard for data transfer using RECOM. However, at this time traditional 1-way nesting is the default in RECOM.

4.8.13 Waves

SWAN has been integrated into the RECOM workflow according to Fig. 4.8.29. The RECOM SWAN model run requires ASCII files for its forcing. After the hydrodynamic model run is finished it produces a `swan_forcing.nc` file from which sea level, currents and bathymetry are extracted in ASCII format for use in SWAN. Additionally, the hydrodynamic model also produces a `shoc_boundary.txt` which combined with the WWIII forcing file is used to create the various boundary files. Wind forcing comes from the same ACCESS forcing file as used in the hydrodynamic runs. RECOM creates a SWAN parameter file named `INPUT` which includes the paths to all of the required forcing files. The SWAN model produces ASCII output files which are then converted into netCDF format to be included in the SHOC BGC/Sediments transport model.

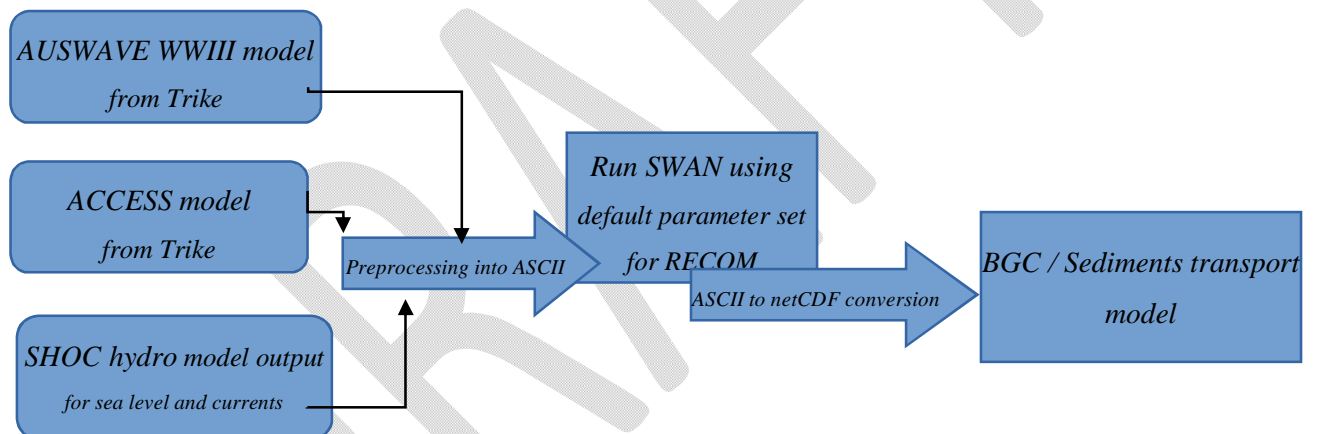


Figure 4.8.29. Workflow to include SWAN waves into RECOM.

4.8.14 RECOM workflow

The elements described above have been assembled into a coherent workflow that allows the user to initiate high resolution simulations with minimal user input via a graphical interface. The grid generation tool, Weplum (Section 4.8.11) has been integrated into the web based webTrike framework which supersedes the previous Java-based RECOM package. The Webtrike/Weplum based framework eases the constraint for users to install the application locally on their machines, exhibits a superior graphical interface and allows for plugins of layers such as model output in the future. This means RECOM is now able to run models using user defined curvilinear grids.

The steps that a user must navigate in order to produce a downscaled hydrodynamic, sediment transport and biogeochemical simulation nested within the GBR4 model (1-way nested at this stage) are:

1. Select RECOM from the list in webTrike,
2. Define the grid using the webPlum grid generation set of panels,
3. Select the time period to use and the forcing dataset to nest the RECOM model in,
4. Define the tracer attribute, parameter and process sets,
5. Schedule the run.

These steps are illustrated graphically using screenshots of the workflow. Here we define a simulation at the mouth of the Fitzroy river from 7 August 2014 for a 3 day simulation using a curvilinear grid. First we select RECOM from the list of available models in webTrike (Fig. 4.8.30). The grid generation workflow next follows that of webPlum (Fig. 4.8.31) exactly as described in section 4.8.11. The user is able to iterate over the steps of webPlum as needed. The final step of generating the bathymetry involves the specification of any river inflows. Freshwater inputs that may be included in RECOM are available from a drop down menu (Fig. 4.8.32) – the user selects the desired river and RECOM will find the cell in the grid closest to the geographic location of the gauging station used to specify that river's flow. Additional rivers not in the list may be uploaded if required. When the final grid has been generated with the appropriate masking and bathymetry applied, we click on the blue next button in the top right to advance to the next step in webTrike's workflow. Each step appears in its own tab within the web page and the user may either select the appropriate step directly by clicking on the tab for any modifications needed or use the Previous/Next buttons, at the top of the page to do so sequentially. The steps within webPlum are selected via orange Prev/Next buttons at the bottom of the right most column. Next we select the Local ocean and Global Atmosphere forcing, in this case we are nesting the model within the GBR4 regional model for ocean variables and ACCESS-R for winds (Fig. 4.8.33). The temporal extents of the forcing data are shown next to each dataset as a time bar. The user manipulates the time slider in the first row to select the period of interest. For any forcing data that falls within this period, a radio button appears next to it to indicate that it is valid and may be selected. Next, the predefined sets of hardwired parameter sets are defined for hydrodynamics, ecology and sediments (Fig. 4.8.34). This includes the BGC processes to invoke (Section 4.8.7) and sediment classes one wishes to use (Section 4.8.8). Note the BGC tracers used are inferred from interrogating the BGC processes, and this specification is therefore invisible to the user. Attributes for tracers (Section 4.8.4) and global parameter sets (Section 4.8.5) must also be defined. Once these sets have been specified, then the model is submitted to run (Fig. 4.8.35).

Once the run is submitted, the simulation can be comprehensively monitored using the webTRIKE interface. This includes an overview of runs submitted (name, time submitted etc.), run status (in-progress, finished, aborted etc.), time to completion, error and status messages, an overview of the grid used for each run (graphically and grid size etc.). From this view the simulation may be stopped, restarted or a new run may be spawned. Once initiated, the TRIKE workflow follows the flow of control shown in Fig. 4.8.1. When complete the workspace is available from downloaded from the "finished" button.

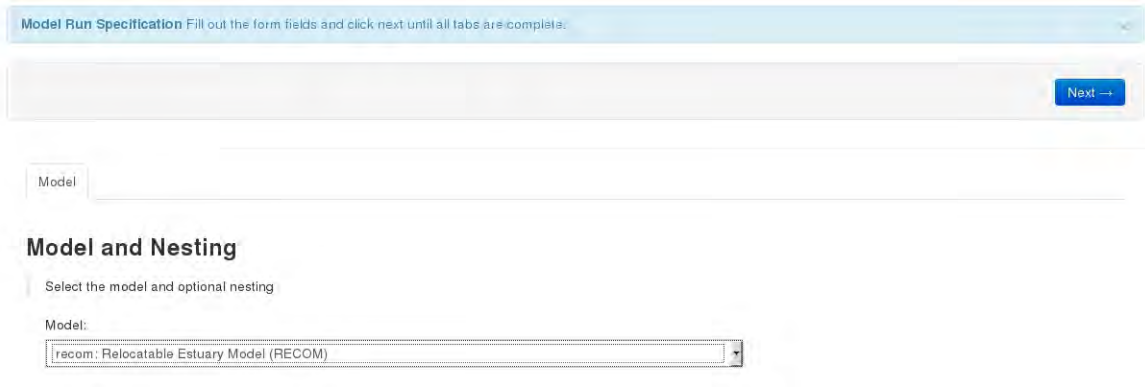


Figure 4.8.30. Screenshot showing model selection.

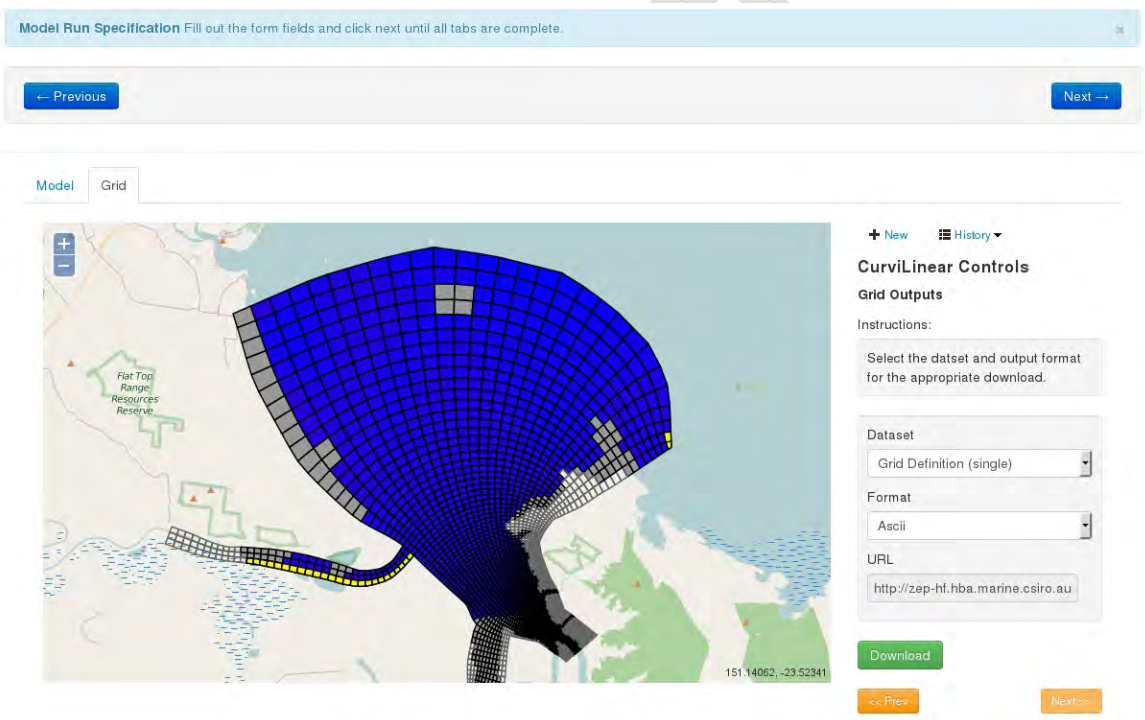


Figure 4.8.31. Screenshot of final grid and bathymetry from webPlum.

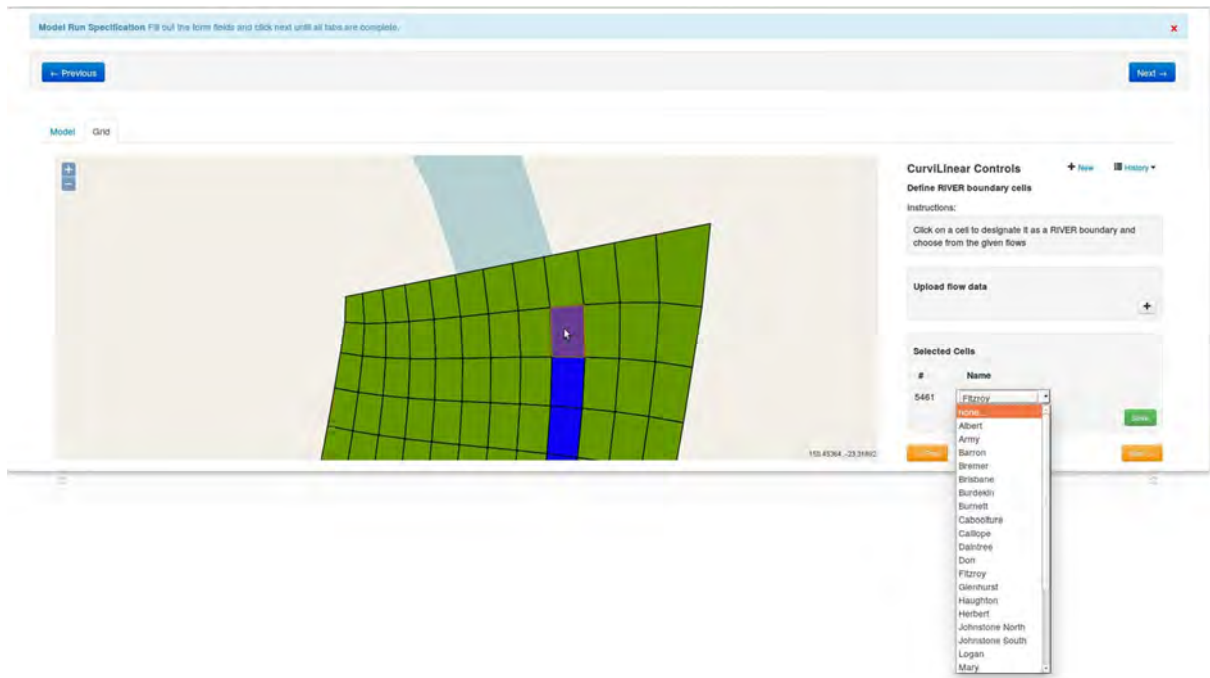


Figure 4.8.32. Screenshot of river specification.

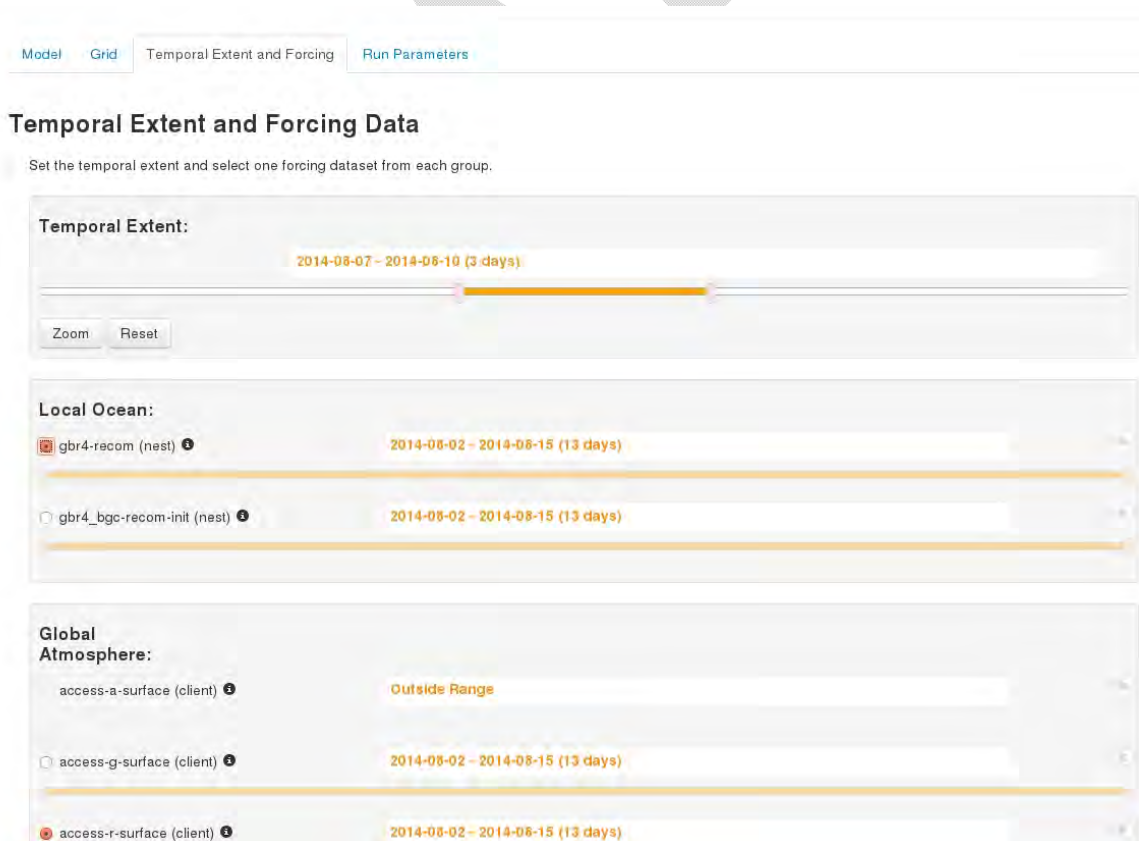


Figure 4.8.33: Screenshot of Temporal Extent and Forcing data selection.

Run Parameters

Set the parameters for the model.

undefined

BIOFNAME	gbr4
	Select Ecological processes
DO_ECOLOGY	YES
	Enable Ecology
DO_SEDIMENTS	YES
	Select Sediment transport
ECO_VARS_ATTS	standard
	Select Ecology parameterisation
PROCESSNAME	gbr4
	Select Ecological processes
ROBUST	
	Robustness Knob. Higher is more robust.
SED_LAYERS	0.005 0.02 0.08 0.32
	List of Sediment layer thicknesses
SED_VARS	Sand Mud FineSed
	List of Sediment types
SED_VARS_ATTS	standard
	Select Sediments parameterisation

Figure 4.8.34. Screenshot of RECOM parameters.

Model Run Specification Fill out the form fields and click next until all tabs are complete.

← Previous

Model Grid Temporal Extent and Forcing Submit

Submit

Run Name:

Model:

- recom

Grid:

- Type: geographic-rectangular
- Ni: 50
- Nj: 75
- X-Origin: 152.8
- Y-Origin: -26.16
- D-Lambda: 0.0225
- D-Phi: 0.0225
- Rotation: 23.5

Temporal Extent:

- Start: 2013-12-10 00:00 +00
- Duration: 22 days

Forcing:

Stream	Dataset	Variable Name	Description
global-atmos	access-r-surface	wind_u_wind_v	U direction wind speed

Submit Run

Figure 4.8.35. Screenshot of model submission.

ReCOM: Model Runs

New Delete Abort

Status Columns Select All Unselect All

10 model runs per page Search:

Run ID	Run Name	Model Name	Run Start	Run Stop	Model Start	Model Stop	Status
51	Fitzroy	recom	-	-	2011-10-27 00:00:00	2014-12-19 00:00:00	Initialising
49	test 7	recom	2014-12-10 04:28:07	2014-12-10 04:54:31	2014-08-04 00:00:00	2014-08-11 00:00:00	Finished
48	test 5	recom	2014-12-10 03:03:01	2014-12-10 03:18:16	2014-08-12 00:00:00	2014-08-17 00:00:00	Finished
47	test 44	recom	2014-12-09 07:08:04	2014-12-09 07:08:15	2014-08-03 00:00:00	2014-08-09 00:00:00	Finished
46	test 4	recom	2014-12-09 06:52:44	2014-12-09 06:52:55	2014-08-03 00:00:00	2014-08-09 00:00:00	Finished
45	test34	recom	2014-12-09 04:33:12	2014-12-09 04:33:22	2014-08-03 00:00:00	2014-08-06 00:00:00	Finished
44	test 33	recom	2014-12-09 04:18:08	2014-12-09 04:18:19	2014-08-07 00:00:00	2014-08-10 00:00:00	Finished
43	test 3	recom	2014-12-09 03:38:34	2014-12-09 03:38:45	2014-08-02 00:00:00	2014-08-05 00:00:00	Finished
42	numerical 3.2	recom	2014-12-05 06:23:55	2014-12-05 06:24:06	2014-08-05 00:00:00	2014-08-09 00:00:00	Finished
41	numerical 3.2	recom	2014-12-05 05:54:28	2014-12-05 05:54:40	2014-08-09 00:00:00	2014-08-12 00:00:00	Finished

Showing 1 to 10 of 48 model runs

← Previous 1 2 3 4 5 Next →

Figure 4.8.36. Screenshot showing list of model runs.

5. Validation

5.1. GBR4 Hydrodynamics

The GBR model is validated using data from the QIMOS node (<http://imos.org.au/httpimosorgauqimoshtml.html>), tide gauges operated by the Queensland Government (<http://www.msq.qld.gov.au/tides.aspx>), Waverider buoys operated by the Queensland Government Department of Environment and Resource Management (<http://www.ehp.qld.gov.au/coastal/monitoring/waves/index.php>) and Argo floats (<http://imos.org.au/argo.html>). An array of delayed mode IMOS moorings (Fig. 5.1.1) on the slope (4 moorings) and shelf (6 moorings) provides spatial coverage from Lizard Island to the Capricorn Bunker Group, and provides time series of water column current profiles, and temperature and salinity at a number of fixed depths on each mooring. A number of these moorings are also augmented with turbidity, chlorophyll and dissolved oxygen sensors (http://data.aims.gov.au/gbroos_moorings/mooringspages/index.html). Sea-level is also monitored in delayed mode at the mooring sites and at a number of offshore reefs. These data are retrieved at ~6 monthly intervals. Outside of QIMOS, AIMS maintains a sea temperature monitoring program with temperature loggers deployed at locations spanning the shelf for the full north-south extent of the GBR. These loggers operate in delayed mode and data are retrieved annually. The delayed mode data is suitable for validating hindcast simulations of the GBR 1km and 4km models. The combination of these data streams allow the hydrodynamic model archive to be validated.

The IMOS National Reference Station (NRS) at the Yongala site (central GBR) provides near-real time observations of temperature, salinity water level, turbidity, chlorophyll and dissolved oxygen at 2 fixed depths near the surface and above the seabed. Water column current profiles and surface waves are also observed at this NRS site and will be transmitted in near-real time in the near future. QIMOS has recently extended near real-time capability to a site at Stradbroke Island, which delivers data at several depths suitable for validation. Near real-time In addition, coastal radar deployed at Tannum Sands and Lady Elliot Island in the southern GBR provides observations of surface currents and wave height and direction in the inner and mid-shelf regions of the southern GBR, including the Capricorn Channel. In collaboration with IMOS, eReefs is extending near real-time capability in the GBR by augmenting the Palm Passage delayed mode mooring with telemetry and deploying a series of gliders in the southern GBR. Tide gauges, Waverider buoy and Argo float data (Figs. 5.1.2 – 5.1.4) also deliver sea surface height, temperature and salinity data in near real-time suitable for validation of the near real-time models (e.g. <http://www.emg.cmar.csiro.au/www/en/emg/projects/eReefs/Results/4km-Near-Real-Time/Time-Series.html>). Note that the Argo floats are not tethered hence their position changes in time. AIMS also maintains a network of offshore automatic weather stations on islands and reefs from Lizard Island to One Tree Island, which transmit in near-real time. These observations will supplement the modelled products used for model forcing. The combination of these data form the basis of model calibration (delayed mode) and data assimilation (near-real time). A summary of the various data streams available for model calibration is provided in Table 5.1.1.

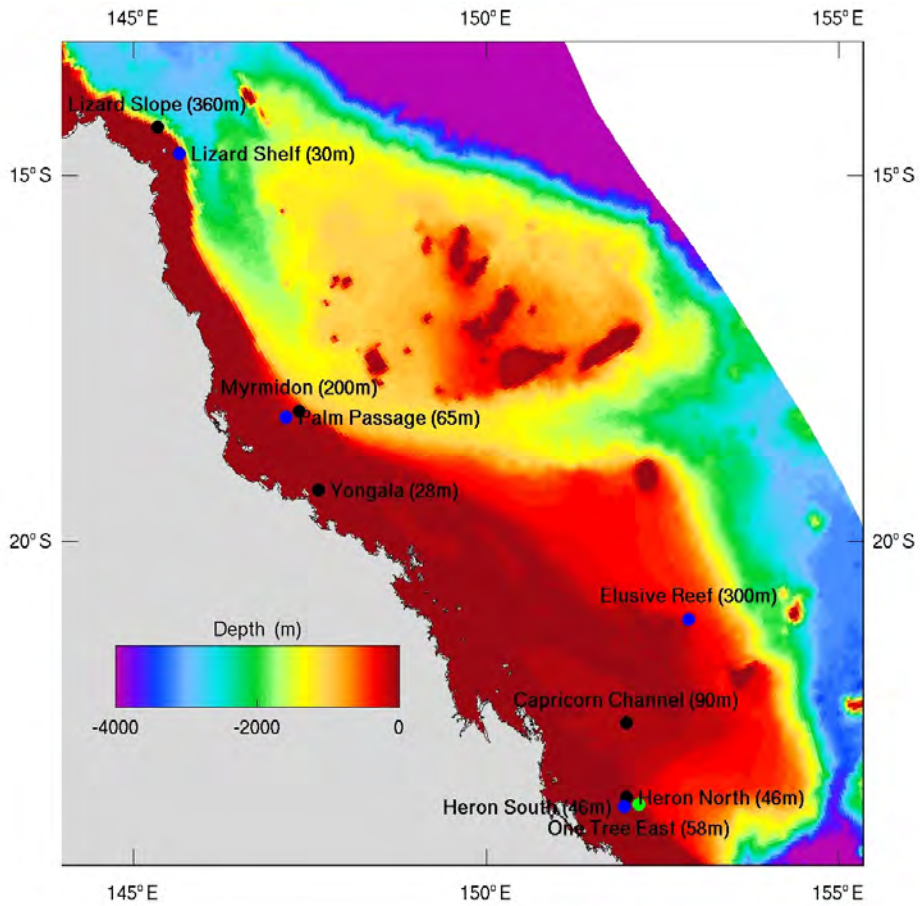


Figure 5.1.1. GBR IMOS delayed mode comparison sites.

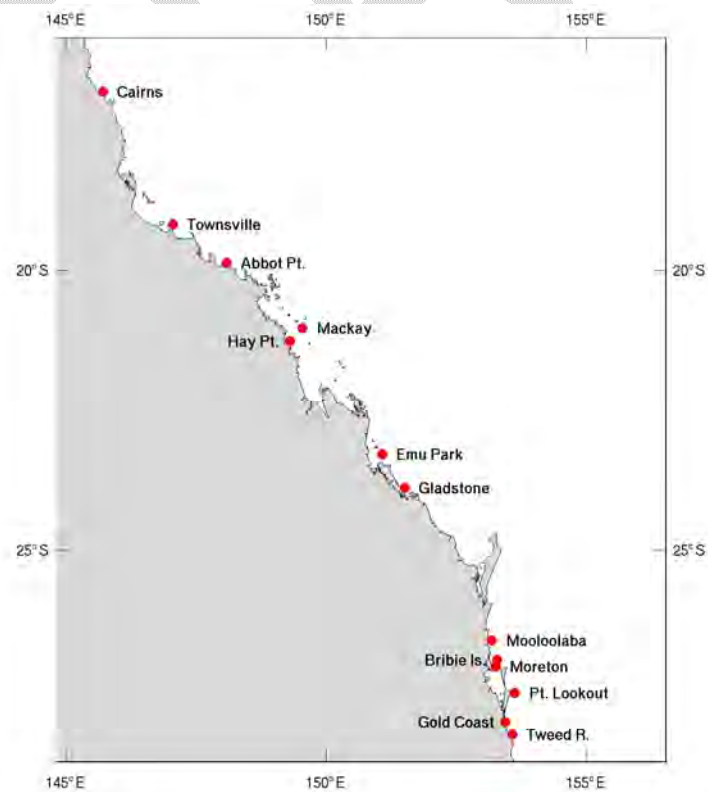


Figure 5.1.2. GBR wave-rider buoy comparison sites.

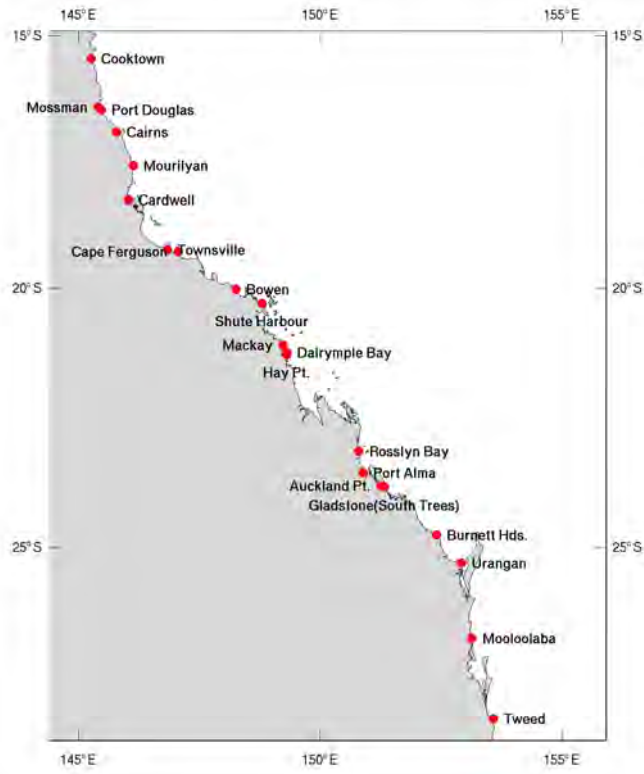


Figure 5.1.3. GBR tide gauge comparison sites.

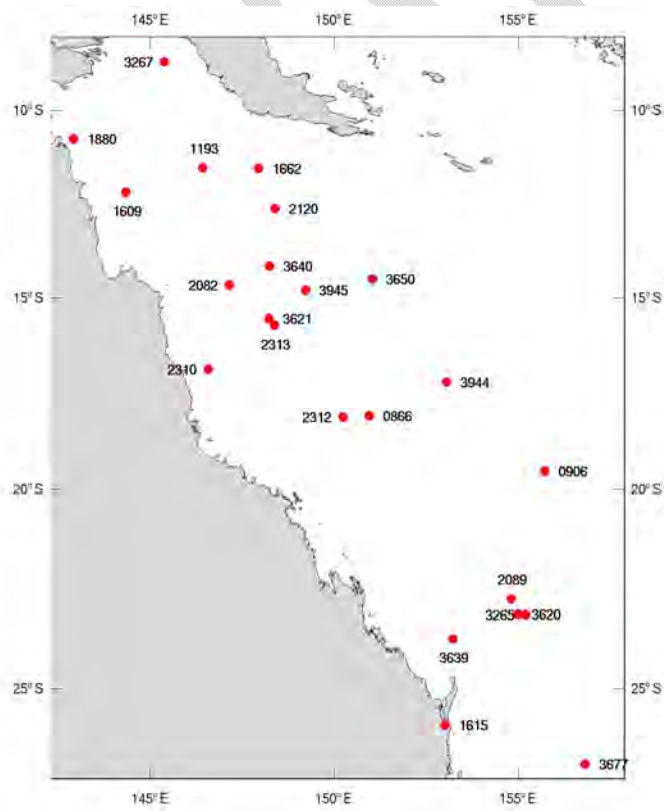


Figure 5.1.3. GBR Argo locations on 24/11/2012.

Table 5.1.1. Model validation data summary

	Real-time	Temperature	Salinity	SSH	Velocity
IMOS delayed		x	x	x	x
Waverider	x	x			
Tide Gauge	x			x	
Argo	x	x	x		

5.1.1 Calibration

Validation of the 4km hydrodynamic model to QIMOS observations is ongoing; solutions from the optimum configuration are presented below. The model configuration used is summarised in Table 5.1.2. Note that this configuration achieves the best comparison to observations across all variables, and alternative configurations may improve one variable at the expense of others. Model skill is quantitatively assessed using root-mean-square error (RMSE), correlation coefficient (cc), bias, mean absolute error (MAE) and the skill metric of Willmott et al. (1985); all these metrics are included in the figures below.

Temperature solutions compare well with delayed mode observations at the surface (Fig. 5.1.4), capturing the seasonal cycle, perturbations at synoptic frequencies and to some extent the diurnal cycle. At depth the temperature exhibits a cool bias (e.g. Myrmidon, 100 m); this is likely a consequence of initial and boundary condition forcing and will be investigated by improving the forcing using data assimilation (Section 4.3.3). At depth the data show large diurnal oscillations of up to 5°C due to internal tides (reference)(e.g. Elusive, > 190m); the resolution of the model is far too coarse to capture these events (resolution of 100s of metres is required), consequently these signals are absent in the model solutions.

Table 5.1.2. Optimum calibration configuration summary.

Parameter	Value
Turbulence closure	k-ε
Background vertical viscosity	$1 \times 10^{-4} \text{ m}^2 \text{ s}^{-1}$
Background vertical diffusivity	$1 \times 10^{-5} \text{ m}^2 \text{ s}^{-1}$
Horizontal viscosity	Smagorinsky, c=0.1
Horizontal diffusivity	Smagorinsky, c=0.1
Horizontal advection	ULTIMATE QUICKEST
Time steps (3D/2D)	90 / 5 s
Bulk scheme	Kondo (1975)
Short wave attenuation	Spatially variable
Short wave transmission	Spatially variable
Short wave bottom absorption	Spatially variable
Open boundary scheme	Herzfeld & Andrewartha (2012)
Boundary relaxation timescale	Dual: 6s / default
Salinity input	Conservative: Flow dependent (Eq. 4.1)

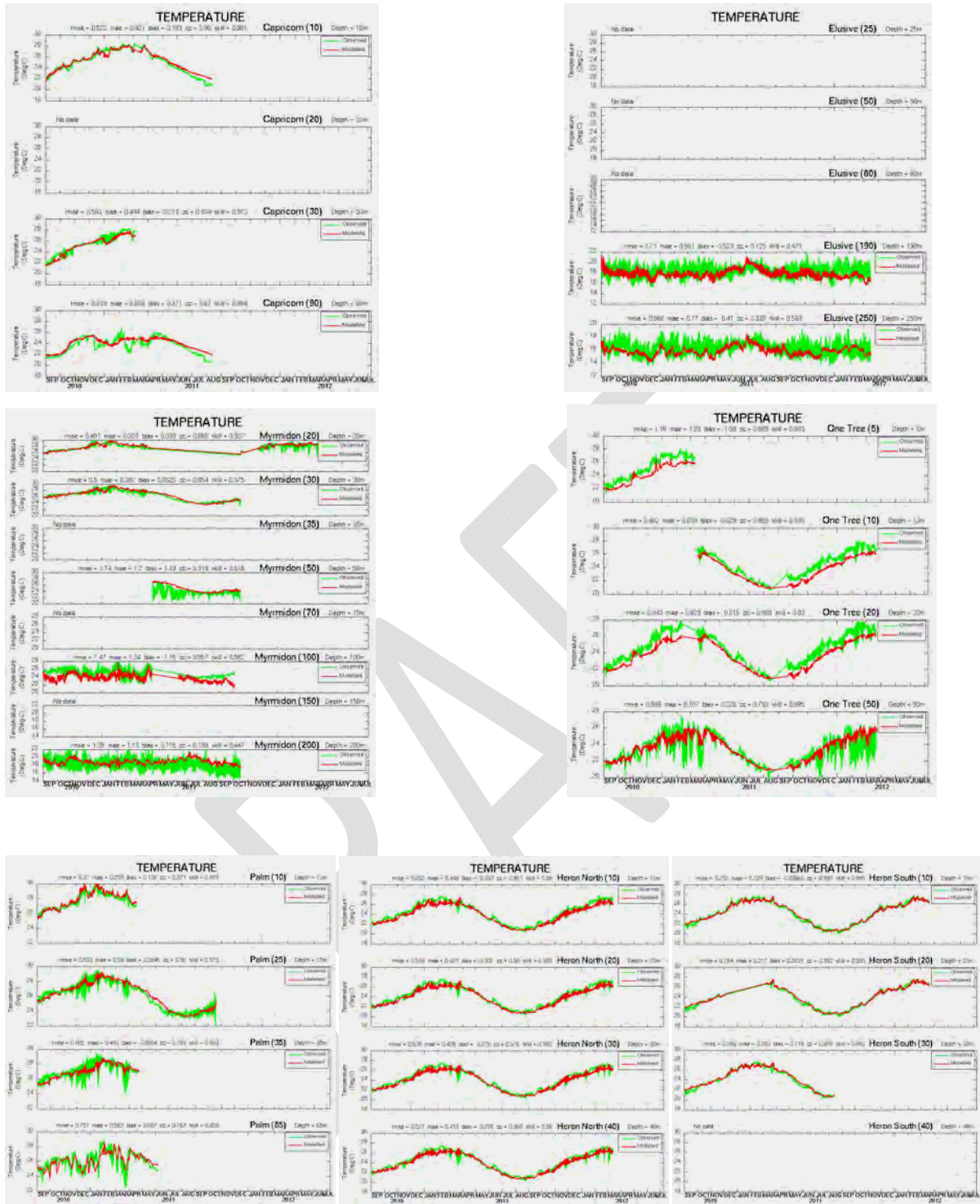


Figure 5.1.4. Temperature comparison with delayed mode QIMOS moorings.

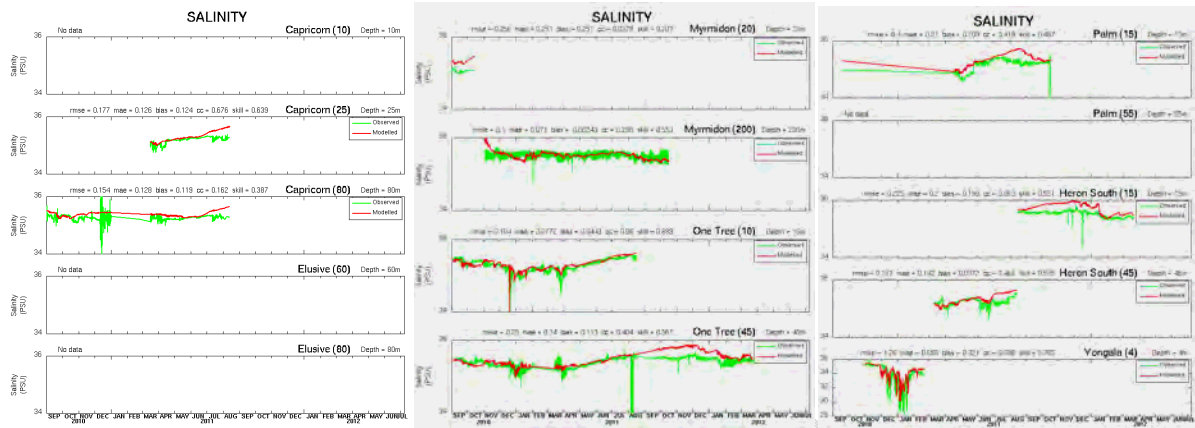


Figure 5.1.5. Salinity comparison with delayed mode QIMOS moorings.

Temperature exhibits a cool bias at the surface across all sites. The spatially variable short wave parameters were generated using EnKF data assimilation (Section 4.3), where the model was parameterised using an earlier configuration than the optimized configuration presented here. Updated shortwave parameters are currently being generated using the optimum configuration, and it is expected this will address the surface temperature bias.

Few sites are available for salinity comparisons; although the coverage of observations could certainly be improved, the lack of data is primarily a consequence of poor data return from the moorings rather than poor coverage. Given this sparse data, Fig. 5.1.5 shows the salinity response does capture mesoscale variability and decreases at the surface due to flow events (One Tree), although observations show larger flow event decreases than the model. This is likely a consequence of the salinity regression biased to low flow (Fig. 4.1.8), where even for high flow events salinity does not approach zero (e.g. ~ 13 psu for $5000 \text{ m}^3\text{s}^{-1}$). A dynamic flow response is under development that addresses several issues encountered when simulating freshwater plumes, and is anticipated to improve the response in this regard. Salinity also exhibits a fresh bias throughout at depth (Myrmidon, 200m). Similar to temperature, this bias may be due to errors in the initial and boundary conditions and will be attempted to be rectified using data assimilation on initial and boundary conditions.

The dual relaxation scheme provides high skill for the tidal response (Fig. 5.1.6). Both the tidal amplitude, phase and neap spring progression is well captured over the latitude range of the model.

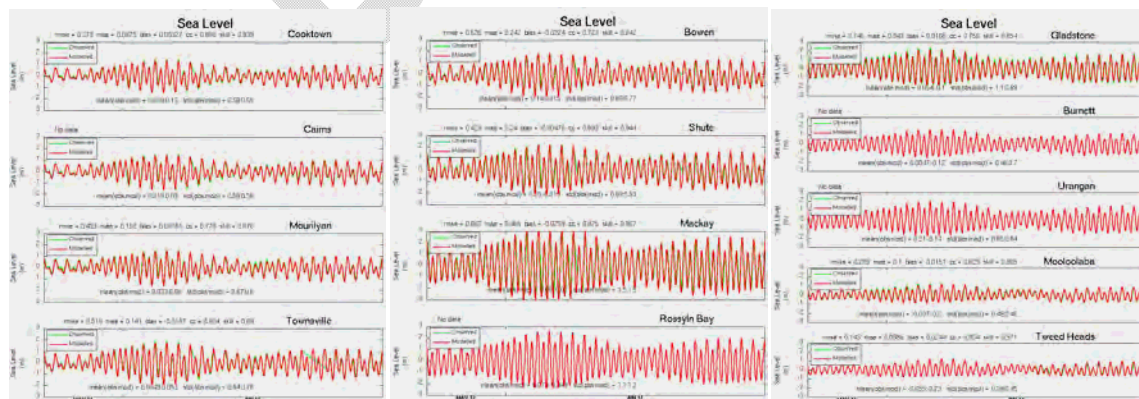


Figure 5.1.6. Sea level comparison with tide gauges.

The low frequency sea level response is indicative of net transport in the domain (as opposed to the tide which is periodic and usually associated with little mean flow) and in the GBR lagoon is largely driven locally by wind stress (Burrage et al, 1991, Brinkman et al, 2002). The low frequency response is assessed by low pass filtering sea level from observation and model (Fig. 5.1.7). Low frequency sea level has generally small amplitude (< 0.25 m), and the model captures the response with adequate skill (mean skill = 65%). This component proved quite sensitive to the open boundary specification (in this case relaxation time-scale) and forcing data (Section 5.1.7 and 5.1.8). The model could provide an improved response under different parameterization regimes, however, at the expense of deteriorating skill in other variables. In particular it is difficult to reconcile the tidal forcing (which requires quite hard boundary relaxation) with the low frequency forcing (which requires a much longer boundary relaxation), and the dual relaxation approach was developed to optimise this tension. However, as will be demonstrated below, there are alternative parameterizations that can improve the low frequency model skill in isolation.

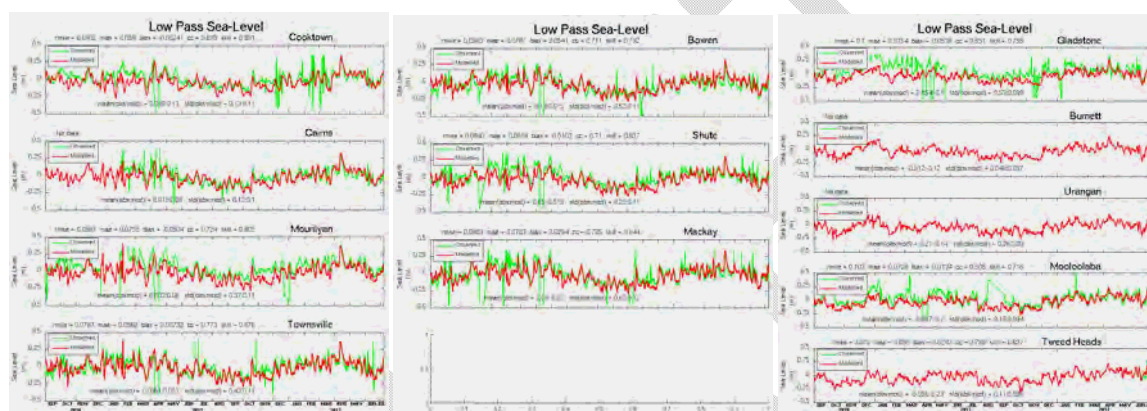


Figure 5.1.7. Low frequency sea level comparison.

The mean model skill across all sites for each variable is listed in Table 5.1.3. Some of these metrics in isolation must be treated with caution for the usual reasons; e.g. for a periodic solution a small error in phase can manifest as a large error in amplitude.

Table 5.1.3. Mean model calibration skill across all sites.

Variable	RMSE	MAE	cc	bias	skill
temp	0.76 °C	0.60 °C	0.81	-0.12 °C	0.86
salt	0.31 psu	0.20 psu	0.49	0.15 psu	0.56
η	0.48	0.21	0.83	-0.005	0.90
η_{low}	0.09	0.07	0.69	-0.002	0.81

5.1.2 Cyclone Yasi

The performance of the model under extreme forcing is examined during the passage of Tropical Cyclone Yasi. This cyclone made landfall in northern Queensland, Australia on 3rd February 2011. It was the most powerful tropical cyclone to cross the Australian coast in a century. As the system moved south-westwards towards the Australian coast, it passed near the QIMOS infrastructure located near the continental shelf break northeast of Townsville

(Fig. 5.1.8). This provided the opportunity to compare the observations of this extreme event with the 3D hydrodynamic model of the whole of the GBR (Fig. 5.1.9).

The IMOS mooring at Myrmidon Reef lies in 200m of water off-shore from the shelf edge of the central GBR, to the south of the path of TC Yasi. The mooring consists of an upward looking Acoustic Doppler Current Profiler at 195m depth, and temperature loggers at 7 locations throughout the water column (<http://data.aims.gov.au/imos-moorings/toc.html>). Vertical profiles of temperature and currents from the Myrmidon mooring were compared with results from the GBR 4km model for January to February 2011 (Figure 5.1.10). Concurrent time series from the observations and model reveal that there is general agreement in the non-tidal variability, particularly in temperature, over the full water column down to 200m. Of note is the observed short-term warming of the water column during TC Yasi, with temperatures at depths of between 160-180m increasing by $>5^{\circ}\text{C}$ during the passage of the cyclone. This response is reproduced by the model, giving confidence to its ability to accurately simulate extreme events. It should be noted that the results present here were produced using the original GBR4 model grid, and the grid has been refined subsequent to these simulations.



Figure 5.1.8. The path of Cyclone Yasi on its approach to northern Queensland and the locations of Myrmidon, Palm Passage and Yongala QIMOS Moorings

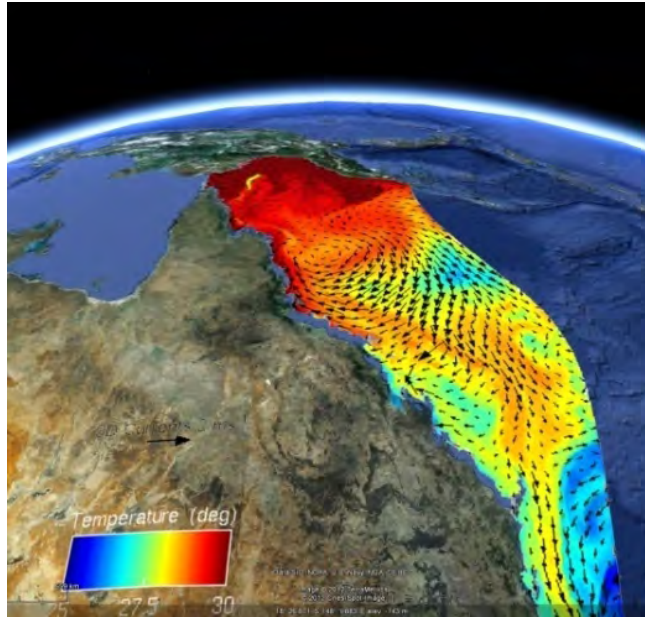


Figure 5.1.9. Snapshot of simulated surface velocity and temperature fields on 02 February 2011, as TC Yasi approached the QLD coast.

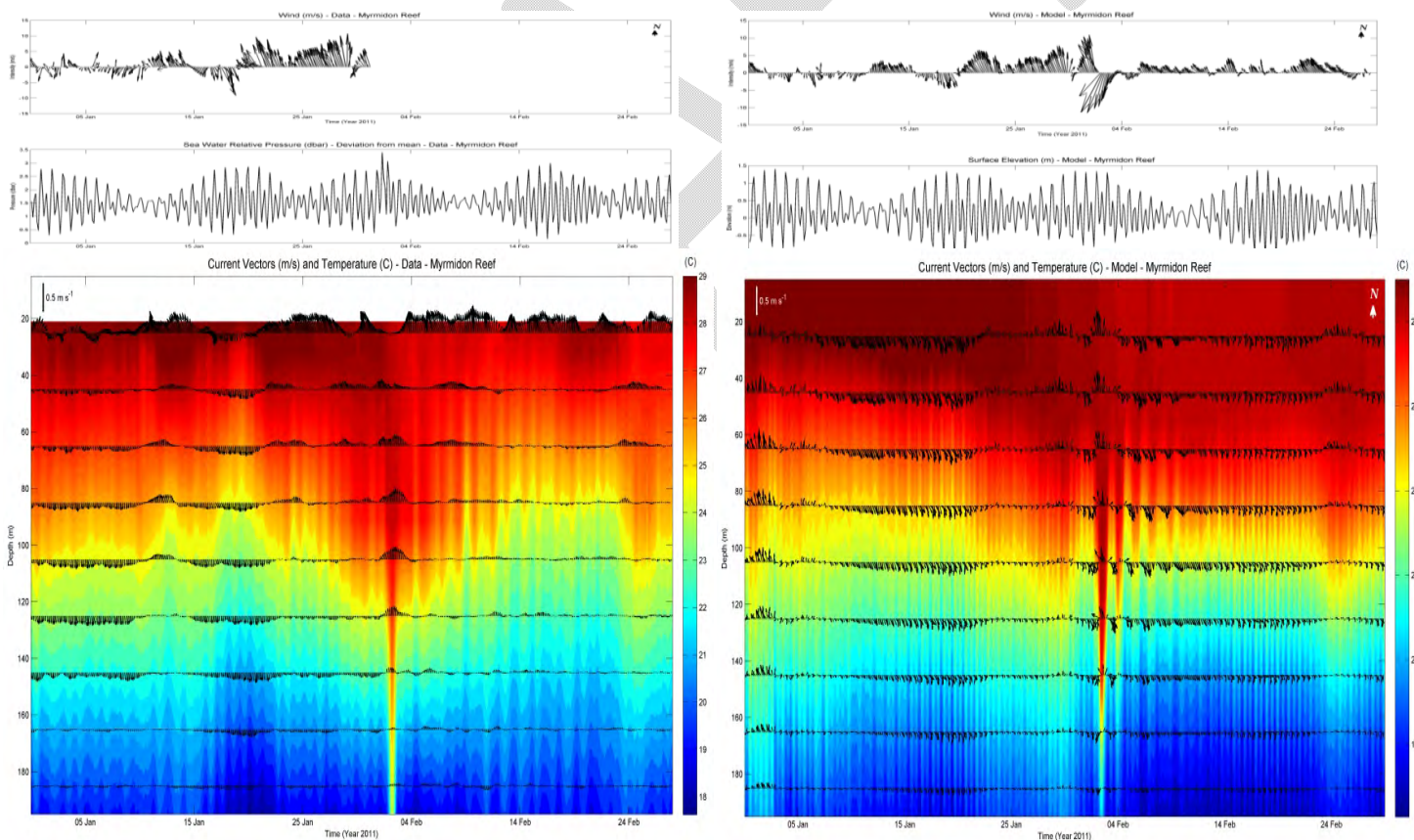


Figure 5.1.10. Time series of wind (top panel) , sea level (middle panel), temperature profiles and currents (bottom panel) from observations and model (shown left and right, respectively) for the period January to February, 2011. Current vectors are shown as black vectors with North directed up the page.

5.1.3 ARGO

Observations derived from ARGO floats can be used to assess the model performance at depth in NRT, although the quantity of these observations varies according to how many floats happen to drift into the region of interest. The distribution as of November 2012 is shown in Fig. 5.1.3. The temperature and salinity comparisons of OceanMAPS and GBR 4km with ARGO observations at selected sites is shown in Figs. 5.1.11 and 5.1.12 respectively. Comparison to ARGO observation is continuously updated in near real-time, and can be viewed at <http://www.emg.cmar.csiro.au/www/en/emg/projects/eReefs/Results/4km-Near-Real-Time/T-S-Profiles--Argo-.html>.

At some sites these comparisons exhibit the biases in the OceanMAPS data at depths 100 – 800m that are the suspected origin of biases evident in Figs. 5.1.4 and 5.1.5. The ARGO data will be particularly useful to constrain sub-surface temperature and salinity when generating analysis products through data assimilation.

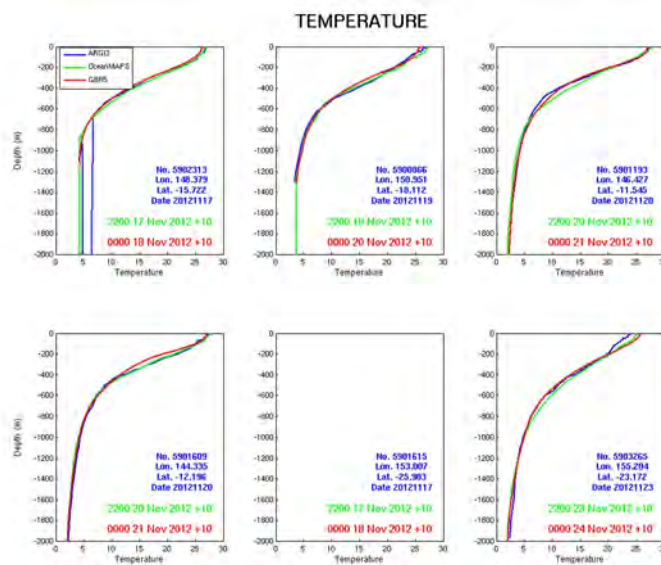


Figure 5.1.11. Temperature comparison with ARGO at selected sites.

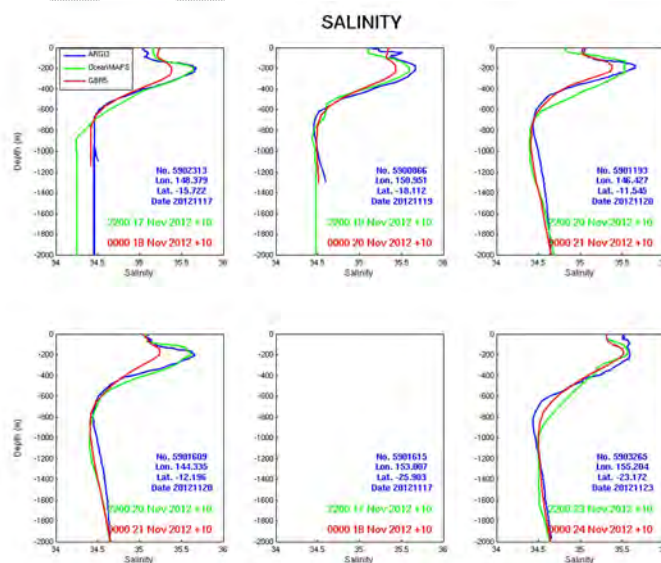


Figure 5.1.12. Salinity comparison with ARGO at selected sites.

5.1.4 Currents

Delayed mode and near real-time ADCP data are available at Yongala, Capricorn Channel and Heron Island South. Comparisons of current speed and direction for various time periods are displayed in Figs. 5.1.13-5.1.15. Current magnitude and direction at the tidal frequency is captured well by the model, as is the increase in speed during the spring tide. Currents are the most difficult variable to tune to observations, since local impacts (wind, bathymetry) not adequately resolved by the model may strongly influence the real flow. For this reason, not as much weight is applied to velocity comparisons as other variables; even so, the model captures the flow at the observation sites with high skill (mean skill ~ 82%).

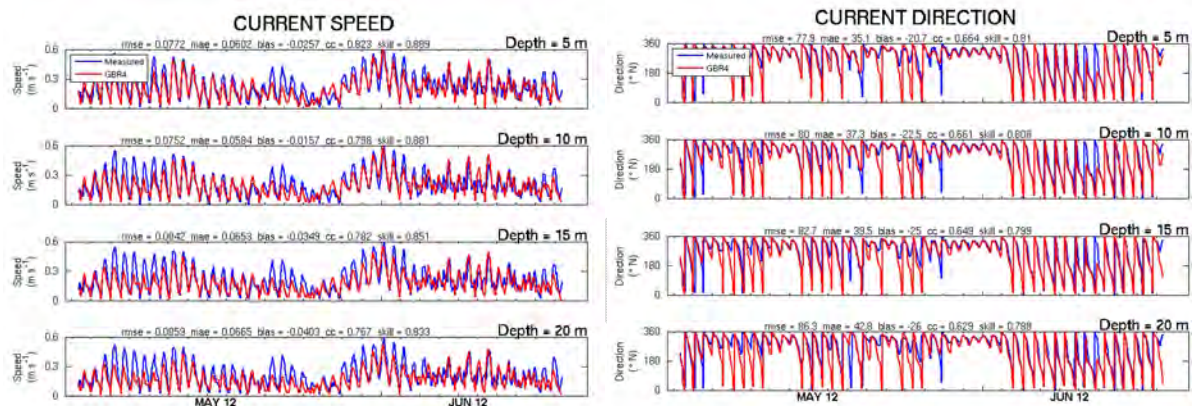


Fig. 5.1.13. Current speed and direction at Yongala.

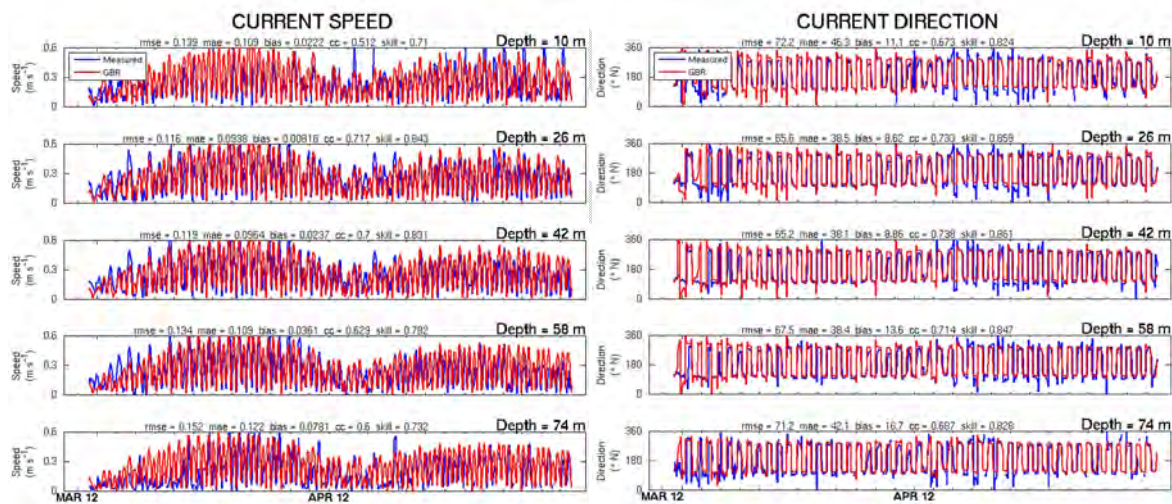


Fig. 5.1.14. Current speed and direction at Capricorn Channel.

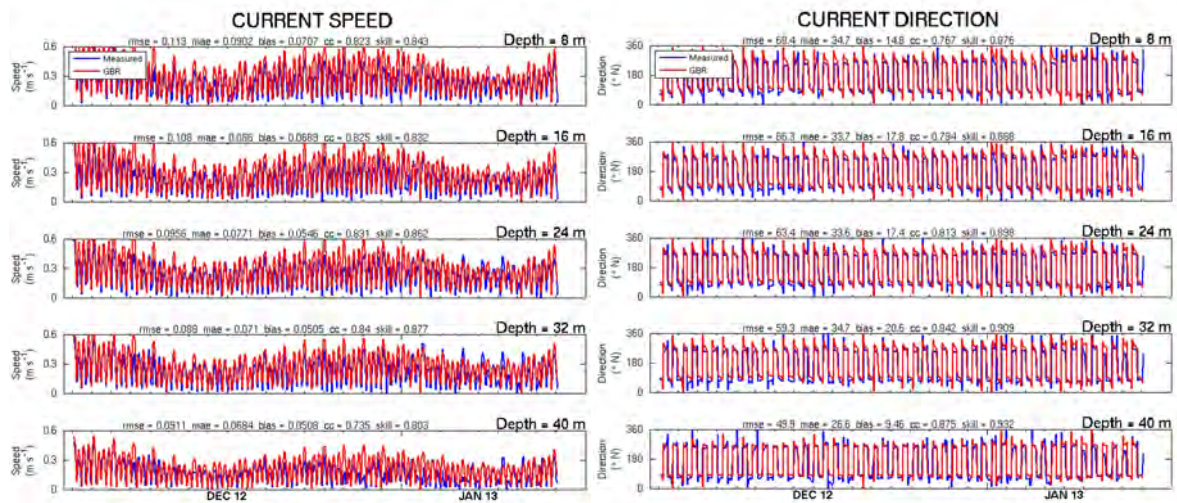


Fig. 5.1.15. Current speed and direction at Heron Island South.

The currents are low pass filtered to gauge the model response to residual flow. Comparisons are displayed in Fig. 16-18. The magnitude of these currents is generally comparable to observation, especially in the northern GBR (Yongala). In the southern GBR, while the magnitude is of the order of observations, not all events are captured accurately and there can be error in the current direction. Skill across all depths is equal to 83% and 87% for speed and direction respectively at Yongala, 45% and 44% at Capricorn Channel and 43% and 88% for Heron Island South. The model shows reasonable skill at reproducing the slowly varying flow fields at these locations.

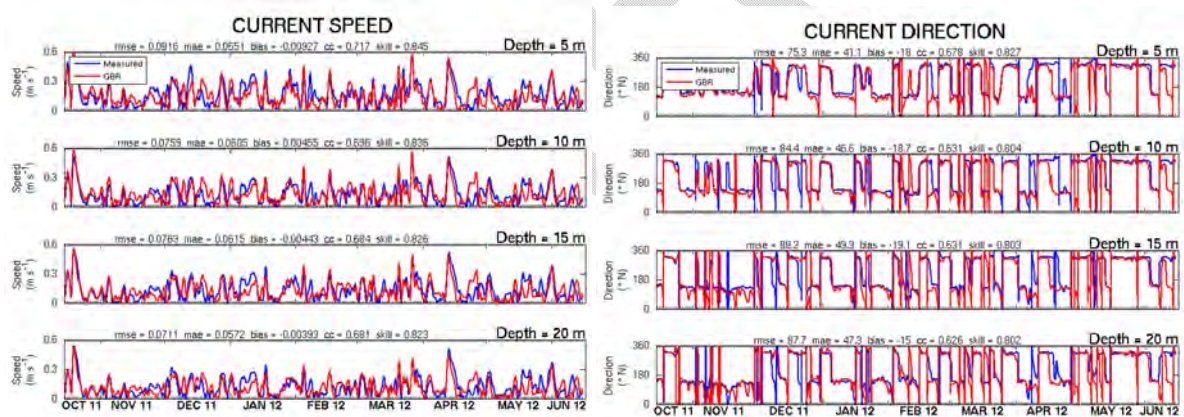


Fig. 5.1.16. Low frequency current speed and direction at Yongala.

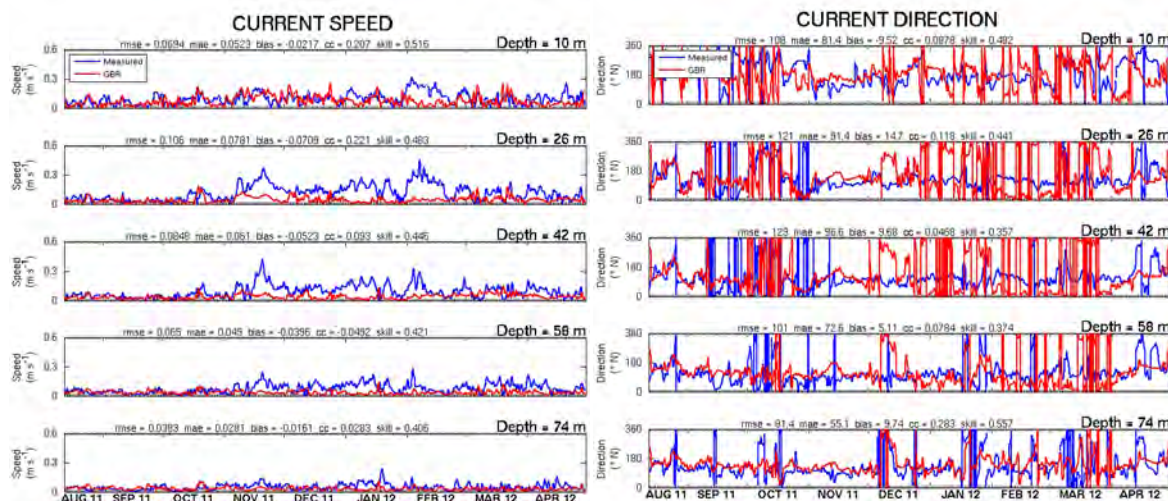


Fig. 5.1.17. Current speed and direction at Capricorn Channel.

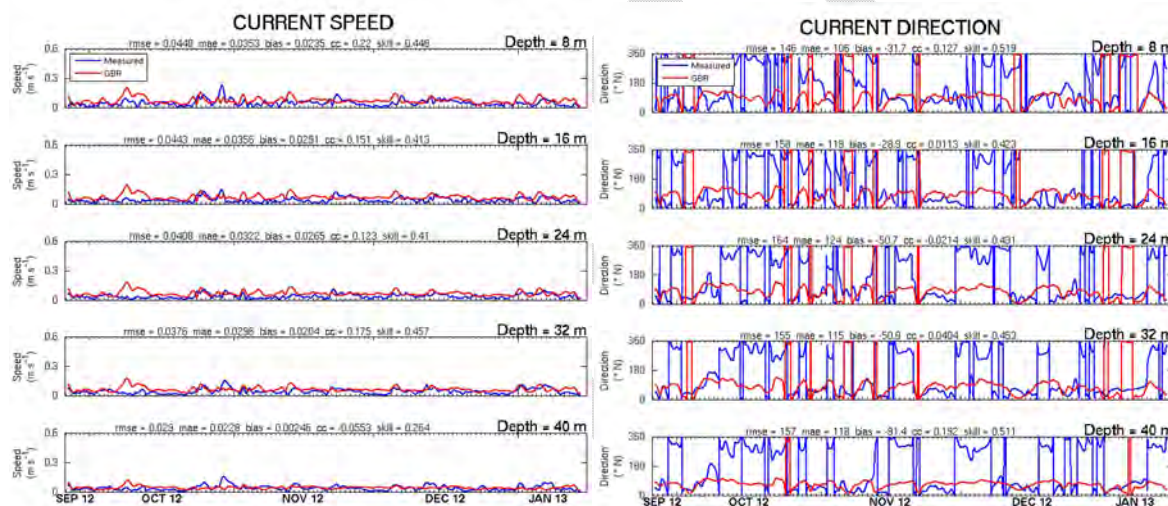


Fig. 5.1.18. Current speed and direction at Heron Island South.

5.1.5 GHRSSST

A comparison between the calibrated run and GHRSSST data over the whole of GBR region can be used to evaluate the performance of the model in the surface layer. To this end, a 2D histogram has been constructed where by data are binned and the frequency of a particular combination of observations vs. model are displayed. This analysis gives more insight than a typically scatter plot. Fig. 5.1.19 displays the results for a one year simulation that spans September 2010 - August 2011. As can be seen, there is a tendency for the model to underestimate the SST by between 0.5 and 1.0 degrees C during the wet season (November - April). However, at the onset of the dry season, the bias reduces to < 0.5 degrees C and most of the frequency mass lies within the standard error of the GHRSSST observations. In part this is related to the calibration period chosen for the SWR parameters. The Calibrated SWR parameters are conditioned on observations from April and May 2011. During this period we see the frequency cloud shift towards and envelope the 1:1 line between the model and observations. Compounding this, as previously noted, the parameter estimation routine is currently being rerun for the final hydrodynamic model configuration.

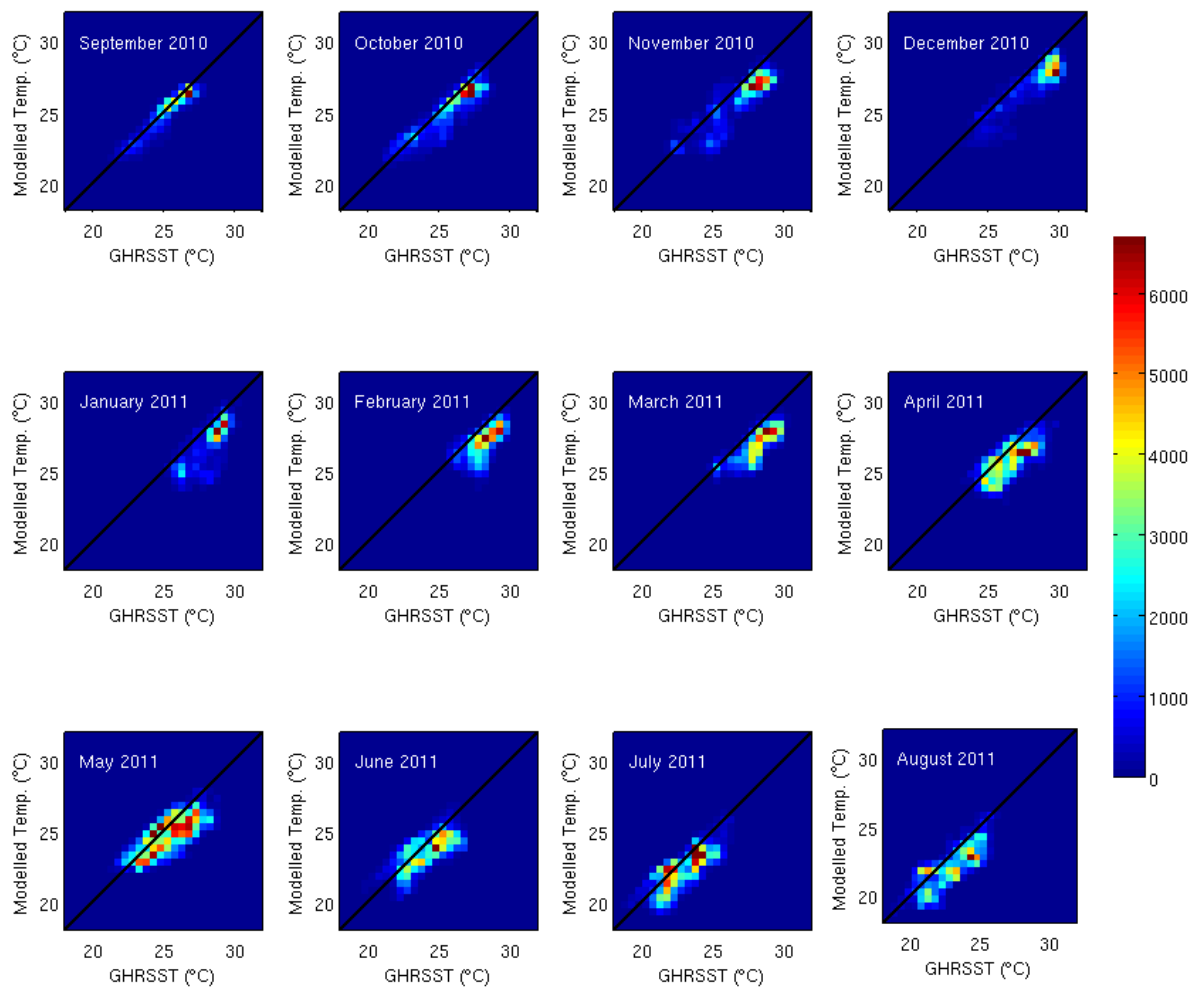


Figure 5.1.19: a 2D histogram of GHRSSST data vs model output for the GBR4 model during the period September 2010 - August 2011. The colour denotes the number of observations (frequency) of a particular combination of GHRSSST and Model output. Dark red denotes the highest mass. The black line denotes the 1:1 relationship between the GHRSSST and model output.

5.1.6 Validation

The model was validated by comparing solutions using the calibration configuration (Table 5.1.2) to independent observations collected from July 2012 to July 2013. These observations again come primarily from delayed mode QIMOS moorings, but also include archived near-real-time data from Waverider buoys, AIMS sensor networks and tide gauges along the GBR.

The temperature solutions continue to compare well to the delayed mode observations at the surface, capturing the seasonal cycle and synoptic scale fluctuations (Fig. 5.1.20). The diurnal temperature oscillations near the surface are less well captured. The observations from depth indicate a warm bias during this period, but the data are too limited to draw firm conclusions. The temperature simulation both at surface and at depth should be improved through the application of data assimilation. As noted in Section 5.1.1, internal wave activity at Elusive Reef and other locations leads to very high diurnal variability in deep water temperatures which we do not expect the 4 km model to reproduce.

Temperature solutions also compare well with observations from Waverider buoys deployed along the Queensland coast (Fig. 5.1.21), albeit with a warm bias of $\sim 1^{\circ}\text{C}$ at the northern sites. Interestingly, comparison to the IMOS data show a slight cool bias hence the warm bias must be restricted to inshore waters, likely due to the interaction of short wave penetration with the bathymetry. Some high frequency variability at Heron Island and One Tree Island is not captured, but these data are acquired from sensors deployed in shallow coral cay lagoons which are not resolved by the GBR4 model; the model is unable to reproduce the temperature variability in these extremely shallow pockets of water. Some abrupt changes in the observational records give the impression of marked discrepancies between the model and the observations either before or after the transition e.g. during September 2012 at Mackay, November 2012 at Hay Point and February 2013 at Tweed River. However, these observations are collected by the Queensland Government Department of Environment and Heritage Protection, and the data quality is uncertain, but must be treated as “unverified” (http://www.ehp.qld.gov.au/coastal/monitoring/wave_monitoring_disclaimer.html). Hence it is not clear whether the large discrepancies between the model and the observations (e.g. during February – June 2013 at Tweed River) are due to poor model performance or a calibration error in the observational sensor. We present the data here as an independent test of the model performance, with the caveat that the observations themselves must be treated with a degree of caution.

Salinity is predicted well in general by the model at the limited observational sites available (Fig. 5.22). As during the calibration period, mesoscale events are reproduced by the model e.g. the freshening at Heron South in January and February 2013. Otherwise, the model largely maintains its performance level over this extended validation period.

Modelling of the tides remains at very high skill levels during the validation period, due to the dual relaxation scheme. Skill levels are in excess of 0.8 at all tide gauge locations (Fig. 5.23. Note that a one month period only is presented for purposes of clarity). The amplitude and phase of the tide at all locations are accurately reproduced. Only at Cairns is there a minor discrepancy, when some of the low tides are not fully simulated.

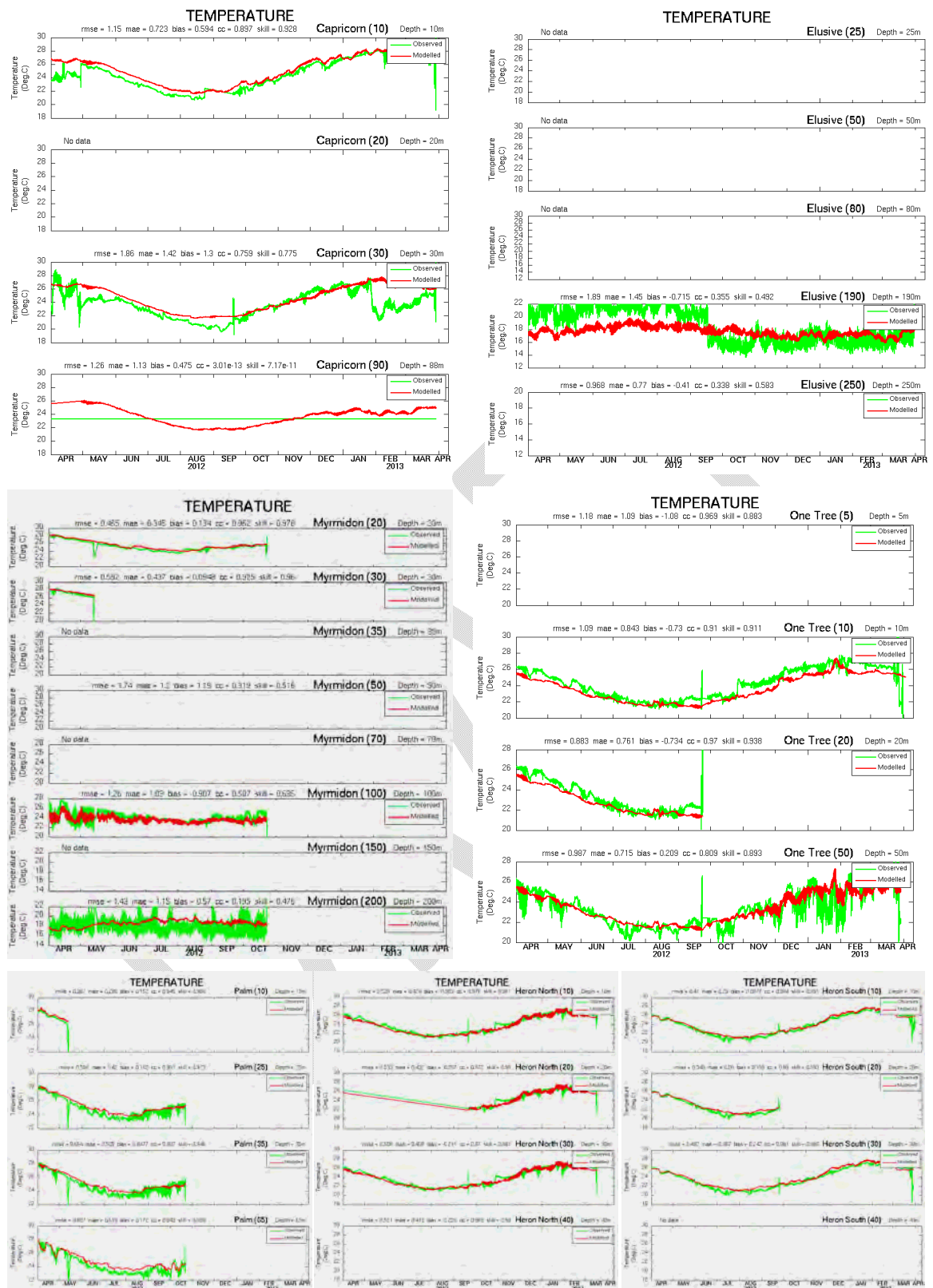


Figure 5.1.20. Temperature comparison with delayed mode QIMOS mooring data for 2012-13.

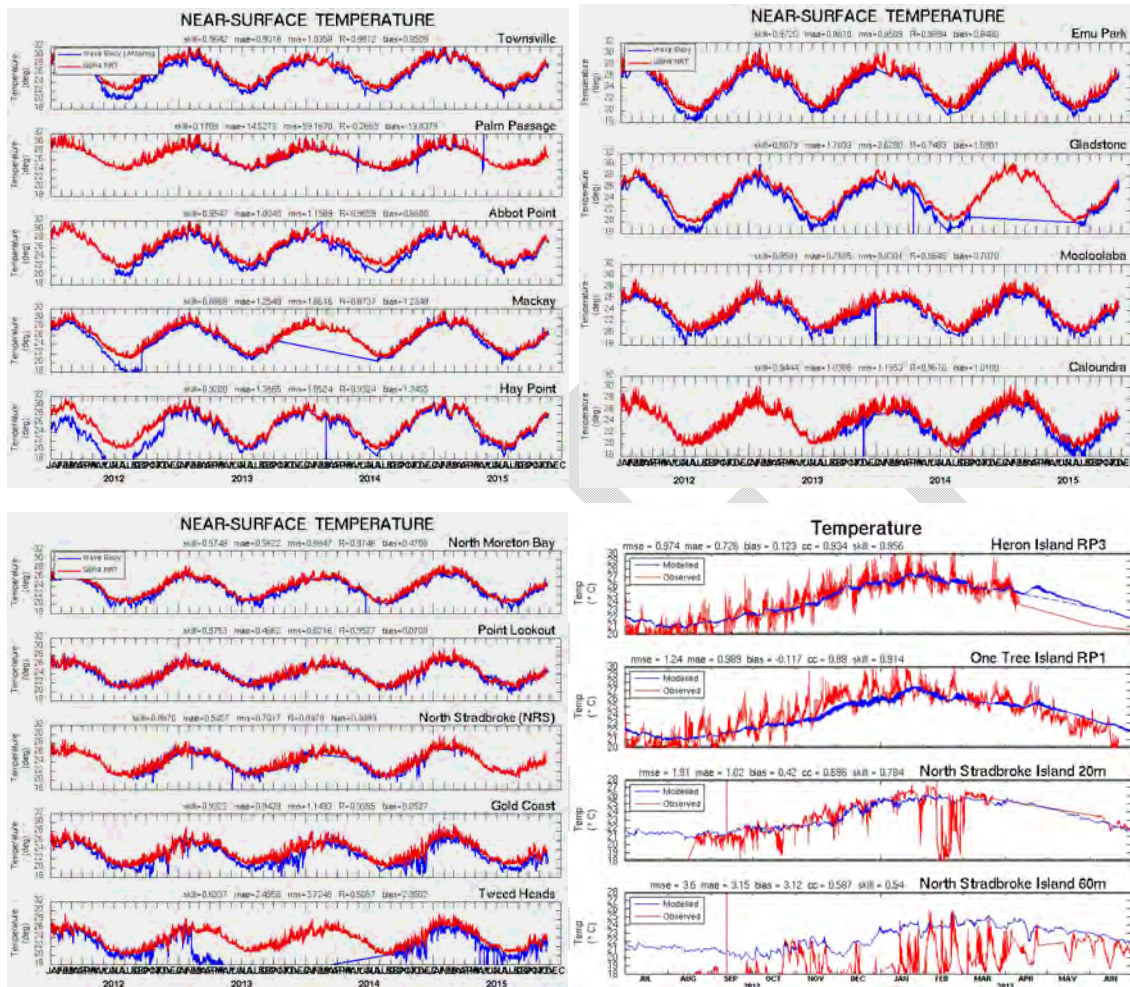


Figure 5.1.21. Temperature comparison with near-real-time sensors deployed on Waverider buoys and as part of the Heron Island and One Tree Island FAIMMS sensor network during 2012-13.

Overall, skill levels for the prediction of the low-frequency sea level response remained the same (mean skill = 79%) as for the calibration period (Fig. 5.1.24). The model therefore maintains performance levels over long simulation periods. In the northern part of the domain, from Cooktown to Gladstone, the model performs slightly better (skill = 74%) than the south (skill = 71%), however, this deterioration is minimal.

Mean skill metrics across all sites are summarized in Table 5.1.4; these are all comparable to the calibration metrics presented in Table 5.1.3.

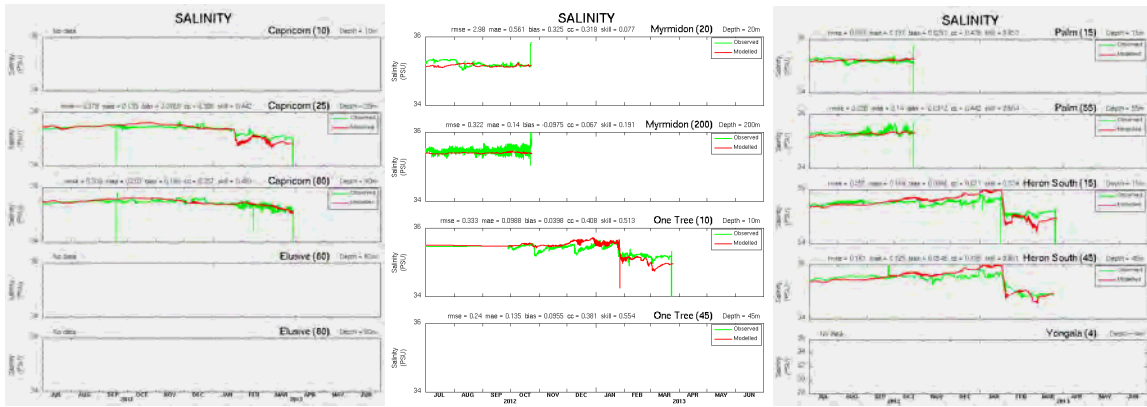


Figure 5.1.22. Salinity comparison with delayed mode QIMOS mooring data for 2012-13.

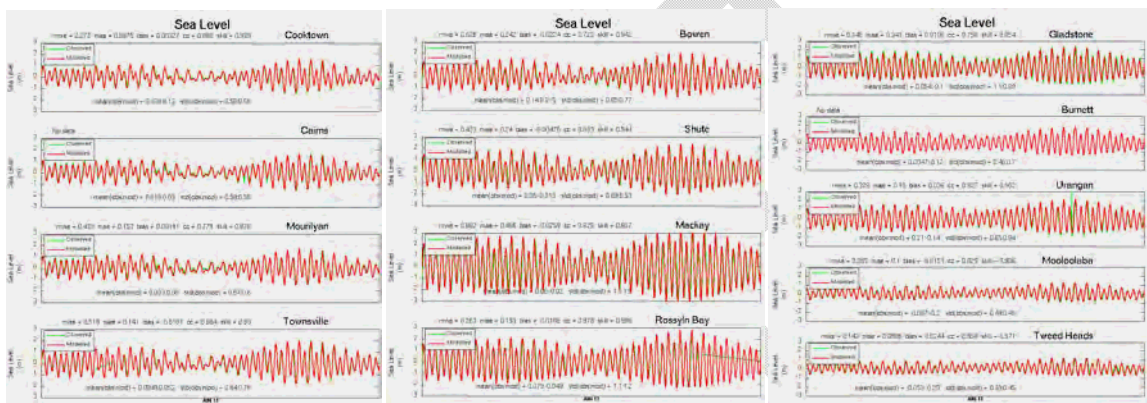


Figure 5.1.23. Sea level comparison with tide gauges for June 2013.

Table 5.1.4. Mean model validation skill across all sites.

Variable	RMSE	MAE	cc	bias	skill
temp	0.90 °C	0.70 °C	0.78	-0.003 °C	0.83
salt	0.57 psu	0.19 psu	0.42	0.08 psu	0.51
η	0.45	0.20	0.85	-0.002	0.92
η_{low}	0.09	0.07	0.69	0.007	0.79

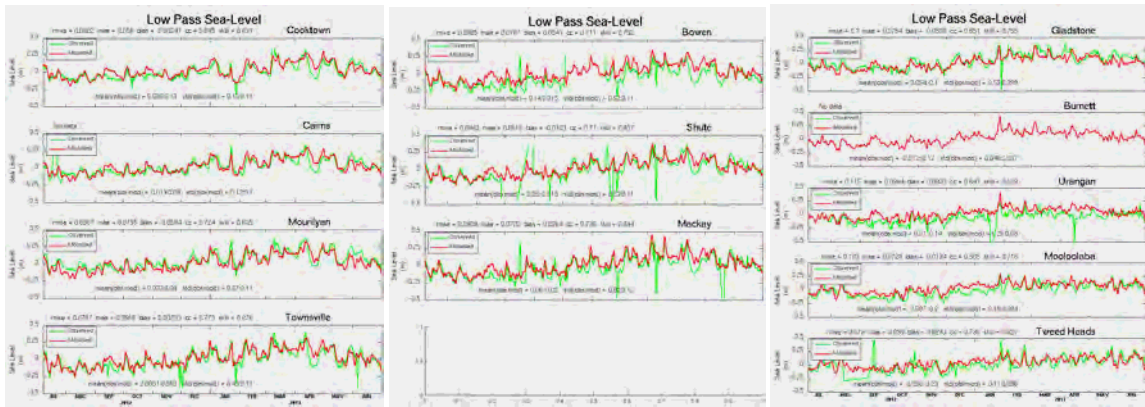


Figure 5.1.24. Low-frequency sea level comparison with tide gauges for 2012-13.

5.1.7 Open boundary specification

In the GBR lagoon high frequency sea level changes exist due to the tide (with period ~12 hours), and a low frequency component which is largely generated locally by wind stress. Open boundaries introducing these motions into the domain may behave in a passive manner that allows transmission of transient waves from the model interior while introducing little of the forcing signal, or an active manner which provides a better correlation to forcing data, but has a reflective nature that prevents energy from readily exiting the domain and can lead to degradation in flow patterns. Therefore, in the GBR any open boundary representing tidal and low frequency motions must behave in an active manner to represent the tide and a passive manner when representing the low frequency motion. These two requirements are in conflict, where an active open boundary (which uses relaxation to forcing data using short relaxation time-scales) will be prone to over-specification error for the low frequency component and may result in instability, and a passive open boundary (which uses long relaxation time-scales) will result in under-specification of the tidal component and an inaccurate solution. Section 4.1.3 introduces the concept of dual relaxation time-scales required to reconcile the short time-scale required for relaxation to oscillations at the diurnal frequency, and much longer time-scales required for low frequency motion. The dual relaxation attempts to allow the tidal component of the forcing to be actively introduced, while the low frequency component is introduced in a more passive manner. It should be noted, however, that regardless of the open boundary treatment, some attenuation and phase shift of the tidal signal would be expected when representing the reef matrix coarsely with 4km resolution.

Various time-scales were implemented in the open boundary specification that demonstrates this effect. The barotropic time-step used in the model is 5s, hence any relaxation time-scale approaching 5s results in the open boundary resembling a clamped condition which can lead to energy build-up and ultimately instability. The single relaxation case falls into this category (6 s relaxation time-scale), and although skill is good for both tidal and low frequency sea level (mean skill of 85% and 75% respectively and RMSE of 0.58 and 0.10 m, Fig. 5.1.25), instability occurs in Broad Sound which is the most energetic region of the domain where tides can have an amplitude > 4 m. While the more passive 'default' single relaxation case maintains good low frequency sea level skill (mean skill of 77%), it has insufficient boundary information

supplied, resulting in an under-specified boundary and deterioration of the tidal signal (RMSE = 0.72 m, Fig. 5.1.26). The dual relaxation significantly improves the tidal response and maintains good skill in the low frequency component (mean skill of 87% and 66% respectively, Fig. 5.1.27). Importantly, the model remains stable by allowing the transmission of energy through a more passive open boundary, and the overall solution is considered a superior compromise.

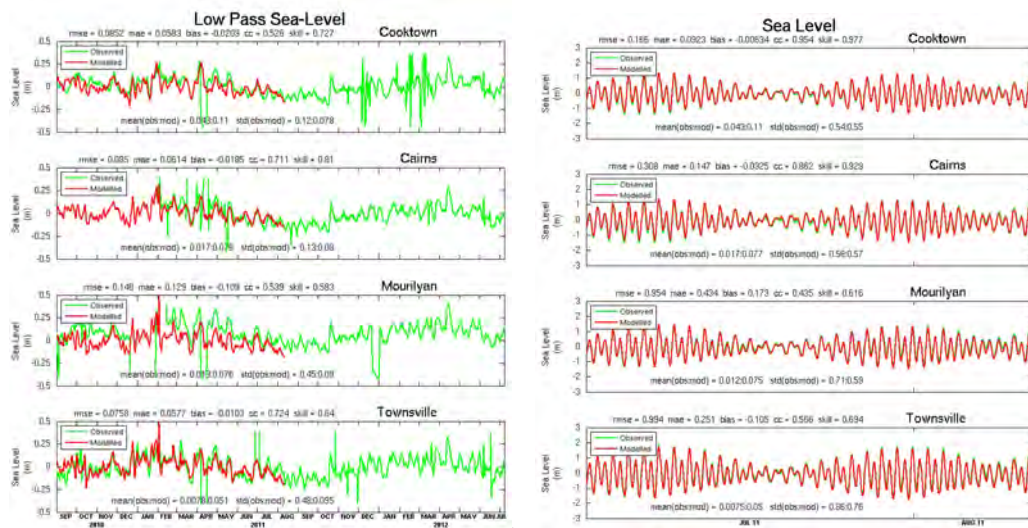


Figure 5.1.25. Low frequency and tidal response using single hard (6s) relaxation.

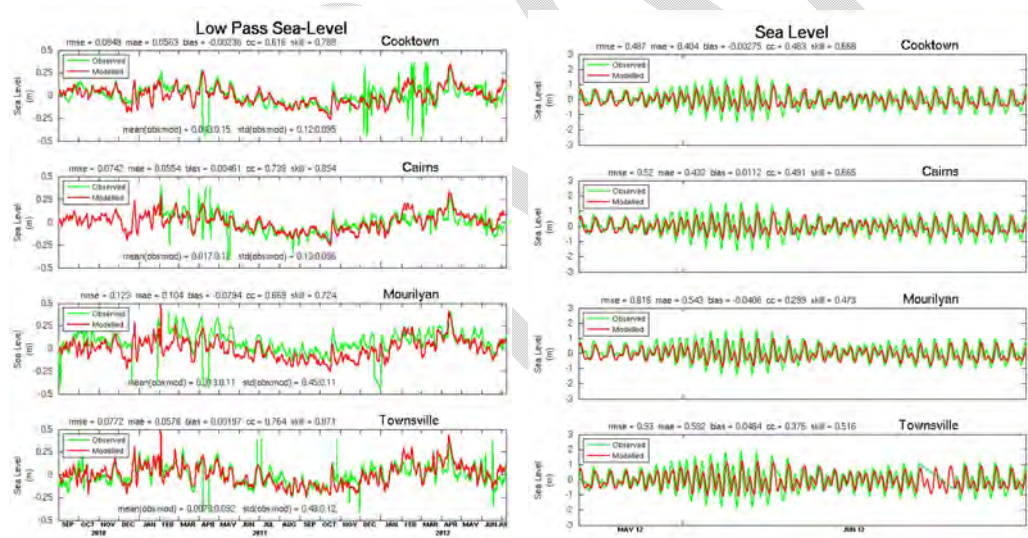


Figure 5.1.26. Low frequency and tidal response using single 'default' relaxation.

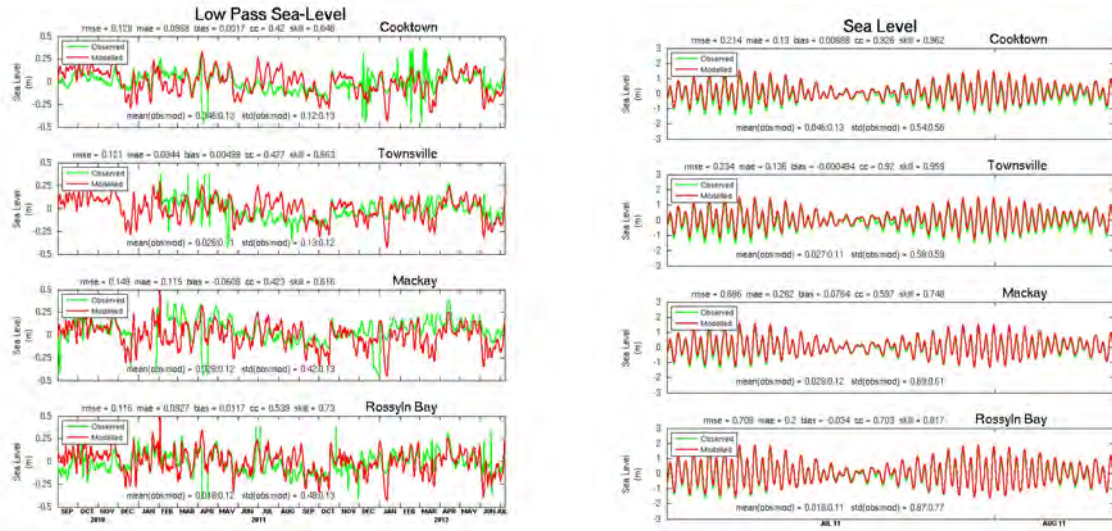
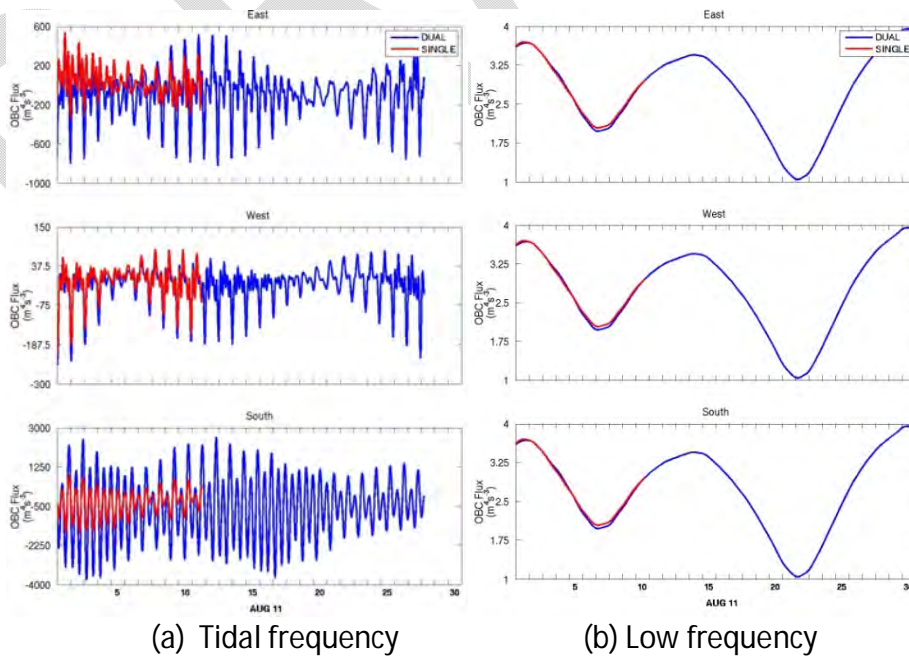


Figure 5.1.27. Low frequency and tidal response using dual 'default' relaxation.

Fig. 5.1.28 shows the energy flux through each open boundary, defined by Palma and Matano (1998) as;

$$OBC_{flux} = \frac{1}{W} \int_W DU_1 (g\eta + 0.5U_2^2) \Delta y \quad (m^4s^{-3}) \quad 5.1$$

where U_1 is the depth-averaged normal velocity at the boundary, U_2 is the depth-averaged tangential velocity at the boundary and W is the width of the open boundary. Eq. 5.1 represents the energy flux through eastern or western boundaries. Note that $\rho(OBC_{flux})$ has units Wm^{-1} where ρ is the water density.



(a) Tidal frequency

(b) Low frequency

Figure 5.1.28. Energy flux through the three open boundaries for dual and single relaxation cases in the period leading up to the model instability on 11th August.

Interestingly, it is observed that the long offshore boundary on the eastern edge of the GBR domain and shorter boundary in the south of the domain are transmitting significantly more energy at the tidal frequency for the dual case than the single case (Fig. 5.1.28a). Low frequency fluxes are similar between the single and dual cases (Fig. 5.1.28b), exhibiting an oscillation at the neap-spring period (~14 days). This suggests that dynamics are at play other than those motivating the application of the dual method in the first place (i.e. transmission of low frequency energy). The long relaxation step in the dual method includes the target tidal elevation in the computation of its flux adjustment (Eq. 4.9), and hence retains some passive character at the tidal frequency. The dual method effectively relaxes toward the tidal target elevation twice, providing a better estimate each time-step. The single relaxation is essentially clamped with no passive character. Tidal amplification occurs across the GBR shelf (Middleton et al., 1984), resulting from a combination of damped semi-diurnal resonance in the southern GBR lagoon and alongshore convergence (e.g. tidal ranges are ~4.5 m at the coast in Broad Sound but have a range of ~ 0.8 m off the shelf along the open boundary). It is this resonant tidal energy that is trapped by the single relaxation case, and allowed to be transmitted through the boundary in the dual case by virtue of the longer secondary relaxation to the tidal plus low frequency target elevation. Consequently, the reflective nature of the single relaxation case, characteristic of clamped style open boundary conditions, is the underlying cause of the observed instability.

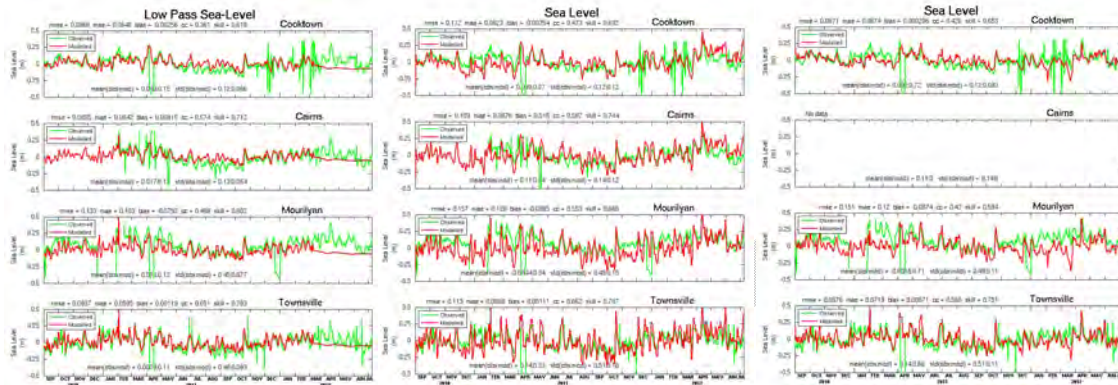
Note that the sea level solutions from the calibration configuration are displayed in Fig. 5.1.7 and 5.1.6, with mean skill of 76% and 89% for low frequency and tidal respectively; overall the 6s/default time-scale configuration (i.e. calibration configuration) was considered better than the default/default dual method. The open boundary relaxation method also impacted the temperature and salinity solutions in addition to sea level. Generally, some sites show degradation in the surface temperature using the calibration configuration compared to the single relaxation and default/default dual methods, but an improvement in sub-surface temperature and near-surface salinity. Overall, the 6s/default dual relaxation was considered the optimum configuration across all variables.

These developments have been published in *Ocean Modelling*; Herzfeld and Gillibrand (2015).

5.1.8 Open boundary data

The previous section demonstrated that the solution within the GBR lagoon was sensitive to the choice of relaxation time-scale used in the open boundary specification. Additionally, the solution is sensitive to the quality of the data applied at the open boundary (velocity, sea level, temperature and salinity) from the global model. It has been shown that the low frequency sea level in the GBR lagoon is primarily locally forced by wind stress (Burrage et al, 1991, Brinkman et al, 2002). A hindcast simulation that crudely emulates this was performed by closing all the open boundaries in the GBR4 domain. This was compared to the sea level directly derived from OceanMAPS and that of BRAN3.5 (BRAN3.5 is a global model hindcast that is considered superior to OceanMAPS due to its greater density of data used in the data assimilation scheme). Low frequency sea level using closed boundaries is displayed in Fig. 5.1.29 (a), and exhibits superior mean RMSE = 0.10m (skill=63%) than the OceanMAPS sea level (Fig. 5.1.29 (b), mean RMSE of 0.125m, mean skill=71%) or BRAN3.5 (Fig 5.1.29 (c), mean RMSE = 0.11m, mean skill=70%). This implies that local forcing is indeed primarily responsible for low frequency sea level changes. Furthermore, when global model forcing is used on the boundaries, any error contained in the global products used for boundary forcing can lead to

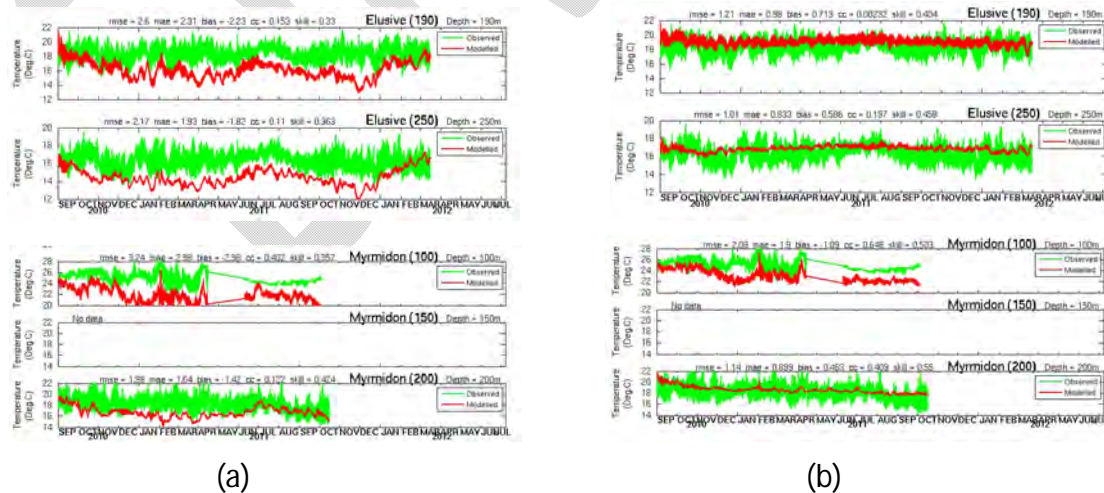
a degradation of the low frequency response in the lagoon. For example, using the BRAN3.5 forcing which is considered to have higher skill than OceanMAPS, the GBR4 low frequency response has RMSE=0.09m and skill 74%, i.e. skill improves over wind forcing alone. However, when a product is used containing more error (OceanMAPS), the RMSE increases compared to the closed boundary case (RMSE=0.13m, skill =65%).



(a) Closed (b) OceanMAPS (c) BRAN3.5

Figure 5.1.29. Low frequency and tidal response. Note (b) and (c) are direct comparisons of the global products rather than GBR4 forced with global products.

Using BRAN3.5 for boundary forcing in preference to OceanMAPS also improves the temperature and salinity solutions within the domain, particularly temperature and salinity at depth (Fig. 5.1.30) and near-surface salinity (Fig. 5.1.31). The only difference between these two runs is the data product used on the open boundary, from which it is observed that the bias at depth of several degrees when using OceanMAPS is absent when forced with BRAN3.5. This implies that the OceanMAPS solutions on the GBR4km domain boundary are the source of these errors. The near-surface salinity shows similar improvement when BRAN3.5 is used (Fig. 5.1.31), although not nearly as marked as temperature at depth. The delivery of fresh water at the coast in coarse regional models also contributes to the fresh model bias in this case.

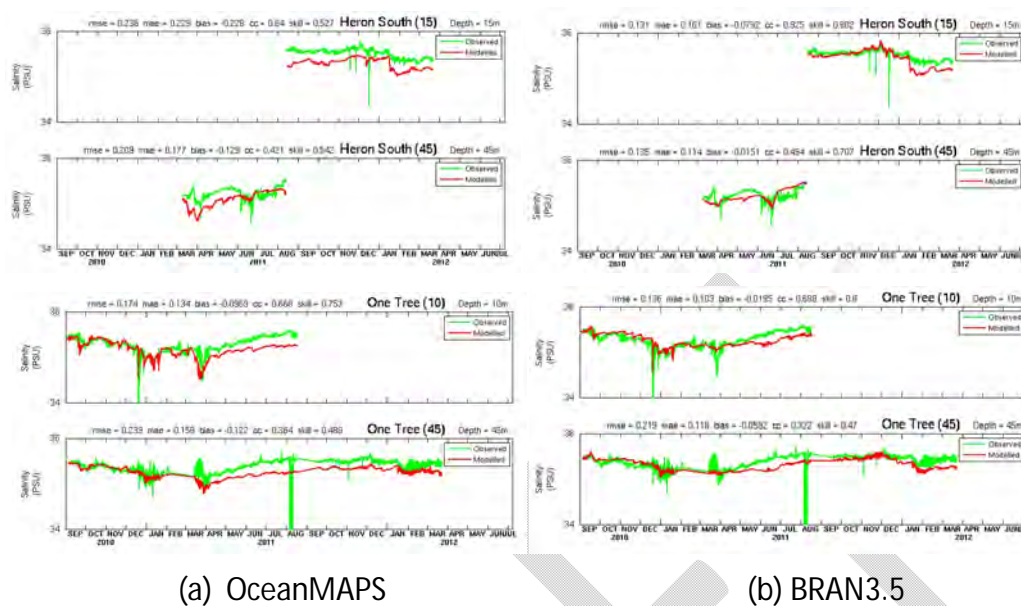


(a) (b)

Fig 5.1.30. Temperature solutions at depth using (a) OceanMAPS and (b) BRAN3.5.

A first order improvement in the 4km model results requires prescribing more accurate open boundary forcing. Unfortunately BRAN3.5 is only run in hindcast mode, and is not available in

near real-time to force the GBR models. One of the objectives in Phase II is to apply data assimilation techniques to OceanMAPS in an attempt to remove the boundary bias.



(a) OceanMAPS (b) BRAN3.5
 Fig 5.1.31. Near-surface salinity solutions at depth.

5.1.9 Short wave parameters

The short wave radiation (SWR) incident at the sea surface penetrates throughout the water column, heating it as it does so via the divergence of radiation. Material resident in the water column attenuates the SWR such that the intensity of radiation decreases exponentially with depth. This decrease in intensity is controlled by the attenuation coefficient. A fraction of SWR may be excluded from this heating of the water column, and used as the surface boundary condition for vertical mixing. The degree to which short wave radiation is excluded from the net heat flux is controlled by the transmission coefficient and is due to the preferential absorption of longer wavelengths of SWR within the first few meters (e.g. Simpson and Dickey, 1981). Transmission varies from approximately 0.42 for Jerlov class I water to 0.22 for class III water. Table 5.1.4 lists attenuation and transmission may as a function of standard water classes according to Mellor (1992). In practice these parameters are tuned heuristically to achieve the optimum model-observation correlation. This procedure is formally achieved through data assimilation (Section 4.3) to provide spatially (and temporally if required) variable distributions of attenuation and transmission.

When the water depth is shallow the SWR may reach the sea floor, and this radiation must be accounted for. We introduce a bottom absorption parameter which takes on the value of 1 if all excess radiation is absorbed into the sea bed with no further heating of the water column, and 0 if all excess radiation is distributed in the bottom layer. Note that the latter may result in an unstable water column that mixes convectively. In practice, this parameter takes on a value between 0 and 1, and this is also prescribed via the data assimilation process.

Table 5.1.4. SWR attenuation and transmission as a function of water class.

Water Type	Attenuation	Transmission
I	0.037	0.32
IA	0.042	0.31
IB	0.056	0.29
II	0.073	0.26
III	0.127	0.24

Fig. 5.1.32 (a) shows the temperature solution at Heron Island North using heuristically tuned constant parameters (attenuation=0.1, transmission=0.7, absorption=0.5), and 5.1.25 (b) that with parameters estimated using data assimilation for the period Feb – May 2011, where all other parameters are identical. The constant SWR solutions clearly show an over-estimation of temperature over all depths whereas this bias is absent in the spatially varying case. This is also observed across the majority of sites. The RMSE and skill scores are superior for the spatially varying case, with mean RMSE of 2.3 vs 0.57 °C and mean skill of 71% vs 98% for constant and varying respectively. This result is not unexpected, since across the breadth of the GBR varying water masses are present as a function of distance offshore, depth and proximity to terrestrial outflows, hence it is difficult for one parameter to accurately represent this variability.

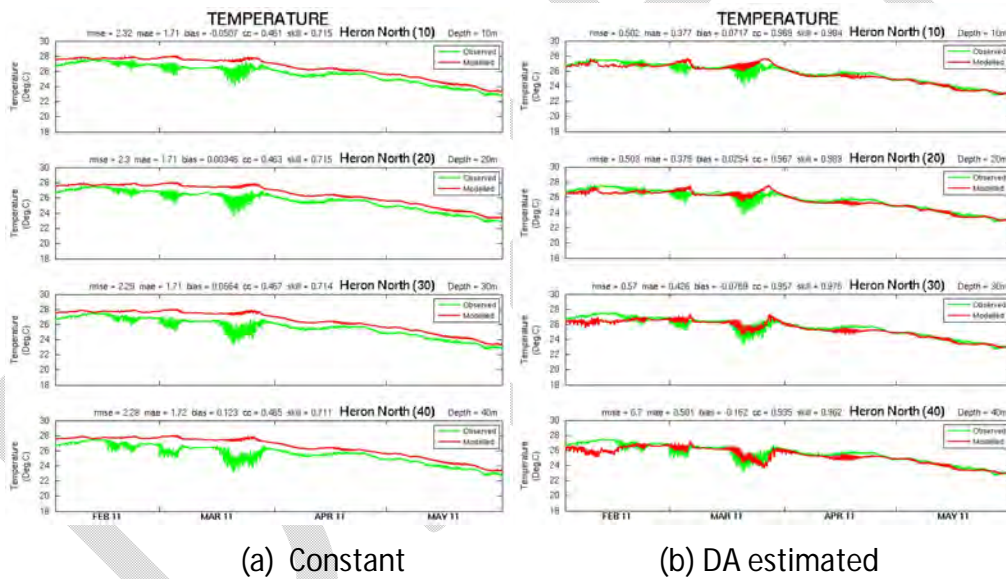


Figure 5.1.32. Surface temperature using constant and DA estimated parameters.

5.1.10 River input

Section 4.1.2 describes the various freshwater input methods and their shortcomings. Using river input having a salinity of zero generally will result in low salinity in the lagoon compared to observation (e.g. Fig. 5.1.33 a). This is due to the absence of an estuary, which entrains salt from the salt wedge into the freshwater outflow, delivering brackish water at the mouth. Improvement of the salinity solution in the lagoon is the cumulative effect of several factors. Flow based salinity (Eq. 4.1.11) may be applied at the river boundary to compensate for the effect of zero salinity input, however, the variability in salinity at the sampling sites is not only due to terrestrial inputs but also influenced by offshore intrusions. This implies that the open boundary data and type of boundary condition can also influence salinity in the lagoon. The

heuristic nature of calibration results in a succession of solutions where individual parameters are not always sequentially perturbed. This was the case with the GBR4 calibration sequence, displayed in Fig. 5.1.33; however, a picture emerges of the influences on salinity in the lagoon. Clearly input of fresh water at the coast creates a lagoon that is too fresh; particularly the response to the flood events in Dec 2010 is too strong. Using a flow based salinity regression in conjunction with BRAN3.5 open boundary forcing improves the solution (Fig. 5.1.33b) by increasing model lagoon salinity, however, the flow events are suppressed (see comments relating to this in Section 5.1.1). Using a default/default dual relaxation open boundary method results in only marginal further improvement (Fig 5.1.33c), while switching to OceanMAPS boundary forcing with this configuration degrades the solution slightly (Fig. 5.1.33d). The use of the 6s/default dual relaxation in this configuration results in another dramatic improvement in the lagoon. The major drivers thus appear to be flow variable salinity prescription in conjunction with the 6s/default dual relaxation method, with a small influence imposed by the global forcing dataset.

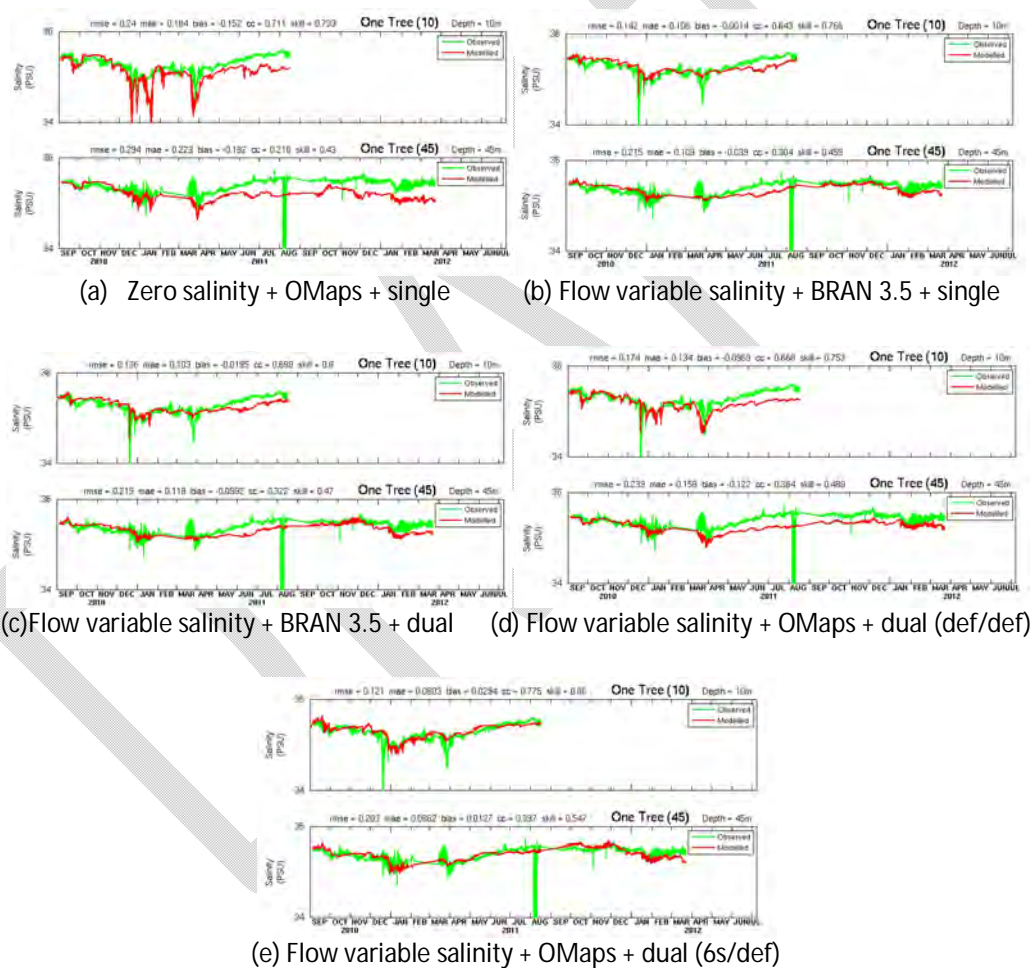


Figure 5.1.33. Salinity at One Tree Island using various OBCs.

5.1.11 Open ocean mean flow

During July the dominant winds in the GBR lagoon are the southeast trades, while during the summer monsoon in January the winds are more variable. Shelf edge flow along the GBR

margin is predominantly controlled by the EAC resulting in a net southward flow. This is strongest during September and October and may occasionally breach the fringing reef onto the shelf (Brinkman et al., 2001), typically accompanied by northerly winds or calm periods. During times when the southeast trade winds are strong (January – August) a reversal of the current can occur (Andrews, 1983) resulting in net northwards flow. Tracer analysis by Luick et al. (2007) confirms this trend for northwards flow in the GBR lagoon during the trade wind season and southward during the monsoon season.

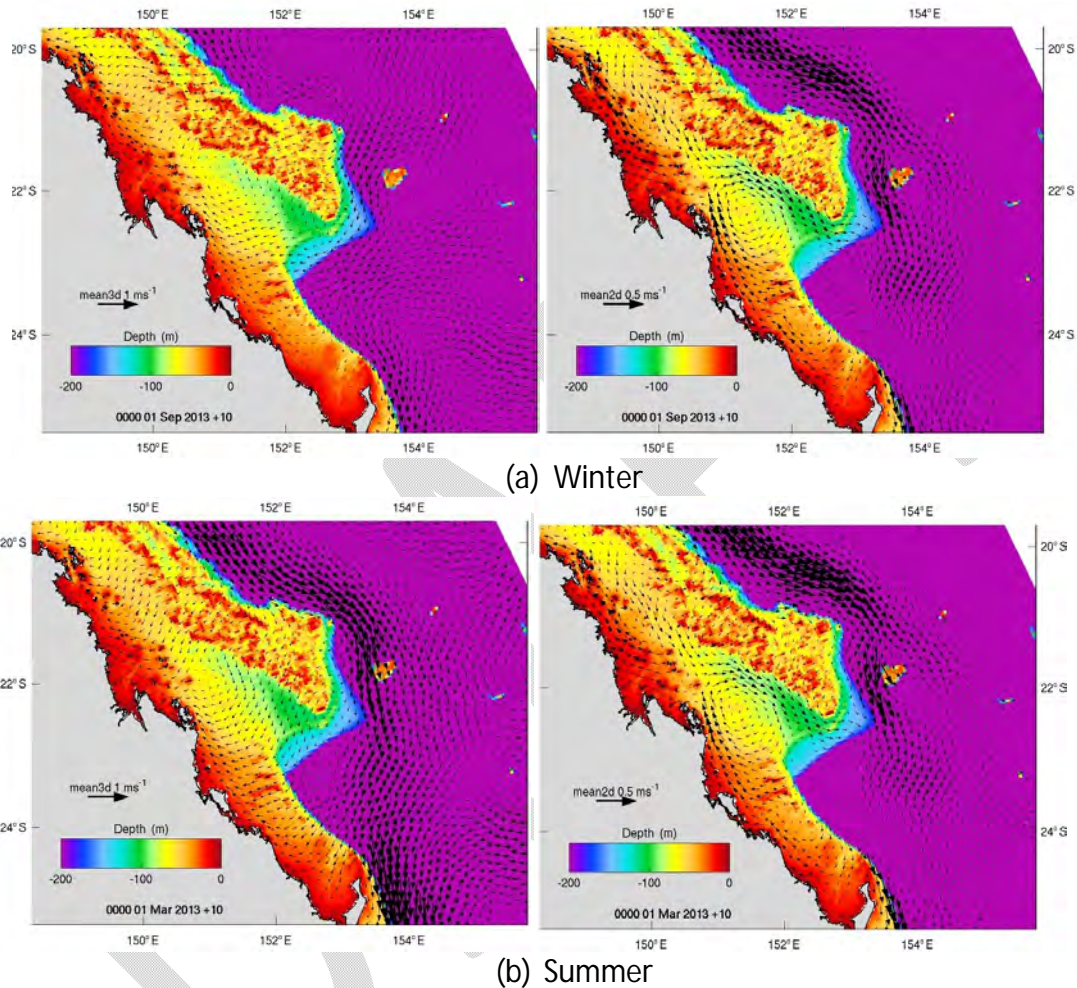


Figure 5.1.34. OceanMAPS seasonal mean velocity over Capricorn Channel. Left column are 3D surface velocities, right column are depth averaged velocities.

The seasonal mean circulation of global model does not capture this reversal of the flow into Capricorn Channel, and exhibits a net southward flow out of the Channel all year with little variability (Fig. 5.1.34), especially evident in the depth averaged component. This is uncharacteristic and in conflict with the current understanding of the system, likely stemming from a lack of fringing reef in the global model which allows onshore intrusions of the EAC, and atmospheric forcing products that poorly capture the southeast trade winds along Australia’s east coast. There is, however, a seasonal variability in the 3D velocity component off the shelf, with the EAC intensifying during summer.

The year-round southward flow in the global model is evident within the boundary forcing applied to the GBR4 model; i.e. the GBR4 boundary forcing attempts to drive southward flow.

However, the EAC signal from the global model is applied on the open boundary with a long time-scale in the dual relaxation method, hence this forcing is prone to under-specification. Additionally, during the trade wind season, strong wind in the interior attempts to create net northward flow, which is in conflict with the open boundary forcing. This generates severe boundary over-specification, and the GBR4 model responds by generating a spurious large anticyclonic eddy in the southern domain (Fig. 5.1.35), particularly strong in winter when this over-specification is greatest.

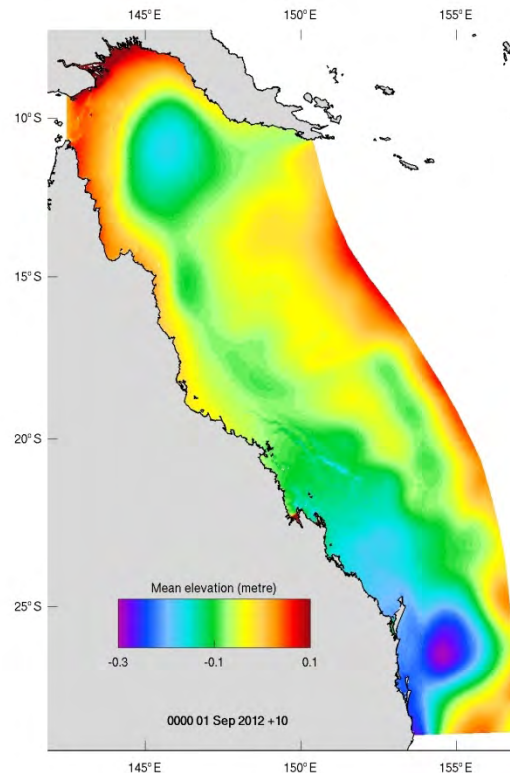


Figure 5.1.35. Winter seasonal mean sea level in GBR4.

The ultimate solution to this problem is to use open boundary forcing that is in harmony with both local forcing over the lagoon while still containing the shelf edge mean southward flow. It is considered important to accurately represent the EAC dynamics, and in the absence of well specified boundary forcing data we seek to implement approaches that impose a dynamic height field in the deep ocean while allowing the lagoon to respond to local forcing. Rendering the open boundary more active will not accomplish this result, as we have seen in Section 5.1.7 that this results in a reflective boundary prone to instability (in this case due to reflection of tidal energy). Tightly constraining the deep ocean dynamic height field to that of the global model is achieved by imposing relaxation on temperature and salinity (i.e. density) using a depth based relaxation constant which is very short in deep water and long in shallow water. The relaxation constant follows an exponential scaling to depth (Fig. 5.1.36). Additionally, to address under-specification of the EAC in the dual relaxation method, the southern boundary was made more active by imposing single relaxation with a time-scale of 6 s (the much longer offshore boundary retains the dual relaxation and is transmissive to energy). This configuration results in seasonal mean flow devoid of the large anticyclonic eddy. Mean flow out Capricorn Channel is much smaller (Fig. 5.1.37), and the depth averaged means suggest a northward undercurrent off the shelf in the deep ocean.

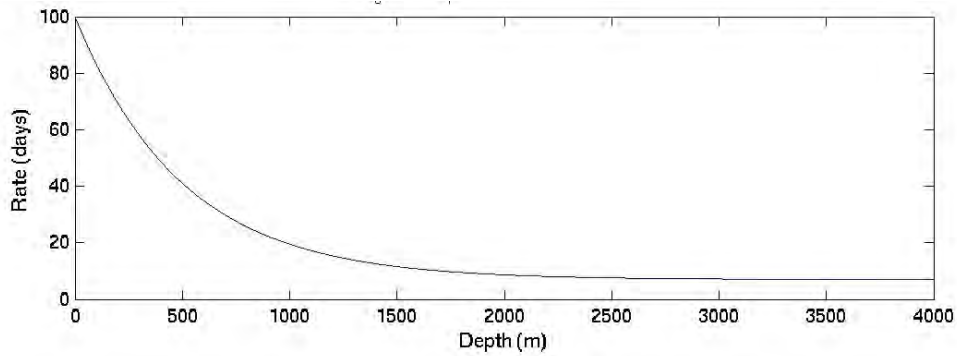


Figure 5.1.36. Depth based relaxation coefficient used for T/S relaxation.

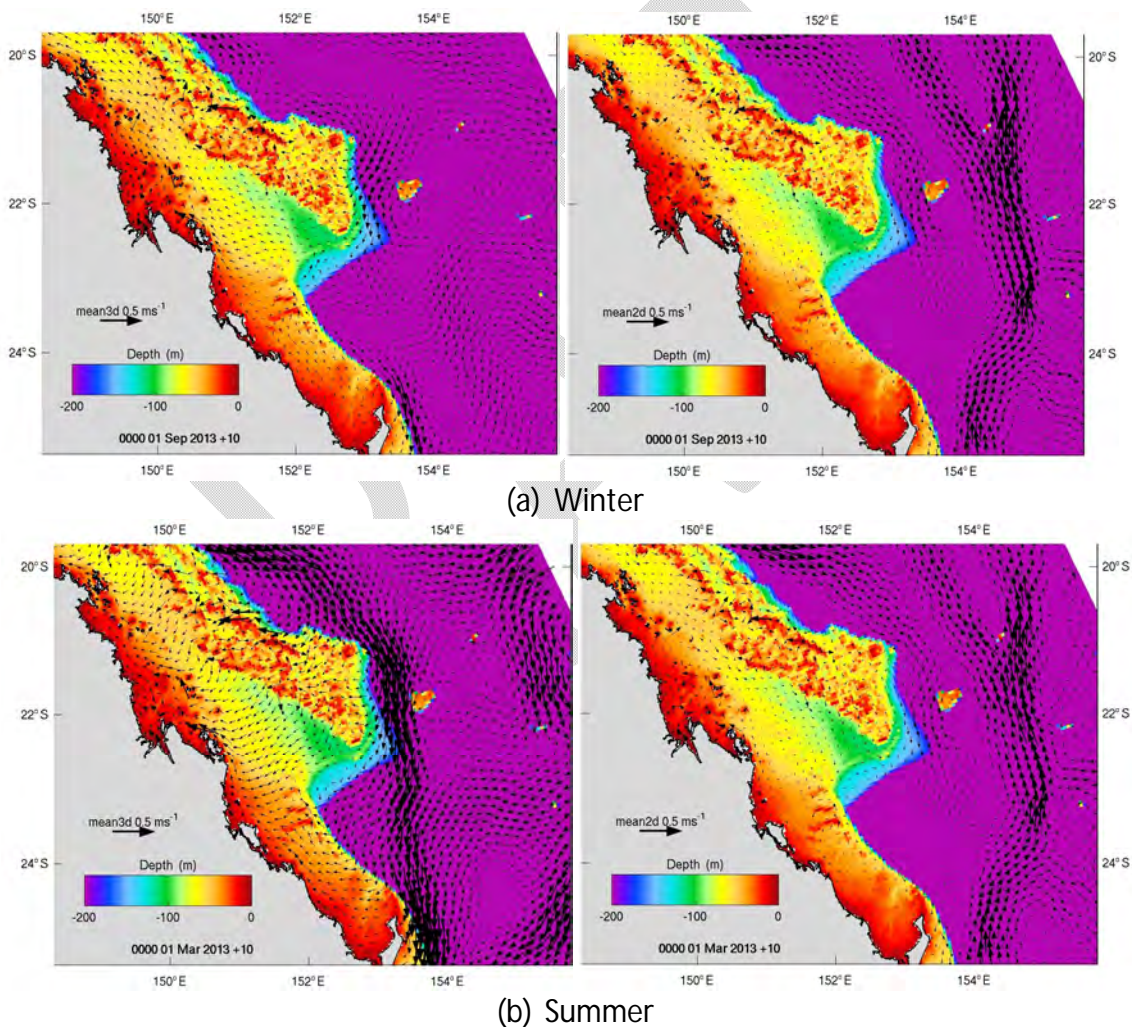


Figure 5.1.37. GBR4 seasonal mean velocity over Capricorn Channel. Left column are 3D surface velocities, right column are depth averaged velocities.

A 'curtain' across the mouth of Capricorn Channel that releases a constant flux of passive tracer results in a spreading of the tracer both northwards and southwards in the median distribution (Fig. 5.1.38), indicating inflow into the Channel at times. This is consistent with the findings of Luick et al. (2007). Since the seasonal means do not strongly show such a

northward flow, the northward transport of tracer is likely due to episodic events of strong north-eastward trade wind activity that does not contribute to a seasonal mean (i.e. balanced by periods of southward flow). The GBR4 parameterisation described above is used in the calibration configuration (Section 5.1.1).

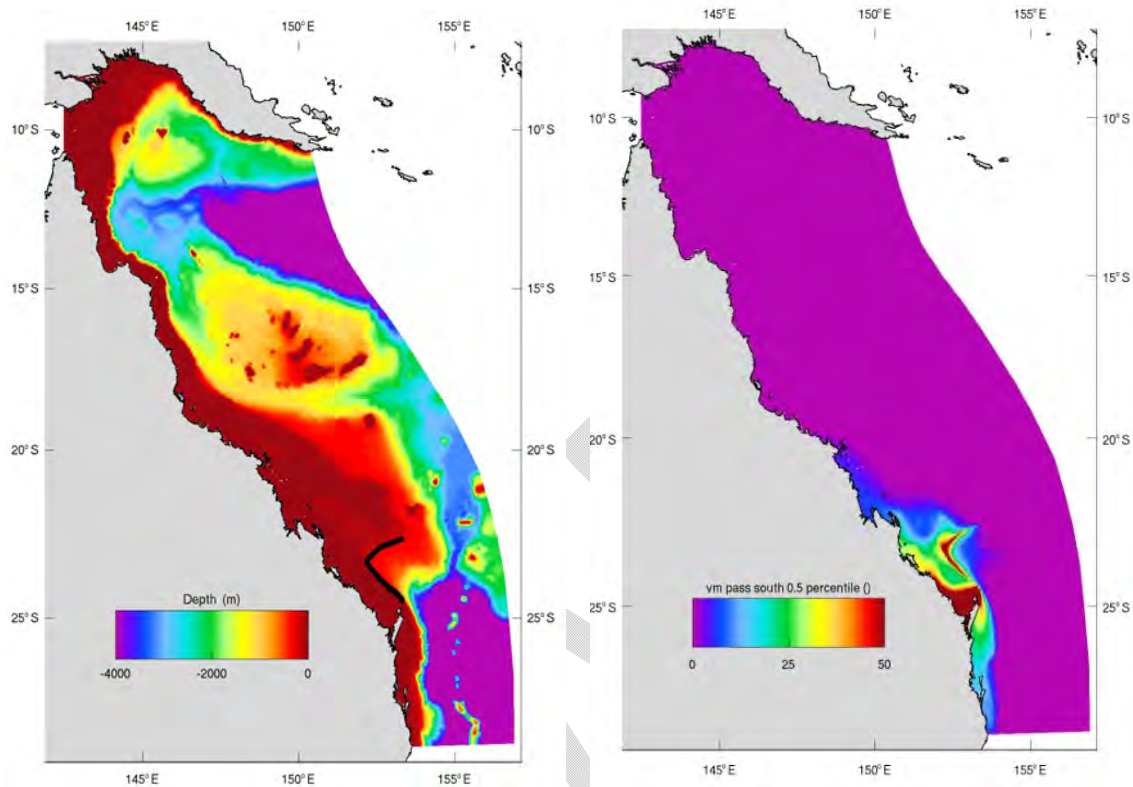
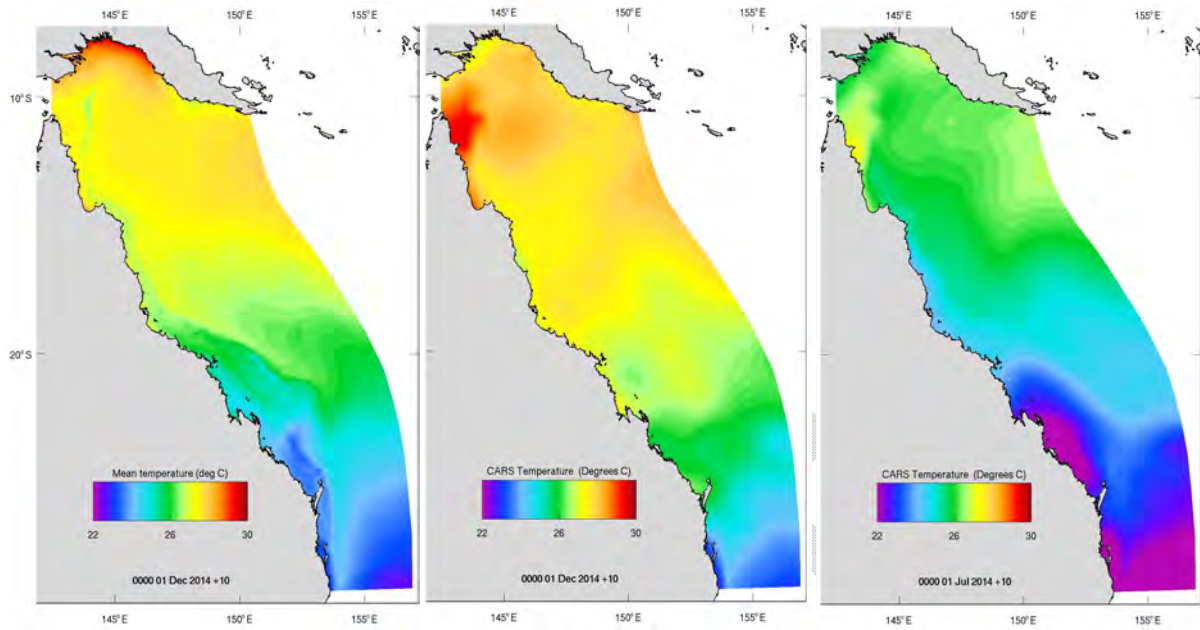


Figure 5.1.38. Passive tracer curtain applied with constant flux release (left, black line) and resulting tracer median distribution (right).

5.1.12 Climatology

The GBR4 simulation is averaged over the period September 2010 to Dec 2014 to produce a climatology that may be compared to the CARS climatology (Ridgeway et al, 2002). The CARS climatology is an observation based climatology that provides a seasonal cycle of SST and salinity. This seasonal cycle cannot adequately be constructed over the period 2010 – 2014 (since it would only include 4 values in the average), hence the mean state is computed as a single mean over the entire four year period. These averages are compared in Fig. 5.1.39 for sea surface temperature and 5.1.40 for sea surface salinity. Overall, the spatial distributions evident in CARS are represented in the model, and the model mean state is encompassed by the seasonal variability evident in CARS, at a location in the central GBR (Fig. 5.1.41).

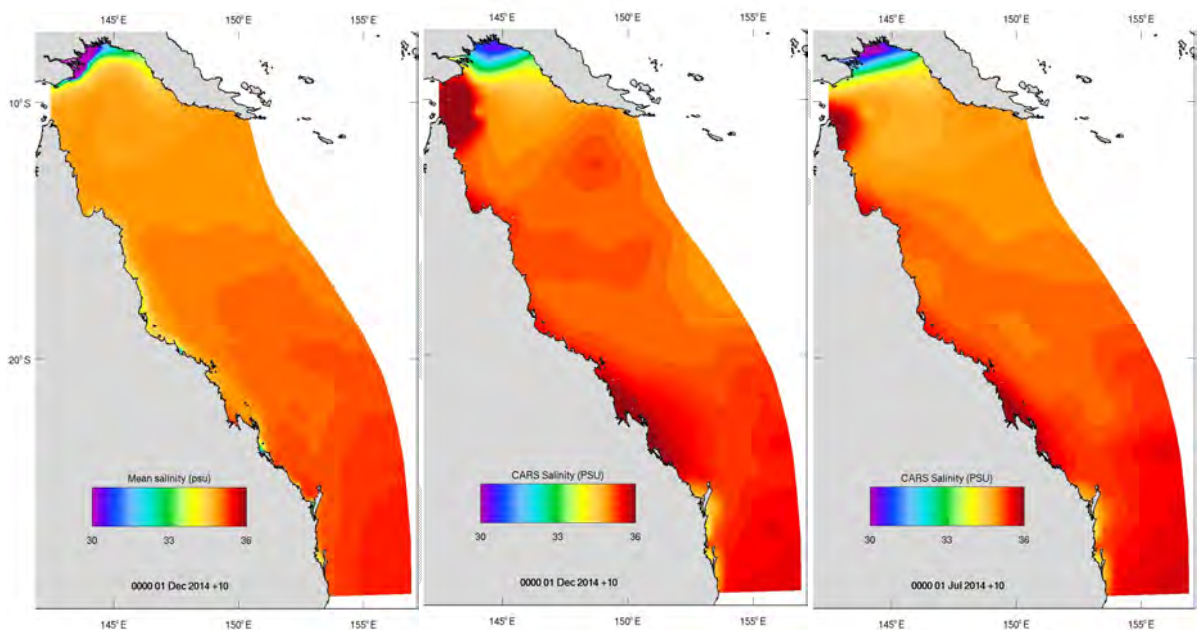


(a) GBR4 SST

(b) CARS summer SST

(c) CARS winter SST

Figure 5.1.39. Mean sea surface temperature.

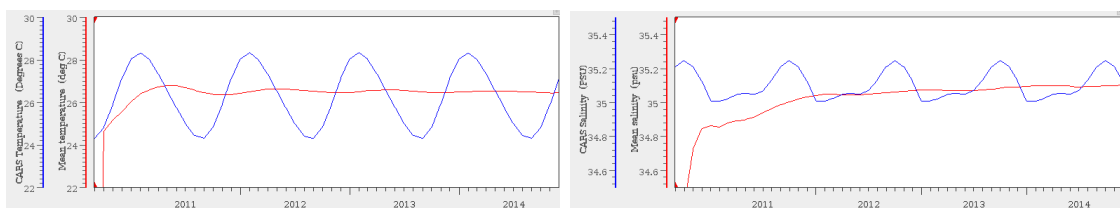


(a) GBR4

(b) CARS summer

(c) CARS winter

Figure 5.1.40. Mean sea surface salinity.



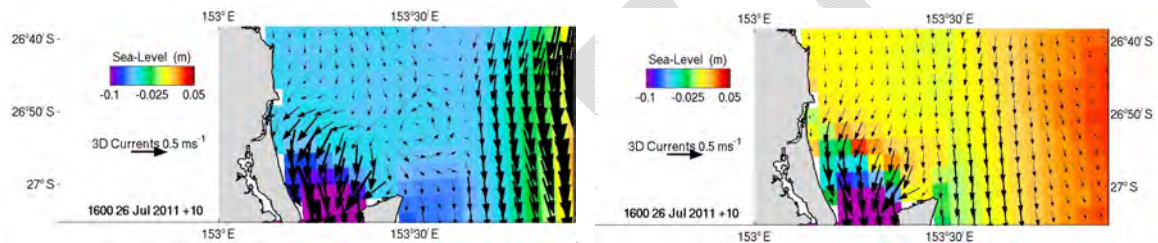
(a) Temperature

(b) Salinity

Figure 5.1.41. Time series in the central model domain.

5.1.13 Other sensitivities

During the course of the calibration procedure various other parameters were perturbed to result in with no significant sensitivity to model results. This included the turbulence closure method ($k-\epsilon$, $k-\omega$, Mellor-Yamada 2.0) and changes to bottom drag (smoothed & unsmoothed). The final configuration used Smagorinsky horizontal viscosity and diffusion; early simulations used a constant value of $2100 \text{ m}^2\text{s}^{-1}$ which resulted in overly smooth flow fields that lacked any detailed structure around obstacles. This was considered unrealistic and the Smagorinsky formulation with empirical constant of 0.1 was used in preference. An example is shown in Fig. 5.1.42, where an eddy forms off the northern tip of Moreton Island in July 2011 using the Smagorinsky mixing. This is likely due to horizontal shear between the strong EAC offshore and weaker oscillating tidal currents inshore generating barotropic instability. Using the constant mixing, this shear is not as strong, and consequently the eddy is absent. The lack of these types of features is typical of the constant horizontal mixing case.



(a) Smagorinsky mixing

(b) Constant mixing

Figure 5.1.42. Flow patterns off Moreton Island.

5.2. GBR1 Hydrodynamics

The 1km model (GBR1) is extremely large and computationally expensive (Section 4.1), and without supercomputing facilities only runs close to near real-time on 12 processor workstations. This means that many calibration simulations cannot be performed as was the case with the 4km model, but the 1km model must be assessed and optimised in near real-time. Fortunately, many of the issues the model faces in the GBR and their solution apply equally to both 1km and 4km models, allowing the 4km calibration configuration to be transported to the 1km model. Using the Smagorinsky horizontal mixing formulation, there are no resolution dependent parameterisations in the model apart from the time-step, and these only have stability implications. It is expected that the transported calibration configuration will largely result in solution containing skill similar to the 4km model, and the calibration approach for the 1km model is to monitor the model's skill in near real-time with this configuration.

5.2.1 Resolution improvements

The circulation over the GBR shelf is primarily driven by the complex topography, winds, tidal motions and the low-frequency circulation in the adjacent western Coral Sea (Wolanski 1994, Brinkman et al, 2001). Low-frequency currents forced by along-shore winds and off-shore pressure gradients are modulated by the tides and the topography, which can create residual currents and strongly deflect the mean current away from areas of high-reef density. The resulting mean circulation is a critical determinant of ecosystem health as it is responsible for net transport of dissolved and particulate material (Wolanski and Spagnol, 2000; Brinkman et al., 2001; Wolanski et al., 2003b; Luick et al., 2007), including the transport of water-borne larvae between reefs (Wolanski et al., 1997, 2004; Armsworth and Bode, 1999) and the transport of nutrients and pollutants by water currents (Done, 1988; Bell and Elmetri, 1995; Wolanski et al., 1999). Tidal jets and eddies in the wake of islands and reefs are ubiquitous feature of GBR circulation and have a significant impact on the circulation, and therefore the ecosystem. Their length scales range from about a 100 m to a few kilometres. In situ measurements, satellite imagery and numerical simulations show that those small-scale phenomena are mainly confined to the neighbourhood of small reefs, islands and passages (Hamner and Hauri, 1981; Wolanski and Hamner, 1988; Wolanski et al., 1988, 1996; Deleersnijder et al., 1992, Lambrechts et al 2008). These processes occur over a wide range of space and time scales, from a few metres to hundreds of kilometres and from a few seconds to several years, and there is significant interaction between small- and large-scale circulation processes (Wolanski et al., 2003a, Wolanski et al., 2003c). There is therefore a clear need for a model aiming to have relevance to the GBR to resolve the impact of the reef on the circulation.

As demonstrated in Section 4.2.1, horizontal resolution has a first order impact on the ability of the model to accurately model the flow through the reef matrix. This is also evident in the 1km model compared to the 4km model. Fig. 5.2.1 and 5.2.2 show snapshots of circulation with a bathymetry underlay in the Palm Passage and Capricorn Channel regions respectively. The shallower regions where reefs exist can be seen in these Figures, and in the vicinity of these regions there is no significant change in circulation patterns using the 4km model, i.e. the 4m model only marginally 'feels' the reef matrix. This is not the case using the 1km model, where it is seen that flow magnitude and direction are perturbed over the individual reefs.

These changes in circulation are qualitatively similar to those displayed in Fig. 4.2.4 when resolution was increased over individual reefs. Therefore, it appears there are benefits gained by increasing resolution over the reef matrix. As mentioned above, the presence of the reef not only impacts circulation at the small scale, but these small scale perturbations feed back to the larger scale. Given the GBR1 model qualitatively improves circulation over the reef, in Phase II we will attempt to quantify the consequences of this on connectivity and retention times within the reef matrix, and reef impacts on the mean circulation. From a downscaling perspective, clearly a more realistic solution will benefit the forcing of finer scale models.

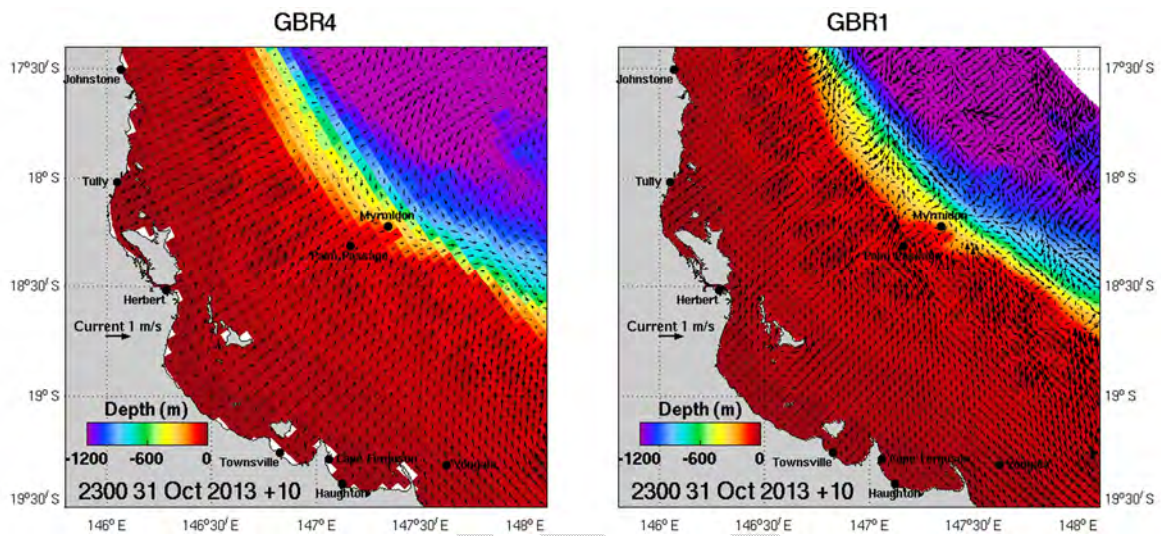


Fig. 5.2.1. GBR4 and GBR1 model in the Palm Passage region.

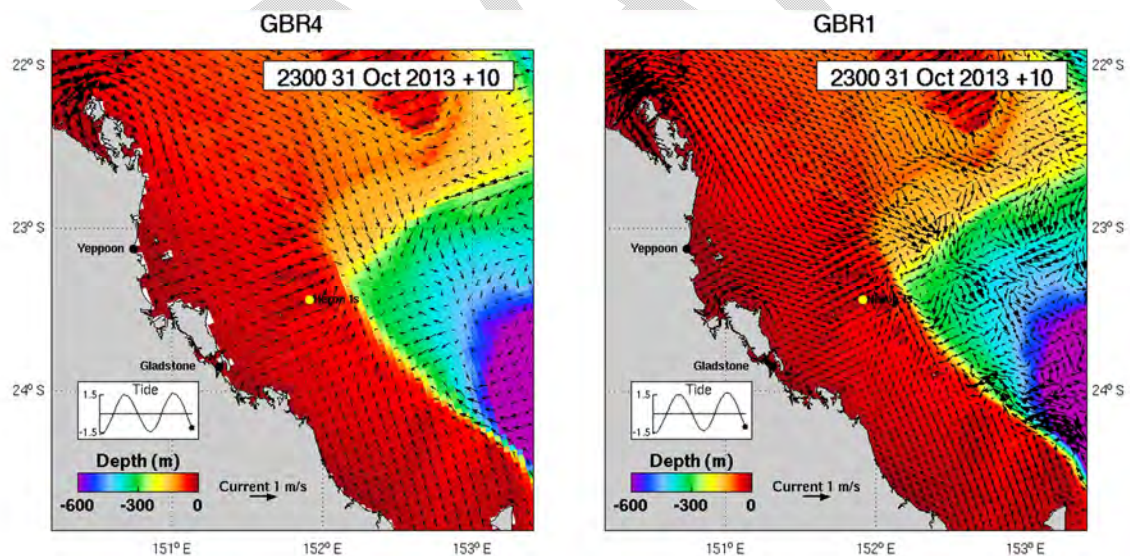


Figure 5.2.2. GBR4 and GBR1 model in the Capricorn Channel region.

5.2.2 NRT comparisons

The final version of the 1 km model was started in December 2014, and at the time of writing this report the GBR1 archive contained the summer of 2014/2015 which could be compared to observations. Time series comparisons of 1km model output and observations of sea level, low frequency sea level, temperature and salinity are displayed in near real-time at www.emg.cmar.csiro.au/www/en/emg/projects/eReefs/Results/1km-Near-Real-Time.html.

Time series of skill scores are also displayed. Delayed mode QIMOS temperature data was retrieved for the 2015 summer, allowing comparisons at depth to be made. The comparison locations and variables displayed are summarised in Table 5.2.1. Sea level comparisons are provided in Fig. 5.2.3, low frequency in 5.2.4, Wave-rider SST in 5.2.5 and delayed mode subsurface temperature in 5.2.6. Model performance is summarized in Table 5.2.2.

Table 5.2.1. Comparison sites for 1 km NRT comparisons.

Variable	Platform	Location
Sea level	Tide gauge	Cooktown, Cairns, Townsville, Bowen, Mackay, Rosslyn Bay, Mooloolaba, Tweed Heads
Low frequency sea level	Tide gauge	Cooktown, Cairns, Townsville, Bowen, Mackay, Rosslyn Bay, Mooloolaba, Tweed Heads
Surface temperature	Wave-rider buoy	Townsville, Palm Passage, Abbot Point, Mackay, Hay Point, Emu Park, Gladstone, Mooloolaba, Caloundra, Bribie Is., Point Lookout, N. Stradbroke Is. Gold Coast, Tweed River
Sub-surface temperature	IMOS NRT	Palm Passage, North Stradbroke Island
Sub-surface temperature	QIMOS delayed	Capricorn Channel, One Tree Is. Heron Is. south, Myrmidon, Palm Passage
Sub-surface salinity	IMOS NRT	Palm Passage, North Stradbroke Island
Sub-surface salinity	QIMOS delayed	Capricorn Channel, One Tree Is. Heron Is. south, Myrmidon, Palm Passage
Profile temperature / salinity	ARGO	Variable

Table 5.2.2. GBR4 and GBR1 metric comparison. GBR1 values in brackets use the best fit neighbourhood technique.

Model	RMSE		MAE		cc		bias		skill	
	GBR4	GBR1	GBR4	GBR1	GBR4	GBR1	GBR4	GBR1	GBR4	GBR1
Wave Temp	0.89	0.79	0.77	0.65	0.88	0.84	0.72	0.28	0.82	0.82
QIMOS Temp	0.95	1.4 (0.48)	0.73	1.1 (0.28)	0.74	0.52 (0.91)	0.03	-0.55 (0.24)	0.81	0.61 (0.9)
η	0.17	0.21	0.14	0.16	0.99	0.97	-0.03	-0.04	0.99	0.98
η_{low}	0.08	0.09	0.07	0.07	0.86	0.84	-0.04	-0.04	0.87	0.86

The comparisons indicate that the 1km model possesses comparable skill to the 4km model across available locations and variables. Note that not all the near real-time instruments have consistent data feeds, and data gaps from the moorings can occur. The ability of the model to capture trends on longer time-scale (e.g. seasonal temperature cycle) can only be assessed once the model has been allowed to run for longer periods of time that encompass these time-scales.

The GBR1 model produces a sea level response that is equivalent in skill to GBR4. Inshore at the surface, temperature also compares well with observations (Fig. 5.2.5) and skill is comparable to GBR4. In this region submesoscale variability is small. Further offshore the model skill deteriorates (Fig. 5.2.6), however, the skill metrics used should be treated with caution in this area. Submesoscale dynamics increase offshore due to the presence of the reef matrix, and large gradients can exist over small spatial scales. For example, Fig. 5.2.7 shows the 17 m temperature solution on 20th January 2015 around the Capricorn Channel mooring region, where it can be seen a cold plume extends into the Channel and the mooring site is located on the front between this plume and warmer lagoon water. At this time a cold bias is seen in the near surface Capricorn comparison; Fig. 5.2.6 17m. At depth (49 m) submesoscale structure is evident, and again the mooring location lies on a frontal boundary. The cold bias observed in the model at Capricorn Channel at this time is due to sampling within the cold plume at 17 m and a cold core submesoscale vortex at 44 m. A small spatial displacement of the modelled sampling location (or conversely, the spatial position of the submesoscale feature) can result in a large change in temperature sampled. This submesoscale variability is not as distinct in GBR4 due to the coarser resolution, with smoother spatial gradients (Fig. 5.2.8), hence this bias is not as large (Fig. 5.2.6).

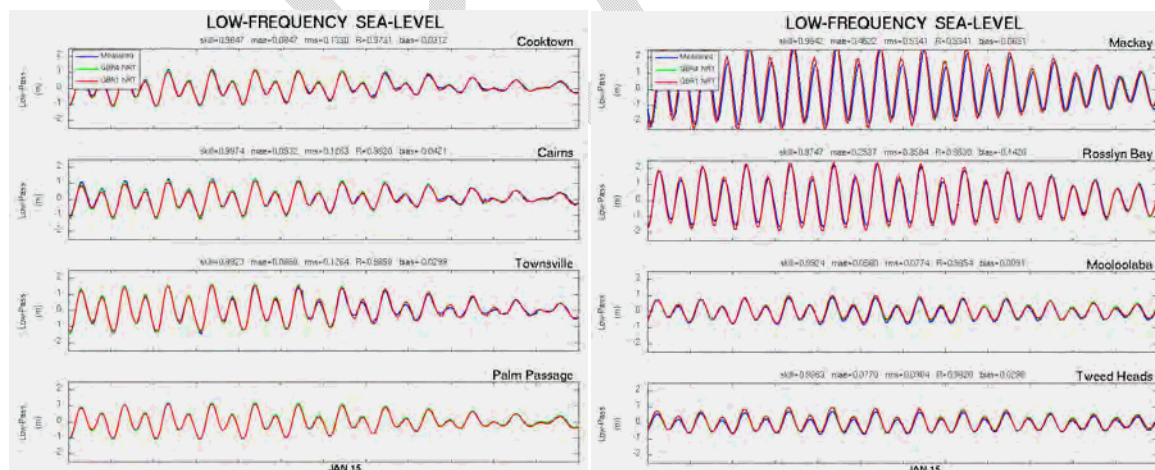


Figure 5.2.3. NRT sea level comparison to data for 4km and 1km models.

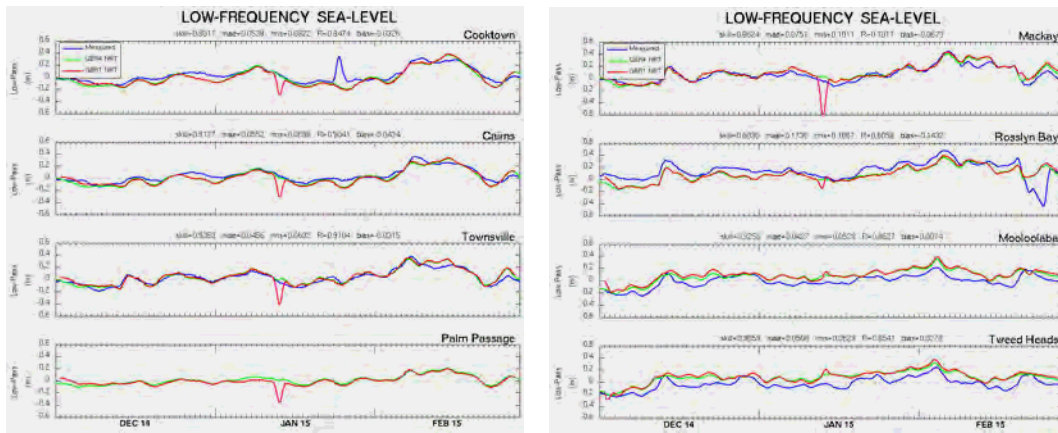


Figure 5.2.4. NRT low frequency sea level comparison to data for 4km and 1km models.

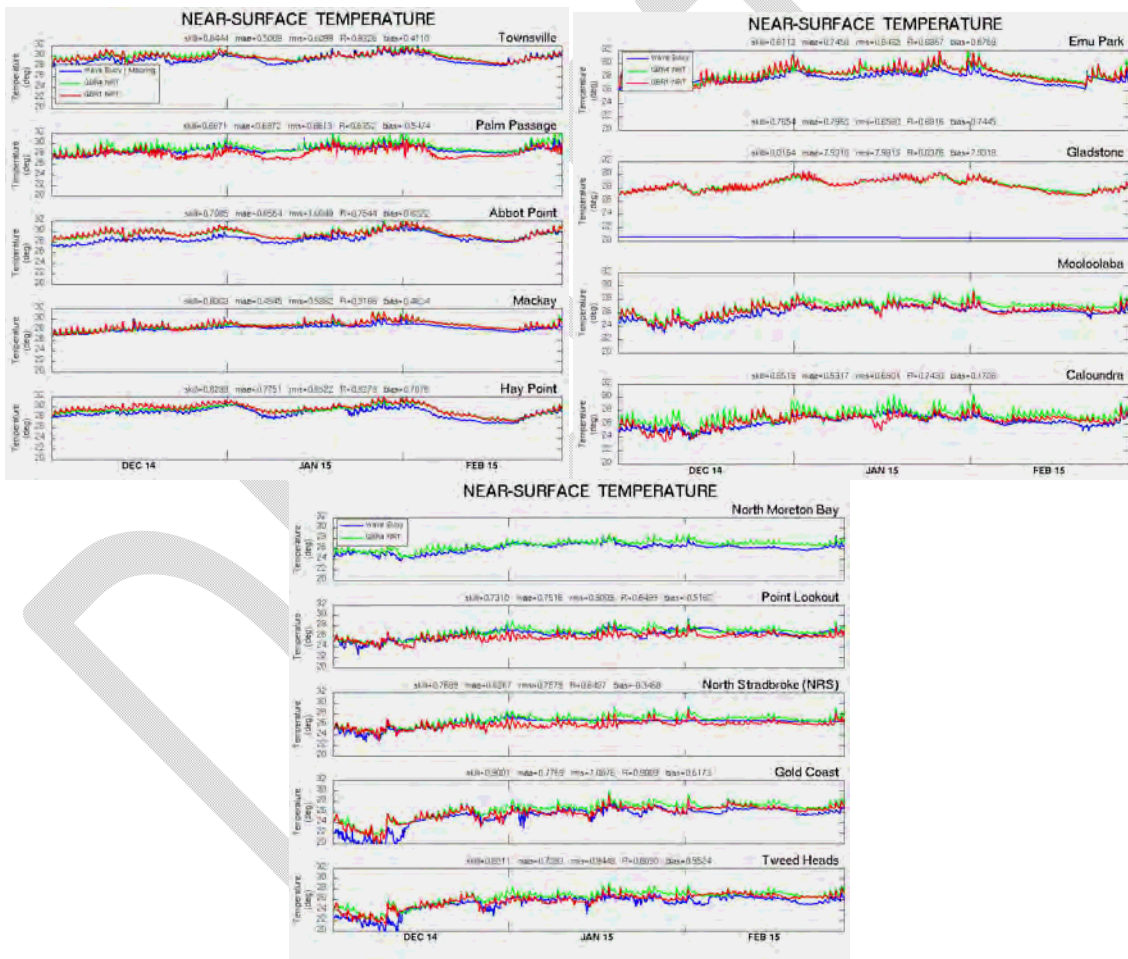


Figure 5.2.5. NRT Wave-Rider (surface) temperature comparison to data for 4km and 1km models.

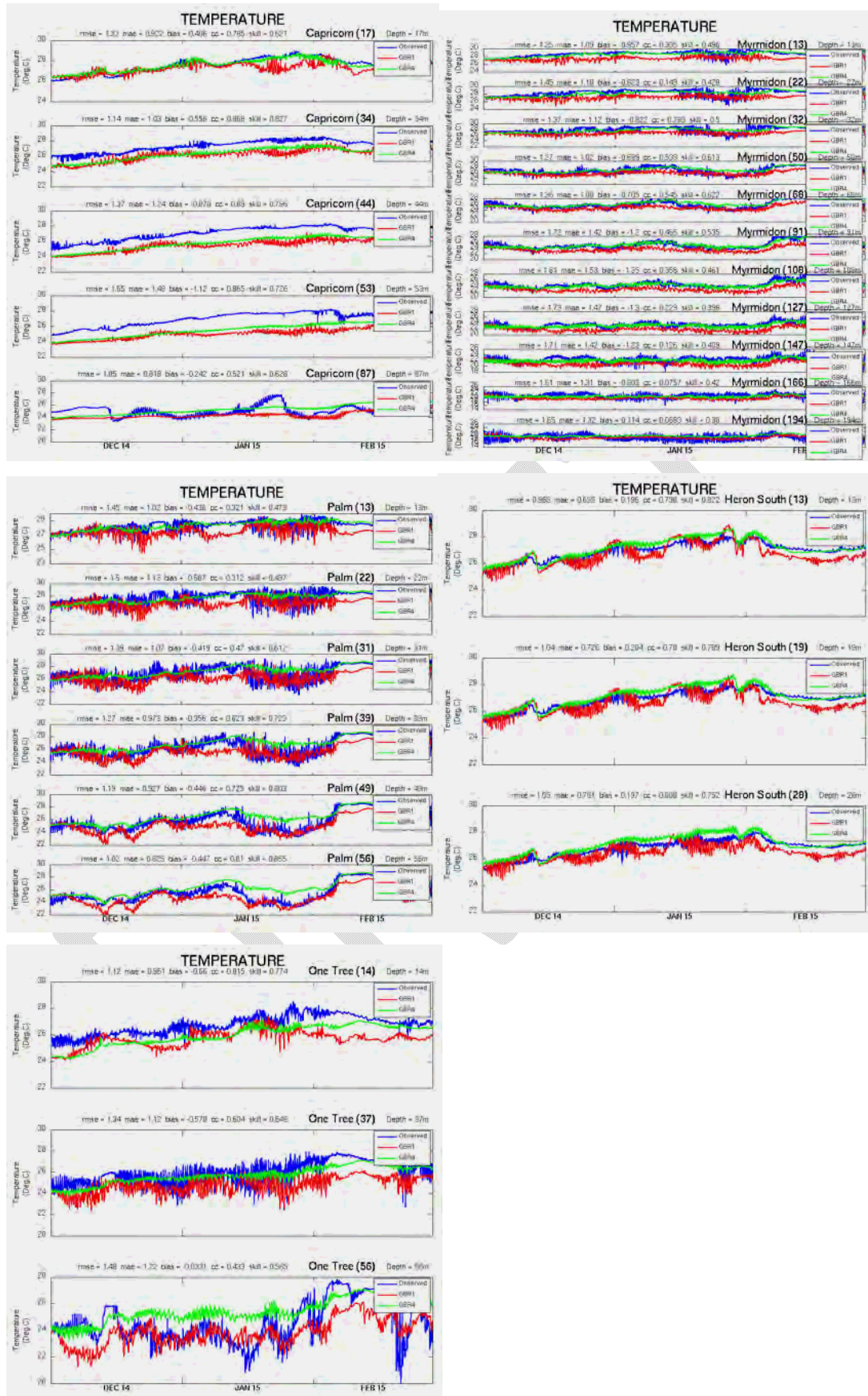


Figure 5.2.6. QIMOS (sub-surface) temperature comparison to data for 4km and 1km models.

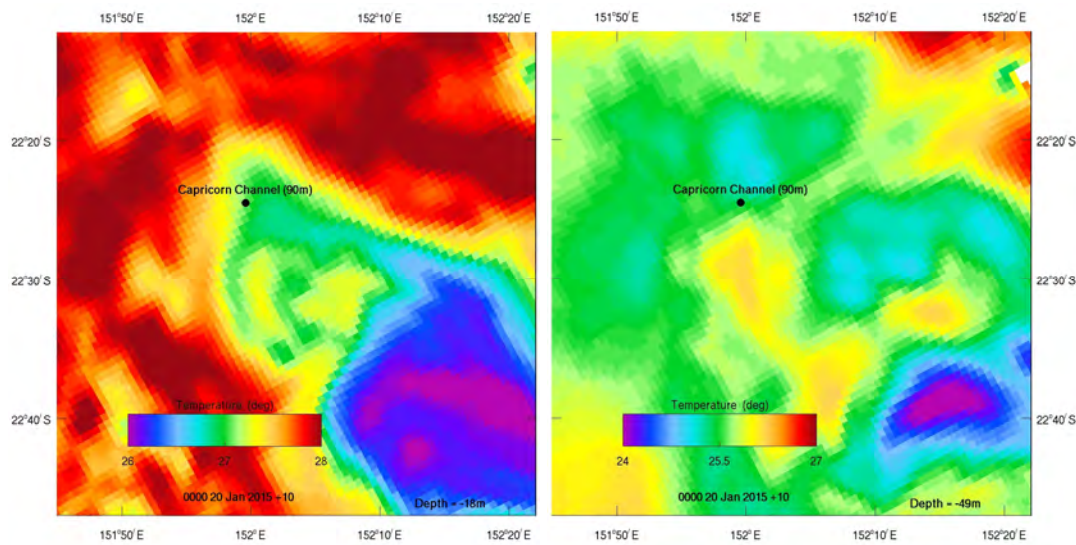


Figure 5.2.7. GBR1 temperature at 18 m (left) and 49 m (right) in the vicinity of the Capricorn Channel mooring on 20 January 2015.

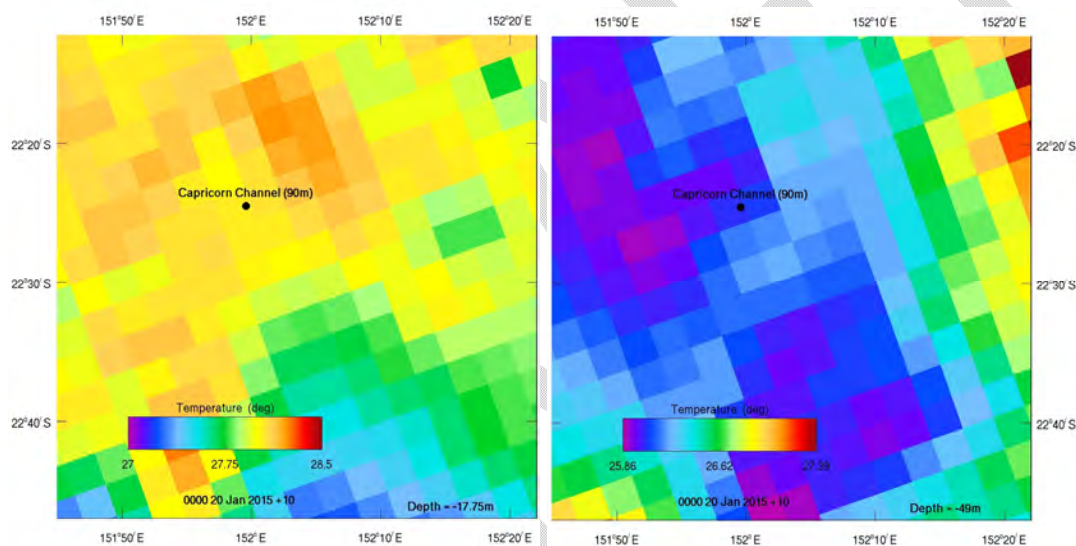


Figure 5.2.8. GBR4 temperature at 17.5 m (left) and 49 m (right) in the vicinity of the Capricorn Channel mooring on 20 January 2015.

In areas with large spatial gradients in GBR1, i.e. areas of submesoscale activity, comparison to observation therefore becomes a problem. Traditional skill metrics (RMSE, CC, bias etc.) no longer become indicative of true model skill as resolution increases and small scale features become more prevalent in the solutions, since small offsets in position of a feature are penalized as severely with these metrics as large bias or displacements of a feature. This problem has long been acknowledged in the meteorology community, and neighbourhood techniques have been developed to address the issue. Neighbourhood techniques attempt to overcome the problem by rewarding predictions where the shape and magnitude of a feature are correctly simulated, but it is slightly offset in time or space (Ebert, 2008). These methodologies are adopted for comparison of GBR1 solutions to observations, where a neighbourhood of the observation location is sampled in the model solution and compared to the measurement. There are many metrics that can be generated with neighbourhood

techniques, many of them categorical, designed to target specific aspects of the model skill. A good overview of common metrics is provided in Ebert (2008); here metrics of interest are upscaling (a neighbourhood average; 5 grid cells to be commensurate with GBR4 resolution), a minimum coverage metric (indicates the % coverage in the neighbourhood where the model – observation difference is less than a threshold, in this case 0.5°C), RMSE over the neighbourhood and the best fit of model to observations in the neighbourhood. The latter three metrics use a neighbourhood of 31 km, which is approximately the mean decorrelation length scale in the area (see Section 5.3.4). The minimum coverage metric tests the assertion ‘A forecast is useful if the event is predicted over a minimum fraction of the region of interest’, Ebert (2008). The most relaxed requirement would be that an event (in this case model-observation difference < 0.5°C) occurs at least once within a neighbourhood. The minimum coverage for temperature is displayed in Fig. 5.2.9; in these figures the ‘cumulative %’ displayed is the percent of time that at least one model cell in the neighbourhood has a value within 0.5°C of the observation. These results indicate that the model has the ability to predict temperatures with low error in the vicinity of the observation point for the majority of the time, with only Capricorn Channel at 53 m, Myrmidon at the surface being the exceptions. Using the best fit in the neighbourhood, the mean metrics are Willmott skill = 0.9, RMSE = 0.48°C, cc = 0.91, bias = 0.24°C and MAE = 0.28°C; a significant improvement on the point-to-point comparisons. Appropriate neighbourhood technique metrics for application to high resolution ocean model solutions remain to be refined.

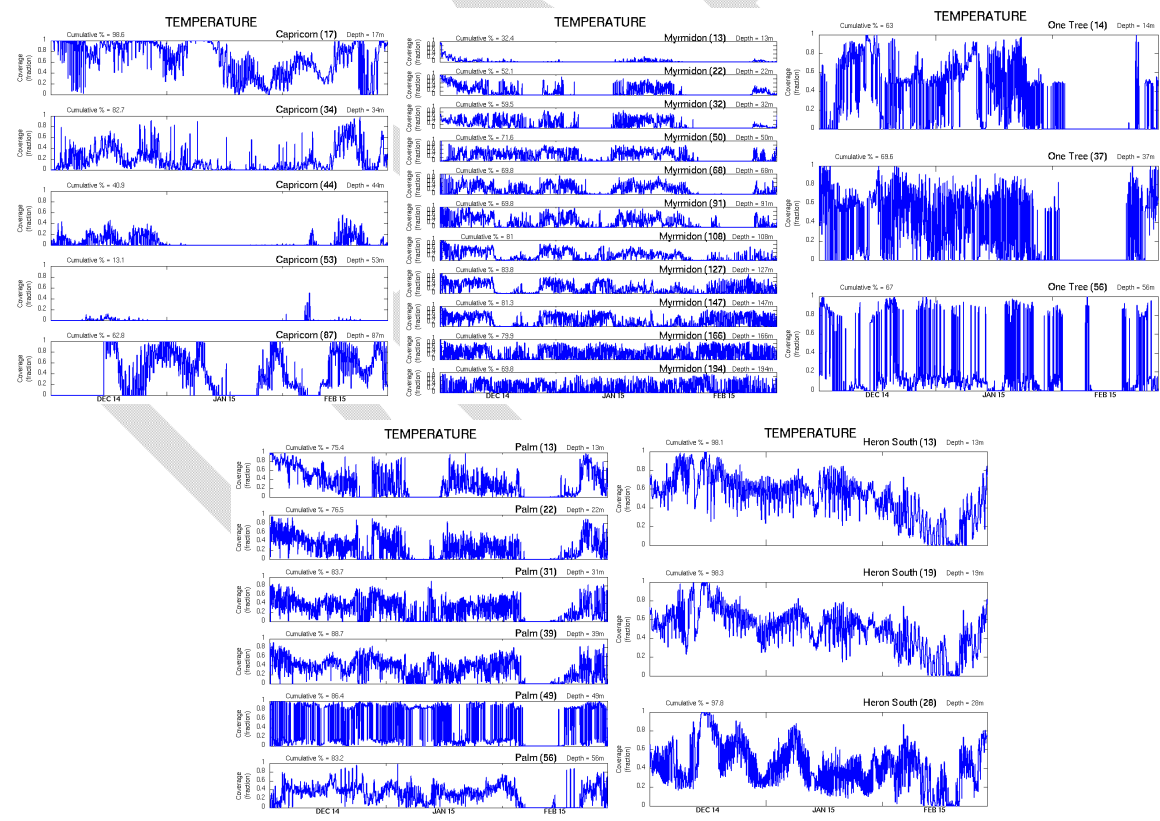


Figure 5.2.9. Minimum coverage metric for temperature using a neighbourhood size of 31 km and model-observation difference threshold of 0.5°C.

Salinity comparisons are displayed in Fig. 5.2.10; these figures demonstrate that all models (GBR1, GBR4 and OceanMAPS) have limited skill in predicting salinity during this time. GBR1

and GBR4 show similar behaviour, with GBR1 and GBR4 exhibiting a fresh bias of -0.49 and -0.41 respectively.

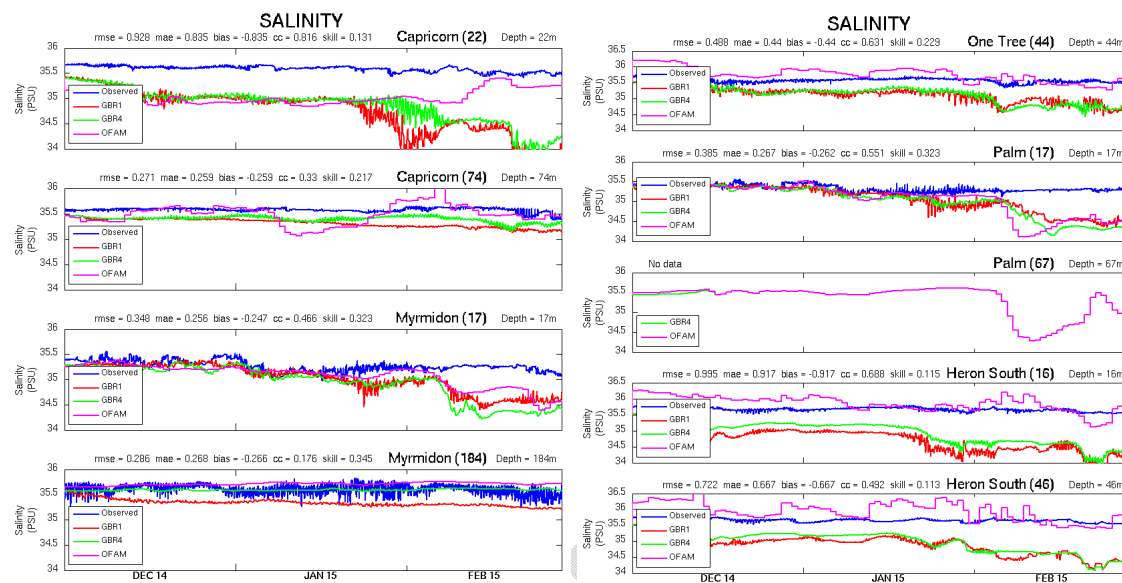


Figure 5.2.10. QIMOS (sub-surface) salinity comparison to data for 4km and 1km models.

During December 2014 and January 2015 there were significant flow and rainfall events into the GBR lagoon (e.g. Fig. 5.2.11 and 5.2.12) which contributed to a freshening of the lagoon water. Notably, on 12 December 2014 a massive rainfall event of over 4 m/day impacted the Capricorn Bunker group (Fig 5.2.12), which contributed to a sharp decrease in salinity from which the model was still recovering well into March 2015 (Fig. 5.2.13). Whether this rainfall volume is realistic remains to be investigated and verified, however, it is responsible for the fresh bias observed in the model-observation comparisons in the southern GBR over the summer of 2015. Additionally, the location of the flood plume resulting from terrestrial runoff due to this rain is critical to correctly predicting salinity, and again the Capricorn Channel, One Tree and Heron Island moorings are located near frontal boundaries of a fresh intrusion emanating from the Fitzroy Estuary (Fig. 5.2.14, 25 Jan). The existence of the fresh intrusion is supported by observing the suspended sediment concentration on 31 January 2015 in a satellite image retrieved from the eReefs BoM Water Quality Dashboard (<http://www.bom.gov.au/marinenwaterquality/>) in Fig. 5.2.15, where elevated levels within the Fitzroy estuary ($> 5 \text{ gm}^{-3}$) and the fresh intrusion ($\sim 1 \text{ gm}^{-3}$) are observed, indicative of terrestrial sediments carried into the lagoon within the plume. A similar plume is seen further north; on 20 January 2015 around the Palm Passage / Myrmidon mooring a fresh bias is seen in the model and is associated with the mooring location on a frontal boundary of a fresh intrusion from the north (Fig. 5.2.16). Again, these spatial gradients mean that traditional metrics can be of limited value, and neighbourhood techniques are more appropriate. Using a neighbourhood equal to the de-correlation length scale in this case only marginally improves model skill; this is expected since points beyond the flood plume are de-correlated with those within it, and hence outside the neighbourhood.

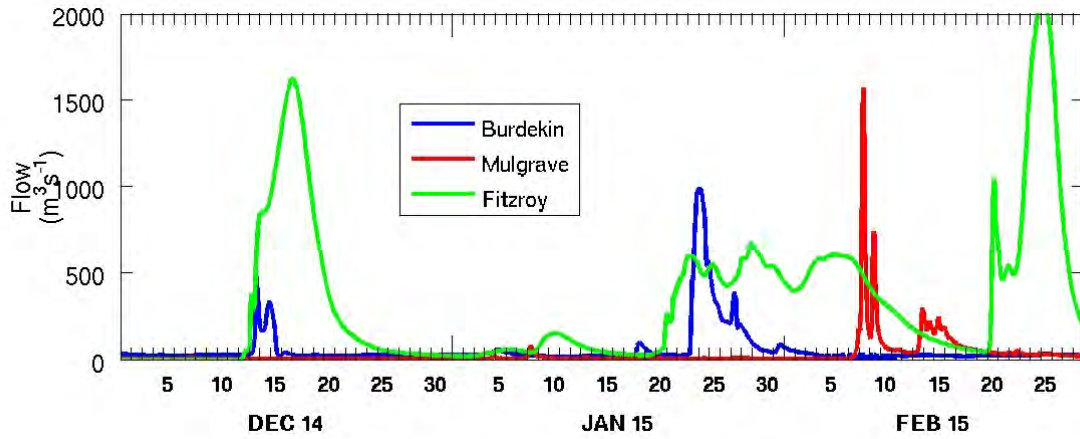


Figure 5.2.11. River flow during the summer of 2014 / 2015.

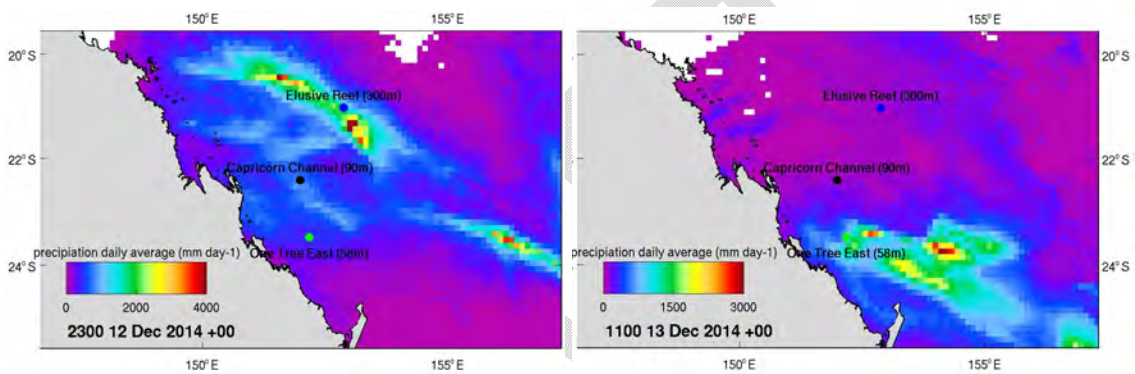


Figure 5.2.12. Rainfall as predicted by ACCESS in the Capricorn Bunker group.

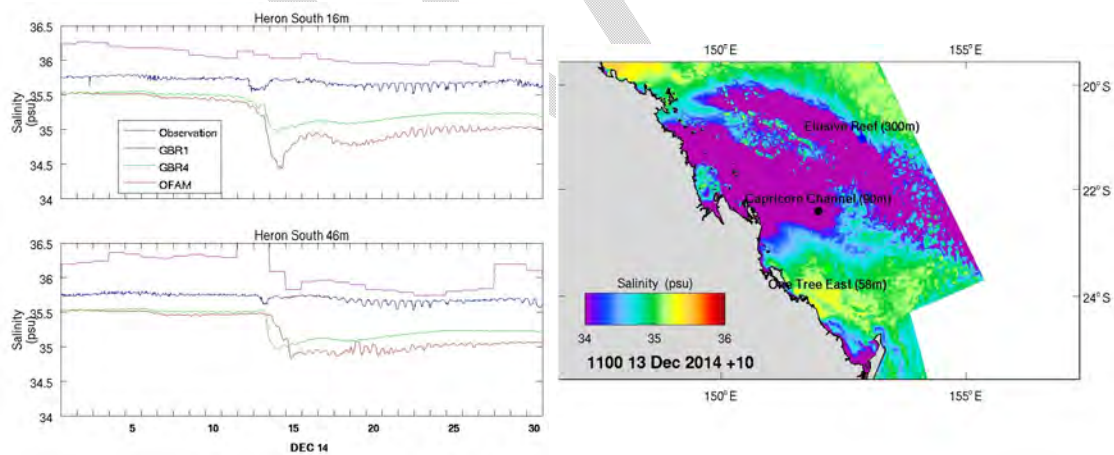


Figure 5.2.13. Salinity response in December 2014; time series at Heron South (left) and surface salinity at 11am on 13 December 2014 (right).

The global model (OceanMAPS) consistently exhibits a salty bias in December and January; in the latter half of February a large fresh bias is often seen. Any fresh signal in this model is a consequence of the data assimilation scheme rather than a dynamic response to fresh water input. Indeed, a flood plume is absent in the Fitzroy River region in this model during the times of large freshwater inflow (Fig. 5.2.17).

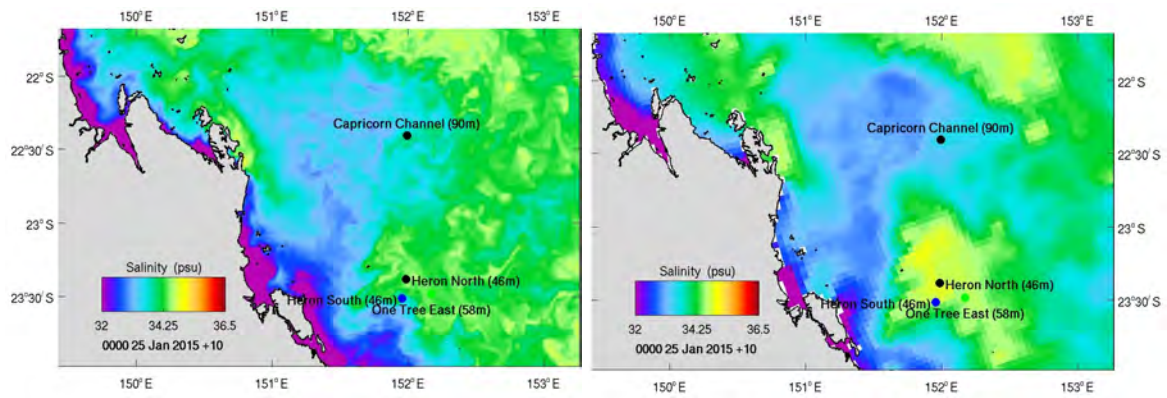


Figure 5.2.14. Surface GBR4 salinity for GBR1 (left) and GBR4 (right) in the vicinity of the Capricorn Channel mooring on 25 January 2015.

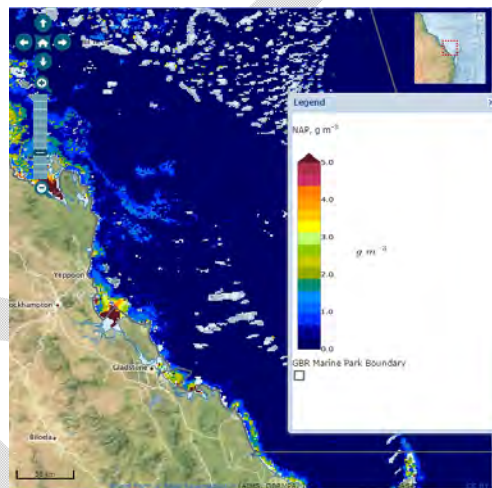


Figure 5.2.15. Non-algal particulates (suspended sediment) on 31 January 2015 from the BoM Water Quality Dashboard.

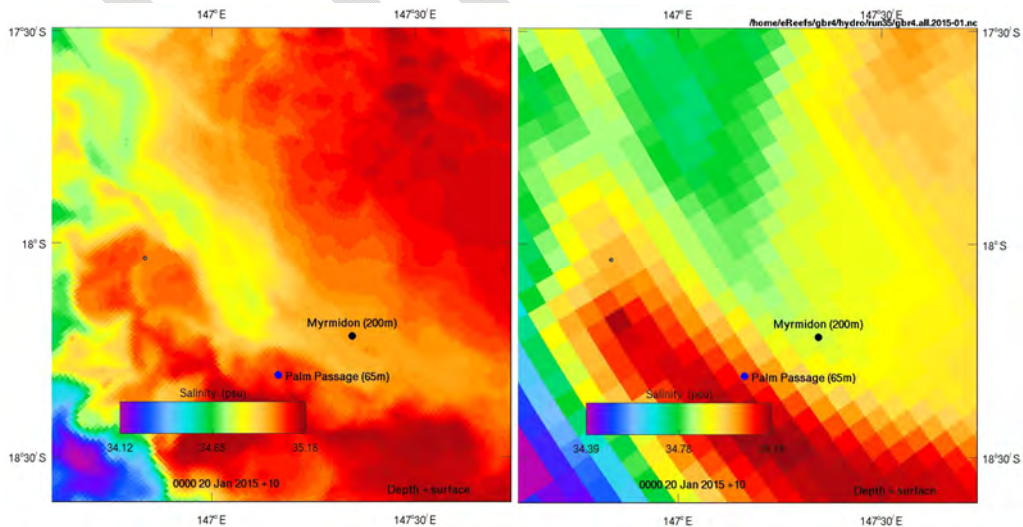


Figure 5.2.16. GBR4 salinity at 17 m for GBR1 (left) and GBR4 (right) in the vicinity of the Palm Passage / Myrmidon mooring on 20 January 2015.

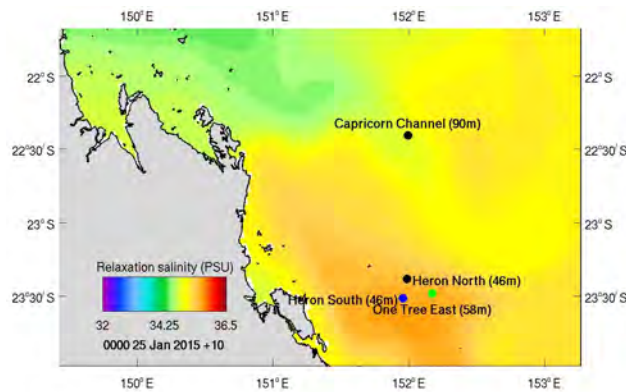


Figure 5.2.17. Surface GBR4 salinity for OceanMAPS in the vicinity of the Capricorn Channel mooring on 25 January 2015.

Discrepancies in model-observation comparisons during the summer of 2014 / 2015 at a single point can be traced to forcing (precipitation) issues or model sampling occurring on the wrong side of sharp frontal gradients. The latter issue is magnified in GBR1. Short term departures from observation have been observed in the GBR4 calibration (Fig. 5.1.5) and validation (Fig 5.1.22) comparisons also. Dry season salinities for 2015 will be monitored as delayed mode observations become available to ensure the mean salinity state (i.e. non rain / flood impacted) is consistent with observation.

Overall, across all variables, the 1km model contains similar skill to the 4km model when compared to observations at a single point, but possesses more realistic circulation at the scale of individual reefs.

5.3 Hydrodynamic analysis

5.3.1 Catchment connectivity using passive tracers

In the context of understanding the impact of riverine discharges on the health of GBR ecosystems, the hydrodynamic models developed as part of eReefs provide a valuable tool in elucidating the spatial impact of discharges from various catchments into the GBR lagoon. Coral cover on the Great Barrier Reef (GBR) has declined by half since 1985, with 42% of the observed decline attributed to coral predation by Crown-of-Thorns Seastar (COTS). Over the last 50 years, COTS populations have exhibited a cyclic pattern of abundance with outbreaks at ~ 15 year intervals. While the underlying cause(s) for the outbreaks are not fully resolved, there is evidence of a link with higher nutrient availability following major flood events (Fig. 5.3.1). River runoff carries enhanced nutrient and suspended sediment loads, and higher nutrient availability can support increased phytoplankton biomass during the period when COTS larvae are in their pelagic filter-feeding stage and increase larval survival above a critical threshold that triggers a primary outbreak. However, existing observational techniques are not able to distinguish the contributions of individual rivers to the region of COTS outbreaks.

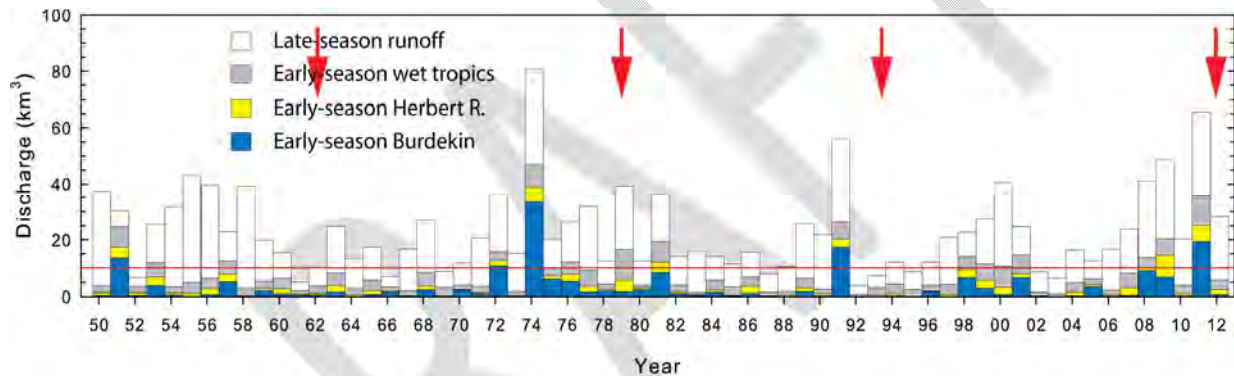


Figure 5.3.1. Estimated wet season river runoff (total bars) from 1949-50 to 2011-12. Coloured sub-bars show estimated early wet season (Nov-Feb) runoff into the north and central GBR potentially able to influence the COTS outbreak initiation region (14.5-17°S). Red arrows indicate nominal years of COTS outbreak initiation. The red horizontal line shows a runoff volume of 10 Km³.

Hydrodynamic models provide a valuable tool for identifying, quantifying and communicating the spatial impact of discharges from various rivers into the GBR lagoon. Hydrodynamic models can simulate the three-dimensional transport and fate of material delivered to the marine environment, and deliver benefits over traditional static observations of river plume distributions. Whilst aerial and remote sensing can track the visual extent of river plumes, it is generally difficult to quantify the contribution of individual rivers to the overall observed spatial impact. The impact of the rivers is often confounded by a number of factors including: plumes from adjacent rivers which spatially overlap and mix; inputs of low salinity tropical water advected from the north and low surface salinity due to rainfall, which is rapidly mixed. Numerical models provide a number of solutions to this problem. During flood events, discharges of freshwater are resolved by the model's salinity solution. Passive tracers overcome the problems of using salinity alone as a tracer, as they allow the water from the individual rivers to be uniquely tagged and their spatial impacts assessed. Passive tracers act

as virtual markers and are conservatively advected and diffused in an identical fashion to physical variables such as temperature and salinity, but play no dynamic role in physical or biogeochemical processes. Distributions of tracers show the transport of river inflows along the GBR and clearly indicate the coastal interactions of inputs from multiple catchments. Importantly, simulation of the transport of unique tracers 'released' from different rivers enables the identification of marine regions influenced by individual catchments, and provides insight into the mixing and retention of river water along various regions within the GBR lagoon (e.g. Brinkman et al., 2001; Luick et al., 2007).

The hydrodynamic models currently being applied to the GBR as part of the eReefs project have provided a valuable tool for identifying, quantifying and communicating the spatial impact of discharges from various rivers into the GBR lagoon. Using a hindcast simulation of the 2010-2011 wet season, river-specific passive tracers were released from each of the major rivers (Table 5.3.1) between the Burdekin River and the Normanby River known to impact the COTS outbreak region in order to elucidate the contribution of each individual river to this region of the GBR (Fig. 5.3.2).

Table 5.3.1 Rivers included in the 2010-2011 wet season hindcast simulation. Rivers in which passive tracers were released are shaded.

Normanby River	Daintree River
Barron River	Mulgrave-Russell Rivers
Johnstone River	Tully River
Herbert River	Haughton River
Burdekin River	Don River
O'Connell River	Pioneer River
Fitzroy River	Burnett River
Mary River	Fly River
Calliope	Boyne
Caboolture River	Pine River
Brisbane River	Logan River

Model simulations of the 3-dimensional distributions of passive tracers for the 2010-2011 wet season were analyzed to produce weekly estimates of cumulative exposure to tracers above a threshold of 1% of the source concentration. The exposure index integrates both concentration above a defined threshold and the duration of exposure, and provides a consistent approach to assess relative differences in exposure of GBR shelf waters to inputs from various rivers.

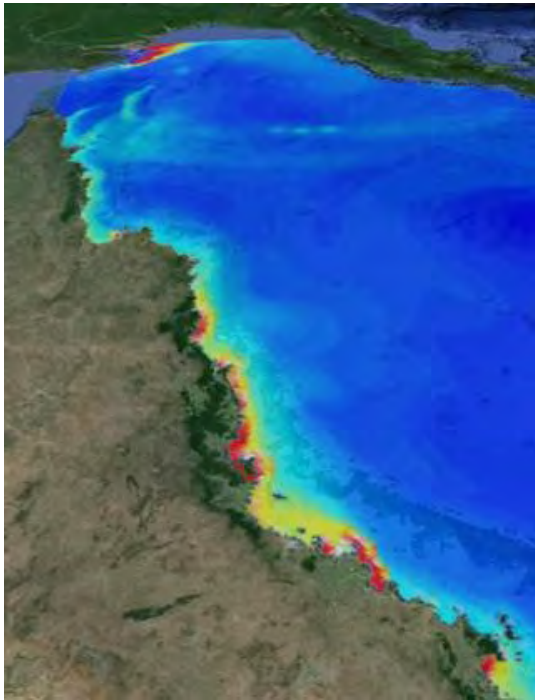


Fig. 5.3.2. Predicted salinity (on a scale of red-yellow-blue showing a gradient from low salinity to full salinity seawater) along the central and northern GBR coast. Freshwater plumes from various river mix along the coast and effects of individual rivers cannot be distinguished.

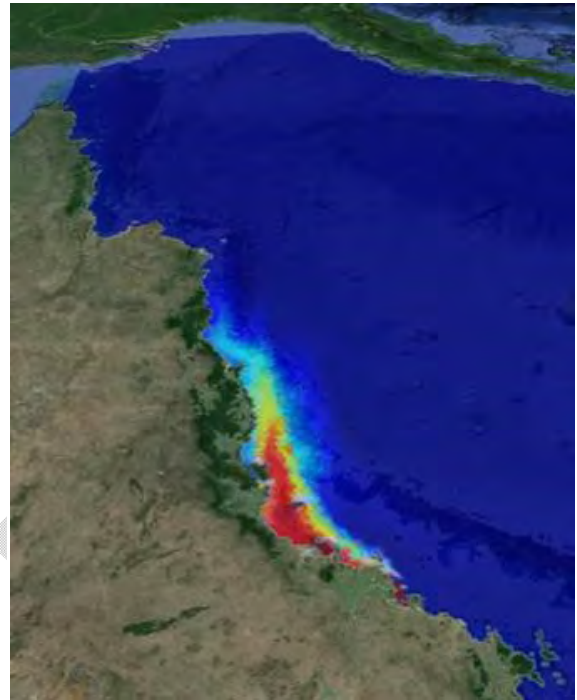


Fig. 5.3.2b. Dispersal of water from the Burdekin River as identified by a virtual tracer model (on a scale of red-yellow-blue showing a gradient of high to low tracer concentration).

Relative contributions of individual rivers to the COTS outbreak region between Cairns and Lizard Island were calculated based on the total cumulative exposure index, aggregated spatially in latitudinal bands covering the region of interest. Because it is the contained nutrients (N,P,Si, etc.) in river runoff rather than freshwater per se which regulates phytoplankton growth and biomass, the major rivers influencing the outbreak area were also ranked on the basis of their estimated DIN (dissolved inorganic nitrogen = $\text{NH}_4^{++}\text{NO}_2^- + \text{NO}_3^-$) inputs to the Cairns-Lizard Island region. Phytoplankton biomass in GBR waters is largely nitrogen-limited (Furnas et al., this volume), so bloom formation relies on the input of externally-sourced, bio-available N to reef waters.

This application of eReefs modelling has provided a quantitative identification of high or extended exposure to individual river plumes and therefore provided a basis for prioritizing catchments for management attention. This work formed a significant part of the background material on the linkages between river runoff, phytoplankton blooms and primary outbreaks of crown-of-thorns starfish in the Northern GBR, which in turn informed the 2013 Scientific Consensus Statement: Land use impacts on Great Barrier Reef water quality and ecosystem condition.

5.3.2 Temperature Exposure

Many of the stressors on reef systems, including coral bleaching, cannot be mitigated through management strategies, however, it is extremely important to know which reef systems are vulnerable to this stress so that other stressors responsive to mitigation strategies can be targeted to reduce the overall negative burden on reef health for these systems. One such approach to identifying reefs that may potentially be impacted by coral bleaching is to use a map of degree heating days (DHD) constructed from satellite sea surface (SST) images. Degree heating days are a measure of the cumulative heat stress on the reef computed by integrating the temperature when it lies above the long term mean. If the SST temperature is one degree above the long term mean for one day, then the DHD value will be 1. Alternatively, if the SST is 0.5°C for 2 days, then the DHD value is also 1. A DHD value of 120 is considered to pose significant risk for coral bleaching. The National Oceanographic and Atmospheric Administration (NOAA) deliver global products in near real-time of Accumulated Heat Indices which provide an indication of the Stage 2 thermal stress. An improved local product tailored to the GBR, ReefTemp, has been developed which allows a now-cast to be provided to assess the risk of bleaching for individual reef (Maynard et al, 2007). The products included in this now-cast are the SST anomaly (the number of degrees above the long term mean for a given month), degree heating days and the heating rate (DHD divided by the number of days temperature exceeds the long term mean). These indices are computed using composite images of SST from satellite thermal imagery using NOAA's environmental AVHRR platforms. ReefTemp can be accessed at <http://www.cmar.csiro.au/remotesensing/reeftemp/web/index.htm>. A map of DHD produced on 1 March 2015 is shown in Fig. 5.3.3. This shows DHD values of between 80 to 100 in the GBR lagoon with a band of lower DHD over the reef matrix in the southern reaches of the GBR. The northern GBR is associated with low DHD values. In the southern limits of the map these exist isolated areas with DHD values greater than 120, but overall during the summer of 2015 there does not appear to be severe risks to the reef from coral bleaching.

Caution must be applied when assessing bleaching stress using remotely sensed surface observations of temperature. Firstly, the satellite only samples the first few microns of the sea surface which may be different to the bulk surface temperature at a few tens of centimetres depth. An outgoing net heat flux across the surface boundary may result in the surface skin being several tenths of a degree colder than the bulk temperature; this is known as the skin effect (Katsaros, 1980). Alternatively, under low wind conditions and high insolation, the first few metres may increase by several degrees more than the main mixed layer (diurnal heating; Stramma et al, 1986). Irrespective of the errors incurred when sampling the sea surface from space, a fundamental problem exists in that corals often grow on the sea floor where the temperature regime can be markedly different from the surface.

The difference between surface and bottom temperatures is controlled by how incident short wave radiation at the surface is attenuated with depth, how heat fluxes across the sea surface are mixed through the water column, and what water masses are transported through the reef matrix. The distribution of short wave radiation is controlled by the clarity of the water; very clear water can transmit shortwave radiation with little loss of energy, allowing much of the heat energy to be delivered to the benthos. Alternatively, turbid water results in little light reaching the bottom, hence heating effects are minimal. Atmospheric heating/cooling of the sea surface due to sensible and latent heat fluxes, longwave radiation loss and absorption of

shortwave radiation at the blue end of the spectrum is distributed throughout the water column as a function of vertical mixing processes. Vertical mixing is promoted by current shear and density convection, and is inhibited by a stably stratified density profile. The mixing response of the water column to shear, buoyancy and transport of turbulent kinetic energy is non-linear and complex, and remains best approximated by numerical turbulence closure schemes (e.g. GOTM, Burchard et al, 1999). Importantly, a stratified water column will typically experience differing thermal regimes at the sea surface and sea floor. In terms of heat stress on coral, the controlling factor is how heat is mixed from the surface to the depths where coral resides. Transport of water masses may also lead to bottom temperature signals that are not observed at the surface. An example of this is upwelling, where cooler water is brought from depth, and may not result in a surface signature if it does not intrude into the base of the mixed layer. The GBR is subject to bottom driven upwelling where the interaction of the East Australian Current (EAC) with the shelf slope results in an upward Ekman transport in the bottom boundary layer. This can slosh cool (and nutrient rich) water into the GBR lagoon, allowing bottom temperatures to differ to that of the surface (Brinkman et al., 2002). It is therefore possible that a large surface derived DHD stress index may not in fact be delivering actual stress to corals on the benthos, or conversely, a critical DHD diagnosed at the surface may not pose a risk on the sea floor.

The GBR4 and GBR1 models possess comparable skill to satellite derived products. One advantage of these products is that they offer a three-dimensional view of a water body, and both sea surface and bottom temperatures can be retrieved. The DHD index can be constructed using temperature from the GBR1 model, employing a long term mean derived from the CARS climatology (Ridgeway et al, 2002). The surface model DHD distribution is shown in Fig. 5.3.4, from which it is seen that the distribution is largely consistent with the ReefTemp distribution; elevated values exist in the southern GBR lagoon with a reduced band over the reef matrix at the shelf edge. The northern GBR has lower values, however, elevated values are observed close inshore. The distribution of DHD at the sea floor as inferred from the model is shown in Fig. 5.3.4; this distribution is significantly different to the surface distribution. Generally two scenarios occur over the reefs; the bottom DHD is zero over the reef matrix whereas the surface values are not; i.e. surface DHDs are over-predicted, or surface and bottom DHDs are about the same resulting in a difference of approximately zero. In the southern GBR within the Capricorn Bunker group (20.5°S, 151°E) the latter situation predominantly occurs, with bottom values slightly larger than surface values to result in a slightly negative difference (Fig. 5.3.5). In the central GBR the former situation is the norm (Fig. 5.3.6), with surface, and therefore DHD differences, of ~30. The northern GBR also approximately zero DHD difference; in this area surface values are greater than bottom values to result in a small positive difference (Fig. 5.3.7). While most of the values lie well below the critical limits for bleaching, in some cases surface values provide a misleading indication of thermal stress the coral is actually exposed to. However, the surface estimate is conservative, in the sense that it usually over-predicts the stress, therefore in most cases bleaching prone regions would be detected using surface derived DHD distributions. Away from the reef matrix, exposure can vary dramatically from surface to bottom. Generally in shallow inshore regions bottom exposure is zero and that at the surface is not, with differences > 150 not uncommon. The largest bottom exposure occurs in the mouth of the Capricorn Channel, where corresponding surface values are modest to result in differences < -200. However, this area is free from shallow coral structures.

The GBR1 model does not exactly emulate reality, and consequently DHDs contain error and are approximate. Although the model resolution (1 km) is sufficient to capture individual reefs, the solutions should still be considered a reef-wide average. This means that the bathymetry in a model grid point is a reef-wide average, and the bottom depth in the model may vary considerably from the depth of an individual coral cluster. Satellites are similarly not without approximations (skin effect and diurnal heating aside); resolution is also coarse (1 km), as are temporal updates where DHDs are assembled (typically using only a day and night pass) which do not capture the diurnal cycle. The model is capable of resolving this cycle since it uses a time-step on the order of minutes. Regardless of the limitations inherent in the model when diagnosing DHDs, the lack of consensus between surface and bottom DHDs cannot be ignored; DHDs rarely are the same at surface and bottom and can vary by 100% when bottom exposure is zero but that at the surface is not. Satellite derived DHDs remain a valid indicator of coral bleaching potential, with the caveat that actual thermal stress at the benthos may be zero whereas that from that diagnosed by satellite imagery is not.

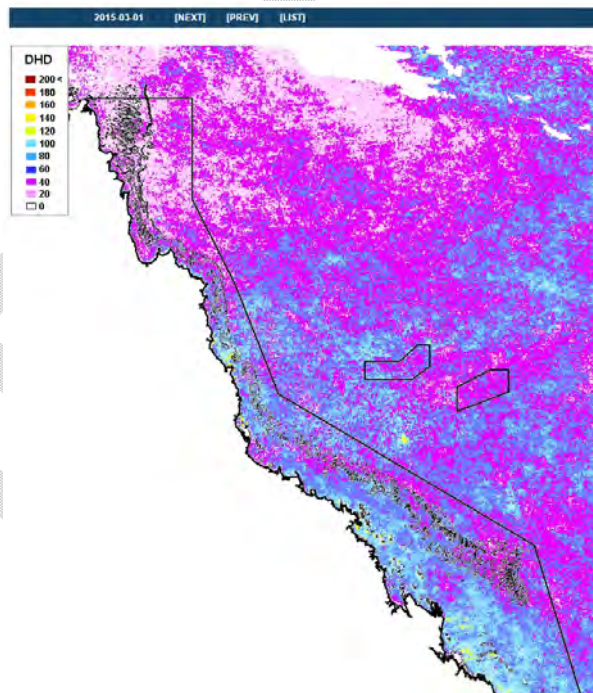


Figure 5.3.3. DHD for 1 March 2015 from ReefTemp

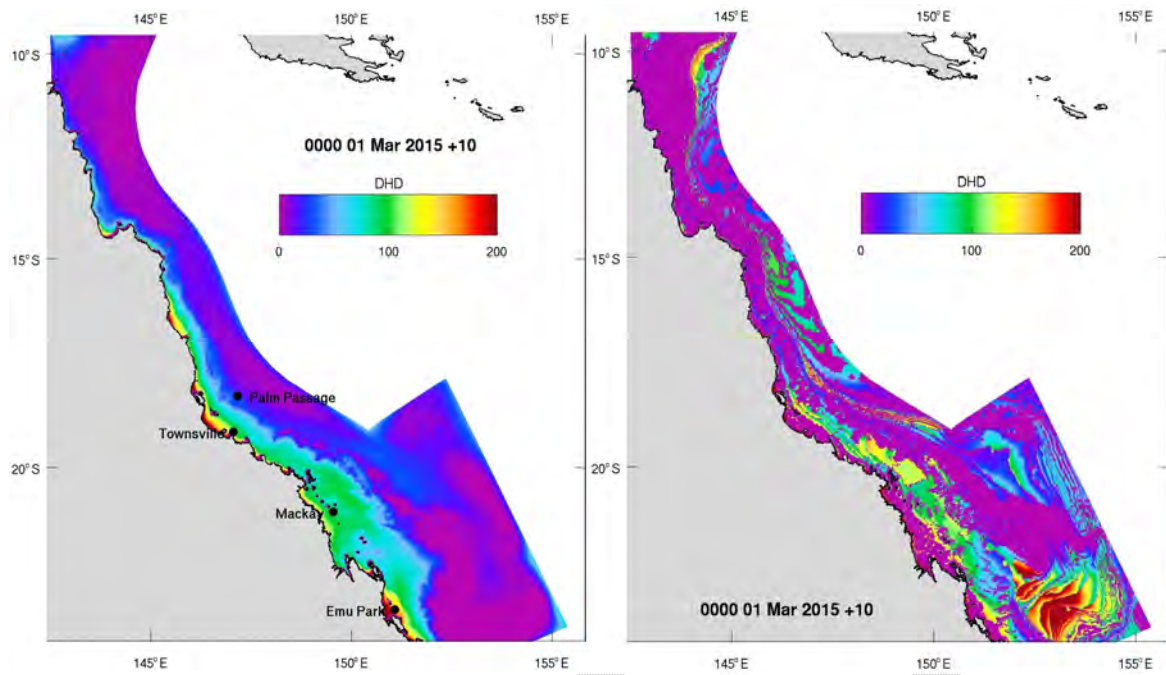


Figure 5.3.4. Surface (left) and bottom (right) DHD from GBR1

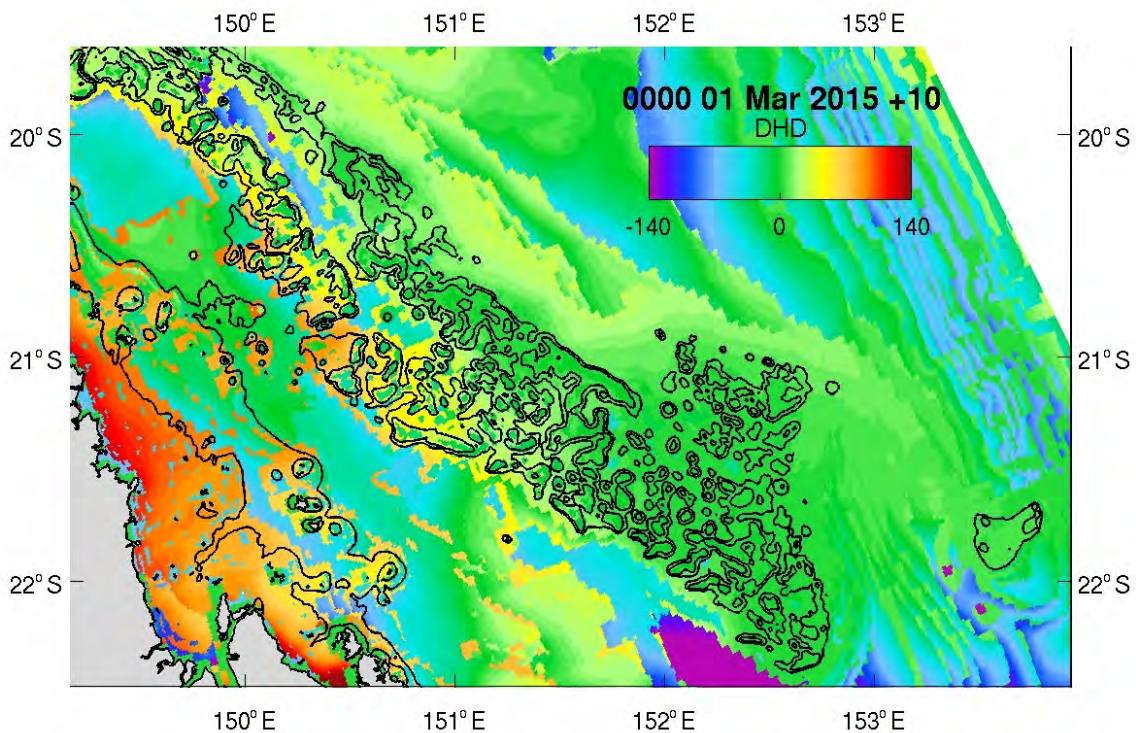


Figure 5.3.5. DHD difference (surface minus bottom) over the southern GBR (Capricorn Bunker Group). Depth contours are overlaid (50 and 25 m) to indicate reef clusters.

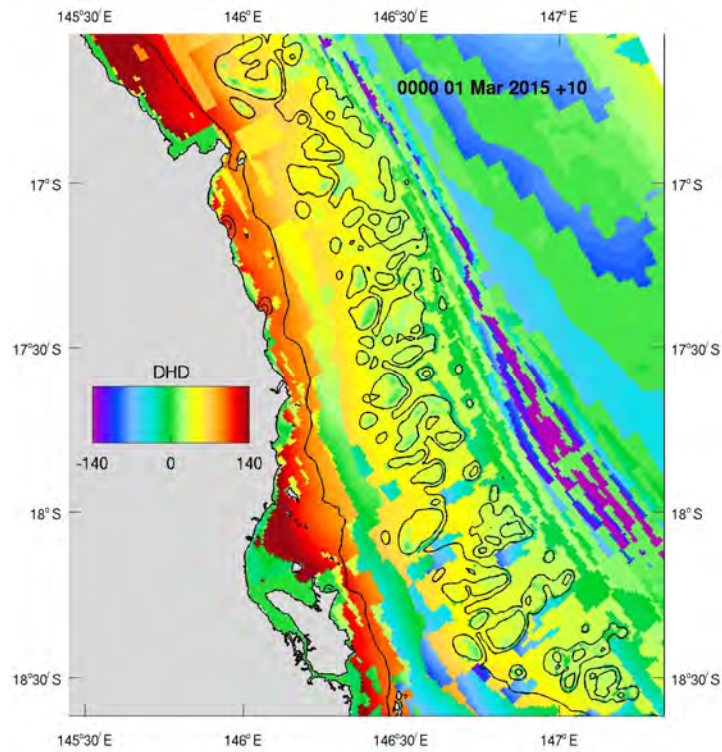


Figure 5.3.6. DHD difference (surface minus bottom) over the middle GBR (Hinchinbrook Islands). Depth contours are overlaid (50 and 25 m) to indicate reef clusters.

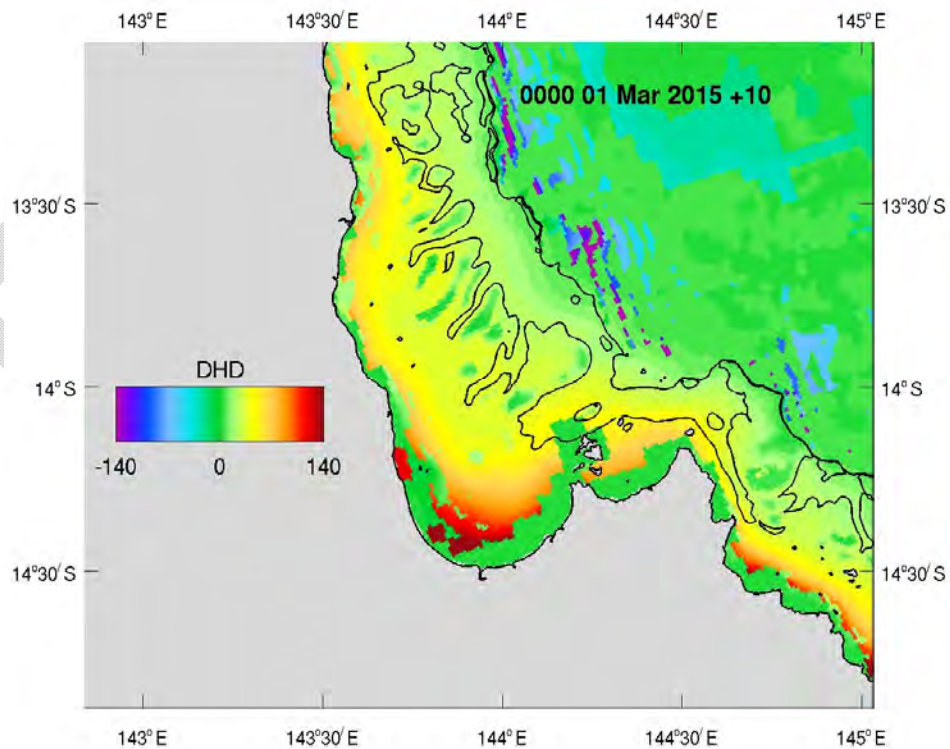


Figure 5.3.7. DHD difference (surface minus bottom) over the middle GBR (Flinders Group). Depth contours are overlaid (50 and 25 m) to indicate reef clusters.

5.3.3 Coral Sea Connections

An analysis of horizontal fluxes through vertical sections corresponding to the open boundaries of the GBR4 domain reveals that ocean temperature and salinity fluxes in the GBR region are dominated by their seasonal cycle. The second-largest contribution to temperature and salinity fluxes are interannual and mesoscale (eddy) velocity anomalies which interact with the seasonal temperature and salinity fields. However, these fluxes are typically much smaller (order 10%-30%) than the seasonal fluxes. The amplitudes of all other terms are negligible.

Residence, or flushing, times are popular metrics to diagnose the dynamics of a water body and to determine the fate of dispersals, nutrients or sediment river plumes (e.g. Bailey and Ollis, 1986; Tartinville et al., 1997). Due to limitations associated with these approaches a statistical method to aid the interpretation of spatial distributions of passive tracer concentrations was used to infer the distribution and magnitude of tracers released along the shelf edge. Two release curtains were implemented to study the impact of different injection zones (Fig. 13), one that followed the shelf-edge and the other one being a cross-shelf section. Generally, the reef matrix forms a barrier to onshore support, except in the vicinity of channels which connect the reef lagoon to the shelf. Furthermore, there are several locations on the shelf edge where enhanced exchange activity occurs. These 'hot spots' have been identified in the 50 percentile distributions of tracer and are located near Pompey Reefs and a region bracketing Palm Passage (Fig. 5.3.8 and 5.3.9).

The tracer experiments present a proxy for understanding the spatial pathways of oceanic derived nutrients delivered from below the surface mixed layer. The tracer source identified along the offshore margin of the Pompey Reefs represents a likely source of the nutrients that supports high rates of bacterioplankton and phytoplankton production and pelagic respiration, which ultimately sustain rich and diverse assemblages of suspension-feeding benthic communities that thrive in this region (Alongi et al., 2015). At Palm Passage, the simulated plume provides evidence of the pathway that contributes and increased fluxes of nutrient into the lagoon. Observational evidence suggests that this region is an important conduit for cool, nutrient rich waters to impact the inner shelf (Furnas and Mitchell 1996) and satellite derived chlorophyll imagery and drifter trajectories show a distinct inflow to the lagoon in this region (Brinkman et al., 2002).

The results of these analysis are described in full in the publication:

Schiller, A., Herzfeld, M., Brinkman, R., Rizwi, F., Andrewartha, A. (2015) Cross-shelf exchanges between the Coral Sea and the Great Barrier Reef lagoon determined from a regional-scale numerical model. *Continental Shelf Res.*, 109, 150-163.

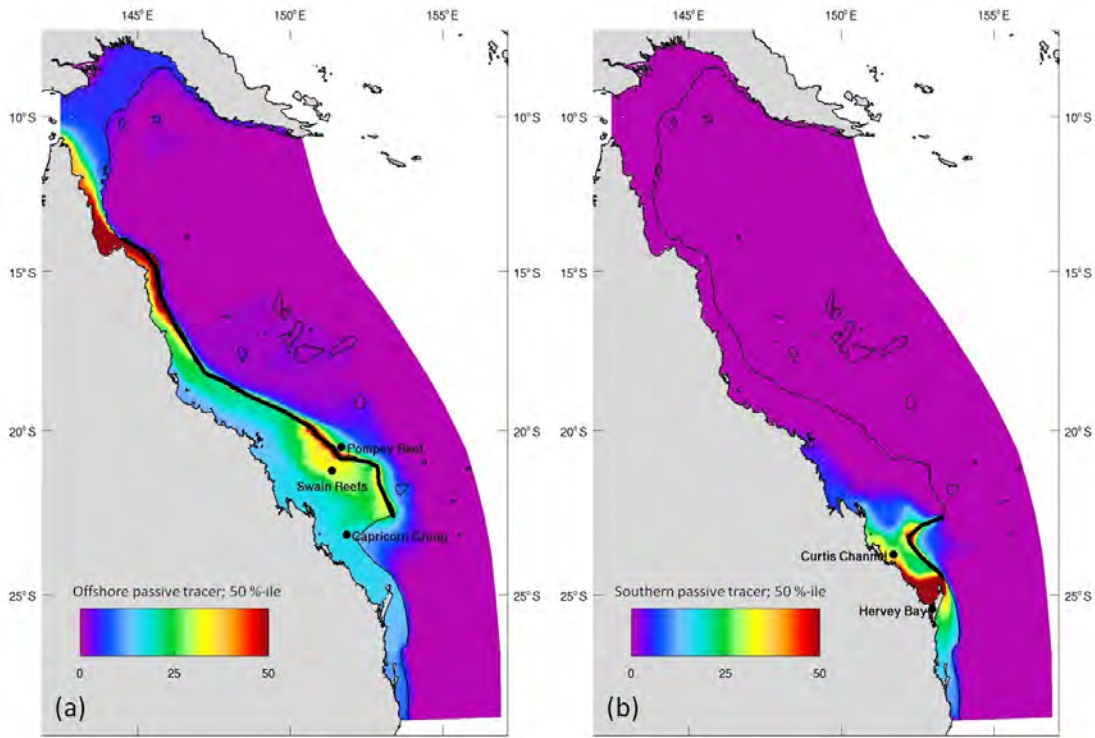


Figure 5.3.8. Median passive tracer distributions due to unit tracer release along the (a) offshore curtain and (b) southern curtain. Thick black lines denote the locations of curtain release. Thin black line is the 200 m isobath.

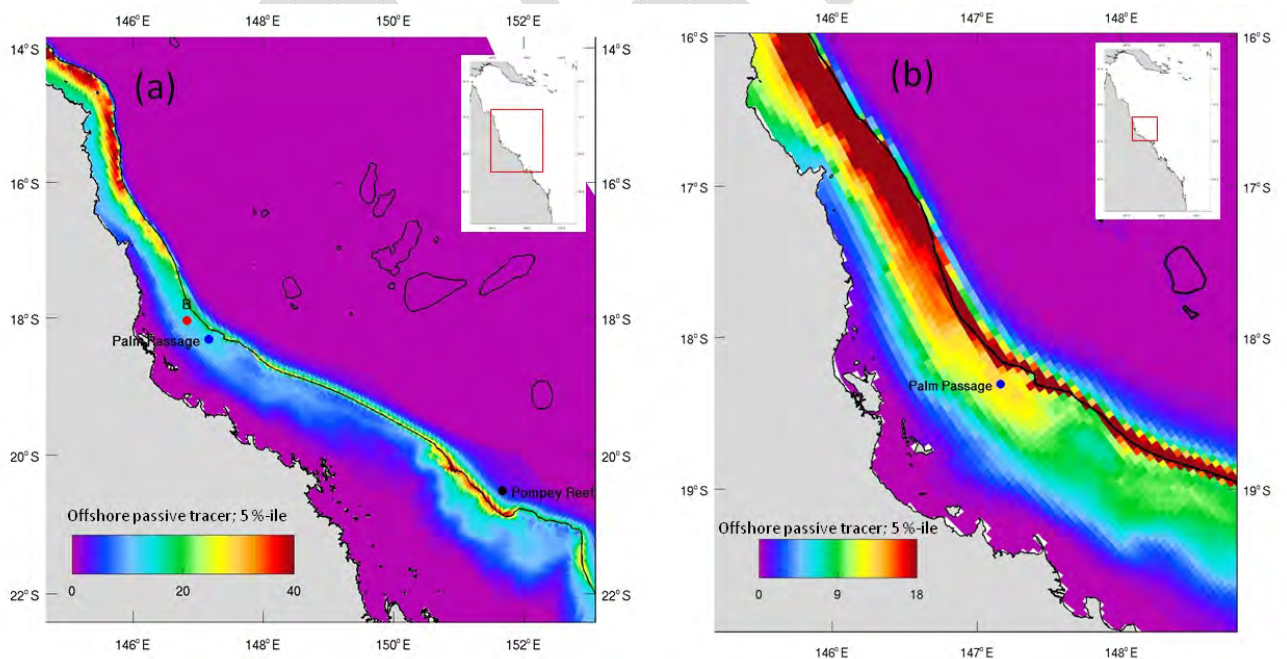


Figure 5.3.9. 5 percentile passive tracer distributions due to unit tracer release along the offshore curtains shown in Fig. 5.3.8. Left panel (a), central lagoon; right panel (b), Palm Passage region. Note different colour scales between plots. The black line is the 200 m isobath.

5.3.4 Decorrelation length scales

Decorrelation length scales are computed using the methodology outlined in Romanou et al, (2006), where the de-correlation length scale is defined as the zero crossing point of the auto-correlated lags. This provides an indication of the spatial scale within which some coherence of the distributions of temperature and salinity can be expected. The mean SST and sea surface salinity decorrelation length scale from the GBR4 model (averaged over December 2014) is presented in Fig. 5.3.10 and Fig. 5.3.11 respectively.

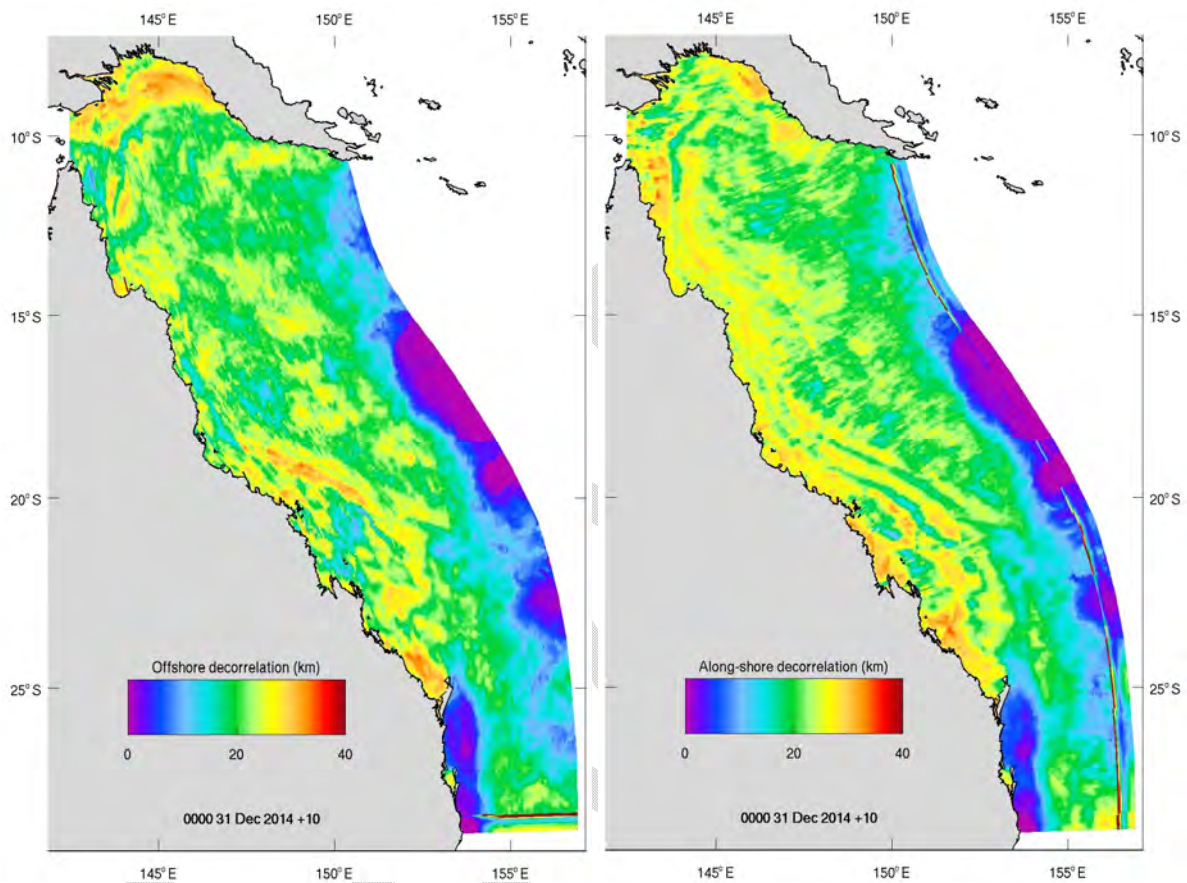


Figure 5.3.10. Mean SST decorrelation in the offshore direction (left) and along-shore direction (right).

Temperature and salinity exhibit similar distributions, with the decorrelation length scale being generally less than 40 km. This means that one cannot expect a sample at any location within the GBR to be representative of its surroundings beyond a 30 – 40 km radius. This is particularly relevant for in situ sampling, where any point measurement is expected to convey characteristics of the water mass within a small area relative to the whole lagoon. Decorrelation length scales are particularly small in the south of the domain, and mid-domain at the offshore boundary. Snapshots of SST decorrelation length scales from the GBR1 model in January 2015 are shown in Fig. 5.3.11. Magnitudes are similar to those computed from the GBR4 model, however, the snapshot provides an indication of the spatial variability around the mean state.

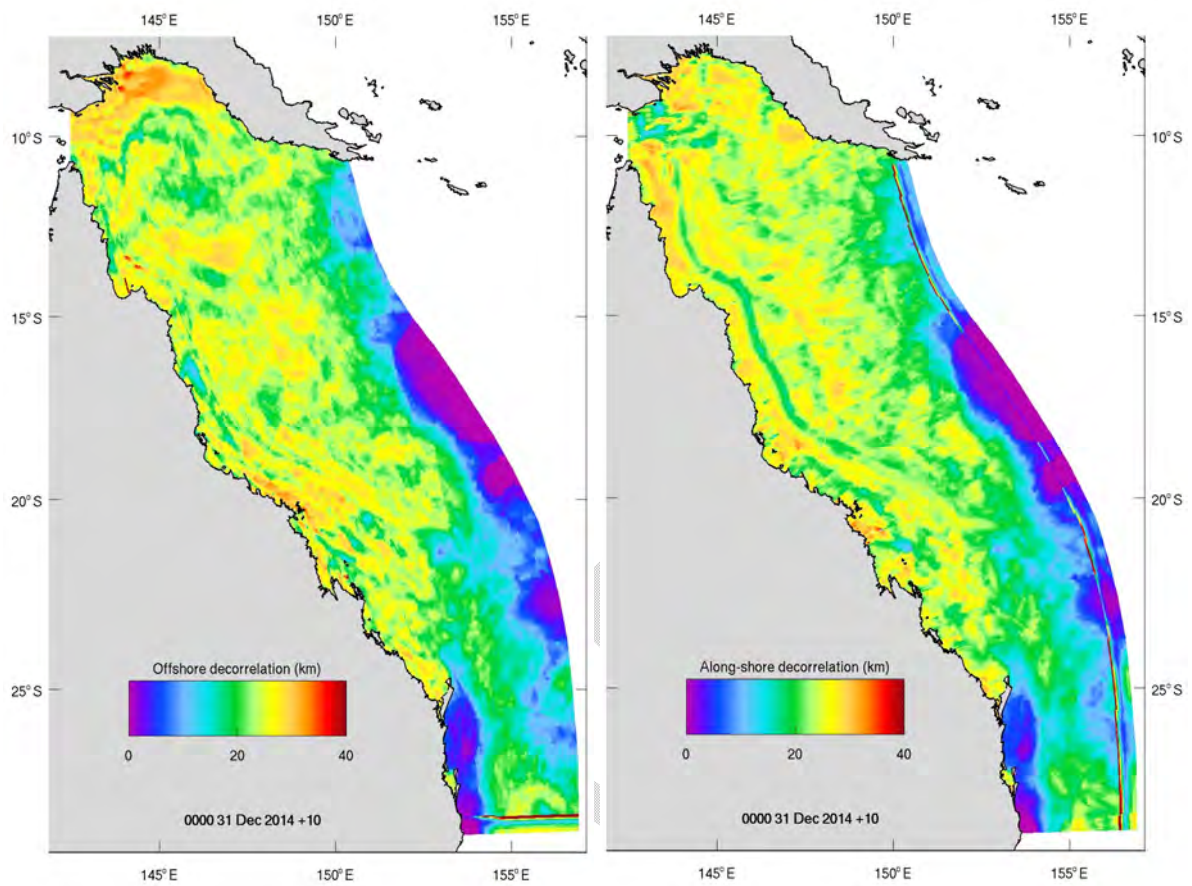


Figure 5.3.10. Mean SSS decorrelation in the offshore direction (left) and along-shore direction (right).

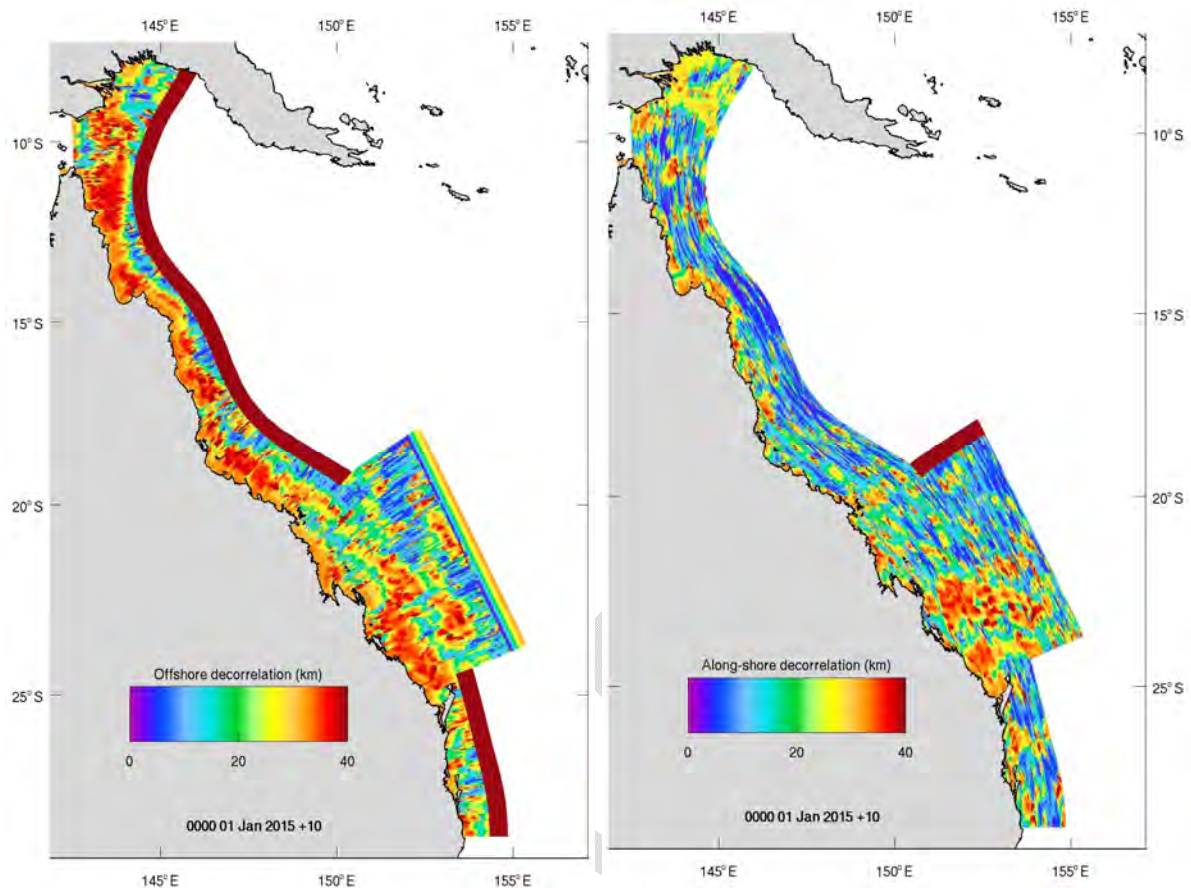


Figure 5.3.10. SST decorrelation in the offshore direction (left) and along-shore direction (right) for 1 Jan 2015.

5.3.5 Submesoscale Coherent Vortices

Submesoscale Coherent Vortices (SCVs) are phenomena observed in the ocean that are characterised by strong horizontal density gradients, vertical velocity and vorticity, horizontal scales of 10s of metres to 10s of kms and lifetimes of hours to days, (McWilliams, 1985). The coherent vortices exist in the surface layer and arise from mesoscale eddies and boundary currents (the EAC in this case). Dynamics within these eddies is no longer in geostrophic or hydrostatic balance, and they arise spontaneously from mesoscale features to advectively transfer energy to smaller scales.

The increased resolution employed in GBR1 allows for the generation of SCVs embedded in the mean flow (Fig. 5.3.11), having characteristics consistent with those reported in the literature; e.g. the modelled surface temperature in the California Current by Capet (2008) shows similar submesoscale structure at frontal boundaries as observed in GBR1. Fig. 5.3.11 (circled) shows several submesoscale features shedding from the edge of the EAC, and the time series shows that temperature decreases by close to 2°C as the SCV traverses the time series location. These SCVs are abundant in the GBR1 output, particularly near the EAC frontal boundaries, and can confound interpretation of larger scale features. The evolution of surface temperature and flow in one particular SCV on 4-5 January 2015 is shown in Fig. 5.3.12 in plan view and 5.3.13 in section view. These figures show that surface divergence of flow initially occurs leading to upward flow and a cooling of the surface. This is followed by a breaking

down of the vortex where surface flow converges and downward vertical flow results. In this case the vortex appears not to be in balance with sea level gradients (Fig. 5.3.14, top row), and is associated with low vertical mixing during its formation (Fig. 5.3.14, bottom row).

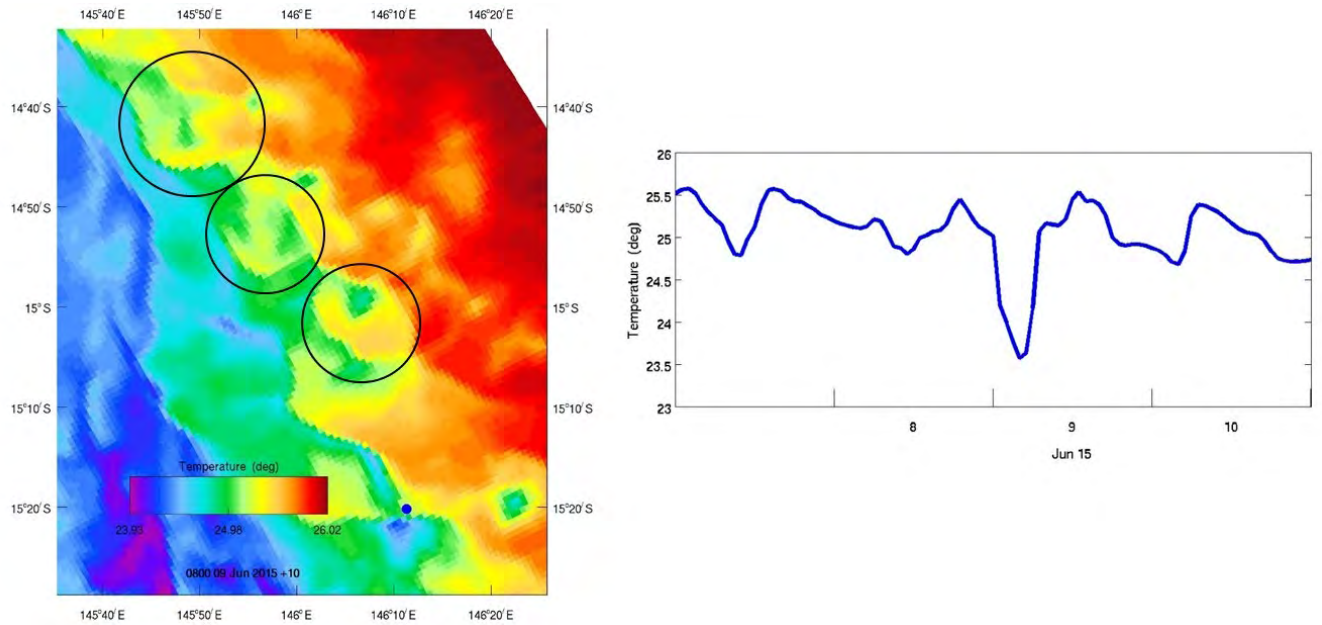


Figure 5.3.11. Snapshot of GBR1 surface temperature showing SCVs characterised by cold core vortices (left panel). A time series at the blue dot is shown on the right panel.

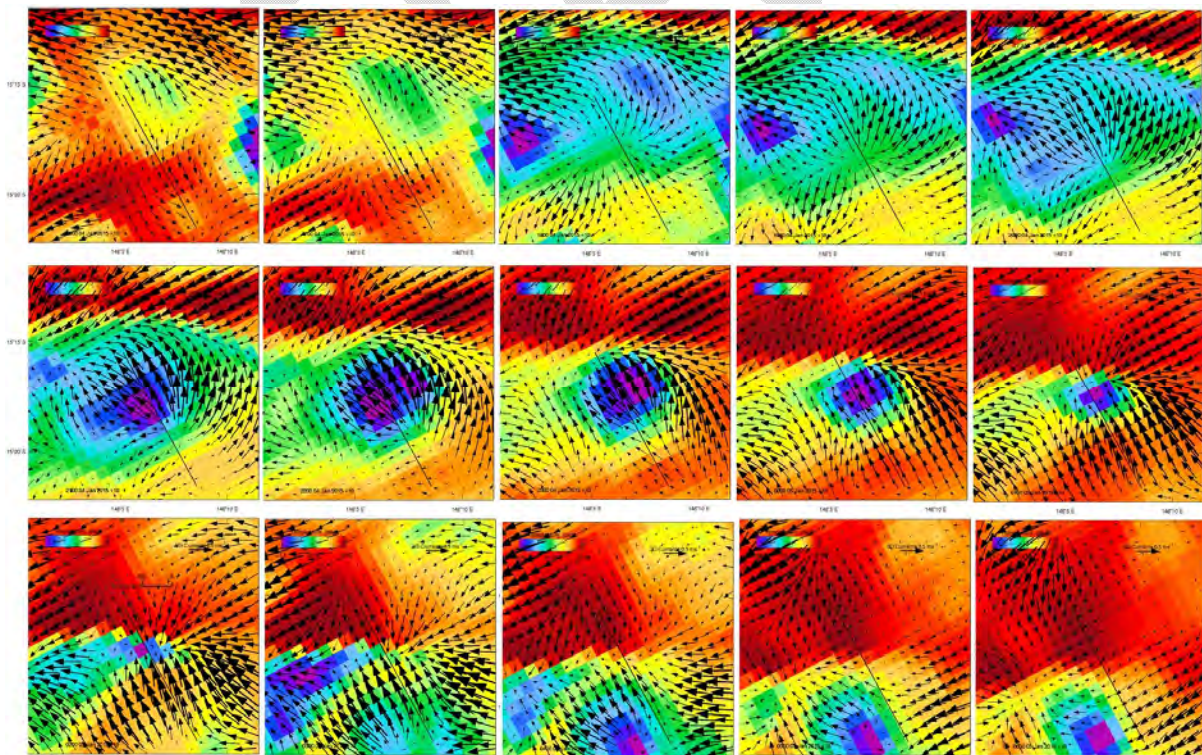


Figure 5.3.12. Surface temperature and flow in a SCV on 1600 4th January 2015 to 0500 5th January 2015 at 1 hour intervals.

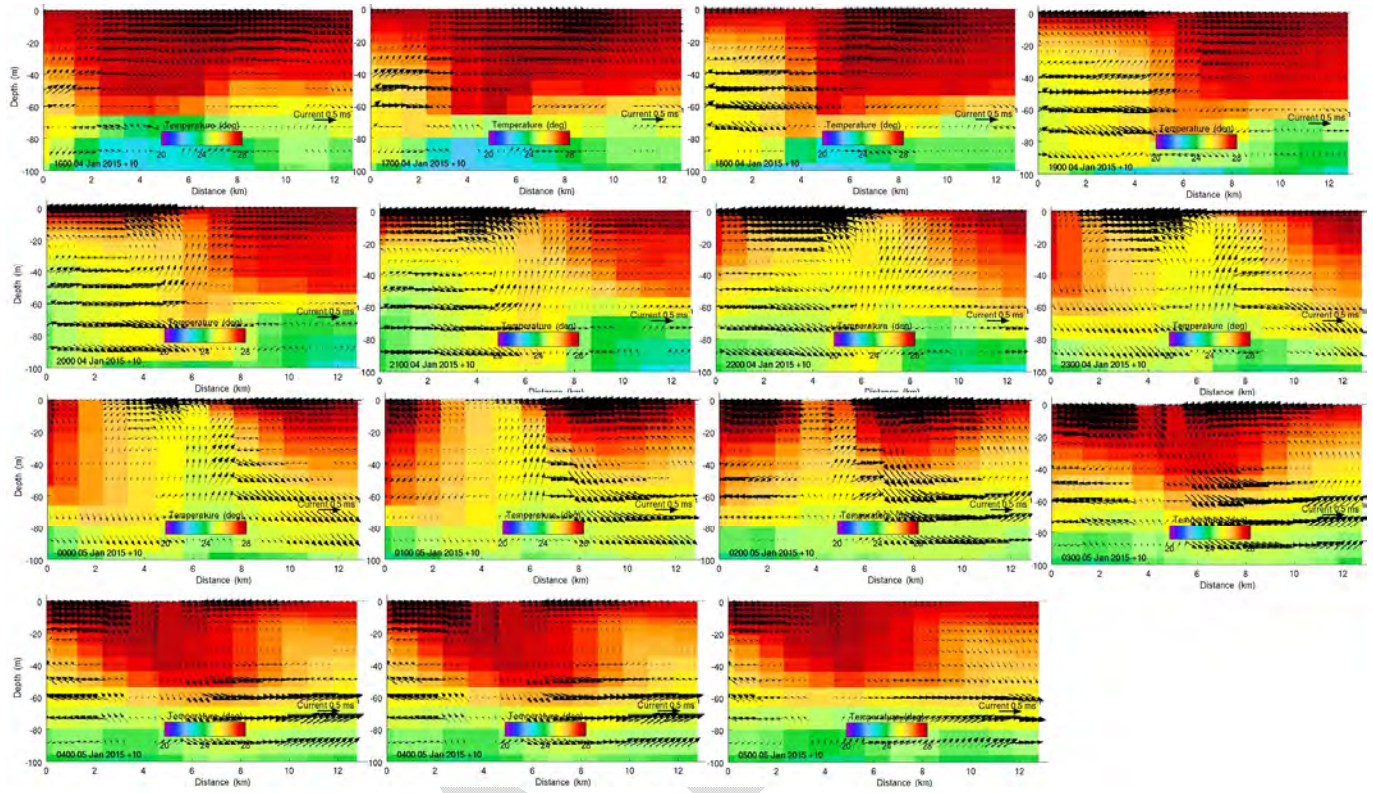


Figure 5.3.12. Cross sectional temperature and flow in a SCV on 4-5 January 2015. The cross section is identified in Fig. 5.3.12.

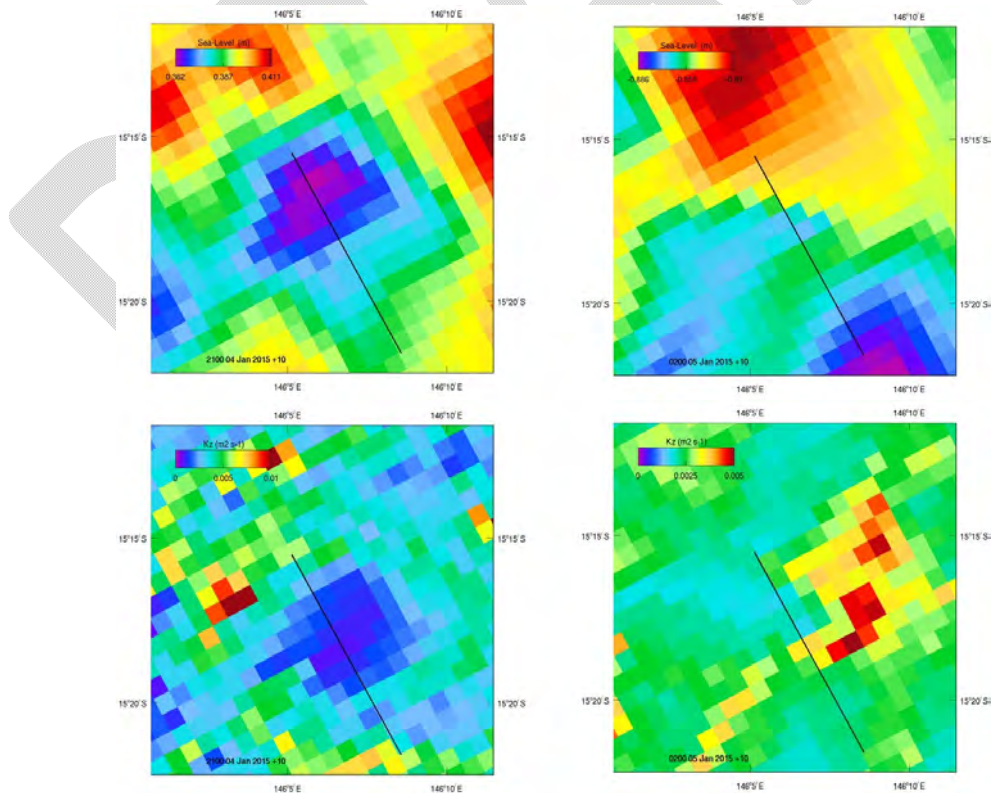


Figure 5.3.14. Surface elevation (top row) and vertical mixing (bottom row) during maximum flow divergence (left column) and flow convergence (right column).

The dynamics controlling SCVs is complex, and although the abovementioned studies provide some insights there appears to be no unifying theory of SCMs. Observations of SCVs are incomplete, theoretical investigations are limited, but modelling investigations provide the best path for further understanding. In numerical investigations of submesoscale effects in the stratified ocean, as the grid resolution increases it is commonly found that submesoscale currents will spontaneously emerge (e.g. http://carthe.org/tutorials_pdf/2013_10/McWilliams_Jim_Oceanic_Phenomena_and_Dynamics_at_the_Submesoscale.pdf). While it is yet to be determined if the SCVs observed in GBR1 can be measured in the field, under the current GBR1 parameterisation the model certainly favours the generation of these features. These features are not present in GBR4, owing to the coarser resolution. The presence of SCVs in GBR1 output should be considered in any analysis (i.e. large small scale, short term changes in flow and density are possible), and warrants future investigation in the field to ascertain their validity.

5.4 Sediment Transport

This section describes data-assimilation experiments and validation of the sediment transport model of GBR followed by a number of the preliminary scenario runs.

5.4.1 Assimilation of the remote sensing TSS

The sediment transport model assimilates suspended sediment concentration inferred from the remote sensing data (Fig. 5.4.1 right plot). The suspended sediment concentrations were estimated from daily MODIS-Aqua observations by coupling two physics-based inversion algorithms – a neural network atmospheric correction based on inverse modelling of radiative transfer simulations (Schroeder et al. 2007) followed by an in-water algorithm based on an adaptive linear matrix inversion (Brando et al. 2012). Extensive algorithm validation showed a mean absolute percentage error of 88% for the retrieval suspended sediments in the GBR region compared to concurrent ground measurements (Brando et al. 2015).

The assimilation scheme updates the initial concentration of benthic sediment and bottom roughness. The model ensemble comprises 32 members of the ensemble, run on National Computer Infrastructure (NCI). The assimilation period is 6 months (January 2011 – June 2011). Emulators are built sequentially in time over 2 days assimilation windows. Spatial fields are approximated via decomposition into truncated set of 3 basis functions. To improve the quality of the emulator, the shelf area is subdivided into 6 subregions shown in Fig. 5.4.1 (left plot; Brisbane, Fitzroy, Mackay, Townsville, North QLD, and Torres Strait). Each of these subregions is further subdivided into shallow coastal area (less than 30 m deep) and relatively deep shelf (from 30 to 100 m deep). For each of these subregions we build a separate emulator and then assimilate observations locally.

eDICE requires observations to be interpolated on the model grid. To speed up processing of the remotely sensed data, observations were sub-sampled with a 10 samples striding step. The minimum of the observed TSS values was set to 0.2 mg/L. The data were interpolated on every 10th model grid node. The assimilation period comprises 6-month and encompasses cyclone Yasi event in January- March 2011. The assimilation window is set to 2 days.

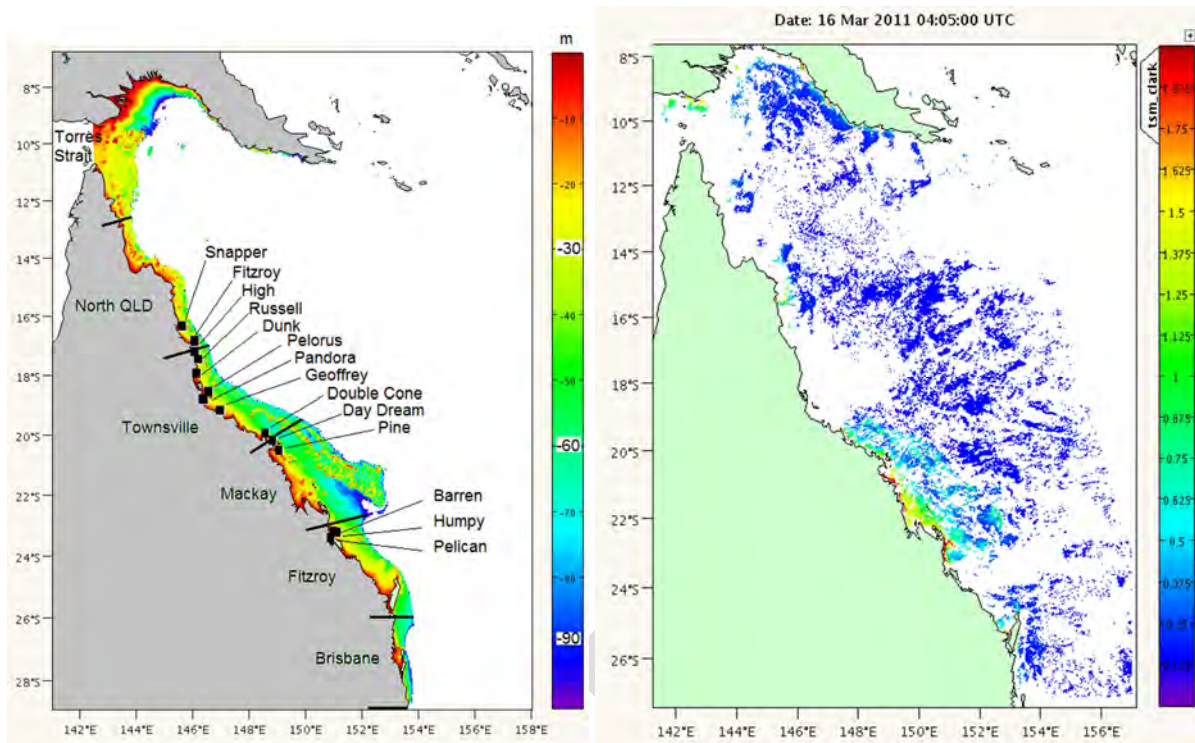


Figure 5.4.1. GBR shelf bathymetry truncated to 100 m depth (left plot). Thick lines indicate cross-shelf boundaries of the emulation and data assimilation subregions. Square dots show water quality monitoring sites. The right plot shows a snap-shot of TSS inferred from the remote sensing data.

The distribution of the bottom roughness inferred through the data-assimilation and validation study is illustrated in Fig. 5.4.2. Elevated levels of the sea-bed roughness are predicted in shallow coastal regions of the PNG shelf, in a macrotidal environment of the Broad Sound, around Fraser Island and over the southern part of offshore GBR. This distribution has been obtained through the assimilation of the remote sensing data and subsequent manual refinement of this map to improve agreement of the model with observations. The manual refinement involved, in particular, reduction of the bottom roughness along the north Queensland coast, in Torres Strait and around Fraser Island.

Patterns of benthic sediment distribution on the shelf (Fig. 5.4.2, right plot) inferred through the data-assimilation, in general, match patterns of the bottom roughness thus suggesting a correlation dependency between these two parameters. One of the implications of such dependency is a non-unique solution for the data-assimilation problem. In other words, the model can be fit to measurements using different sets of the tuning parameters. For example, having high roughness and limited amount of benthic sediments may produce the same levels of the suspended sediment as that for a scenario with small roughness and higher concentration of benthic sediments.

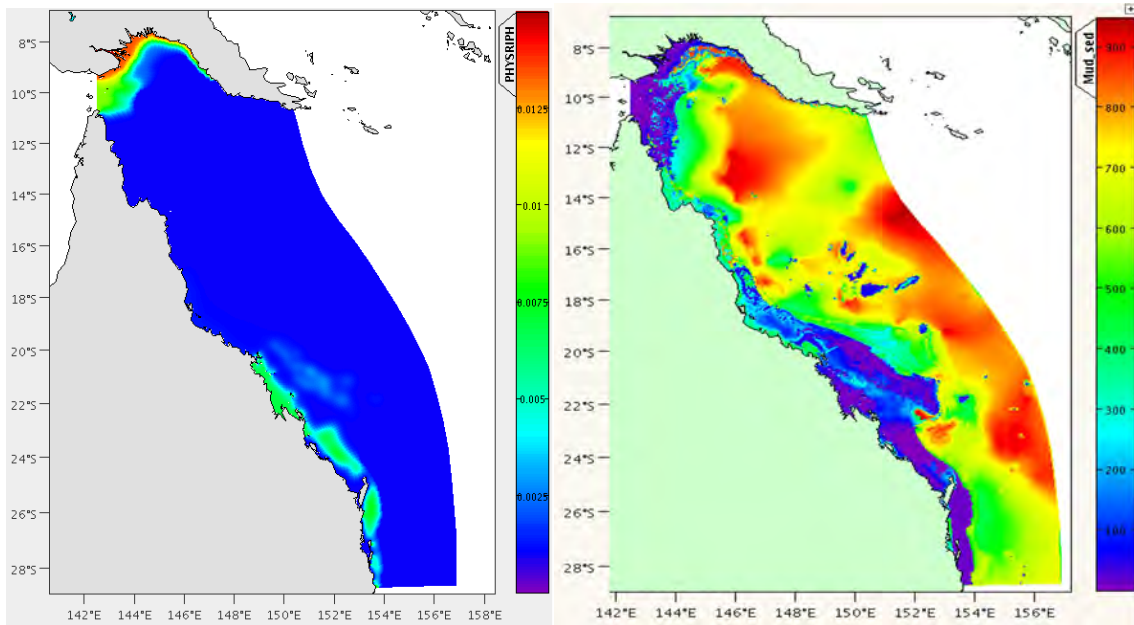
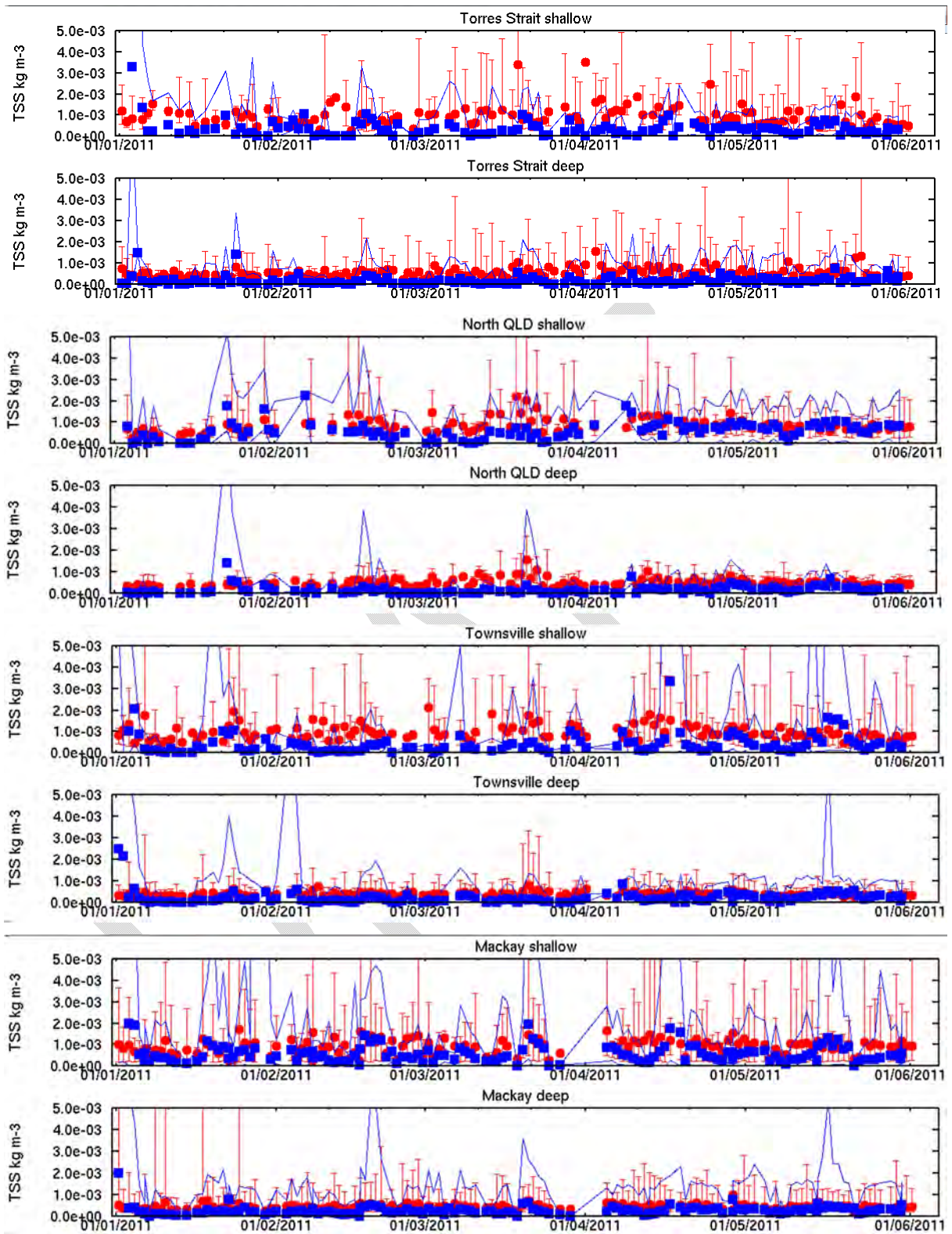


Figure 5.4.2. Bottom roughness and benthic mud estimated through the data assimilation and validation study

Fig. 5.4.3 illustrates comparison of the data-assimilating model against observations for individual subregions of the study area. As expected, the quality of the model varies across the region. The model tends to reproduce spatial gradients of the TSS levels across shallow coastal waters and relatively deep shelf waters. The data assimilating ensemble tends to underestimate sediment concentrations in the coastal Torres Strait and Townsville region. In northern QLD the simulated data are in general within the ballpark of observations. The model is, in general, consistent with observations in Mackay and Fitzroy regions and tends to miss high resuspension events in Brisbane area.

To illustrate improvements that the data-assimilation procedure brings into the model, in Fig. 5.4.4 an ensemble of the data-assimilating models is compared to the ensemble of unconstrained models initialised with a prior distribution of the parameters. The free-run of the ensemble of prior models grossly overestimates suspended sediment concentrations in the regions. The assimilation procedure “cools down” the ensemble of models and improves agreement between model and observations.



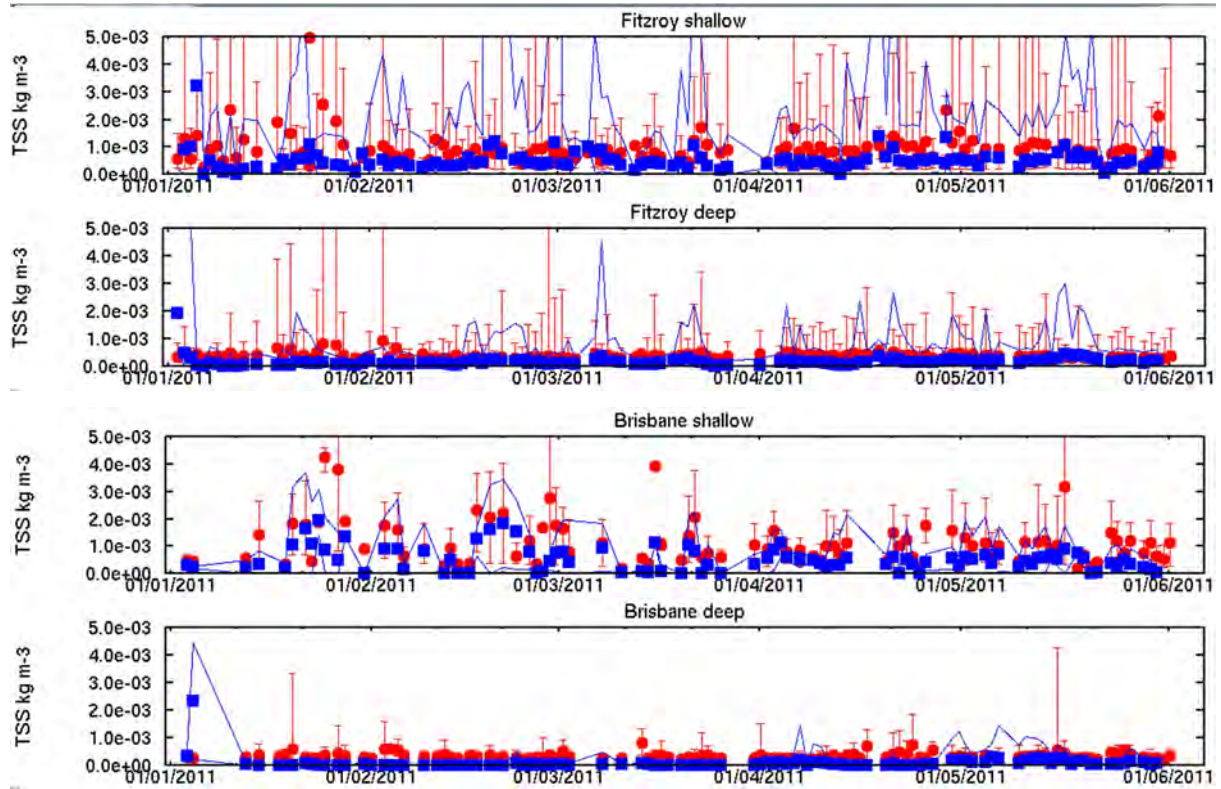


Figure 5.4.3. Data-assimilating run of the ensemble of models vs observations for different subregions. Red dots show observations integrated over the subregion. Blue dots show modelled data integrated over the subregion and over the ensemble members. Thin blue line shows modelled minimum and maximum values. See subregions map in fig. 5.4.1.

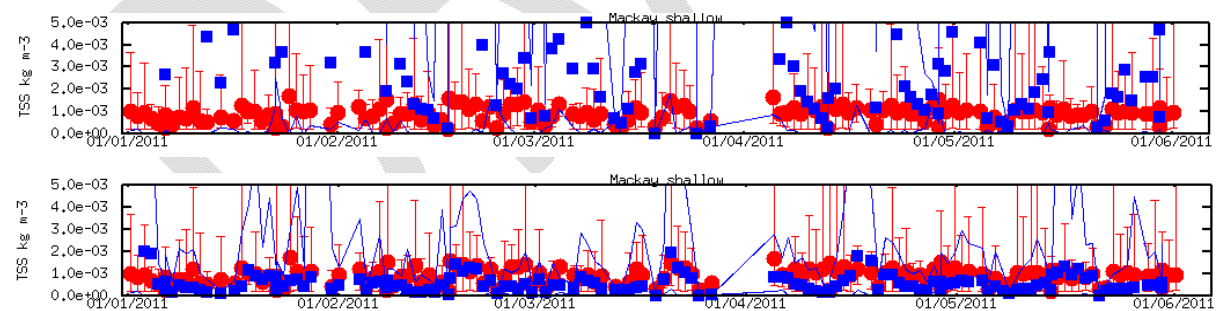


Figure 5.4.4. Control run of the ensemble of models vs observations (top plot). Data-assimilating run of the ensemble of models vs observations (bottom plot). Mackay coastal subregion. Red dots show observations integrated over the subregion. Blue dots show modelled data integrated over the subregion and over the ensemble members. Thin blue line shows modelled minimum and maximum values.

5.4.2 Model vs coastal records

Assimilation of the remote sensing data, as outlined in the previous section, produces an ensemble of the data-assimilating models. Because of the high computational expenses, operational run of such ensemble is not feasible. Instead, these models are integrated through time and across members of the ensemble to produce one single model of the sediment transport on GBR. To have a better understanding of the quality of such model, it was tested against 4 years of turbidity records taken at a number of locations along the GBR coast (Schaffelke et al., 2012). An assumption underpinning this comparison is that TSS scales with turbidity linearly and the scaling coefficient equals 1.3 (Schaffelke et al., 2011).

The sediment transport model initialised with the mean parameters (estimated through the data assimilation) shows a long-term drift of the sediment concentration on the shelf (not shown here). To remove this drift, vertical profile of critical shear stress in sediments has been manually adjusted making deep sediments less resistant to resuspension. Fig. 5.4.5 shows comparison of records of TSS simulated by this refined model against measurements at coastal observation sites (see site map in Fig. 5.4.1). According to this data, the quality of the model varies across the region and with time. The model tends to capture major resuspension events but overestimates peak sediment concentrations in the northern part of the region. In a macrotidal environment it predicts about the correct range of sediment concentrations and their seasonal and annual variability. The model grossly underestimates sediment concentrations at the Pelican site.

Quantitative estimates of the data-model agreement for different sites is shown in Fig. 5.4.6. A number of comparison metrics is used to evaluate the model. Mean absolute error (MAE), root-mean-square error (RMSE), and willmott-index are calculated as follows

$$MAE = \frac{1}{N} \sum_{i=1}^N |M_i - O_i| \quad 5.4.1$$

$$RMSE = \left(\frac{\sum_{i=1}^N (M_i - O_i)^2}{N} \right)^{0.5} \quad 5.4.2$$

$$WMT = 1 - \frac{\sum_{i=1}^N |M_i - O_i|}{\sum_{i=1}^N (|M_i - \bar{O}| + |O_i - \bar{O}|)} \quad 5.4.3$$

Here M is model, O is observation, and O with a horizontal bar is mean observation. Note that RMSE is known to be sensitive to the presence of outliers. The Willmott-index ranges from 0 to 1, and for a perfect agreement between model and data, it reaches the value of 1.

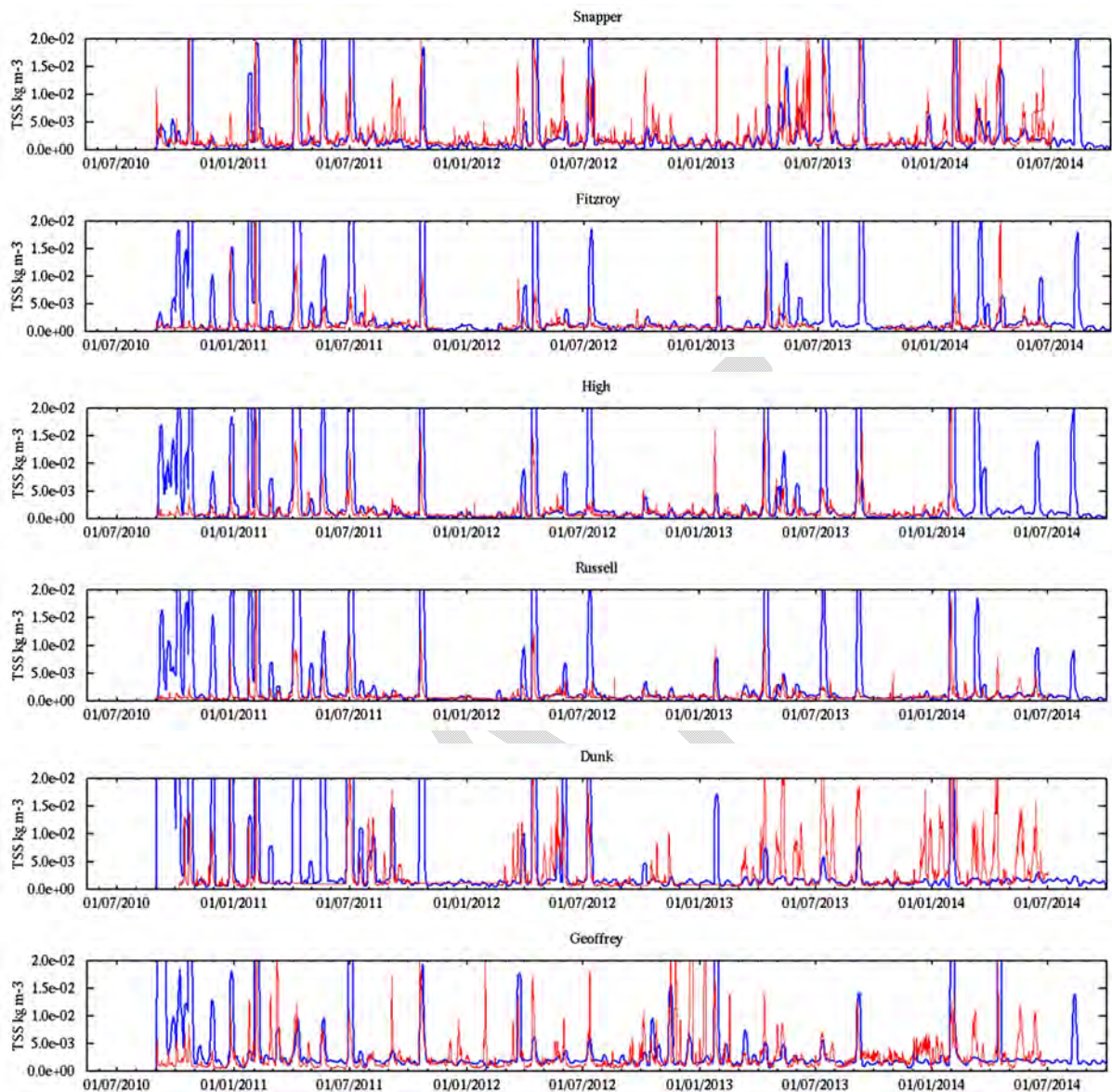


Figure 5.4.5a. Simulated sediment concentration (blue) vs observations (red). Both model and observations are passed through the low-pass filter with a 1 day cut-off period. See site map in Fig. 5.4.1.

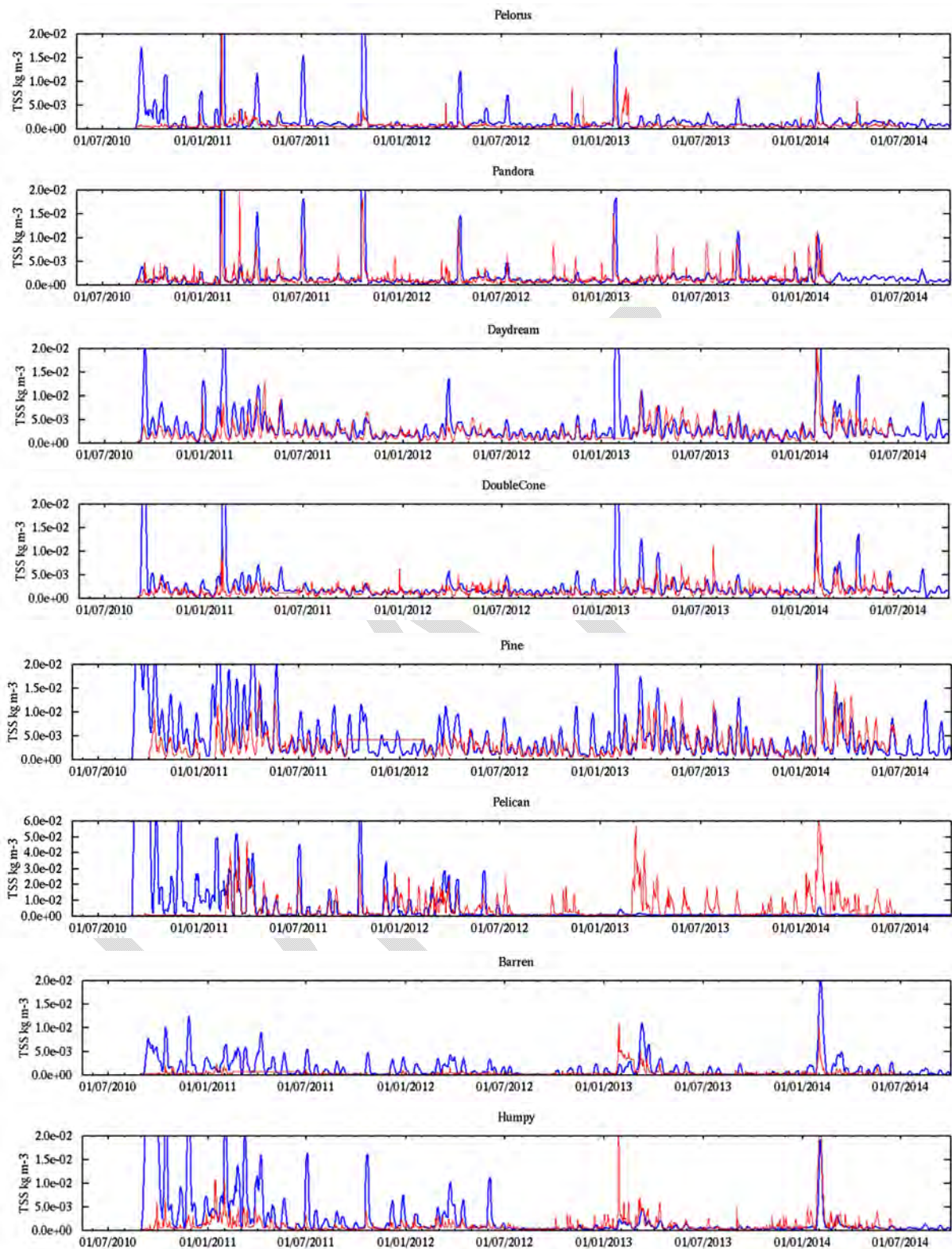


Figure 5.4.5b. Simulated sediment concentration (blue) vs observations (red). Both model and observations are passed through the low-pass filter with a 1 day cut-off period. See site map in Fig. 5.4.1.

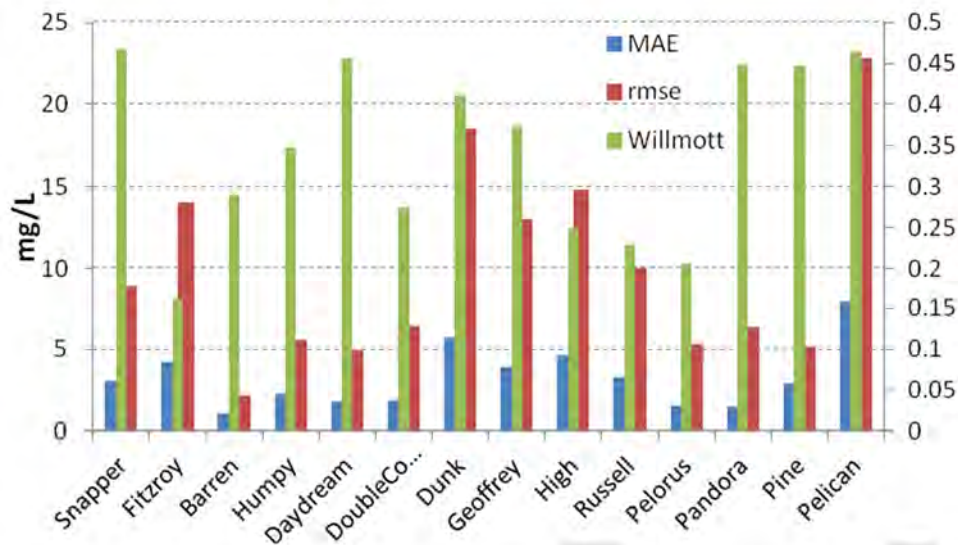


Figure 5.4.6. Mean Absolute Error (MAE), RMSE and Willmott-index of the simulated TSS records at observation sites. See site map in Fig. 5.4.1.

5.4.3 Model vs GBROOS data

In the previous section the model was tested against coastal records of turbidity. In this section it is evaluated against records of turbidity from GBROOS moorings representing offshore shelf regions and characterised with relatively low levels of turbidity. The mooring sites considered in this study (Heron South, Heron East, Capricorn Channel, Palm Passage, and Lizard Shelf) represent the southern, central and northern parts of GBR (Fig. 5.4.7). At each site the data is taken at 2 depths - near the surface and in deep water.

A number of factors are likely to influence the quality of this evaluation of the model against GBROOS data. Because of the increasing height of the model grid-cells in deep waters, the deeper the measurement site and the closer it to the seabed the larger discrepancies between the modelled variables (which represent data integrated over the grid-cell) and observations (representing point measurements). In Heron Island site, for example, deep sensor located within a meter to the seabed is likely to be sensitive to the bedload processes not resolved by the model. Another source of the discrepancy is that observed turbidity levels on the GBR shelf typically are very low and could be close to the detection limit. Further, the conversion factor between NTU and TSS for this data is not known and was set 1 mg/L – 1 NTU. Finally, this evaluation of the model has been carried out with a stand-alone sediment transport model decoupled from the biogeochemistry model. The biogeochemical cycling of the organic particulates has not been simulated.

Evaluation of the model against the GBROOS data suggests that the model overestimates suspended sediment levels on the Lizard Shelf site (LSH, Fig. 5.4.8). In Palm Passage (PPS), Capricorn Channel (CCH), and Heron East (OTE) sites both the model and observations show very low levels of TSS and the modelled levels, in general, are consistent with observations.

In Heron Island South (HIS) the model predicts higher levels of the suspended sediment in surface layers and underestimates sediment concentration in deep water. The later can be attributed to the mismatches of the modelled variables integrated over the grid-cell volume and the point measurements taken near the seabed.

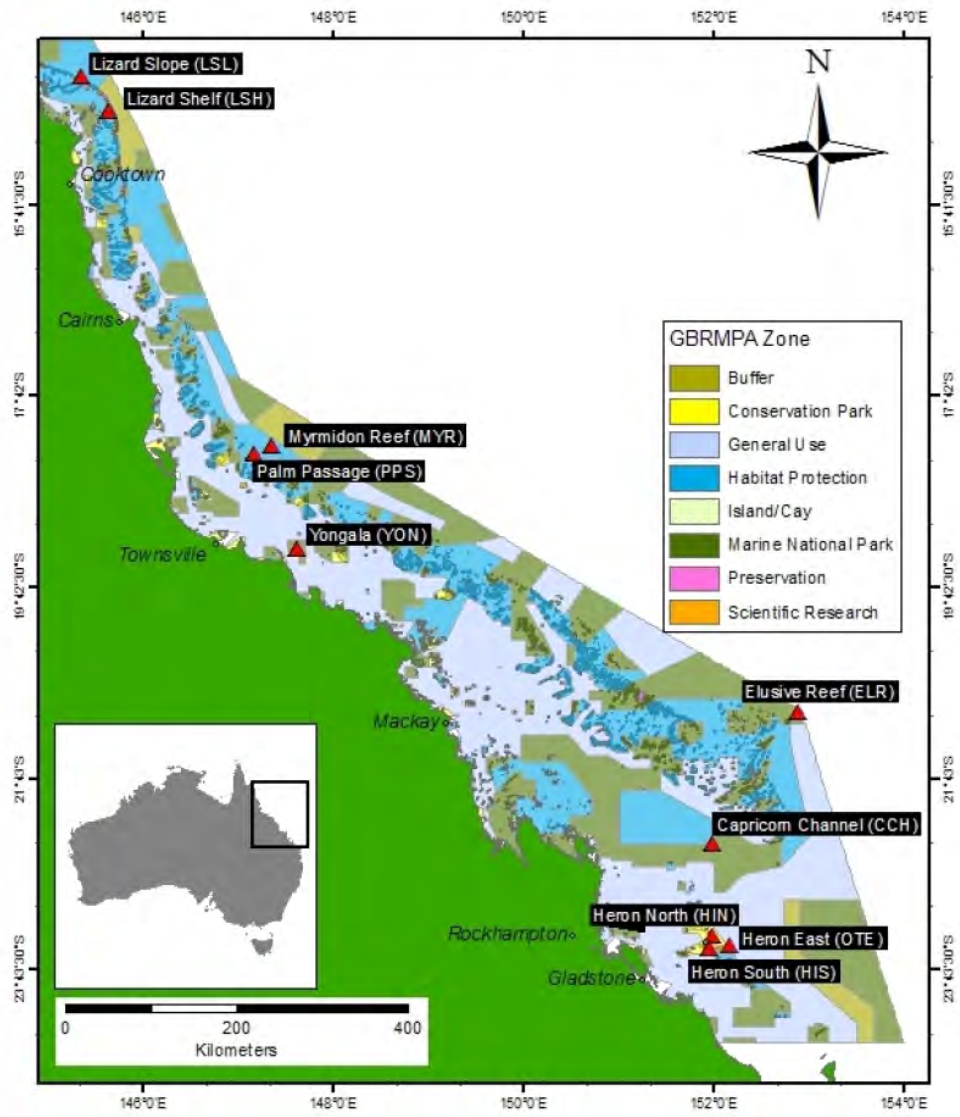


Figure 5.4.7. GBROOS mooring sites location map (<http://data.aims.gov.au/imos-moorings/>)

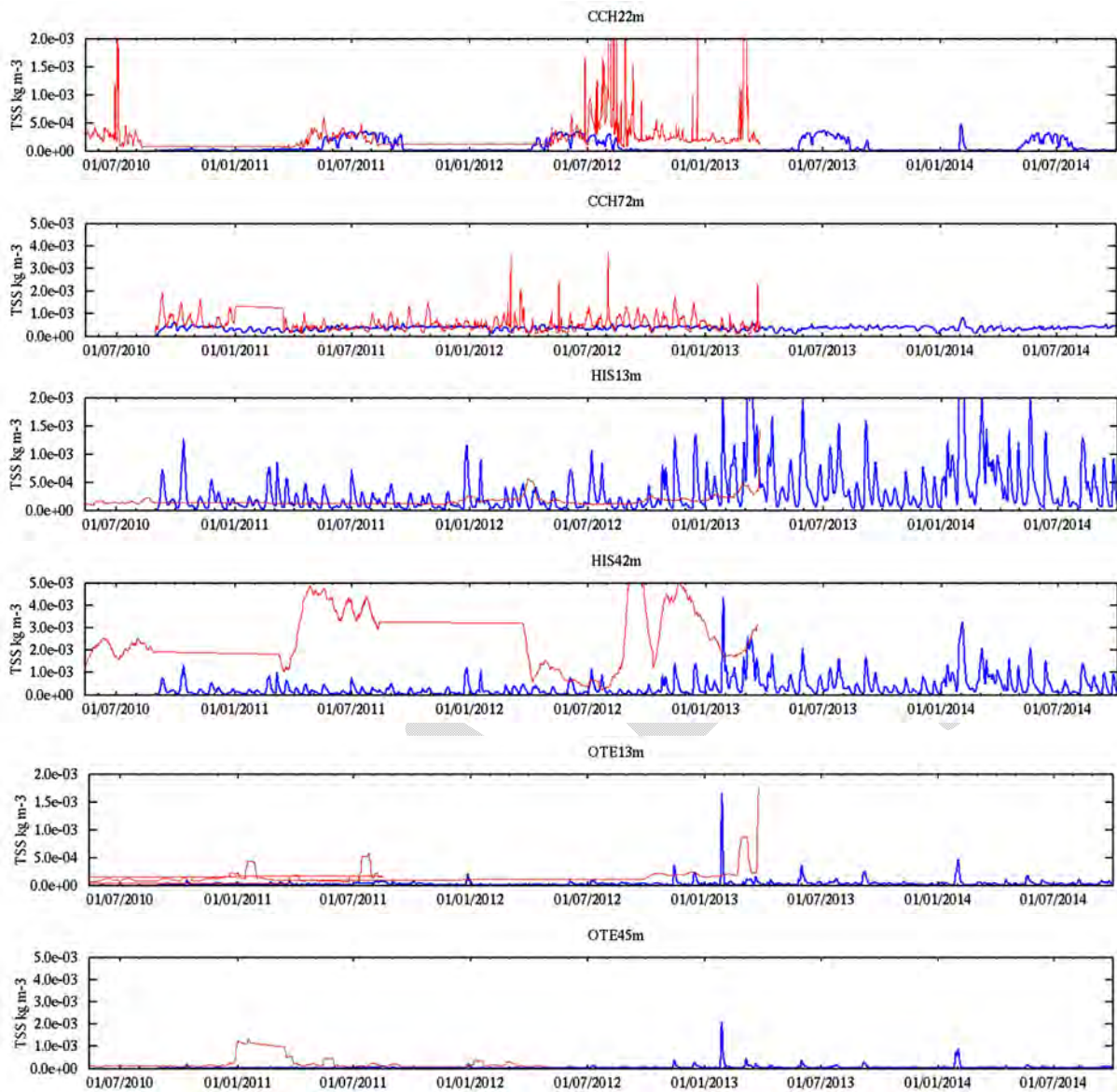


Figure 5.4.8a. Model (blue) vs observations (red) at GBROOS sites. Both model and observations are passed through the low-pass filter with a 1 day cut-off period. See site map in Fig. 5.4.7.

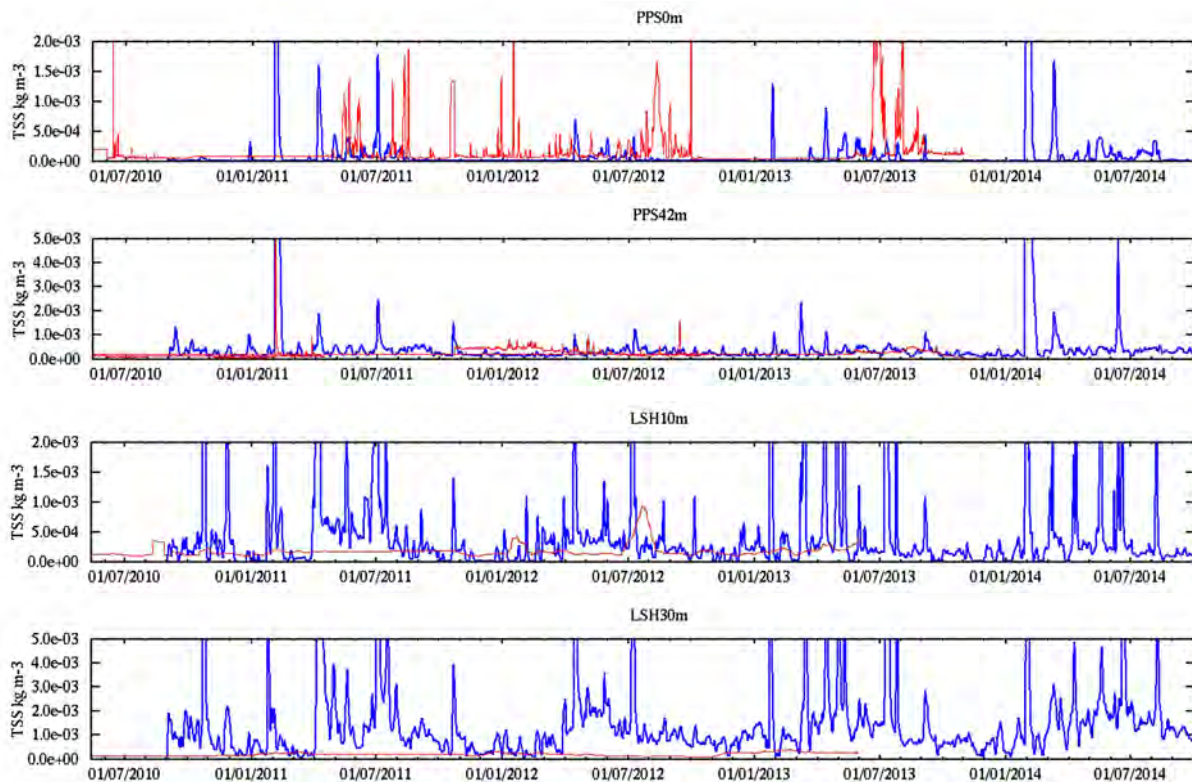


Figure 5.4.8b. Model (blue) vs observations (red) at GBROOS sites. Both model and observations are passed through the low-pass filter with a 1 day cut-off period. See site map in Fig. 5.4.7.

5.4.4 GBR1: 1 km GBR sediment model

Figures 5.4.9 and 5.4.10 illustrate predictions by two sediment transport models of the GBR having varying horizontal resolution of the study region. The fine resolution 1x1 km model (GBR1) is compared to the coarser resolution 4x4 km model (GBR4) whose validation is described above. The GBR1 model archive began in December 2014, only allowing three months of simulation to compare to GBR4. According to fig. 5.4.9, both models predict similar patterns of the large-scale distribution of the suspended sediment on the shelf. The details of these distributions, including the magnitude of the TSS levels, however, vary across the region and through time. As illustrated in figure 5.4.10, GBR1 tends to predict higher diurnal variability of the TSS signal. On most sites (except Heron Island and Lizard Shelf) the peak levels of TSS simulated with GBR1 tend to exceed analogous data simulated by GBR4. In the coastal sites the discrepancies between two models often exhibit an intermittent character – both fine and coarse resolution models might be close to each other except a succession of the high resuspension events predicted by the fine-resolution model. Given GBR4 both under and over-predicts observations at times (Fig. 5.4.5), it is difficult to attribute any one model with greater skill. However, GBR4 performs well at the Daydream site, and comparison with GBR1 at this site indicates an over-prediction by GBR1. When observations concurrent with the GBR1 archive are available the GBR1 skill will be able to be thoroughly assessed.

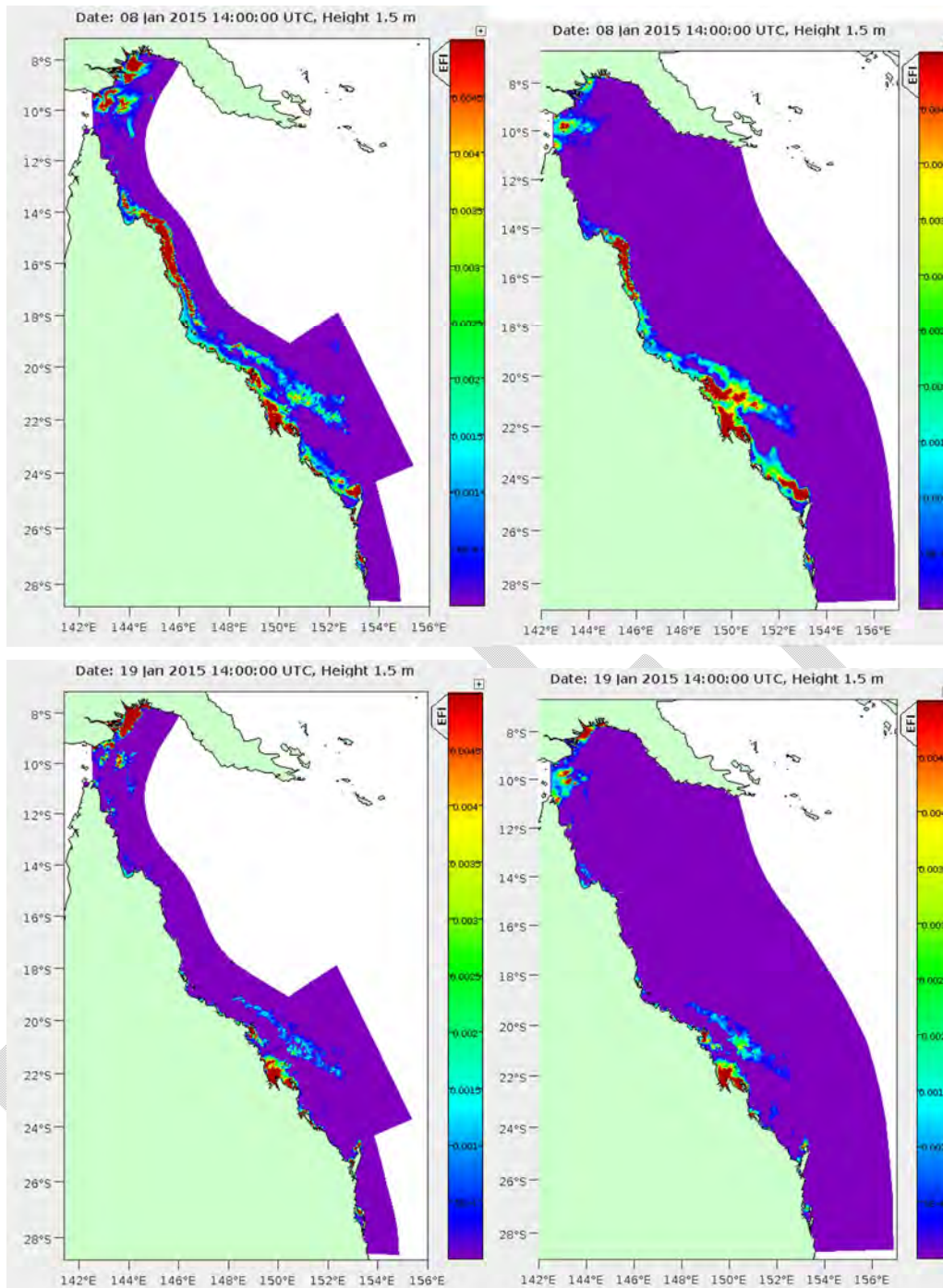


Figure 5.4.9. Snapshots of surface tss produced by GBR sediment transport models using GBR1 (left plots) and GBR4 during periods of high (top plots) and moderate resuspension events (kg m⁻³).

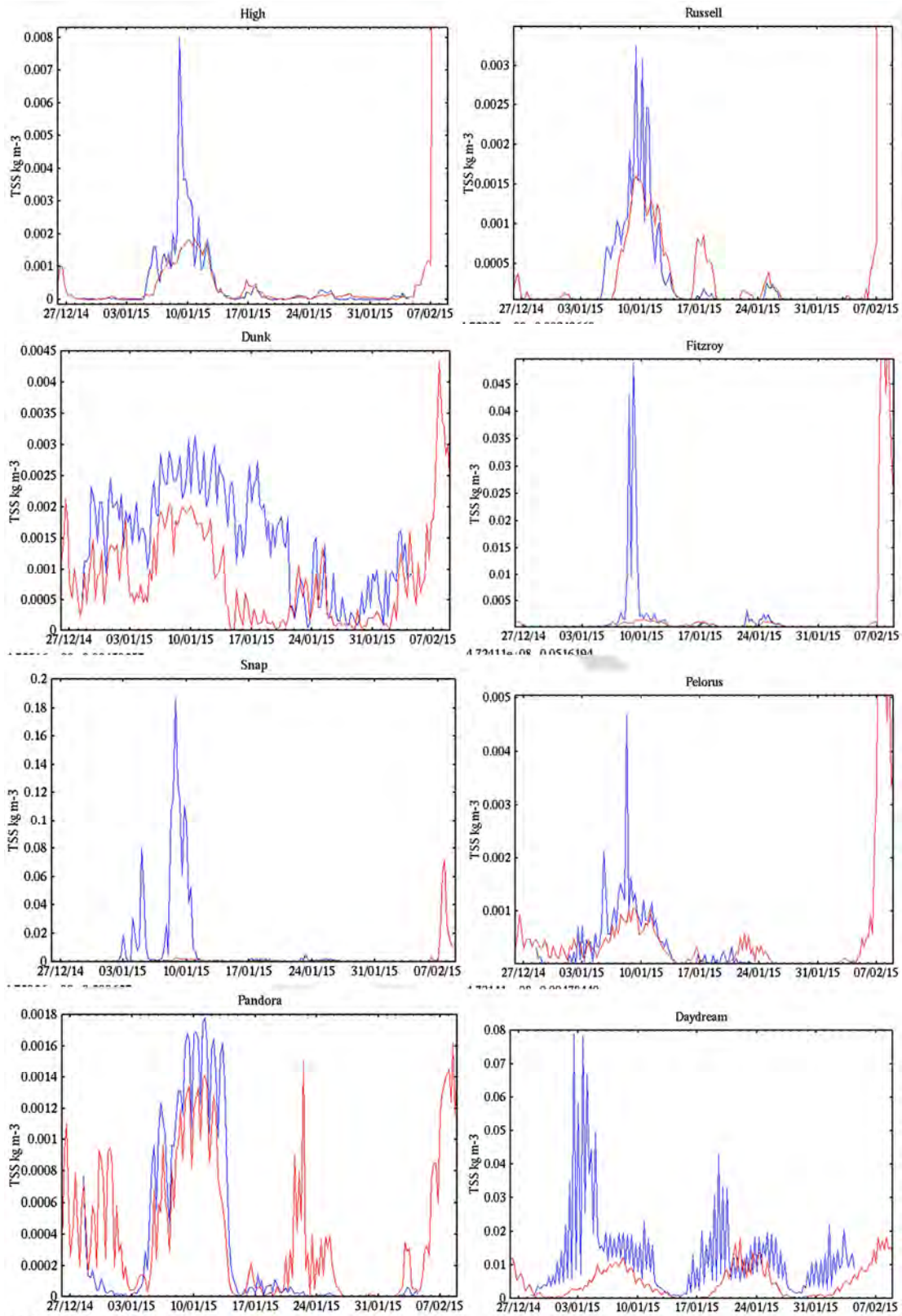


Figure 5.4.10a. Time series of TSS simulated with GBR sediment transport model GBR1 (blue) and GBR4 (red) (see site maps in Figs. 5.4.1 and 5.4.7).

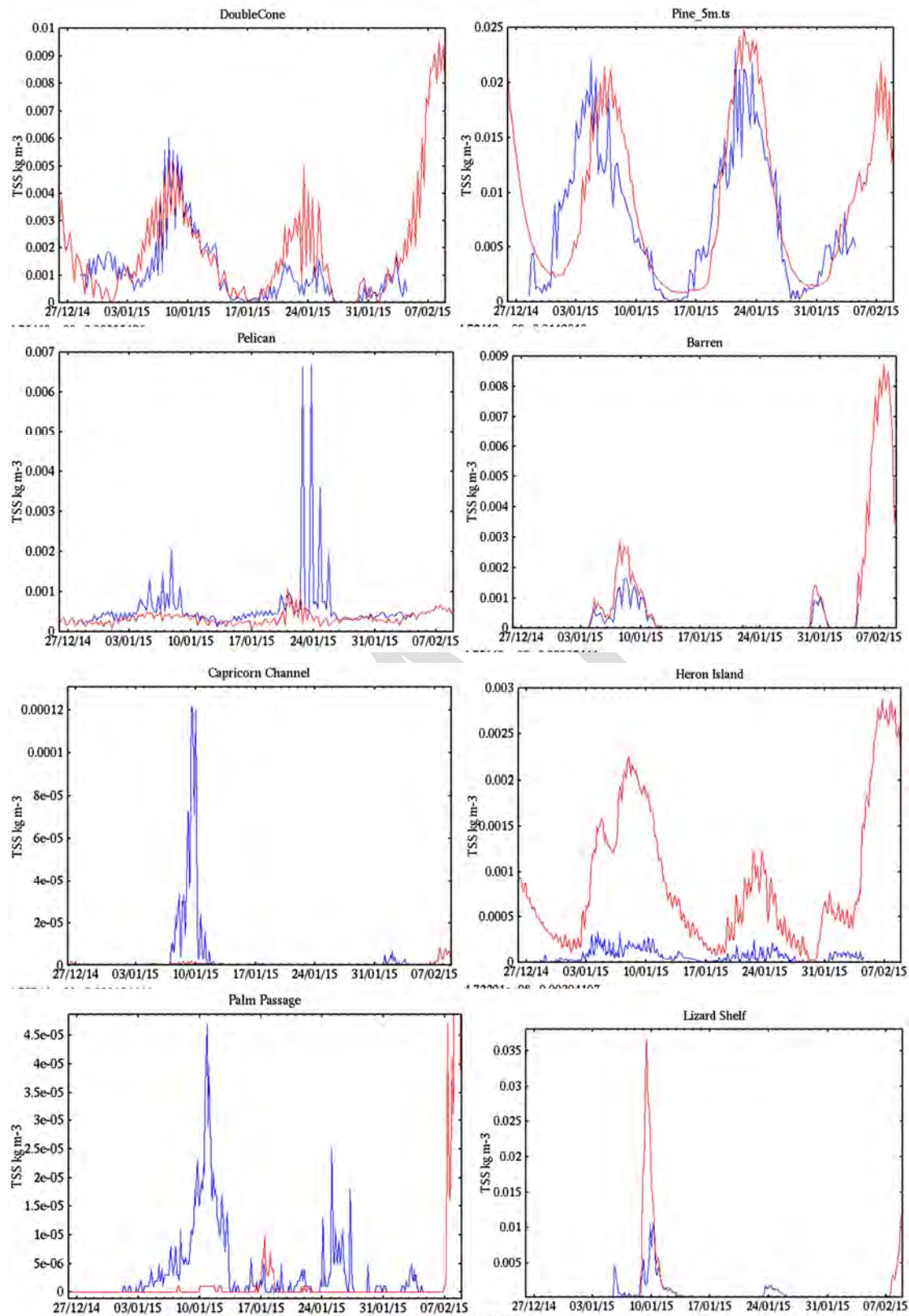


Figure 5.4.10b. Time series of TSS simulated with GBR sediment transport model GBR1 (blue) and GBR4 (red) (see site maps in Figs. 5.4.1 and 5.4.7)

5.4.5. Baseline Scenario

Fig 5.4.11 shows annual-mean surface TSS over the 4-year simulation period. Consistent across the years, the highest levels of the mean TSS are predicted in macrotidal environments of the PNG shelf and in Broad Sound. The model suggests significant annual variability of the mean fields, contrasting analogous data from the remote sensing showing relatively little variability of annual TSS across years (Fig. 5.4.12). One of the reasons for such a discrepancy between the model and the remote sensing could be attributed to the sparse temporal coverage of the remote sensing data which is likely to miss some resuspension events.

Benthic distribution of sediments released from all GBR catchments (as implemented in this study) over the simulation period is illustrated in Fig. 5.4.13. Left plots show benthic footprints of catchment sediments in May 2011 (note that the model is hot-started from a 4-years spin-up run and certain amount of catchment-sediment has been released into the region during the spin-up). Right plots illustrate the distribution of these sediments after 4 years of simulation. As expected the light fraction of sediment ("dust") has a larger footprint compared to the heavier sediments. Deposits of "dust" are clearly visible in the Capricorn Channel, while heavier sediments tend to be allocated within a narrow strip along the coastline. These simulated patterns are, in general, consistent with the observed patterns of the distribution of terrestrially-derived sediments in GBR (Alongi et al., 2005). The simulated distribution of the heavier sediments is characterised with high spatial gradients - the peak concentrations are allocated in the vicinity of the source points and only traces of these sediments tend to spread along the coastline. According to the model, large-scale patterns of the sediment distribution in GBR after the 4-year simulation period do not undergo significant changes.

Transport pathways of sediments released from two largest catchments in the region (Fitzroy and Burdekin) are illustrated in Figs. 5.4.14 and 5.4.15. Consistent with the general understanding of the sediment transport in these regions, the model predicts a net north-eastward orientation of benthic patterns associated with catchment loads. Heavier sediments are allocated in a closer proximity to the source points as compared to "dust". Reduced concentration of benthic "dust" after the relatively dry years of 2013 and 2014 is indicative of a certain "recovery" of benthic sediments from the previous loads accumulated during the wet years of 2011 and 2012.

Simulated erosion-deposition map (Fig. 5.4.16) illustrates high variability of the sediment processes across the region. Benthic sediments tend to erode in Torres Strait and there are intermittent patches of erosion and deposition over the most of the GBR shelf. Sediments tend to deposit and accumulate in deep waters beyond the shelf break. Extending simulation period from 4 to 8 years (right plot) shows patterns of the erosion and deposition similar to that obtained after the 4-year run.

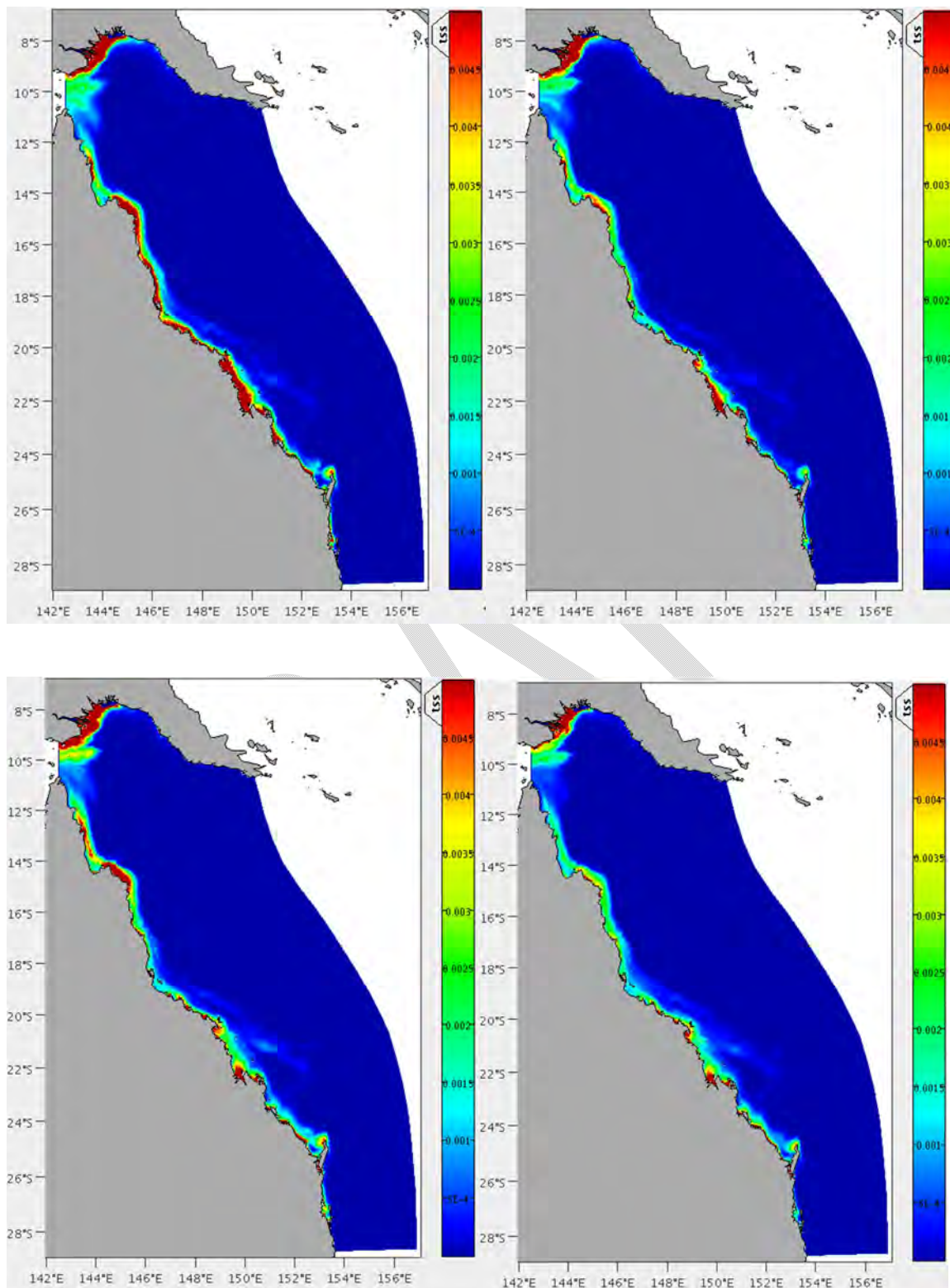


Figure 5.4.11. Simulated annual mean TSS (kg m⁻³). October 2010-September 2011 (top left), October 2011-September 2012 (top right), October 2012-September 2013 (bottom left), October 2013-September 2014 (bottom right).

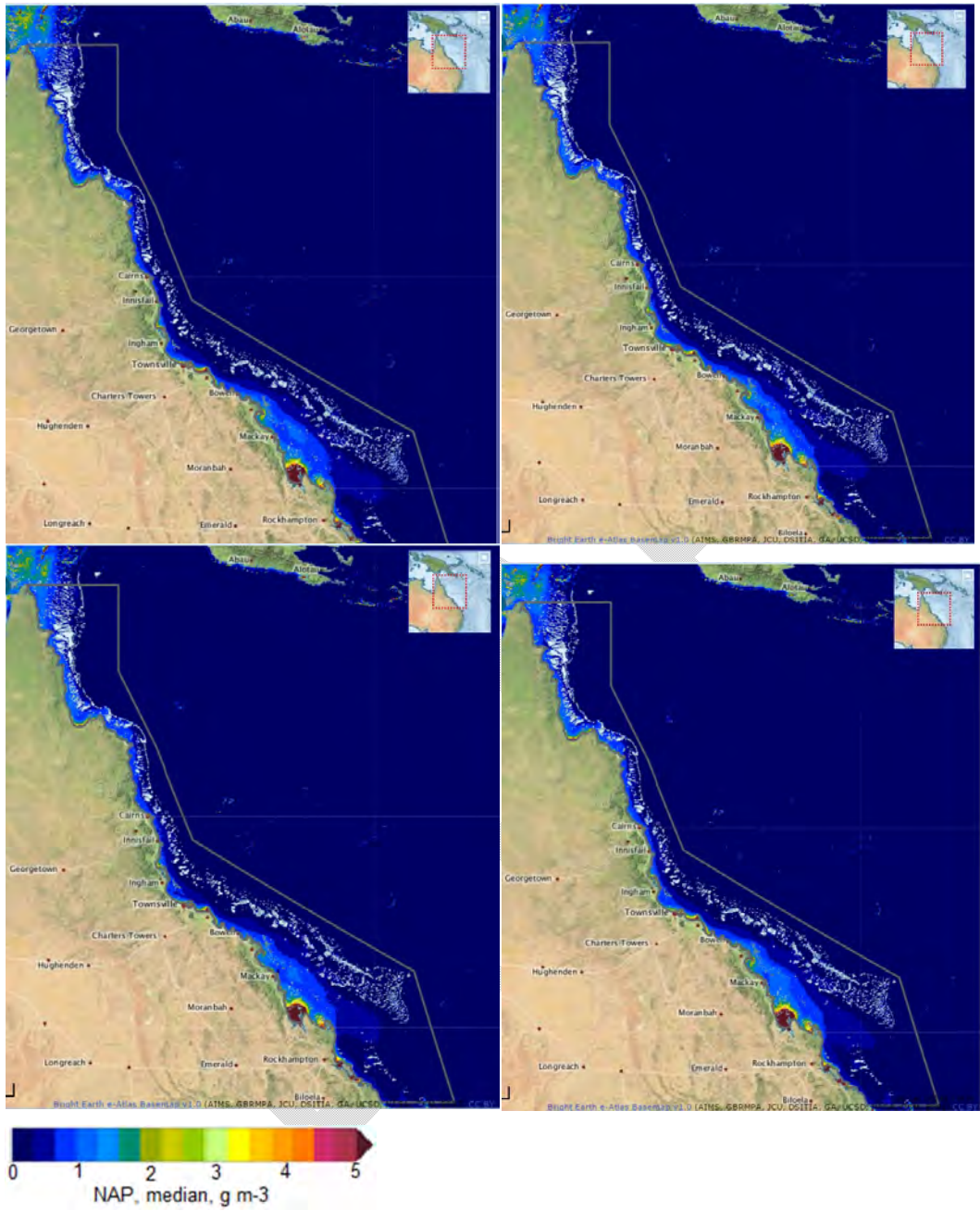


Figure 5.4.12. Annual median of TSS inferred from the remote sensing data for 2010 (top left), 2011 (top right), 2012 (bottom left), and 2013 (bottom right) (<http://www.bom.gov.au/marinewaterquality/>).

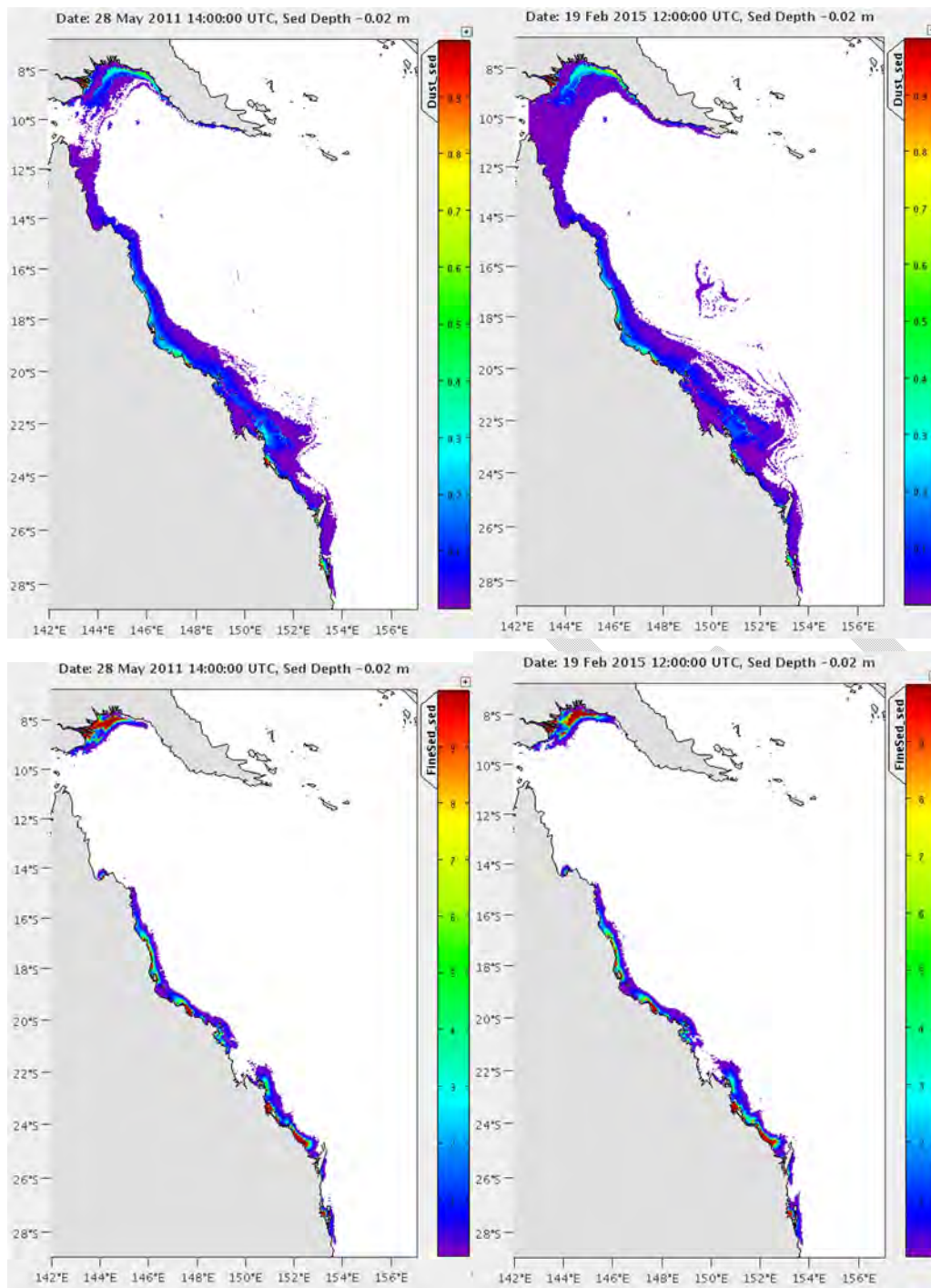


Figure 5.4.13. Benthic concentration of sediments delivered from all catchments (kg/m³). Fine sediment (bottom plot), dust sediment (top plot).

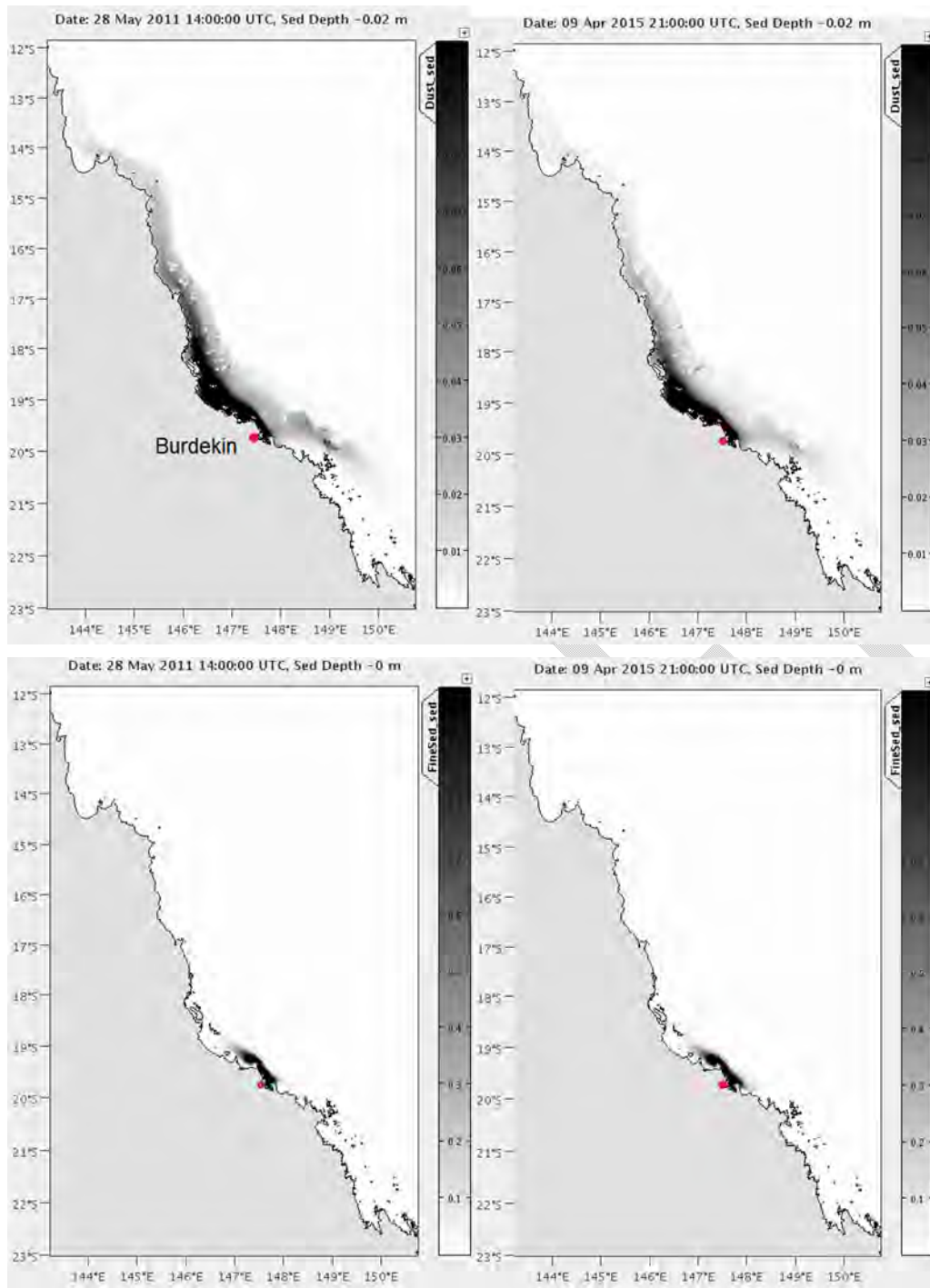


Figure 5.4.14. Benthic concentration of sediments delivered from the Burdekin catchment (kg/m³). Fine sediment (bottom plot), dust sediment (top plot).

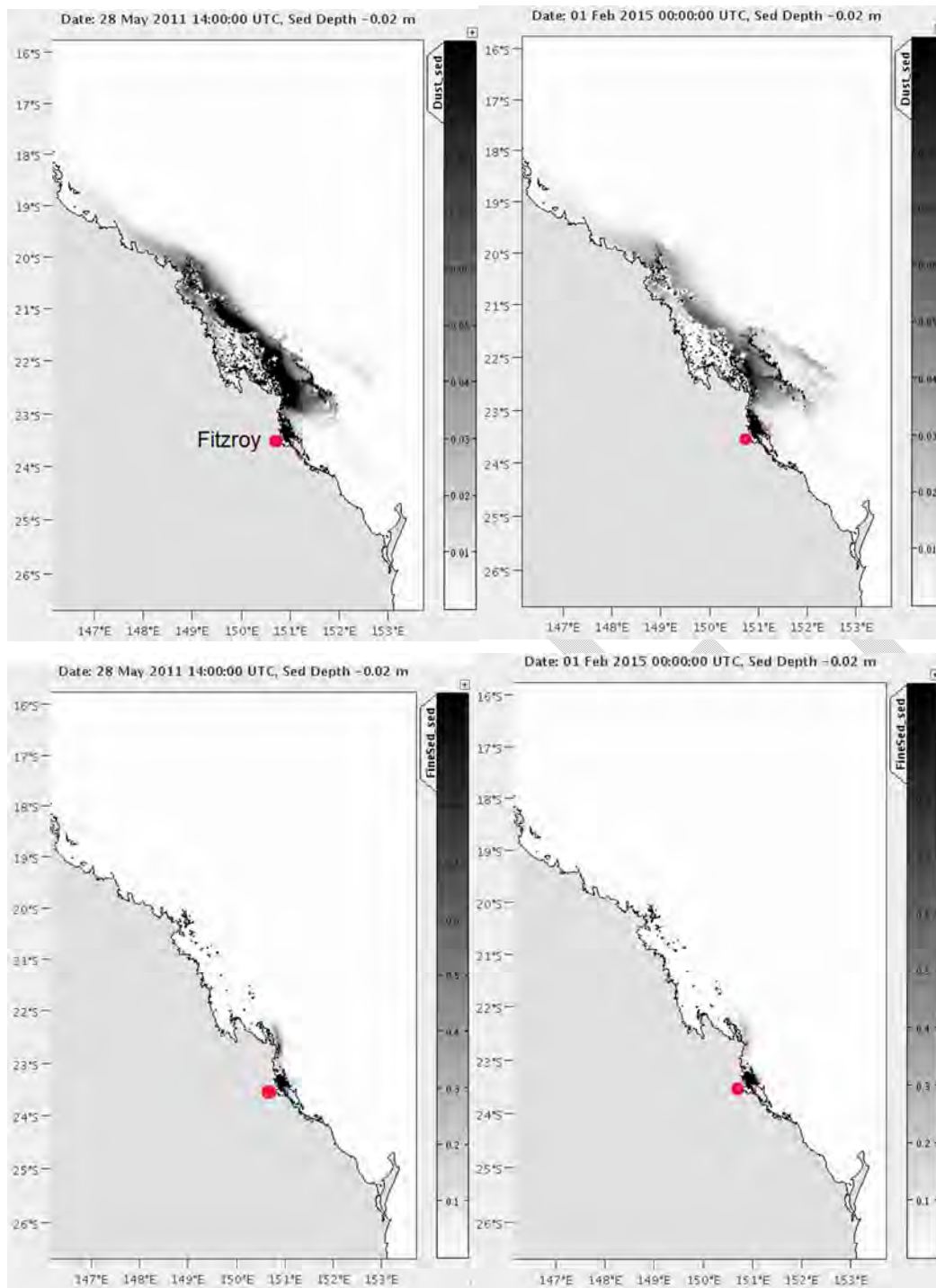


Figure 5.4.15. Benthic concentration of sediments delivered from the Fitzroy catchment (kg/m³). Fine sediment (bottom plot), dust sediment (top plot).

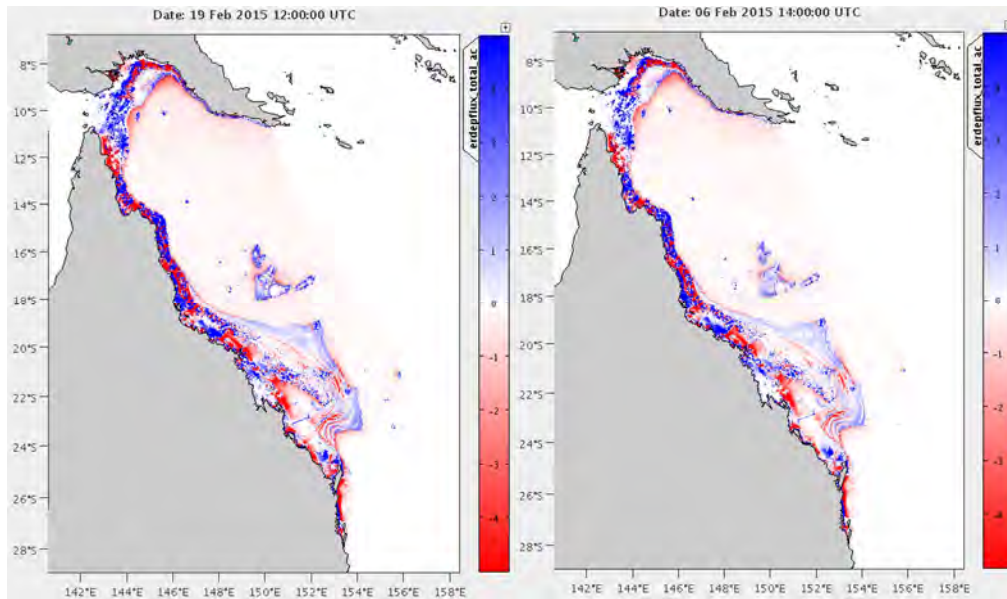


Figure 5.4.16. Simulated erosion map after 4 (left) and 8 (right) years of simulation. Colour scale units in $\text{kg}/(\text{sec m}^2)$. Red is deposition.

5.4.6. Perturbation scenarios

A number of preliminary scenarios have been simulated with the calibrated model in order to understand better sensitivity of the TSS levels on GBR to sediment loads from catchments. The main goal of these simulations is to provide material for a subsequent design of the model scenarios in consultation with stakeholders. The simulated scenarios are as follows:

1. Baseline scenario. All parameters of this scenario are equal to the parameters of the calibrated sediment transport model. Input of "dust" from catchments comprises 3% of the total load.
2. Sterile-catchments scenario assumes zero discharge of all sediments from all catchments over the 4-year simulation period (and except 4-year spin-up period when fine sediments were allowed to discharge from catchments on GBR).
3. Moderate-load scenario assumes that the mass content of "dust" delivered from catchments comprises 10% of the total sediment loads to GBR.
4. High-load scenario assumes the mass content of "dust" is 20% of the total sediment loads from catchments to GBR.

Fig. 5.4.17 illustrates how the probability for TSS to exceed 2 mg/L changes across scenarios with varying loads from catchments. According to idealistic "sterile-catchments" scenario, having all sediment loads from catchments on GBR switched off, results (as expected) in a decline of the probability of the shelf TSS to exceed 2 mg/L. Compared to the baseline scenario, the greatest decline of this probability (exceeding 0.05) is predicted on the PNG shelf and in localised coastal regions around river-discharge points. Over the rest GBR shelf, characterised with a relatively low probability to exceed 2 mg/L, the corresponding changes are small too and typically do not exceed 0.015. Increasing the content of "dust" in catchment loads from 3 to 20%, tends to increase considerably the probability for TSS to exceed 2 mg/L (by more than 0.05 over the significant part of the shelf).

Annual changes of the perturbation of probability (Fig. 5.4.18), suggests a relatively short term-response of the system to the changes in the catchment loads. The model does not show an accumulative, multi-year build-up of the excessive TSS levels in the region one would expect due to the elevated discharge from catchments. Instead, altered loads from catchments are most pronounced during the wet years, and these changes have a smaller impact on the probability for TSS to exceed 2 mg/L during the subsequent dry years.

All perturbation runs considered earlier in this section are based on catchment loads as simulated by catchment model. Analogous simulations have been carried out with catchment loads based on linear scaling of the river flow. Results produced by both models, in general, are similar to each other, except that scenarios with scaled loads show higher sensitivity of TSS levels on GBR in dry 2013 to catchment loads in 2011 and 2012 (not shown).

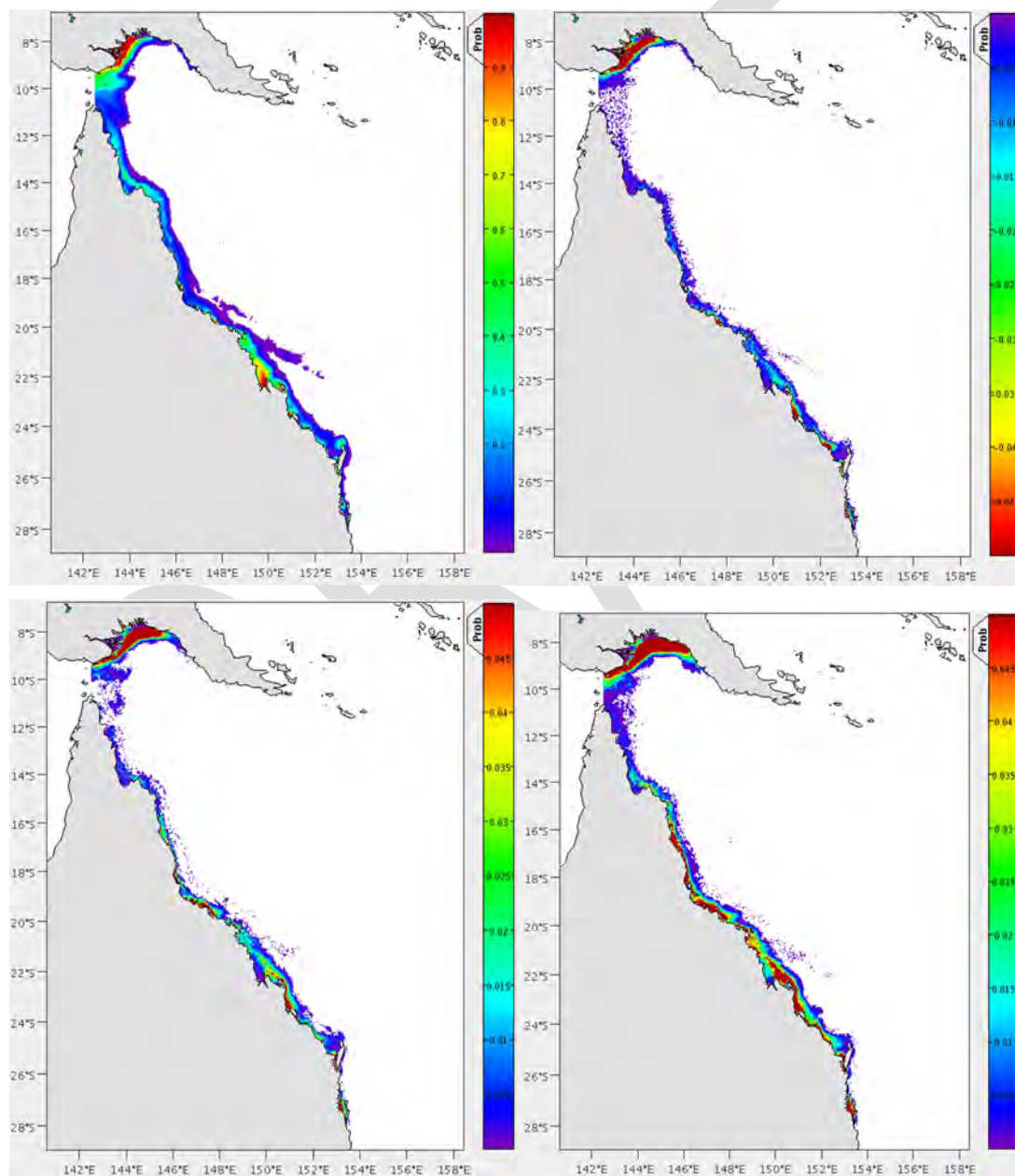


Figure 5.4.17. Four-year mean probability for TSS to exceed 2 mg/L according to baseline scenario (top left plot) and the perturbation of this probability for scenarios with no river load

(top right), scenario with moderate dust load (bottom left) and scenario with high dust load (bottom right).

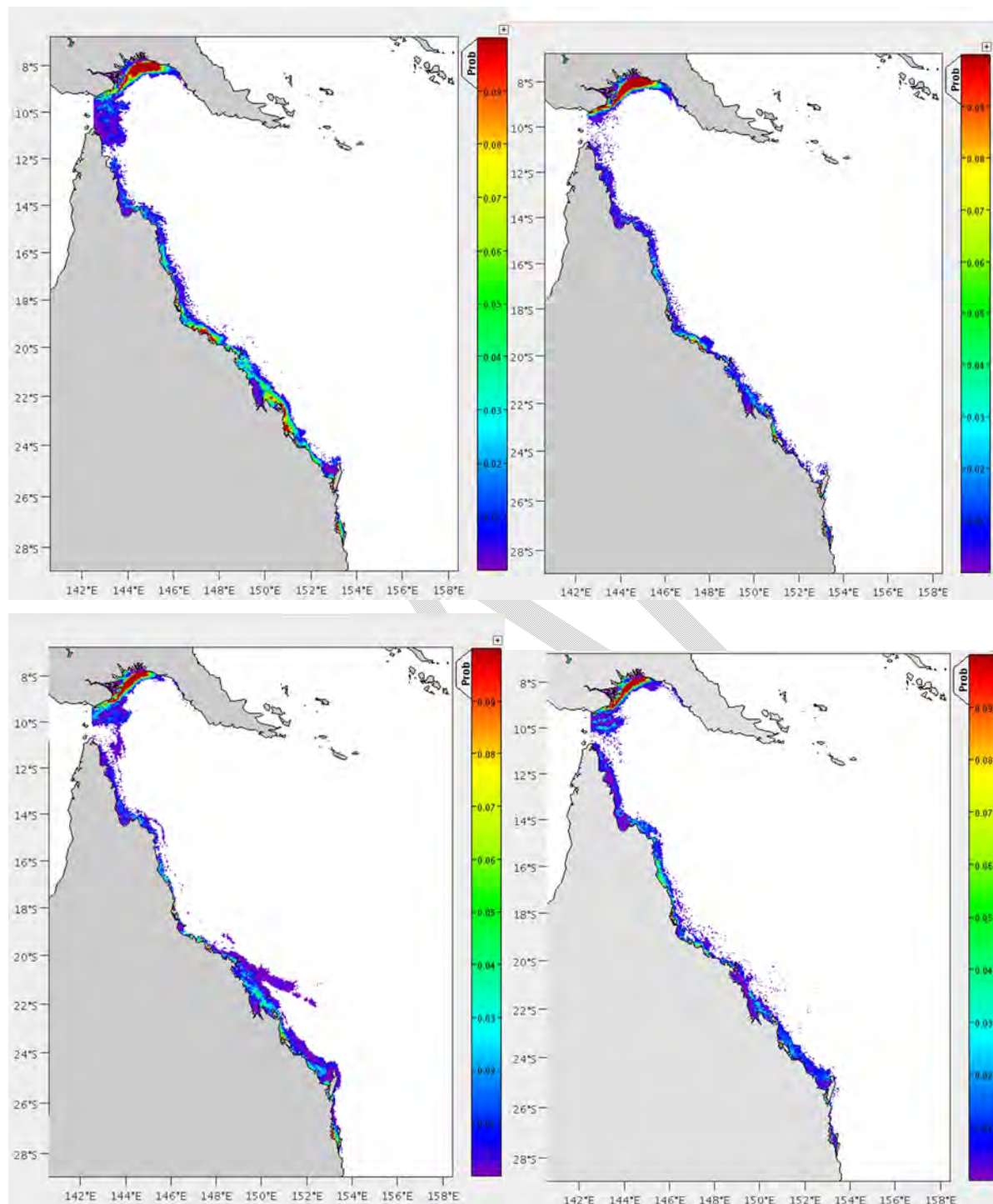


Figure 5.4.18. Perturbation of the annual mean probability for TSS to exceed 2 mg/L for the scenario with moderate dust load against baseline scenario. October 2010-September 2011 (top left), October 2011-September 2012 (top right), October 2012-September 2013 (bottom left), October 2013-September 2014 (bottom right).

5.4.7 Conclusion

A numerical model of the suspended sediment transport on the GBR shelf has been developed. The model is initialised with the observed distribution of gravel, sand and mud in the seabed of the shelf region. Catchment sediments discharged into the GBR are represented in the model by two classes of particles having varying settling velocities. The transport of modelled sediments is driven by simulated hydrodynamics and wave data. The model resolves the study region into 4x4 km grid-cells in horizontal directions and 50 layers in vertical direction, including 4 benthic layers in sediments. The model is intended as a decision support tool to estimate GBR-wide distribution of fine sediments; it also supports biogeochemical model simulations and provides initial and boundary conditions for a nested fine-resolution relocatable model RECOM.

The sediment transport model was calibrated in two stages. First, the model parameters (initial conditions and spatially varying bottom roughness) have been refined through the ensemble assimilation of the 6 month remote sensing data for TSS. Ensemble of models, produced through the assimilation step, has been reduced then to a single model, which was subsequently validated against time-series of the observed turbidity (i.e. data from coastal sensors and GBROOS shelf moorings). The validation of the 4-year run of the model revealed a long-term drift of the solution which was handled through the manual adjustment of the model parameters. The quality of the calibrated model varies across the GBR region and with time (as was expected). The distribution of the simulated suspended sediment on GBR, in general, is consistent with observations. The model tends to overestimate suspended sediment levels in northern QLD and underestimate TSS levels in Torres Strait. The validation study indicates considerable uncertainty of the calibrated model.

A number of preliminary scenarios have been simulated with the calibrated model. The main goal of these runs is to provide material for a subsequent discussion with stakeholders to design further scenarios relevant to GBR management and research practices. Numerical experiments highlight the role of very fine fraction of catchment sediments (called "dust" in this report and representing tails of the sediment size-distribution) as a carrier of sediment signals propagating from catchments to the GBR region. Scenarios with varying loads of sediments from catchments illustrate spatial and temporal variability of changes of suspended sediment levels on GBR. Preliminary analysis of the annual mean probability for TSS to exceed 2 mg/L suggests a relatively short term-response of the GBR system to changes in catchment loads. The 4-year run of the model does not show an accumulative, multi-year build-up of the excessive TSS levels in the region one would expect due to the elevated discharge from catchments. Instead, altered loads from catchments are most pronounced during wet years, and these changes have a smaller impact on the probability for TSS to exceed 2 mg/L during the subsequent dry years.

5.5 Biogeochemistry

Scope of BGC model Validation

Quoting from Rykiel (1996) 'Before validation is undertaken, (1) the purpose of the model, (2) the performance criteria, and (3) the model context must be specified.' For the eReefs BGC model validation the model purpose, performance criteria, context and also what the model will not do are clarified below:

1. **Model Purpose:**
To reliably represent the spatially resolved water quality dynamics (phytoplankton, nutrients, turbidity, oxygen) of the GBR World Heritage Area for informed management (tourism, conservation, recreation, aquaculture, development, land use) via hindcast, near real time and scenario simulations (e.g. how is the GBR shelf going to respond to catchment loads, natural loads). Model results will be suitable to assess WQ guidelines.
2. **Performance Criteria:**
 - 2.1 Model conserves mass (C, N, P, O) to confirm that the model is logically and numerically accurate.
 - 2.2 Simulated state variable concentrations resemble the regional climatology for offshore-reef, lagoon-reef and near-shore zones.
 - 2.3 Simulated state variable concentrations resemble WQ observations under contrasting seasons/loads (wet vs dry) and significant events (e.g. 1/10 yr flood). Model results are consistent with specific data sets available to the project.
 - 2.4 The model produces a credible nutrient budget (including pelagic + benthic fluxes).
3. **Model Context:**
The model will be assessed for the GBR World Heritage Area including the near-shore coastal waters, the GBR lagoon, the shelf reef and adjacent offshore waters. At the regional scale model parameters will be optimised for the 4km model grid and generalised onto the 1km model grid, for more precise simulation of fine-scale features (e.g. reef topography, river plumes).
4. **What we will not do:**
We will not assess the model performance out-with the GBR World Heritage Area; model results on the periphery of the region will remain 'pilot' (e.g. PNG coastal waters, Fraser Island, Coral Sea). Benthic processes in the model are relatively coarsely resolved by the whole of GBR scale models; most accurate simulation of these components will be achieved at finer scales using RECOM. Prior to the provision of a sophisticated catchment model, basic flow-concentration relationships are unlikely to accurately resolve the WQ evolution of a flood plume.

Model skill metrics and a selection of results will be provided on the CEM team web page; more detailed model analysis tools will be provided by the 'dashboard' and visualisation team.

5. Model Skill Metrics:

A number of indicators will be used to assess the quality of the model, including RMS errors, Pearson's correlation coefficients, Willmott's skill indicators (Willmott (1981); see formula below, and visual comparison of time series of simulated and observed data. RMS errors will be evaluated by comparing the model solution with observations at every site separately and then estimating an integral error of the solution. RMS errors are known to perform poorly in applications with noisy data and high spatial variability of the fields when small mismatches between model and data tend to produce large errors even for distributions of similar patterns. To reduce uncertainty of the data, we also present the data-model comparison for observations and the model which have high-frequency fluctuations of the sediment concentration filtered out. Observations were filtered by estimating mean and the range of the observed values over a particular space and time window. The time window over which the data were integrated varied from one subregion to another depending on the duration of the monthly sampling campaign in that particular area. Such integrated data were particularly useful for visualisation purposes when comparing time series of the model solution with observations. Having stochastic component of observations filtered out, reduced the level of noise in this data and uncovered seasonal and inter-annual variability in the subregions. Unless otherwise specified, exactly the same filtering was applied to both observations and model simulations.

The skill of the model was additionally assessed using the definition of Willmott (1981), used by Warner et al. (2005):

$$skill = 1 - \frac{\sum_{t=1}^N |mod(t) - obs(t)|^2}{\sum_{t=1}^N \left(|mod(t) - \overline{obs}| + |obs(t) - \overline{obs}| \right)^2}$$

where a skill of 1 indicates model and measurements agree perfectly, and 0 indicates total disagreement.

5.5.1 Mass Conservation

There are two parts to the evaluation of mass conservation in the model: firstly, the conservation of mass within the biogeochemical model process transformations, for example the uptake of nutrients into autotrophic biomass must equal the equivalent loss of nutrient from the dissolved pool; and secondly the conservation of mass during physical movement of tracers between grid cells by advection, diffusion, sinking and resuspension.

The biogeochemical model code is processed in columns equating to the model grid. At the start of each time step the total mass of carbon, nitrogen and phosphorus in the water column, epi-benthos and sediment across all biogeochemical model tracers are summed. Computations then proceed for the uptake and transformation of substances within the

biogeochemical model. At the end of the biogeochemical model time step the mass of all tracers are summed and checked against their initial value to confirm conservation of mass for all biogeochemical model processes. In the eReef biogeochemical process model, mass conservation has been achieved for carbon, nitrogen and phosphorous; mass balance of nitrogen includes numerical accounting for the generation of nitrogen by *Trichodesmium* nitrogen fixation and the loss of nitrogen to the atmosphere by denitrification.

Biogeochemical model tracers are advected and diffused by an offline transport model with flow fields generated by the free-running hydrodynamic model. Initially the biogeochemical model was hosted in the semi-Lagrangian transport model (Section 4.5.2). This transport model was computationally efficient but the numerical scheme was inherently non-conservative of mass. To achieve mass balance for the transport of biogeochemical model tracers, 'fill' options in the code could be invoked to allowed calculation and reintroduction of the un-conserved mass as a diffuse flux across the model grid. A more rigorous transport model using a Flux Form scheme (Section 4.5.3), which conserves mass has since been implemented. Biogeochemical model tracers are now advected and diffused with this scheme and mass is locally conserved during the physical movement of tracers throughout the model grid.

The eReefs biogeochemical model achieves mass balance for carbon, nitrogen and phosphorous in all biogeochemical model processes, and during the movement of tracers throughout the model grid in pelagic, epibenthic and sediment layers.

5.5.2 Comparison of Model with Climatology

The eReefs 4km biogeochemical model 3D nutrient field was compared with the *CSIRO Atlas of Regional Seas Climatology 'CARS Coast8' of the Queensland shelf* (www.marine.csiro.au/atlas). The CARS Coast8 climatology comprises 100 million nutrient observations between longitude 142 – 157°E and latitude 7 - 29°S. Comparisons between the CARS observations and the model were made at 0, 50, 110 and 220m as well as water column profiles for sub-regions of the shelf.

The CARS nutrient climatology shows very low <5 mg N m⁻³ nitrate concentrations in shallow waters (0-50m) in general across the whole Queensland shelf Table 5.5.1, Fig. 5.5.1, although coastal concentrations south of Fraser Island (25°S) were greater (up to 40 mg N m⁻³ at 50 m). Modelled nitrate concentrations were similarly low in shallow waters throughout the domain, although in 2011 elevated concentrations were simulated adjacent to the coast likely associated with river discharge during the intense wet season of 2011. The model also shows persistent elevated nitrate concentrations in coastal waters off the Fly River in Papua New Guinea and at 50 m along the south eastern PNG peninsular; both of these regions are beyond the scope of the CARS data set.

At greater depths (110 – 220 m) the CARS climatology shows a progressive increase in nitrate concentration, particularly along the shelf edge and in the northern Coral Sea. Annual mean nitrate distributions from the model show similar patterns and concentrations of nitrate. In 2011-2012 nitrate concentrations in the northern Coral Sea were slightly greater than the climatology at 110m, whilst in 2013–2014 nitrate concentrations along the shelf edge were slightly higher.

Subregions from Cape York to Palm Passage (~19°S) and Palm Passage to Fraser Island were used to characterise mean inshore lagoon and offshore lagoon plus reef, nutrient conditions (Fig. 5.5.2). In general modelled profiles matched the nitrate climatology well in all regions and years with simulated nitrate concentrations falling within the 10-90 percentile of observations. In the northern inner lagoon simulated nitrate concentrations in 2011 were greater than the climatology likely associated with river discharge during the intense wet season in 2011. In the southern lagoon and the offshore lagoon plus reef regions the simulated depth of the nitricline shoaled as the model run progressed, due to evolution in the physical representation of the density structure.

Table 5.5.1 Summary of CARS nitrate climatology and eReefs 4km model 4 year mean nitrate concentrations for sub-regions of the shelf.

	Whole shelf		North Inner Lagoon		South Inner Lagoon		Reef + Outer Lagoon	
	CARS	Model	CARS	Model	CARS	Model	CARS	Model
No. NO3 Obs.	49.59E 6	1296.3E 6	3.51E 6	50.89E 6	13.68E 6	377.93E 6	24.12E 6	867.49E 6
Mean NO3 0m	3.39	3.05	3.58	3.87	2.80	2.22	2.41	0.35
Mean NO3 30m/27m	2.68	2.25	2.12	4.41	2.31	2.75	1.83	0.64
Mean NO3 60m/66m	6.49	11.05	7.36	10.41	8.57	13.53	2.56	8.07
Mean NO3 100m/96m	19.81	26.02						
Mean NO3 200m/220 m	95.34	85.10						

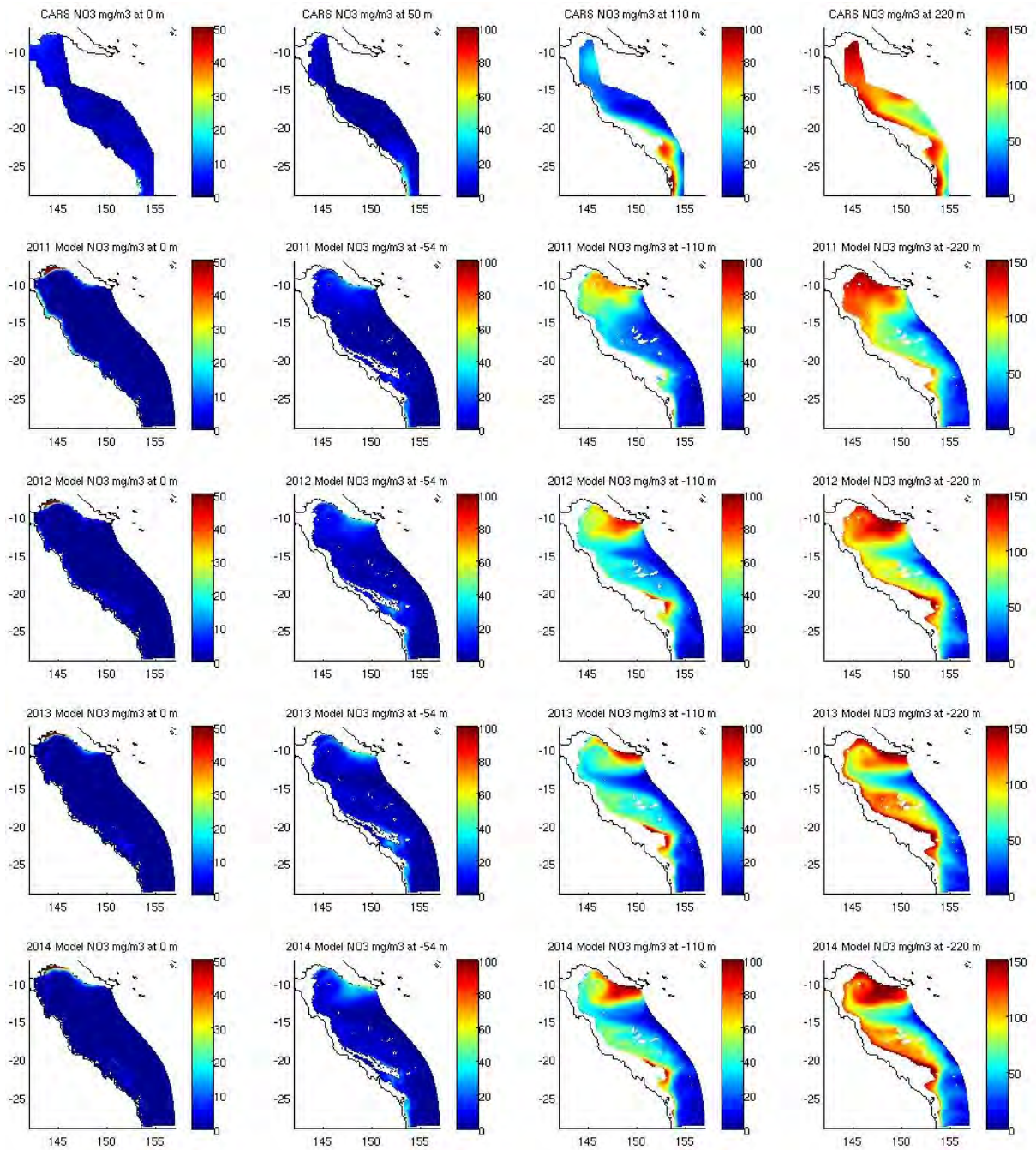


Figure 5.5.1. CSIRO Atlas of Regional Seas Coast 8 nitrate climatology (top) compared with annual mean GBR 4km modelled nitrate for 2001, 2012, 2013 & 2014 at various depths (0, 50, 110 & 220 m).

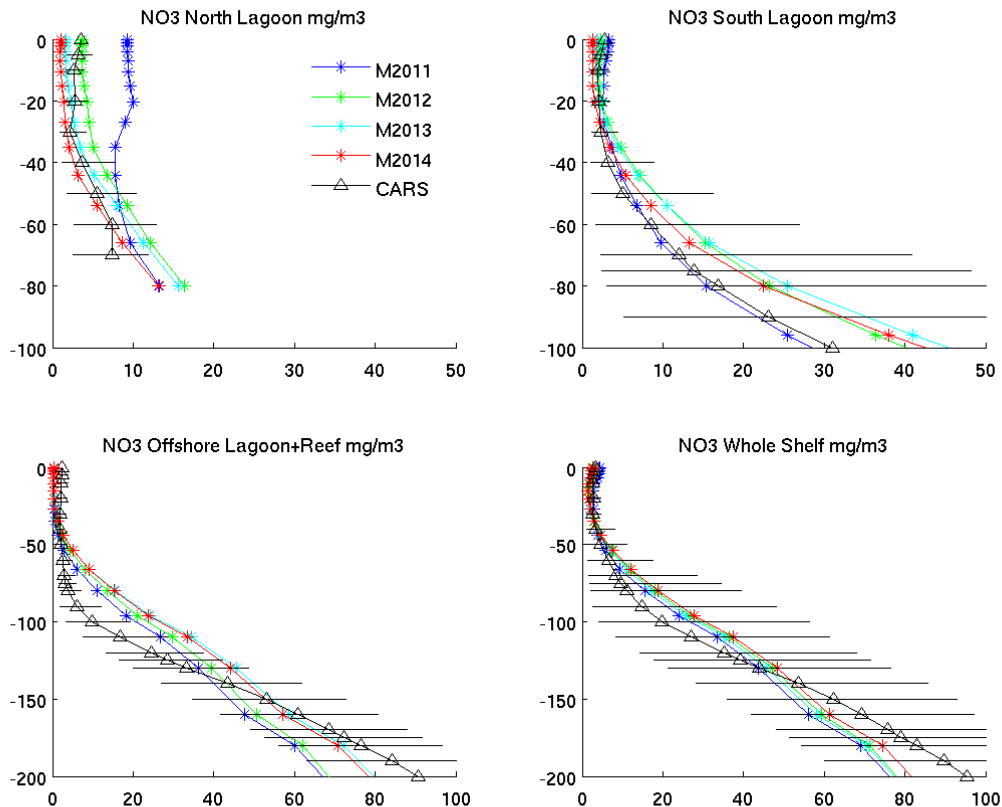


Figure 5.5.2. Mean model and CARS nitrate profiles for subregions from Cape York to Palm Passage, Palm Passage to Fraser Island, offshore lagoon plus reef, and the whole shelf. Horizontal error bars show the 10 – 90 percentile CARS nitrate concentration.

The CARS phosphate climatology shows low concentrations ($<5 \text{ mg P m}^{-3}$) of phosphate in shallow waters (0-50m) similar to the distribution of nitrate (Table 5.5.2, Fig. 5.5.3). Simulated phosphate concentrations in the eReefs 4km BGC model are however systematically lower than in the climatology by $\sim 2\text{-}4 \text{ mg P m}^{-3}$. This can be clearly seen in the sub-region analysis of mean phosphate profiles (Figure 5.5.4). In the CARS data set very few values of phosphate concentration were reported less than 3 mg P m^{-3} suggesting that the general limit of phosphate detection was $\sim 3 \text{ mg P m}^{-3}$ or $0.1 \mu\text{M PO}_4$.

In deeper water the CARS climatology showed an increase in phosphate concentration along the shelf edge and in the northern Coral Sea. These features were well reproduced by the model both spatially and in approximate magnitude. In 2011-12 simulated offshore phosphate concentrations were $\sim 5 \text{ mg P m}^{-3}$ lower than the CARS climatology, but concentrations recovered in the mid and northern parts of the shelf in 2013-14.

On the shelf the regional analysis (Fig. 5.5.4) suggests that simulated phosphate concentrations were systematically underestimated, notwithstanding a possible omission of low values (beyond detection limit) in the CARS data set. This model bias of up to 5 mg P m^{-3} in deep water could lead to phosphate depletion in photoautotrophs and potentially curtail primary production if phosphate then became the nutrient in least supply relative to the Redfield ratio for phytoplankton and the Atkinson ratio for benthic macrophytes.

Table 5.5.2 Summary of CARS phosphate climatology and eReefs 4km model 4 year mean DIP concentrations for sub-regions of the shelf.

	Whole shelf		North Inner Lagoon		South Inner Lagoon		Reef + Outer Lagoon	
	CARS	Model	CARS	Model	CARS	Model	CARS	Model
No. DIP Obs.	50.57E 6	1296.3E 6	3.57E 6	50.89E 6	13.94E 6	377.93E 6	24.70E 6	867.49E 6
Mean DIP 0m	4.60	1.18	3.85	1.50	4.13	1.74	4.03	0.11
Mean DIP 30m/27m	3.87	0.81	3.78	1.68	4.13	1.46	3.72	0.19
Mean DIP 60m/66m	4.91	2.03	4.95	2.30	5.45	3.07	4.44	1.43
Mean DIP 100m/96m	7.47	4.21						
Mean DIP 200m/220 m	17.21	12.97						

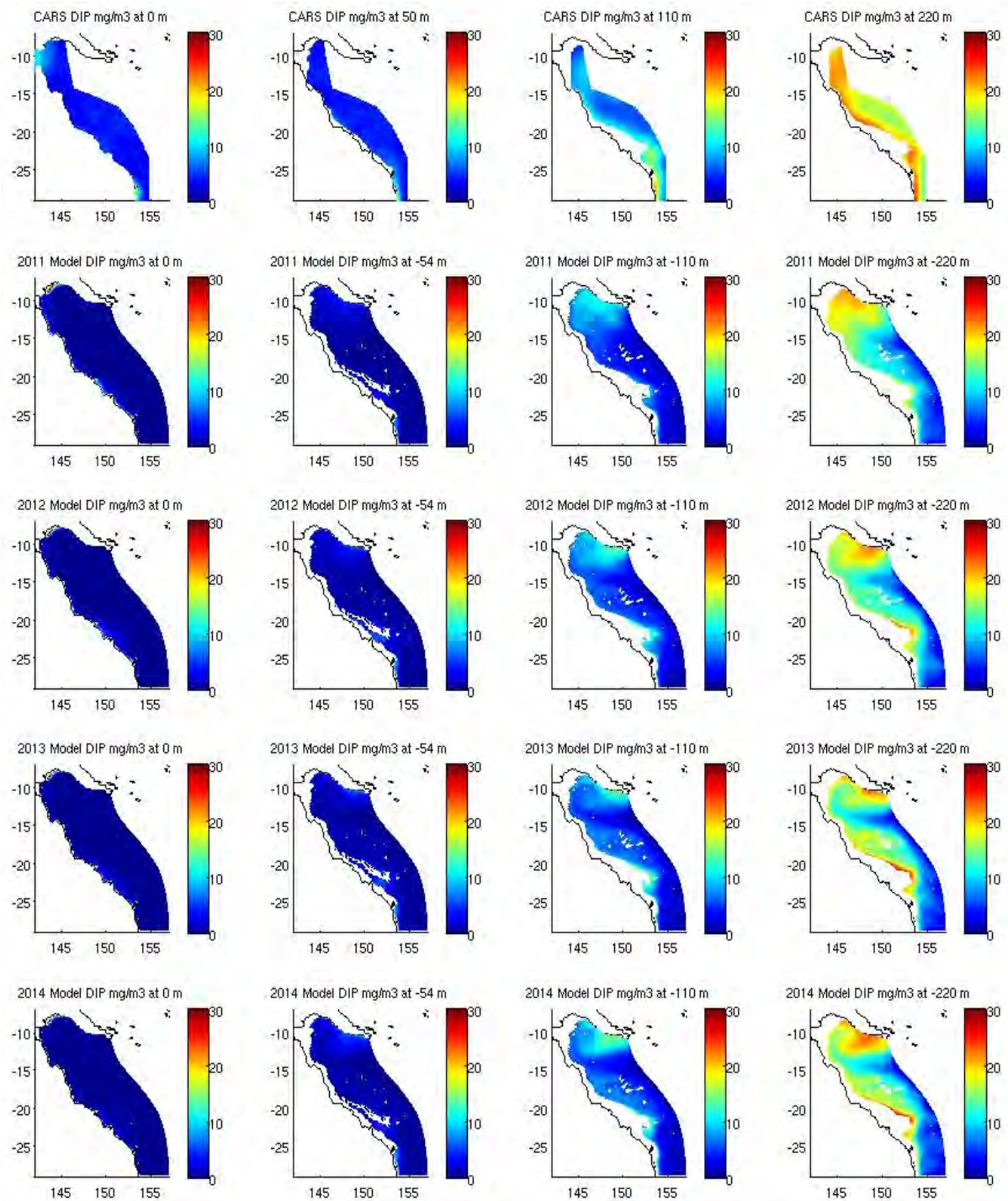


Figure 5.5.3. CSIRO Atlas of Regional Seas Coast 8 phosphate climatology (top) compared with annual mean GBR 4km modelled nitrate for 2001, 2012, 2013 & 2014 at various depths (0, 50, 110 & 220 m).

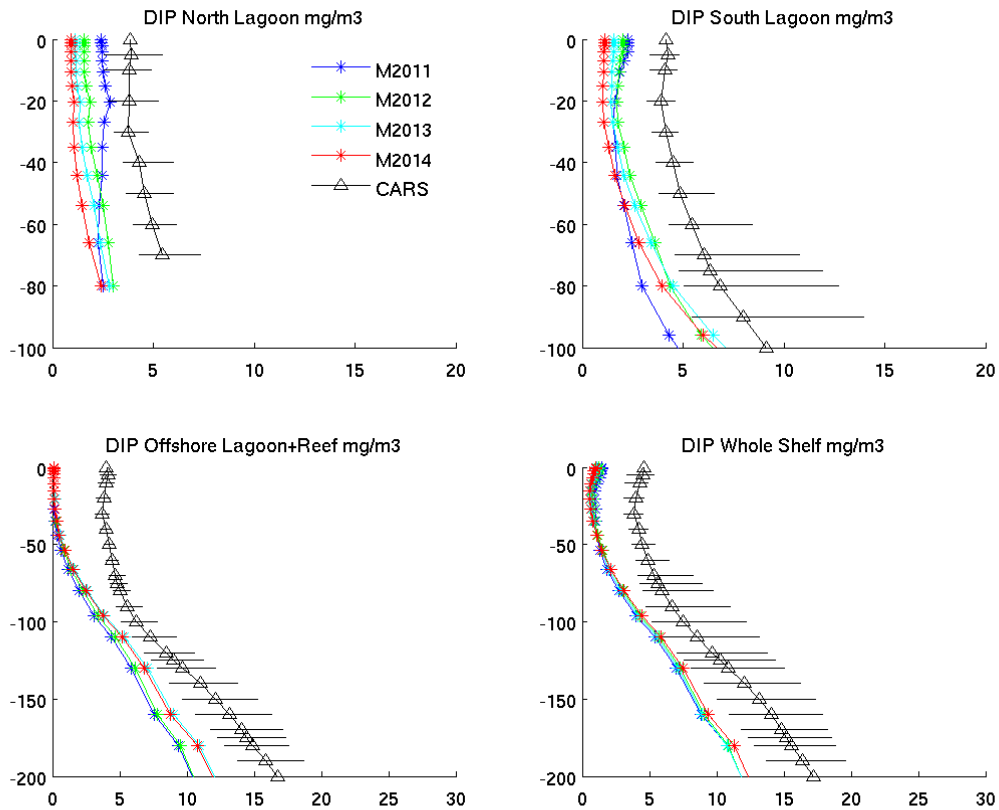


Figure 5.5.4. Mean model and CARS phosphate profiles for subregions from Cape York to Palm Passage, Palm Passage to Fraser Island, offshore lagoon plus reef, and the whole shelf. Horizontal error bars show the 10 – 90 percentile CARS phosphate concentration.

The molar nitrate to phosphate ratio was calculated from the CARS Coast 8 climatology and for annual means of simulated nitrate and phosphate (Fig. 5.5.5). Values below 16 indicate the system is below Redfield ratio with primary production (at 106C:16N:1P) potentially limited or controlled by the availability of nitrate [phosphate is in excess of Redfield requirement]. In the CARS climatology the N:P ratio was well below Redfield in surface waters (0-110m), indicating nitrate was the nutrient in least supply for primary production; at 220m the N:P ratio approached Redfield ratio. In the model the molar N:P was well below Redfield in surface waters, and approached Redfield ratio at depth. In surface waters at the offshore model boundary there was a mis-match in the supply of nitrate and phosphate in the Coral Sea and off PNG such that the N:P ratio exceeded Redfield so that these locations were limited by the supply of phosphate. However, in general, over the whole Queensland shelf and GBR reef, the CARS climatology and model agree that the N:P ratio is below Redfield and primary production in the system is therefore limited by the supply of nitrogen.

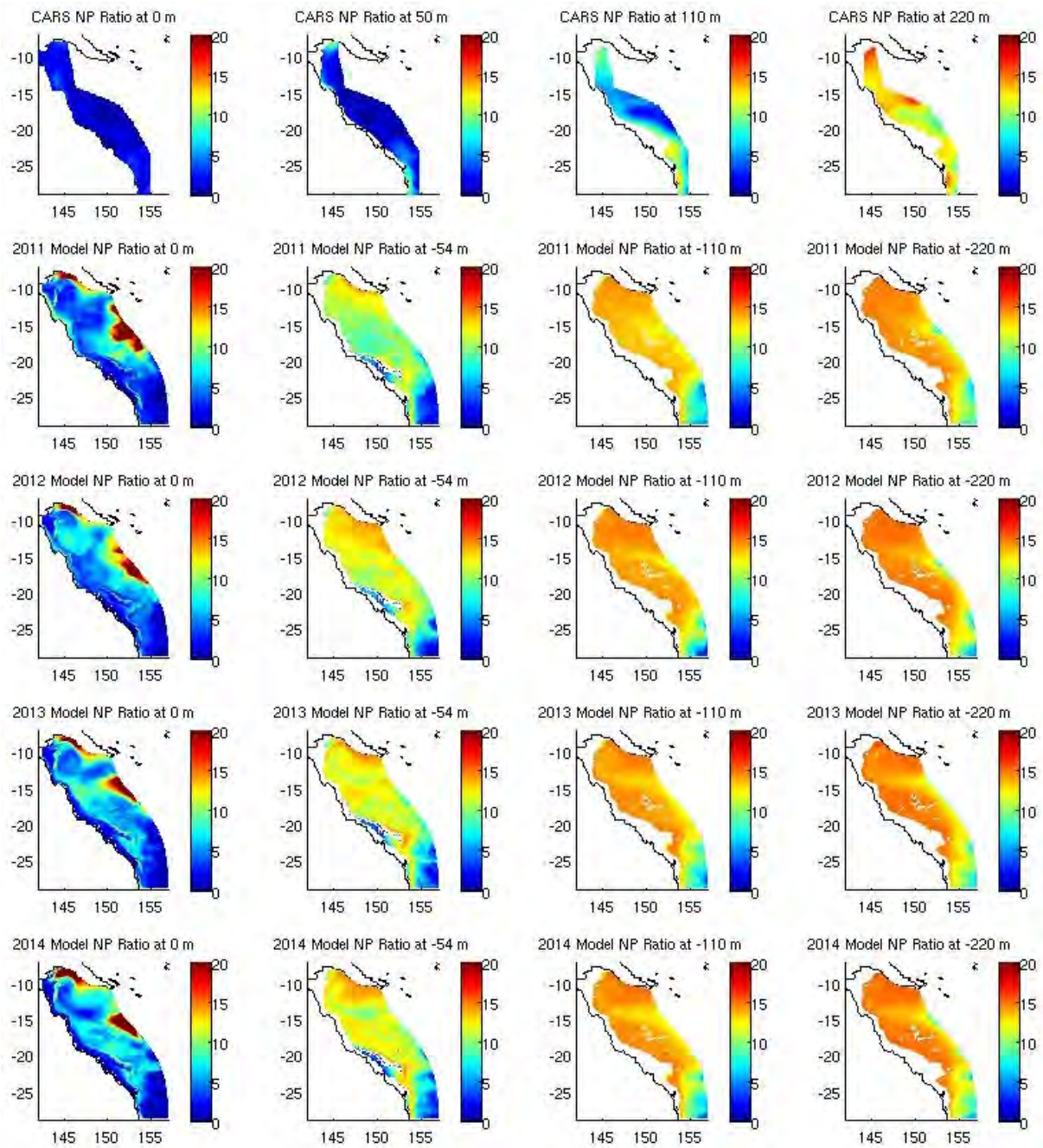


Figure 5.5.5. Molar N:P ratio calculated from the CSIRO Atlas of Regional Seas Coast 8 phosphate climatology (top) compared with annual mean GBR 4km modelled nitrate:phosphate ratio for 2001, 2012, 2013 & 2014 at various depths (0, 50, 110 & 220 m).

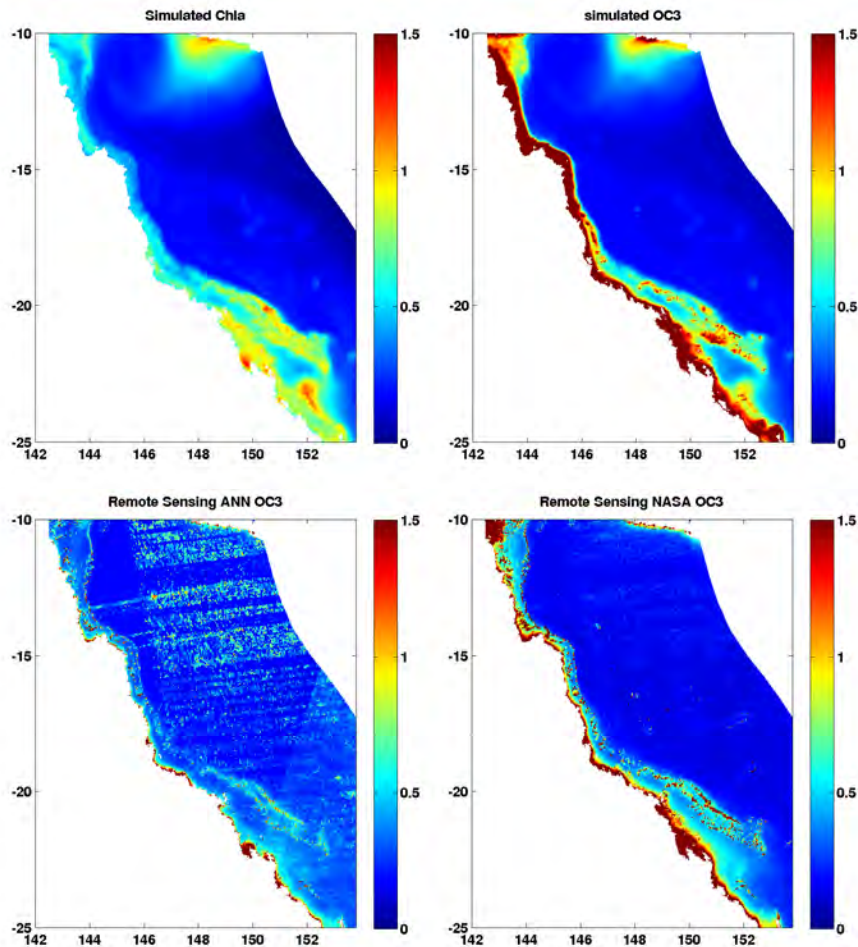


Figure 5.5.6. Climatology (June 2011 – June 2014 average) of: Top left, simulated surface Chla (mg m^{-3}). Top right simulated OC3 (combining simulated reflectance using the NASA OC3 algorithm). Bottom left, remote sensing ANN OC3 (Artificial neural network regional atmosphere correction product from Schroeder et al 2012). Bottom right, remote sensing NASA OC3, standard NASA product.

The eReefs biogeochemical model simulates individual reflectances. It is therefore possible to combine these reflectances into standard, well recognized remote sensing products. Fig. 5.5.6 presents mean simulated Chla concentration and equivalent simulated OC3 product, as well as in situ remotely sensed products (regional ANN OC3 and standard OC3 Chla estimate).

The 2 panels that can be truly compared are the one on the right side of Fig. 5.5.6, representing the simulated and remotely sensed OC3 estimate of Chla concentration. Both combine individual reflectance into proxies for Chlorophyll-a concentrations (using the NASA OC3 algorithm, this product degrades closer to the coast where CDOM signal dominates).

By comparing the 2 panels, we can conclude that the model represents accurately the general distribution throughout the region, with high values along the coast and above each reef systems, and low concentrations offshore. The simulated concentration inside the coastal band is higher than in the remotely sensed observation.

The 2 panels on the left represent simulated Chlorophyll-a concentration and regionally optimized remotely sensed product (ANN OC3). The bands on the offshore region of the

bottom left panel are artifacts of the climatology and interpolation schemes used to grid the ANN OC3 product (the ANN OC3 is only valid for the coastal inshore band). Similar to standard OC3 products, but looking inside the coastal band this time, the general gradient of concentrations are similar in both the model and the remote sensing estimate, but the model overestimate slightly the Chla concentrations. The later comparison is challenging. The estimation of Chla in high CDOM coastal waters with remote sensing is difficult and prone to errors.

5.5.3 Observations used for Model Comparison

Observations from a number of databases for the model hindcast period of October 2010 to present are listed in Table 5.5.3. These datasets range from intermittent or short term/short scale sampling, to quarterly or monthly individual water quality management samples, to high temporal observations (e.g. fluorescence on an IMOS mooring, 10 minutes). The time and space scales covered by the various data sets are summarised and compared with the eReefs model resolution (Fig. 5.5.7). Data at finer spatial scales than the model needs to be interpreted with care as fine-scale observations rarely capture broad-scale features accurately. In this context the role of mid-scale AUV and towed vehicle observations is very important for scaling up the fine-scale observations with understanding of the broader-scale natural variability. In the GBR region AUV and towed vehicle observations are limited to a few estuarine plume studies and the Heron Island glider transect. In these regions the model can be evaluated with appropriately scaled observations with more confidence.

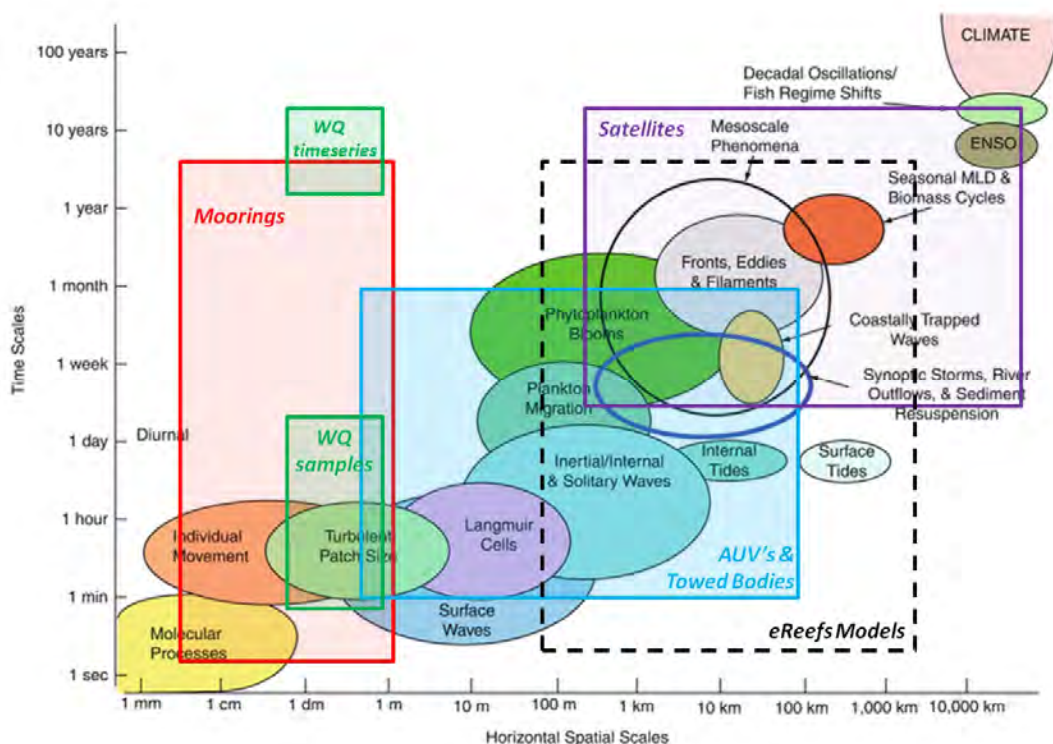


Figure 5.5.7. Time and space scales of GBR processes and observations.

Table 5.5.3. Observations used in 2010-present model comparison [Blue: direct model comparison; White: informs initial conditions and model performance in remote areas].

Database type	Number of sites/voyages with WQM	Holdings	BGC Parameters
AIMS WQM standard sites	16- 20 sites with many taken at 2 depths most at approx 3 month intervals	AIMS WQM	NH ₄ , NO _x , DIP Chla (HPLC), TSS, DOC, DON, DOP
Reef rescue Sites	14 Sites that correspond with AIMS WQM sites above (continuous from 2009)	Reef Rescue/AIMS	Chl (fluorescence), turbidity
IMOS moorings chlorophyll	6 moorings with WQM instruments, generally 2 WQM depths per mooring (continuous Fluorescence)	IMOS	Chl (Fluorescence)
NRS Moorings chlorophyll	Two continuous Chl (fluorescent) moorings Yongala and Stradbroke. Yongala is in both IMOS and AIMS database separately Yongala is usually more up to date in AIMS for WQ data than in IMOS. Sometimes a little different ion data due to burst data we being available after a time	Aims database and IMOS	Chl (Fluorescence)
NRS IMOS Moorings	WQM monthly samples and Chl generally every month at two moorings: Yongala and Stradbroke,	Aims database and IMOS	NH ₄ NO _x DIP Chla (HPLC) TSS
Alkalinity Surveys	Sample set from mid 2011 to present of 14 sample sites (same as Reef Rescue sites)	Miles Furnas	Aragonite saturation state, DIC, pH, alkalinity
HPLC chlorophyll samples	assorted HPLC chls samples from moorings and voyages and one off transects in the barrier reef region and at model boundaries	AESOP and IMOS and Data Trawler	Chla (HPLC)
Flood plumes	4 regional areas of datasets where flood plume WQ samples are taken (15 per site over the flooding period(weekly): Burdekin, Burnett Mary, Fitzroy and wet tropics	James Cook University	Note some parameters not always taken: Kd, TSS, Chla (HPLC), turbidity, NH ₃ , NO _x DIP, DON, DOP
Samples North of the Noosa River to Fitzroy	Received 4 WQ datasets 21 Nov 2014 that are predominantly very close to shore and up into estuaries from Noosa to Fitzroy mainly close inshore and estuary samples	Jonathon Hodge via CQAMP	Alkalinity, Chl-a, NH ₄ , NO _x , DON, DOC, Oxygen, DIP, TSS,
Sporadic Aims WQM sites throughout the 2010 to 2014 period, underway or special research	~50 sites temporally sporadic or ad hoc most near the coast or very close to inner reef Islands	Aims WQM	NH ₄ , NO _x , DIP, CHL, TSS, DOC, DON, DOP, NO _x
Voyage sites Coral Sea	Historic: 1920 until present (~100 sites) sporadic or ad hoc	marlin and data trawler	NH ₄ NO _x DIP Chl TSS
Voyages near Fly river	Historic: 1920 until present (~20 sites) sporadic or ad hoc	marlin and data trawler	NH ₄ NO _x DIP Chl TSS
Voyage sites Coral Sea near PNG gulf	Historic:1920 until present (~50 sites) sporadic or ad hoc	marlin and data trawler	NH ₄ NO _x DIP Chl TSS
Voyage sites Torres strait	Historic:1920 until present (~30 sites) sporadic or ad hoc	marlin and data trawler	NH ₄ NO _x DIP Chl TSS
Voyage sites or longitudinal surveys from new and Queensland border	Historic:1970 until present (~200 sites) sporadic or ad hoc	marlin and data trawler	NH ₄ NO _x DIP Chl TSS

Most monthly and quarterly in situ water quality samples came from AIMS and the National reference stations (NRS) and most of the high temporal observations are from IMOS and the NRS and the Reef Rescue program (AIMS). The sites of the major AIMS Water Quality stations

(taken 3 monthly) and the IMOS and NRS moorings are shown in Figure 5.5.8. The IMOS moorings provide hydrodynamic data at a number of fixed depths on each mooring with spatial coverage from Lizard Island to the Capricorn Bunker Group. A number of these moorings as shown on Figure 5.5.8 are augmented with turbidity, chlorophyll and dissolved oxygen sensors (http://data.aims.gov.au/gbroos_moorings/mooringspages/index.html).

It should be noted that most of these sites and moorings are near shore with regard to the extent of the GBR4 model domain. There is a large area of the GBR4 model that is not covered by consistent sampling. In order to set up the initial conditions and have a general understanding of the entire spatial area of the model grid we used a variety of historical voyage datasets from the regions (1930 to present) where there were limited routine datasets. These regions were Torres Strait, the Gulf of Papua, the QLD/NSW boundary of the model and the Coral Sea. These historical datasets were primarily housed within the CSIRO public databases: DataTrawler (<http://www.cmar.csiro.au/trawler/>) and Marlin (<http://www.cmar.csiro.au/marlin/>). Other additional datasets within some of these regions were obtained from glider profiles (IMOS) (see Section 5.5.5). The period of in water IMOS and Reef Rescue moorings for the 2010 to present model calibration are shown in Figure 5.5.9.

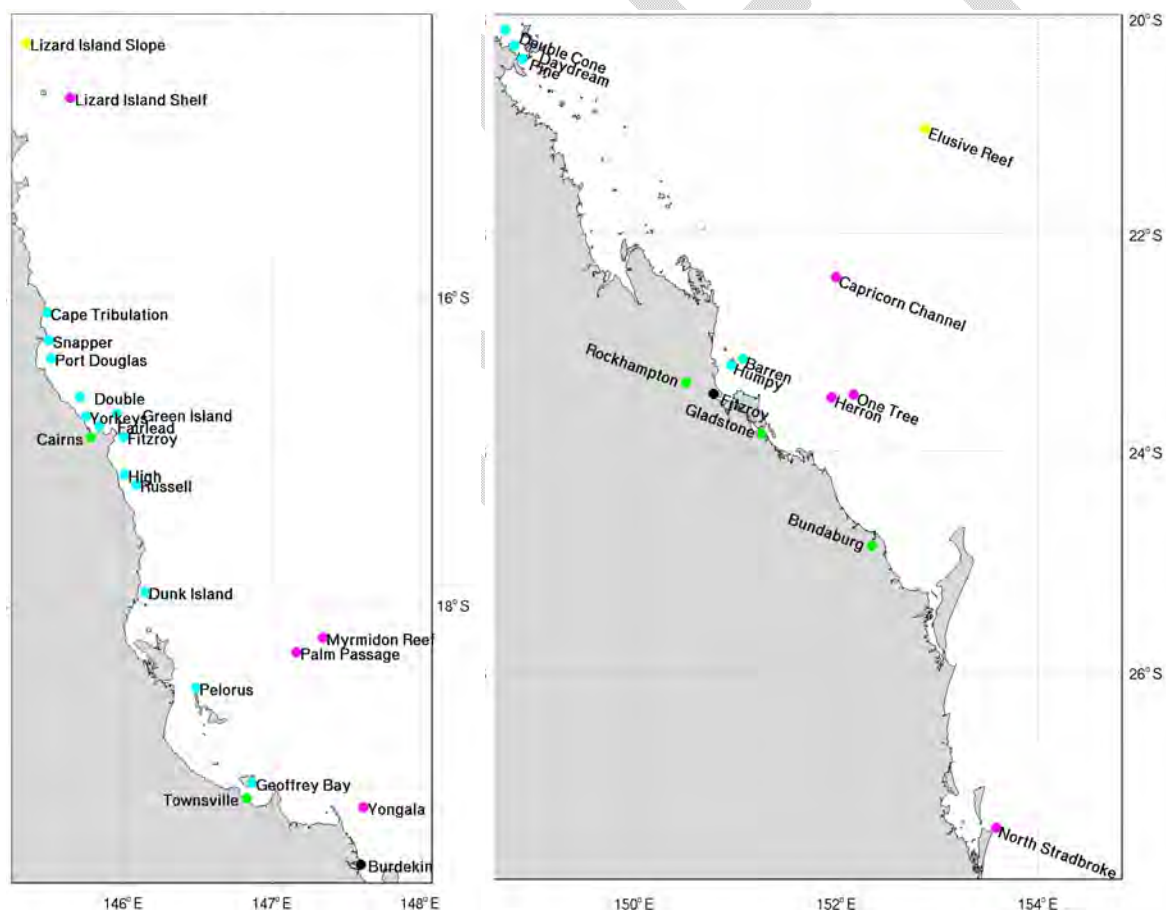


Figure 5.5.8. Primary observational data sites used for model calibration for the GBR4 eReefs model. Pink are IMOS and NRS moorings, Blue are AIMS water quality monitoring (WQM) sites. Yellow are IMOS moorings without BGC observations.

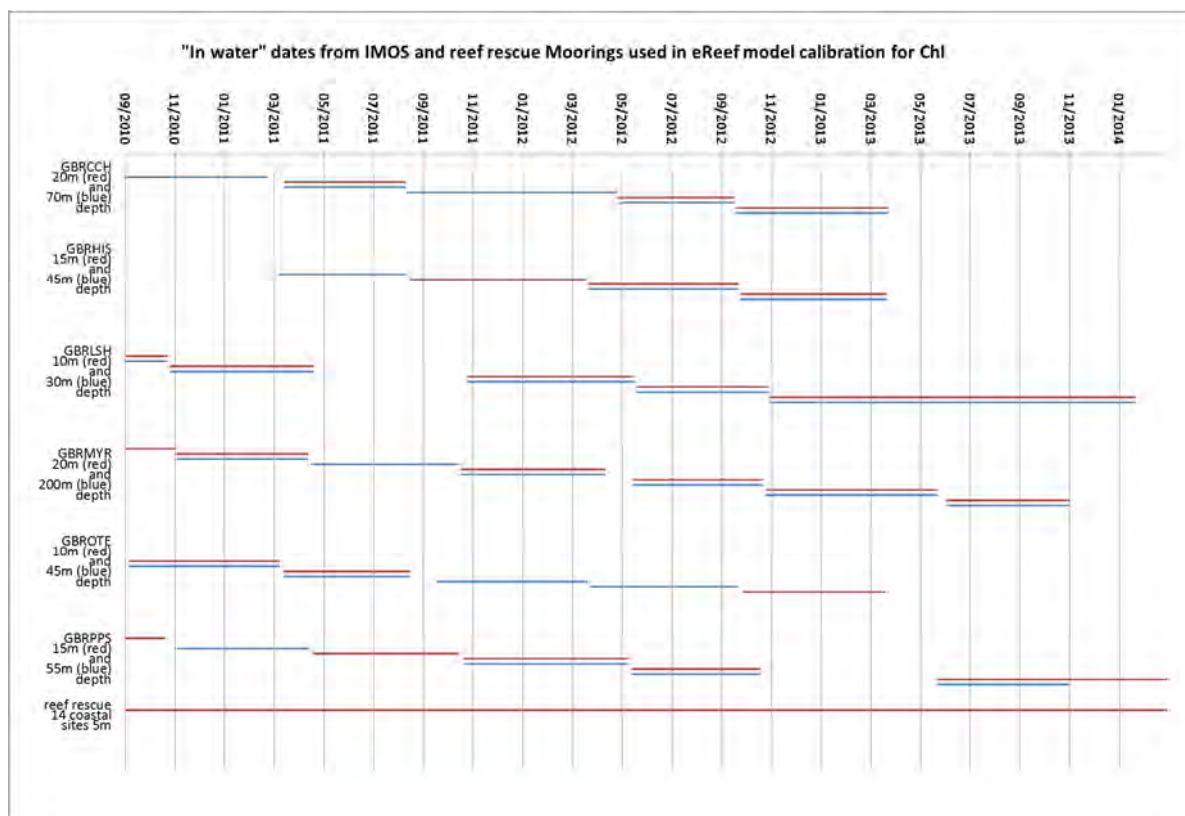


Figure 5.5.9. Gantt chart of IMOS and Reef Rescue moorings fluorescence measurements used for the model calibration of chlorophyll showing availability of data over the model 2010 to 2014 hindcast run.

5.5.4 Skill assessment of biogeochemical model against water quality time series observations

Biogeochemical model skill can be quantitatively assessed in the model using root-mean-square error (RMS), correlation coefficient (r), bias, mean absolute error (MAE) and the skill metric of Willmott et al. (1985) ($d2$). All these metrics are included in Fig. 5.5.10 – 5.5.14 which contain a comparison of the GBR4 BGC model with chlorophyll (fluorescence) at the IMOS and NRS BGC moorings and their respective monthly nutrient observations as well as a comparison of the AIMS chlorophyll (fluorescence) moorings at the 14 water quality sites.

As noted in Section 5.5.3, the comparison of mooring and bottle water samples with 4km resolution model output requires some care as the observations are unlikely to fully represent broad-scale patterns in water quality. Nevertheless these preliminary direct model comparisons against observations demonstrate that the model is operating in the right order of magnitude with generally good agreement for simulated chlorophyll and nitrate.

5.5.4.1 Observations

Observations were compared with model simulations for a number of individual sites and moorings within the GBR domain. The eReefs BGC model analysis would not be possible without the continuing observational analysis datasets which play a highly significant role in the successful interpretation of the biogeochemical cycles and management of our eReef model suite. Our primary observational data sources were from the Integrated Marine Observing System (IMOS) which include the National Reference Stations (NRS- Yongala and North Stradbroke Island) and AIMS-WQM and Reef Rescue Sites and moorings (see BGC Appendix A for all results statistics and comparisons). We also use satellite data calculated using MODIS OC3 and TSS 625 (Goyens et al. 2013) algorithms from simulated remote sensing reflectance and chl *a* and TSS from the MIM algorithm using remotely sensed MODIS-Aqua observations ((Goyens et al. 2013) see BGC Appendix A pages 153-184 for all results and comparisons).

Due to the size and nature only a few examples of direct comparison are shown in this report, all other direct one to one observational/model simulation comparisons are shown in the BGC Appendix A attached to this report or are also shown in other sections in more sophisticated representations.

Due to the location and bathymetry of the observational sites within the model grid, some sites were flagged for potential issues (Table 5.5.4). Note that some of the sites with poor flags compared favourably with the model simulations (e.g. Fig. 5.5.13 Snapper Island, Double Cone Island and Fitzroy Reef had poor flags but observations compared well with model simulation). The attached BGC Appendix A contains comparisons of all sites and model simulations. No IMOS and NRS moorings had site location or depth issue flags with respect to their placement within the model grid. Sites that did have issues were generally AIMS-WQM sites that were close to the coast or islands or enclosed in embayments or mismatched between the observed and modelled water column depth.

Overall, comparisons were very difficult with triannual/quarterly sampling of the 20 WQM sites and the modelling simulations which were 2 hourly. The WQM sites were generally highly detailed in their nutrient analysis and often had three depths. However, for use in the model comparison there was no ability for these sites to capture any temporal variation. Most of these sites were also very close to coasts and Islands (Table 5.5.4). We have done comparisons for all these sites with the model simulations and these and their statistics are shown in the BGC Appendix A pages 111-146. It is perhaps surprising that over the 20 sites the observations and model simulations and their statistics do compare favourably (BGC Appendix A page 38).

A summary of the statistics for all sites and parameters can be found in the BGC Appendix A on pages 36-41.

Table 5.5.4. Observational sites used to compare model simulations showing flagging of any potential issues with site within the GBR4 model grid (WQM-RR are AIMs Reef Rescue sites). 0 is no flag to 3 which is poor.

Site grouping	Site	Site depths flag	Site location flag	Site names	Field sample depth	Max obs. depth	Max model depth	Comment on potential conflicts within model grid with respect to observational sites, locations and depths
IMOS	Capricorn Channel	0	0	GBRCCH_22m	-22	-92	-91.17	no site location or depth issue flags with respect to model simulation
IMOS	Capricorn Channel	0	0	GBRCCH_72m	-72	-92	-91.17	no site location or depth issue flags with respect to model simulation
IMOS	Heron Island South	0	0	GBRHIS_13m	-13	-46	-47.01	no site location or depth issue flags with respect to model simulation
IMOS	Heron Island South	0	0	GBRHIS_42m	-42	-46	-47.01	no site location or depth issue flags with respect to model simulation
IMOS	Lizard Shelf	0	0	GBRLSH_10m	-10	-31	-30.32	no site location or depth issue flags with respect to model simulation
IMOS	Lizard Shelf	0	0	GBRLSH_30m	-30	-31	-30.32	no site location or depth issue flags with respect to model simulation
IMOS	Myrmidon Reef	0	0	GBRMYR_17m	-17	-203	-220	no site location or depth issue flags with respect to model simulation
IMOS	Myrmidon Reef	0	0	GBRMYR_200m	-200	-203	-220	no site location or depth issue flags with respect to model simulation
IMOS	One Tree Island	0	0	GBROTE_13m	-13	-58	-62.61	no site location or depth issue flags with respect to model simulation
IMOS	One Tree Island	0	0	GBROTE_45m	-45	-58	-62.61	no site location or depth issue flags with respect to model simulation
IMOS	Palm Passage	0	0	palm_passage_0	-1	-70	-71.9	no site location or depth issue flags with respect to model simulation
IMOS	Palm Passage	0	0	palm_passage_15	-15	-70	-71.9	no site location or depth issue flags with respect to model simulation
IMOS	Palm Passage	0	0	palm_passage_60	-60	-70	-71.9	no site location or depth issue flags with respect to model simulation
IMOS/NRS	North Stradbroke	0	0	North_Stradbroke_0	-1	-67	-66	no site location or depth issue flags with respect to model simulation
IMOS/NRS	North Stradbroke	0	0	North_Stradbroke_10	-10	-67	-66	no site location or depth issue flags with respect to model simulation
IMOS/NRS	North Stradbroke	0	0	North_Stradbroke_20	-20	-67	-66	no site location or depth issue flags with respect to model simulation
IMOS/NRS	North Stradbroke	0	0	North_Stradbroke_30	-30	-67	-66	no site location or depth issue flags with respect to model simulation
IMOS/NRS	North Stradbroke	0	0	North_Stradbroke_40	-40	-67	-66	no site location or depth issue flags with respect to model simulation
IMOS/NRS	North Stradbroke	0	0	North_Stradbroke_50	-50	-67	-66	no site location or depth issue flags with respect to model simulation
IMOS/NRS	Yongala	0	0	Yongala_0	-1	-27	-28.62	no site location or depth issue flags with respect to model simulation
IMOS/NRS	Yongala	0	0	Yongala_10	-10	-27	-28.62	no site location or depth issue flags with respect to model simulation
IMOS/NRS	Yongala	0	0	Yongala_20	-20	-27	-28.62	no site location or depth issue flags with respect to model simulation
IMOS/NRS	Yongala	0	0	Yongala_26	-26	-27	-28.62	no site location or depth issue flags with respect to model simulation
WQM	Cape Tribulation	0	0	CapeTrib356_10m	-10	-18	-20.5	no site location or depth issue flags with respect to model simulation
WQM	Double island	0	0	DoubleI520_0m	-1	-31	-22.05	no site location or depth issue flags with respect to model simulation
WQM	Double island	0	0	DoubleI520_18m	-18	-31	-22.05	no site location or depth issue flags with respect to model simulation
WQM	Green island	0	0	Green830_0m	-1	-38	-34.66	no site location or depth issue flags with respect to model simulation
WQM	Green island	0	0	Green830_18m	-18	-38	-34.66	no site location or depth issue flags with respect to model simulation
WQM	Green Island	0	0	Green830_36m	-36	-38	-34.66	Green WQM is 38m and model depth is 35 meters. Model will automatically take lowest depth in model grid (i.e. 35m) and assign this to this point
WQM	Port Douglas	0	0	PortD_0m	-1	-18.44	-18.44	no site location or depth issue flags with respect to model simulation
WQM	Port Douglas	0	0	PortD_15m	-15	-17.1	-18.44	no site location or depth issue flags with respect to model simulation
WQM-RR	Daydream	0	1	Daydream_5m	-5	-26	-16.76	Daydream WQM max depth is 26 m and model is 17 m. Model will automatically take lowest depth in model grid and assign this as the bottom layer. suitable for 10 and 5 m. Resuspension and mixing occurs at this site
WQM-RR	Daydream	0	1	Daydream330_10m	-10	-26	-16.76	Daydream WQM max depth is 26 m and model is 17 m. Model will automatically take lowest depth in model grid and assign this as the bottom layer. suitable for 10 and 5 m. Resuspension and mixing occurs at this site
WQM-RR	High Island	0	1	High_5m	-5	-25	-17.64	no site location or depth issue flags with respect to model simulation
WQM	High Island	0	1	HighI_10m	-10	-25	-17.64	no site location or depth issue flags with respect to model simulation
WQM	High Island	0	1	HighI697_0m	-1	-25	-17.64	no site location or depth issue flags with respect to model simulation
WQM	High Island	0	1	HighI697_10m	-10	-25	-17.64	no site location or depth issue flags with respect to model simulation
WQM-RR	Russell Island	0	1	Russell_5m	-5	-22	-19.94	good for depth but poor location placement
WQM	Russell Island	0	1	Russell695_0m	-1	-22	-19.94	good for depth but poor location placement
WQM	Russell Island	0	1	Russell695_10m	-10	-22	-19.94	good for depth but poor location placement
WQM	Russell Island	0	1	Russell695_20m	-20	-22	-19.94	Russell WQM max depth is 22 m model depth is -19.94m. Model will automatically take the lowest depth in the model grid and assign this to this point. Assigning 19.94 m in the model to a point taken at 22 as they are both in the same depth layer
WQM	Yorkeys Knob	0	1	Yorkeys519_0m	-1	-10.6	-10.5	good for depth but poor location placement
WQM	Yorkeys Knob	0	1	Yorkeys519_8m	-8	-10.6	-10.5	good for depth but poor location placement
WQM	Daydream	1	1	Daydream_23m	-23	-26	-16.76	Daydream WQM max depth is 26 m and model is 17 m. Model will automatically take lowest depth in model grid and assign this as the bottom layer. Possible concern for TSS in the bottom layer. Resuspension and mixing occurs at this site
WQM-RR	Dunk Island	0	2	Dunk859_5m	-5	-10	-9.15	good for depth but poor location placement. The site is close to the Island and enclosed and the grid cells border land.
WQM	Fairlead Buoy	0	2	FairleadBuoy518_0m	-1	-8.5	-9.63	good for depth but poor location placement. The site is close to the Island and enclosed and the grid cells border land.
WQM-RR	Fitzroy Reef	1	1	Fitz_5m	-5	-16.5	-27	Max obs depth for Fitz by WQM is 16.5. Model depth is 27 m. The model will be reading this value as mid water column when obs will have it as bottom depth. Probably not suitable for deep obs but possible suitable for 0 and 5 m

WQM	Fitzroy Reef	1	1	FitzCoral852_0m	-1	-16.5	-27	Max obs depth for Fitz by WQM is 16.5. Model depth is 27 m. The model will be reading this value as mid water column when obs will have it as bottom depth Probably not suitable for deep obs but possible suitable for 0 and 5 m
WQM-RR	Pandora	0	2	Pandora_5m	-5	-12	-16.98	Pandora WQM sample is taken at 5 m but the max obs bottom depth is 12 m so a model depth of 16.98 is reasonable as only 1 layer difference good for depth but poor location placement
WQM-RR	Pelican	2	0	Pelican_5m	-5	-9.7	-4.47	Pelican WQM is taken at 5 m max obs depth is 9.7. The model max depth of -4.97 maybe suitable as the model automatically takes the lowest depth layer however 5 m is meant to be mid water column in the obs whereas its bottom in the model
WQM-RR	Pelorus Island	0	2	Pelorus_5m	-5	-31	-24.64	good for depth but poor location placement
WQM	Pelorus Island	0	2	Pelorus686_0m	-1	-31	-24.64	good for depth but poor location placement
WQM	Pelorus Island	0	2	Pelorus686_14m	-14	-31	-24.64	good for depth but poor location placement
WQM-RR	Barren Island	1	2	Barren_5m	-5	-18	-24.26	Barren WQM max depth is 18m and model is 24 m. We only compare 5 and 10 m depths. This site is therefore suitable for these depths. The depth of 18 (obs) to 24 (model) m is also only one model layer difference. The site is close to the Island and enclosed and the grid cells border land. This site has effects from Fitzroy
WQM	Barren Island	1	2	Barren411_10m	-10	-18	-24.26	Barren WQM max depth is 18m and model is 24 m. We only compare 0 and 5 and 10 m depths. This site is therefore suitable for these depths and bottom sites. The depth of 18 (obs) to 24 (model) m is also only one model layer difference. The site is close to the Island and enclosed and the grid cells border land. This site has effects from Fitzroy
WQM-RR	Geoffrey Bay	0	3	GeoffreyBay336_5m	-5	-10	-10.42	Flag is good for depth but poor location placement in the model grid as it is in an enclosed bay and borders land for 4 grid cells. Note that it is also a resuspension site and is affected by Burdekin run off
WQM	High Island	2	1	Highl_20m	-20	-25	-17.64	High l max obs depth is 25 m model is -18. Model will automatically take lowest depth in model grid (i.e. 18 m). The model grid cell is in the grid layer one up from the observation.
WQM-RR	Humpy Island	0	3	Humpy_5m	-5	-14	-12.86	good for depth but poor location placement due to closeness of Island. This site has effects from Fitzroy
WQM	Humpy Island	0	3	Humpy873_0m	-1	-14	-12.86	good for depth but poor location placement due to closeness of Island. This site has effects from Fitzroy
WQM	Humpy Island	0	3	Humpy873_10m	-10	-14	-12.86	good for depth but poor location placement due to closeness of Island. This site has effects from Fitzroy
WQM	Pelorus Island	1	2	Pelorus686_28m	-28	-31	-24.64	Pelorus WQM max depth is 31 m yet model depth is 24.64 meters in the model. Model will automatically take the lowest depth in the model grid (i.e. 24.64m) and assign this to this point. Assigning 24.64 m in the model to a point taken at 28 as the obs layer is only one layer below
WQM-RR	Pine	1	2	Pine_5m	-5	-25	-18.14	Pine WQM max obs depth is 25 m yet model depth is -18.14m. Model will automatically take the lowest depth in the model grid (i.e. 18.14m) and assign this to this point. They are both in the same depth layer however a 20 obs depth is 5 m above the bottom whereas it is bottom of the model not suitable for deepest sample but suitable for 0 and 5. This site has strong tides and waves and a long fetch.
WQM	Pine	1	2	Pine329_0m	-1	-25	-18.14	Pine WQM max obs depth is 25 m yet model depth is -18.14m. Model will automatically take the lowest depth in the model grid (i.e. 18.14m) and assign this to this point. Assigning 18.14 m in the model to a point taken at 20m ? They are both in the same depth layer however a 20 obs depth is 5 m above the bottom whereas it is bottom of the model not suitable for deepest sample but suitable for 0 and 5. This site has strong tides and waves and a long fetch.
WQM	Snapper Island	3	0	Snap_10m	-10	-11.2	-22.14	Depth for Snapper by WQM is 11.2 m Model depth is 22.14 m. Given that the 10 m is close to bottom water column and the model will be reading it as mid water column possibly not suitable
WQM-RR	Snapper Island	3	0	Snap_5m	-5	-11.2	-22.14	Depth for Snapper by WQM is 11.2 m Model depth is 22.14 m. Given that the 10 m is close to bottom water column and the model will be reading it as mid water column possibly not suitable
WQM-RR	Double cone	2	2	DoubleCone_5m	-5	-31	-17.03	Double cone WQM max depth is 31 m and model is 17 m. Model will automatically take the lowest depth in the model grid (i.e. 17 m) and assign this to this point. True layer being only one layer below the model depth of 17m means that 17m is closer to observed mid rather than bottom for this site
WQM	Double cone	2	2	DoubleCone334_10m	-10	-31	-17.03	Double cone WQM max depth is 31 m and model is 17 m. Model will automatically take the lowest depth in the model grid (i.e. 17 m) and assign this to this point. True layer being only one layer below the model depth of 17m means that 17m is closer to observed mid rather than bottom for this site
WQM	Fitzroy Reef	3	1	FitzCoral852_15m	-15	-16.5	-27	Max obs depth for Fitz by WQM is 16.5. Model depth is 27 m. The model will be reading this value as mid water column when obs will have it as bottom depth Probably not suitable for deepest obs
WQM	Pine	2	2	Pine329_10m	-10	-25	-18.14	Pine WQM max obs depth is 25 m yet model depth is -18.14m. Model will automatically take the lowest depth in the model grid (i.e. 18.14m) and assign this to this point. Assigning 18.14 m in the model to a point taken at 20m ? They are both in the same depth layer however a 20 obs depth is 5 m above the bottom whereas it is bottom of the model makes this mid depth possibly not suitable for 10 m. This site has strong tides and waves and a long fetch.
WQM	Double cone	3	2	DoubleCone_23m	-23	-31	-17.03	Double cone WQM max depth is 31 m and model is 17 m. Model will automatically take the lowest depth in the model grid (i.e. 17 m) and assign this to this point. True layer being only one layer below the model depth of 17m means that 17m is closer to observed mid rather than bottom for this site. Worse for deepest later of 23 m
WQM	Pine	3	2	Pine329_20m	-20	-25	-18.14	Pine WQM max obs depth is 25 m yet model depth is -18.14m. Model will automatically take the lowest depth in the model grid (i.e. 18.14m) and assign this to this point. Assigning 18.14 m in the model to a point taken at 20m ? They are both in the same depth layer however a 20 obs depth is 5 m above the bottom whereas it is bottom of the model not suitable for deepest sample of 20 meters but suitable for 0 and 5. This site has strong tides and waves and a long fetch.

5.5.4.2 Model and Observation comparison example: Yongala

Due to the extensive amount of data comparisons completed (see BGC-Appendix) only one site and depth is shown in this report. Figs. 5.5.10 and 5.5.11 compares of carbon chemistry, chl *a*, remote sensing data and nutrient observations with the model simulation for the National Reference station Yongala (NRSYON) (surface). The statistics show good agreement with the monthly nutrient observations (Fig. 5.5.10). Fig. 5.5.11 shows the comparison of the eReef designed algorithm of chl *a* from MIM or TSS 645 algorithm using remotely sensed MODIS-Aqua observations (Goyens et al 2013) with MODIS and the model simulation. Also shown is the comparison of the IMOS mooring chlorophyll fluorescence at surface with the model simulations. Further comparisons at Yongala at different depths and at other IMOS and Reef Rescue moorings are shown in the attached BGC Appendix A. The BGC Appendix A also shows 31 other sites within the GBR where satellite data and model observations are compared.

DRAFT

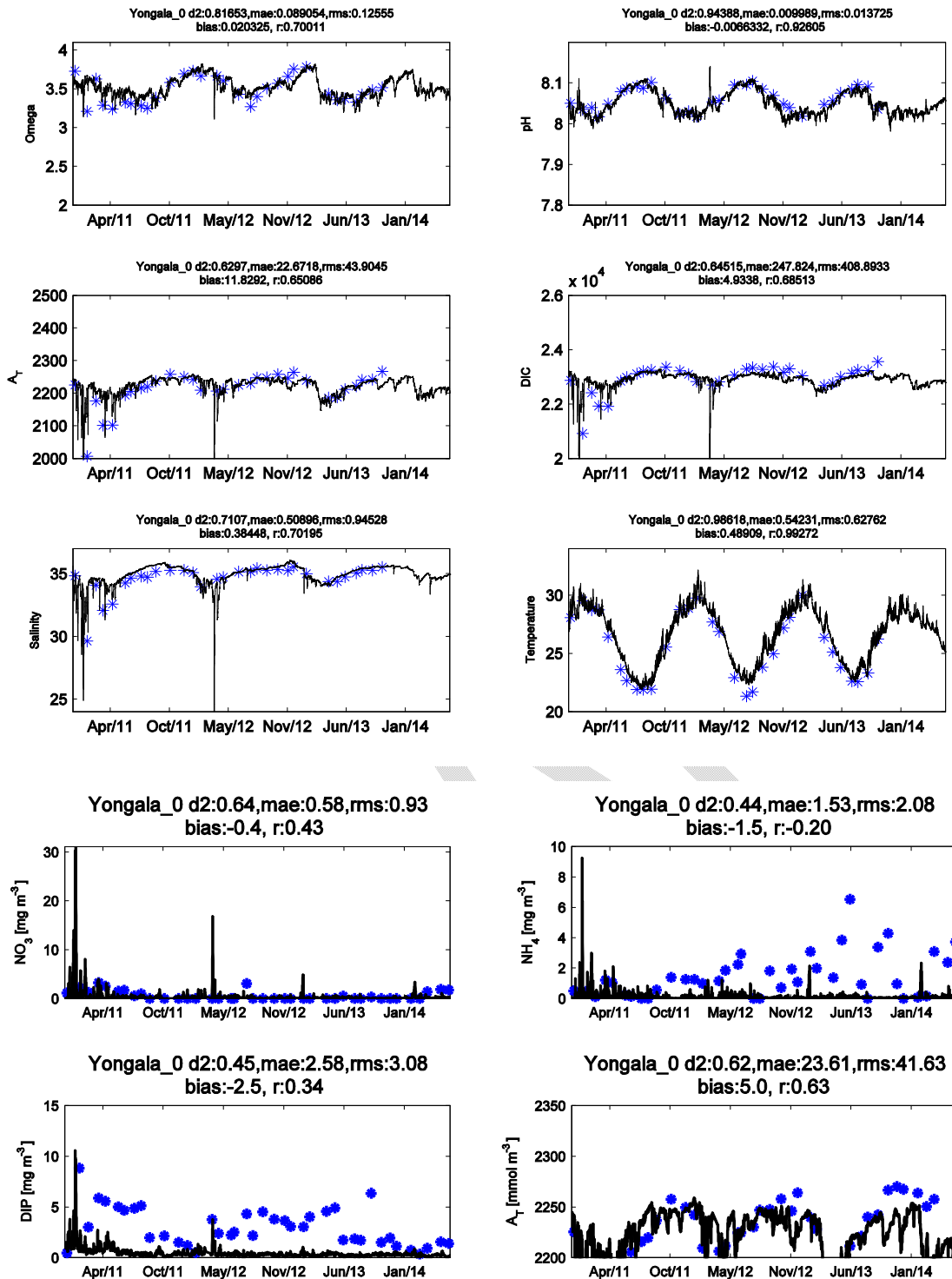


Figure 5.5.10. IMOS National Reference station NRSYON (Yongala) showing model and observational comparison at 0 m. **Blue stars:** observations, **Black line:** Model simulation, (see BGC Appendix A for further details on NRS and other AIMS WQM sites comparison of observation and model simulation). Parameters from top left across – degree of saturation for aragonite (Omega), pH, Alkalinity (A_T), Dissolved Inorganic Carbon (DIC), Salinity, Temperature, Nitrate (NO_3), Ammonia (NH_4), Phosphate (DIP). Statistics shown at the top of each comparison d2 (Willmott index), MAE (mean absolute error), Bias, r (see section 5.4.2 and BGC Appendix A page 12 for equations).

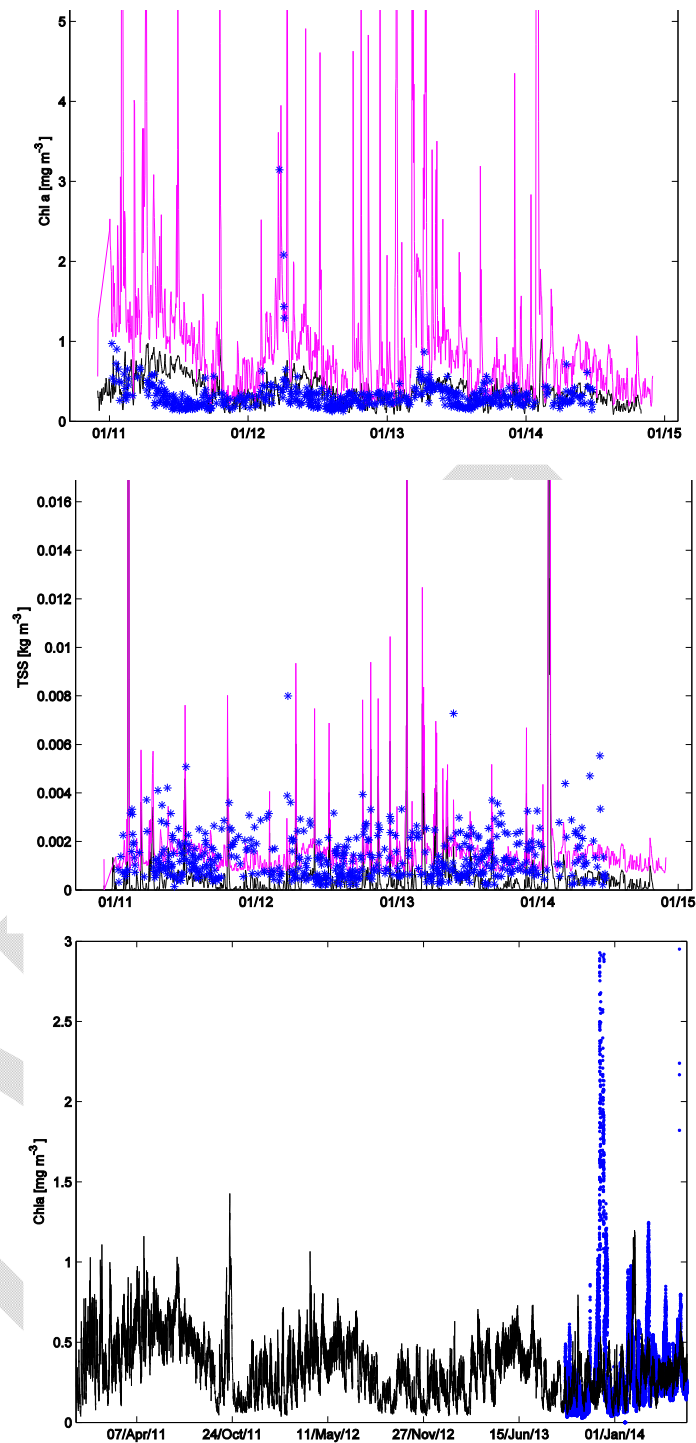
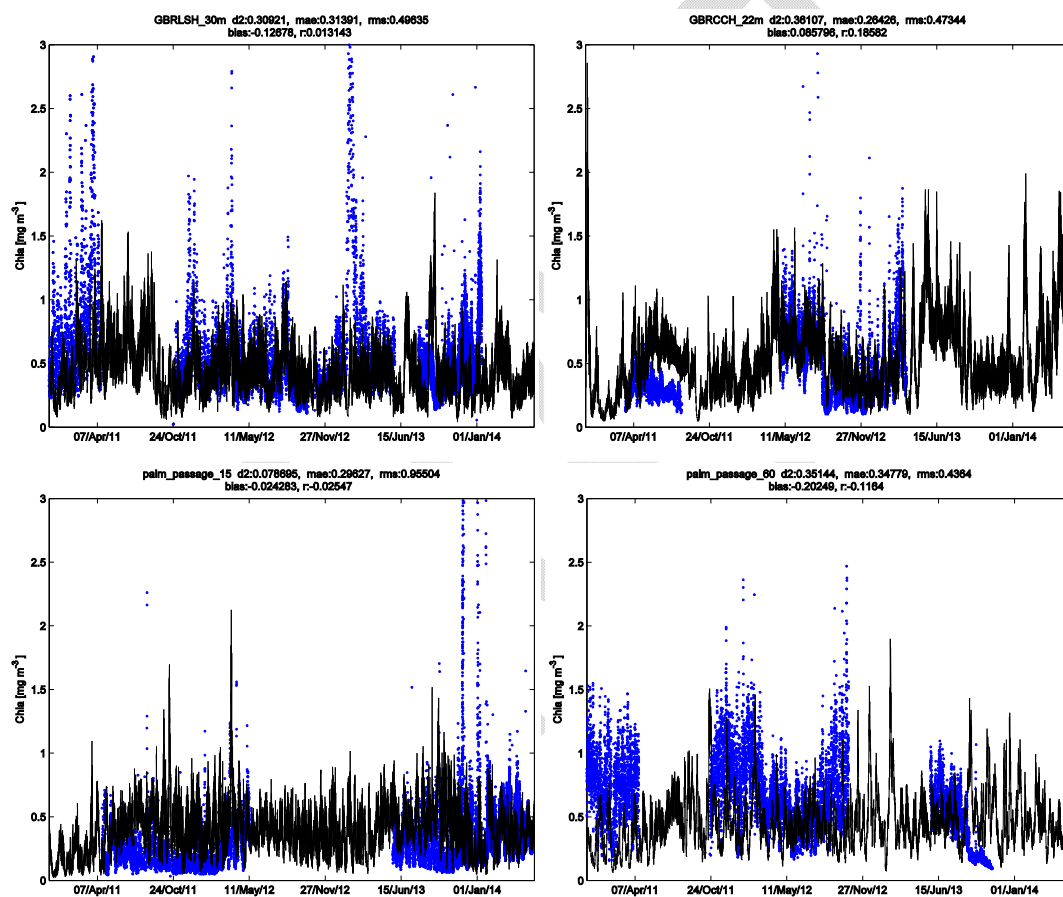


Figure 5.5.11. IMOS National Reference station NRSYON (Yongala) showing simulated in situ model and observational comparison at 0 m. – Top figures: **Blue stars**: Chl *a* or TSS from MIM algorithm using remotely sensed MODIS-Aqua observations, **Black line**: Model simulation, **Pink line**: Chl *a* calculated using MODIS OC3 algorithm from simulate remote-sensing reflectance (top fig) or TSS calculated using MODIS TSS 645 algorithm from simulated remote-sensing reflectance (middle fig). Bottom figure **Blue stars**: Chl *a* fluorescence from IMOS NRSYON mooring at 0 m, **Black line**: Model simulation (see BGC Appendix A for further details on Yongala and other remotely sensed data, moorings and model comparison).

5.5.4.3 Chlorophyll comparisons

Examples of model simulation with chlorophyll fluorescence at IMOS moorings can be seen in Fig. 5.5.12 for 4 locations. The model simulates Chl *a* at each of the locations and depths. Similarly the Reef Rescue moorings (Fig. 5.5.13) show good agreement of chlorophyll fluorescence and TSS with model simulations. The sites shown are from south to north with the two top figures showing sites closest to the Fitzroy River, the middle two sites representing the middle of the GBR and the bottom two sites represent the northernmost Reef Rescue moorings. All Reef Rescue sites are relatively close to shore and show slightly higher chlorophyll fluorescence in the model simulations when compared with the mooring fluorescence results. A preliminary comparison was done for Yongala to find the closest model value to the observations within the 9 grid cells surrounding the site at each depth (i.e. the best fit neighbourhood technique described in Section 5.2.2). Fig. 5.5.14 shows that cells surrounding the site reached lower values closer to the observed for the time period shown.



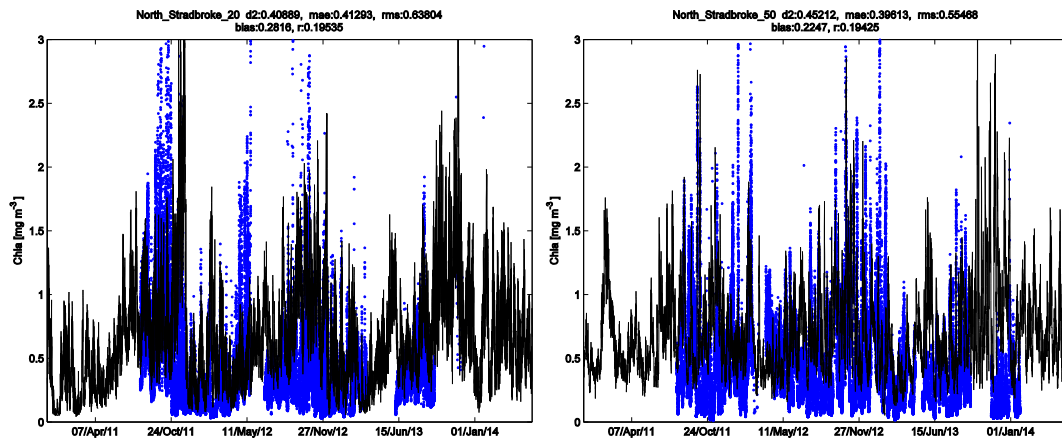
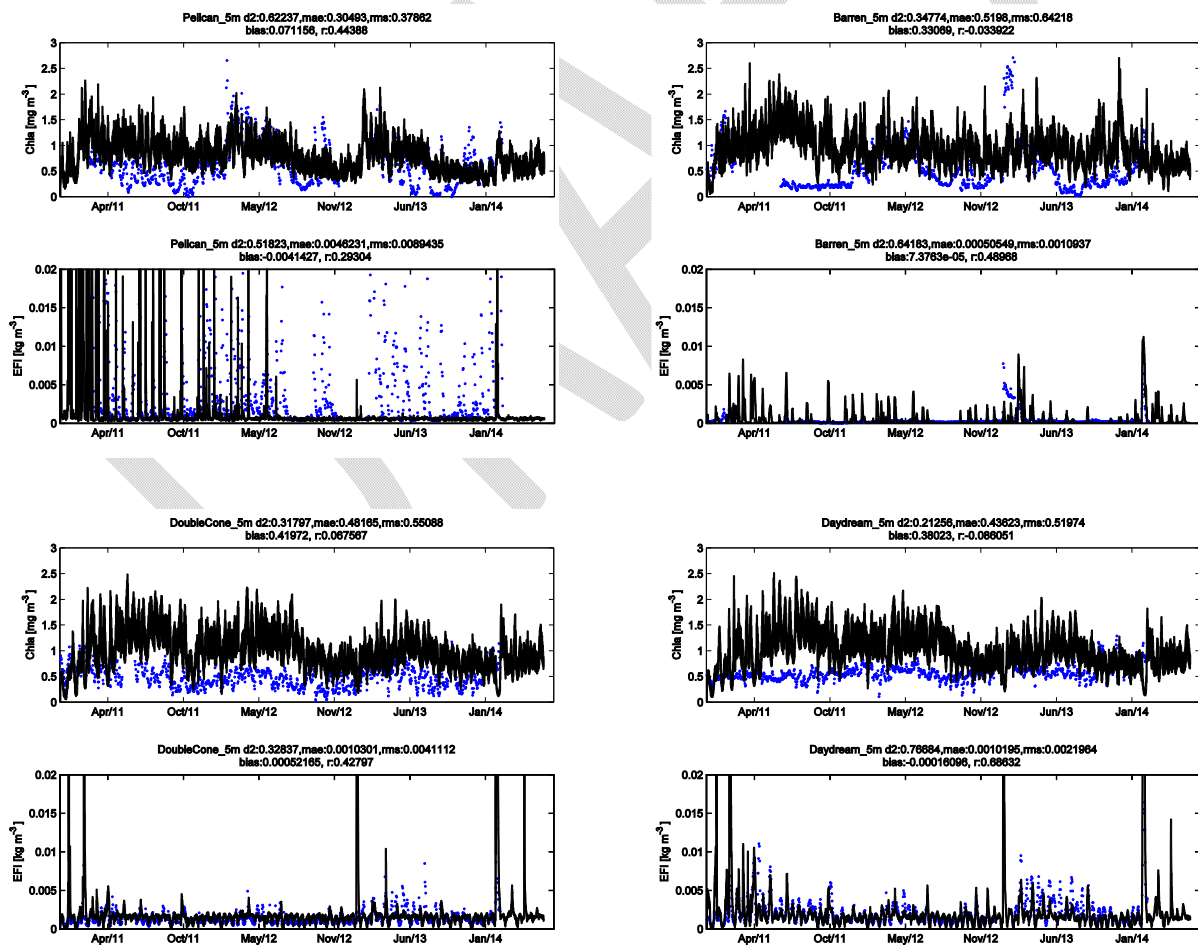


Figure 5.5.12. IMOS/NRS moorings at model simulations showing simulated in situ model and observational comparison at Lizard Shelf (GBRLSH) 30m, Capricorn Channel (GBRCCH) 22m, Palm Passage (GBRPPE) (15 m and 60m) and North Stradbroke Island (NRSNSI) – **Blue**: Chl *a* fluorescence from IMOS mooring, **Black line**: Model simulation. (see BGC Appendix A for further comparisons and details of IMOS moorings and model simulations). Statistics shown at the top of each comparison d2 (Willmott index), MAE (Mean absolute error), Bias, r (see BGC Appendix A page 12 for equations).



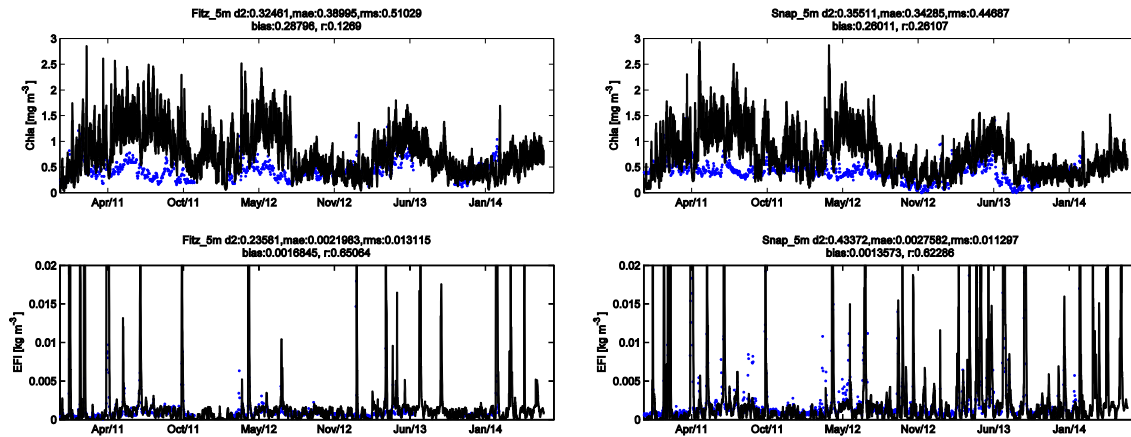


Figure 5.5.13. Reef Rescue moorings (AIMS) observations at 5 m against GBR4 model simulation: Observation (blue), model (black): Parameters = EFI (TSS) and chlorophyll (fluorescence). From top – Barren and Pelican Islands are closest Reef Rescue moorings to Fitzroy River; Double Cone and Daydream Islands are midway along GBR and Snapper Island and Fitzroy Reef are northern Reef Rescue mooring sites (see BGC Appendix A for further comparisons and details of Reef Rescue moorings and model simulations). Statistics shown at the top of each comparison d2 (Willmott index), MAE (Mean absolute error), Bias, r (see BGC Appendix A page 12 for equations).

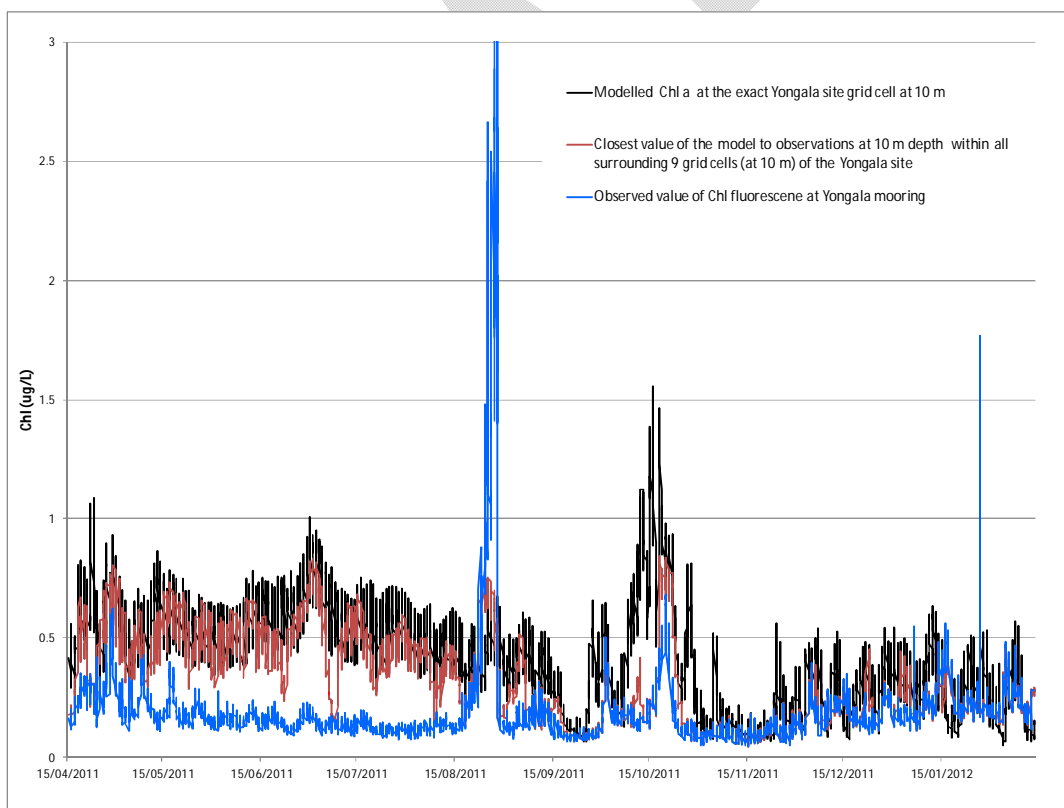


Figure 5.5.14. Shows an example of how the model varies spatially. Black line: modelled Chl a at the location of the mooring at 10 m. Blue line: observed value of chlorophyll fluorescence at the Yongala mooring. Red line: Closest value at 10m of the model to observations within surrounding 9 grid cells (at 10 m) at the Yongala site.

5.5.4.4 Zooplankton

Fig. 5.5.15 shows a snapshot of small and large zooplankton and phytoplankton biomass during January 2014. The large zooplankton and large phytoplankton are shown close to the shore while the small zooplankton and phytoplankton are highest out in the Coral Sea which compares well with observational studies (McKinnon et al 2015).

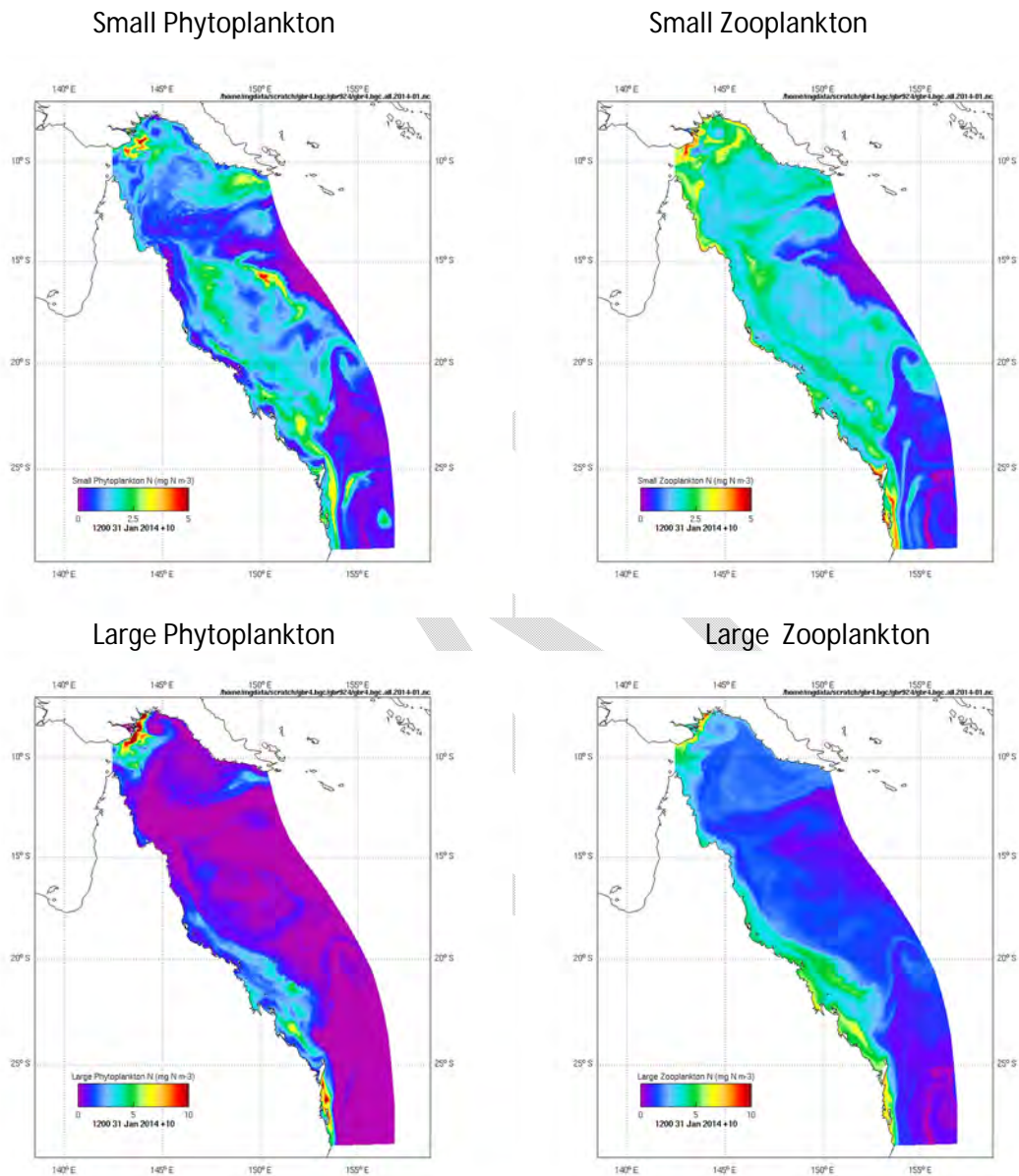


Figure 5.5.15. Large and small phytoplankton biomass (LHS figures) and large and small zooplankton (RHS) for the GBR4 model simulation on 31 January 2014.

5.5.4.5 Seagrass

The model predicts the above- and below-ground biomass of *Zostera* and *Halophila* in each 4 km grid cell. We compare the total seagrass distribution on 1 Dec 2014 (after the model has been running 5 years) with polygons representing locations where seagrass has been observed (McKenzie, L. J., Yoshida, R. L., Grech, A., Coles, R., 2014. Composite of coastal seagrass

meadows in Queensland, Australia - November 1984 to June 2010. Tech. rep., doi:10.1594/PANGAEA.826368.).

The model predicts that an area 8,500 km² has a seagrass biomass greater than 0.1 g N m⁻² (~ 15 % covered) on 1 Dec 2014, while the MacKenzie database has identified an area of 18,400 km² where seagrasses have ever been identified (but GBR1 configuration produces approximately double the area of GBR4). Fig 5.5.16. shows the model predictions on 1 Dec 2014 around the Burdekin region. In this region of the model, seagrasses are generally restricted to areas within 1 pixel of the coast due to the 4 km resolution leading to waters being too deep for seagrass more than 1 pixel from the coast.

To better understand the light and nutrient conditions under which seagrass prosper, scatter plots of light and nutrient conditions are shown (Fig. 5.5.17). *Zostera* has less non-zero points than *Halophila*, indicating its distribution is more limited. *Zostera* has high biomass above a monthly mean bottom light of 10 mol photon m⁻² d⁻¹, while *Halophila* prospers at a bottom light as low as 4 mol photon m⁻² d⁻¹. At high biomasses, both *Halophila* and *Zostera* reduce the dissolved inorganic nitrogen below the half-saturation constant for uptake (500 mg N m⁻³), indicating that at high biomass growth has become to some extent nutrient limited. The porewater nutrient reduction is more consistent in *Zostera* communities than *Halophila* due to the higher above-ground and below-ground biomass, and therefore productivity of *Zostera* facilitating a greater drawdown of nutrients.

Finally, we show the coverage of seagrass in Moreton Bay, beyond the GBR marine park, but an area for which many seagrass assessments have been undertaken (Fig. 5.5.18).

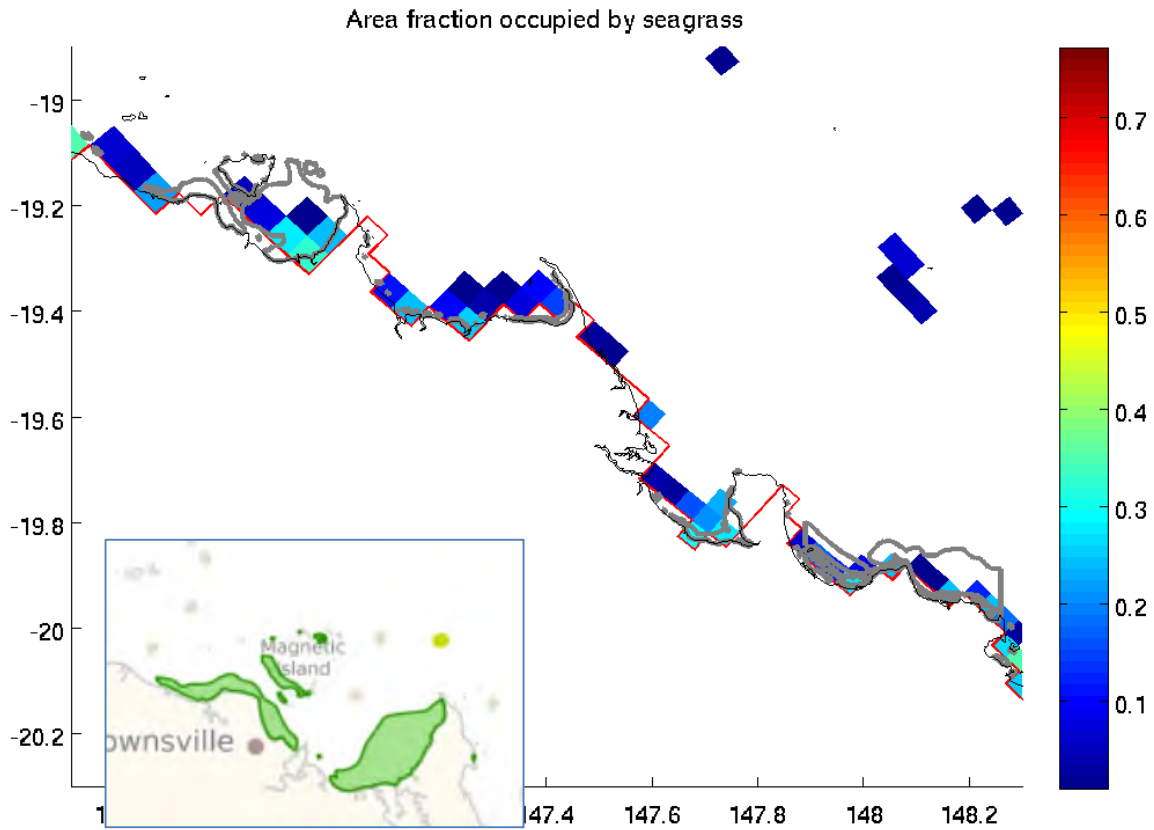


Figure 5.5.16. Area of the bottom covered by seagrass (*Zostera* + *Halophila*) [cover = $1 - \exp(-\Omega B)$ where B is the seagrass biomass, Ω is the nitrogen-specific leaf density]. The black line is the observed coastline, the red line the model coastline, the thick grey lines show seagrass distribution maps from MacKenzie et al. (2010), and the colour pixels are the cell centred area of the bottom covered by seagrass on 1 Dec 2014, 4 years after the simulation began. The insert shows the distribution of seagrass in the e-Atlas, with a smaller extent in Cleveland Bay than seen in the MacKenzie (2010) data set.

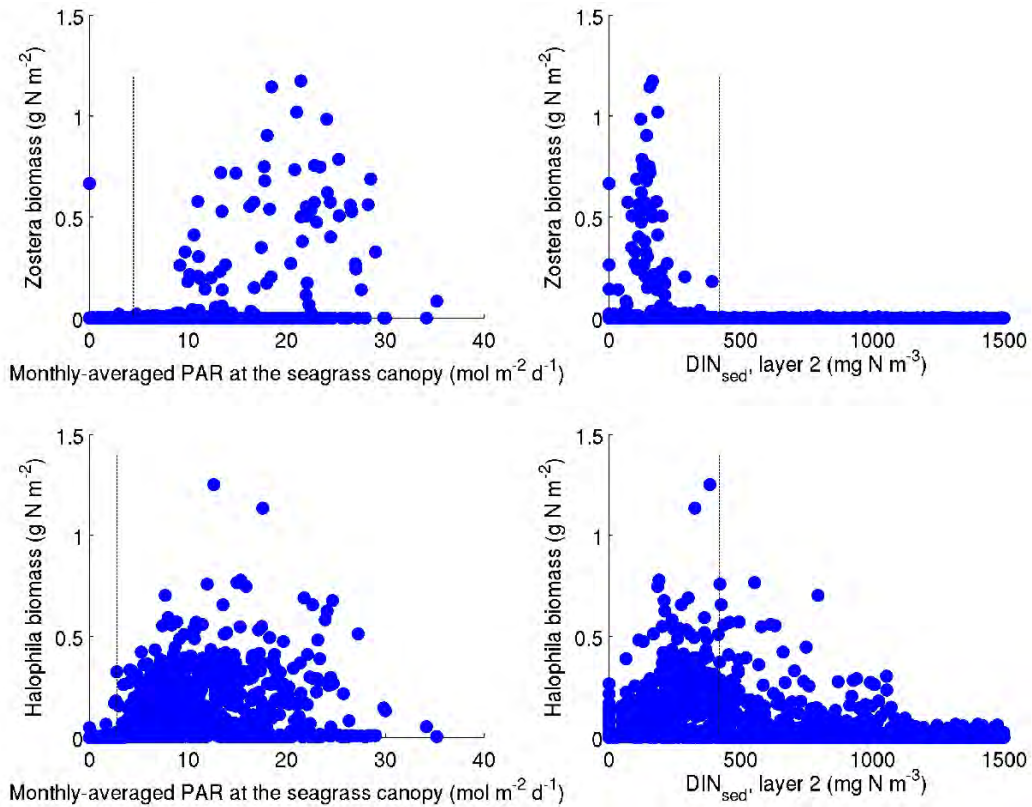


Figure 5.5.17. The above-ground biomass of *Zostera* (top row) and *Halophila* (bottom row) throughout the model domain on the 1 Dec 2014 as a function of the monthly-mean of the daily dose of photons above the seagrass canopy (right) and sediment porewater concentration (between 5 - 25 mm depth).

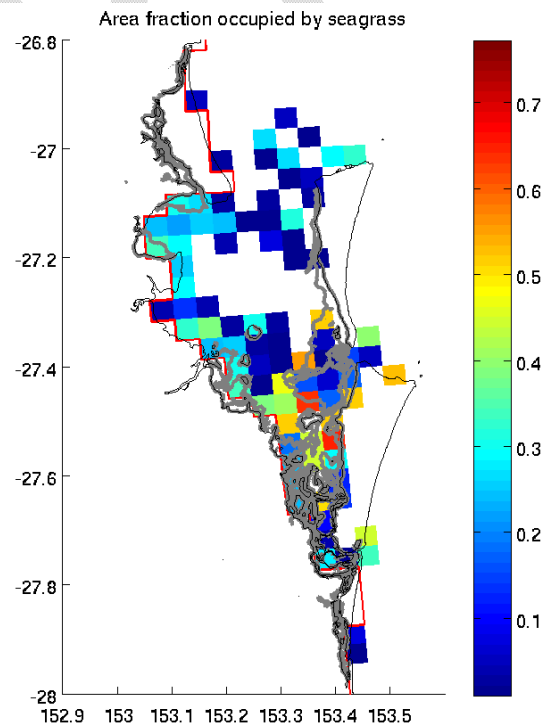


Figure 5.5.18. Area fraction in Moreton Bay.

5.5.4.6 Corals

The model predicts the areal biomass of coral host, zoothaxellae and chlorophyll concentration within the zoothaxellae. Processes resolved include coral host and zoothaxellae growth and mortality, inorganic nutrient and organic particulate uptake, and translocation of organic matter from the zoothaxellae to host. Coral processes also include precipitation (calcification) and dissolution of calcium carbonate, leading to a change in the overlying water column chemistry. Coral communities are assumed to take up only an approximately 0.1 fraction of each 16 km² grid cell.

The model is initialised with a low coral biomass in the 1,825 grids cells that correspond with the location of the 3,651 reefs identified in the GBRMPA features map. Elsewhere biomass is initialised as zero, and, as the model does not represent the process of spawning, remains zero throughout the simulation.

It is difficult to make quantitative comparisons of the model with observations, as GBR-wide observations of corals are typically presence / absence. A further complication is that loss of corals due to extreme events (cyclones, bleaching, COTS outbreaks) are not at present represented. Thus model predictions represent the impact of water clarity, nutrient dynamics and ocean acidification pressures, but not extreme events.

Nonetheless, interesting phenomena can be considered. The accuracy of the prediction of carbon chemistry (alkalinity, pH, see later section) indicates that the rates of calcification, a function of the predicted biomass, are reasonable.

Biomass distribution

In the model, coral cover is highest on the outer reefs (Fig. 5.5.19), reducing to less further north. As a result of less cover, the areal zoothaxellae nitrogen and chlorophyll concentrations are reduced. The northern fringing reefs have an anomalously low cover and biomass because the reefs in the 4 km grid are too deep, so light limitation reduced growth and therefore cover. Some of the most inshore reefs also have lower cover, presumably due to reduced light associated with reduced water clarity.

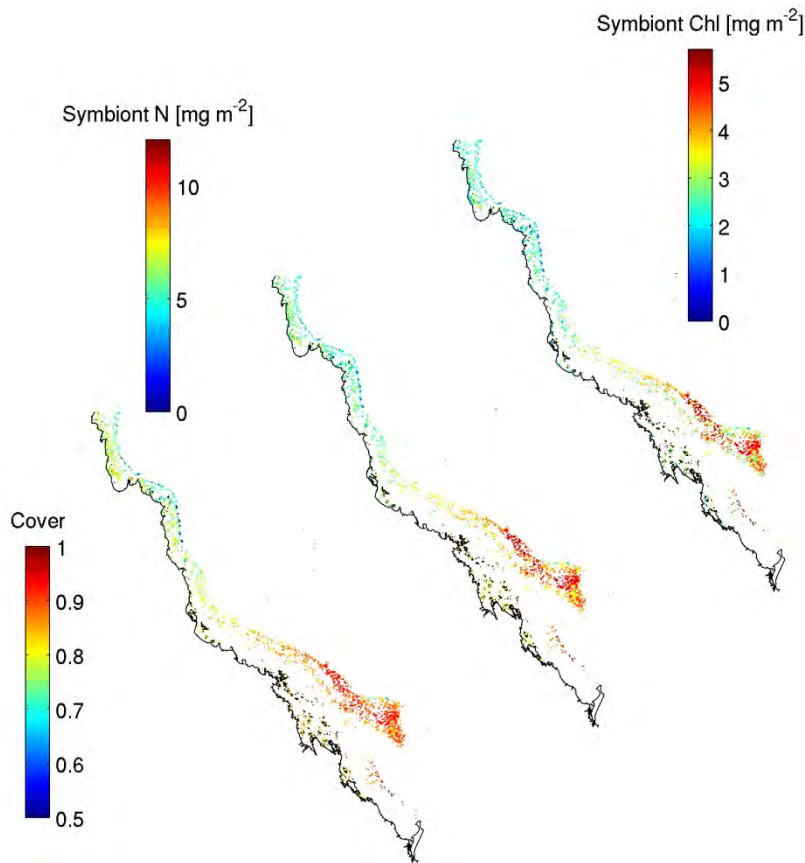


Figure 5.5.19. Fraction of coral cover as seen from above [cover = $1 - \exp(-CH \Omega_{CH} / A_{CH})$ where CH is the coral host biomass, Ω_{CH} is the nitrogen specific polyp density and $A_{CH} = 0.1$ is the grid scale to reef scale ratio], symbiont (zoothaxellae) nitrogen and symbiont chlorophyll concentration.

Organic nitrogen vs. Inorganic nitrogen uptake

Corals play a fascinating biogeochemical role due to their ability to use both organic and inorganic nitrogen. The relative uptake rate of organic and inorganic nitrogen has a new importance due to the increased thermal coral bleaching of corals (Gustafsson et al., 2014). Fig. 5.5.20 shows generally low levels of inorganic nitrogen uptake throughout the GBR, with only a few isolated regions of strong uptake generally on the outer edges where continental shelf upwelling delivers high nutrient concentrations. Thus zoothaxellae growth is generally N limited. In contrast, organic matter uptake is more spatially variable, with the highest uptake rates in the centre of the outer reef matrix in the Swain's region. The model indicates that the regional oceanography determines that these reefs are less susceptible to thermal bleaching events than would be predicted from SST metrics such a degree heating weeks alone.

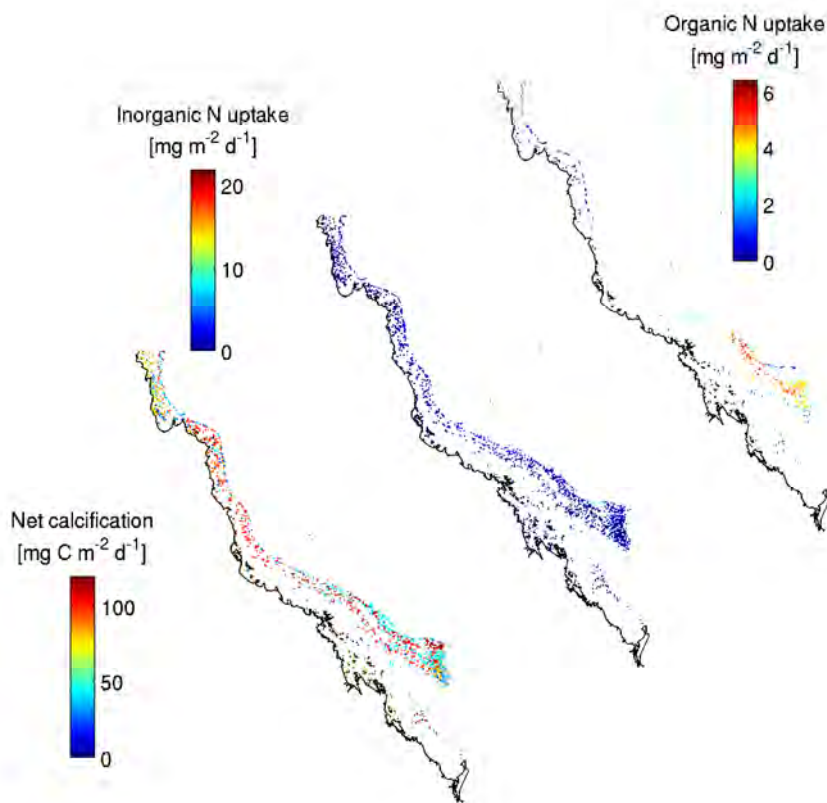


Figure 5.5.20. Flux of carbon associated with calcification – dissolution, and nitrogen due to inorganic and organic uptake.

5.5.4.7 Macroalgae and benthic microalgae

The model predicts a quite limited distribution of macroalgae, with the only significant areas in coastal embayments, offshore of the Fly River, and in upwelling areas (Fig. 5.5.21). In contrast, the sediment concentrations of microalgae at inshore sites above 20 mg chl m^{-2} . The model predictions in the upwelling region off North Stradbroke Island are interesting, as the model predicts non-zero macroalgae biomass in three regions where macroalgae are known to flourish (Fig. 5.5.22).

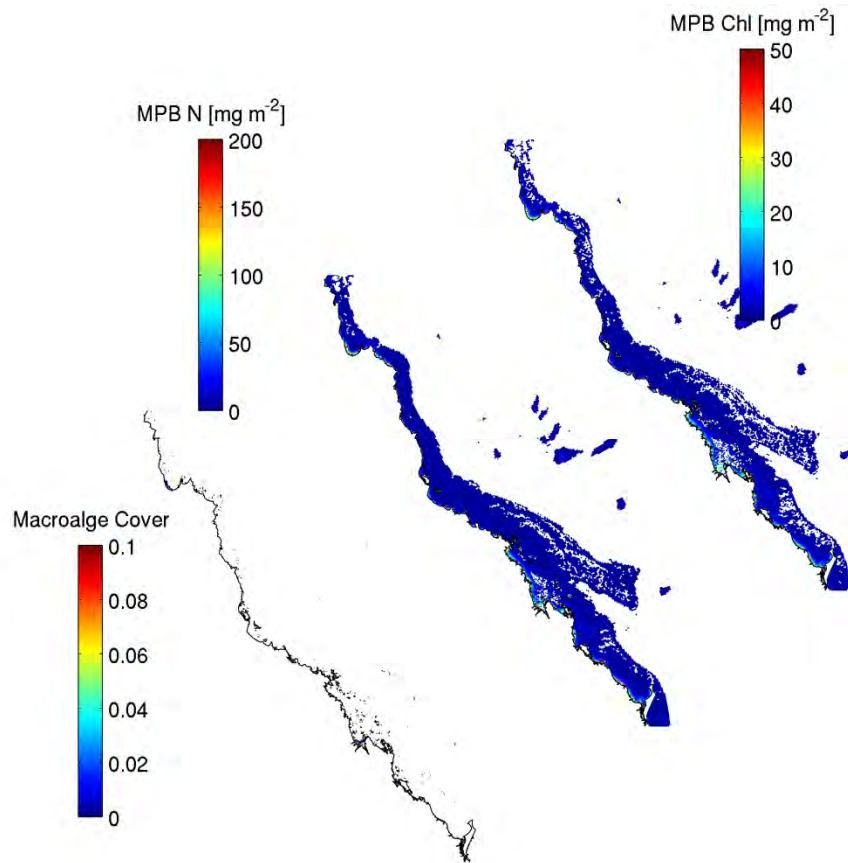


Figure 5.5.21. The macroalgal cover [cover = $1 - \exp(-MA \Omega MA)$], and areal biomass of benthic microalgae quantified by nitrogen and by chlorophyll on 1 Dec 2014.

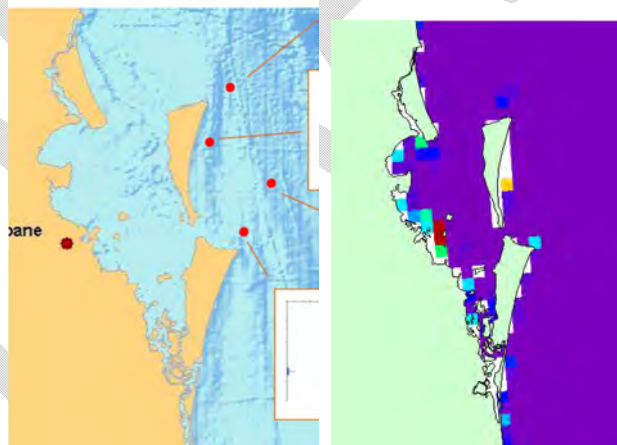


Figure 5.5.22. Location of significant kelp beds identified as Flinders, Henderson and Deep Tempest and Flat Rock (left, from north to south) using an AUV (Marzinelli EM, Williams SB, Babcock RC, Barrett NS, Johnson CR, Jordan A, et al. (2015) Large-Scale Geographic Variation in Distribution and abundance of Australian Deep-Water Kelp Forests. PLoS ONE 10(2): e0118390. doi:10.1371/journal.pone.0118390), and the model biomass.

5.5.4.8 Remote-sensing reflectance

The spectrally-resolved optical model (Baird et al., 2016) allows, for the first time, the state of the optically-significant components of the biogeochemical model (including benthic plants and corals) to be assessed through comparison of the model predicted remote-sensing surface reflectance and the atmospherically-corrected satellite-observed remote-sensing reflectance.

The biogeochemical model has 20 optically-active components, including 4 phytoplankton classes with two pigments each, CDOM, two particulate categories, and a variety of bottom substrates and vegetation. The error in the observed remote-sensing reflectance (due to atmospheric effects, sensor error etc.) is approximately one third of the error in the simulated remote-sensing reflectance (Baird et al., 2016). Thus, the errors in simulated remote-sensing reflectance represent errors in the prediction of the state of the optically-active components – that is, in the biogeochemical model.

The errors in the wet season of 2013, which for the optically-active components is more dynamic, are larger than in the whole year (i.e. 2011, Baird et al., 2016). But we learn more analysing this period. The individual bands, averaged over the period, meet our expectations, with the shorter wavelengths being relatively constant and close to clear water, except for a reduction in coastal waters due to CDOM absorption (Fig. 5.5.23). The central wavelengths (green) show the most spatial variability, with greater reflectance in coastal waters due to scattering (without strong absorption) and bottom reflection. The longer wavelengths are strongly attenuated, with reflectance only seen in regions of high surface suspended concentrations.

The absolute errors in the reflectance are generally greater in the regions of higher reflectance. Importantly, the bias for 547 nm bands and below is much less than the error (Fig. 5.5.24), so that skill assessment, and assimilation (see earlier section), is not unduly affected by bias. As mentioned above, this is another demonstration that the optical model is sufficiently accurate, such that errors are dominated by the errors in the estimation of biogeochemical state (and not the calculation of the reflectance from the estimated state).

Finally, analysis of the mean absolute percent error (Fig. 5.5.25) shows that the model is most skilful at short wavelengths, and in inshore regions. The outer offshore regions have a lower reflectance, so errors in phytoplankton concentration (or vertical distribution) cause greater errors in reflectance. In regions where bottom reflectance is important, errors in bottom substrate state (mud vs. sand) or model depth, introduce large errors.

For a more in depth discussion, the reader is referred to Baird et al. (2016).

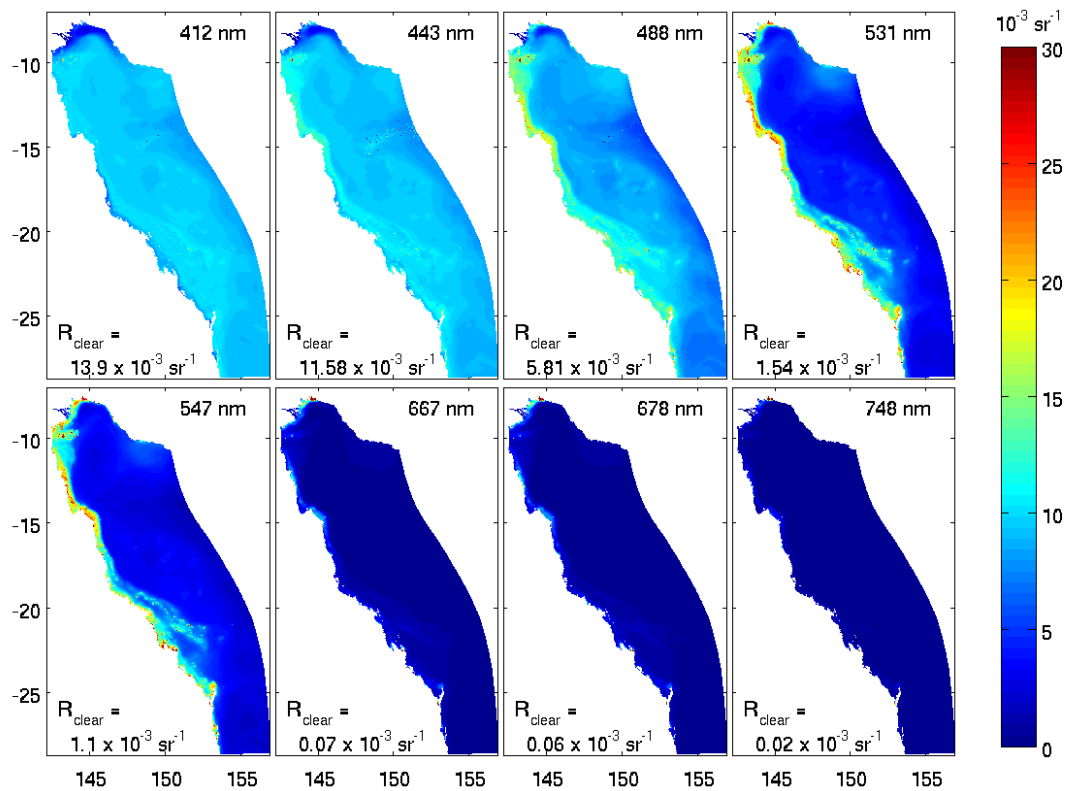


Figure 5.5.23. Spatially-resolved temporal mean for 2013 of the simulated remote-sensing reflectance at the centre of the 8 MODIS ocean colour bands. For reference, the model calculated remote-sensing reflectance of pure seawater at each band is given.

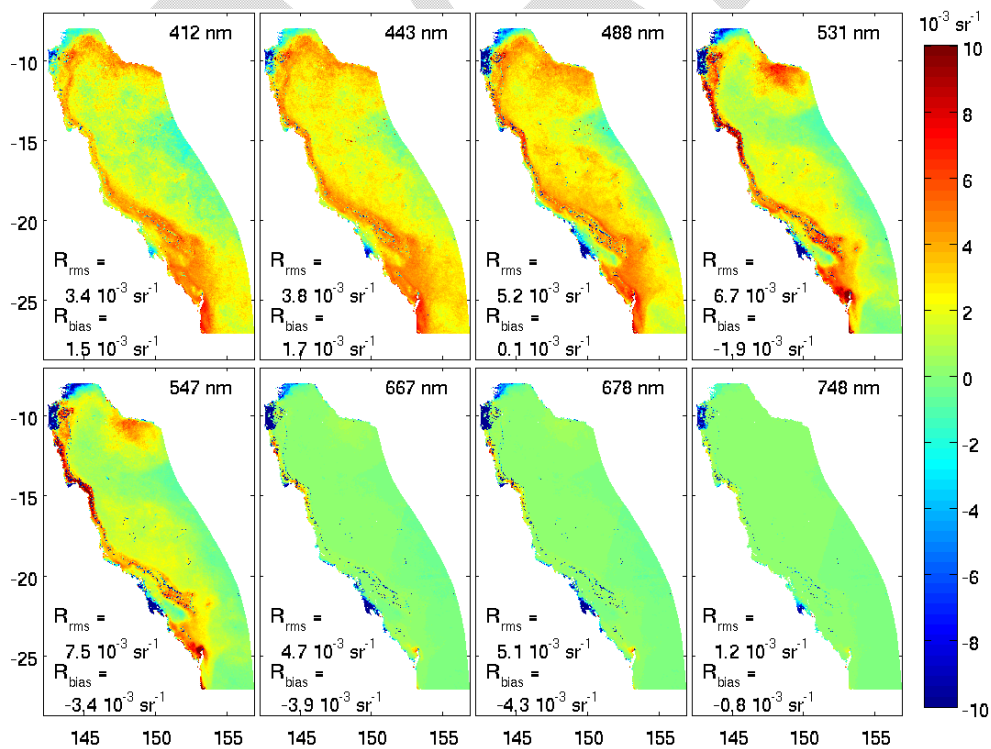


Figure 5.5.24. Spatially-resolved temporal mean remote-sensing reflectance rms error (simulated at midday minus observed atmospherically-corrected) for Jan – Jun 2013 at the centre of the 8 MODIS ocean colour bands. Within each panel the spatial mean of the rms error of the temporal mean, and the spatially- and temporally-averaged model bias is given.

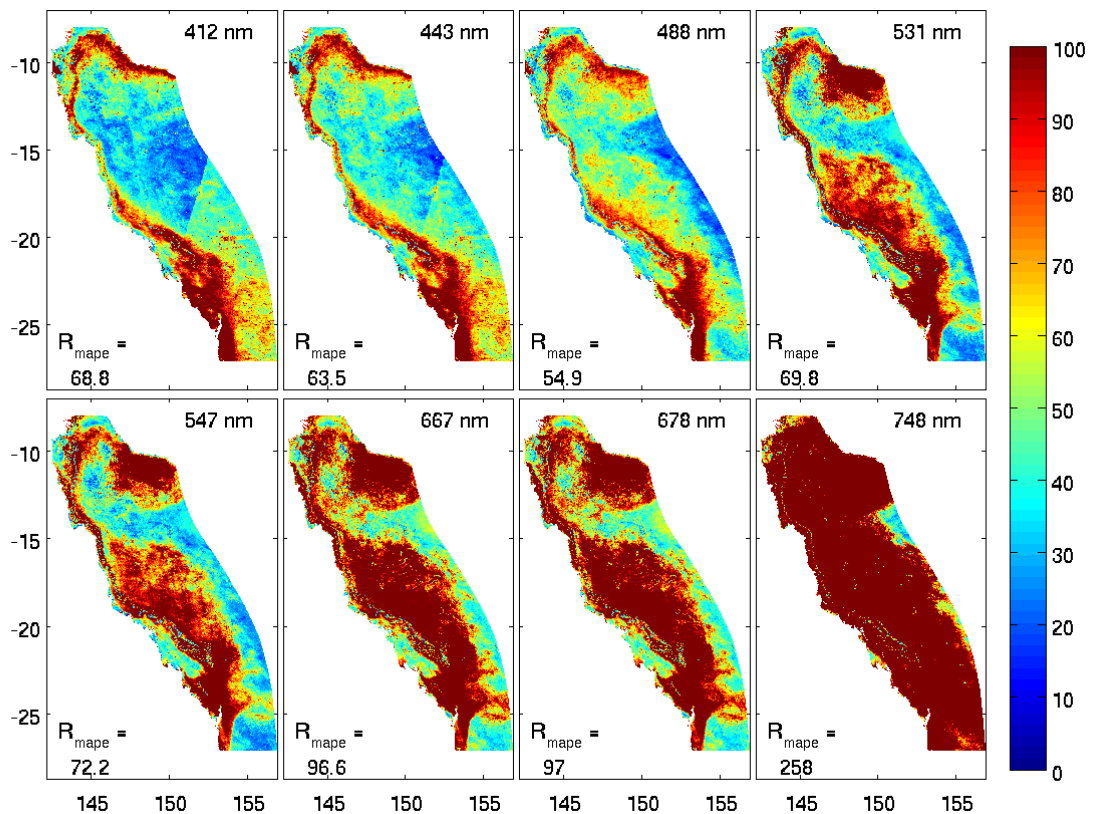


Figure 5.5.25 Spatially-resolved mean absolute percent error (MAPE) for Jan – Jul 2013 for the eight ocean colour bands.

5.5.4.9 Optical plume dynamics

To assess the ability of the model to determine the extent of optical plumes in the GBR, we concentrate on the Burdekin region (17-20 °S). Using the atmospherically-corrected remote-sensing reflectance that is obtained through the dashboard, we match the observed spectra at the MODIS ocean colour bands with a six plume classification, as used by Devlin et al. Averaged over Jan-Apr, we see the extent of each of the plume classes in the wet season of 2014 (Jan-Apr).

As we calculated the simulated (model-generated) remote-sensing reflectance from the model state variables (Baird et al., 2016), we can now undertake the identical spectral matching technique to determine the extent of the optical plumes calculated by the coupled hydrodynamic / sediment / biogeochemical GBR4 model (Fig. 5.5.26, bottom right). Initially we undertake this by taking the mean of the class on the days the remote-sensing reflectances are reported (i.e. cloud free). This provides a measure of the accuracy of the coupled hydrodynamic / sediment / biogeochemical to predict the 3 dimensional distribution of optically active constituents (four phytoplankton types, sediments), subject to circulation, sediment dynamics and biogeochemical transformations, for the purposes of classifying coastal water colour. The mean of the error is given at the top right, where red

occurs where the model predicts a more open ocean class, and blue a more turbid class, when compared to the observations.

On average the model is generally within 1 class of the observations with the exception when the bottom is visible, and in highly turbid waters where plumes generate variability over small spatial scales.

Finally, because the simulated (model-generated) remote-sensing reflectance is calculated every day, we can determine the plume class distribution without the bias of excluding cloudy days. Considering only sunny days, as determined by the model, results in an underestimate of the plume extents, although this underprediction is surprisingly small.

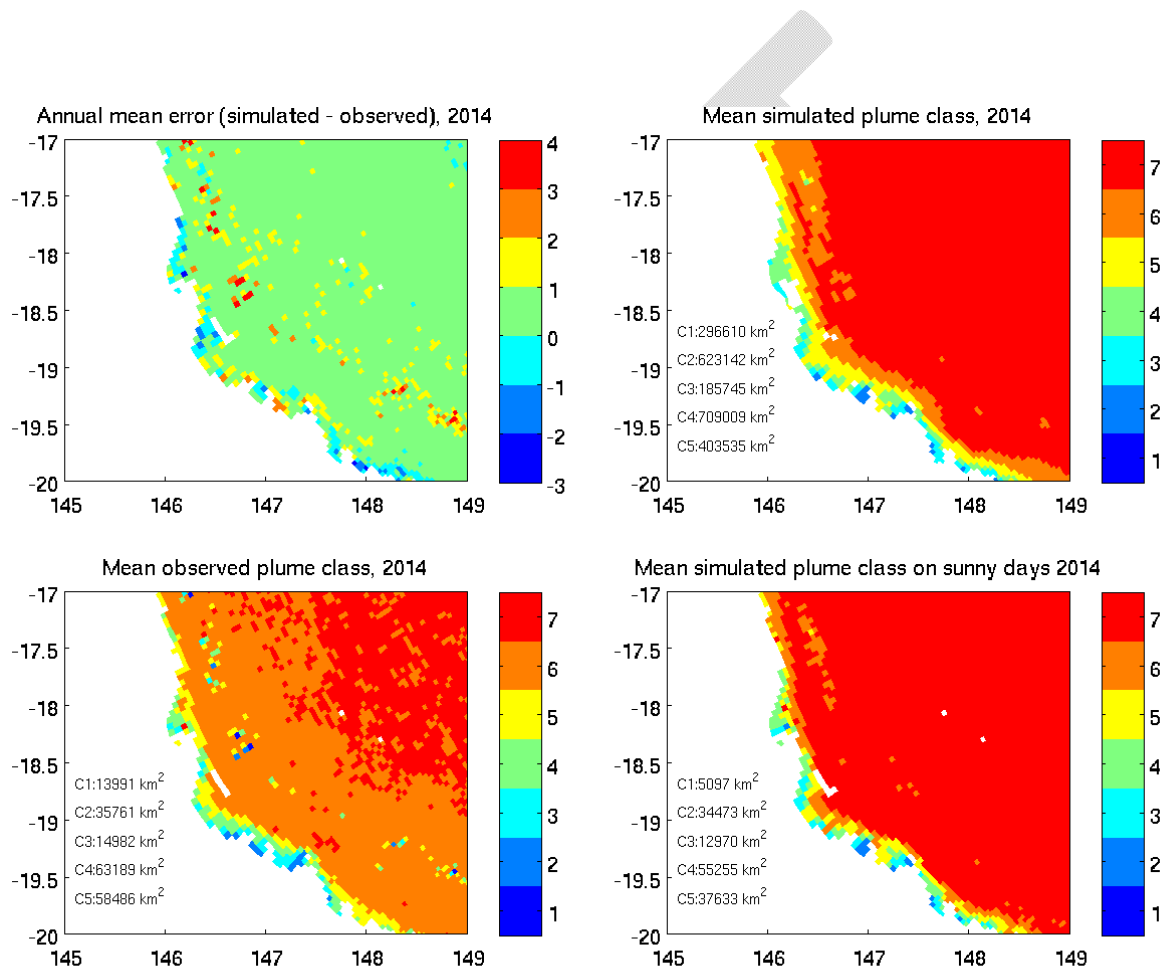


Figure 5.5.26. The mean observed (bottom left) and simulated (bottom right) plume class with cumulative plume class extent in km², for Jan-Apr, on cloud free days. The mean simulated minus observed plume class on cloud-free days (top right) with red occurring where the model predicts a more open ocean class, and blue a more turbid class, when compared to the observations. Top right shows the mean simulated plume extent on all (120) days. Thus the C1-C5 plume extents between in the Burdekin region (17-20 °S) for 2014 were on average 2,471; 5,192; 1,548; 5,908; and 3,362 km². For a 400 km long coastline, this represents 6.2; 13.0; 3.9; 14.77 and 8.4 km thick.

5.5.4.10 Carbon chemistry

The eReefs model represents the state of the inorganic carbon system using total alkalinity, A_T , and dissolved inorganic carbon, C_T , from which pH, amongst other quantities, can be calculated. The skill of the model assessed at the 22 observational sites provided a measure of the uncertainty of the aragonite saturation, Ω_a , predictions at the 3,581 reef locations. The root mean square (rms) error of time-series of A_T , C_T , S and temperature at each site was calculated (Fig. 5.5.27). The mean (and range) of rms errors across the 22 sites were: A_T : 39.90 (8.5, 91.5) mmol m^{-3} ; C_T : 35.9 (12.5, 63.97) mmol m^{-3} ; S : 0.47 (0.15, 0.93); temperature: 0.87 (0.63, 1.24) $^{\circ}\text{C}$, resulting in an error in the calculated Ω_a of 0.23 (0.09, 0.54).

With an error of only 0.23, it is therefore possible to map the aragonite saturation on all 3,581 reefs on the GBR, a resolution not possible through observations alone (Fig. 5.5.27).

For more information, see Mongin et al. (2016).

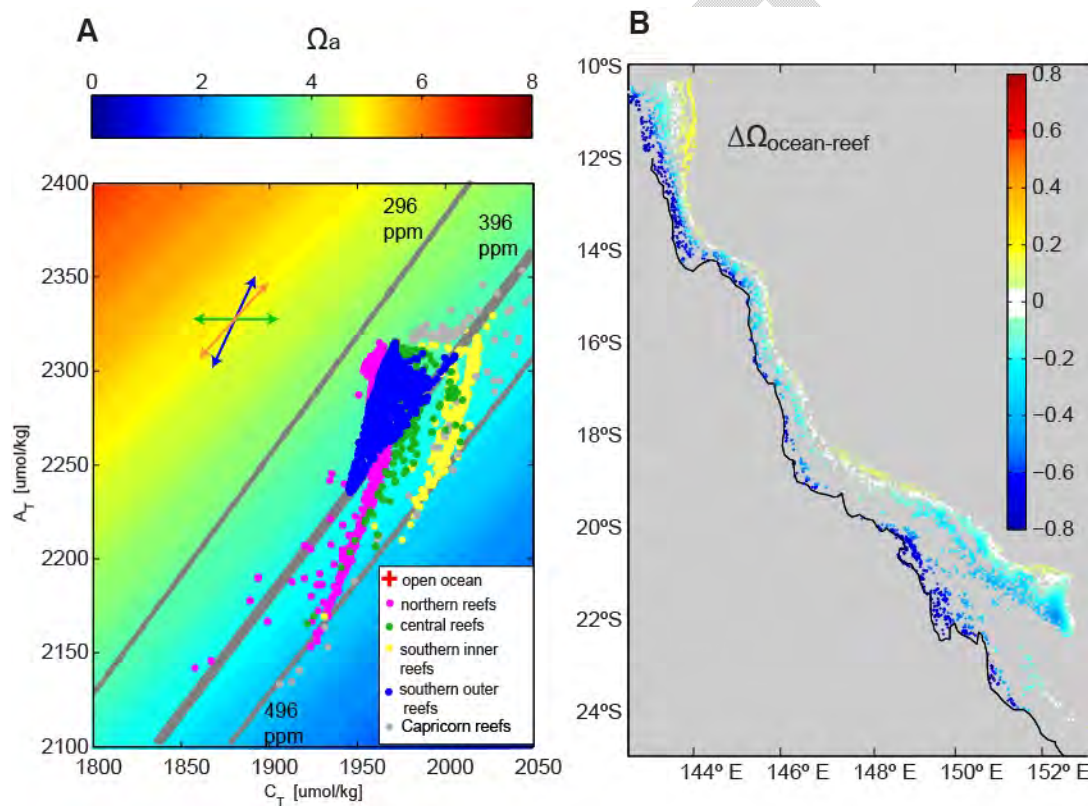


Figure 5.5.27. Simulated mean (from daily Sept. 2010 – Sept. 2012 values) aragonite saturation state for the 3,581 individual coral reefs that make up the Great Barrier Reef. **a)** Simulated aragonite saturation state (as background shading) versus dissolved inorganic carbon, C_T , and total alkalinity, A_T , for the individual coral reefs. Grey lines show the surface $p\text{CO}_2$ of 396 and 296 ppm. The Ω_a was calculated at a temperature of 25°C and salinity of 35. If the Ω_a used as the background shading in a) is calculated at 21 and then 27°C , the range observed in the GBR surface waters, Ω_a at a constant C_T and A_T changes by less than ± 0.07 from the shaded values. The process arrows are approximations that are further discussed in Figure 3. **b)** For the individual reefs the mean difference in aragonite saturation state between the open ocean value and the value simulated at the reef ($\Delta\Omega_{\text{ocean-reef}} = (\Omega_{\text{ocean}} - \Omega_{\text{reef}})$).

5.5.4.6 Summary of model vs. observations metrics

Comparisons and statistical metrics were completed for model simulations and observational sites. These included root mean square (RMS), r , bias, mean absolute error (MAE) and Willmott's skill metrics ($d2$). The Willmott's skill metric is the ratio of the MAE and the mean absolute deviation about the observed mean (Willmott et al. 1995, Willmott et al. 2012). Equations for these metrics can be found in the BGC Appendix A p12. The following Figs. 5.5.28 to 5.5.30 show the Willmott and bias metrics as bar graphs for the observed sites which include AIMS water quality sites, IMOS moorings, Reef Rescue moorings and carbon chemistry surveys. Further analysis of the other metrics can be found in the BGC Appendix A with all model and observational comparisons.

The complexity of 3D coastal models and the associated observations makes model simulations very difficult to evaluate on a spatial and temporal scale against observational sites. Arhonditis and Brett (2004) analysed 153 biological BGC models and reported that only half had performance related accuracy assessments and only 30% of these determined goodness of fit with respect to observed values. Reasons for this is not the reluctance on the part of modellers or observationalists but primarily due to observational programs being originally set up for reasons other than calibrating a models high temporal and spatial comparison. For this reason the WQM sites (Figure 5.5.30, bottom figure) which are sampled 3 to 4 times a year at 2 to 3 depths are not ideal to compare with a model sampled every 2-6 hours with 46 depths. However the model simulation does represent the nutrients and TSS and chlorophyll a for many of these WQM sites. The WQM sites are also all close to the coast and often impinged by local currents and islands (see Table 5.5.4 and Fig. 4.7.39). In contrast the Reef Rescue moorings sites and the IMOS/NRS moorings are more suitable due to their high temporal sampling of chlorophyll and TSS, thus make them a more suitable choice with which to compare the eReef models. Evaluation of the observations from these sites can also be affected by the nature of the 4 km model grid which cannot achieve the local changes that occur within the area of the actual moorings. Care should be taken with statistical results without consideration of the direct comparisons. All comparisons are shown in the BGC Appendix A. Fig. 5.5.31 shows examples of the statistical difference and discrepancy and the importance of using a variety of statistics to compare models. The site with the poorest Willmott score (0.07, Palm Passage) has a lower bias compared with the figure with the highest Willmott score (0.34, Heron Island). Due to the low bias Palm Passage can visually appear a better calibrated comparison of model and observation.

A summary of the model skill statistics for the Reef Rescue and AIMS WQM sites is given in Table 5.5.5. These include a comparison of the WQM sites at Reef Rescue site locations plus an average of all the metrics for all the WQM monitoring sites ($n=37$). Comparison with chlorophyll fluorescence from the Reef Rescue mooring sites with simulated chlorophyll a showed a bias of only $-0.07 \text{ mg chl } a \text{ m}^{-3}$, and a RMS error of $0.33 \text{ mg chl } a \text{ m}^{-3}$. The least skilful site was Geoffrey Bay, which is sited within metres of the Magnetic Island shoreline. Excluding Geoffrey Bay from the overall average of the Reef Rescue sites reduces the average bias from -0.07 to $-0.05 \text{ mg chl } a \text{ m}^{-3}$, and a RMS error reduction from 0.33 to $0.30 \text{ mg chl } a \text{ m}^{-3}$.

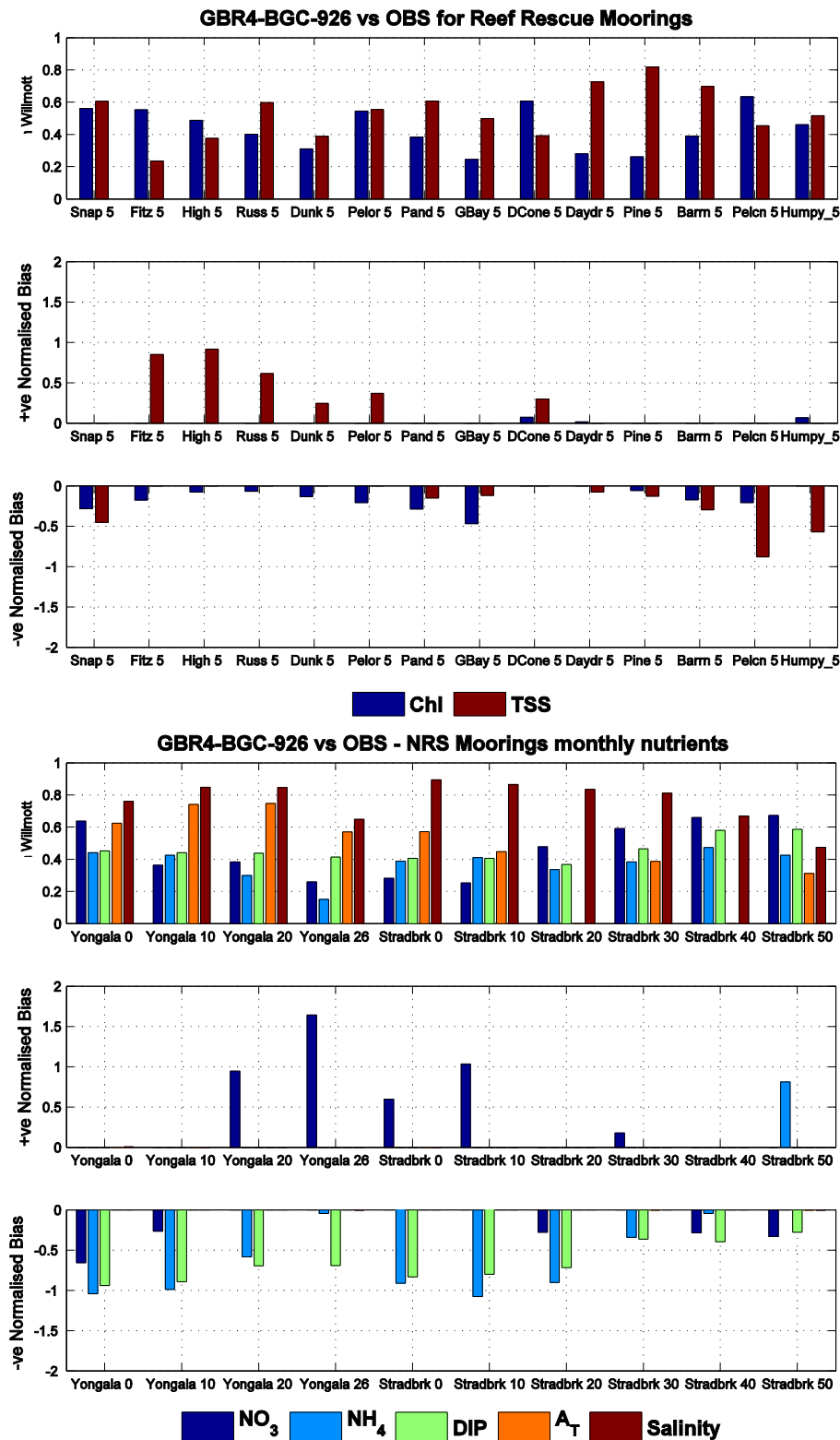


Figure 5.5.28. Top: Reef Rescue mooring statistics of Willmott and model normalised bias compared with observations for chlorophyll fluorescence and TSS. Bottom: IMOS NRS stations at Yongala and Stradbroke showing Willmott and model normalised bias for nutrients NO₃ NH₄ DIP and Alkalinity (see BGC Appendix A for details).

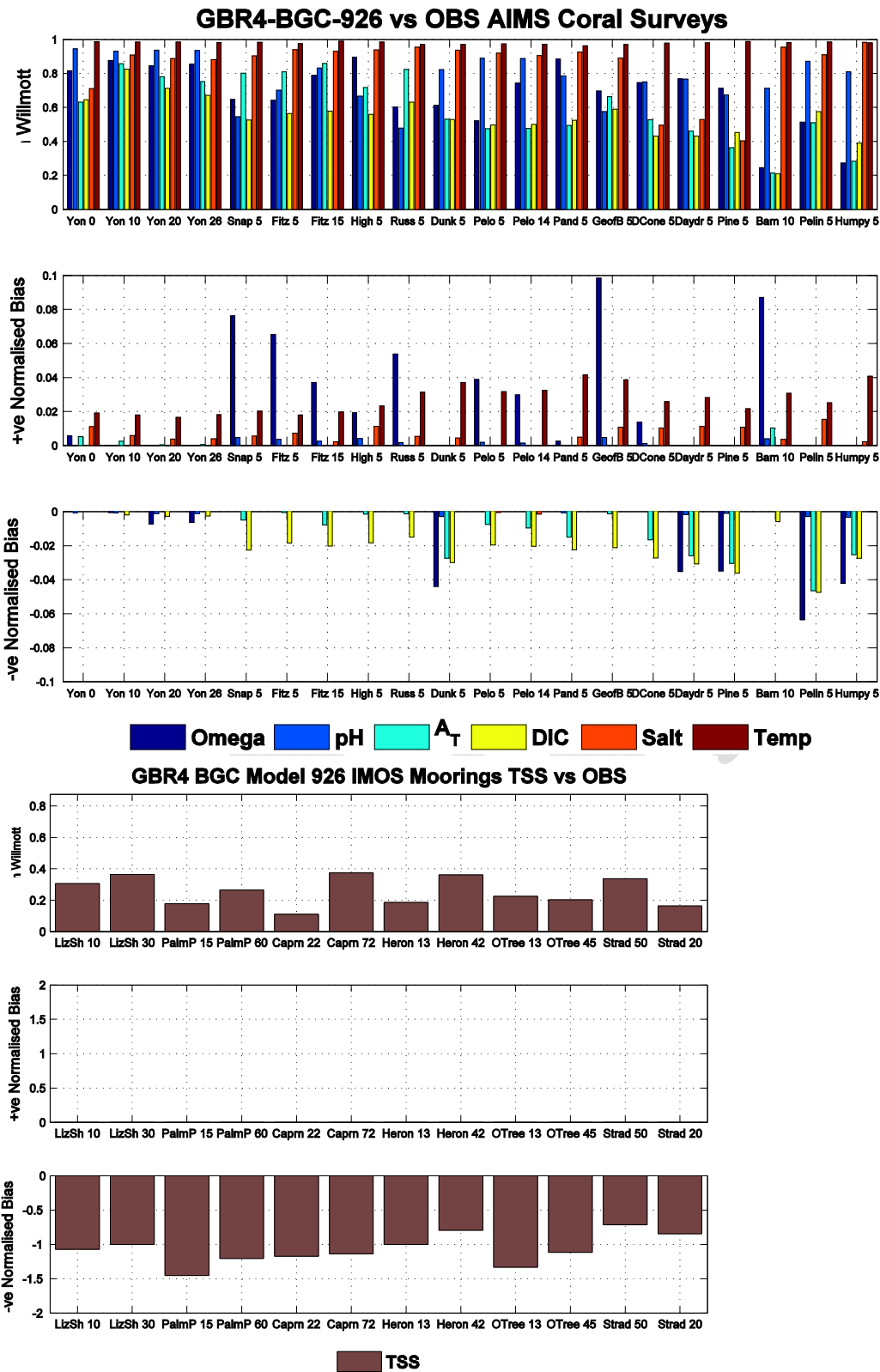


Figure 5.5.29. Top: Carbon Chemistry statistics of Willmott and model normalised bias compared with observations for pH, Alkalinity, Omega, DIC, Salinity and Temperature. Bottom: IMOS and NRS station statistics of Willmott and model normalised bias compared with observations for TSS. Bottom (see BGC Appendix A for details).

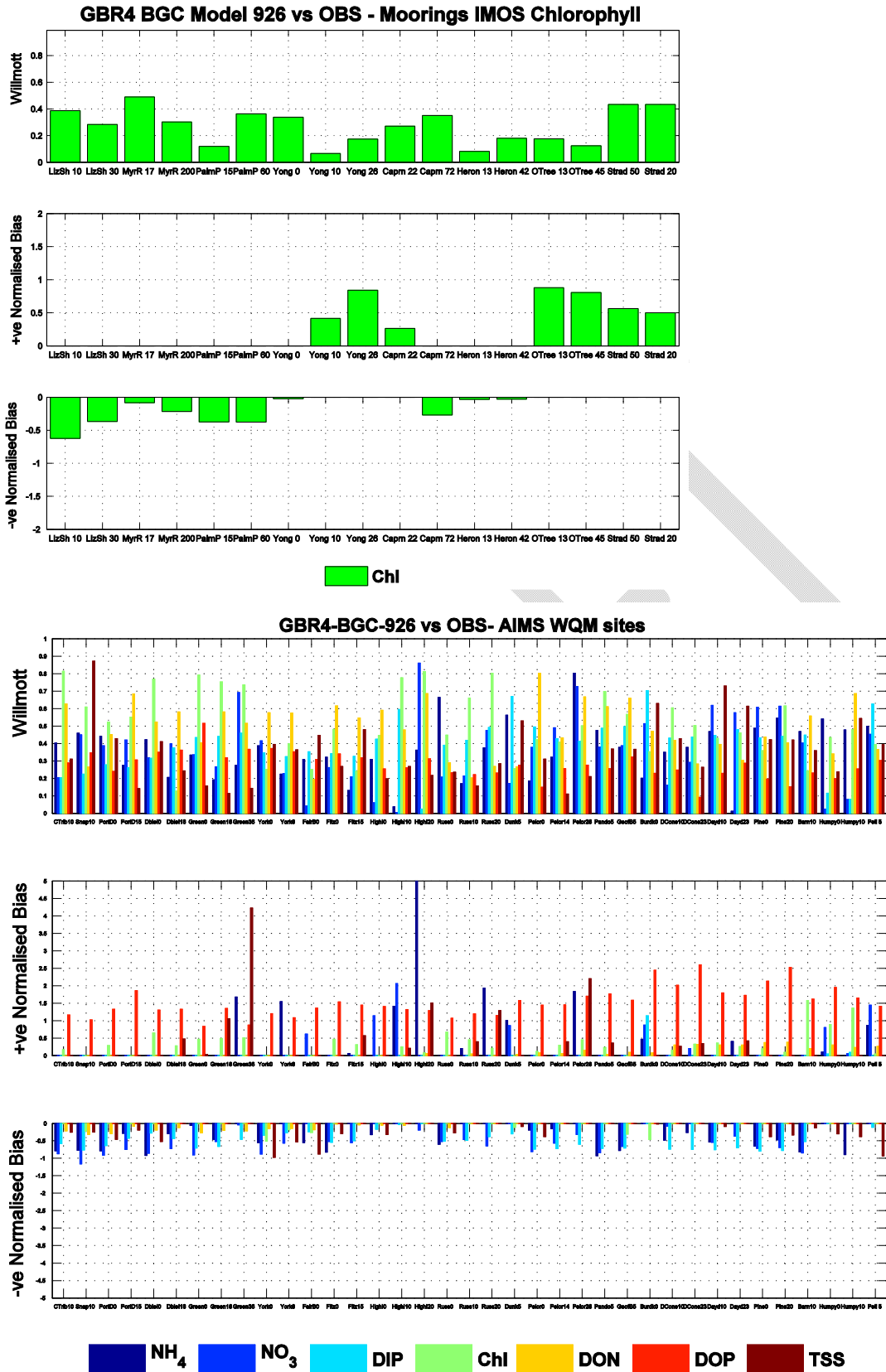


Figure 5.5.30. Top: IMOS and NRS station statistics of Willmott and model normalised bias compared with observations for Chlorophyll fluorescence. Bottom: AIMS WQM site (sampled 3 to 4 times a year) statistics of Willmott and model bias compared with observations for nutrients, TSS and Chlorophyll (see BGC Appendix for details).

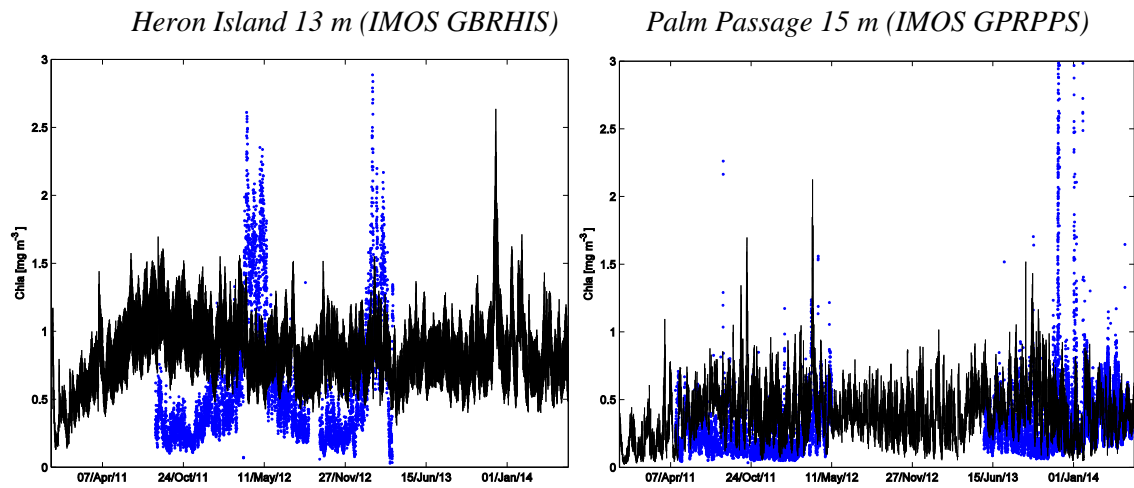


Figure 5.5.31. An example of the discrepancy and difference in the use of statistics when comparing models. * Chlorophyll fluorescence — model simulation of chlorophyll *a*. Heron Island Willmott d2 index = 0.34 while Palm Passage Willmott d2 index = 0.07 (very poor). In comparison, the bias for Heron Island is higher: GBRHIS bias 0.34, root mean square (RMS) 0.65, mean absolute error (MAE) 0.64, GBRPPS bias -0.02 RMS 0.96, MAE 0.30.

Table 5.5.5

Skill metrics for the Reef Rescue and AIMS WQM sites.

Willmott index	Chlorophyll		TSS			
	Reef Rescue moorings	AIMS WQM triannual sampling	Reef Rescue moorings	AIMS WQM triannual sampling		
Snapper Island	0.56	0.61	0.60	0.87		
Fitzroy Reef	0.55	0.48	0.24	0.27		
High Island	0.49	0.78	0.38	0.27		
Russell Island	0.40	0.66	0.60	0.16		
Dunk Island	0.31	0.26	0.39	0.53		
Pelorus Island	0.54	0.42	0.55	0.31		
Pandora Island	0.38	0.70	0.61	0.37		
Geoffrey Bay	0.24	-	0.50	-		
Double Cone Island	0.61	0.60	0.39	0.43		
Daydream Island	0.28	0.43	0.73	0.73		
Pine Island	0.26	0.36	0.82	0.42		
Barren Island	0.39	0.24	0.70	0.36		
Pelican Island	0.63	0.39	0.45	0.39		
Humpy Island	0.46	0.48	0.52	0.54		
Wilmot average	0.44	0.49	0.53	0.43		
RMS						
Snapper Island	0.23	0.23	0.0027	0.0004		
Fitzroy Reef	0.25	0.27	0.0105	0.0008		
High Island	0.25	0.28	0.0111	0.0009		
Russell Island	0.24	0.30	0.0053	0.0006		
Dunk Island	0.44	0.38	0.0224	0.0007		
Pelorus Island	0.23	0.33	0.0051	0.0005		
Pandora Island	0.28	0.20	0.0074	0.0007		
Geoffrey Bay	0.70	-	0.0143	-		
Double Cone Island	0.25	0.36	0.0038	0.0015		
Daydream Island	0.29	0.26	0.0027	0.0016		
Pine Island	0.27	0.26	0.0033	0.0059		
Barren Island	0.47	0.48	0.0008	0.0005		
Pelican Island	0.38	0.44	0.0087	0.0009		
Humpy Island	0.33	0.63	0.0023	0.0013		
RMS average	0.33	0.34	0.0072	0.0013		
Bias						
Snapper Island	-0.11	-0.08	-0.0009	-0.0003		
Fitzroy Reef	-0.08	0.16	0.0009	-0.0002		
High Island	-0.03	0.12	0.0011	0.0002		
Russell Island	-0.02	0.17	0.0005	0.0003		
Dunk Island	-0.06	-0.06	0.0007	-0.0002		
Pelorus Island	-0.09	0.04	0.0003	-0.0003		
Pandora Island	-0.11	0.07	-0.0002	0.0002		
Geoffrey Bay	-0.28	-	-0.0003	-		
Double Cone Island	0.04	0.08	0.0004	0.0004		
Daydream Island	0.01	0.21	-0.0002	-0.0002		
Pine Island	-0.04	0.12	-0.0004	-0.0018		
Barren Island	-0.09	0.40	-0.0001	0.0001		
Pelican Island	-0.13	0.03	-0.0047	-0.0036		
Humpy Island	0.03	0.53	-0.0006	-0.0004		
Bias average	-0.07	0.14	-0.0003	-0.0005		
Statistical averages for all WQM sites 926 (n=37) triannually monitored						
	NH4	NO3	Chlorophyll	DON	DOP	TSS
WILMOT average	0.36	0.36	0.51	0.48	0.28	0.35
RMS average	1.70	3.48	0.31	30.65	8.10	0.0019
BIAS average	0.06	-0.24	0.09	1.77	7.35	-0.0002

5.5.5 Skill assessment of biogeochemical model against glider data

At Heron Island a Slocum Glider has been deployed by IMOS since 2012 on cross shelf missions ranging from a few days to several weeks (e.g. Fig. 5.5.32). Data from the glider transects show the cross shelf profile of water column properties including temperature, salinity, chlorophyll and for a few missions nitrate (as measured optically by a SUNA probe). Repeat transects show the short term and longer term evolution of the water column with very high resolution.

For model comparison glider data was averaged over a 4km spatial footprint equivalent to the model grid. Visual comparison between glider data in January 2013 and model output from an early simulation show good agreement, including a fair capture of the change in water column properties following the passage of ex-cyclone Oswald (Fig. 5.5.33 and Fig. 5.5.34 pre- and post-storm break in observations). Before the storm the water column is well stratified with a strong thermocline and nutricline below 60m and a subsurface chlorophyll maximum at 40m. Following the storm low salinity water floods the surface layer (likely from coastal runoff), nutrient concentrations in the surface layer are elevated (Fig. 5.5.35) and peak chlorophyll concentrations occur at shallower depths (Fig. 5.5.34).

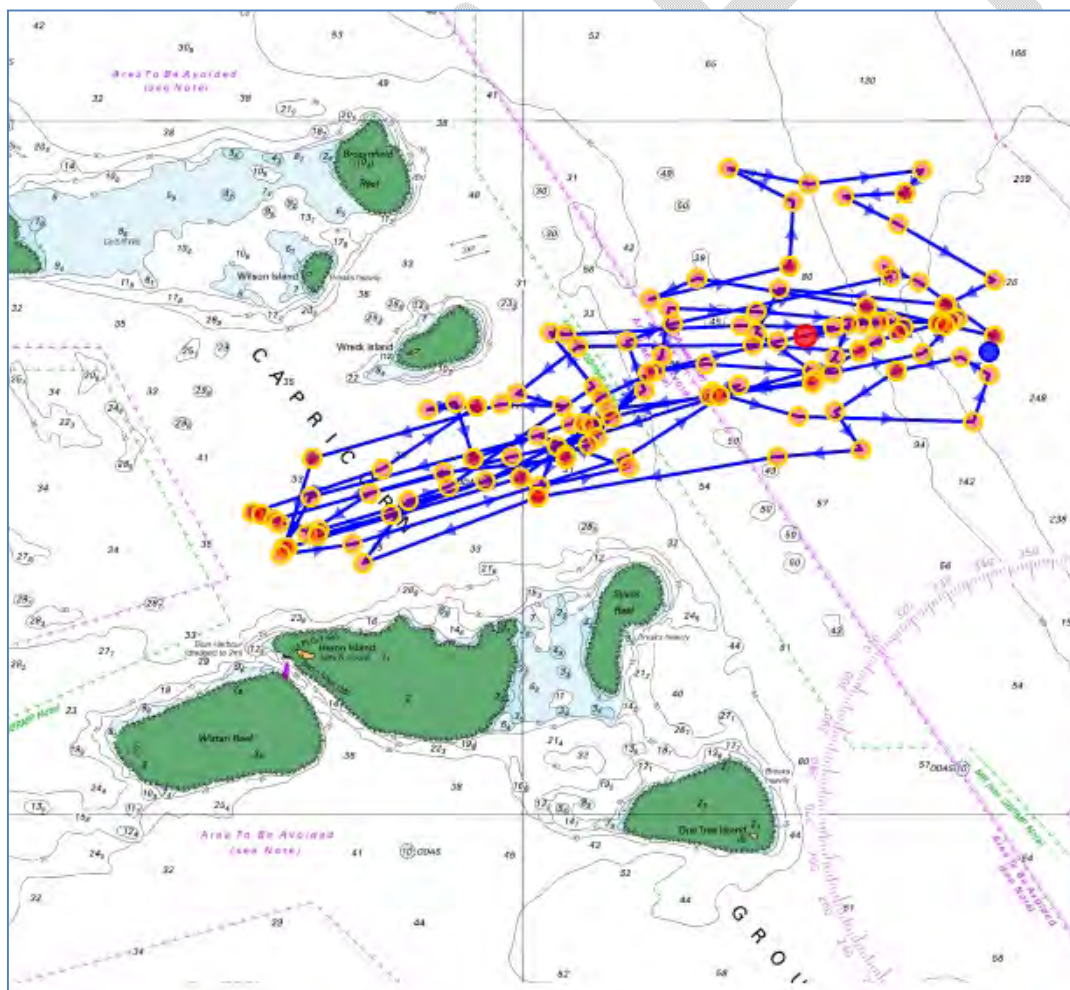


Figure 5.5.32. Cross shelf track of the final Betsy glider mission in January 2013.

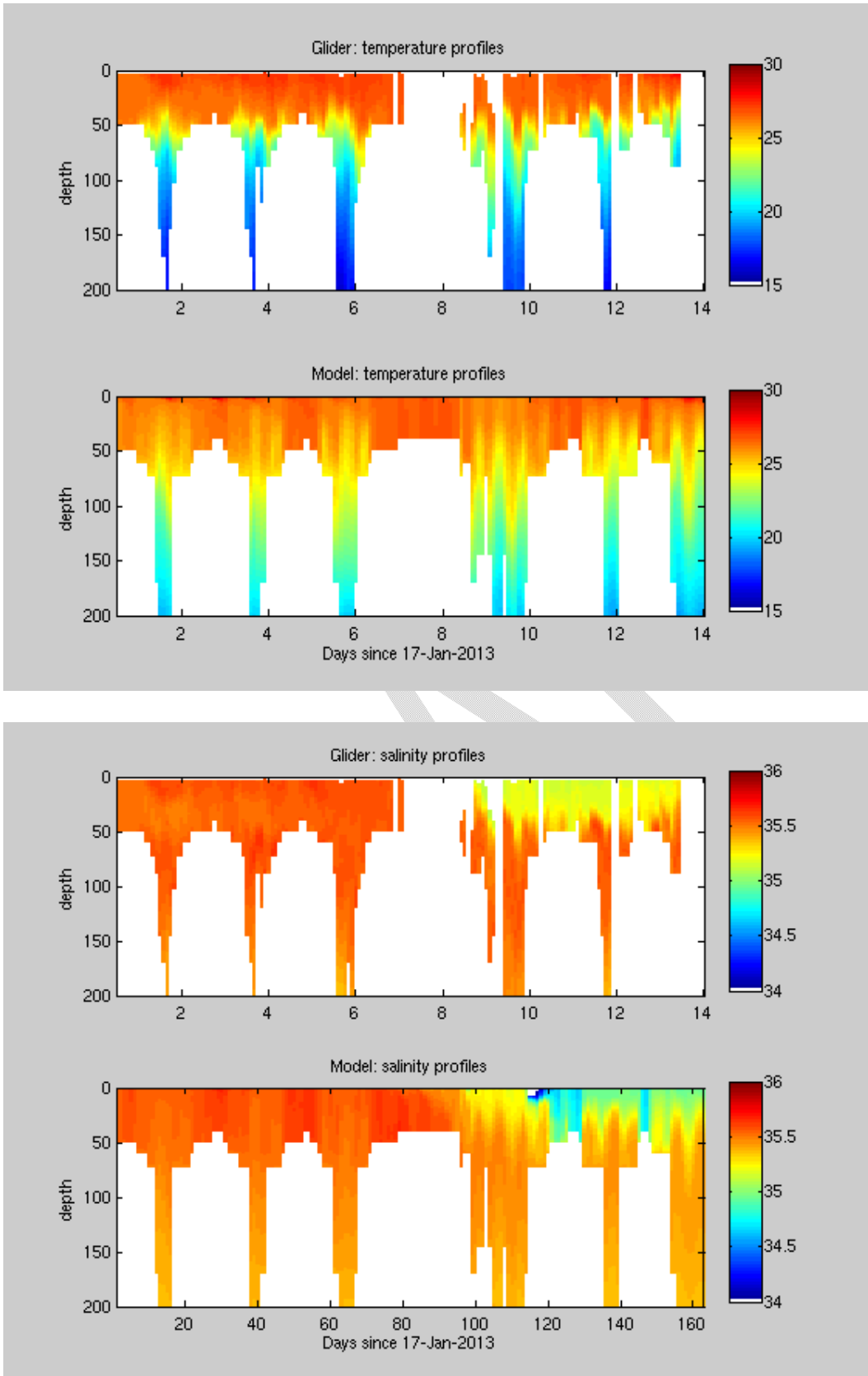


Figure 5.5.33. Comparison of observed and simulated cross shelf transects of temperature and salinity.

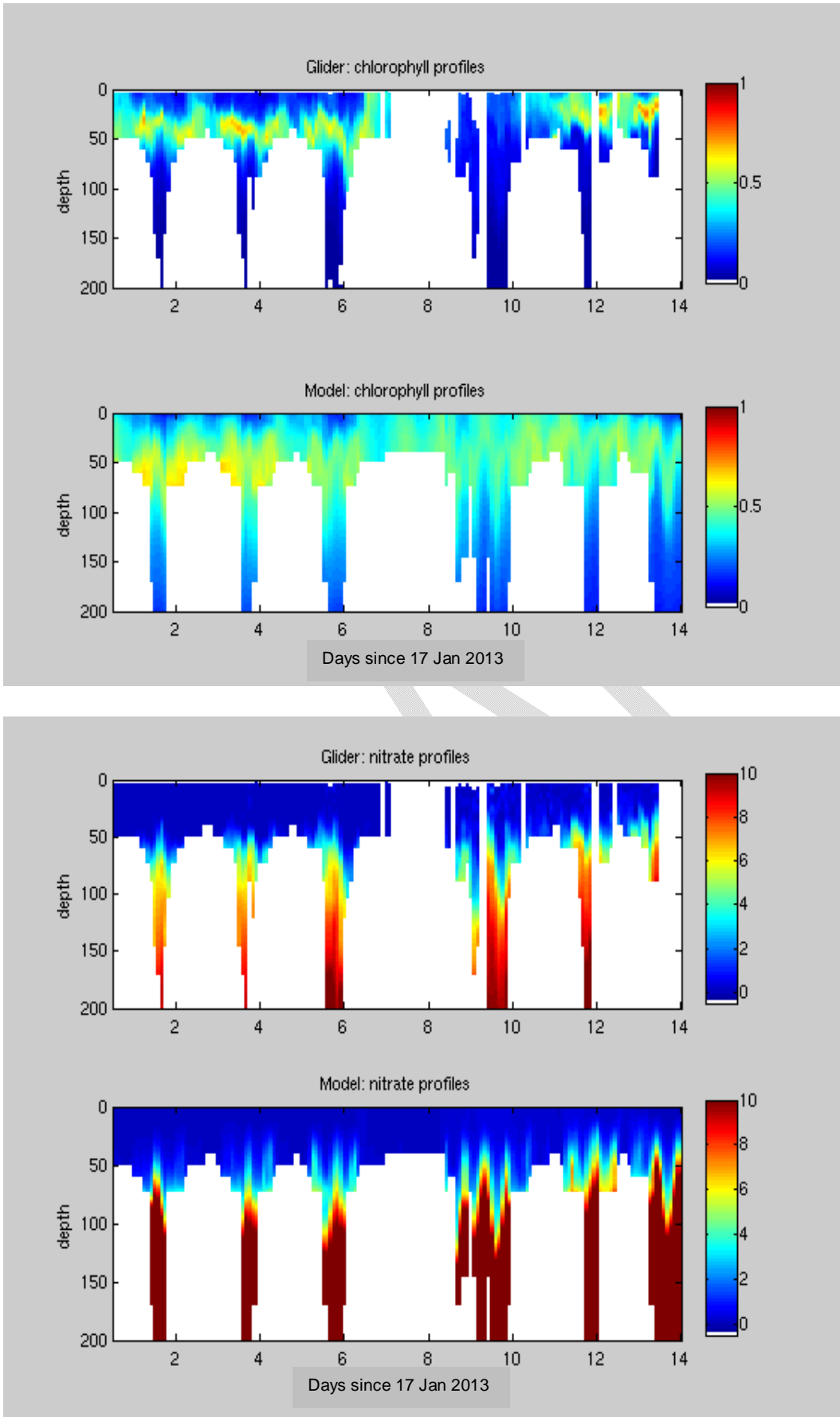


Figure 5.5.34. Comparison of observed and simulated cross shelf transects of chlorophyll and nitrate.

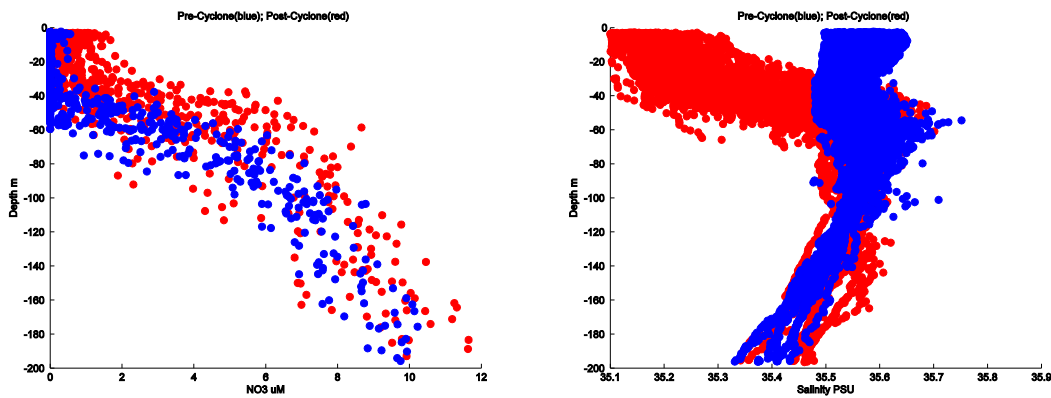


Figure 5.5.35. Nitrate (left) and salinity (right) glider profiles before (blue) and after (red) the passage of ex-cyclone Oswald.

5.5.6 *Trichodesmium*

Although the data available to quantify the role of *Trichodesmium* in the Great Barrier Reef Lagoon (GBRL) are very limited, it is believed that this marine cyanobacterium plays an important role in the nitrogen budget of the region (Bell et al., 1999; Messer, 2015). *Trichodesmium* are able to fix atmospheric nitrogen, providing a nitrogen source to drive production when dissolved inorganic phosphorus is available, but dissolved inorganic nitrogen is critically low. It has been speculated that nitrogen-fixation by *Trichodesmium* and other diazotrophs in the GBRL is increasing over time due to changes in river nutrient loads (Bell et al., 2014)

A physiology-based *Trichodesmium* model has been developed as part of the eReefs biogeochemical model (Section 4.7.4.2). The model is described in detail by Robson et al. (2013) and in the EMS biogeochemical model description (Baird et al., 2015). This section describes some of the *Trichodesmium* model outputs and how they compare with what is known.

Fig. 5.5.36 shows snapshots of *Trichodesmium* concentrations just below the surface of the water column during July (left) and December (right). The model shows considerable spatial variability, higher *Trichodesmium* concentrations inshore than offshore, higher concentrations in the southern Great Barrier Reef than in the north, and greater coverage mid-year than in summer. All of this is in accordance with expectations.

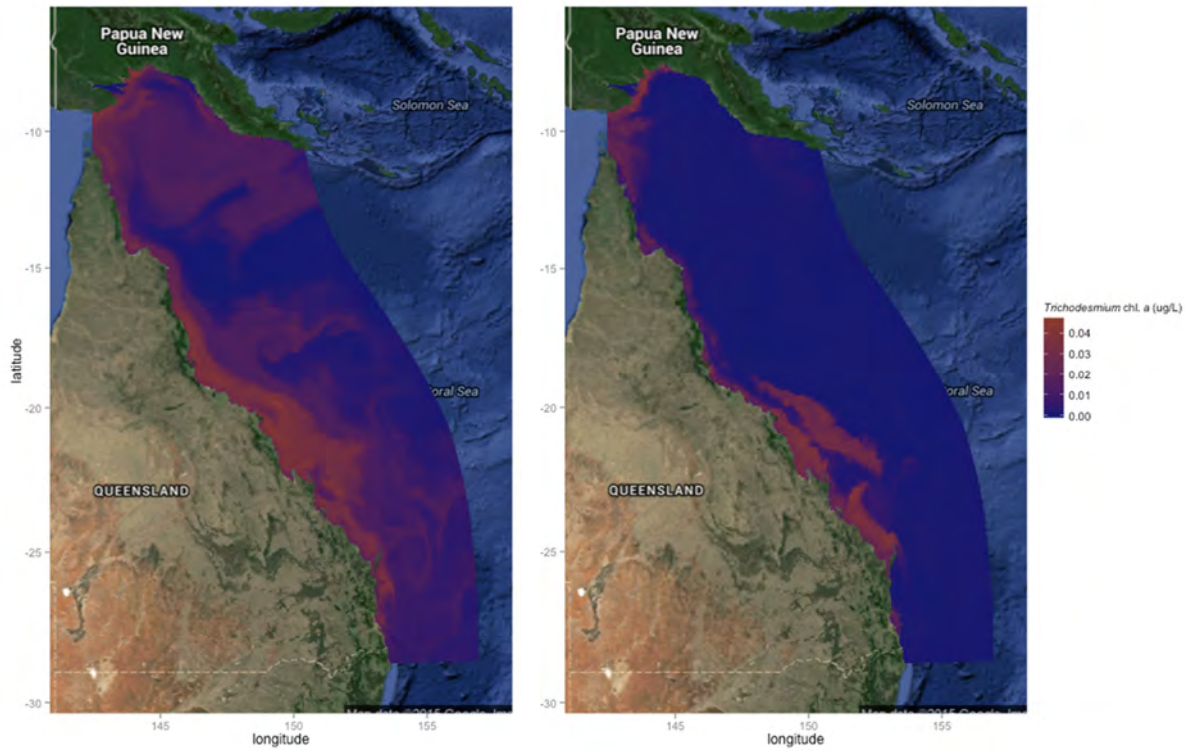


Figure 5.5.36. Simulated surface *Trichodesmium* concentrations, left: July 2013, right: December, 2013. Note that the colour scale used here does not represent the visual appearance of *Trichodesmium* at the concentrations indicated. Base map copyright Google Inc.

The spatial distribution of *Trichodesmium* shown in Fig. 5.5.36 is plausible in comparison with satellite estimates currently available (e.g. Fig. 5.5.37, taken from McKinna, 2010 and images not yet released from more recent work by David Blondeau-Patissier), however we do not yet have access to satellite estimates from matching times to allow a more direct comparison.



Figure 5.5.37. Estimated distribution of *Trichodesmium* in the Fitzroy region (approximately 23°S) during October 2007 according to the satellite classification algorithm of McKinna (2011) (figure reproduced from that McKinna, 2010).

Simulated *Trichodesmium* concentrations are generally low relative to total chlorophyll a. Because the model simulates mean concentrations in each 4x4 km grid cell while *Trichodesmium* blooms tend to aggregate on a much smaller scale and are typically reported in terms of cell counts or presence/absence (McKinna et al., 2011), it is not possible at this time to quantitatively assess the accuracy of these concentrations, however this finding is consistent with reports that measurable *Trichodesmium* blooms are only occasionally observed in routine sampling (David Alongi, pers. comm.)

To facilitate interpretation of model output, we will consider seasonal patterns in each of 7 overlapping regions, as indicated in Fig. 5.5.38.

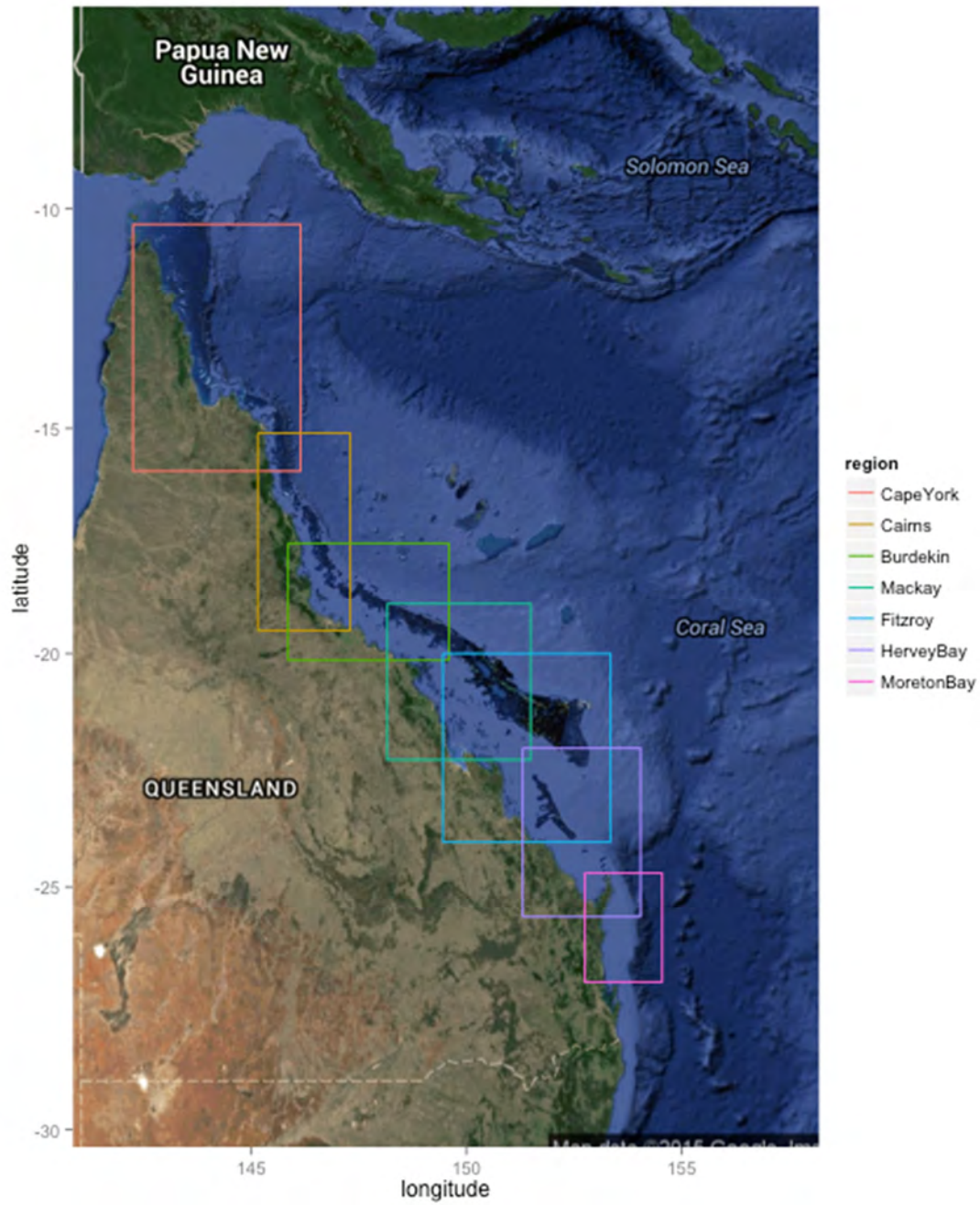


Figure 5.5.38. Boundaries of regions, as defined for further analysis of *Trichodesmium* outputs. These regions were chosen to match regions currently being used to assess satellite *Trichodesmium* estimates (David Blondeau-Pattisier, pers. comm.)

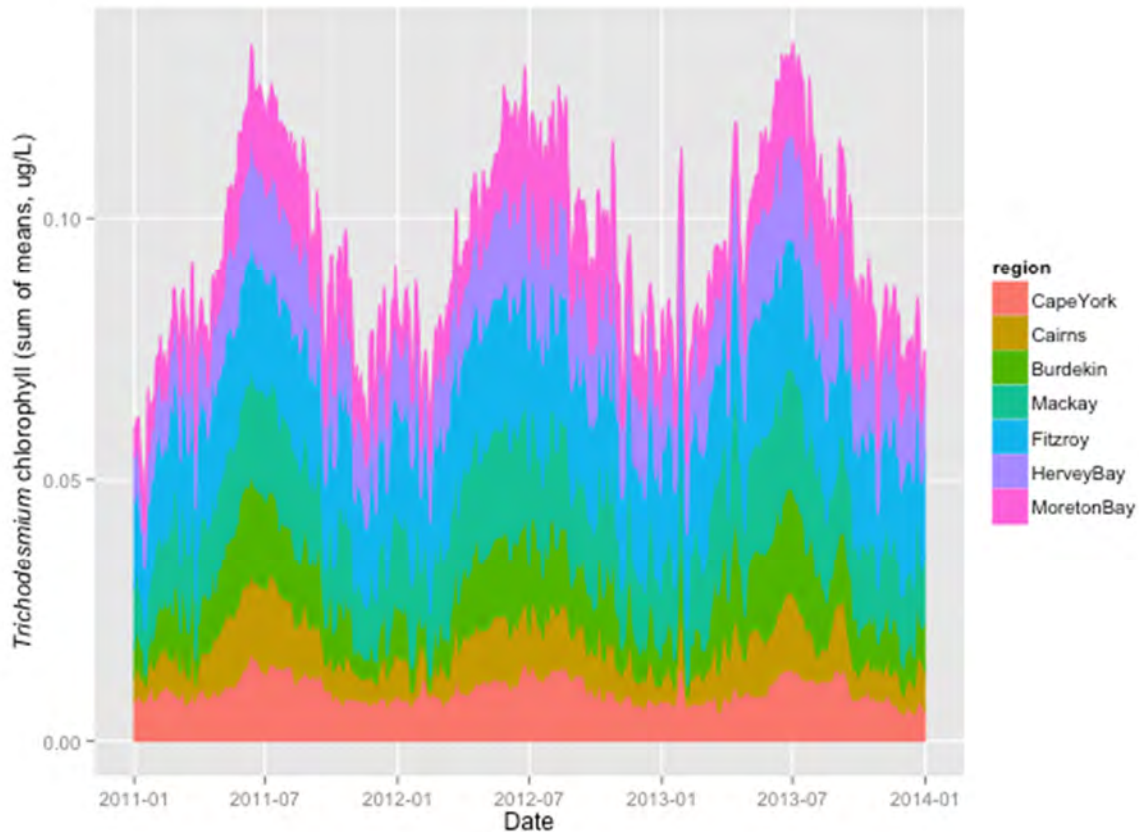


Figure 5.5.39. Simulated *Trichodesmium* time series, 2011-2013. The area of each colour-coded region shows the mean value of *Trichodesmium* at the depth of maximum concentrations.

As the seasonal pattern in Fig. 5.5.39 is relatively consistent, we can aggregate monthly values across all years of the simulation to more clearly show seasonal and spatial patterns Fig. 5.5.40. Simulated *Trichodesmium* chlorophyll concentrations are higher in the mid- and southern GBR than in the northern GBR, and peak slightly later in the year in the South. This is consistent with observed higher total primary production in the southern GBR lagoon (Furnas et al., 2005) and satellite estimates of *Trichodesmium* occurrence in each region (David Blondeau-Patissier, pers. comm.). The mid-year peak in simulated *Trichodesmium* concentrations occurs earlier than the peak coverage estimated from remote sensing products, which occurs in August in Cape York and not until October in the Fitzroy and Hervey Bay regions (David Blondeau-Patissier, pers. comm.). This could indicate an error in the model results, or could reflect the fact that *Trichodesmium* is most visible at the surface when a bloom is in decline and forms a surface scum with increased PSII pigmentation (Miles Furnas, pers. comm.) so peak visibility in satellite images may in fact occur later than peak *Trichodesmium* chlorophyll concentrations in the water column. Satellite detection of *Trichodesmium* blooms and measurement of diazotrophic nitrogen fixation activity is a topic of active current research, and more evidence to evaluate and improve the model is likely to emerge in the coming few years.

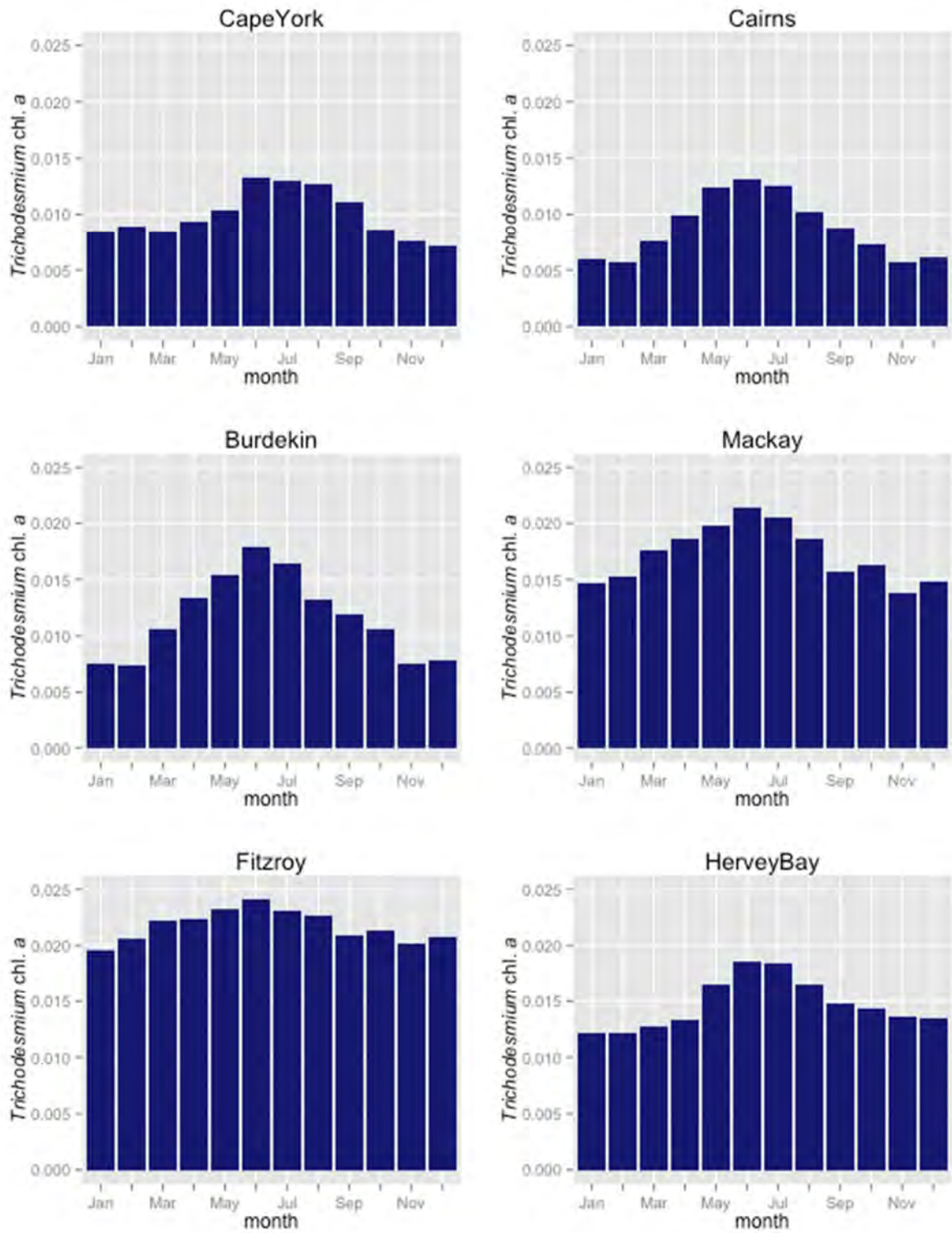


Figure 5.5.40. Mean *Trichodesmium* concentration in each region, 2011-2013 model output aggregated by month of the year.

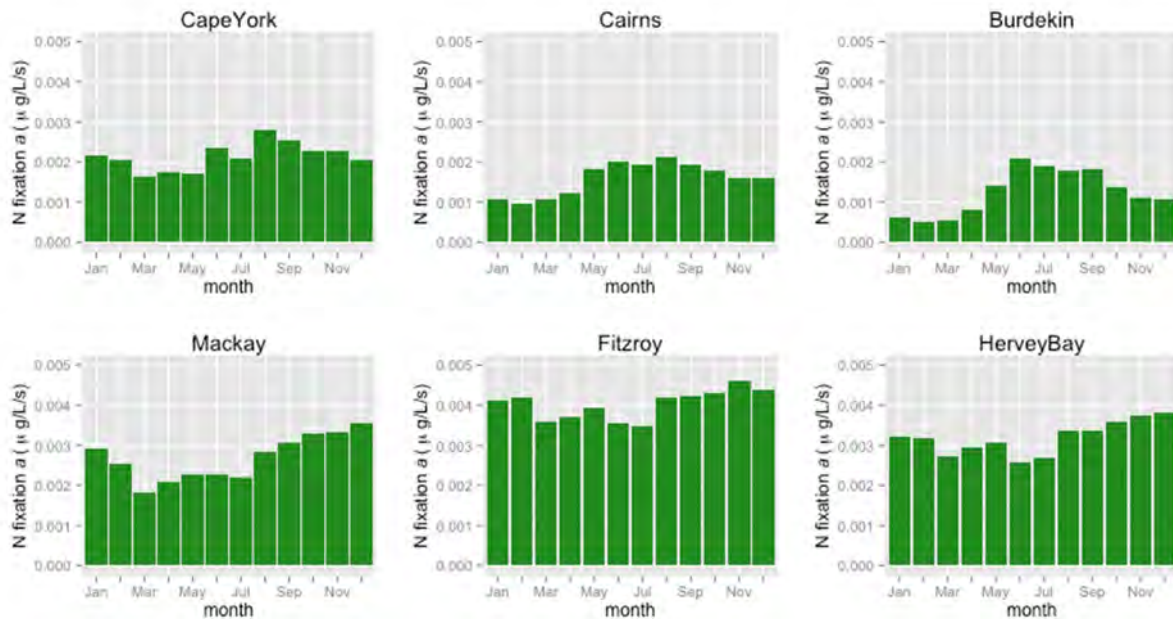


Figure 5.5.41. Instantaneous simulated nitrogen fixation rates near the surface (mean of snapshots taken in each region at midday each day). Nitrogen fixation by *Trichodesmium* is typically at its highest near midday (Oliver et al., 2012).

Interestingly, while simulated nitrogen fixation rates parallel simulated *Trichodesmium* concentrations in the northern GBR, the seasonal pattern is reversed in the southern GBR (Fig. 5.5.41), reflecting the complex relationship between nutrient availability, photosynthesis, and nitrogen fixation.

5.5.7 Emergent properties

Complex aquatic ecological models like the eReefs marine model contain many parameters representing biogeochemical process rates. Tuning these parameters within the bounds of the ranges supported by experimental and observational data allows the model to be calibrated to improve its match with in situ observations at monitoring stations. With many parameters and limited observational data, it is sometimes possible for models to be over-fitted, achieving “the right results for the wrong reason”. To guard against this, we can look for independent ways to evaluate the performance of models.

A particularly powerful means of evaluating the predictive capacity of models is to test the degree to which the model reproduces patterns in observational data that emerge only when data are aggregated or considered at large temporal or spatial scales (de Mora, 2015). In this section, we consider relationships of this type, which have been observed in the real world, which would not necessarily or directly result from a good match between the model output and the time-series monitoring data against which the model was calibrated, and which were not themselves used in calibration of the model. Two emergent properties are discussed. (a) Following the lead of Hirata et al. (2013) and de Mora et al. (2015), we consider whether the model reproduces expected patterns in phytoplankton community structure. (b) Following the work of Fabricius et al. (2013, 2014), we consider whether the model reproduces the observed relationship between total annual freshwater discharge from the Burdekin River and water clarity in the central Great Barrier Reef during the dry season.

We did not look at these relationships until after model calibration was complete – this provides assurance that the calibration was not biased to achieve a favourable result on emergent properties.

5.5.7.1 Phytoplankton community structure

Phytoplankton cell size influences function in several ways. Large cells have lower maximum nutrient uptake rates and (assuming negative buoyancy) higher sinking rates, but are also able to harvest more light for photosynthesis and are less susceptible to grazing by small zooplankton. Large phytoplankton such as diatoms will therefore thrive in different conditions than small phytoplankton. In the eReefs marine model, we simulate two phytoplankton size classes: large phytoplankton (or micro-phytoplankton) and small phytoplankton (corresponding to pico- and nano-phytoplankton). The implementation and mechanistic basis of these size-based phytoplankton groups is described in detail by Baird and Emsley (1999), Baird et al. (2007) and Baird et al. (2015). Phytoplankton size classes are not routinely monitored in the GBR, so the phytoplankton model was calibrated only against total chlorophyll a observations.

Hirata et al. (2011) used a global phytoplankton pigment dataset derived from several coastal monitoring programmes and oceanographic cruises between 1992 and 2008 to estimate the contribution of several phytoplankton function groups and three phytoplankton size classes (micro-, pico- and nano-phytoplankton) to total chlorophyll. When the data were aggregated, they found strong relationships, with the contribution of small (pico- and nano-) phytoplankton increasing as total chlorophyll decreases.

Fitting a curve through the observational data presented by Hirata et al. (2011) produces the black lines shown in Fig. 5.5.42. Output from the eReefs marine model (2011-2014) is shown as a cloud of coloured points. We conclude that the model does reproduce the expected relationship between total chlorophyll a and phytoplankton community structure. This provides strong evidence that the way the model handles phytoplankton functional responses is realistic.

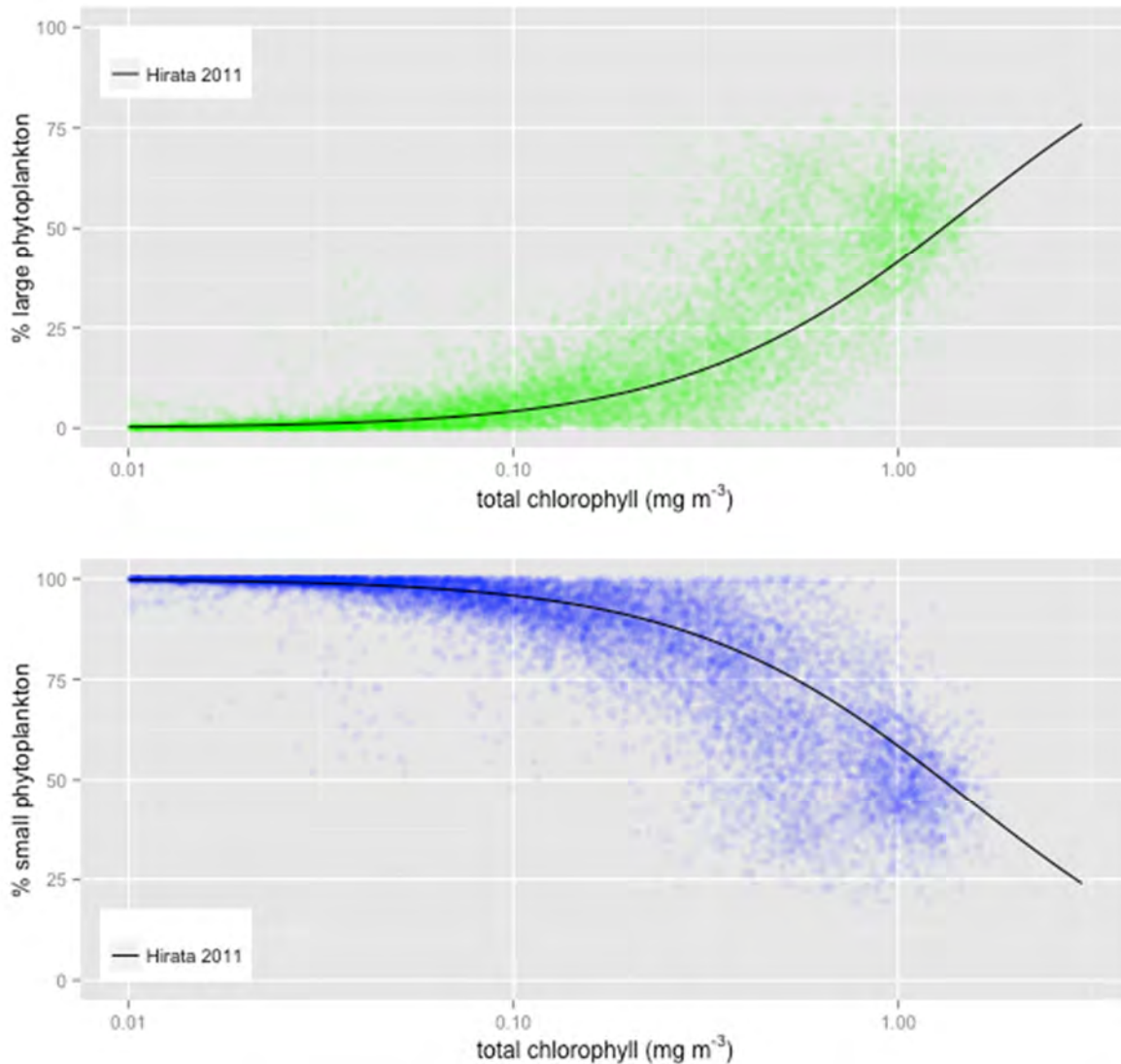


Figure 5.5.42. Percent large phytoplankton (microplankton) and percent small phytoplankton (picoplankton plus nanoplankton) plotted against total chlorophyll a concentrations. Coloured dots are a random sample of 20,000 values from the surface layer of the 4km grid-cell eReefs model during the 2011-2014 simulation. Black lines show the expected values: a fit to the global ocean observational dataset presented by Hirata et al. (2011).

5.5.7.2 Relationship between wet-season total flow and dry-season water clarity in the central Great Barrier Reef

Wet season river discharges bring heavy loads of sediments, nitrogen and phosphorus into near-shore Great Barrier Reef waters. Fresh water flood plumes typically extend up to 50 km from the coast. The vast majority of particulate material (and hence also the majority of nitrogen and phosphorus) is deposited to the sediments within 10 km of the coast, but dissolved nutrients remain with the flood plumes and are dispersed further (Devlin and Brodie, 2004). It is believed that this drives increased phytoplankton production and crown of thorns starfish outbreaks following large flood events (De'ath et al., 2012).

Although flood plumes typically disperse by April, recent work by Fabricius et al. (2014) has demonstrated that river run-off affects water clarity in the central Great Barrier Reef for several months after plume dispersal. Annual mean photic depth (calculated from the start of the wet season to the start of the following wet season) decreases linearly as annual discharge from the Burdekin River increases and water clarity is reduced even four months after the end of wet-season flows (Fabricius et al. 2014).

Fig. 5.5.43 shows the relationship between total wet-season discharge from the Burdekin in the marine models and mean dry season (June to October) surface chlorophyll a in the “central Great Barrier Reef” region defined by Fabricius et al. (2014), i.e. from 20.1°S to 17.9°S and from 146.3°E to 149.4°E for 2011, 2012, 2013 and 2014. Across these four years, there appears to be a strong relationship between wet-season flow and simulated phytoplankton production and hence chlorophyll concentrations during the dry season, persisting for months after the dispersal of flood plumes. Elevated chlorophyll production in years with large flow events leads to increased turbidity, increased light attenuation (Fig. 5.5.44) and reduced photic depth.

Average simulated chlorophyll a concentrations, by region and month of the year, are given in Fig. 5.5.45 for reference.

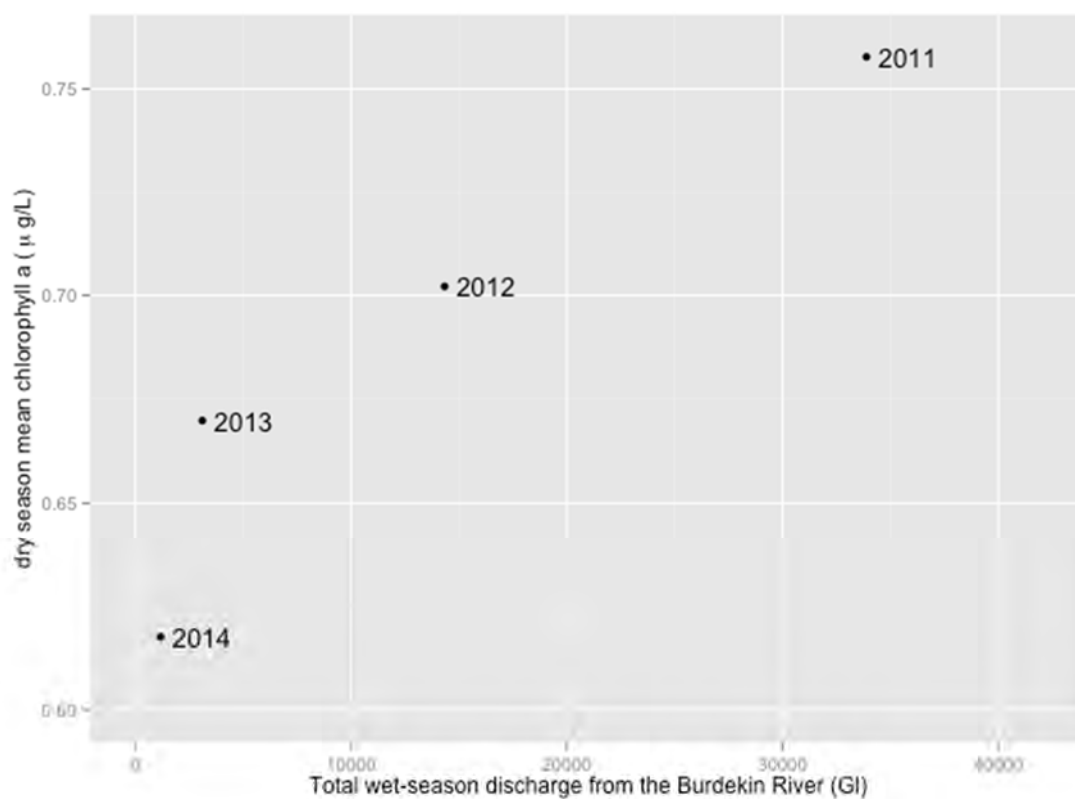


Figure 5.5.43. Total wet season (November to April) flow versus mean dry season surface chlorophyll a concentrations in the central GBR during the following wet season (June to October).

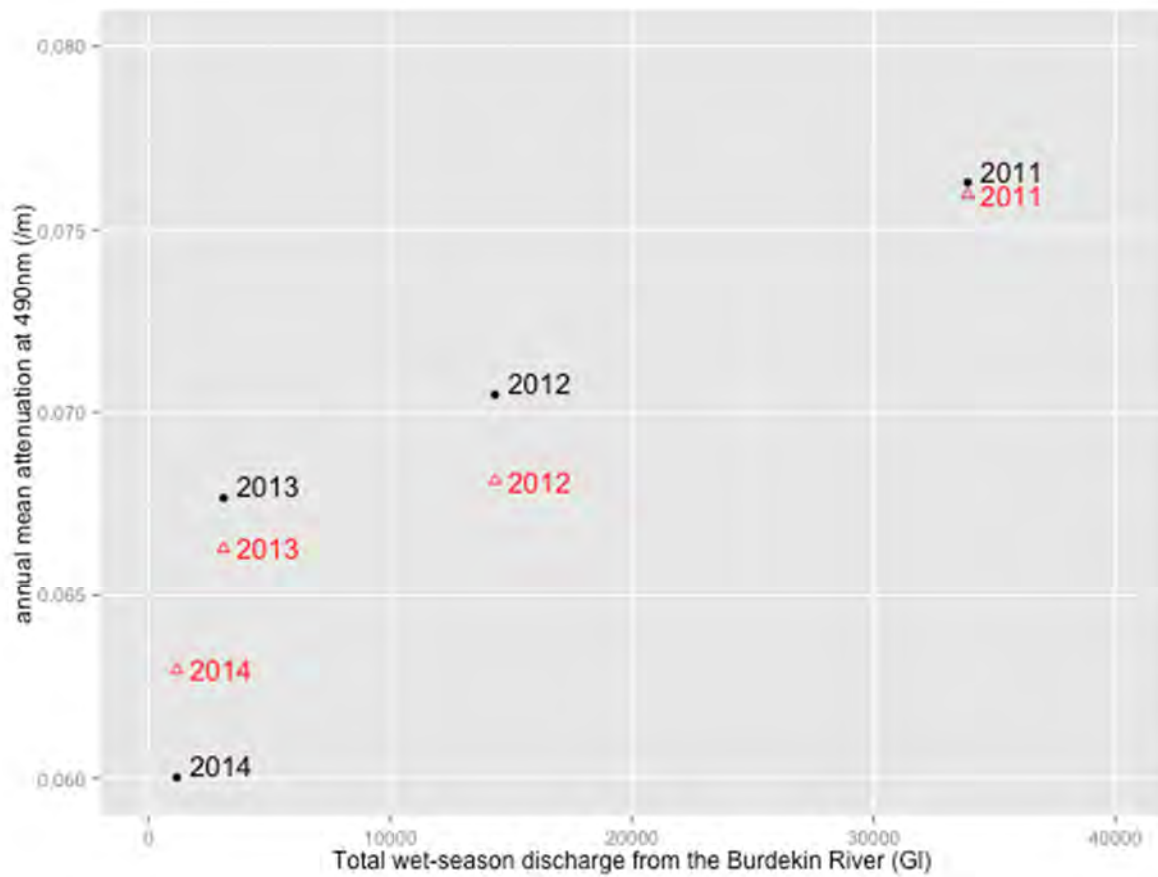


Figure 5.5.44. Mean annual attenuation of light at 490nm in the surface layer of the model, plotted against total wet-season discharge from the Burdekin River. Blue: Dry-season mean. Red: annual mean.

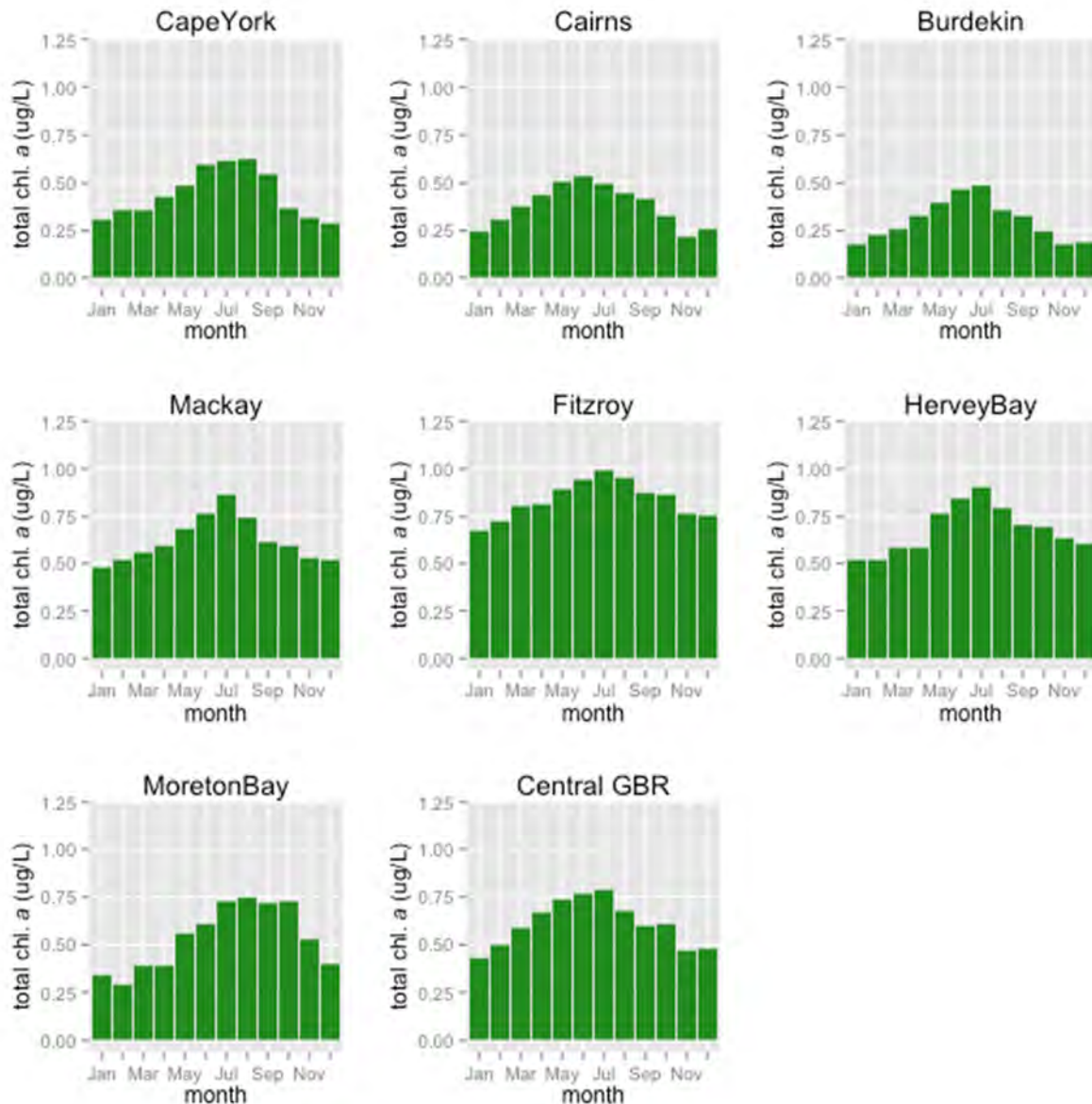


Figure 5.5.45. Mean simulated chlorophyll a (taken as the maximum in the top eight layers of the model) in each month in each region as defined in Fig. 5.5.38 plus the central GBR region discussed in this section, averaged over 2011-2014.

5.5.8 Regional budgets

Regional budgets were calculated for 3 subregions of the eReefs biogeochemical model grid: Northern Inner Lagoon, Southern Inner Lagoon and Outer Lagoon and Reef (Fig. 5.5.46). These budgets were calculated for specific months of simulation to explore contrasts in wet and dry season nutrient pools. Scaled pie charts illustrate the total nitrogen concentration in each model pool as well as the proportional contribution from each part e.g. small, large and *Trichodesmium* phytoplankton nitrogen (Fig. 5.5.46). Similar budgets were constructed for pelagic and sediment nitrogen to summarise the distribution of mass (Fig. 5.5.47).

Results for January 2013 showed a greater concentration of nitrate and detrital nitrogen in the Northern Inner Lagoon with smaller concentrations of phytoplankton and zooplankton.

In the Southern Inner Lagoon nitrate and detrital nitrogen concentrations were lower but in similar proportion; phytoplankton nitrogen was marginally greater. In the Outer Lagoon and Reef dissolved nutrient concentrations were greater than in the Inner lagoons, and zooplankton nitrogen biomass, dominated by large zooplankton, was marginally greater than phytoplankton nitrogen biomass. In the Outer Lagoon and Reef the phytoplankton biomass in January 2013 was dominated by *Trichodesmium*.

The comparative analysis of water column and sediment nutrient pools (Fig. 5.5.47) demonstrates clearly that in the lagoon, the concentration of nutrients in the sediment is much greater than in the pelagic layer (0-110 m). Microphytobenthos also dominates the phytoplankton biomass in the lagoon. In the Outer Lagoon and Reef pelagic nitrogen pools are comparatively larger for dissolved nitrogen and plankton biomass compared to sediment pools.

These monthly budget analyses vary over a seasonal cycle which demonstrates that the GBR region is a dynamic system which evolves rapidly in response to coastal and shelf nutrient input.

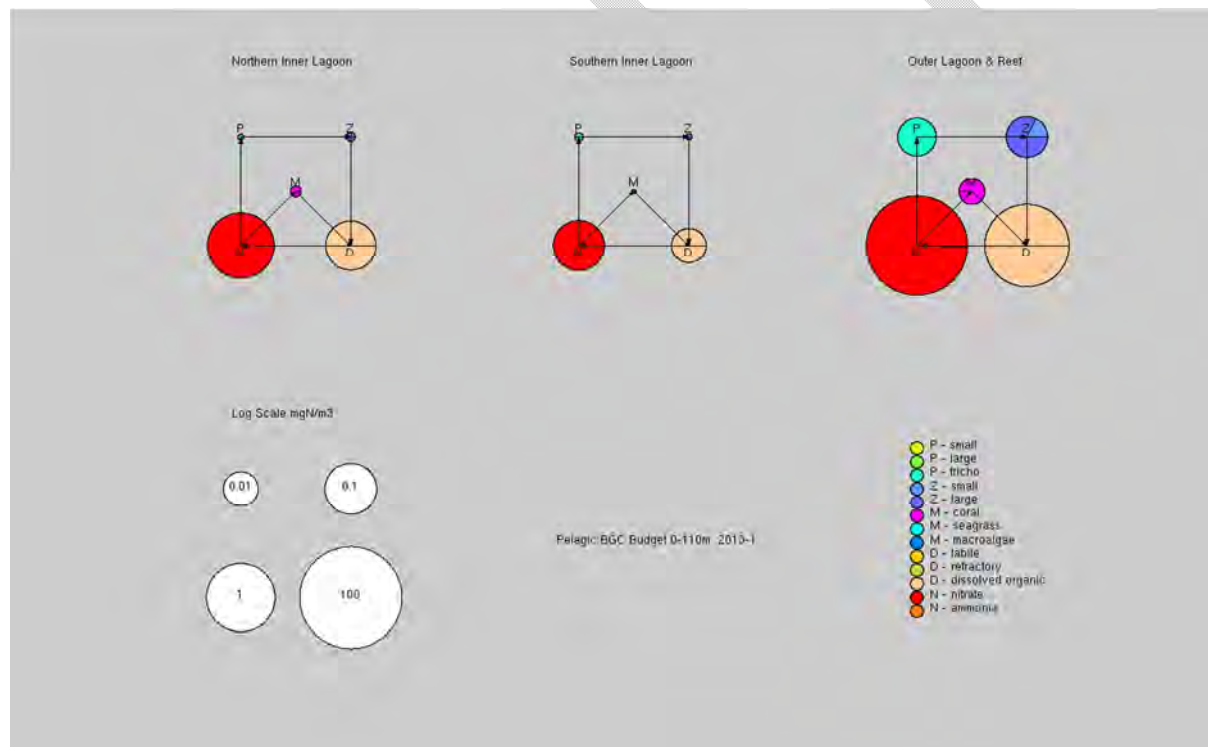


Figure 5.5.46. Nitrogen budget for Northern and Southern Inner Lagoon regions and the Outer Lagoon + Reef. Circle size represents mean January 2013 concentration of nitrogen in the top 110 m on a log scale.

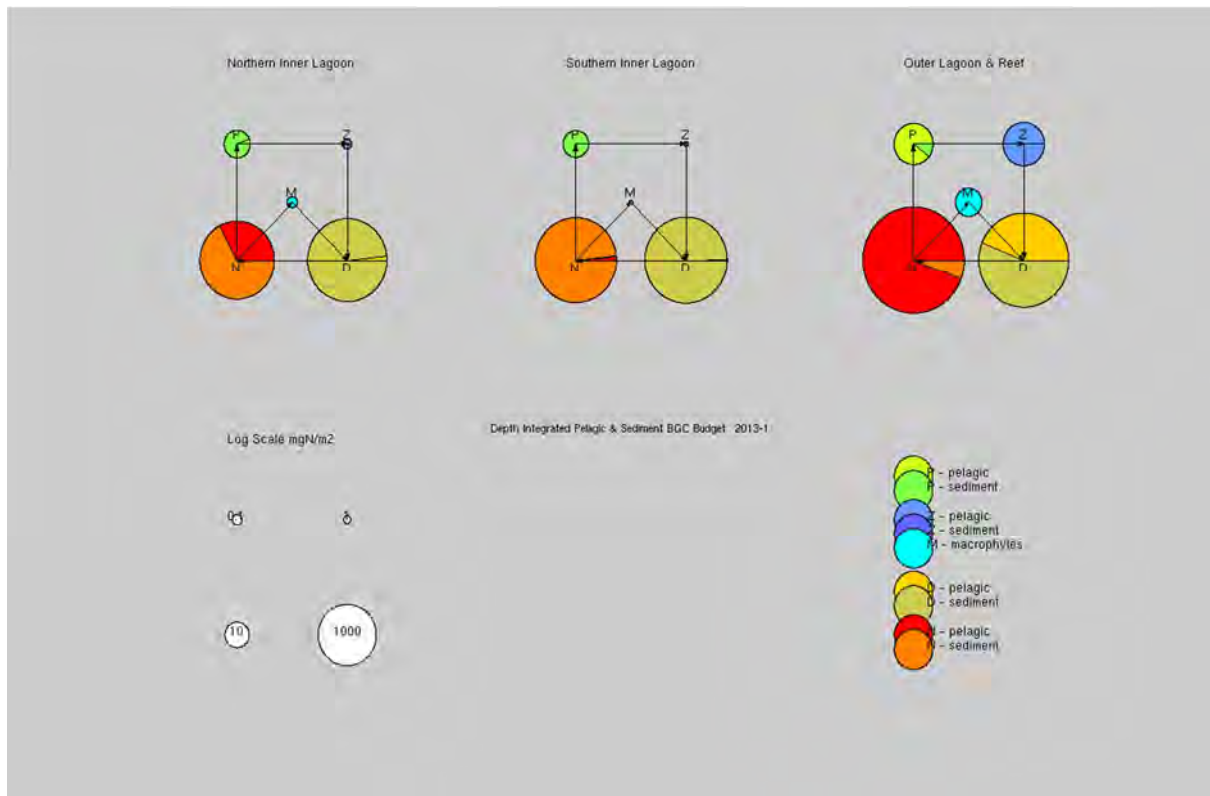


Figure 5.5.47. Nitrogen budget for Northern and Southern Inner Lagoon regions and the Outer Lagoon + Reef. Circle size represents mean January 2013 concentration of nitrogen in the top 110 m of the water column and top 40mm of the sediment on a log scale.

5.5.9 Primary production and zooplankton grazing

Simulated phytoplankton primary production and zooplankton grazing are shown in Fig 5.5.48. The model simulates persistent spatial gradients in production and grazing with elevated levels on the QLD shelf and off the PNG coast. Whilst chlorophyll pigment concentration is often greater at depth forming a subsurface chlorophyll maximum, phytoplankton primary production is typically greatest in surface waters, where phytoplankton have greatest exposure to light. Variability in primary production is related to a combination of phytoplankton population history, nutrient supply, light intensity and zooplankton grazing.

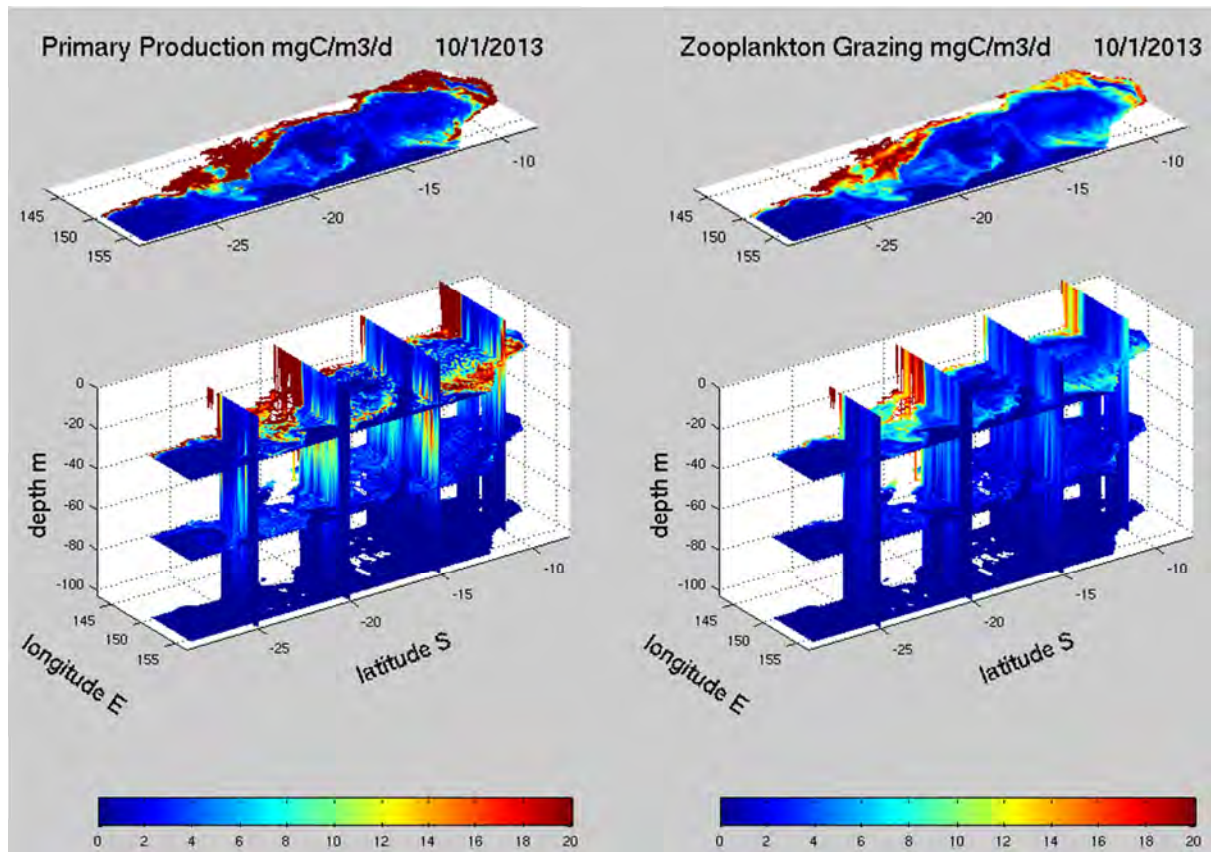


Figure 5.5.48. Modelled primary production (left) and zooplankton grazing (right) in January 2013. The 3D view is taken from offshore south east looking northwest towards the QLD coast/shelf.

Annual depth integrated (0-110m) phytoplankton primary production (Fig. 5.5.49) was calculated for the 4 years of model simulation and shows persistent gradients in intensity. Lagoon and shelf waters in the southern GBR have the greatest productivity ($>400 \text{ gC m}^{-2} \text{ y}^{-1}$), whilst offshore reefs and ocean waters have the lowest productivity ($<100 \text{ gC m}^{-2} \text{ y}^{-1}$). Whilst these patterns are similar each year, productivity in 2012 was greater than in other years.

Subregions of the model are compared in Figs. 5.5.50 & 5.5.51. Profiles of mean daily phytoplankton production generally show peak productivity in surface waters declining to near zero at 100m depth (the practical limit of the euphotic zone). In the Northern Lagoon there was a decline in production from 2011 to 2014 that may be linked to the climatic change from an intense wet season in 2011 to drier conditions in subsequent years. Phytoplankton primary production was lower in the Offshore Lagoon + Reef area, particularly in surface waters. This is likely due to very low nutrient supply to the surface as the principle nutrient resource to this region is the supply from deep water.

Modelled phytoplankton primary production is of the same order of magnitude as observations made by Furnas & Mitchell 1987. They estimated annual primary production in 1983 as 183, 167 and 211 $\text{gC m}^{-2} \text{ y}^{-1}$, on the mid-shelf, the shelf break and in offshore waters. Our model results show comparable levels of productivity in offshore waters with a 2 fold increase in production in inshore waters (not sampled by Furnas & Mitchell in 1983).

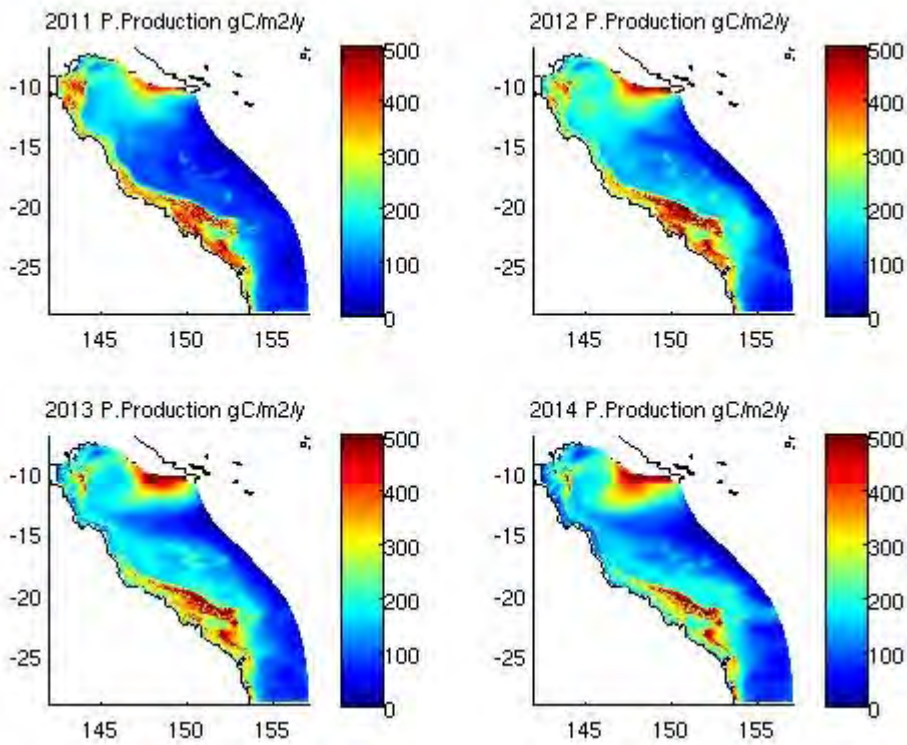


Figure 5.5.49. Annual depth integrated (0-110m) phytoplankton primary production.

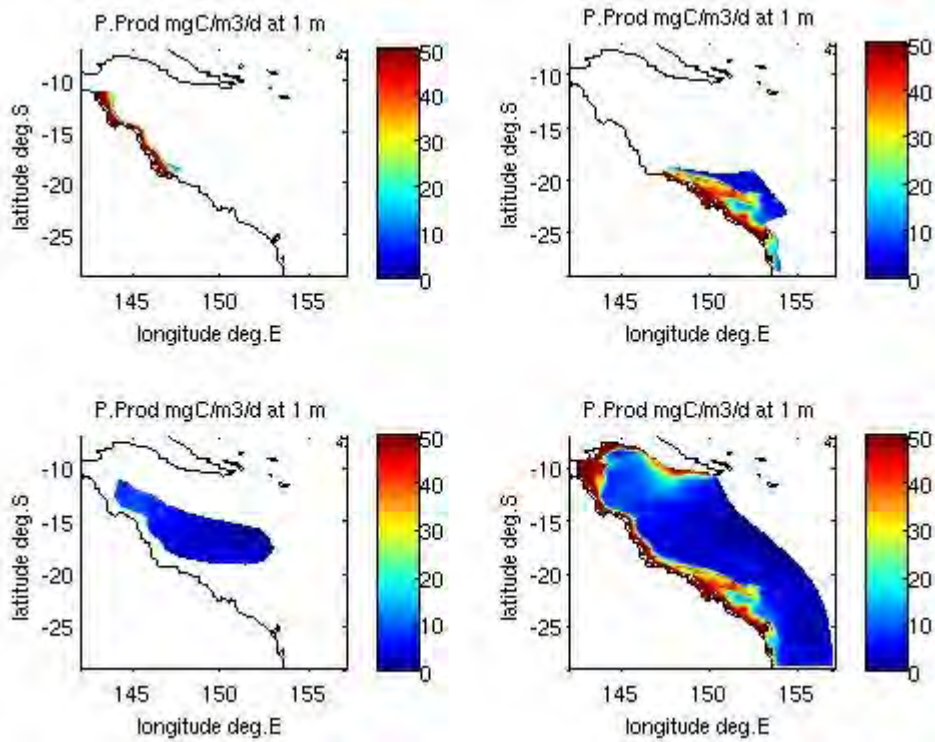


Figure 5.5.50. 2011 Annual mean phytoplankton primary production in subregions of the model [clockwise from top left: Northern Lagoon, Southern Lagoon, Outer Lagoon + Reef, Whole Region].

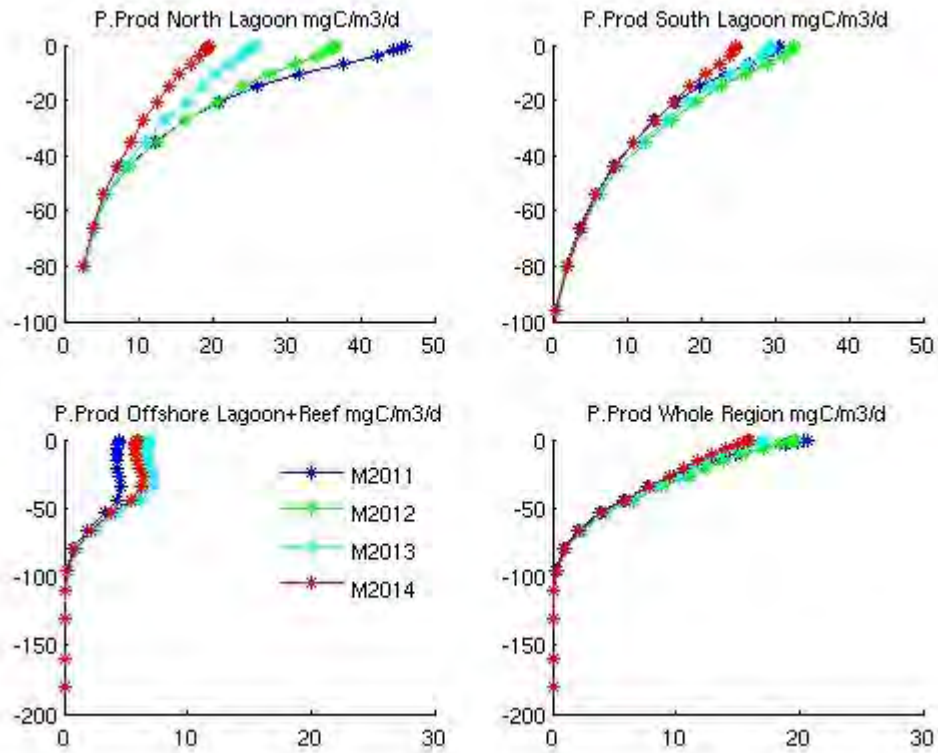


Figure 5.5.51. Profiles of modelled annual mean phytoplankton primary production for sub regions of the model.

Zooplankton grazing has a similar footprint to the distribution of primary production, although with lesser magnitude. Total grazing comprises micro- and meso-zooplankton ingestion with micro-zooplankton responding very rapidly (near synchronous) to small phytoplankton growth. Large zooplankton respond more slowly to the availability of large phytoplankton and also consume micro-zooplankton, which can at times result in a reduction in small phytoplankton grazing and thus allow the small phytoplankton to bloom. The introduction of these trophic links in the model has resulted in greater patchiness in the phytoplankton dynamics than previously simulated.

Total annual depth integrated zooplankton grazing ranged from $<100 \text{ gC m}^{-2} \text{ y}^{-1}$ in offshore waters to $>300 \text{ gC m}^{-2} \text{ y}^{-1}$ in the Southern GBR Lagoon (Fig. 5.5.52). Depth profiles of zooplankton grazing for subregions of the model (Figs. 5.5.53 & 5.5.54) show similar patterns to the distribution of phytoplankton primary production with greatest grazing occurring in surface waters tending to zero at $\sim 100\text{m}$ (the bottom of the euphotic zone). As noted previously for primary production, zooplankton grazing in the Northern Lagoon was greatest in 2011 with declining trend in subsequent years, likely due to the influence of the strong wet season in 2011.

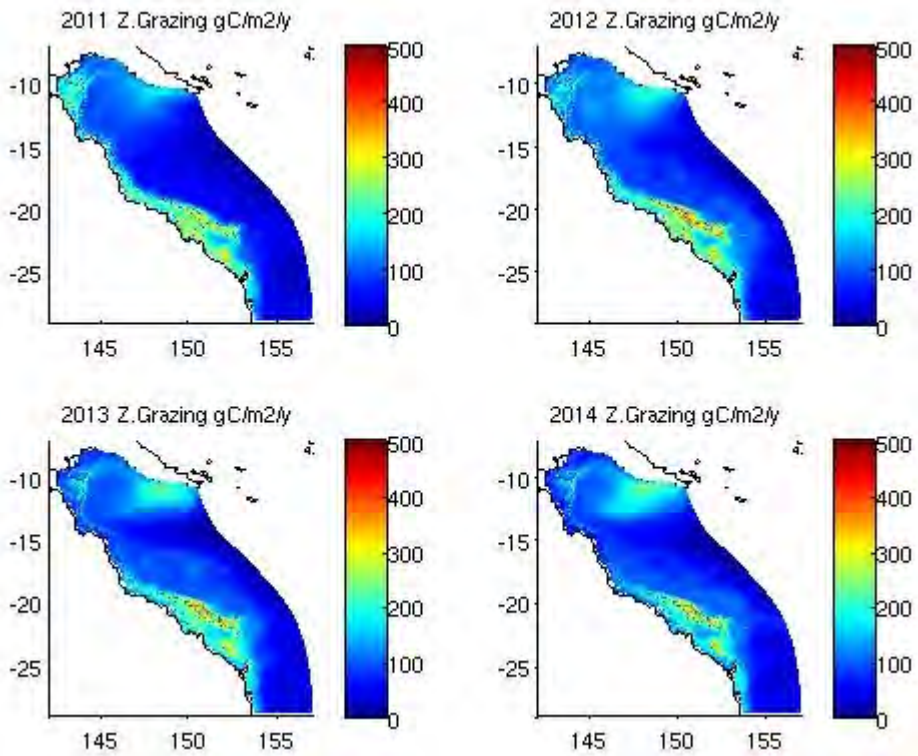


Figure 5.5.52. Annual depth integrated (0-110m) total zooplankton grazing.

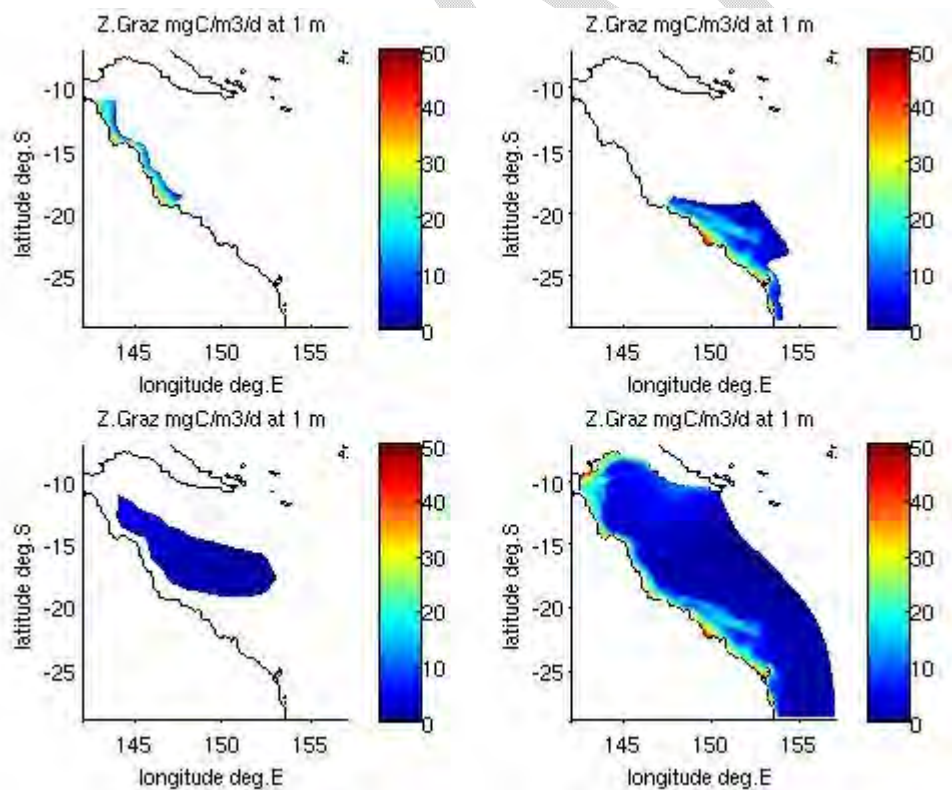


Figure 5.5.53. Annual surface zooplankton grazing in subregions of the model [clockwise from top left: Northern Lagoon, Southern Lagoon, Outer Lagoon + Reef, Whole Region].

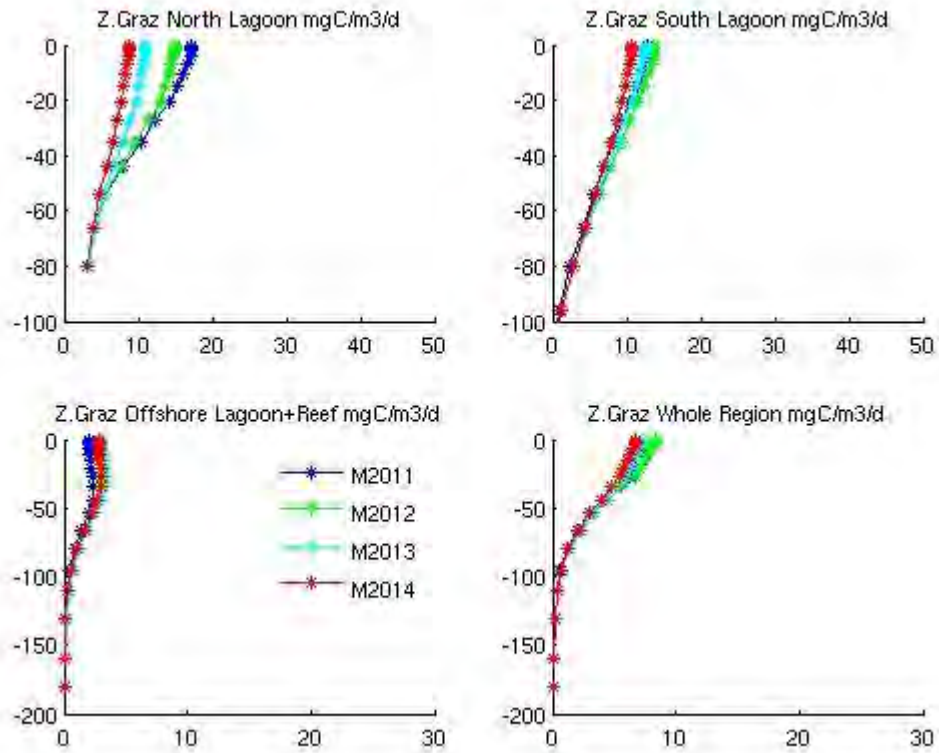


Figure 5.5.54. Profiles of modelled annual mean total zooplankton grazing for sub regions of the model.

Table 5.5.6. Modelled phytoplankton primary production and zooplankton grazing, 4 year depth integrated (0-110m) means for subregions of the model.

	Whole Region	Northern Inner Lagoon	Southern Inner Lagoon	Outer Lagoon + Reef
Primary Production $gC\ m^{-2}\ y^{-1}$	212	345	330	127
Total Zooplankton Grazing (Large + Small on phytoplankton, + large on micro zooplankton) $gC\ m^{-2}\ y^{-1}$	132	241	226	73
Small Zooplankton Grazing on phytoplankton $gC\ m^{-2}\ y^{-1}$	73	130	113	48
% of P.Prod (+ Small Zoo) grazed by large Zooplankton	62	70	68	57
% of P.Prod grazed by Small Zooplankton	29	20	21	45

Comparing modelled phytoplankton primary production with zooplankton grazing (Table 5.5.6) we see that zooplankton grazing accounts for 57-70% of production. However it should be noted that this ratio includes the carnivorous grazing of large zooplankton on small zooplankton and is therefore an over estimation of trophic transfer from primary to secondary production. Considering the small zooplankton grazing in isolation we see that 20-45% of the primary production is grazed by the small zooplankton, with greatest grazing occurring in the outer lagoon and reef. In inshore waters the phytoplankton population includes a greater fraction of larger cells which support large zooplankton; this leads to a greater grazing pressure on the small zooplankton in inshore waters.

Observations by McKinnon et al., 2015 indicate that large zooplankton grazing in the GBR accounts for 7% of phytoplankton production. Whilst a global review by Schmoker et al., in 2013 showed that small zooplankton grazing accounts for 49-77% of phytoplankton production. Our model results suggest large zooplankton grazing may account for a greater proportion of phytoplankton primary production particularly in the southern lagoon and small zooplankton grazing playing a smaller role.

5.5.10 Summary of the 4 km BGC model Skill assessment against Observations

The purpose of the eReefs biogeochemical model is to simulate the spatially resolved water quality dynamics (phytoplankton, nutrients, turbidity, oxygen) of the GBR World Heritage Area with hind cast, near real time, and in the future, scenario simulations. Model results and insight will be suitable to be used to inform management (tourism, conservation, recreation, aquaculture, development, land use) of WQ throughout the region. Validation of the model for this purpose was assessed against 4 performance criteria:

- Conservation of mass (C, N, P, O) to confirm that the model is logically and numerically accurate.

- Simulated state variable concentrations resemble the regional climatology for offshore-reef, lagoon-reef and near-shore zones.

- Simulated state variable concentrations resemble WQ observations under contrasting seasons/loads (wet vs dry) and significant events (e.g. 1/10 yr flood). Model results are consistent with specific data sets available to the project.

- The model produces a credible nutrient budget (including pelagic + benthic fluxes).

The biogeochemical model hosted in the flux form hydrodynamic transport scheme was assessed for conservation of mass and achieved mass balance for C, N, P and O. Mass was conserved in all biogeochemical model processes and during movement of tracers throughout the model grid in pelagic, epibenthic and sediment layers. This confirms the numerical and logical accuracy of the code.

Annual mean model results for nitrate and phosphate were compared with the CSIRO Atlas of Regional Seas ('CARS Coast 8') climatology of the Queensland Shelf, and 4 years of remotely sensed ocean colour products for chlorophyll. Simulated nitrate was generally in good agreement with the observed climatology throughout the region, although the modelled nutricline was ~40 m shallower than climatology in the Offshore Lagoon and Reef. In 2011

modelled surface nitrate concentrations were $\sim 5 \text{ mg N m}^{-3}$ greater than climatology in the Northern Lagoon, likely due to the intense wet season that year. Modelled phosphate concentrations had good spatial agreement with the CARS Coast 8 data set, but were systematically lower than the climatology by $2\text{-}4 \text{ mg P m}^{-3}$. Comparison of the N:P ratio over the whole Queensland shelf confirms that nitrogen is the nutrient in least supply for primary production (molar N:P ratio < 16) in both the climatology and the model. Simulated surface chlorophyll concentrations agree well with remotely sensed chlorophyll estimates, notwithstanding the differences in the computation and applicability of NASA OC3 and ANN OC3 chlorophyll products. Gradients in chlorophyll from inshore to offshore are well reproduced and the optical models direct simulation of the NASA OC3 chlorophyll product has equivalent features.

The biogeochemical model was compared with observations from numerous sites, platforms, sensors and analytical methods, although most observations were focussed on inshore and local reef dynamics. This mis-match in time and space scales between observations and model (cm^{-3} vs km^2 of water) precludes direct comparison and so we have used local knowledge, statistical analysis and common sense to evaluate model skill and for completeness the full analysis is included as an appendix.

Comparison of the model with the 20 WQM sites with triannual/quarterly sampling was difficult but overall the statistical analysis showed the model had acceptable skill (Willmott score of >0.3) for the majority of sites for chlorophyll, DIP, DON and TSS, with weaker skill for NH_4 , NO_3 and DOP due to a general positive bias of up to 10%. Comparison of the model with the AIMS Coral Reef Survey Site carbon chemistry observations showed that the model had good levels of skill at the majority of stations for Omega, pH, alkalinity and DIC. Data from the Reef Rescue moorings for chlorophyll and TSS also showed that the model had acceptable levels of skill especially considering the location of these sites were in very close proximity to reefs. The IMOS NRS moorings and monthly nutrient samples from Yongala and Stradbroke provided the most useful data set with which to compare the model; at these stations the model had acceptable skill at multiple depths for NO_3 , NH_4 , DIP and chlorophyll. There was no evidence of a systematic negative bias in modelled DIP compared to these inshore data sets despite the evidence to the contrary at climatic scales. The comparison of the model with these time-series observations provides evidence that the biogeochemical model has general skill in reproducing the observed seasonal cycles and events such as storms and floods as captured in the observed data set.

The biogeochemical model was also compared with glider data from the Heron Island region during the passage of ex-cyclone Oswald. Model and observations show the transition from a pre-storm stratified water column with a deep subsurface chlorophyll maximum and nitricline to post-storm conditions with these subsurface features elevated in the water column.

Underpinning the simulation of water quality are the more subtle dynamics of the phytoplankton community and its interaction with light. Simulated *Trichodesmium* patterns agree broadly with expert knowledge, whilst the proportions of large and small phytoplankton relative to chlorophyll concentration, match observed global relationships. In inshore waters there is a strong relationship between wet season flow and phytoplankton production, with elevated chlorophyll concentrations increasing light attenuation for several months after the dispersal of flood plumes.

Modelled nitrogen budgets for the shelf are seasonally dynamic, but in general show largest supply of pelagic nitrate to the Offshore Lagoon and Reef, whilst the Southern Lagoon has the largest sediment pool of nitrogen. Modelled phytoplankton primary production is similar in magnitude to observations in offshore waters, but 2 fold higher inshore, modulated by coastal nutrient supply. Modelled zooplankton grazing is within the range of observations, although the contribution of size fractions maybe bias towards consumption by large zooplankton of large phytoplankton in inshore waters.

It has not been possible to constrain all the variables and processes employed in the biogeochemical model at all spatial and temporal scales against observations, due to omissions in the time and space scales and range of observed parameters. These variables and processes are consistent with the components of the model that have been validated, however, less confidence is placed the accuracy of their outputs until such a time as observations become available with which to validate them.

We conclude that the eReefs 4km biogeochemical model is suitable to simulate the spatially resolved water quality dynamics (phytoplankton, nutrients, turbidity, oxygen) of the GBR World Heritage Area with hind cast, near real time, and scenario simulations.

5.5.11 Comparison of the 4 km and 1 km BGC configurations

At the time of reporting, the 1 km biogeochemical configuration (GBR1) had been run from 28th December 2014 until 28th February 2015. The assessment of GBR1 is undertaken by comparing its output with the 4 km configuration (GBR4). The general response of GBR1 is comparable to GBR4, but differs in detail; GBR1 contains more realistic fine scale structure. Dynamics that are known to exist at small scales are present in GBR1 but not represented in GBR4. This is due the inability of the coarse resolution to adequately resolve bathymetry and geography that are often the sources of turbulence, as well as the dynamics at small scales of the energy cascade. In this regard, GBR1 is a better model than GBR4, even though the formal quantitative skill assessment of GBR4 illustrates that its skill makes GBR4 suitable for a broad range of applications.

Later in 2016, when the GBR1 simulation will have run for more than a year, and in situ observations for this period are available, a more thorough assessment of the performance of the GBR1 will be possible. The comparison undertaken here will focus on the Fitzroy and Burdekin River regions.

The GBR1 biogeochemical processes (e.g. the model equations) and parameters values are identical to the GBR4 configuration, as reported in Section 4.7 (with the exception of A_{CH} , the maximum fraction of a grid cell that corals can occupy, which increases from 0.1 in GBR4 to 0.36 in GBR1). The biogeochemical model tracers are initialized with the GBR4 model results on December 28th, 2014, using EMS interpolation capabilities. This initialization does not utilize the higher resolution benthic layers that are available for some variables (seagrass and coral presence / absence).

Due to differences in the vertical density structure of GBR4 and GBR1 on 28th December 2014 at mid depth, the profiles of DIN and DIP concentration where re-initialized with climatology and interpolated onto the GBR1 28th December density profile (equivalent to the initialization procedure for GBR4 on 1 December 2010). The GBR1 BGC open ocean conditions use the GBR4 BGC water column tracer concentrations. The river boundaries in GBR1 have equivalent

fluxes to the GBR4 near real time model, albeit the cell size within which the fluxes exchange is ~16 times smaller.

Burdekin region

As expected the model bathymetry in the Burdekin region is similar in the two configurations, as both configurations are based on the same 100 m resolution data set (Fig. 5.5.55). Along the coast, shallower regions that are resolved as water in GBR1 appear as land in GBR4. Significant differences exist on the outer reef, where water column depth varies between GBR1 and GBR4 by more than 10 m at some locations.

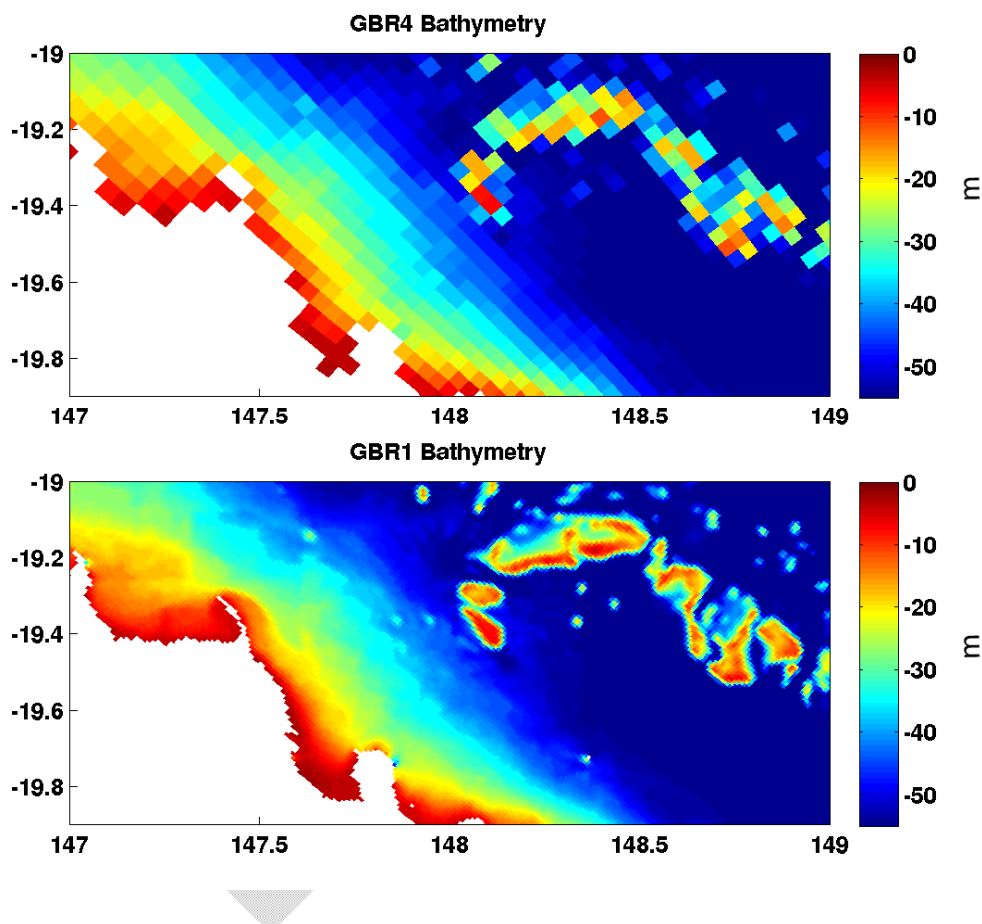


Figure 5.5.55. GBR4 (top) and GBR1 (bottom) bathymetry in the Burdekin River region. Note the entrance to the Burdekin River (19.65 S, 147.6 E) is resolved as a 2 x 2 grid cell entrance in GBR1, but is a straight coastline in GBR4.

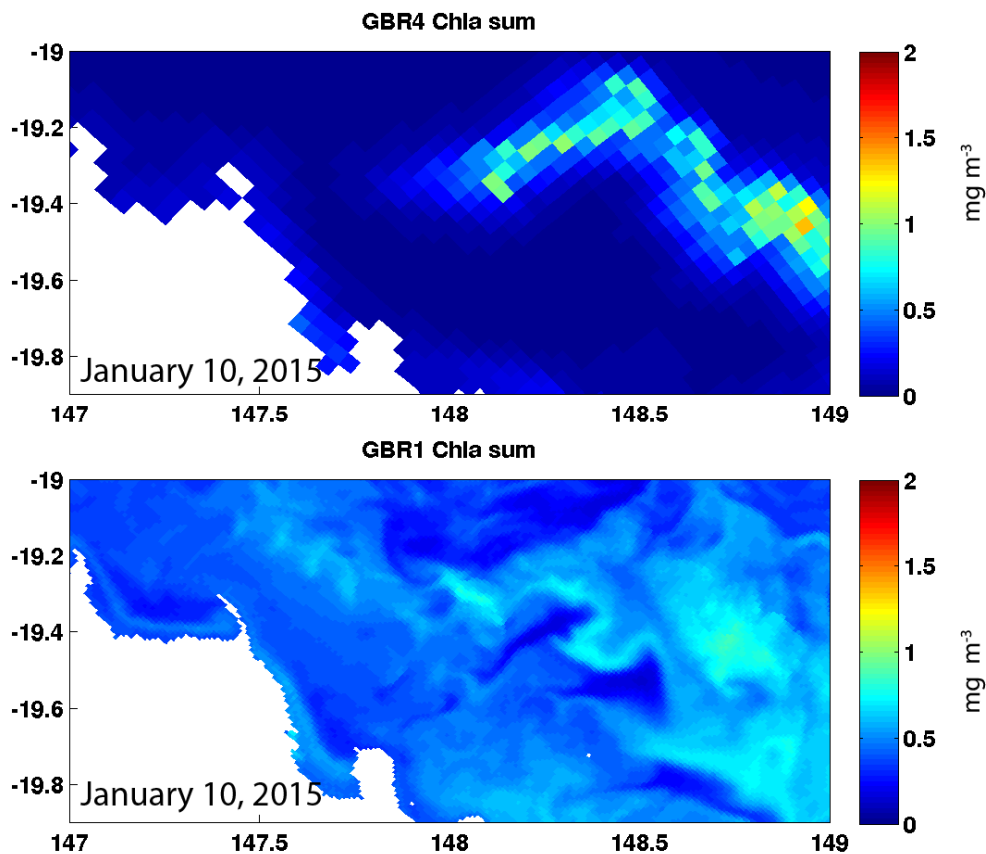


Figure 5.5.56. GBR4 (top) and GBR1 (bottom) simulated surface chlorophyll a (sum of 4 phytoplankton types) on January 10th in the Burdekin river region.

Simulated chlorophyll a is presented in Figure 5.5.56. Overall chlorophyll concentration is higher, with more detailed features evident, in GBR1 than GBR4. Areas where chlorophyll a is the largest (on Jan 10, 2015) are similar (i.e on the reef) in both configurations. Simulated chlorophyll a in GBR1 shows structures in the GBR lagoon, and narrow plumes along the shoreline, that are absent in GBR4. Simulated chlorophyll a in GBR1 also has more fine-scale circulation-generated structures over the reef than in GBR4.

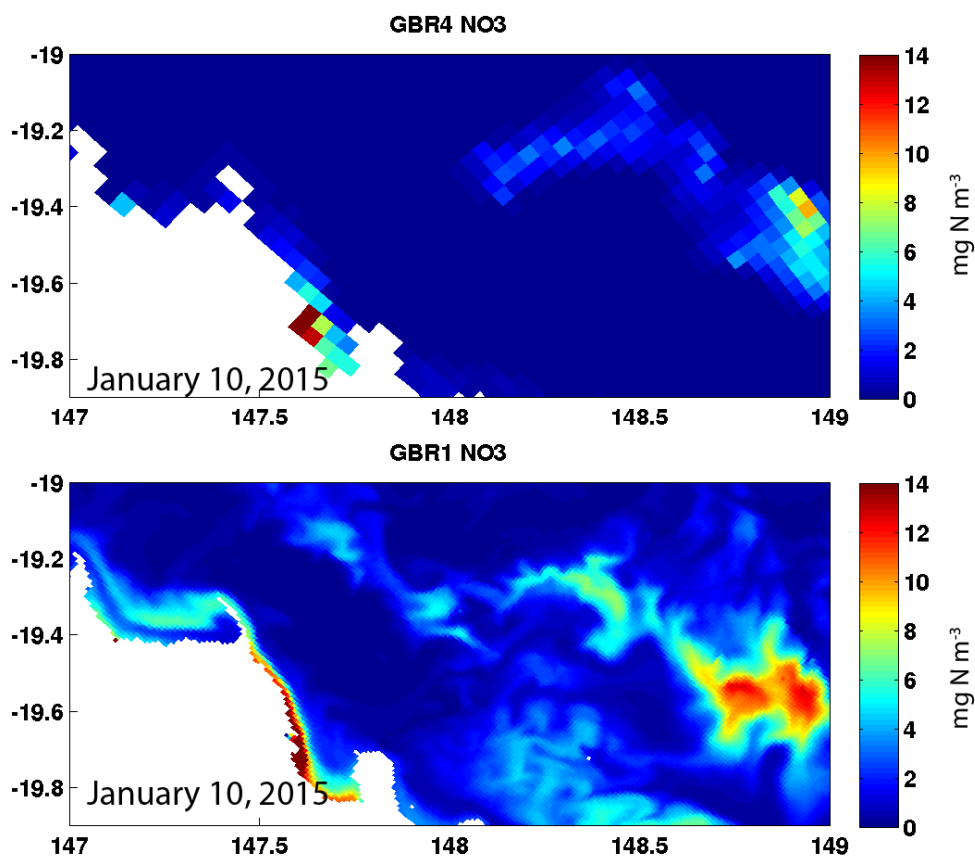


Figure 5.5.57. GBR4 (top) and GBR1 (bottom) simulated surface nitrate on January 10th, around the Burdekin River region.

Similar differences exist between configurations for simulated nitrate (Fig. 5.5.57) as were seen for chlorophyll. Additionally, the Burdekin River coastal plume is a more coherent feature in GBR1. The high nutrient plume extends along a narrow band (< 4 km wide), from the Burdekin entrance to Cape Cleveland with a region of elevated nitrate in southern Upstart Bay (southeast of the river mouth). As found for simulated chlorophyll a, fine scale nitrate structures are simulated in GBR1 in the lagoon and over the reef.

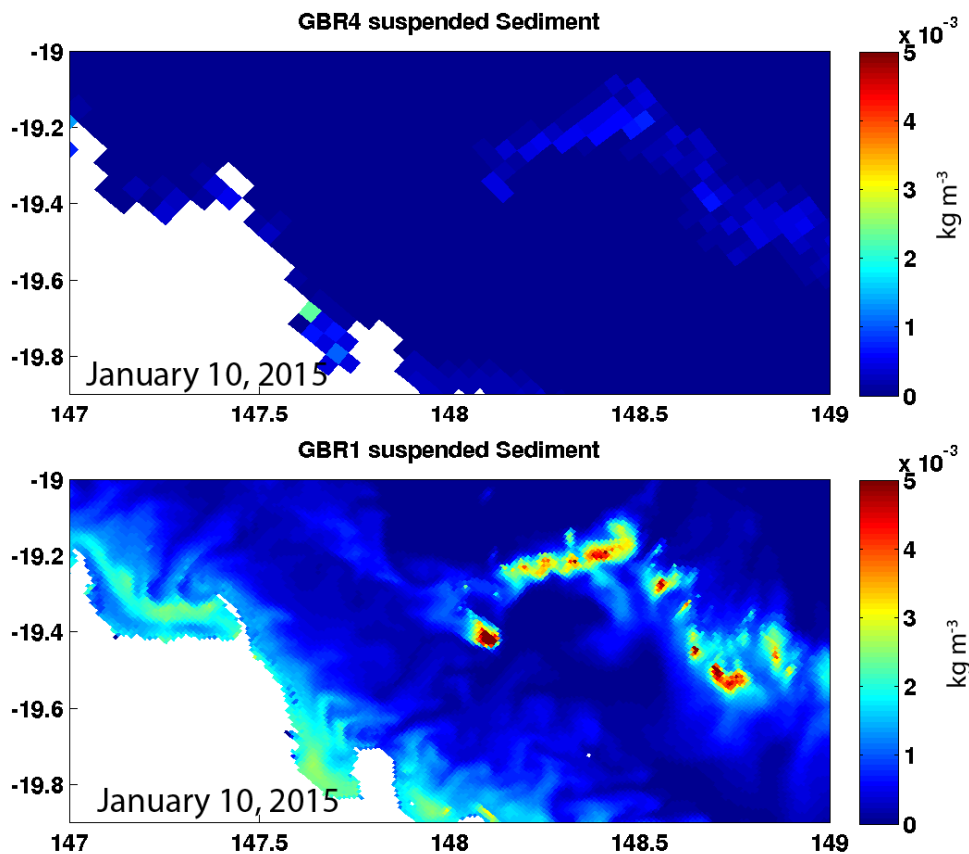


Figure 5.5.58. GBR4 (top) and GBR1 (bottom) simulated surface Ecological Fine Sediment Inorganic (Finesed + Mud) on January 10th, in the Burdekin River region.

The differences between the two configurations are larger for suspended sediment (Fig. 5.5.58) than nitrate or chlorophyll. Large sediment plumes are present in GBR1, as well as large re-suspension patches on the reef, both absent in GBR4. Time series analysis of the sediment model (Section 5.4.4) shows that while GBR1 generally has higher suspended sediment concentrations, that it also often has lower concentrations.

In summary differences between GBR4 and GBR1 in the Burdekin region, over the reef are the result of a better-resolved reef matrix, with shallower areas, triggering larger re-suspension events leading to more surface nutrient, chlorophyll and suspended solids than in GBR1. The elevated concentrations are advected off individual shallow reefs into the lagoon creating small-scale circulation-driven structures.

Fitzroy region

The Fitzroy region is another area of interest, containing the Fitzroy River, the isolated Capricorn Bunker reefs, and with continental shelf only 80 km wide.

Like in the Burdekin region, the two configurations show significant bathymetric differences over the reef matrix (Fig. 5.5.59). The coastline, with small bays and coastal channels, is better resolved in GBR1.

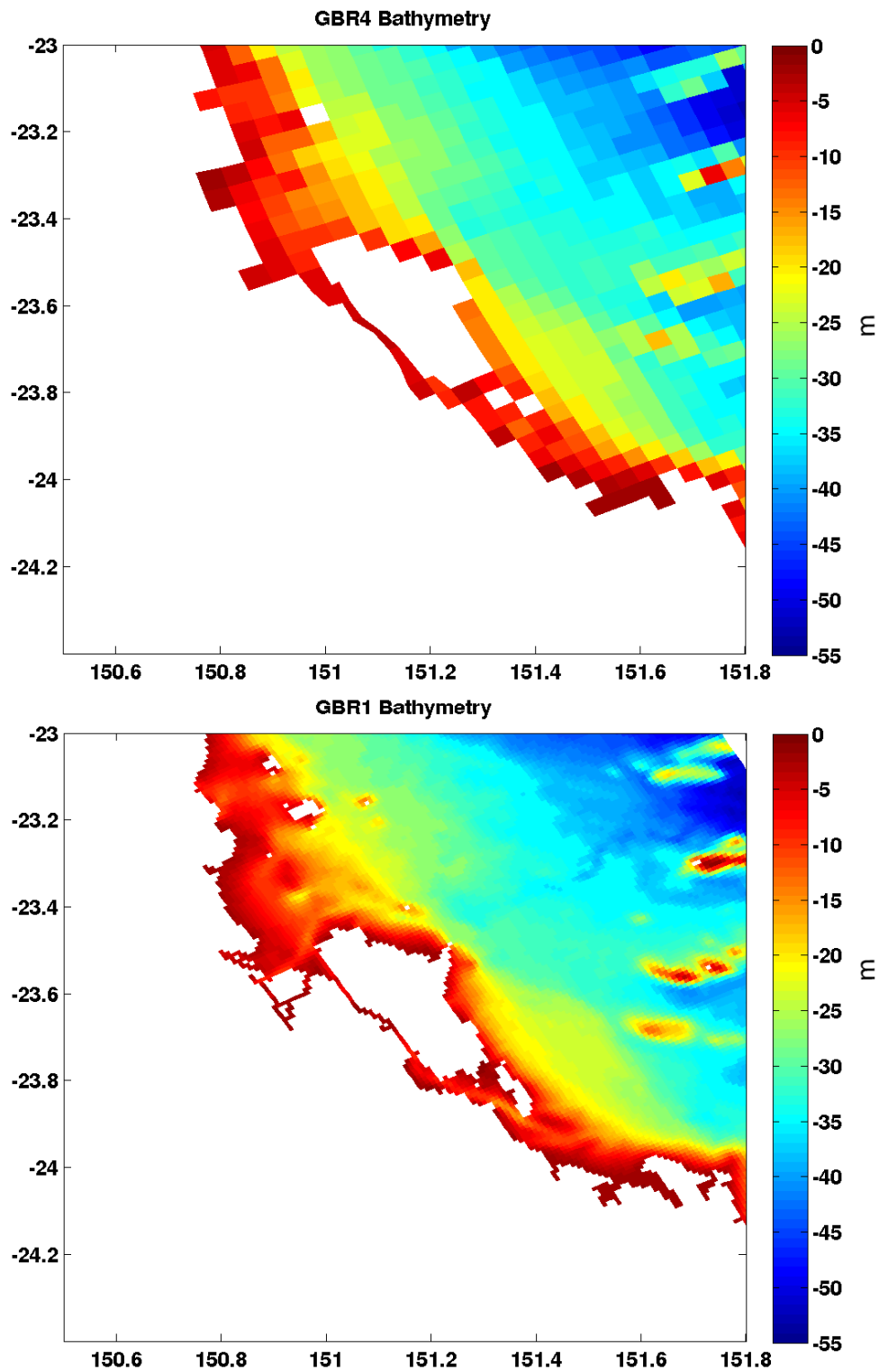


Figure 5.5.59. GBR4 (top) and GBR1 (bottom) bathymetry around the Fitzroy River region.

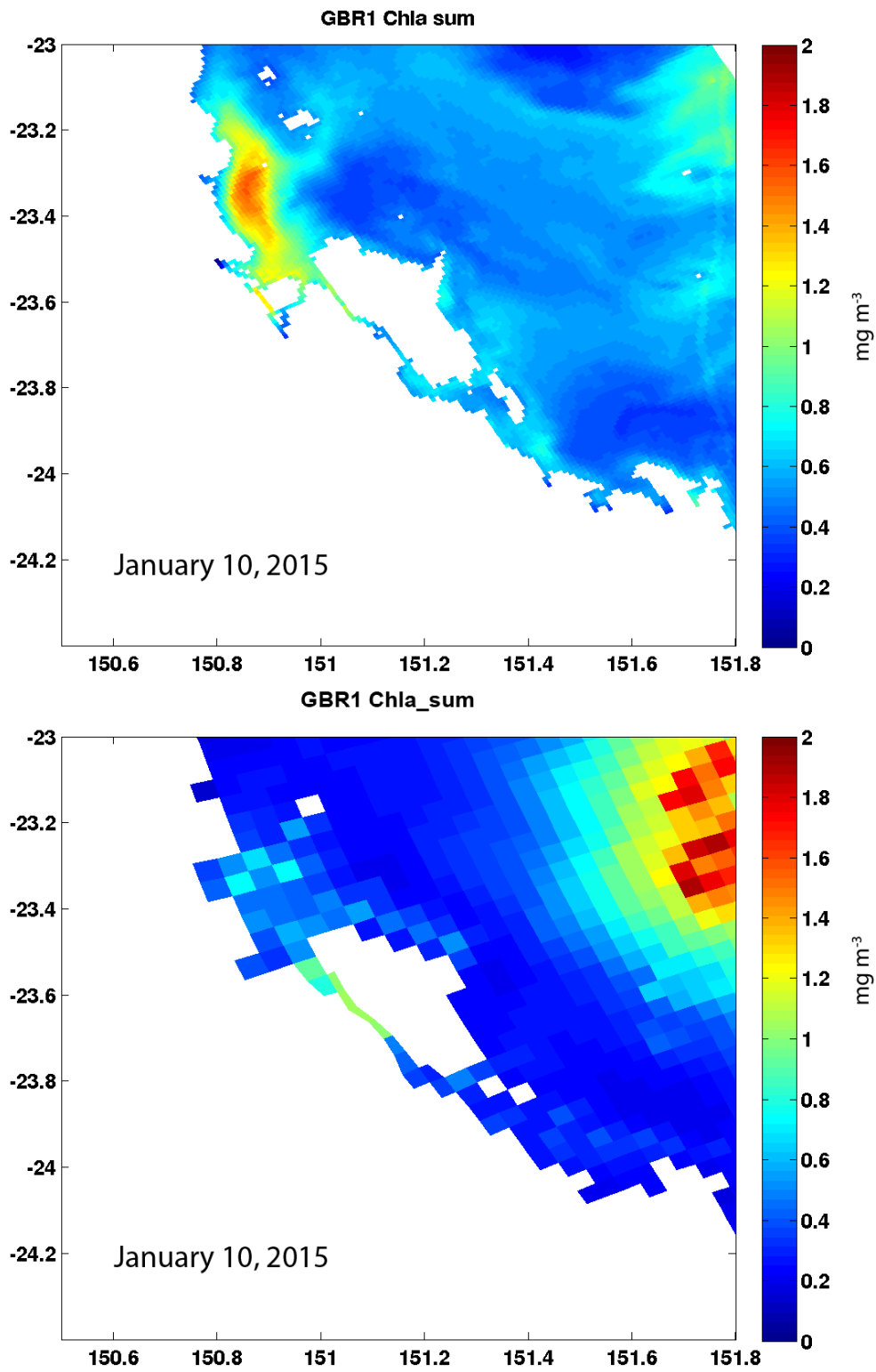


Figure 4.4.60. GBR4 (top) and GBR1 (bottom) simulated surface chlorophyll a on January 10th, around the Fitzroy River region.

The Fitzroy region simulated chlorophyll a (Fig. 5.5.60) shows larger differences than in the Burdekin region. A maximum chlorophyll a (1.5 mg m^{-3}) is located just north of the Fitzroy River mouth in GBR1, while GBR4 only produces 0.8 mg m^{-3} chlorophyll a over a much smaller area. Over the reef, GBR4 produces higher chlorophyll a than GBR1.

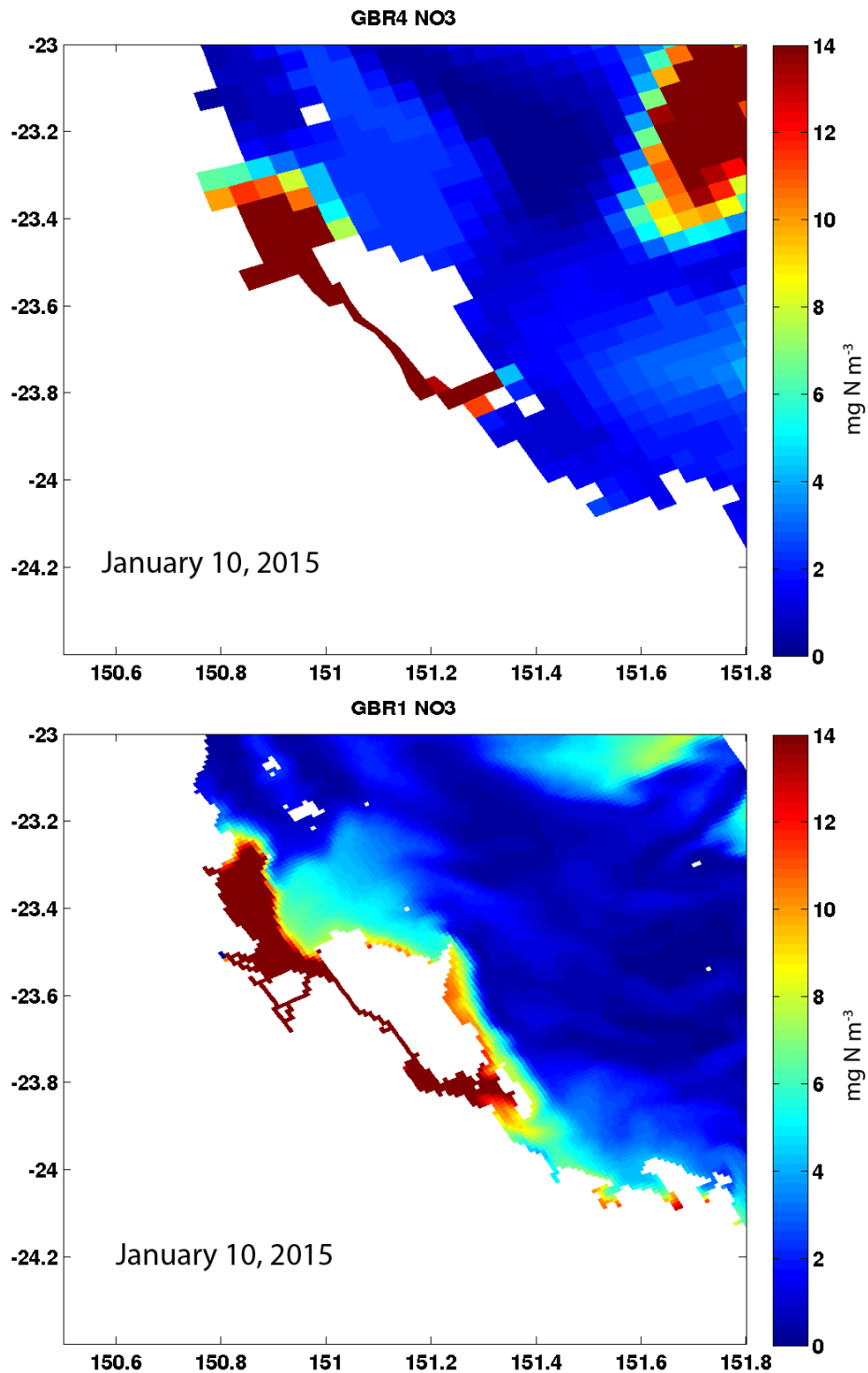


Figure 5.5.61. GBR4 (top) and GBR1 (bottom) simulated surface nitrate on January 10th, in the Fitzroy River region.

The differences in simulated chlorophyll a can be explained by the differences in nitrate (Fig. 5.5.61). A significant upwelling event led to high nitrate concentrations at the shelf edge in GBR4 (in a form of large patch > 50 km wide), while this patch is absent in GBR1. Thus the supply of nutrient following upwelling events is quite different in the two configurations. This is not surprising, as one would expect the continental slope and deep channels to be better resolved in GBR1, leading to different pathways and structures in water circulation.

Along the coastline, the size of the high nitrate area is similar in both configurations, but the gradient from high to low concentrations is smoother with more structure in GBR1. In the south of the region, the better resolved bays display more nitrate in GBR1.

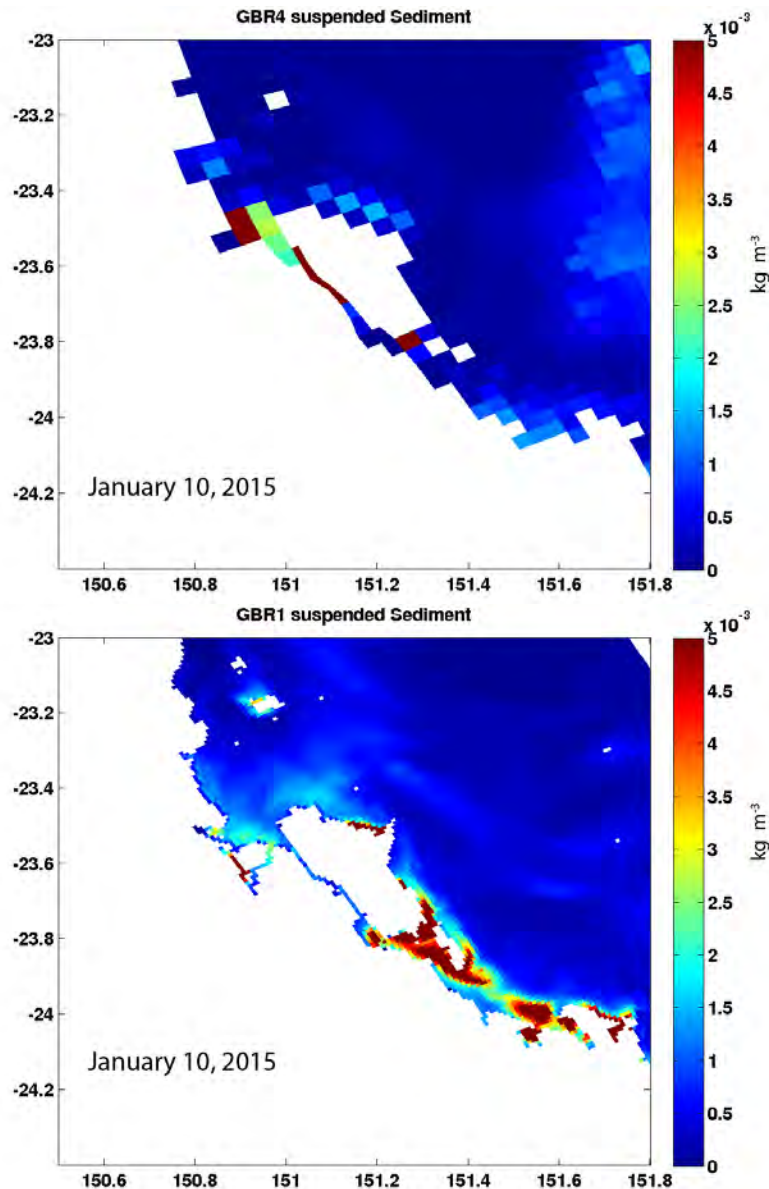


Figure 5.5.62. GBR4 (top) and GBR1 (bottom) simulated surface Ecological Fine Sediment Inorganic (Finesed + Mud) on January 10th, in the Fitzroy River region.

In the Fitzroy region, the sediment re-suspension above the reef (Fig. 5.5.62) is not larger in GBR1 than GBR4 (in line with the difference in upwelling explanation suggested above). On the other hand, the coastal bands of suspended sediment are different between the two configurations. GBR4 simulates high suspended sediment concentrations at the mouth of the Fitzroy River, and in a small area (~ 4 km wide) just south of Curtis Island, while GBR1 simulates area of high suspended sediment in a much larger region that extends south of Curtis Island. These differences result from the southern (main) entrance to Gladstone Harbour being represented by one grid cell with a diagonal width of 5.7 km that is 12.82 m deep in GBR4, while in GBR1 has a width of 7.1 km, and cells with depths of 13.3, 10.3, 6.3, 4.4 and 2.34 m.

Time series at Yongala

Time series of salinity, chlorophyll a, NO₃ and suspended sediment (Figs. 5.5.63 – 5.5.66) do not show major differences at the Yongala sampling site. Chlorophyll a concentration is higher at the surface in GBR1 than GBR4 with the inverse occurring at depth. This suggests a difference in vertical stratification and mixing, with the integrated biomass being equal in the two configurations.

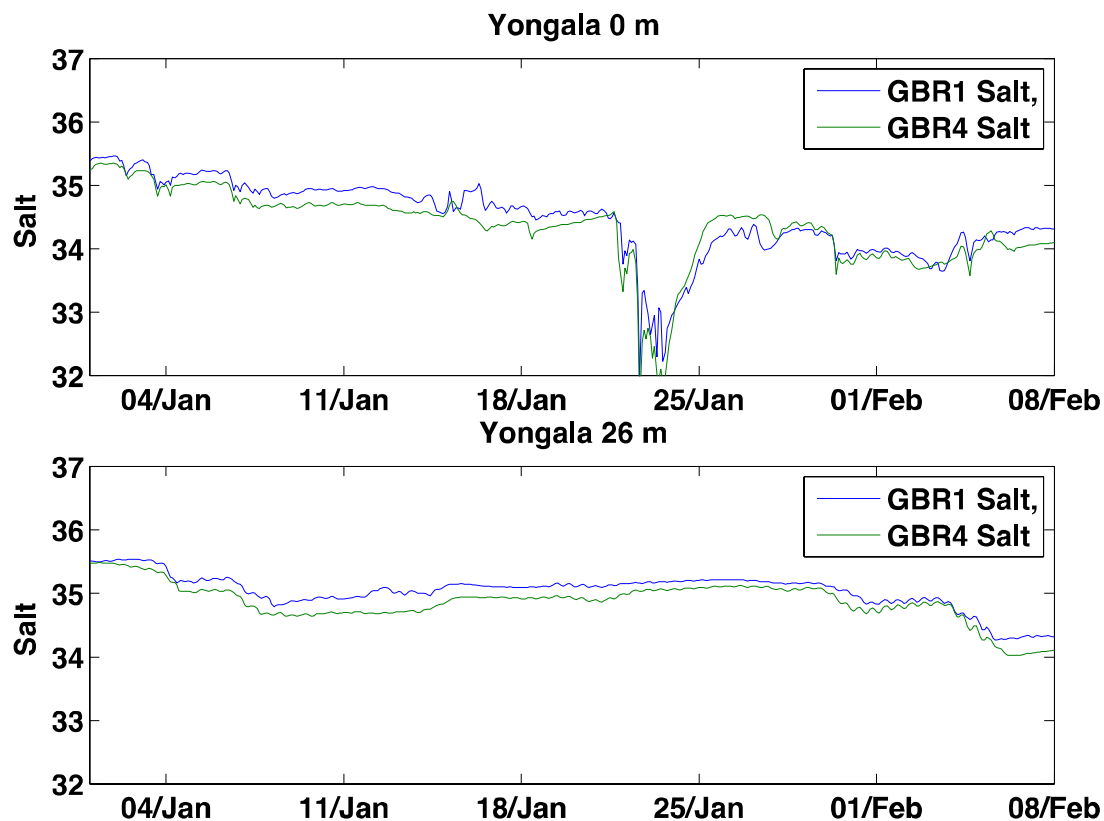


Figure 5.5.63. Times series of salinity at the Yongala sampling site, surface (top) and 26 m deep (bottom) for the GBR4 (green) and GBR1 (blue).

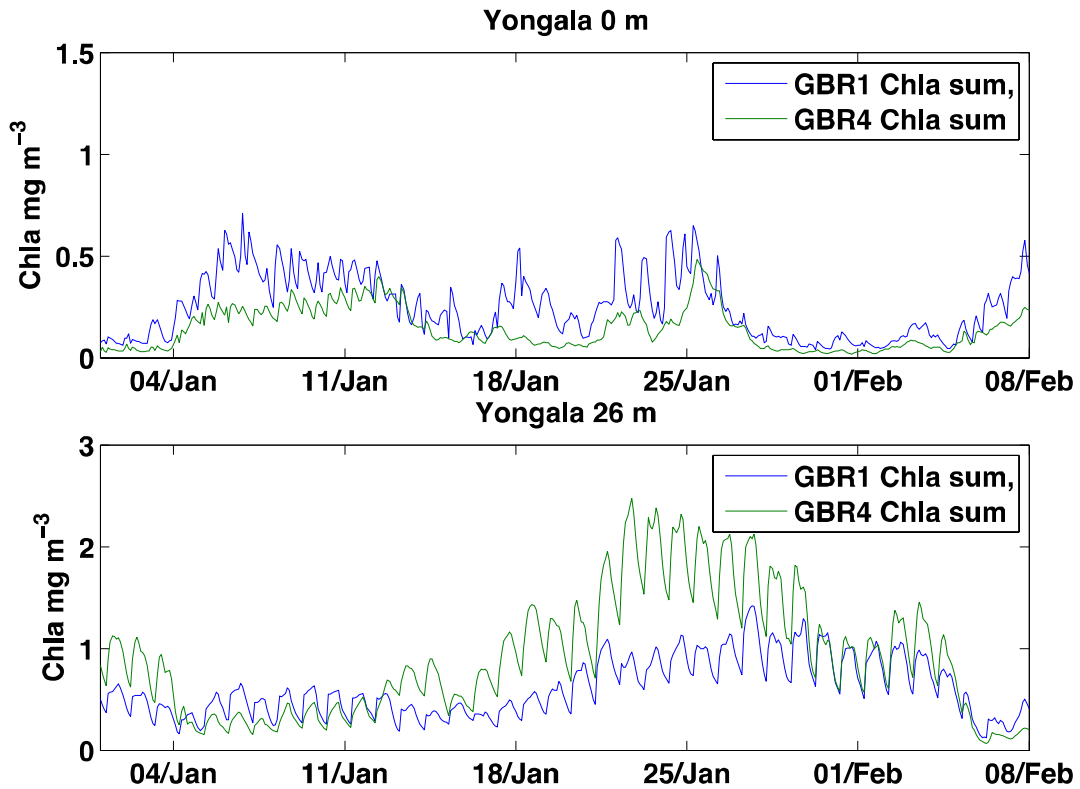


Figure 5.5.64. Times series of Chlorophyll-a sum at the Yongala sampling site, surface (top) and 26 m deep (bottom) for the GBR4 (green) and GBR1 (blue).

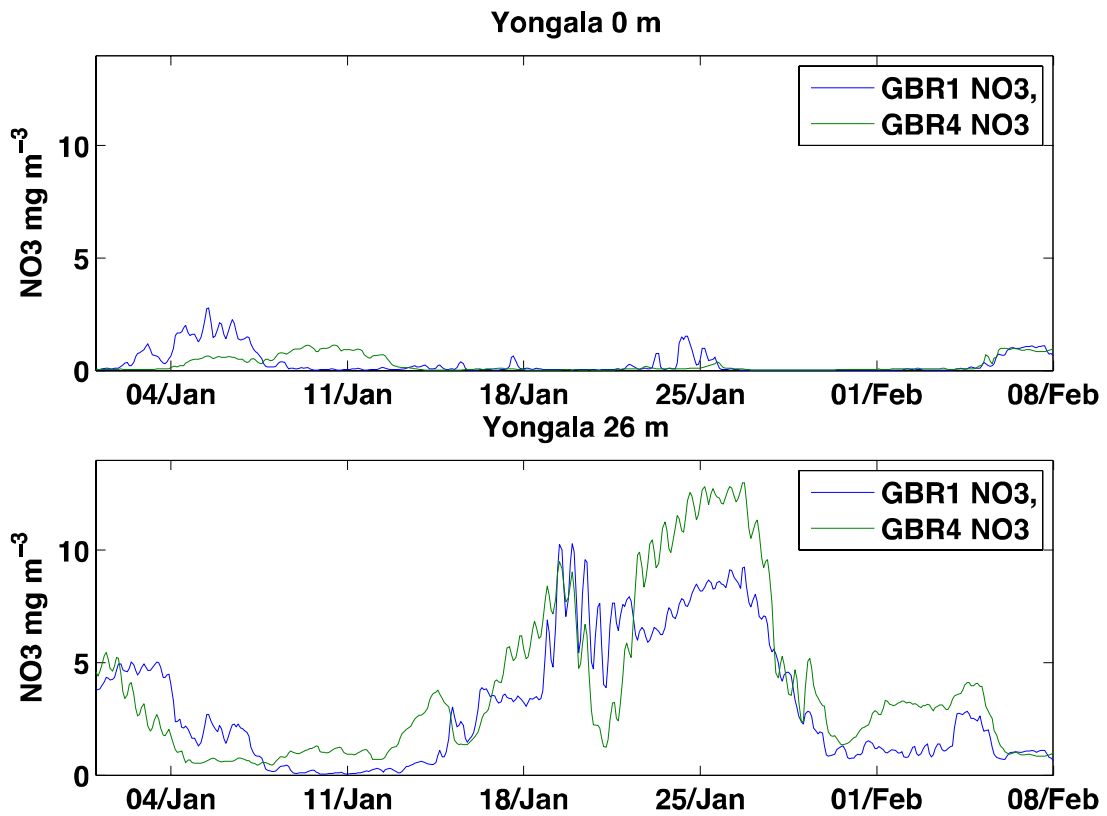


Figure 5.5.65. Times series of nitrate at the Yongala sampling site, surface (top) and 26 m deep (bottom) for the GBR4 (green) and GBR1 (blue).

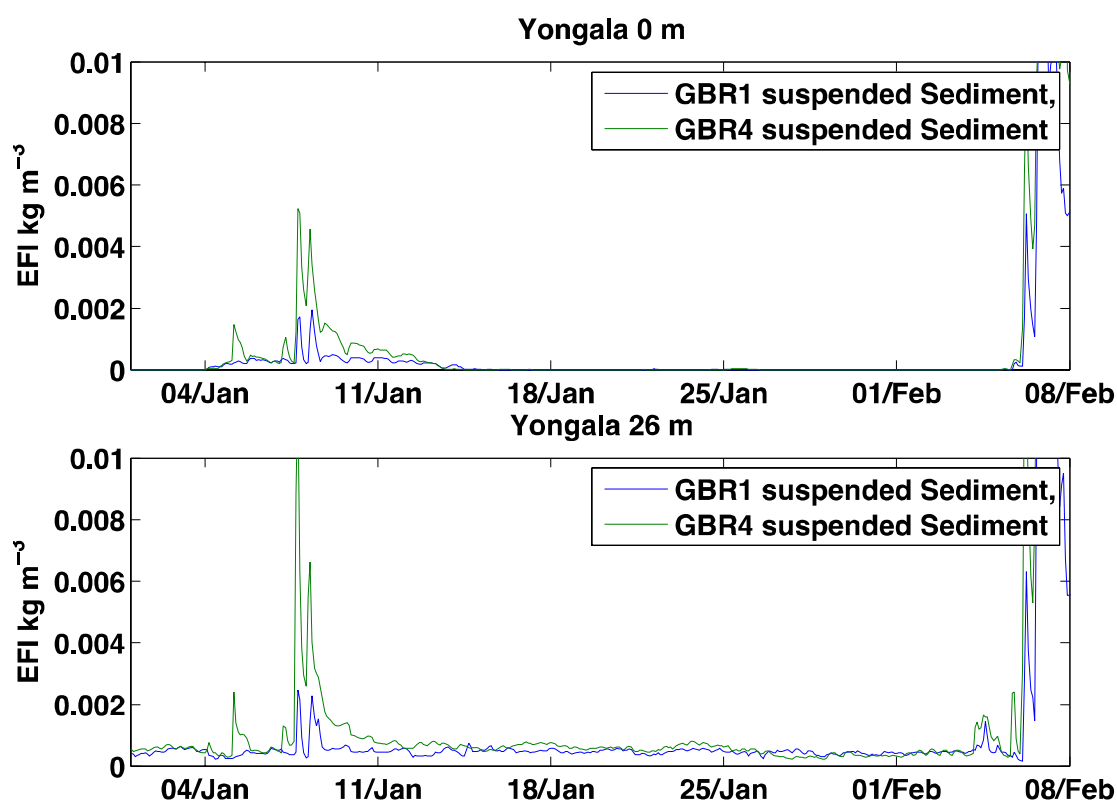


Figure 5.5.66. Times series of surface Ecological Fine Sediment Inorganic (Finesed) at the Yongala sampling site, surface (top) and 26 m deep (bottom) for the GBR4 (green) and GBR1 (blue).

Optical properties

The differences in biogeochemical state of the water column and bottom depth of the two configurations result in changes in the apparent optical properties. Here we consider in detail some of the optical properties in the Burdekin River region.

In the simulated true colour image (Fig. 5.5.67), the 16-fold increase in pixels, and better resolution of coastlines and bathymetry, produces interesting differences. Notable improvements in GBR1 are a more coherent, thinner and longer Burdekin River plume (Fig. 5.5.68), the more obvious presence of the Haughton River plume (with the first pixel being dark green, and the next a beige), and more detailed circulation-driven structure evident in the suspended colour. GBR1 shows greater resuspension of sediment along the coast (and especially near Cape Bowling Green) and on the offshore reefs, a result primarily of GBR1 better resolving shallower regions, as described above. Resuspension above the offshore reefs results in a brighter surface colour in the GBR1 (note the image is one day before the new moon, and halfway between the high high tide and the high low tide of the day resulting in near maximum tidal currents of the month).

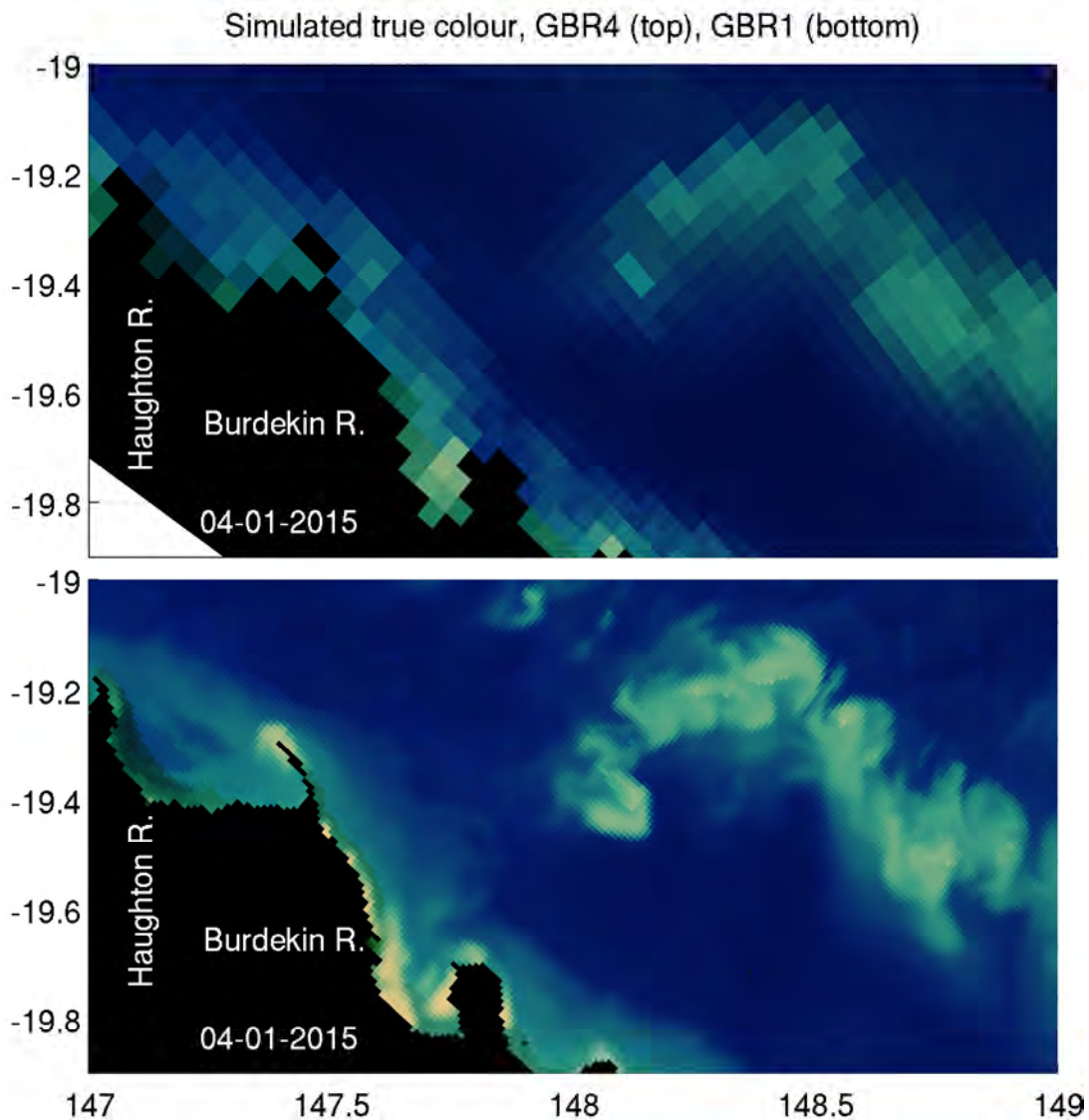


Figure 5.5.67. Simulated true colour on the 4 Jan 2015 from GBR4 (top) and GBR1 (bottom). The location of the Burdekin River entrance is shown. GBR1 has 5 grid cells that are wet in the mouth of the Burdekin that appear as land in the GBR1. True colour is rendered from a scaled Red/Green/Blue colour map using the remote-sensing reflectance at 645, 555 and 470 nm, following the MODIS protocols (Baird et al., 2016).

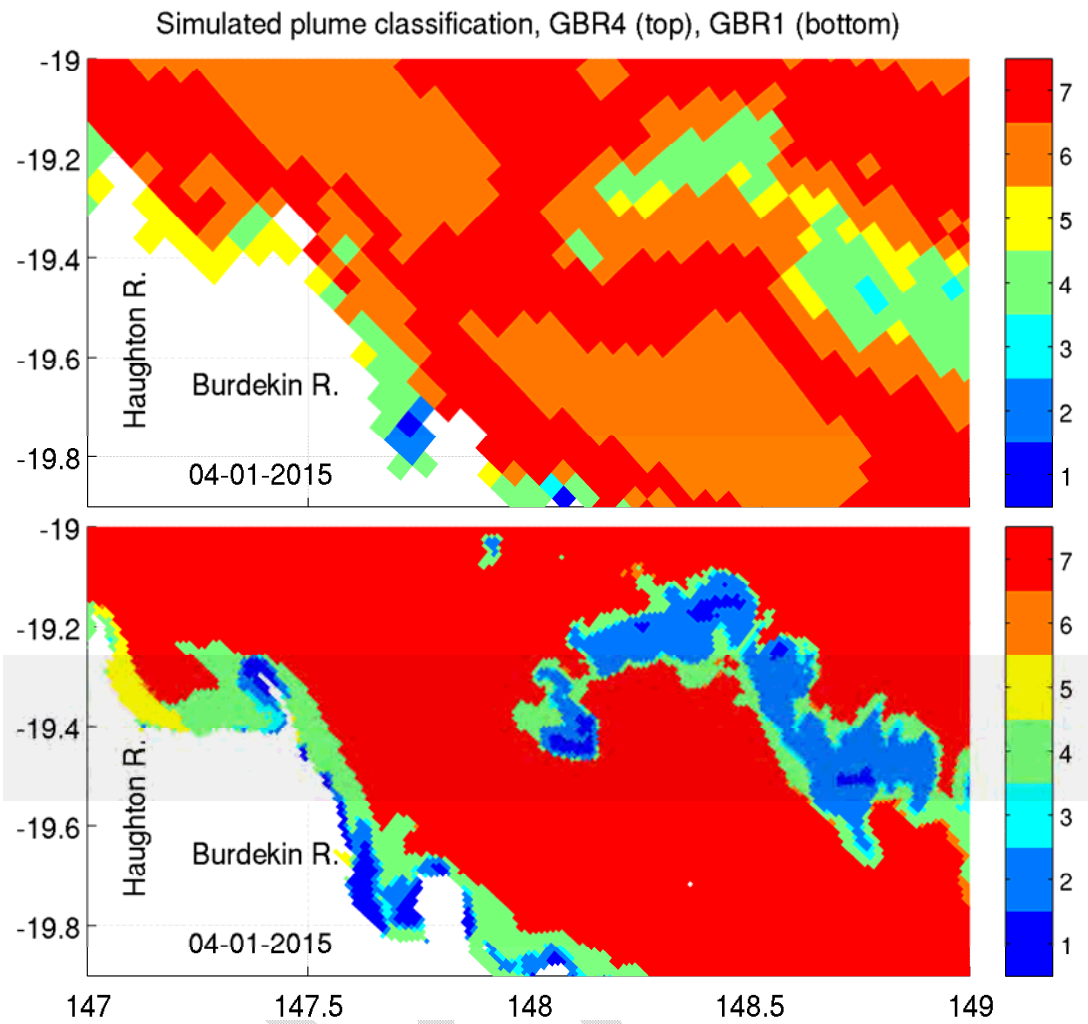


Figure 5.5.68. Plume classification on the 4 Jan 2015 from the 4 km model (top) and 1 km model (bottom). The location of the Burdekin River entrance is shown with the 1 km model have 4 grid cells that are wet in the mouth of the Burdekin that appear as land in the 4 km model. Plume classification are categorical based on spectral mapping comparison with the plume classification of Delvin (Baird et al., 2016).

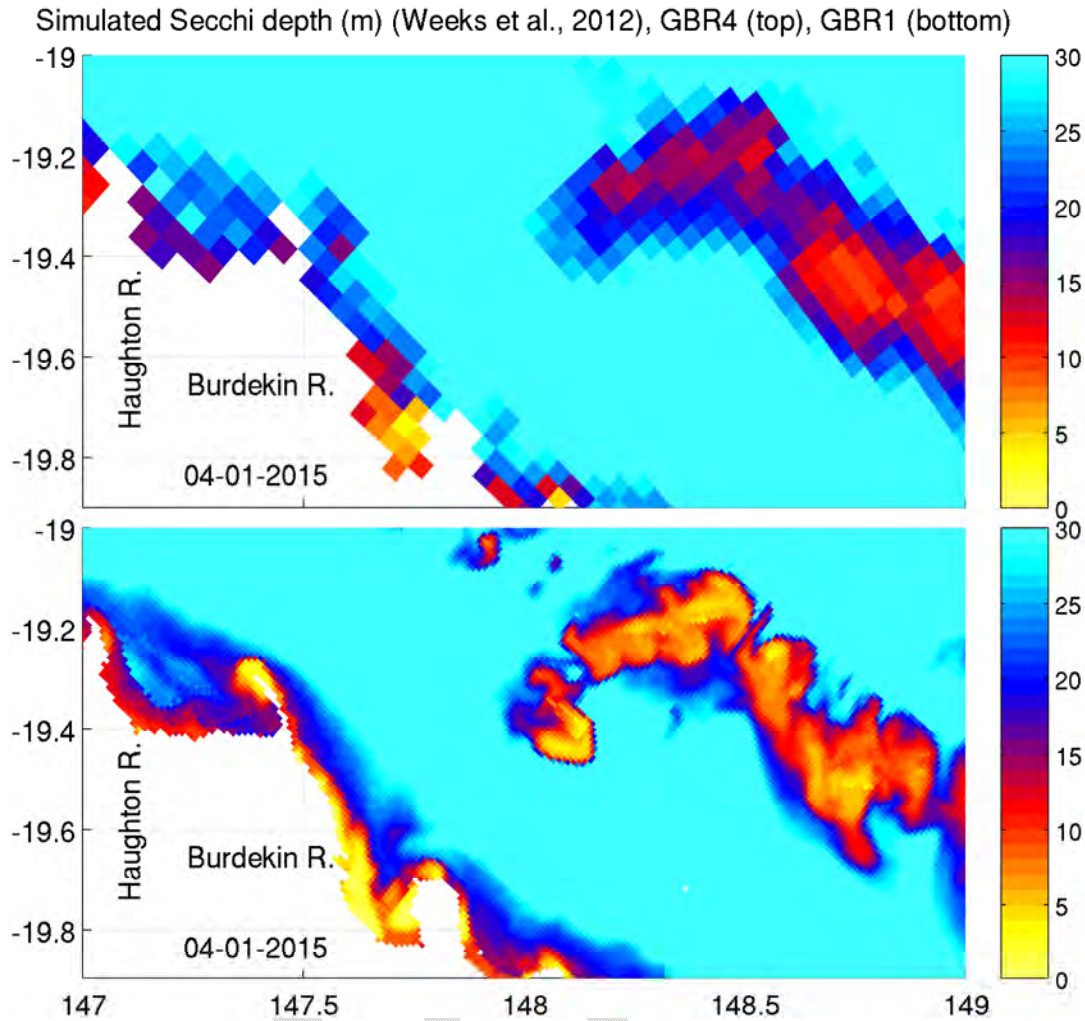


Figure 5.5.69. Simulated Secchi depth determined using simulated remote-sensing reflectance at 488 nm, and the Weeks et al., (2012) correction for the GBR on the 4 Jan 2015 from the GBR4 (top) and GBR1 (bottom). To interpret this figure, Secchi depth estimated here is identically equivalent to the remotely observed GBR-corrected Secchi depths, although may differ from the both the simulated Secchi depth, or the in situ observed depth.

Accompanying the greater surface reflectance in GBR1 is a reduction in Secchi depth (Fig. 5.5.69), although Secchi depth remains greater than 10 m for most of the region. More complex is the changes in the daily dose of photons reaching the bottom, as this changes with both water column properties and bottom bathymetry (Fig. 5.5.70). The most significant change in bottom light is in the inshore strip that is represented as land in GBR4, but is wet in GBR1. As a result, it is expected that over time GBR1 will develop a larger area of seagrass, especially *Zostera*, than captured in GBR4 model. On the offshore reefs there is also a greater area of bottom for which benthic production will be significant.

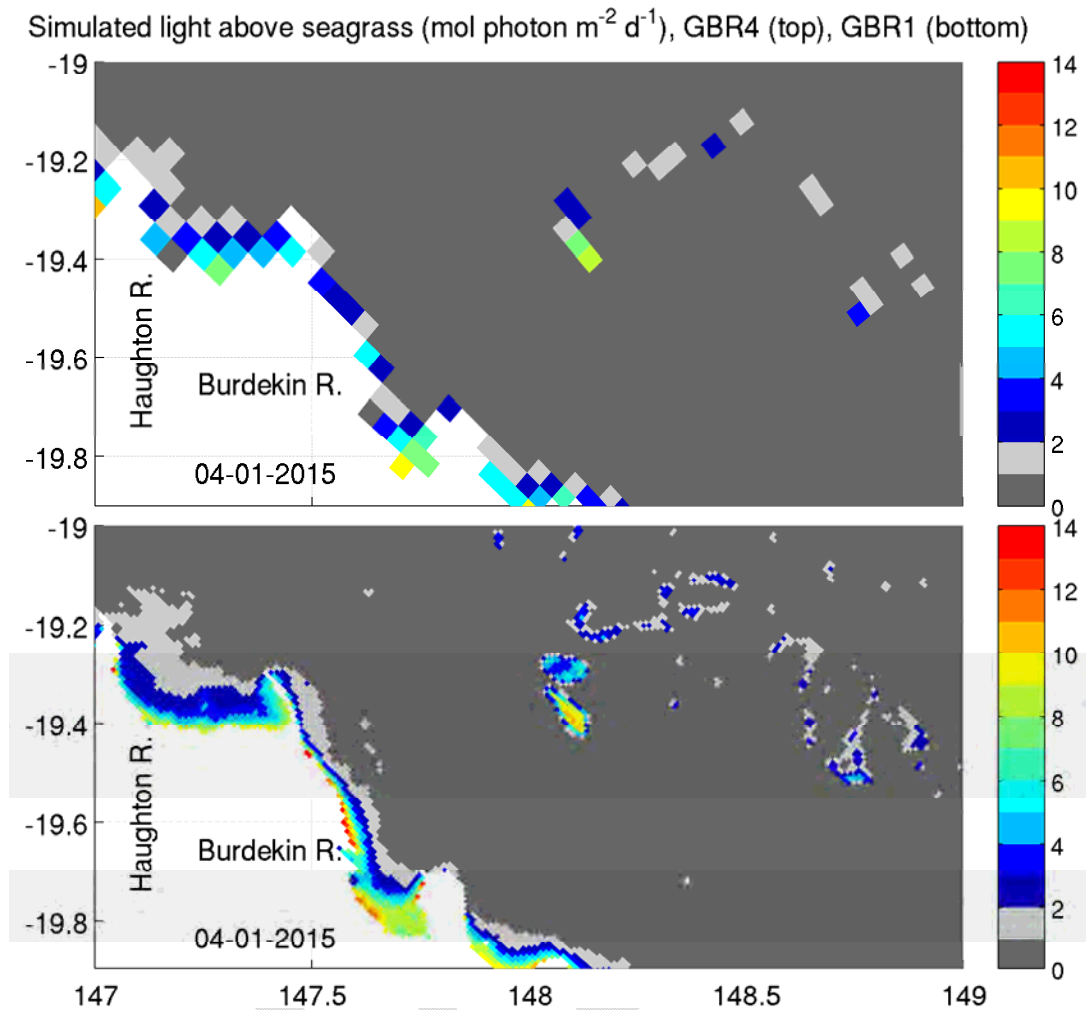


Figure 5.5.70. Simulated running monthly mean bottom light (above the seagrass canopy) on the 4 Jan 2015 from GBR4 (top) and GBR1 (bottom). Grey areas have a daily dose of photons $< 2 \text{ mol photon m}^{-2}$, and will have a negative net seagrass growth. Dark blue areas have sufficient light for *Halophila*, but not *Zostera*. Above a daily dose of $4 \text{ mol photon m}^{-2}$ (sky blue to red) both seagrass types are viable. Significant areas that are viable for seagrass in GBR1 are land in GBR4, illustrating the improvement in GBR1 for modelling seagrass due to the better resolved coastline.

Summary.

The 1 km resolution coupled hydrodynamic, sediment, biogeochemical model configuration of the entire Queensland coast (GBR1) is running in near-real time, generating an archive from 28th December 2014 onwards. The finer resolution has produced a variety of features that are clear improvements on the GBR4, and will be of added value when considering coastal processes, and to provide biogeochemical boundary conditions for RECOM.

The most obvious improvements for biogeochemical representation is the improved resolution of shallow regions, due to either resolving the shallowest components of the offshore reefs, or simply improving the coastline, and thus better resolving bays, inlets etc. For some iconic benthic communities on the GBR, such as seagrass meadows, initial estimates

suggest that GBR1 has approximately double the viable area compared to GBR4. The resolution of sub-mesoscale features such as island wakes, headland and frontal eddies and river plumes noted earlier in the report can also be seen in the brief analysis above to drive biological responses.

Most biogeochemical processes have been parameterized independent of grid resolution, as they needed to be implemented across scales (including RECOM). For example, the light-dependence of seagrass growth was parameterized according to physiological studies, not to match directly observations. Thus, as mentioned above, because GBR4 does not resolve all shallow regions, the bottom light levels are too low, and the GBR4 seagrass areal extent is smaller than observed. But with improved resolution, *for the same parameterization of seagrass growth*, it is anticipated that the areal extent will increase to better match observations.

A longer run, and more dedicated skill assessment, is required to quantitatively assess the improvements in GBR1. Such an assessment may identify some processes that were not resolved in the GBR4 and thus were implicitly included in the parameterisation, but are now being resolved in the GBR1 (such as higher resuspension rate to account for a lack of shallow regions and topographic steering acceleration of bottom currents). In these cases, some adjustment of model parameters may improve the model skill.

Comparison of the GBR1 model to in-situ observations remains to be undertaken. It should be noted that the observations currently collected are not adequate to assess a high resolution model such as GBR1 that contains an abundance of sub-mesoscale structure. This was evident in the hydrodynamic assessment of the 1 km model (Section 5.2), where although high frequency time series data were available from moored instruments, comparison was confounded by large small scale gradients from submesoscale structure. Traditional metrics for model validation are no longer adequate at these resolutions when small scale features become more prevalent in the solutions (Ebert, 2008) because small offsets in position of a feature are penalized as severely with these metrics as complete absence of a feature. This problem has long been acknowledged in the meteorology community and alternative methods developed to assess skill. Similar effort is required to be invested in similar techniques in order to confidently assess GBR1 BGC, most likely based on categorical metrics using neighbourhood techniques that target specific aspects of predictability. This is a research question that goes beyond the scope of eReefs, but requires attention in the future in order to produce meaningful quantitative metrics to place bounds on predictability of GBR1.

While the skill assessment of sub mesoscale biogeochemical features is a research question beyond the scope of eReefs, it is worth highlighting that the optical and biogeochemical data assimilation developments in eReefs allows remotely-sensed products to be used in a more robust manner than previously possible (Baird et al., 2016). On cloud-free days remote-sensing is the only means to resolve the extent of sub-mesoscale features. Further should we hope to predict sub-mesoscale biogeochemical features, this will require data assimilation for which much of the initial system development work has already been completed.

Finally, the logistics of running GBR1 is challenging. The hydrodynamic simulations run at 3:1 on a 20 processor system (i.e. one 24 hour day to run 3 model days), while the biogeochemical simulations run at 10:1. As a result we do not have a long hindcast to assess model

performance, and to improve parameterisations. But once a year-long hydrodynamic archive exists, biogeochemical experiments to assess and improve GBR1 will be possible.

5.5.12 Demonstration scenarios

The eReefs biogeochemical model has been run using two different catchment forcings:

1. Gauged flows with constant particulate and dissolved loads using the Furnas relationship.
2. Gauged flows with particulate and dissolved loads determined from the SOURCE catchment modelling.

Analysis of the difference between model state under these two estimates of catchment forcings provides both an indication of the sensitivity of the model within the bounds of uncertainty in the catchment loads, and a prototype analysis of how more detailed scenario analysis may be undertaken. Both scenarios are run from the same initial condition (a spin-up of 4 years of the constant concentration run) with output analysed after running a further 3.5 years.

At the scale of the central GBR, the surface chlorophyll concentration varies from 1 mg m^{-3} inshore to virtually zero offshore. As the simulations have identical forcing except for their catchment loads, the offshore chlorophyll concentrations are low and identical (Fig. 5.5.71). The greatest difference is in Upstart Bay into which the Burdekin River discharges, where the SOURCE catchment model loads result in a 0.5 mg m^{-3} smaller surface chlorophyll concentration, a result of lower loads.

Interestingly, the SOURCE catchment has a higher load of suspended solids, although this elevated surface concentration is only seen within 10 km of the coast, due to the elevated surface signal sinking. DIN is lower in the SOURCE simulation near the coast due to lower loads, but with elevated suspended solids resulting in greater light limitation, the smaller DIN loads actually penetrate further offshore, resulting in a higher concentration. Nonetheless, as noted above, chlorophyll concentration is lower throughout Upstart Bay. This dynamic, although not unexpected, demonstrates the important role of a model simulations in understanding the non-linear dynamic between loads and receiving water response.

An understanding of the ecosystem response can be gauged by studying the water column optical properties (Fig. 5.5.72 and 5.5.73), or perhaps more difficult to anticipate, the macrophyte biomass and bottom light. In Upstart Bay there is more light reaching the bottom in the SOURCE catchment simulation, resulting in more seagrass, but less seaweed. Interestingly this trend is reversed near river mouths further south, illustrating the sensitivity of the coastal waters to catchment discharges.

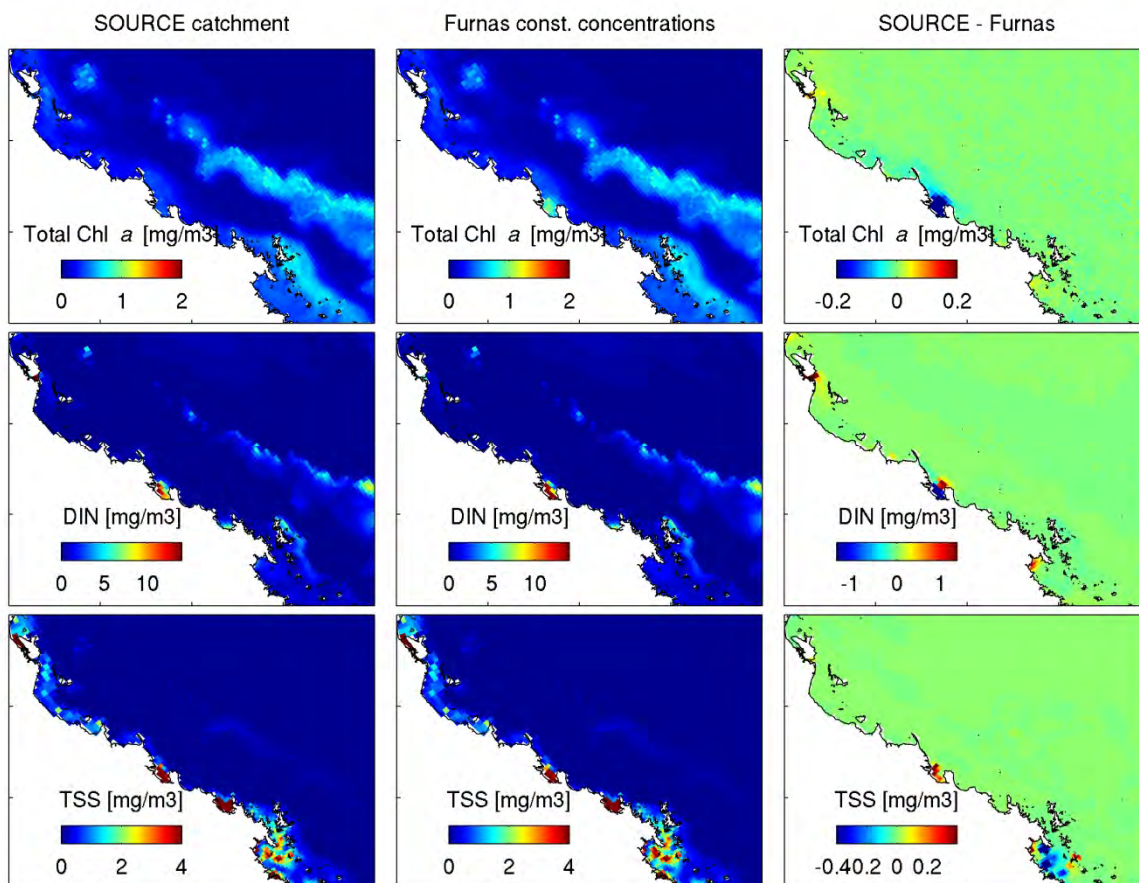


Figure 5.5.71. The total chlorophyll concentration (top row), dissolved inorganic nitrogen concentration (middle row) and total suspended solids (bottom row) for loads estimated using the catchment model (left column), the gauged flows with constant particulate and dissolved concentrations (middle row), and the difference between the two (right column) at the surface on the 1st July 2014. That is the right column is the impact (positive red, negative blue) of using the catchment model instead of the constant constituents.

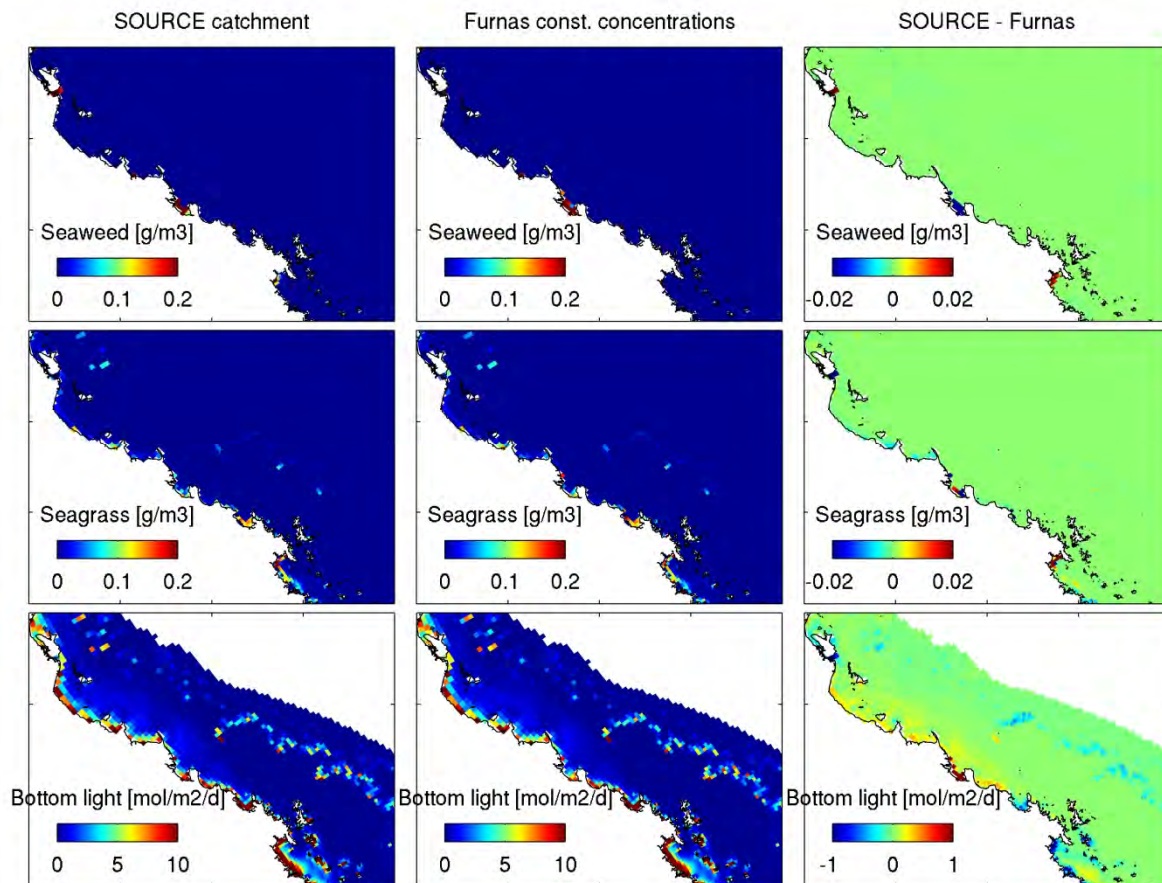


Figure 5.5.72. The seaweed biomass (top row), seagrass biomass (middle row) and running monthly mean bottom light (bottom row) for loads estimated using the catchment model (left column), the gauged flows with constant particulate and dissolved concentrations (middle row), and the difference between the two (right column) at the surface on the 1st July 2014. That is the right column is the impact (positive red, negative blue) of using the catchment model instead of the constant constituents.

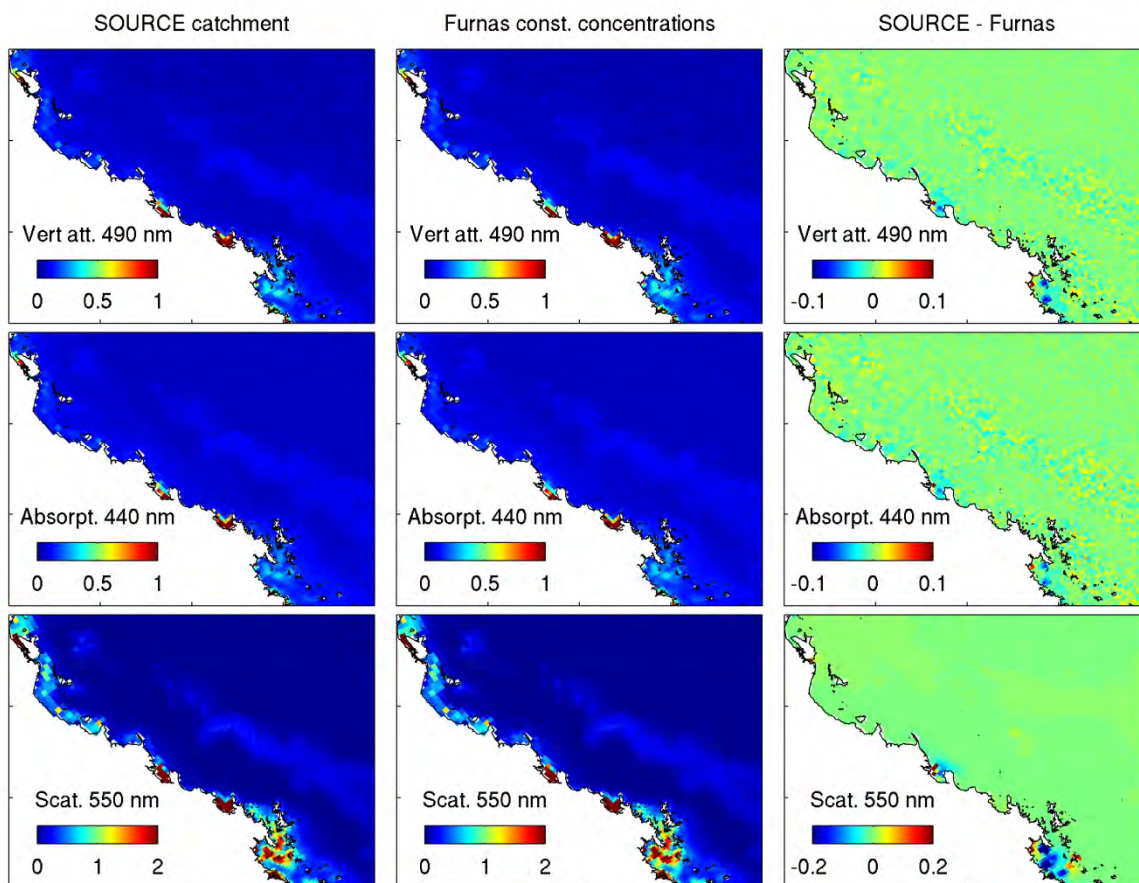


Figure 5.5.73. The vertical attenuation of light at 490 nm (top row), total absorption at 440 nm (middle row) and total scattering at 550 nm (bottom row) for loads estimated using the catchment model (left column), the gauged flows with constant particulate and dissolved concentrations (middle row), and the difference between the two (right column) at the surface on the 1st July 2014. That is the right column is the impact (positive red, negative blue) of using the catchment model instead of the constant constituents.

5.6 RECOM

The validation of RECOM is accomplished by comparing a RECOM implementation of a case study with previously optimized and calibrated models of the same region. We choose two regions as the focus of this validation exercise which have been subject to development of calibrated models under separate projects:

1. The Fitzroy Estuary, developed within the CRC for Coastal Zone, Estuary and Waterway Management in 2006.
2. Heron Island, developed within the Ocean Acidification component of the ACCSP (Australian Climate Change Science Program) project.

The approach to validation is to generate a hydrodynamic-sediment-wave-BGC model using the RECOM infrastructure, configured using the RECOM default parameterization, and compare the results to the previously optimized model to gauge the skill of the RECOM application. The two priority areas are considered in turn. In addition, a demonstration region around the Whitsunday Islands is performed to demonstrate the utility of the system. This application is associated with limited validation.

5.6.1 Fitzroy Estuary

The Fitzroy River, located on the Tropic of Capricorn and running past the city of Rockhampton, rivals the Burdekin River as the single largest terrestrial source of sediments and nutrients to the Great Barrier Reef Lagoon (Robson and Dourdet, 2015). As such, the Fitzroy Estuary and Keppel Bay (into which the estuary discharges) have been the focus of intensive measurement and modelling activities over many years (e.g. van Woesik, 1991; Webster et al., 2003; Douglas et al., 2005; Ford et al., 2005; Quin et al., 2007; Ryan et al., 2007; Radke et al. 2010; Webster and Ford, 2010; Jones and Berkelmans, 2014). Considerable expert effort was invested into the development, calibration, validation and subsequent refinement of a detailed local model for this system between 2003 and 2013 while, in parallel, equal effort was invested in understanding and modelling sources of sediments and nutrients in the Fitzroy catchment (e.g. Fentie et al., 2005; Douglas et al., 2006; Cogle et al., 2006; Hughes and Croke, 2011; Carroll et al., 2012).

Receiving water modelling efforts included the initial development, calibration and validation of a coupled hydrodynamic-biogeochemical model for Fitzroy estuary, (Webster et al., 2003; Margvelashvili et al., 2003), the extension of this model into Keppel Bay with further validation (Herzfeld et al., 2006; Margvelashvili et al., 2006; Webster et al., 2006; Wild-Allen et al., 2006; Robson et al., 2008), its application to understanding carbon and nutrient budgets and cycling for the system (Douglas et al., 2005; Robson et al., 2006) application of the model with catchment models to simulate the effects of land management scenarios (Robson et al., 2006), use of satellite observations to improve the biogeochemical and sediment models (Robson and Brando, 2007; Brando et al., 2007; Cherukuru et al., 2008; Cherukuru et al., 2009; Margvelashvili et al., 2012), further validation of the model during an extreme flood event, and application to additional land-management scenarios (Robson and Brando, 2008), and the development and testing of data assimilation to improve parameterisation of the sediment model (Margvelashvili et al., 2013).

The Fitzroy Estuary and Keppel Bay constitute one of the most intensively studied regions of the Queensland coast. This, in combination with the complex bathymetry, extensive mudflats and coastal creeks, extreme flows and tidal ranges in the system make it an ideal case study and stress test for the eReefs relocatable model, RECOM.

Unfortunately, routine in situ monitoring of Keppel Bay was discontinued in 2014 (Ryan Turner, Government of Queensland, pers. comm.) while RECOM forcing files are currently available only from December 2014 onwards, so we cannot directly compare results of the RECOM case study with field observations. Instead, we compare the RECOM implementation with the optimised EMS model application developed previously, and with the full-scale eReefs biogeochemical marine model.

5.6.1.1 Optimized model

The Fitzroy project was conducted within the Coastal CRC (http://www.ozcoasts.gov.au/search_data/crc_pubs.jsp) to assess suspended sediment and nutrient delivery through the Fitzroy Estuary and into the Great Barrier Reef lagoon. A hydrodynamic, sediment transport and BGC model were developed within this initiative. The model was further refined for wet-season conditions during subsequent CSIRO strategic projects and a project conducted for the Fitzroy Basin Association. Relevant publications describing these models are listed above, some of which can be downloaded from http://www.ozcoasts.gov.au/search_data/crc_rpts.jsp.

The methodology applied to these models and model code compatibility has changed considerably in the 8 years since these models were initially developed, and some alignment was necessary when resurrecting these models for RECOM comparisons. In particular, a series of nested domains were originally used in the hydrodynamic model to downscale to the local domain, whereas now the local domain may be nested directly within the GBR4 model. Meteorological forcing originally consisted of interpolation from land-based BoM observation sites, whereas the model now uses ACCESS-A model products for atmospheric forcing. The boundary temperature from GBR4 was also required to be reduced by 1.05°C for interior solutions to be comparable to observation (the original CRC model also used boundary scaling on both temperature and salinity). Apart from differences in the forcing products, and associated boundary condition forcing methodologies, the original parameterisation remains largely unchanged. The model grid and bathymetry is displayed in Fig. 5.6.1.

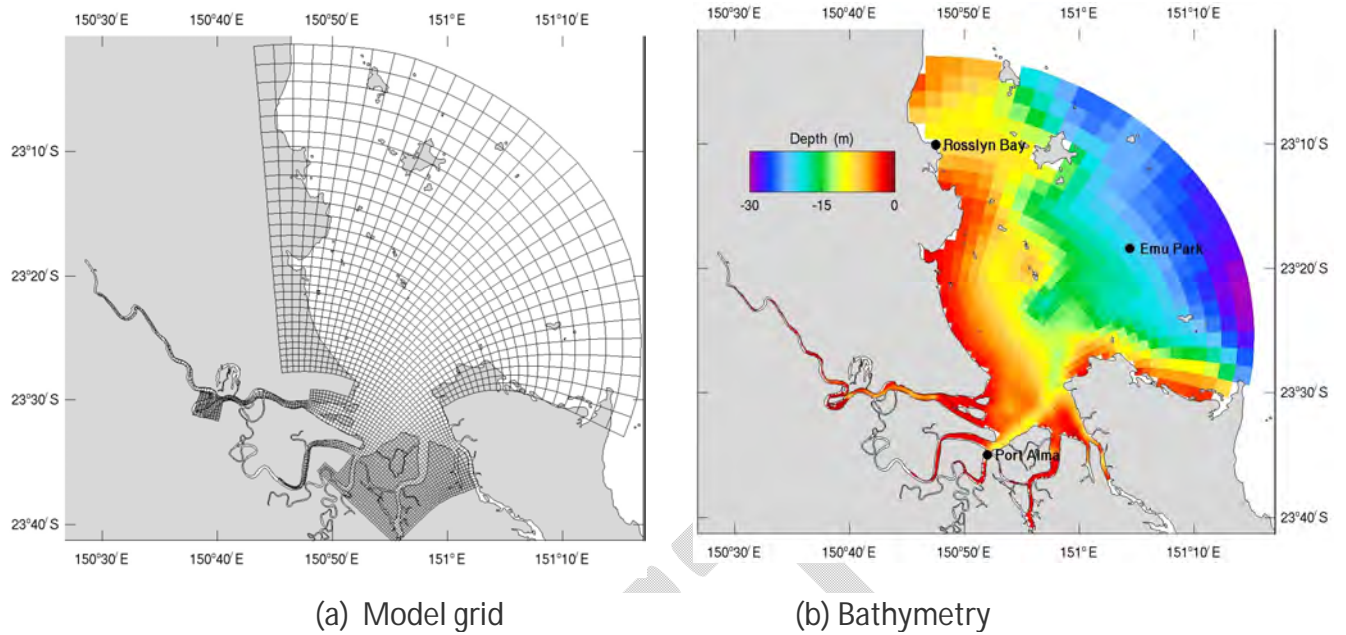


Figure 5.6.1. Model grid and bathymetry for Fitzroy region.

To verify that the altered forcing conditions still produced accurate solutions, the sea level was compared at Port Alma and Rosslyn Bay, and temperature was compared to the wave-rider buoy at Emu Park (Fig. 5.6.1 b). Results are shown in Figs. 5.6.2 – 5.6.4 for October–November 2014. The global model (OceanMAPS) and GBR4 model low frequency sea level and temperature are included for reference. It can be seen the Fitzroy model accurately reproduces the tidal, low frequency and temperature observations in the Bay, and moreover, does so with greater skill than either the global model or GBR4.

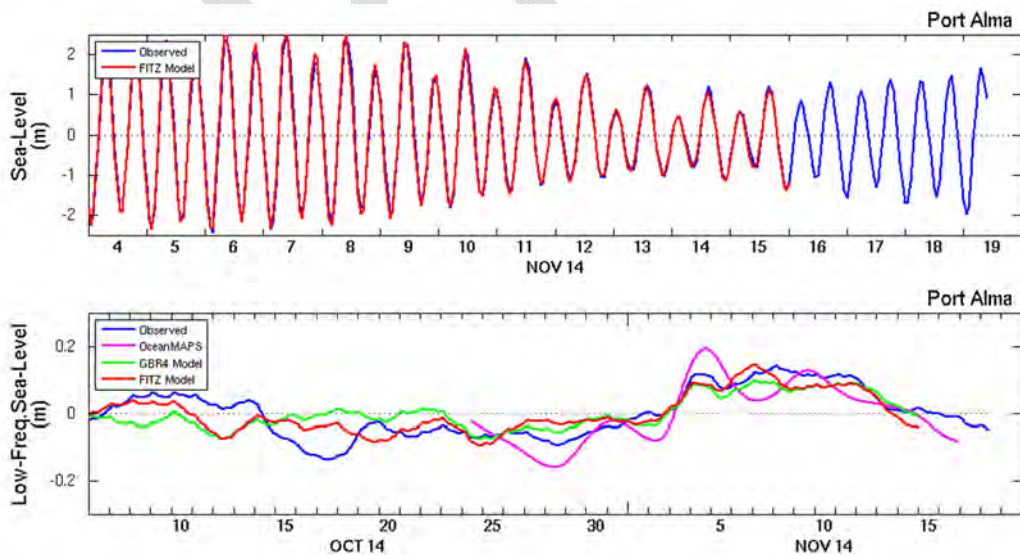


Figure 5.6.2. Sea level at Port Alma.

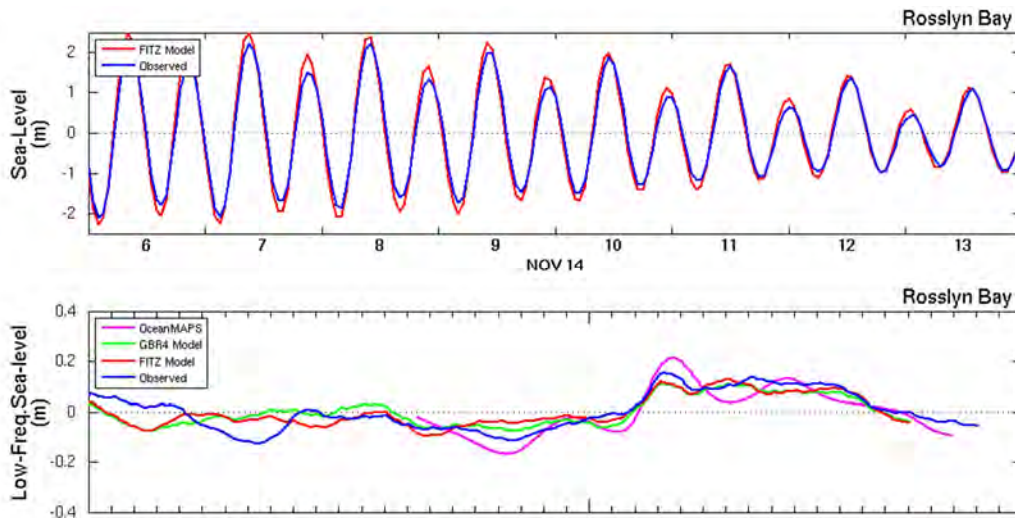


Figure 5.6.3. Sea level at Rossllyn Bay.

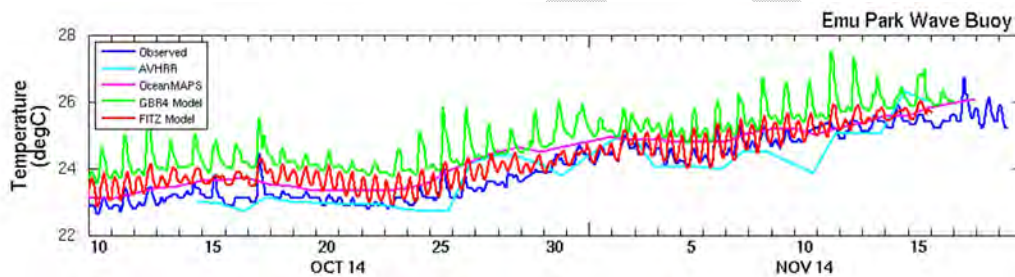


Figure 5.6.4. Sea level at Emu Park.

This Fitzroy model is operating in NRT and outputs can be viewed at:

<http://www.emg.cmar.csiro.au/www/en/emg/projects/Fitzroy/eReefs-NRT.html>

The model has also been updated to reflect improvements in the sediment dynamics and biogeochemical models, including:

- Updating the handling of light and optics to match that now used in the eReefs models;
- Adjustment of phytoplankton growth rate parameters to reflect improvements in the optical code (and to match the values being used in the GBR4 BGC model);
- Alteration of the handling of fine sediments in the biogeochemical code, including the removal of the distinction between flocculated and unflocculated sediments;
- Adjustment of phosphorus adsorption/desorption parameters in association with correction of bugs that existed in the phosphorus adsorption code in older versions of EMS;
- Updating of the seagrass model and parameters to match the more advanced seagrass model now available;
- Inclusion of *Trichodesmium*, as per the current GBR4 model.

This model is considered to be suitably accurate to benchmark a RECOM configuration against.

5.6.1.2 Grid development and set-up

An experienced user of RECOM was able to quickly set up the grid shown in Fig. 5.6.5 (top left), which resolves the shape of the Fitzroy River with a similar resolution to the previously developed optimised Fitzroy grid (top right), while also capturing key features of tidal creeks and islands around Keppel Bay. As with the optimised Fitzroy grid, the RECOM grid takes advantage of the curvilinear grid system to produce fine resolution within the estuary channel and near its mouth, expanding to larger cells near the ocean boundary. The estuary channel was slightly deepened in the RECOM application relative to its depth as indicated in the digital elevation map for the region to ensure smooth hydrodynamic model operation. In the optimised Fitzroy grid, the depth of the estuary channel was tuned to achieve an optimal calibration of the hydrodynamic model (Herzfeld et al., 2006). Both the RECOM application and the manually optimised Fitzroy grid allow much finer resolution to be achieved than is possible with the 'parent' (GBR4 or GBR1) eReefs marine model, within which the local models are nested.

RECOM was run at robustness level 6 (see Section 4.8.12) with catchment loads from the Fitzroy river matching those used in the final version of the hindcasting 4km-scale eReefs biogeochemical model (GBR4) and initial conditions and ocean boundary conditions derived from the 1km scale eReefs hydrodynamic model and GBR4 biogeochemical model. The run is preserved as RECOM exec ID 419. The model was run from 1 Jan 2015 through to 30 Jan 2015, a period which included a wet-season flow event.

The optimised Fitzroy grid was also nested within the eReefs GBR4 model, finally overcoming a major shortcoming of the original Fitzroy modelling, which was the need to assume fixed nutrient and chlorophyll concentrations at the open ocean boundary (Robson et al., 2008; Robson and Brando, 2008). For consistency, Fitzroy River loads were also specified as in the RECOM and GBR4 models.

5.6.1.3 Initialisation

Previous work (Douglas et al., 2006; Ryan et al., 2007; Webster and Ford, 2010) has shown that large quantities of particulate sediment and nutrient material are delivered to and deposited within the estuary mouth during every flood event and that these materials are subsequently redistributed within Keppel Bay over the course of months to years following a major flood event, with some proportion eventually exported to the Great Barrier Reef Lagoon (Radke et al., 2010; Robson and Brando, 2008). Unlike most of the Great Barrier Reef Lagoon, sediments at the mouth of the Fitzroy Estuary are muddy, store large quantities of nitrogen, phosphorus and carbon, and vary substantially from year to year depending on flow conditions in the preceding several years. Water-column sediment, nutrient and chlorophyll concentrations in the custom Fitzroy model are very sensitive to assumed initial sediment stores, and choosing appropriate values for these initial stores on the basis of recent field sampling (Radke et al., 2010) and model spin-up was a key pre-requisite to achieving satisfactory agreement with Keppel Bay water quality observations (Margvelashvili et al., 2006; Robson et al., 2006; Robson and Brando, 2008). Hydrodynamic initial conditions, by contrast, are rapidly 'forgotten' by the model.

In the current version of RECOM, initial conditions are set from the GBR4 model, which in turn are specified from large-scale Geoscience Australia maps based on observations made several years ago. It is not yet possible to specify customised initial conditions in RECOM. For this case study, therefore, we have compared (1) a standard implementation of RECOM with (2) the

optimised Fitzroy grid set up with the same initial conditions as the RECOM application, (3) the low-resolution 'parent' GBR4 model, and (4) the optimised Fitzroy grid set up with initial conditions derived from the original custom Fitzroy modelling, as described by Robson and Brando (2008) and Margvelashvili et al. (2013a).

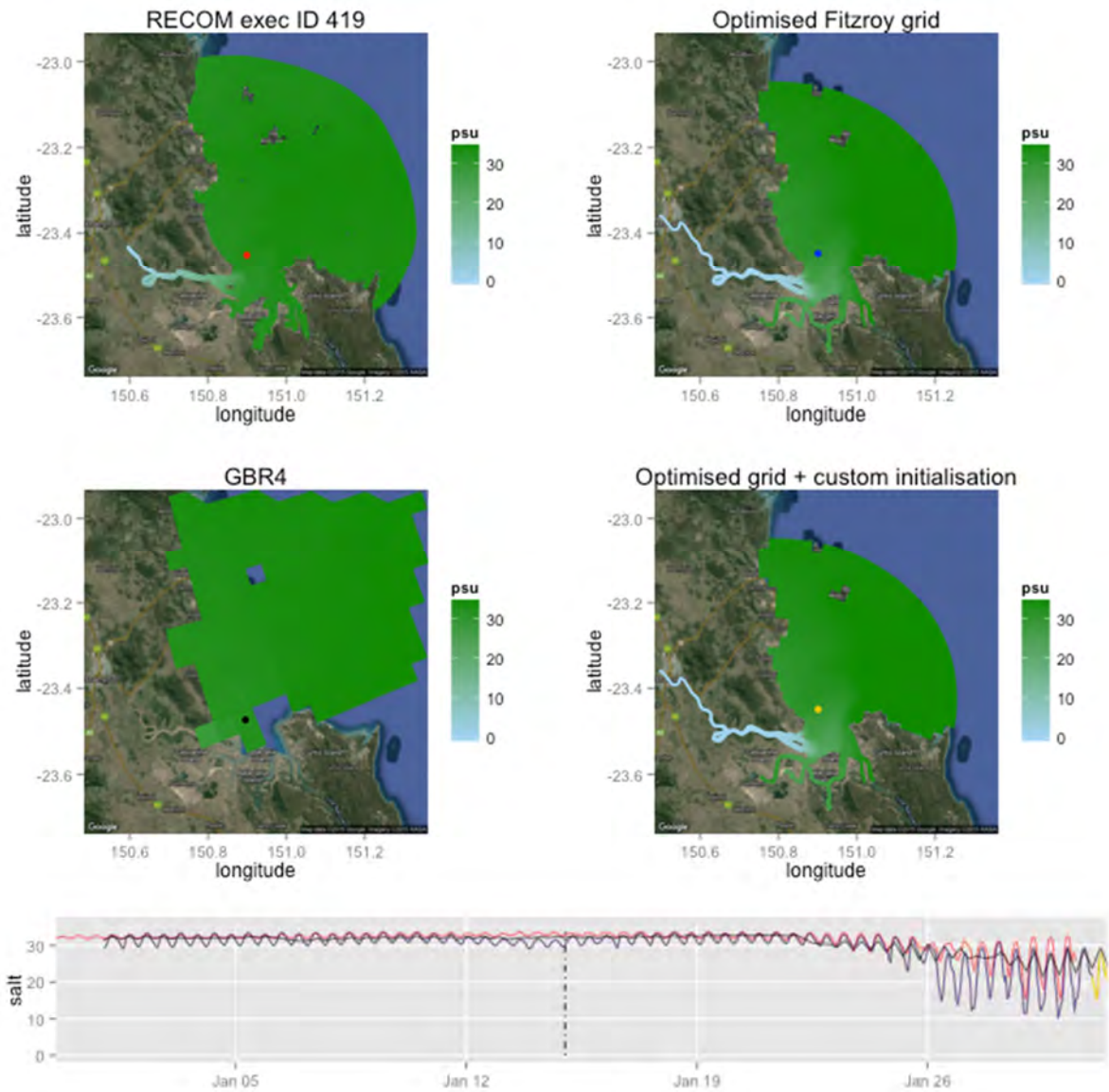


Figure 5.6.5. Surface salinity in the Fitzroy Estuary and Keppel Bay, January 2015, in four model implementations: top left: as implemented in RECOM, without customisation. Top right: using the optimised Fitzroy/Keppel Bay grid developed during previous projects, initialised from and nested within the 4km x 4km grid eReefs Great Barrier Reef model (GBR4). Bottom left: as represented in the parent model, GBR4. Bottom right: Using the optimised Fitzroy/Keppel Bay grid developed during previous projects in combination with customised initial conditions. Far bottom: time-series of surface salinity at the location indicated by the coloured dots. Vertical dashed line indicates the time for which the maps were produced. Line colours match the colours of the dots on the corresponding Fitzroy/Keppel Bay grid.

5.6.1.4 Hydrodynamics

Salinity (Fig. 5.6.5) and temperature (Fig. 5.6.6) were almost identical in the RECOM application and the optimised grid, though the difference in the estuary channel depth in the two grids can be seen in the slightly different extent of fresh water in the river. Both grids resolved much more spatial detail and stronger salinity and temperature gradients than were evident in the GBR4 grid. The optimised Fitzroy grid includes some areas of very shallow mudflats that have not been resolved in this RECOM application, and this can be faintly observed as slightly cooler areas around the edge of Keppel Bay and in the tidal creeks (the snapshot maps show model output at midnight).

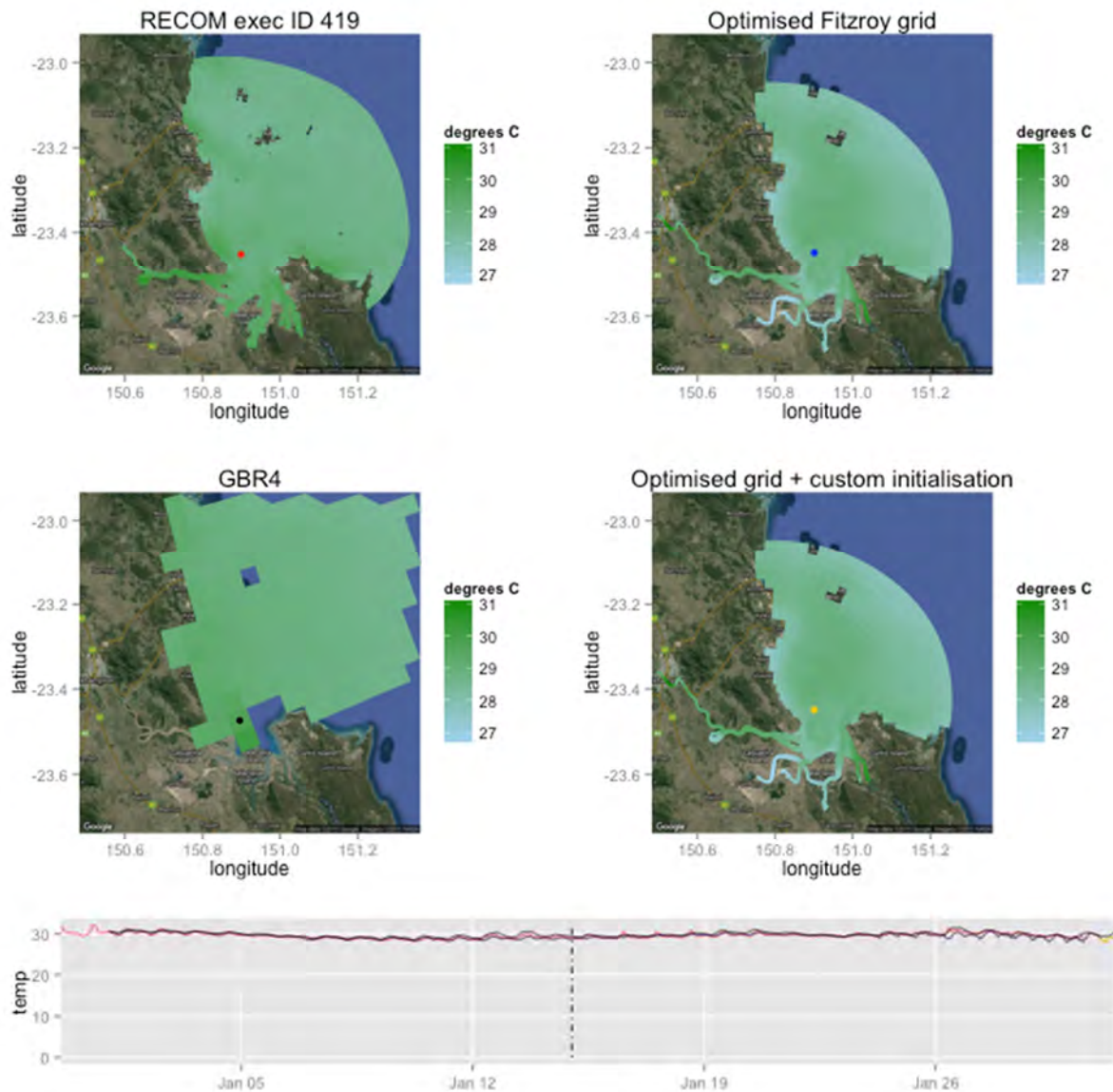


Figure 5.6.6. Surface temperature in the Fitzroy Estuary and Keppel Bay, January 2015, in four model implementations: top left: as implemented in RECOM, without customisation. Top right: using the optimised Fitzroy/Keppel Bay grid developed during previous projects, initialised from and nested within the 4km x 4km grid eReefs Great Barrier Reef model (GBR4). Bottom left: as represented in the parent model, GBR4. Bottom right: Using the optimised Fitzroy/Keppel Bay grid developed during previous projects in combination with customised

initial conditions. Far bottom: time-series of surface temperature at the location indicated by the coloured dots. Vertical dashed line indicates the time for which the maps were produced. Line colours match the colours of the dots on the corresponding Fitzroy/Keppel Bay grid.

5.6.1.5 Fine sediments

Simulated fine sediment concentrations in the RECOM application and the similarly initialised optimised Fitzroy grid are very similar, with small differences due to differences in the representation of the estuary channel and interpolation of the bathymetry of Keppel Bay (Fig. 5.6.7; top left and top right). Both are very different from the output of the coarse-resolution GBR4 model (bottom left), which is unable to resolve the fine sediment resuspension dynamics near the mouth of the estuary. The results of both grids are also very different from those of the optimised Fitzroy model with customised initial sediment stores (Fig. 5.6.7; bottom right).

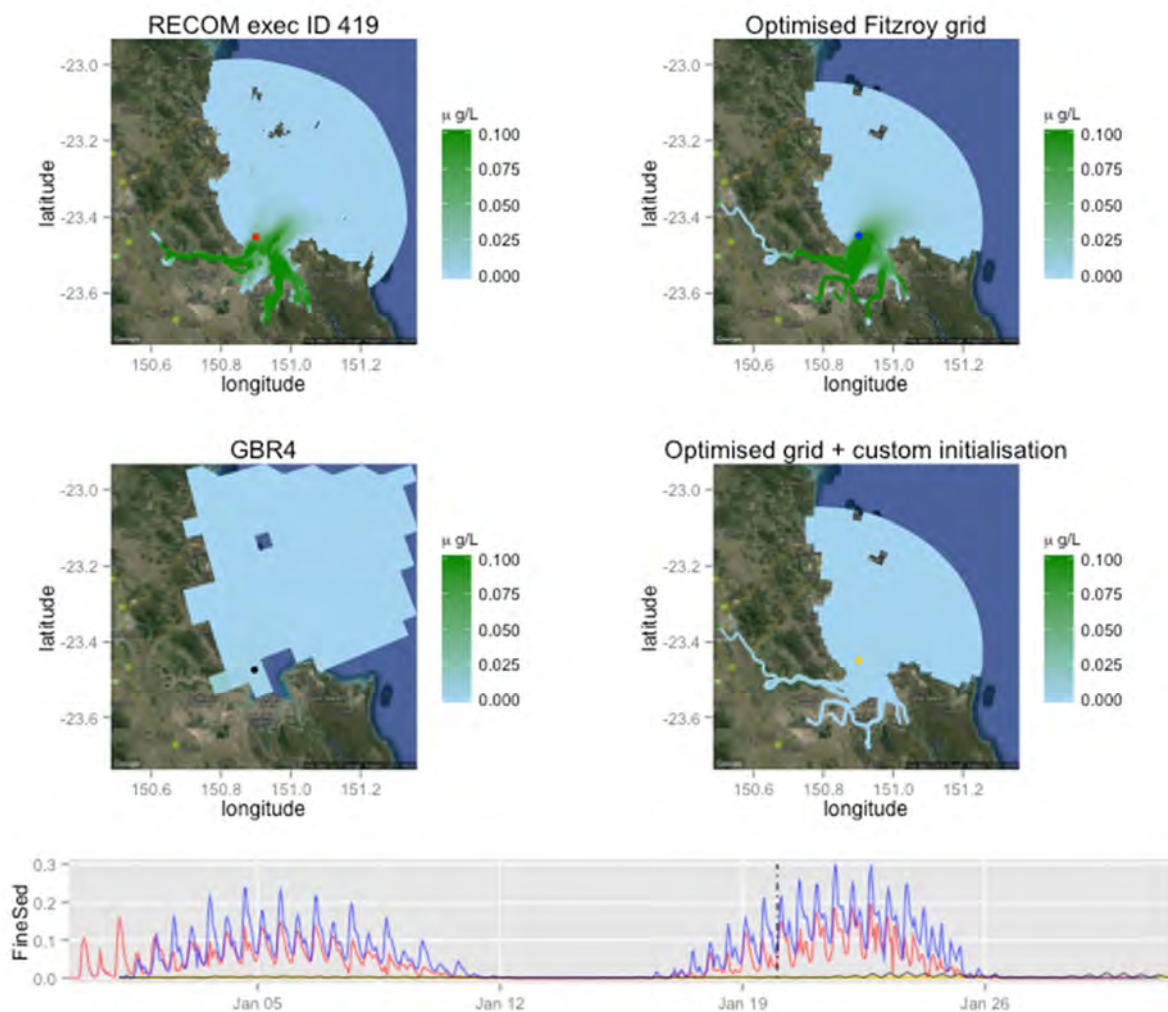


Figure 5.6.7. Surface fine sediment concentrations in the Fitzroy Estuary and Keppel Bay, January 2015, in four model implementations: top left: as implemented in RECOM, without customisation. Top right: using the optimised Fitzroy/Keppel Bay grid developed during previous projects, initialised from and nested within the 4km x 4km grid eReefs Great Barrier Reef model (GBR4). Bottom left: as represented in the parent model, GBR4. Bottom right: Using the optimised Fitzroy/Keppel Bay grid developed during previous projects in

combination with customised initial conditions. Far bottom: time-series of surface fine sediment concentrations at the location indicated by the coloured dots. Vertical dashed line indicates the time for which the maps were produced. Line colours match the colours of the dots on the corresponding Fitzroy/Keppel Bay grid.

5.6.1.6 Nitrogen and phosphorus

Total nitrogen (Fig 5.6.8) and total phosphorus (Fig 5.6.9) concentrations, dominated by nutrients in particulate form, show similar spatial and temporal patterns in the RECOM application and the optimised Fitzroy grid. Differences are larger than differences in fine sediment concentrations, as the small differences resulting from the effects of small differences in bathymetry on particle transport are compounded by subsequent biogeochemical processing and by small differences in the biogeochemical parameterisation of the two models. Again, both models resolve resuspension and deposition processes that are not resolved by the GBR4 model, and both models produce very different results from the optimised grid with customised initial conditions.

The same observations about the comparisons can be made when we consider nutrients in dissolved form, e.g. dissolved inorganic nitrogen, which combines simulated nitrate and ammonium (Fig. 5.6.10) and dissolved inorganic phosphorus (5.6.11).

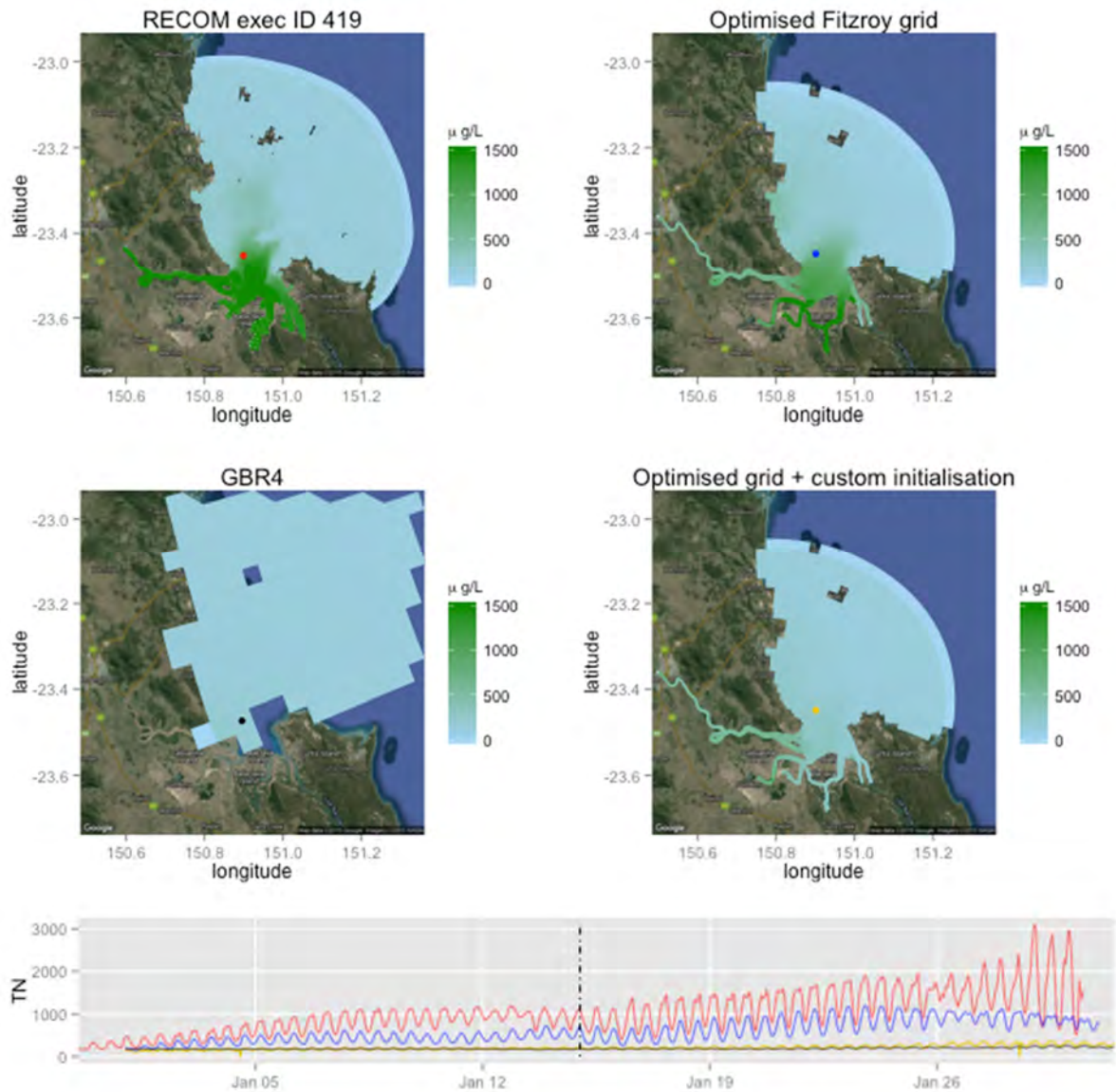


Figure 5.6.8. Surface total nitrogen in the Fitzroy Estuary and Keppel Bay, January 2015, in four model implementations: top left: as implemented in RECOM, without customisation. Top right: using the optimised Fitzroy/Keppel Bay grid developed during previous projects, initialised from and nested within the 4km x 4km grid eReefs Great Barrier Reef model (GBR4). Bottom left: as represented in the parent model, GBR4. Bottom right: Using the optimised Fitzroy/Keppel Bay grid developed during previous projects in combination with customised initial conditions. Far bottom: time-series of surface TN at the location indicated by the coloured dots. Vertical dashed line indicates the time for which the maps were produced. Line colours match the colours of the dots on the corresponding Fitzroy/Keppel Bay grid.

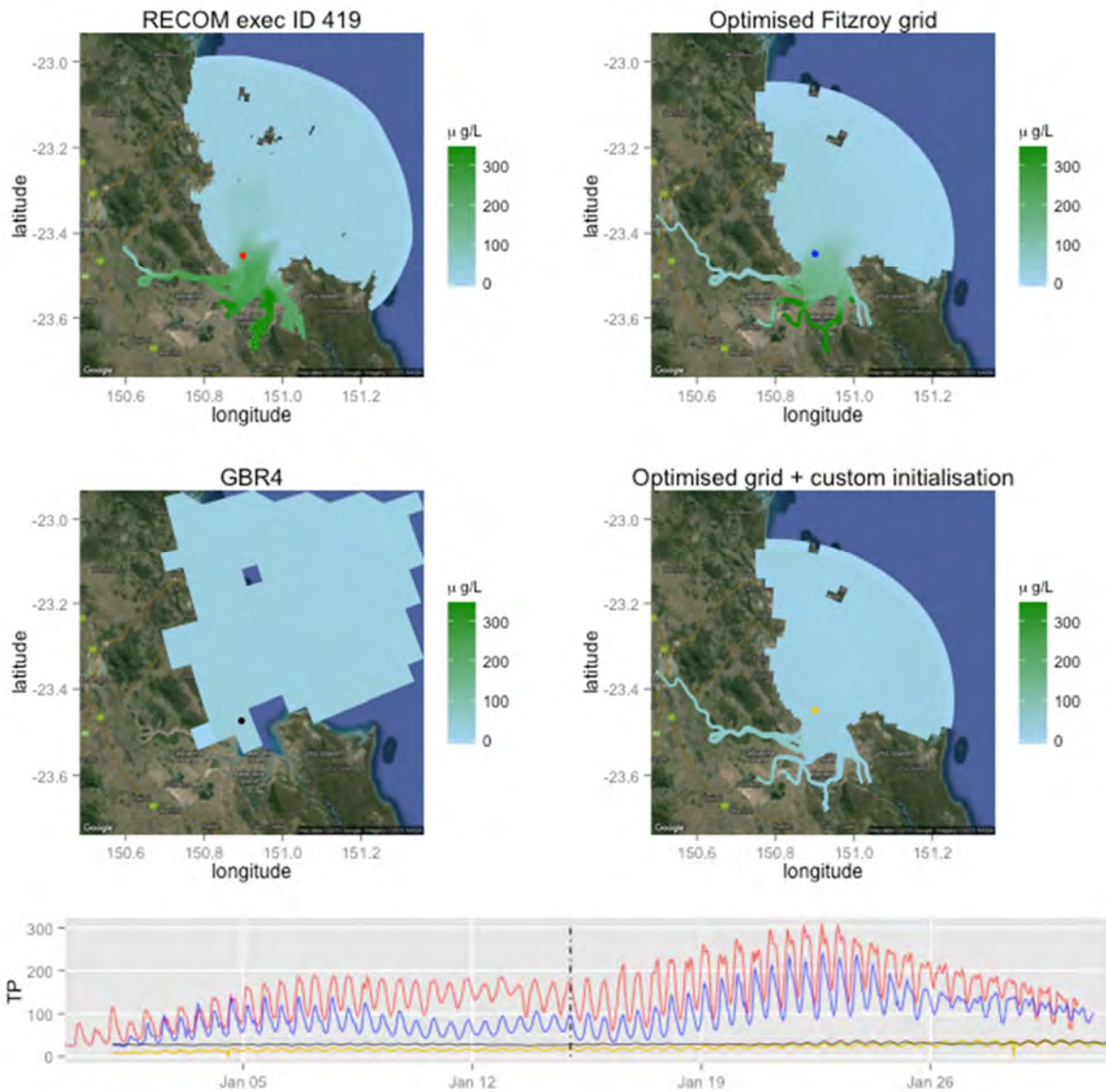


Figure 3.6.9. Surface total phosphorus in the Fitzroy Estuary and Keppel Bay, January 2015, in four model implementations: top left: as implemented in RECOM, without customisation. Top right: using the optimised Fitzroy/Keppel Bay grid developed during previous projects, initialised from and nested within the 4km x 4km grid eReefs Great Barrier Reef model (GBR4). Bottom left: as represented in the parent model, GBR4. Bottom right: Using the optimised Fitzroy/Keppel Bay grid developed during previous projects in combination with customised initial conditions. Far bottom: time-series of surface TP at the location indicated by the coloured dots. Vertical dashed line indicates the time for which the maps were produced. Line colours match the colours of the dots on the corresponding Fitzroy/Keppel Bay grid.

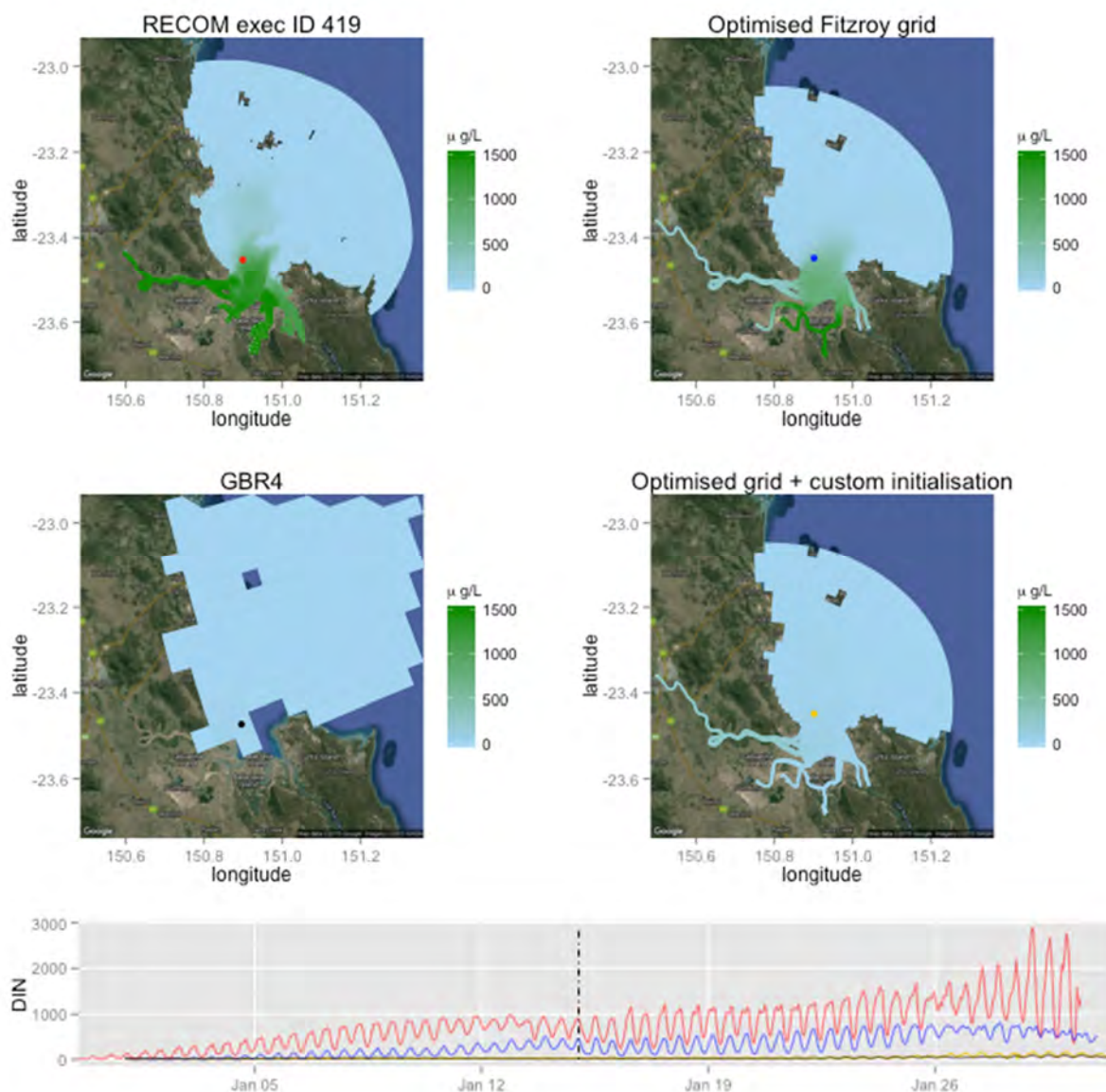


Figure 5.6.10. Surface dissolved inorganic nitrogen in the Fitzroy Estuary and Keppel Bay, January 2015, in four model implementations: top left: as implemented in RECOM, without customisation. Top right: using the optimised Fitzroy/Keppel Bay grid developed during previous projects, initialised from and nested within the 4km x 4km grid eReefs Great Barrier Reef model (GBR4). Bottom left: as represented in the parent model, GBR4. Bottom right: Using the optimised Fitzroy/Keppel Bay grid developed during previous projects in combination with customised initial conditions. Far bottom: time-series of surface DIN at the location indicated by the coloured dots. Vertical dashed line indicates the time for which the maps were produced. Line colours match the colours of the dots on the corresponding Fitzroy/Keppel Bay grid.

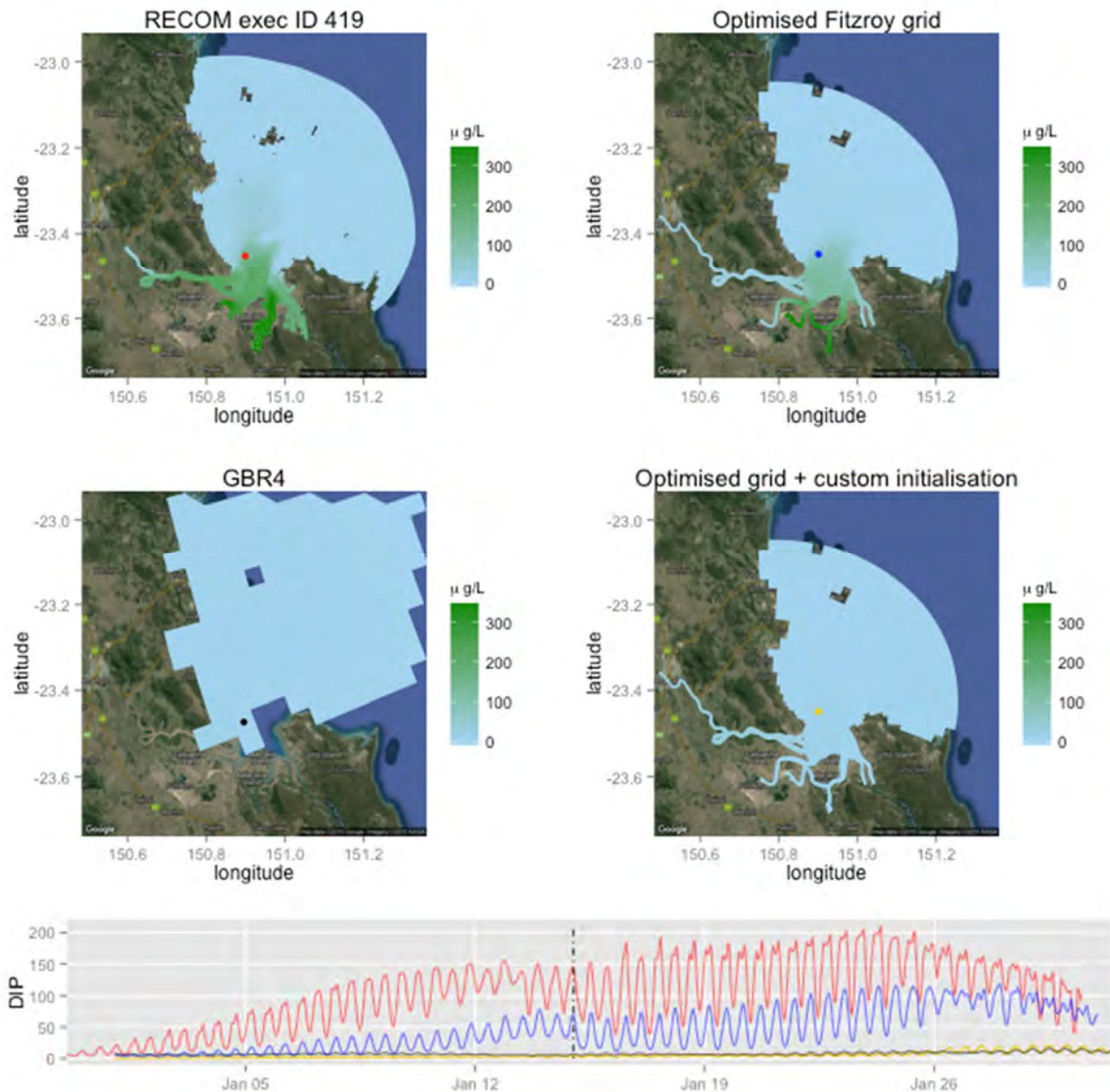


Figure 5.6.11. Surface dissolved inorganic phosphorus in the Fitzroy Estuary and Keppel Bay, January 2015, in four model implementations: top left: as implemented in RECOM, without customisation. Top right: using the optimised Fitzroy/Keppel Bay grid developed during previous projects, initialised from and nested within the 4km x 4km grid eReefs Great Barrier Reef model (GBR4). Bottom left: as represented in the parent model, GBR4. Bottom right: Using the optimised Fitzroy/Keppel Bay grid developed during previous projects in combination with customised initial conditions. Far bottom: time-series of surface DIP at the location indicated by the coloured dots. Vertical dashed line indicates the time for which the maps were produced. Line colours match the colours of the dots on the corresponding Fitzroy/Keppel Bay grid.

5.6.1.7 Chlorophyll a

The greatest differences between the four models emerge when we consider higher-order biogeochemical and ecological properties such as chlorophyll a concentrations and concentrations of specific phytoplankton and zooplankton groups. Relatively small differences in fine sediment concentrations produce difference in light conditions, and hence differences in photosynthetic rates. Moderate differences in dissolved nutrient concentrations produce differences in nutrient uptake rates and hence (in combinations with differences in photosynthesis), differences in pigment synthesis. Differences in chlorophyll production and phytoplankton growth result in differences in zooplankton growth, and ultimately, differences in grazing pressure and phytoplankton loss terms. All of these combine to produce chlorophyll a concentrations that are sometimes very different from one model implementation to the next. Nonetheless, spatial patterns are broadly similar and remain within plausible bounds (Fig. 5.6.12).

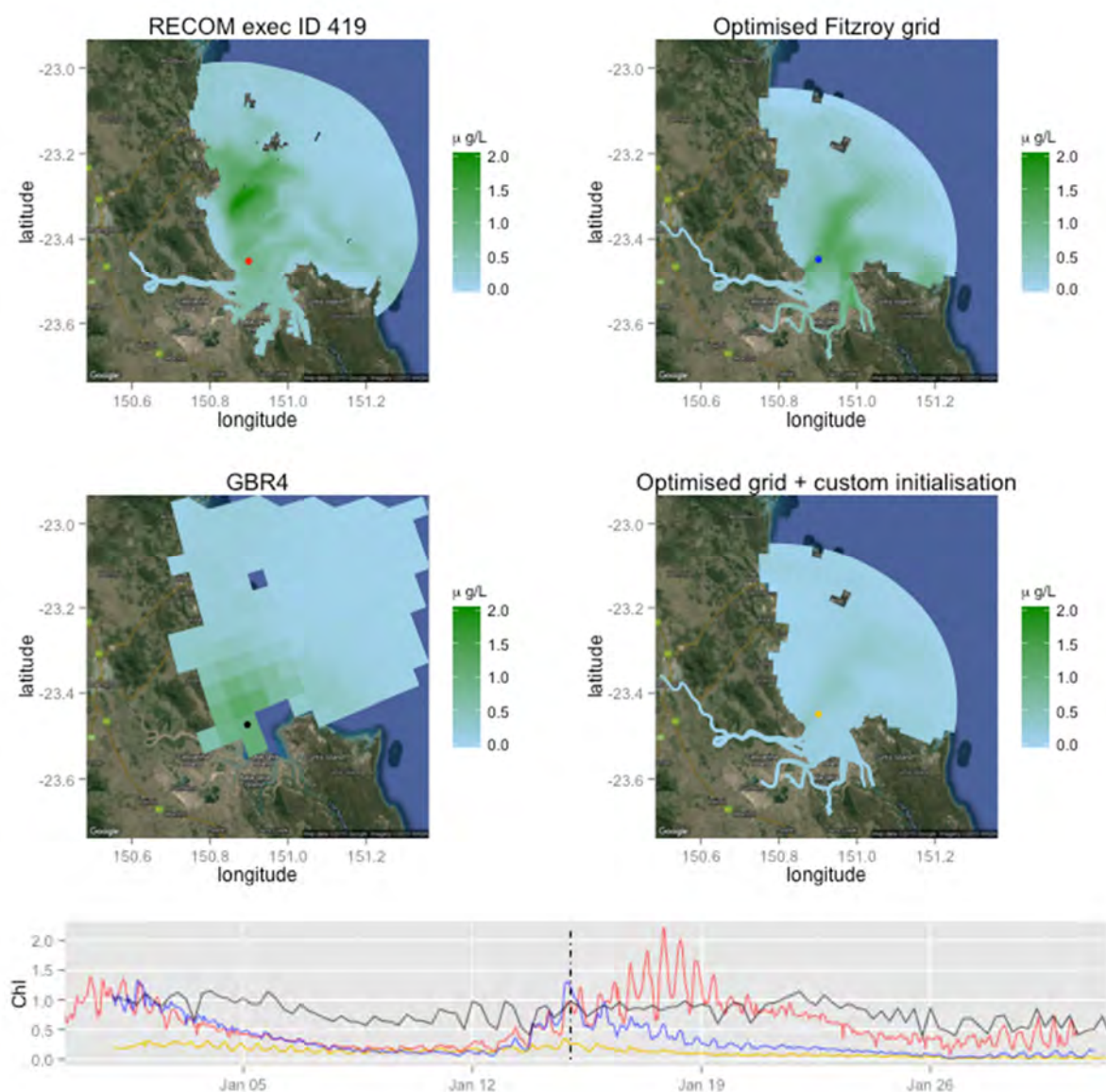


Figure 5.6.12. Surface chlorophyll a in the Fitzroy Estuary and Keppel Bay, January 2015, in four model implementations: top left: as implemented in RECOM, without customisation. Top

right: using the optimised Fitzroy/Keppel Bay grid developed during previous projects, initialised from and nested within the 4km x 4km grid eReefs Great Barrier Reef model (GBR4). Bottom left: as represented in the parent model, GBR4. Bottom right: Using the optimised Fitzroy/Keppel Bay grid developed during previous projects in combination with customised initial conditions. Far bottom: time-series of surface chlorophyll at the location indicated by the coloured dots. Vertical dashed line indicates the time for which the maps were produced. Line colours match the colours of the dots on the corresponding Fitzroy/Keppel Bay grid

5.6.1.8 Concluding remarks

This case study clearly illustrates both the capabilities and limitations of RECOM: the system is capable of producing a model that closely matches the dynamics simulated by an expensive custom-developed model and will produce plausible results, but the results will not be accurate unless the inputs (both catchment river loads and, in muddy coastal areas, initial sediment conditions as well as meteorological conditions) are accurate.

Previous work (Robson and Brando, 2008) suggests that the initial conditions will have less impact after the model has been run for a period of several years. This will eventually be possible in RECOM, as the near real-time eReefs model is running continually to build up a multi-year archive within which RECOM runs can be nested.

In the short term, planned further development of RECOM includes adding the ability to upload customised initial conditions. Specification of accurate initial conditions will require expert knowledge and local observational data, but implementation of accurate local models will still be substantially faster and less expensive using RECOM than using previously existing tools.

In the medium term, improvements to the biogeochemical data assimilation technologies that have been developed through eReefs may reduce the need for expert customisation where sufficient local or remotely-sensed observational data are available.

As things stand, implementations of RECOM that have not been subject to expert customisation must be considered pilot models: they can be used to simulate the hydrodynamics of the system and simulate the types of biogeochemical and sediment responses that might be expected under defined scenarios, but cannot be expected to accurately match in situ observations at any particular time.

5.6.2 Heron Island

The Heron Island domain was chosen as a priority area for validation of RECOM primarily due to the existing body of work carried out in the region under the ACCSP, buffering effect (GBRf) and carbon cluster projects.

5.6.2.1 Optimized model

The Heron Island project (Mongin et al, 2014) was conducted under the Ocean Acidification component of the ACCSP (Australian Climate Change Science Program) project to understand how reef biogeochemical processes impact the water carbon chemistry. The project included the development and calibration of a high-resolution model around the Heron Island reef (Mongin and Baird, 2014) capable of simulating the flushing of the water in and out of the lagoon and flux of carbon associated with photosynthesis and calcification processes. The original model was calibrated against the Queensland Integrated Marine Observed System (Q-IMOS) monitors the reef lagoon continuously (Bainbridge et al., 2010). The model domain and observation sites are illustrated in Fig. 5.6.13.

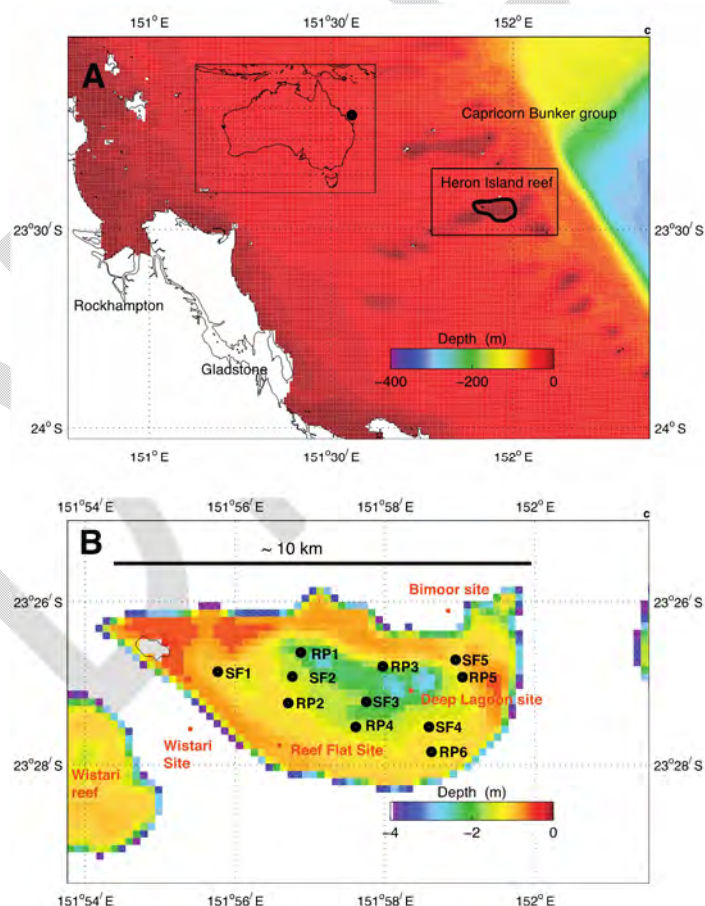


Figure 5.6.13. Model grid and bathymetry for Heron Island region.

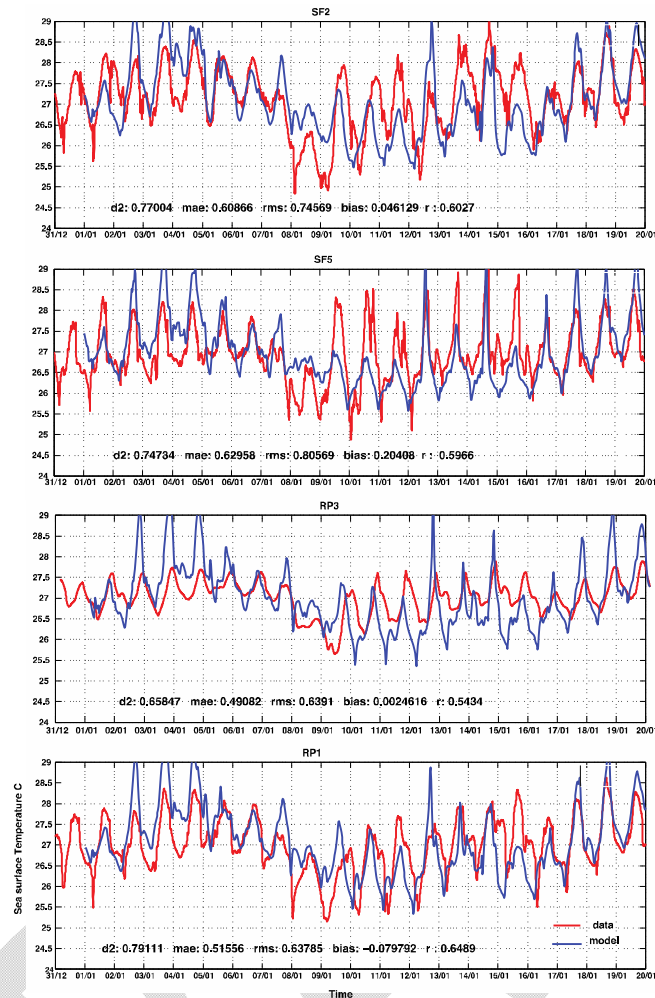


Figure 5.6.14. Modelled and observed lagoon temperature time series at the six relay pole (RP) stations, January 2010.

A second version of the model (*Gillibrand et al. , In Prep*) was nested inside the eReefs GBR1 model and waves were added. The optimized model uses the best available bathymetry (high resolution above 10 m only) and best mapping of the coral reef habitat. The model was calibrated against available observations of currents, waves and water temperature from winter 2009 and summer 2010. Selected temperature comparisons are presented at 4 sites in Fig. 5.6.14. The model output was then used to investigate the general circulation of Heron Island lagoon, and to isolate the roles of tides, winds and waves in driving the circulation. Modelled tidal currents through the region were strongly steered by the local reef topography around the lagoon. Residual (mean) currents across the reef were westward in summer 2010, driven by the prevailing wind, and of similar magnitude to residual surface flows in deeper water around the lagoon. The model showed that elevated mean sea level inside the lagoon relative to that outside drove a barotropic circulation expelling water from the lagoon. The role of waves in driving exchange across the reef crest was moderate, even during a storm event during February 2010, largely because Heron reef is protected from the prevailing swell by Sykes and One Tree Island Reefs to the east. Waves were modelled using SWAN and calibrated to observation (Fig. 5.6.15), and the radiation stresses supplied from this model were used to force the hydrodynamics model. The subsequent effect of waves on the

circulation is shown in Fig. 5.6.16, from which it is seen that wave influence is small. The flushing of the lagoon (defined as the time taken for a mass of passive tracer to fall to e^{-1} of its initial mass) took place in hours rather than days, and was moderately enhanced by wave effects.

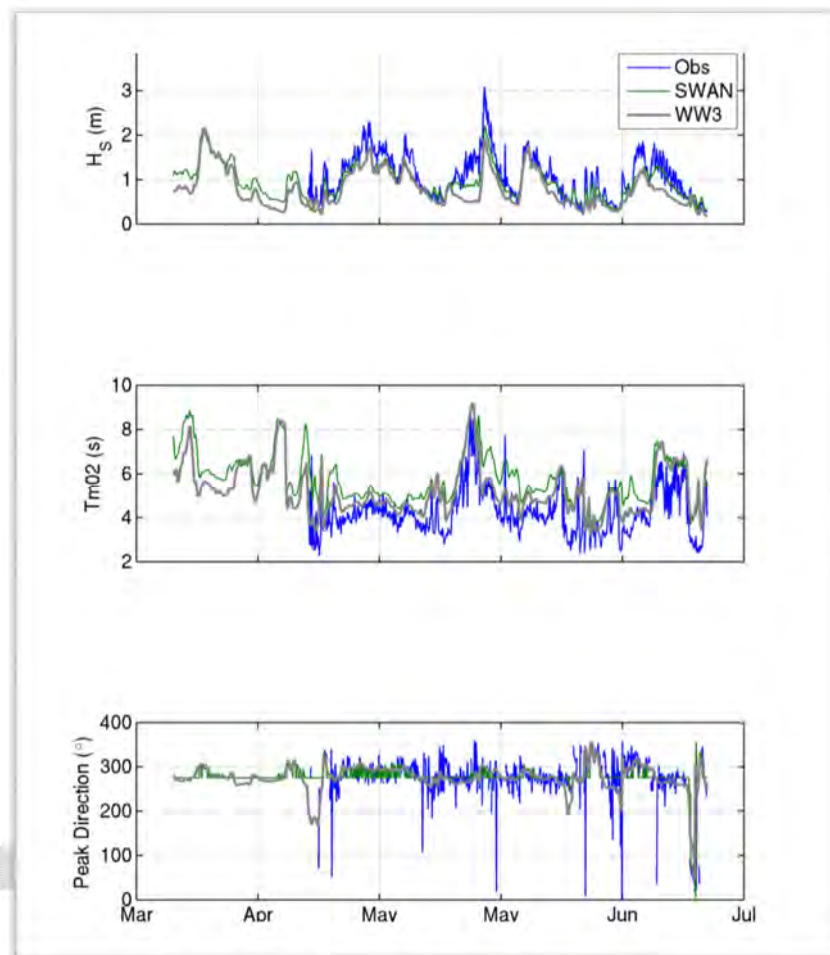


Figure 5.6.15. Modelled and observed time series of significant wave height, H_s (top panel), wave period (T_{m02} , middle panel), and direction (bottom panel) for April - June 2009.

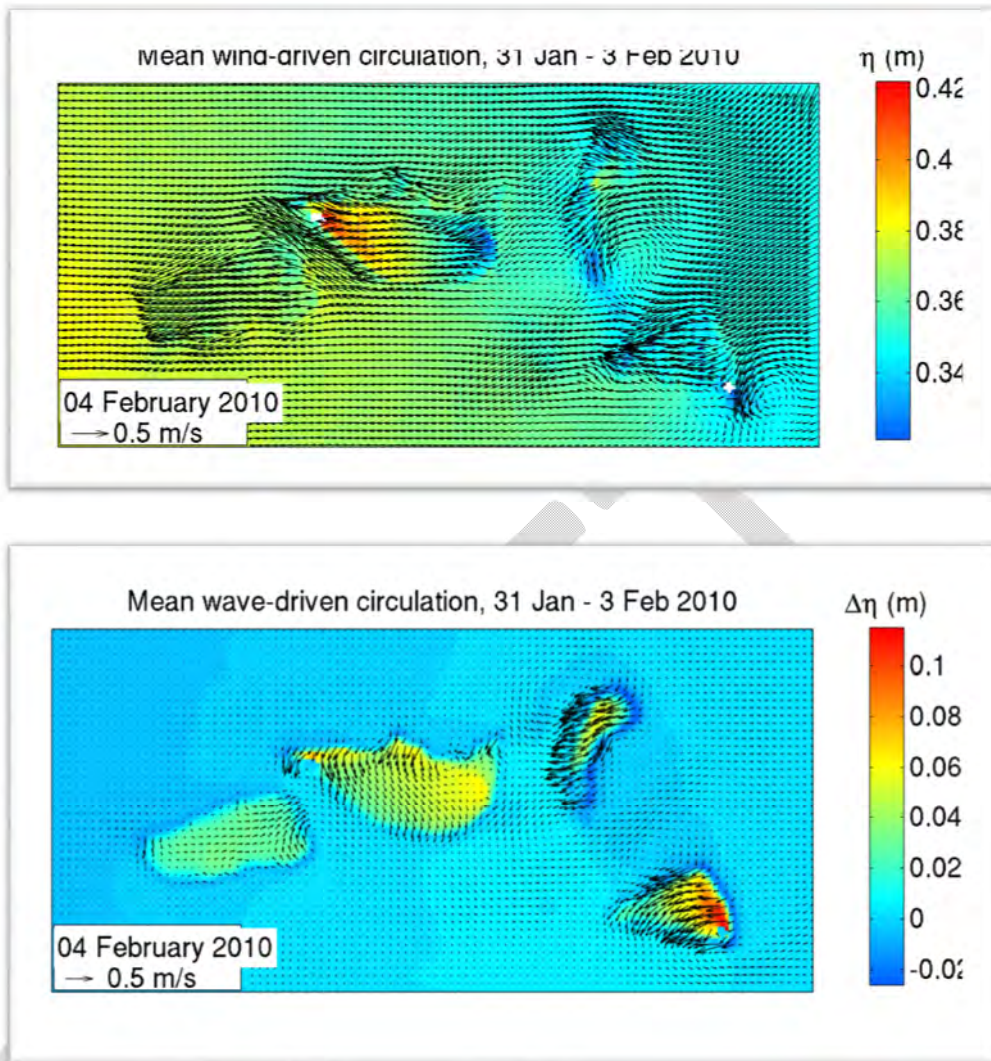


Figure 5.6.16. Modelled mean sea surface height (η) and wind-driven circulation for the period 31 January – 3 February 2010 (top). Modelled mean wave-driven circulation and the change in mean sea surface height ($\Delta\eta$) due to the presence of wave forcing (bottom) for the same period.

This Heron Island model is operating in NRT and outputs can be viewed at:

<http://www.emg.cmar.csiro.au/www/en/emg/projects/Heron-Island/Near-Real-Time-Results.html>

This model is considered to be suitably accurate to benchmark a RECOM configuration against.

5.6.2.2 Heron model RECOM test case strategy

In order to test the RECOM model framework of a similar domain, we chose to build a RECOM model grid which is as close as possible to the original model grid (in contrast to the other test cases this easily accomplished, since as the original optimized model, the grid is rectangular with 167 m horizontal resolution). The RECOM grids therefore cover the same area, with the same number of grids cells and the same horizontal resolution as the optimized version (see Fig. 5.6.17). Additionally, we ensured that the different models (optimized and RECOM) were nested into the same regional model, using the same temporal frequency of nesting. The hydrodynamics (temperature, salinity, surface elevation and currents) are nested in the eReefs GBR1 model, the biogeochemical tracers are nested in the GBR4 eReefs model.

In order to test all the different options of RECOM, we build two versions of the model (both using the same grid). The first one (RECOM1) uses the default GBR100 (Beaman, 2010) bathymetry, while the second (RECOM2) uses the option that enables merging of the default bathymetry with the high resolution product similar to that used in the optimized model.

All three models (called optimized, RECOM1 and RECOM2 thereafter) run for 2 months (December – January 2014/2015) using the same meteorological forcing. Similarly, we ran the optimized version of the model with the default set of parameter (similar to RECOM).

The only differences between the 3 simulations will therefore be due to:

- The RECOM grid generation and bathymetry interpolation,
- Automation of forcing files extraction, and model parameterization (for hydrodynamic, sediment and biogeochemistry all have the same default eReefs parameters),
- Vertical layer structure,
- Initial conditions of the benthic and sediment variables,
- Different parameters for diffusion, friction and stability in the hydrodynamic model.

5.6.2.3 Bathymetry

The bathymetry of the optimized heron model was manually modified to ensure that the reef crest is located at the right level, and that no cells would protrude above the surface layer. The bathymetry that was generated within RECOM was not modified in any way.

The interpolation of the bathymetry in the RECOM models produces bathymetry field that is quite good in the deeper sections (Fig. 5.6.17). The RECOM bathymetry manages to separate the different reefs and channels, as well as reproducing the steep slopes toward the east. However, RECOM bathymetry is quite poor at detailing the reef crest (see on the cross section on Fig. 5.6.18). The merging of the GBR100 and Heron bathymetries assist in resolving the issue of the lagoon being too deep in the RECOM1 model, but still failed to resolve the reef crest (and has some artifacts following the merging).

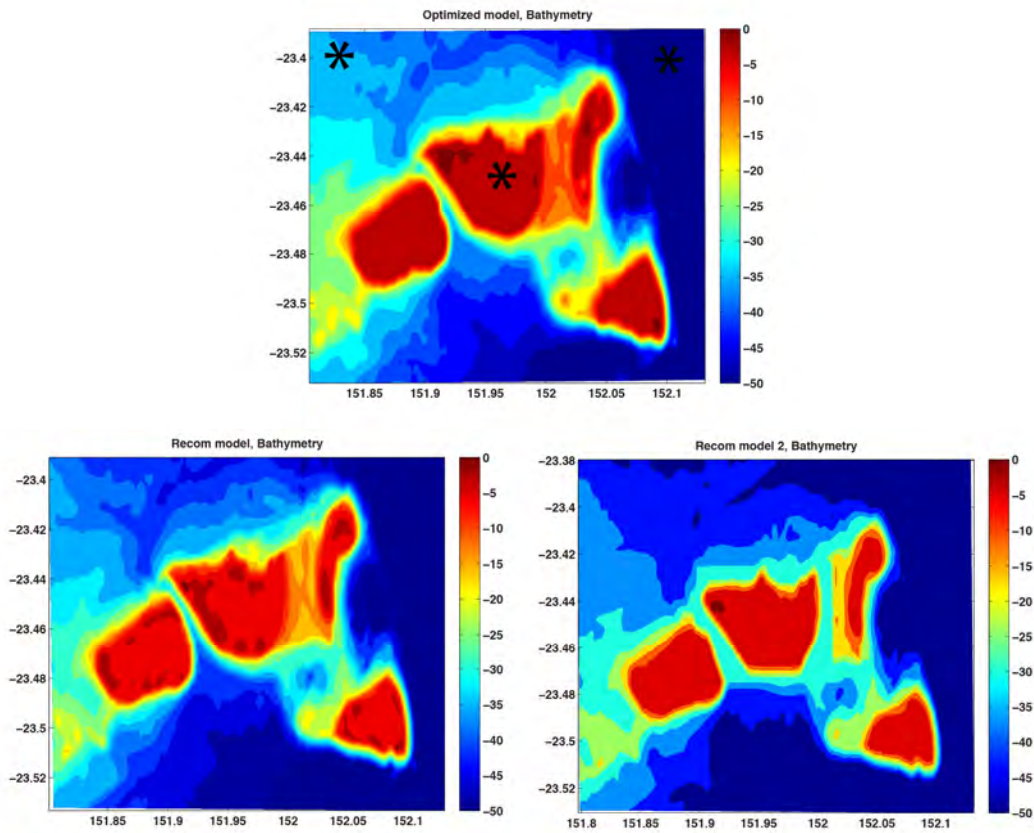


Figure 5.6.17. Heron model domain and bathymetry. Top panel shows the optimized Heron model (Mongin et al 2014). Bottom left show the automated RECOM version of the grid with default bathymetry (GBR 100, Beaman 2010). Bottom right panel shows the automated RECOM version of the grid with the merging bathymetry option used (GBR100 and Heron high resolution). The stars on the top panel shows the locations of the time series in the following figures.

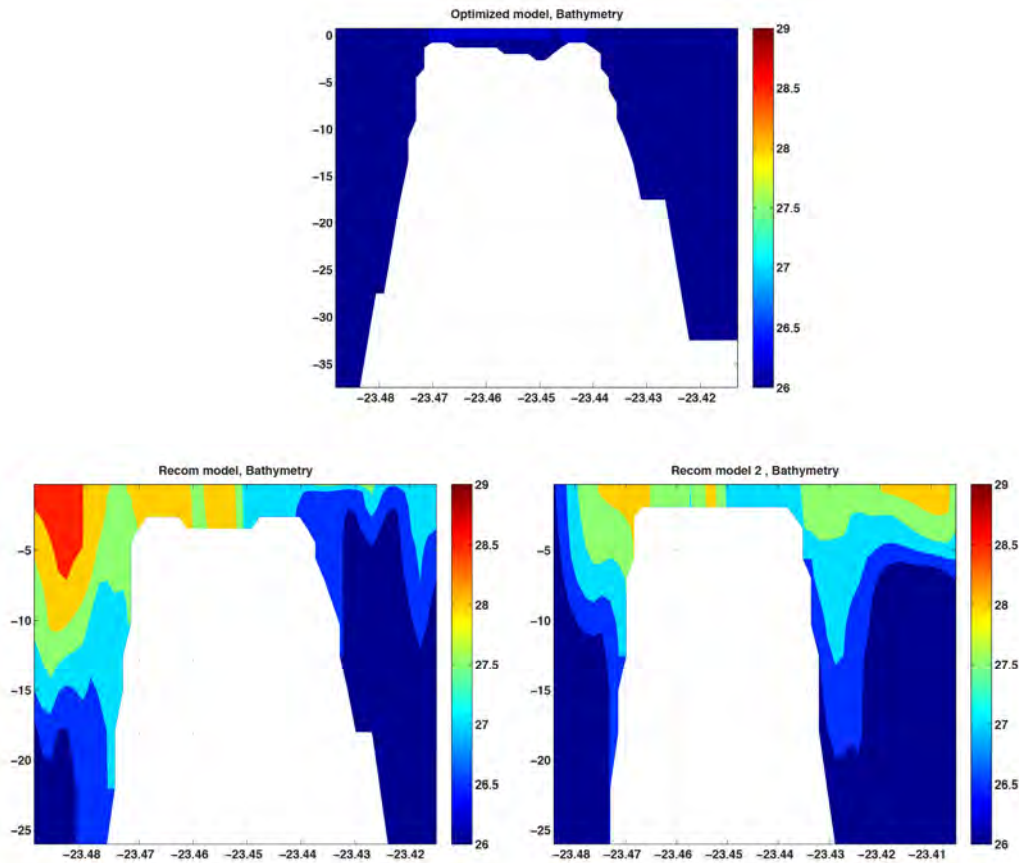


Figure 5.6.18. Heron model cross section (south-north in the middle of the Heron reef). Top panel shows the optimized Heron model (Mongin et al 2014). Bottom left show the automated RECOM version of the grid with default bathymetry (GBR100, Beaman, 2010). Bottom right panel shows the automated RECOM version of the grid with the merging bathymetry option used (GBR100 and Heron high resolution).

5.6.2.4 Sea surface height

The three models have a very similar sea surface height (Fig. 5.6.19) indicating that the tides and therefore a large fraction of the water circulation are well represented in the RECOM models. Tidal amplitude and phase is well represented, as is the neap-spring cycle. The circulation on the Heron reef is strongly dominated by tides and their interactions with bathymetric features. The simulation period had little wind to enhance the flushing the lagoon.

It is difficult to completely assess the difference of ocean circulation between the different models without invoking detailed diagnostics and the simulations of passive tracers. These additional diagnostics are not currently set up automatically in RECOM and will therefore be left for further analysis.

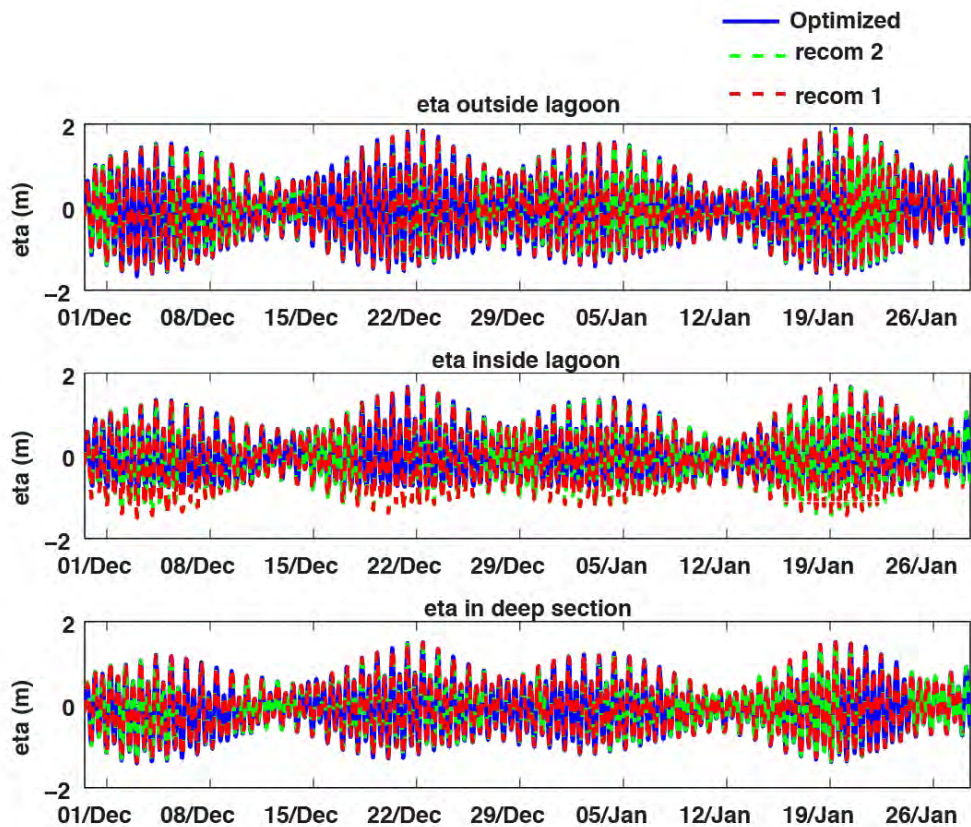


Figure 5.6.19. Time series of sea surface elevation in the optimized (Blue) and RECOM models (red & green). Top panel is on the North West corner of the model domain, middle panel inside the deep lagoon inside the Heron Island reef bottom panel is on the north east corner in the 50 m deep waters.

5.6.2.5 Sea Surface Temperature

Over the two months simulation, on average both RECOM models are able to represent the large fraction the spatial variability in the sea surface temperature (Fig. 5.6.20). Most of the features of the optimized model are well represented in the RECOM models. The temperature over the shallowest areas over the reefs and inside the lagoon is, however, quite different.

The analysis of the simulated sea surface temperature over time (Fig. 5.6.21) reveals that the RECOM models do not represent well the diurnal preferential heating and cooling typical of shallow reef system. Inside the lagoon (Fig. 5.6.21 middle panel), the RECOM models are 2-4°C too cold compared to the optimized model. This is a consequence of the deeper water in the lagoon and the corresponding decrease in differential heating. The low temperatures are quite similar which indicate that the flushing time is accurate. This indicates that despite having a lagoon that is too deep (therefore having a larger volume than the optimized version) the flushing time of the water is similar. We conclude that the flushing is probably happening too fast in the RECOM models (less so in the RECOM2 version), but the large volume of water compensate, leading to a similar flushing timeframe.

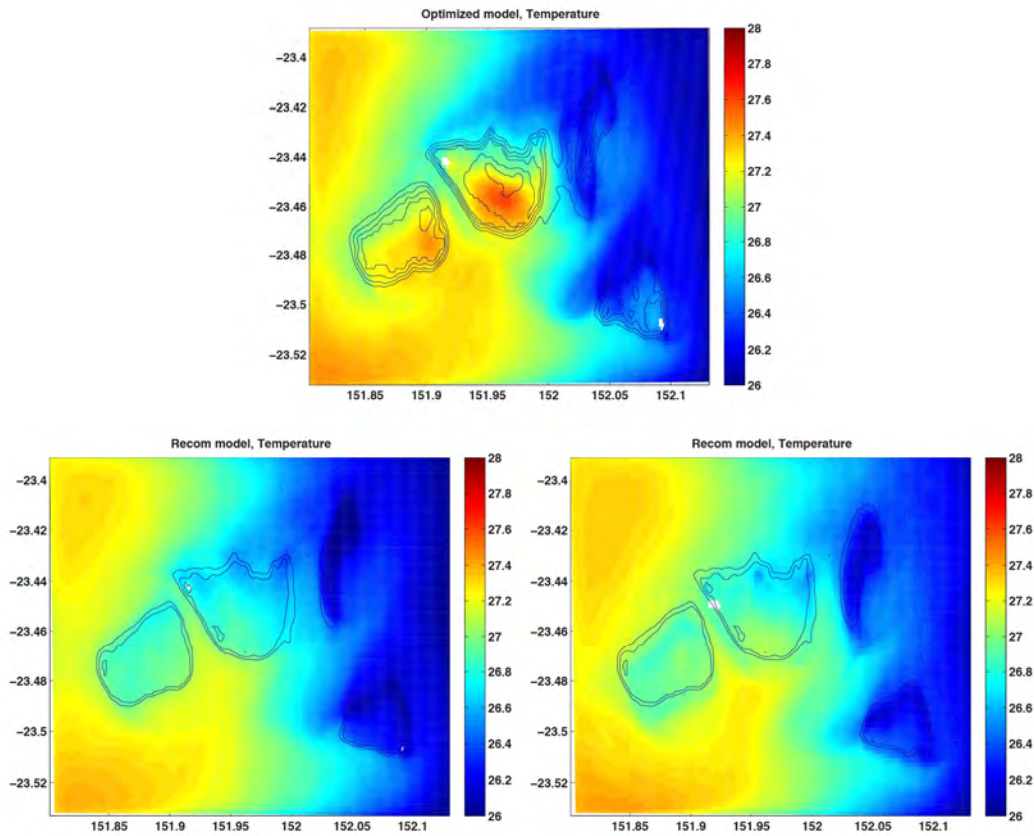


Figure 5.6.20. Heron model average simulated temperature. Top panel shows the optimized Heron model (Mongin et al 2014). Bottom left show the automated RECOM version of the grid with default bathymetry (GBR100). Bottom right panel show the automated RECOM version of the grid when the merging bathymetry option is used (GBR100 and Heron high resolution).

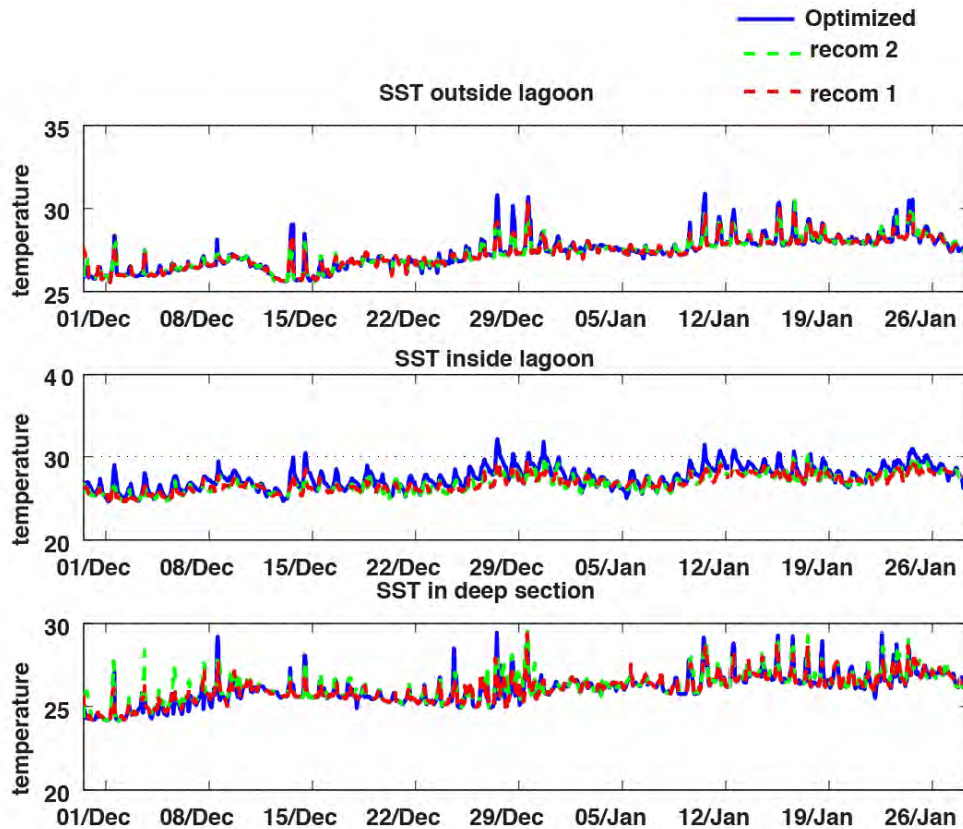


Figure 5.6.21. Time series of Sea Surface Temperature in the optimized (Blue) and RECOM models (red & green). Top panel is on the north-west corner of the model domain, middle panel inside the deep lagoon inside the Heron Island reef, bottom panel is on the north east corner in the 50 m deep waters.

5.6.2.6 Biogeochemistry

The Heron island system is an oligotrophic system, isolated from major riverine inputs, hence the input of nutrient is dominated by large scale feature provided through the open boundaries. As a result, the NO_3 concentration in all three models is quite similar and low enough to have minimum impact (Fig. 5.6.22).

Chlorophyll-a integrates many processes in the biogeochemistry model, therefore we expect the model's response to be quite different. The analysis of the time series of Chlorophyll-a at different locations in the models domain (Fig. 5.6.23) shows that the difference between the RECOM models is as large as the differences with the optimized model. The variability in Chlorophyll-a is best explained by small changes in water circulation and release /uptake of nutrient via benthic and sediment processes.

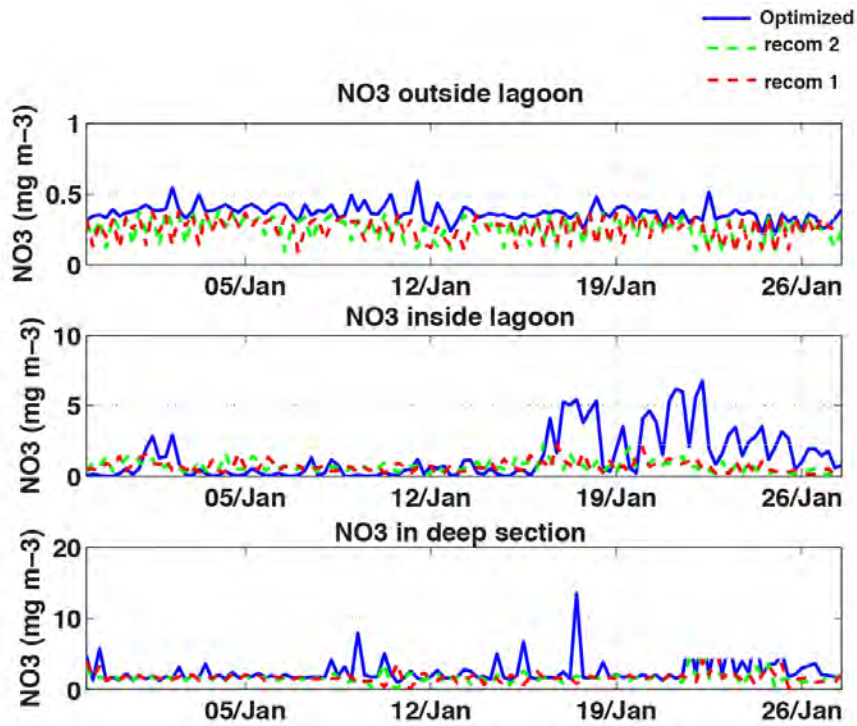


Figure 5.6.22. Time series of NO₃ in the optimized (Blue) and RECOM models (red & green). Top panel is on the north-west corner of the model domain, middle panel inside the deep lagoon inside the Heron Island reef, bottom panel is on the north east corner in the 50 m deep waters.

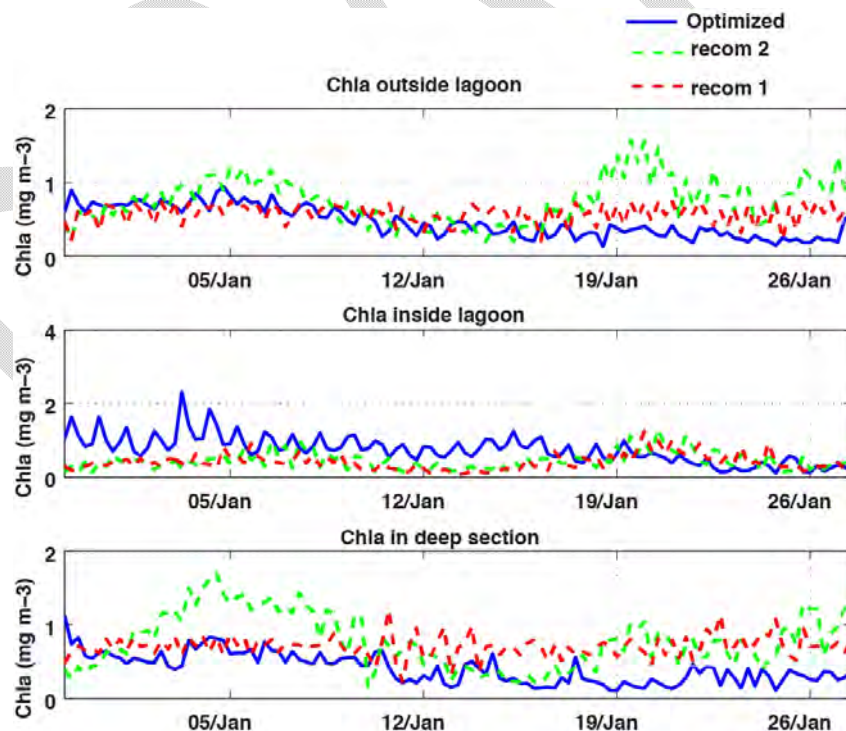


Figure 5.6.23. Time series of Chlorophyll-a in the optimized (Blue) and RECOM models (red & green). Top panel is on the North West corner of the model domain, middle panel inside the deep lagoon inside the Heron Island reef, bottom panel is on the North East corner in the 50 m deep waters.

One of the major differences between RECOM and optimized models is the initial conditions. The water column tracers are all initialized by interpolating from the GBR4 model, which produces the same profiles between the RECOM and optimized models (being on a similar grid). For the benthic variables, the optimized model was initialized using detailed maps of benthic habitats, the coverage of which is only available for Heron Reef; these maps were not used in the GBR4 model. As a consequence, the RECOM models benthic habitat are initialized from a much coarser GBR wide map.

The difference on the coral distribution between the optimized and RECOM models is presented in Fig. 5.6.24. While the magnitude of biomass is similar, the distribution is quite different. In both RECOM models, the coral does not sit on the reef but on deep sections, as a consequence coral do not grow and decay slowly. While it is difficult to relate the coral biomass to the Chlorophyll concentration, it is much more straightforward to look at the low coral biomass impact on the carbon chemistry. Indeed, coral reef strongly modulates the carbon chemistry over and around coral reef systems.

Aragonite saturation state, a measure of the ability for coral reef to calcify is presented on Fig. 5.6.25. While the differences outside the reef are quite low (less than 0.1), the response is completely different inside the lagoon. Aragonite saturation state is almost always 0.5 to 0.8 lower in the optimized model. The RECOM models act as if no reef processes modify the Aragonite saturation state and simulate constant values reflecting the open ocean. The ability of the RECOM model to simulate coral reef processes depends on the ability to position accurately the corals in the first place.

High detailed maps of benthic habitat at the scale of each individual reefs are rare and Heron Island is one of the only places within the GBR where they are available. This application highlights how the interpolation of benthic distribution from the regional models in RECOM impacts the model results. Accuracy can be dramatically improved in this case by choosing bathymetries and benthic distributions commensurate with the higher resolution used.

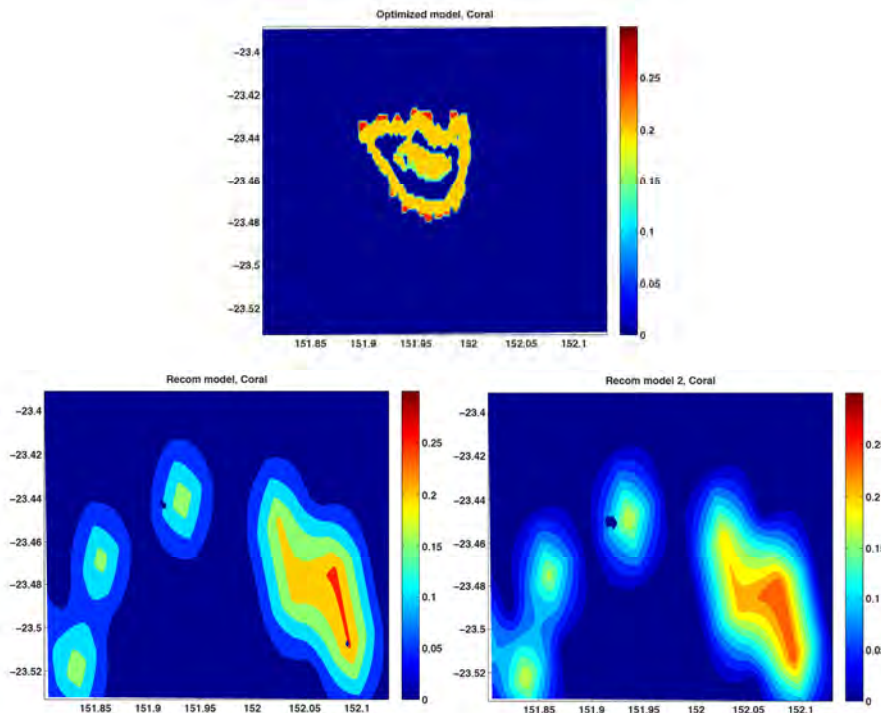


Figure 5.6.24. Heron model Coral reef distribution. Top panel shows the optimized Heron model (Mongin et al 2014). Bottom left show the automated RECOM version of the grid with default bathymetry (GBR100) and coral interpolated from the GBR4 model. Bottom right panel show the automated RECOM version of the grid when the merging bathymetry option is used (GBR100 and Heron high resolution) and coral interpolated from the GBR4 model.

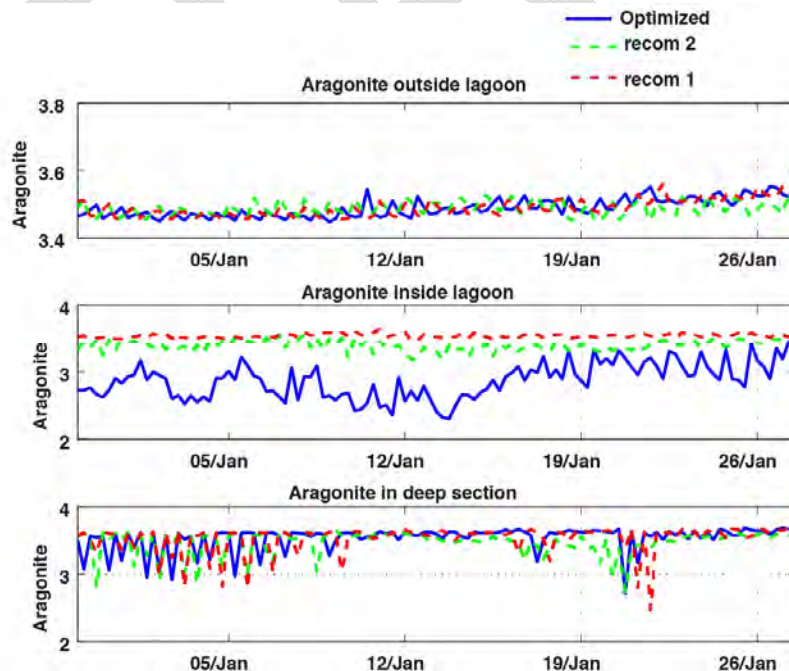


Figure 5.6.25. Time series of Aragonite Saturation state in the optimized (Blue) and RECOM models (red & green). Top panel is on the North West corner of the model domain, middle panel inside the deep lagoon inside the Heron Island reef, bottom panel is on the north east corner in the 50 m deep waters.

5.6.2.7 Conclusion

The RECOM version of the Heron reef domain proved to be generally accurate, but lack the fine scale refinement of the benthic layers (both for the bathymetry and benthic habitat). The fine-tuning of these model characteristic are lengthy processes that currently goes beyond the ability of an automated system such as RECOM.

The merging of the two bathymetric datasets did not enhance the model results as expected; the automated interpolation procedure does produces some artifacts when the two bathymetry are joined (this obvious in Fig. 5.6.17) that requires manual intervention to optimize.

The simulation of water circulation around a coral reef is challenging due to the relatively large gradient in bathymetry and speed of the current. The RECOM interface managed to deliver a product that is comparable to the manually optimized model. Most importantly, RECOM delivered a model that is stable, robust, a solid platform to build upon. For this application, we recommend that the user be cognizant of the limitations about the benthic layers and importance of reef crest location.

5.6.3 Whitsundays

The Airlie Beach region, adjacent to the Whitsunday Island Group, was chosen as a third application for RECOM to demonstrate its utility. Limited validation was undertaken for this region; the objective is to demonstrate that RECOM is capable of producing realistic outputs. Optimized models were developed for the region against which RECOM could be benchmarked. These models employed finer resolution than that used in previous applications, which presented the opportunity to investigate whether higher resolution might improve circulation and calculation of benthic properties. The domain is not impacted by river inputs, and there are limited observations available.

Note that the optimized Whitsunday model was developed as a hydrodynamic model only, and so can only be used to compare with the hydrodynamics of the RECOM model. The latter was however run as a complete hydrodynamic, sediments and BGC simulation, enabling an assessment of the sensibility of the BGC outputs for this region.

5.6.3.1 Optimized model

Two optimized model approaches were developed; the first (WHIT1) involved nesting the local domain in a regional polar model (POLW) (which was in turn nested inside BoM's global model OceanMAPS), while the second methodology (WHIT2) was to nest the local domain inside GBR1. Thus, the 2 versions of the optimized model could be compared with one another, as well as with the RECOM model.

Bathymetry data used for the optimized mode was mostly obtained from the GBR100 product (Beaman, 2010). However, inaccuracies were noted in this data in the region of Molle Channel, where the depths were far too shallow, and also adjacent the coast where there were a few 'deep holes'. These regions were treated instead using data from Geoscience Australia's 250m product (2003).

All regional models used ACCESS-A model products for atmospheric forcing, and OceanMAPS for salinity, temperature and low-frequency sea-level forcing. The POLW model was tidally-forced using global OTPS tidal harmonics in preference to the CSR model used in GBR4 and GBR1, as these were found to be more accurate in the relatively shallow waters of the POLW boundaries.

The optimized Whitsunday model configuration is displayed in Fig. 5.6.26, while the regional polar model (POLW), used to nest version1 of the Whitsunday model (WHIT1) is displayed in Fig. 5.6.27. Version2 of the Whitsunday model (WHIT2) was nested directly inside the GBR1 model (Fig. 4.1.2).

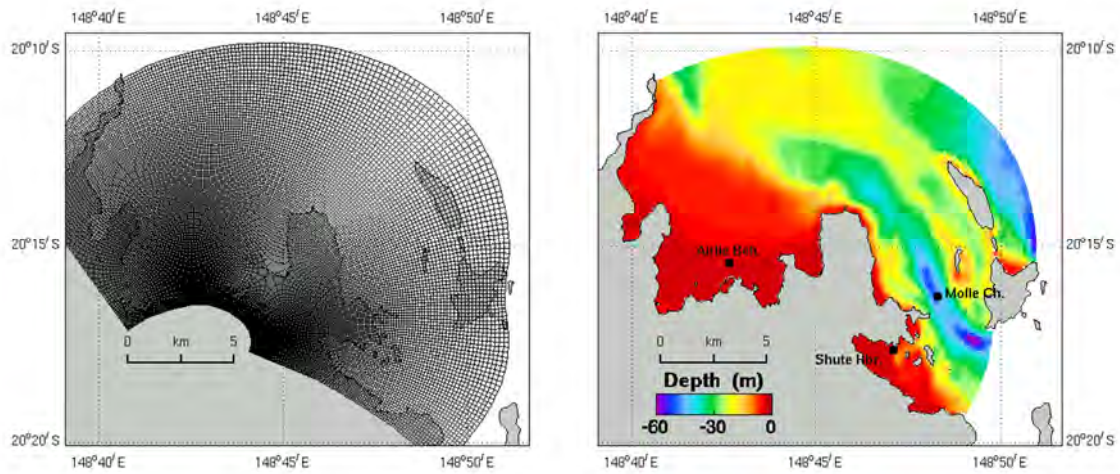


Figure 5.6.26 Model grid and bathymetry for optimized Whitsunday model.

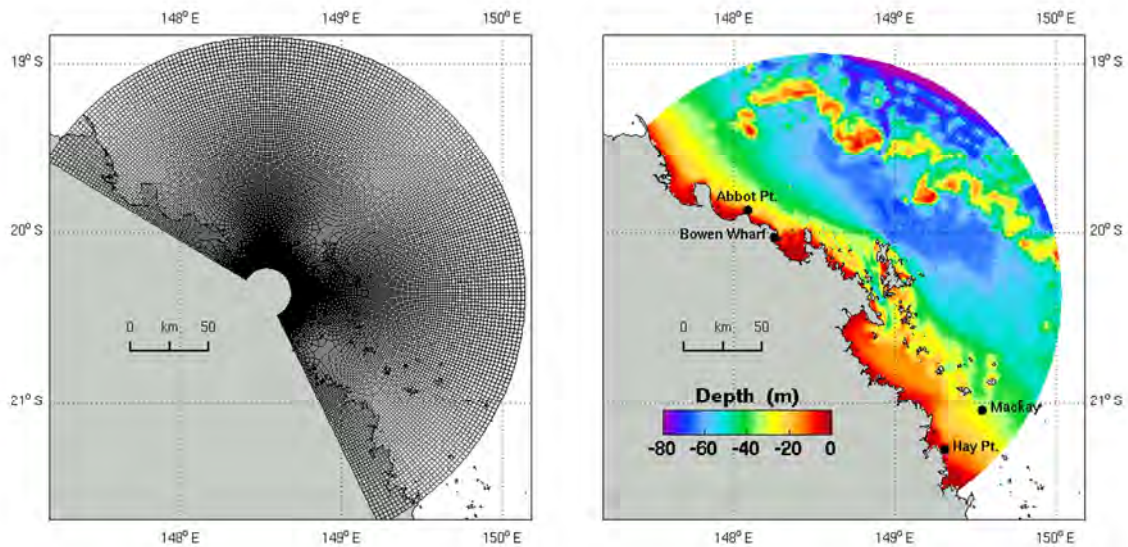


Figure 5.6.27 Model grid and bathymetry for polar regional model (POLW).

Verification of the Whitsunday models against observations was limited because the model domain is so compact as to only encompass very few measurement stations. The only continuous and contemporaneous data set that could be found was sea-level at Shute Harbour, just south of Airlie Beach. However, accuracy of both sea-level and surface

temperature could be inferred by first verifying the accuracy of the polar forcing model (POLW), which does encompass some measurement stations, and then by comparing the POLW output with the Whitsunday output at sites within the latter where they overlap. A similar procedure was carried out using the GBR1 forcing model. Salinity is not assessed due to lack of observations.

The sea-level for the POLW & WHIT1 models was compared with observations at 3 stations; Bowen Park, Shute Harbour and Mackay (Fig. 5.6.28). The POLW model accurately predicts the tidal sea-levels at all three sites. WHIT1 only includes Shute Harbour and also predicts the tidal height accurately. Similarly, WHIT2 compares well to observations, albeit with a slight degradation in skill compared to WHIT1 (Fig. 5.6.29; Willmott skill value of 0.96 and 0.99 for WHIT1 and WHIT2 respectively). Spring tides were slightly over-estimated and there was a slight phase difference. The low-frequency sea-level signals were similarly compared and are presented in Fig. 5.6.30, again showing good correlation to observations.

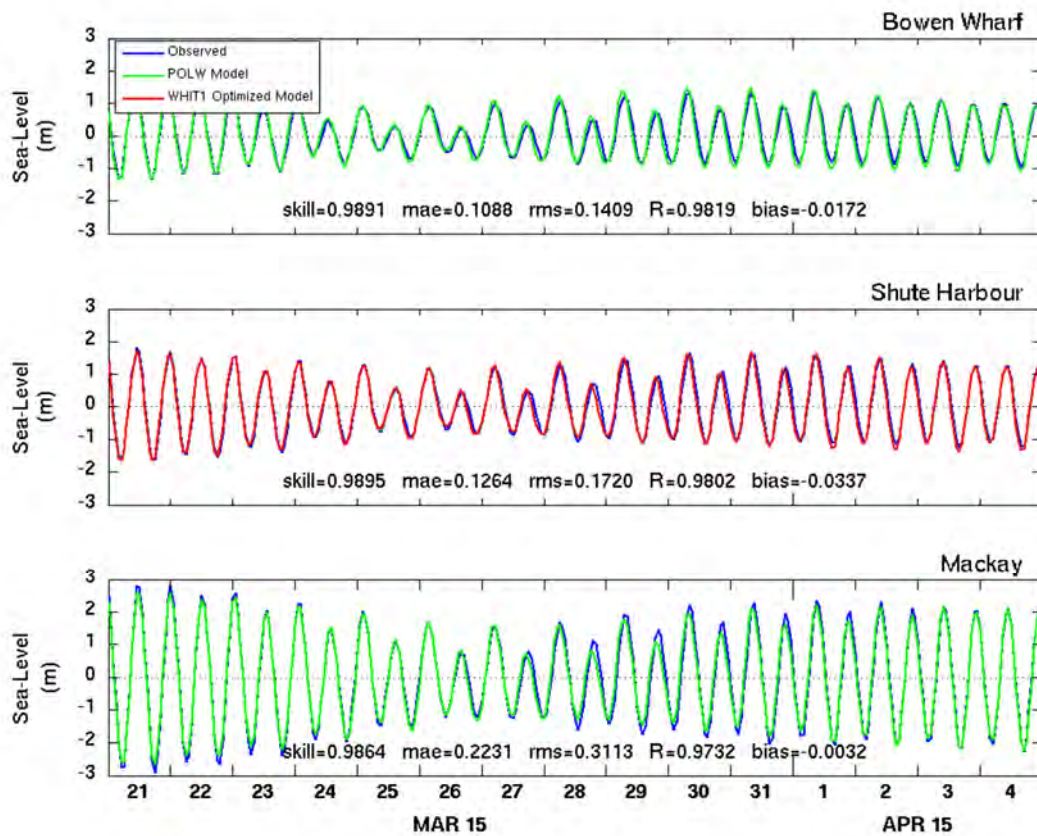


Figure 5.6.28. Sea-level comparisons for POLW at 3 stations and for WHIT1 at 1 station.

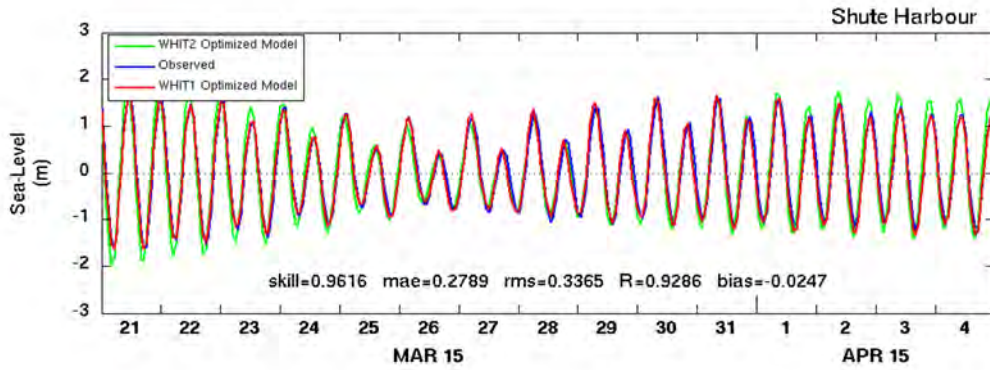


Figure 5.6.29. Sea-level comparisons between WHIT1, WHIT2 and the observations.

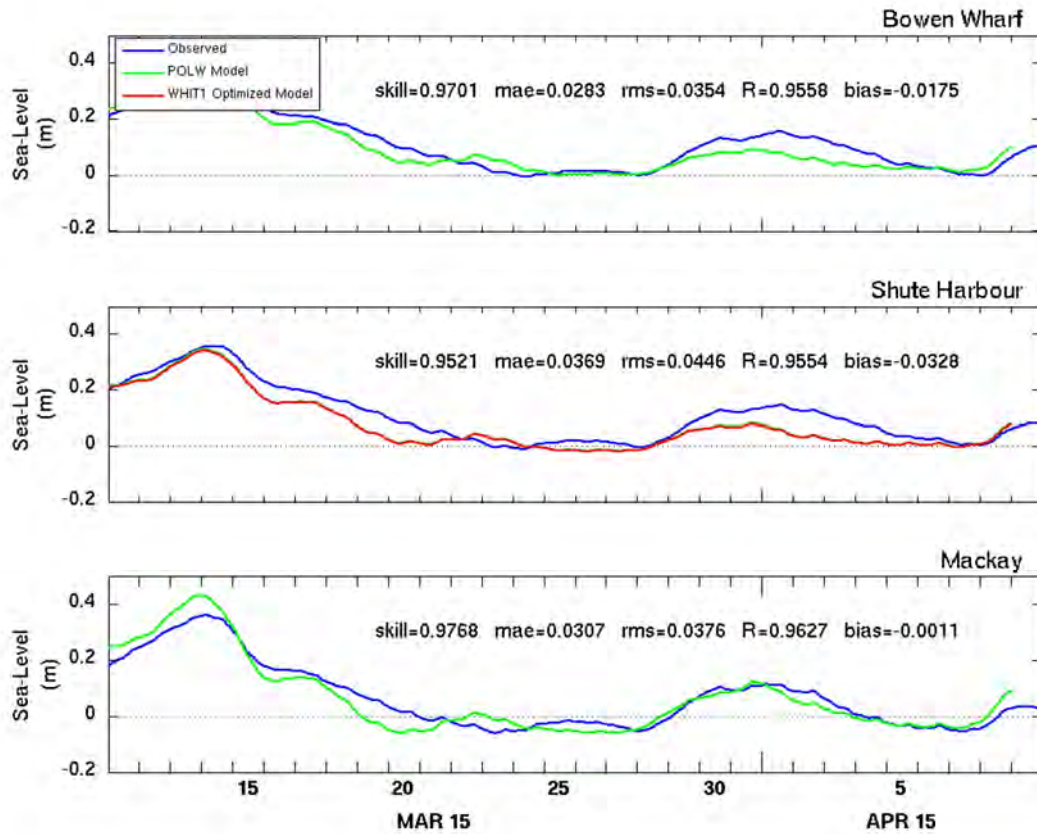


Figure 5.6.30. Low-frequency sea-level comparisons for POLW and WHIT1.

Accuracy of sea-surface temperature predictions from the models was assessed using observations from wave-buoys stationed at Abbot Point and Mackay. Results are shown in Fig. 5.6.31. Here POLW is seen to be in good agreement with the observations at both stations, although skill level is reduced at Mackay, while WHIT1 is in close agreement with POLW at 2 other sites, namely Airlie Beach and Molle Channel (see Fig. 5.6.26). At Molle Channel, the POLW and WHIT1 temperatures are virtually identical. The optimized model

suite is considered to be suitably accurate for the purposes of benchmarking a RECOM configuration.

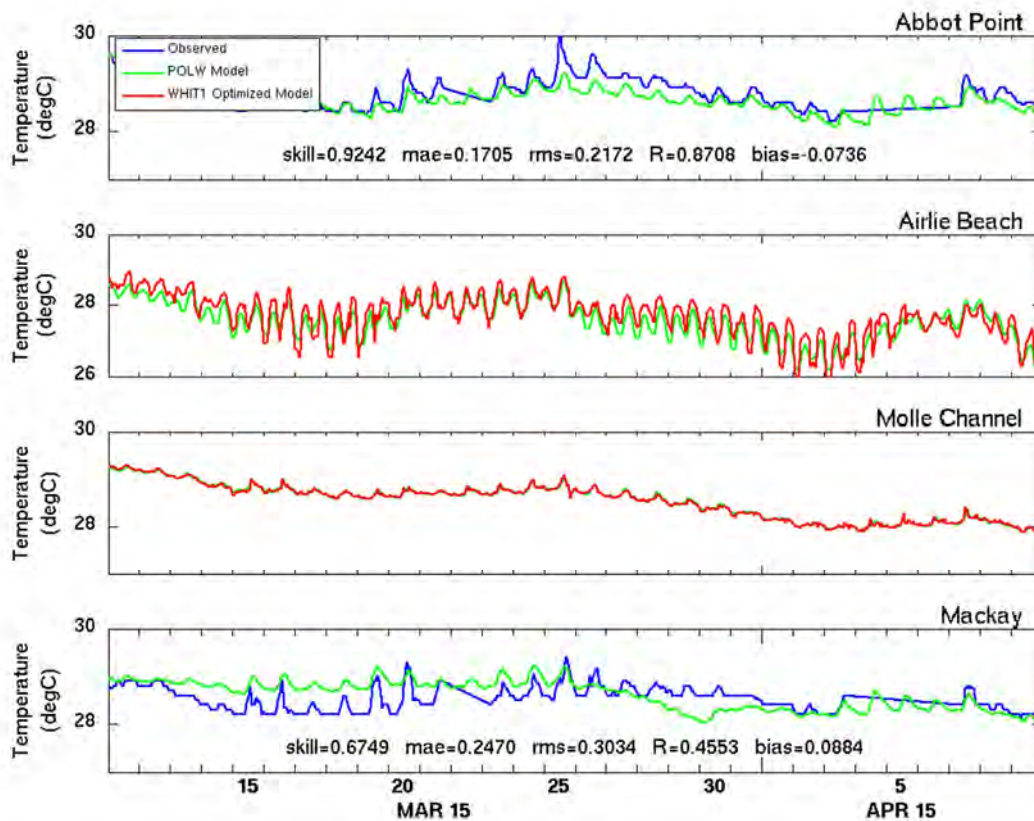


Figure 5.6.31. Surface temperature comparisons for POLW and WHIT1.

5.6.3.2 RECOM model

The RECOM web-tool was used to create a grid configuration as similar as possible to the optimized model shown in Fig. 5.6.26. Differences to the optimized grid arose due to slight differences in input coastline and bathymetry data. Also, limitation on the time-step allowed by RECOM prohibited grid resolution to be as finely resolving as the optimized model. There is the possibility of relaxing these limitations, however, this may result in users generating grids with unacceptably long run-times. Maximum resolution in the RECOM application was 80 m, i.e. twice that of the optimized model. The RECOM grid configuration is displayed in Fig. 5.6.32. A notable difference with the optimized model, as described earlier, is the much shallower bathymetry in the region of Molle Channel.

RECOM was initialised using the GBR4 model, ACCESS surface fluxes, GBR1 boundary forcing for temperature, salinity and surface elevation, and GBR4 boundary forcing for BGC variables. The ROBUST level 4 was used throughout (see Section 4.8.11).

The following simulations were implemented for the RECOM model:

- Run1. 01 March to 28 March, 2015
- Run2. 01 January to 28 February, 2015

Note that forcing for WHIT1 was only available from March onwards, and for RECOM BGC it was desirable to perform a longer simulation.

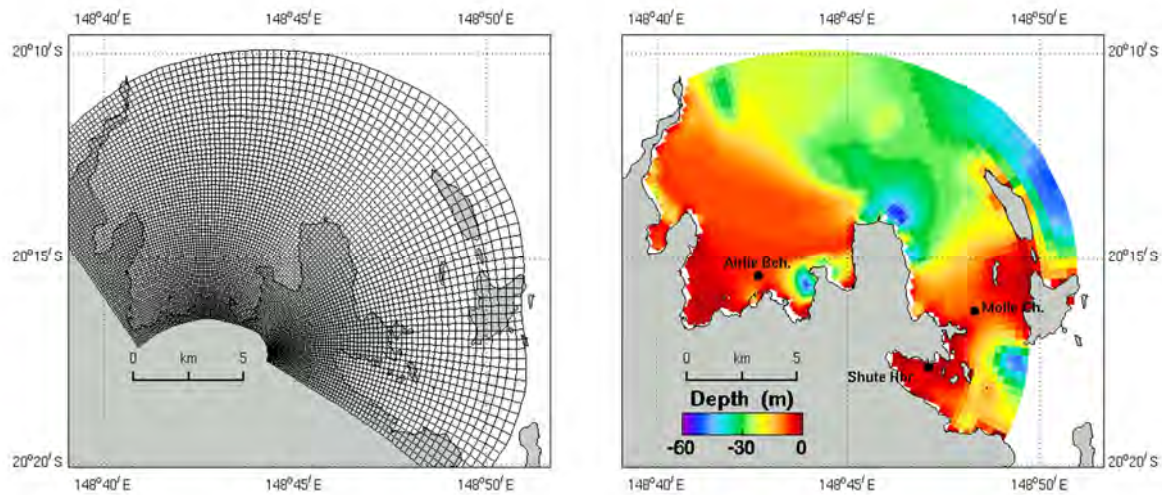


Figure 5.6.32. Model grid and bathymetry for Whitsunday RECOM model.

RECOM sea level from Shute Harbour was compared with both the observations and the output from the WHIT1 optimized model in Fig. 5.6.33. The results show that the RECOM model performs well through the neap tides, but over-estimates the spring tides of both WHIT1 and the observations by ~10-15%. The Willmott skill level of 0.97 is only slightly less than the 0.99 obtained for the optimized model.

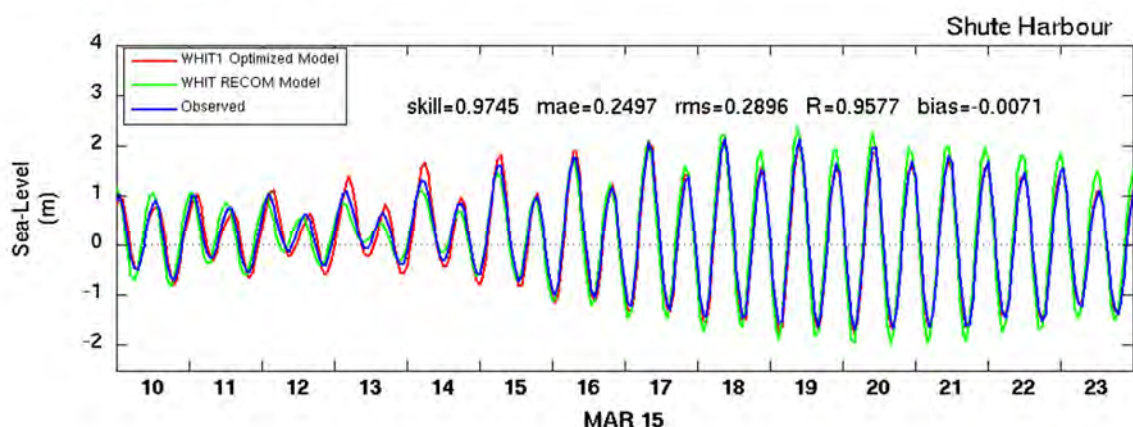


Figure 5.6.33. Sea-level comparisons between WHIT1, RECOM and the observations.

The low-frequency sea-level signals are compared in Fig. 5.6.34. The RECOM model and WHIT1 model both perform reasonably well in matching the observations, but the length of

the model runs is too short to make a definitive comparison. The RECOM Willmott skill level is 0.94 compared with 0.95 obtained for the optimized model.

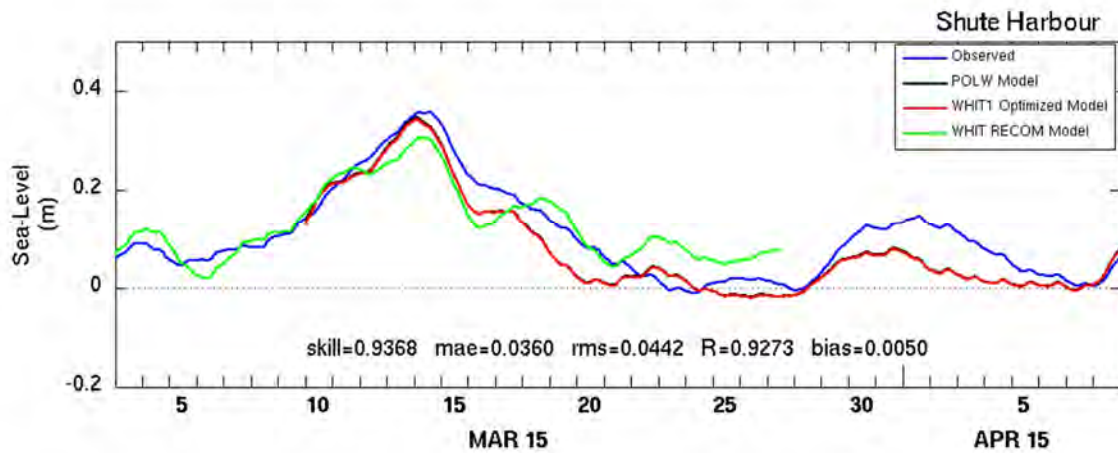


Figure 5.6.34. Low-frequency sea-level comparisons between POLW, WHIT1, RECOM and the observations.

Figures 5.6.35 and 5.6.36 present snapshots of sea-level and surface currents from WHIT1 and RECOM. These plots highlight the effect of the bathymetry differences on the currents in Molle Channel. Also, the overall current speeds of RECOM are lower than those of WHIT1 at this particular time, but this (and the small differences in sea-level) can be attributed to a small shift in phase of the tide for the RECOM model.

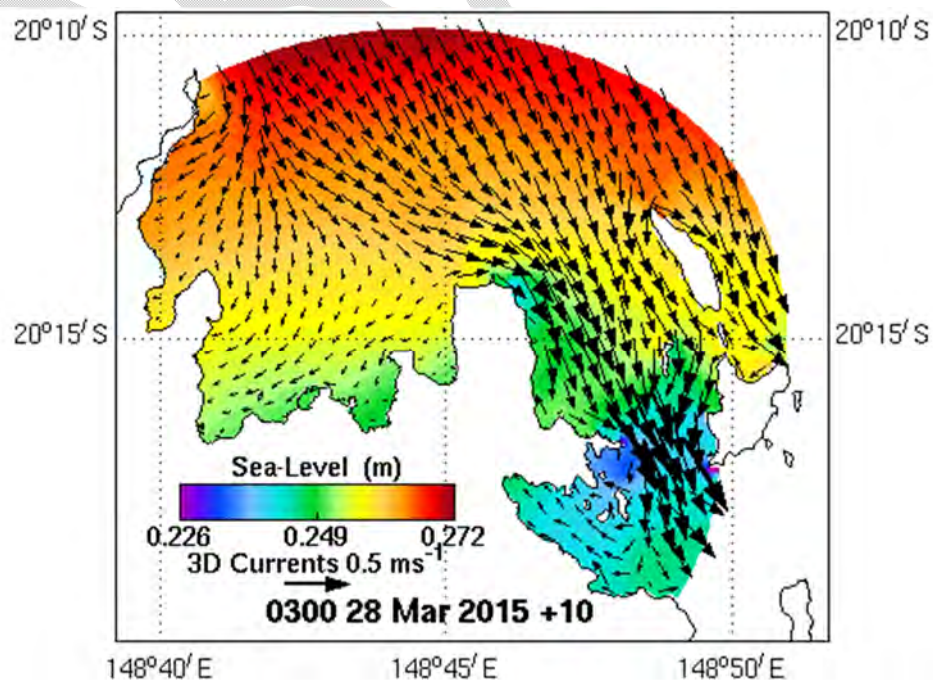


Figure 5.6.35. Sea-level & surface currents as predicted by the WHIT1 optimized model.

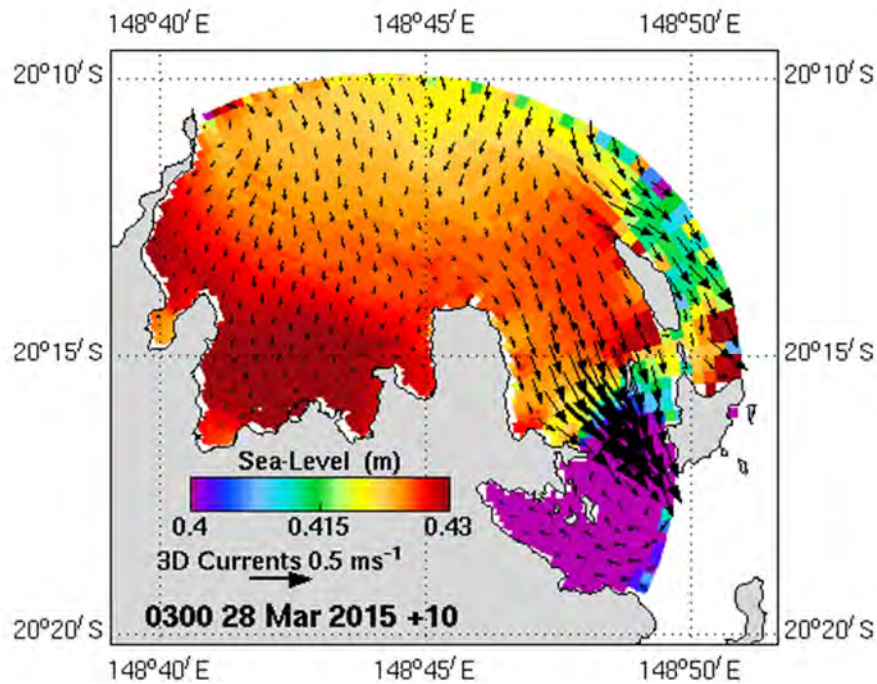


Figure 5.6.36. Sea-level & surface currents as predicted by the RECOM model.

To assess the surface temperature predictions for the RECOM model, output from Run1 for two sites was compared with the output from the WHIT1 optimized model (Fig. 5.6.37) and surface temperature near the end of the simulation in Fig. 5.6.38. Note that observations of temperature were not available for the Whitsunday domain hence quantitative skill metrics cannot be produced. The results show that the RECOM model has higher temperature at the Airlie Beach site by $\sim 1\text{-}2^{\circ}\text{C}$ relative to the optimized model, whereas differences are small at the Molle Channel site. The higher temperature at Airlie Beach is likely due to differential heating impacts between the two models as a result of any shallow inshore bathymetry differences. Certainly, the source of the cool water in WHIT1 near midday when surface heat fluxes are near maximum appears anomalous (Fig. 5.6.38). When these heating effects are less dominant in deeper, better flushed water, temperature differences are less. Note that GBR1 temperature (which is used as boundary forcing for RECOM) possesses a good level of skill at Mackay (Fig. 5.2.5) and develops a small bias in December 2014 and early January 2015 further north at Abbot Point. The optimized models have a warm bias at Mackay in March 2015, and small cool bias at Abbot Point (Fig. 5.6.31). In the absence of observations, within the sheltered regions of Airlie Beach it is debatable which model is actually performing better.

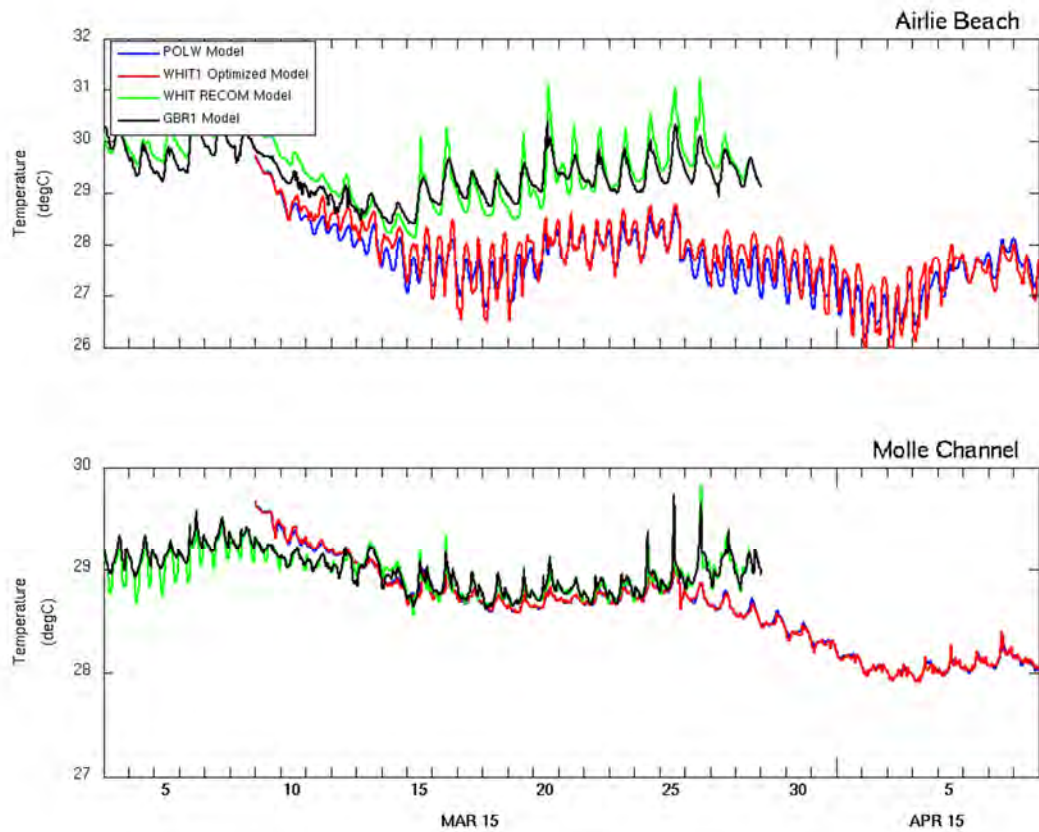


Figure 5.6.37 Surface temperature comparisons for RECOM model.

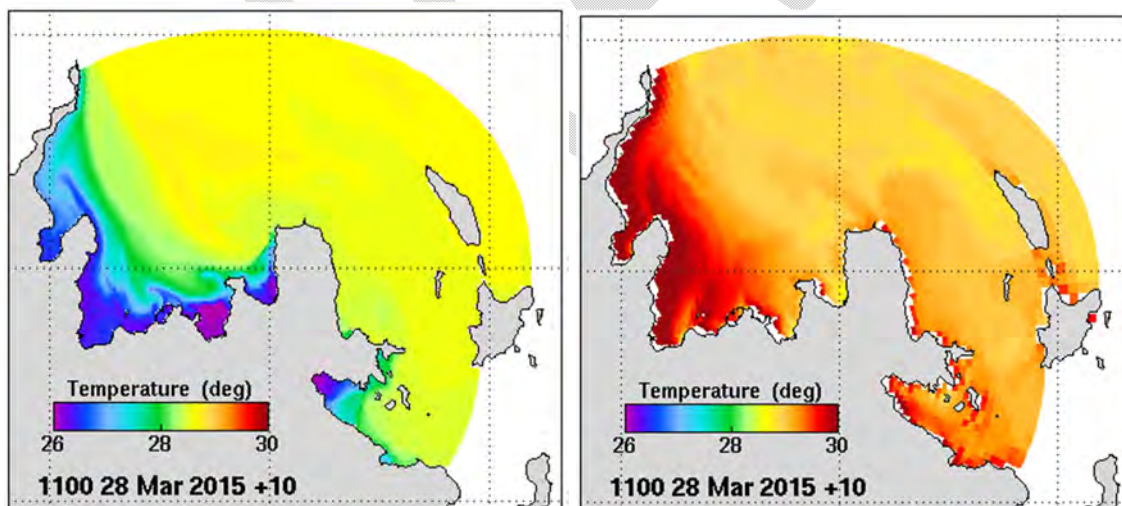


Figure 5.6.38. Surface temperature from WHIT1 (left) and RECOM (right).

The above RECOM comparisons are for the relatively short period of March-April 2015, when WHIT1 output was available. A second RECOM run (Run2) was carried out for the longer period January - February 2015 and fine sediment transport, Chla and nitrate are presented in Figs. 5.6.39-41.

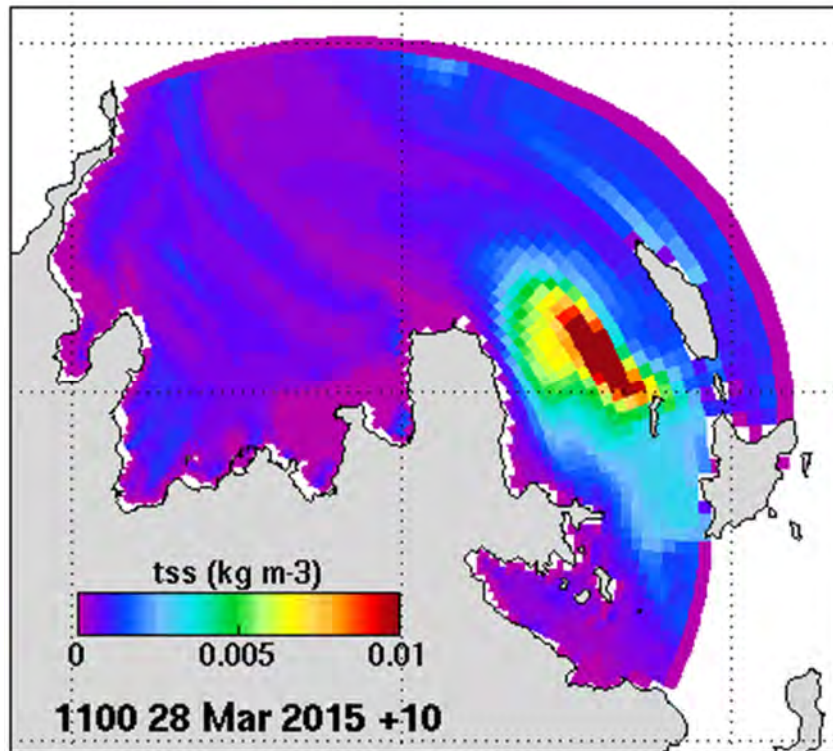


Figure 5.6.139. Total Suspended Solids as predicted by the RECOM model.

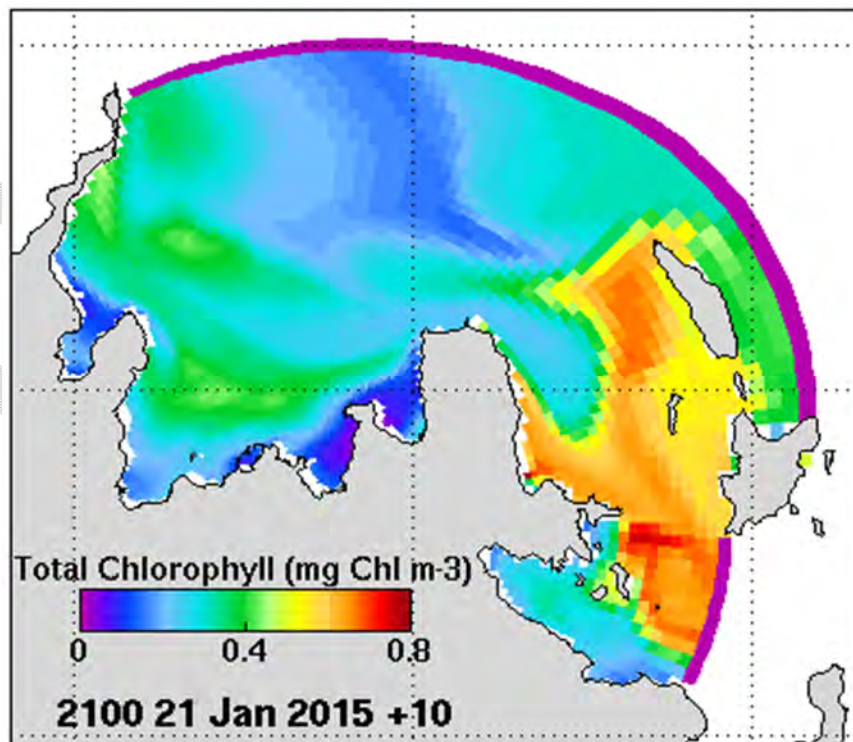


Figure 5.6.40. Total Chlorophyll as predicted by the RECOM model.

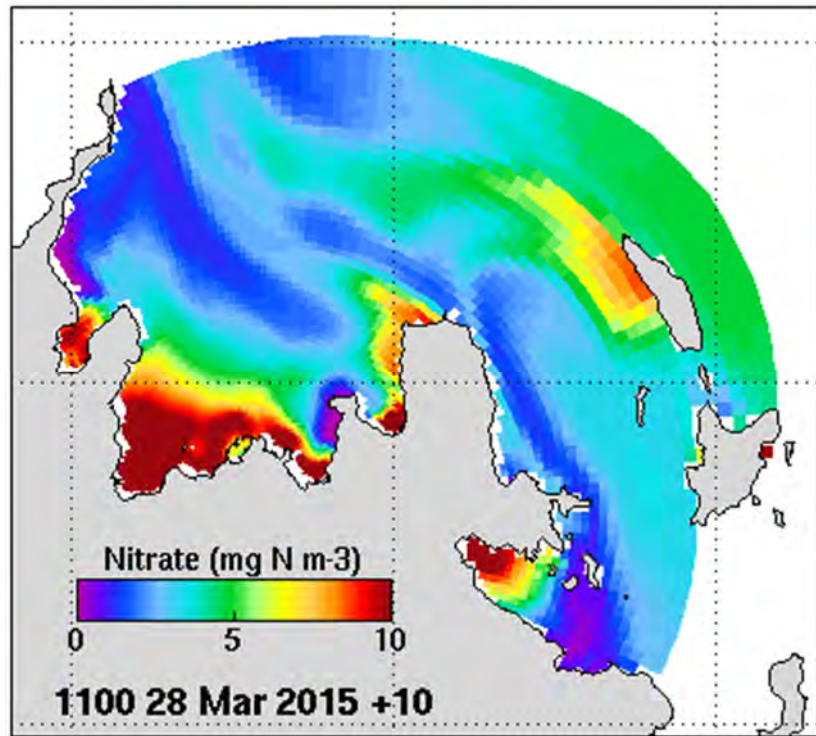


Figure 5.6.41. Total Nitrate as predicted by the RECOM model.

5.6.4 Summary and recommendations

The RECOM software has been tested on three regions possessing contrasting characteristics, by users who were not intimately familiar with the package through involvement in the software development. The users were able to successfully generate high resolution model implementations of the domains and produce outputs that are realistic. The basis of the hydrodynamic component in RECOM is that used in ROAM, developed over many years under BLUElink, and it is therefore a mature, robust and well tested piece of software. It is therefore unsurprising that the hydrodynamic component performed the best in the tests presented, correlating well with both observation and optimized models used as benchmarks. RECOM presents for the first time the inclusion of sediment transport and BGC components in an automated, re-locatable model, and consequently these components do not possess the level of maturity in terms of universal parameterisation and error handling as the hydrodynamic component. We see this reflected in decreasing levels of skill as the model progresses through hydrodynamics, sediment transport and BGC. However, a large contributor to differences in RECOM and optimized models lies in the initial conditions used in each, particularly the benthic components of the BGC, to which some components of RECOM are very sensitive. The ability of the user to import, and modify, benthic initial conditions from third-party sources is a modification to RECOM that will have direct consequences on the accuracy of the outputs. The error handling in sediments and BGC is implemented at the most basic level (i.e. if an error is detected the model does not integrate the water column). Having the benefit of greater development attention within BLUElink, the hydrodynamics is more sophisticated,

whereby the model is self-monitoring for the sources of instabilities, and attempts to rectify itself if trending towards instability. There remains much scope to implement similar error handling strategies within the sediment transport and BGC components of RECOM. That said, the RECOM sediment and BGC components in the above test cases were largely error free. Ultimately model applications require some optimization by expert users, and generally the more experienced the modeller, the better the model will be. RECOM cannot take the place of such expert input, and there will always be room for fine tuning of the model after scrutiny of model outputs by experts familiar with the dynamics of the ocean and the numerical implementations that approximate them. However, RECOM will produce an application that is around 90% along the road toward optimization, with minimal user effort. While the RECOM outputs should always be carefully appraised against observations, they can be considered useful pilot models 'out of the box' that accurately capture first order dynamics.

The workflow of RECOM is impressive and makes available unprecedented ease of generation of sediment and BGC models, such that non-specialist operators can now have access to these model outputs without the requirement of becoming intimately familiar with the underlying model codes and their methods of operation. Outputs of RECOM are self-contained transportable bundles that contain all the information required to run the model offline if required. This has the potential to open uptake of model products to a much wider audience than is currently possible. The user interaction with RECOM through the graphical interface is intuitive and simple. Nevertheless, practice using RECOM, especially the grid generation, will lead to improvements to the outputs RECOM generates. As more users are exposed to RECOM, there will undoubtedly be usability improvements that will be desired to be included in the RECOM workflow. Our limited experience indicates this is already the case, both in terms of generating better grids, and initializing the models to make outputs more accurate. We recommend that next developments of RECOM include:

1. The ability to import customized initial conditions for benthic variables,
2. The ability to move individual grid nodes in the grid generator,
3. Ability to see and share grids between users,
4. Ability to name grids; clone and resubmit model runs with only minor changes,
5. Consolidate the bathy tabs for improved editing; adding scale and coasts as well as optionally showing the regional model's grid/bathymetry or even the raw bathy,
6. Better control over outputs and provision for time-series files,
7. The ability to import a custom BGC parameter or process file to run on the RECOM server,
8. User profiles, so you can log in and see either just your own RECOM runs, or everyone's, and add notes to runs after they are complete,
9. Ability to revert a selected area of bathymetry during bathymetry editing to the original GBR100 or GA 2012 bathymetry. Additional options for fine-tuning bathymetry,

RECOM is currently operated in a development environment within the CSIRO computing architecture. The interface to RECOM is currently web based (<http://recom.it.csiro.au/>). Ultimately it is envisioned that RECOM be made accessible to anyone who wishes to model a section of the GBR at high resolution, and the next challenge is to determine a deployment

strategy for RECOM. This is not a trivial exercise, as the choices made in how users can access RECOM will dictate its uptake, flexibility, longevity, and ultimately the success of the product. There are various deployment strategies that could be used; the user could download, install and run the package in its entirety, the system could reside completely on a server and users could interact via a web GUI, or there could be a combination of both. The recent ability to generate a 'lightweight' virtual machine image, e.g. using docker (<https://www.docker.com/what-docker>) raises the possibility using this to deploy an embedded image of RECOM. It is recommended that the implementation of a deployment strategy be treated with the highest priority.

It is recommended that we view RECOM not as a final product, but as one capable of evolving to end user requirements. Any enhancements of RECOM should integrate this philosophy at the design stage to render RECOM flexible to change. We would hope that user feedback on usability and accuracy of RECOM would trigger enhancements to the system. RECOM also is built on the foundation of several other development initiatives in CSIRO, notably ROAM, TRIKE and MARVL, where many components are common to all systems. Some of the development expertise of these other systems lies elsewhere in CSIRO, however, development of RECOM was tightly coordinated with this expertise. It is recommended that RECOM maintains this tight coupling, with the objective to bring these software packages into a more unified single system in the longer term. Divergence of the software packages would be detrimental to the long term development of RECOM.

6. Summary

Although the GBR is recognised as one of the best managed reefs in the world, coral cover has continued to decline over the last decades at rates similar to less well managed reefs (Brodie and Waterhouse, 2012), and research based management and policy is recognised as a pathway for mitigating this trend. Model development to guide management actions is considered a criterion for the effective integration of science and management (Boesch, 1996). In this context, the outcome of eReefs is expected to be an information system that will assist regulatory authorities with issues relating to reef management. These include prediction of coral bleaching hotspots, ocean acidification and coral calcification effects, catchment impacts on reef health (sedimentation issues, eutrophication), dredging management, crown of thorns starfish (COTS) infestations, hypoxia, shipping management, fisheries management, search and rescue, larval connectivity and prediction of floods or extreme weather events. The modelling package will operate routinely in near real-time, delivering up-to-date information on the state of the GBR so that emergent events such as floods, dredge plumes, phytoplankton blooms, cyclones, vessel groundings, bleaching events etc. may be investigated in a timely manner. Maintaining a current archive of the state of the GBR assures that any investigations of processes and dynamics remain relevant, and account for shifts in the state of the system. The relocatable coastal modelling system will be made available to commercial consultants, state agencies and university staff and students who may wish to use a coastal modelling package to implement and analyse models.

Additionally, a strategic outcome is the production of next-generation prediction systems through pursuing state-of-the-art methodologies. These include reef processes, autonomous 2-way nesting, automated relocatable estuary models and model-data fusion.

The ultimate goal of major management initiatives such as Reef Plan and Reef Rescue is to protect the health of GBR ecosystems and the ecosystem services they support. These initiatives rely on a cause-effect chain linking land use and practices in catchments, to end of catchment flows and loads, to water quality in the GBR lagoon, to reef ecosystem health. These are complex systems, and there is inevitably uncertainty around all of these links. Quantitative links between end of catchment loads and reef performance measures are critical in order to set, e.g. end of catchment load targets, and to assess the relative benefits arising from load reductions in different catchments.

The modeling system developed under eReefs will provide a capacity to predict impacts of catchment loads on water quality under acute flood event conditions, and chronic post-flood and dry season conditions. The combined water quality model would provide a single integrated and consistent platform to predict changes in water quality in space and time in response to land use and load scenarios for any or all GBR catchments. Such model scenarios could be used directly to support the development of water quality targets for the GBR Lagoon, and to link these targets to end-of-catchment load targets. Further, ecological response models can employ output from the water quality model to simulate coral cover, coral recruitment, macroalgae and COTS as indicators of reef health.

There are a number of ways in which the modelling framework as described above could be used to support management decisions. A standard use of models is to predict system responses under alternative management scenarios and use this to assist in planning actions. In this form, models link management actions to performance indicators. Models can also be

used for diagnostic purposes; e.g., the model could be used to disentangle effects of interannual variability, or other pressures including climate change, from effects of actions in the catchment, and to explore the interactions among them. They can also be used to assess current compliance against set water quality targets. Models of this kind serve as an infrastructure platform for research as well as management. They provide an environment for evaluating new hypotheses about processes and system interaction and for designing field experiments and observing programs.

DRAFT

7. References

- Alongi, D. M. and McKinnon, A. D. 2005 The cycling and fate of terrestrially-derived sediments and nutrients in the coastal zone of the Great Barrier Reef. *Marine Pollution Bulletin* . 2005; 51:239-253
- Amos K.J, Alexander J., Horn A., Pocock G., Fielding C. 2004. Supply limited sediment transport in a high-discharge event of the tropical Burdekin river, north Queensland, Australia. *Sedimentology* 51, 145–162.
- Andrews, J.C. (1983) Water masses, nutrient levels and seasonal drift on the outer central Queensland shelf (Great Barrier Reef). *Aust. J. Mar. Freshw. Res.*, 34, 821-834.
- Andrews, J.C. and Furnas, M.J., 1986. Subsurface intrusions of Coral Sea water into the central Great Barrier Reef – I. Structures and shelf-scale dynamics. *Continental Shelf Res.*, 6(4):491-514.
- Andrews, J.C., Bode, L. (1988) The tides of the central Great Barrier Reef. *Continental Shelf Research* 8: 1057-1085.
- Andutta, F.P., P.V. Ridd and E. Wolanski (2011). Dynamics of hypersaline coastal waters in the Great Barrier Reef. *Estuarine, Coastal and Shelf Science*, 94:299:305
- Anthony, K. R. N., Kleypas, J. A., Gattuso, J.P. 2011. Coral reefs modify their seawater carbon chemistry - implications for impacts of ocean acidification, *Global change biology*, 17, 3655–3666.
- Ardhuin, F., E. Rogers, A.V. Babanin, J. Filipot, R. Magne, A. Roland, A. van der Westhuysen, P. Queffeulou, J-M. Lefevre, L. Aouf and F. Collard, 2010: Semiempirical dissipation source functions for ocean waves. part i: definition, calibration, and validation. *J. Phys. Oceanogr.*, **40**, 1917–1941.
- Ariathurai, R., Krone, R. B., 1976. Finite element model for cohesive sediment transport. *Journal of the Hydraulics Division, ASCE*, 104, HY2, 323–328.
- Armsworth, P., Bode, L., 1999. The consequences of non-passive advection and directed motion for population dynamics. *Proceedings of the Royal Society A: Mathematical, Physical and Engineering Sciences* 455, 4045–4060.
- Bailey, J.E., D. F. Ollis, 1986: *Biochemical engineering fundamentals*. McGraw-Hill Book Company, New York, 984pp.
- Baird, M. E., Ralph, P. J., Rizwi, F., Wild-Allen, K. A., Steven, A. D. L., 2013. A dynamic model of the cellular carbon to chlorophyll ratio applied to a batch culture and a continental shelf ecosystem. *Limnol. Oceanogr.* 58, 1215-1226.
- Beaman, R. 2010. Project 3DGBR: a high-resolution depth model for the Great Barrier Reef and Coral Sea. Final Report to Marine and Tropical Sciences Research Facility Final Report, June 2010
- Bell, R., Elmetri, I., 1995. Ecological indicators of large-scale eutrophication in the Great Barrier Reef lagoon. *Ambio* 24, 208–215.

- Bell, P.R.F., Elmetri, I., Uwins, P. (1999) Nitrogen fixation by *Trichodesmium* spp. in the central and northern Great Barrier Reef lagoon: relative importance of the fixed nitrogen load. *Marine Ecology Progress Series* 186: 119-126.
- Bell, P.R.F., Fu, F. (2005) Effect of light on growth, pigmentation and N₂ fixation of cultured *Trichodesmium* sp. from the Great Barrier Reef lagoon. *Hydrobiologia* 543: 25-35.
- Blumberg, A.F., Herring, J., 1987. Circulation modelling using orthogonal curvilinear coordinates, in *Three-Dimensional Models of marine and Estuarine Dynamics*, Ed. J.C.J. Nihoul and B.M. Jamart, Elsevier.
- Boesch, D.F., 1996. Science and management in four U.S. coastal ecosystems dominated by land-ocean interactions. *Journal of Coastal Conservation*, 2, 103-114.
- Brando, V. E., Robson, B. J., Cherukuru, N. R., Dekker, A. G., & Webster, I. T. (2007). Toward assimilation of ocean colour satellite observation into coastal ocean biogeochemical models: the tropical Fitzroy River Estuary case study. In *Optical Engineering+ Applications* (pp. 66850D-66850D). International Society for Optics and Photonics.
- Brando, V.E., Schroeder, T., Dekker, A.G., Park, Y.J., Reef Rescue Marine Monitoring Program: Using remote sensing for GBR-wide water quality. Final Report for 2009/2010 Activities. 2010, CSIRO Land & Water: Canberra [http://www.gbrmpa.gov.au/_data/assets/pdf_file/0007/46528/Remote_sensing_final_annual_report_2009_10.pdf]
- Brassington, G. B.; Pugh, T.; Spillman, C.; Schulz, E.; Beggs, H.; Schiller, A. & Oke, P. R. (2007), BLUElink development of operational oceanography and servicing in Australia, *Journal of Research and Practice in Information Technology*, 39(2), 151-164.
- Brodie, J., Waterhouse, J. (2012) A critical review of environmental management of the 'not so Great' Barrier Reef. *Estuarine, Coastal and Shelf Science*, 104-105, 1-22.
- Bowie, G. L., Environmental Research Laboratory (Athens Ga.) and Tetra Tech inc. (1985). Rates, constants, and kinetics formulations in surface water quality modeling. Athens, Ga., Environmental Research Laboratory, Office of Research and Development, U.S. Environmental Protection Agency,
- Brinkman, R.M., Wolanski, E.J., Deleersnijder, E., McAllister, F.A., Skirving, W.J., 2002. Oceanic inflow from the Coral Sea into the Great Barrier Reef. *Estuarine Coastal and Shelf Science* 54: 655-668.
- Brodie, J., Furnas, M., 2001. Status of nutrient and sediment inputs from Great Barrier Reef catchments and impacts on the Reef. Paper in proceedings of the 2nd National Conference on Aquatic Environments: Sustaining Our Aquatic Environments – Implementing Solutions. 20-23 November, 2001, Townsville, 14 p.
- Brodie, J., L.A. McKergow, I.P. Prosser, M. Furnas, A.O. Hughes and H. Hunter 2004 Sources of sediment and nutrient exports to the Great Barrier Reef World Heritage Area. ACTFR Report No. 03/11 to Environment Australia
- Brodie, J., Waterhouse, J., 2012. A critical review of environmental management of the 'not so Great' Barrier Reef. *Est, Coastal and Shelf Sci.*, 104-105, 1-22.

- Brodie J., Kroon F., Schaffelke B., Wolanski E., Lewis S., Devlin M., Bohnet I., Bainbridge Z., Waterhouse J., Davis A. 2012. Terrestrial pollutant runoff to the Great Barrier Reef: An update of issues, priorities and management responses. *Marine Pollution Bulletin* 65, 81–100.
- Brodie J., Waterhouse J., Schaffelke B., Kroon F., Thorburn P., Rolfe J., Johnson J., Fabricius K., Lewis S., Devlin M., Warne M., McKenzie L. 2013. Scientific Consensus Statement Land use impacts on Great Barrier Reef water quality and ecosystem condition. The State of Queensland 2013. Published by the Reef Water Quality Protection Plan Secretariat, July 2013.
- Browne N.K., Smithers S., Perry C., Ridd P. 2012. A Field-Based Technique for Measuring Sediment Flux on Coral Reefs: Application to Turbid Reefs on the Great Barrier Reef. *Journal of Coastal Research* 28, 5, 1247–1262.
- Bureau of Meteorology, 2010. The Implementation of the AUSWAVE wave model at the Australian Bureau of Meteorology. NMOC Operations Bulletin No. 84, 12 pp.
- Burford, M. A., A. Revill, D. Palmer, L. Clementson, B. Robson and I. Webster (2011). "River regulation alters drivers of primary productivity along a tropical river-estuary system." *Marine and Freshwater Research* 62(2): 141-151.
- Burrage, D. M., Church, J. A., Steinberg, C. R. 1991 Linear systems analysis of Momentum on the continental shelf and slope of the Central Great Barrier Reef. *Journal of Geophysical Research* 96 (C12), 22 169–22 190.
- Burrage, D.M., C. R. Steinberg, W. J. Skirving and J. A. Kleypas, 1996. Mesoscale circulation features of the Great Barrier Reef lagoon inferred from NOAA satellite imagery. *Remote Sens. Environ.*, 56, 21 – 41.
- Burrage, D.M., M.L. Heron, J.M. Hacker, J.L. Miller, T.C. Stieglitz, C.R. Steinberg and A. Prytz (2003). Structure and influence of tropical river plumes in the Great Barrier Reef: application and performance of an airborne sea surface salinity mapping system. *Remote Sensing of Environment*, 85:204-220
- Butler, A.J. 1999. Seagrass in Australia: Strategic Review and Development of an R&D Plan, FRDC Project 98/223.
- Calbet, A. and M.R. Landry 2004 Phytoplankton growth, microzooplankton grazing, and carbon cycling in marine systems. *Limnology and Oceanography* 49: 51-57.
- Capet, X., McWilliams, J.C., Molemaker, M.J., Shchepetkin, A.F. (2008). Mesoscale to submesoscale transition in the California Current system. Part II: Frontal processes. *J. of Phys. Oceanog.*, 38, 44-64.
- Capone, D.G., Bronk, D.A., Mulholland, M.R., Carpenter, E.J. (2008) Nitrogen in the Marine Environment 2nd Edition, Academic Press, San Diego.
- Carroll, C., Waters, D., Vardy, S., Silburn, D. M., Attard, S., Thorburn, P. J., Clark, A. (2012). A paddock to reef monitoring and modelling framework for the Great Barrier Reef: paddock and catchment component. *Marine Pollution Bulletin*, 65(4), 136-149.
- Cartwright, D.E. and R.D. Ray (1990) Oceanic tides from Geosat altimetry. *J. Geophys. Res.*, 95 C3, 3069-3090.

- Chang, J. (2000). "Precision of different methods used for estimating the abundance of the nitrogen-fixing marine cyanobacterium, *Trichodesmium* Ehrenberg." *Journal of Experimental Marine Biology and Ecology* 245(2): 215-224. Doi 10.1016/S0022-0981(99)00163-X.
- Cherukuru, N. R. C., B. J. Robson, V. E. Brando and A. G. Dekker (2008). Improving light propagation in coastal biogeochemical models: A case study in tropical coastal waters of Australia. *Ocean Optics Conference XIX, Italy*
- Cherukuru, N., Robson, B., Brando, V., & Dekker, A. G. (2009). Assimilation of optical remote sensing data into coastal aquatic biogeochemical models. In 5th WMO Symposium on Data Assimilation, Melbourne (Aus.) (pp. 5-9).
- Cogle, A. L., Carroll, C., & Sherman, B. S. (Eds.). (2006). The use of SedNet and ANNEX models to guide GBR catchment sediment and nutrient target setting. *Natural Resources, Mines and Water*.
- Condie, S. A., M. Herzfeld, N. Margvelashvili and J. R. Andrewartha (2009). "Modeling the physical and biogeochemical response of a marine shelf system to a tropical cyclone." *Geophysical Research Letters* 36Artn L22603 Doi 10.1029/2009gl039563.
- Connell, D. W., B. M. Bycroft, G. J. Miller and P. Lather (1981). "Effects of a Barrage on Flushing and Water-Quality in the Fitzroy River Estuary, Queensland." *Australian Journal of Marine and Freshwater Research* 32(1): 57-63.
- Crane M & C D Burke (2007). "Primary Porosity in Modern Coral Patch Reefs". *Proceedings of AAPG Mid-Continent Section Meeting, Wichita, Kansas*
- Crosbie, N.D., Furnas, M. (1999) Distribution of photosynthetic prokaryotic picoplankton in GBR shelf waters. *Bulletin de l'Institute oceanographique Monaco* 19(Special): 377-386.
- Darnell R., Henderson B., Kroon F., Kuhnert P. 2012. Statistical power of detecting trends in total suspended sediment loads to the Great Barrier Reef *Marine Pollution Bulletin* 65, 203–209.
- Davies, P. L. and B. D. Eyre (2005). "Estuarine modification of nutrient and sediment exports to the Great Barrier Reef marine park from the Daintree and Annan River catchments." *Marine Pollution Bulletin* 51(1-4): 174-185. DOI 10.1016/j.marpolbul.2004.11.008.
- Dickson, A. 1990. Standard potential of the reaction - $\text{AgCl(s)} + \frac{1}{2}\text{H}_2(\text{g}) = \text{Ag(s)} + \text{HCl(aq)}$ and the standard acidity constant of the ion HSO_4^- in synthetic sea-water from 273.15 to 318.15 K. *Journal of Chemical Thermodynamics*, 22, 113–127.
- De'ath George, Fabricius K., 2008 *Water Quality of the Great Barrier Reef: Distributions, Effects on Reef Biota and Trigger Values for the Protection of Ecosystem Health Report to the Great Barrier Reef Marine Park Authority*, N 89, 105 p.
- Debreu, L. and E. Blayo (2008). "Two-way embedding algorithms: a review." *Ocean Dynamics* 58(5-6): 415-428. DOI 10.1007/s10236-008-0150-9.
- Debreu, L., P. Marchesiello, P. Penven and G. Cambon (2012). "Two-way nesting in split-explicit ocean models: Algorithms, implementation and validation." *Ocean Modelling* 49-50: 1-21. DOI 10.1016/j.ocemod.2012.03.003.
- Debreu, L., Vouland, C., Blayo, E., 2008. AGRIF: adaptive grid refinement in Fortran. *Comput. Geosci.* 34 (1), 8–13.

- Deleersnijder, E., Norro, A., Wolanski, E., 1992. A three-dimensional model of the water circulation around an island in shallow water. *Continental Shelf Research* 12, 891–906.
- Deltares (2011). Delft3D-FLOW. Simulation of multi-dimensional hydrodynamic flows and transport phenomena, including sediments. User Manual. Version: 3.15. The Netherlands.
- Done, T., 1988. Simulations of the recovery of pre-disturbance size structure in populations of *Porites* spp. damaged by crown-of-thorns starfish. *Marine Biology* 100, 51–61.
- Douglas, G., Ford, P., Moss, A., Noble, B., Packett, B., Palmer, M., ... & Webster, I. (2005). Carbon and nutrient cycling in a subtropical estuary (the Fitzroy), Central Queensland. Cooperative Research Centre for Coastal Zone, Estuary and Waterway Management. Technical Report, 14, 72.
- Douglas, G. B., Ford, P. W., Palmer, M., Noble, R. M., & Packett, R. (2006). Fitzroy River Basin, Queensland, Australia. I. Identification of sediment sources in impoundments and flood events. *Environmental Chemistry*, 3(5), 364-376.
- Durrant, T., M. Hemer, C. Trenham and D. Greenslade (2013). "CAWCR Wave Hindcast 1979-2010, v4. CSIRO. Data Collection. DOI: 20.4225/08/523168703DCC5
- Donnelly, T., M. Grace and B. Hart (1997). "Algal blooms in the Darling-Barwon River, Australia." *Water, Air, & Soil Pollution* 99(1): 487-496.
- Dunn, R. J. K., A. Ali, C. J. Lemckert, P. R. Teasdale and D. T. Welsh (2007). "Short-term Variability of Physico-chemical Parameters and the Estimated Transport of Filterable Nutrients and Chlorophyll-a in the Urbanised Coombabah Lake and Coombabah Creek System, Southern Moreton Bay, Australia." *Journal of Coastal Research*: 1062-1068.
- Eanes, R., Bettadpur, S., 1995: The CSR 3.0 global ocean tide model. Center for Space Research, Technical Memorandum, CST-TM-95-06.
- Ebert, E.E. (2008). Fuzzy verification of high-resolution gridded forecasts: a review and proposed framework. *Meteorological Applications*, 15, 51-64.
- Evensen, G. (2009), The Ensemble Kalman Filter for Combined State and Parameter Estimation Monte Carlo techniques for data assimilation in large, *IEEE Control Systems Magazine*, 29(3), 83-104.
- Eyre, B. and P. Balls (1999). "A comparative study of nutrient behavior along the salinity gradient of tropical and temperate estuaries." *Estuaries* 22(2A): 313-326. Doi 10.2307/1352987.
- Fabricius, K.E., 2005. Effects of terrestrial runoff on the ecology of oral and coral reef: review and synthesis, *Marine Pollution Bulletin* 50, 12 -1.
- Fabricius K., De'ath George, Humphrey C., Zagorskis I., Schaffelke B. 2013. Intra-annual variation in turbidity in response to terrestrial runoff on near-shore coral reefs of the Great Barrier Reef Estuarine, *Coastal and Shelf Science* 116, 57-65.
- Fabricius K., Logan M., Weeks S., Brodie J. 2014. The effects of river run-off on water clarity across the central Great Barrier Reef *Marine Pollution Bulletin* 84, 191–200.
- Farraday, R.V. and F.G. Charlton (1983). Hydraulic factors in bridge design. Hydraulic Research Station Ltd., Wallingford, Oxfordshire, England. 314p

- Fentie, B., Joo, M., Yu, B., Hunter, H., Marsh, N., Carroll, C., & Dougall, C. (2005). Comparison of mean annual suspended loads estimated by the SedNet model and rating curves in the Fitzroy Catchment, Australia.
- Flores, E. and A. Herrero (2005). "Nitrogen assimilation and nitrogen control in cyanobacteria." *Biochemical Society Transactions* 33: 164-167.
- Ford, P., P. Tillman, B. Robson and I. T. Webster (2005). "Organic carbon deliveries and their flow related dynamics in the Fitzroy estuary." *Marine Pollution Bulletin* 51(1-4): 119-127. DOI 10.1016/j.marpolbul.2004.10.019.
- Fujii, M., E. Boss and F. Chai (2007) The value of adding optics to ecosystem models: a case study. *Biogeosciences*, 4, 817–835.
- Furnas, M., (2003). *Catchments and corals: terrestrial runoff to the Great Barrier Reef*. Australian Institute of Marine Science, Queensland., 334 p.
- Furnas, M.J., (1991). Net in situ growth rates of phytoplankton in an oligotrophic, tropical shelf ecosystem. *Limnol. Oceanogr.*, 36(1): 13-29.
- Furnas, M and Mitchell, A.W., (1986). Phytoplankton dynamics in the central Great Barrier Reef – I. Seasonal changes in biomass and community structure and their relation to intrusive activity. *Continental Shelf Res.*, 6(3): 363-384.
- Furnas, M and Mitchell, A.W., (1996). Nutrient inputs into the central Great Barrier Reef (Australia) from subsurface intrusions of Coral Sea waters: a two-dimensional displacement model. *Continental Shelf Res.*, 16(9): 1127-1148.
- Furnas, M., Mitchell A.W., Skuza M. (1995) Nitrogen and Phosphorus budgets for the central Great Barrier Reef. Shelf Research Publication No 36 Great Barrier Reef Marine Park Authority, Townsville 193 p.
- Furnas, M., Mitchell, A., Skuza, M. and Brodie, J., (2005). In the other 90%: phytoplankton responses to enhanced nutrient availability in the Great Barrier Reef Lagoon. *Mar. Poll. Bull.*, 51: 253-265.
- Furnas, M., D. Alongi, D. McKinnon, L. Trott and M. Skuza (2011) Regional-scale nitrogen and phosphorus budgets for the northern (14°S) and central (17°S) Great Barrier Reef shelf ecosystem. *Continental Shelf Research* 31: 1967-1990.
- Ganachaud, A.; Kessler, W.; Wijffels, S.; Ridgway, K.; Cai, W.; Holbrook, N.; Bowen, M.; Sutton, P.; Qiu, B.; Timmermann, A.; Roemmich, D.; Sprintall, J.; Cravatte, S.; Gourdeau, L. & Aung, T. (2007), Southwest Pacific Ocean Circulation and Climate Experiment (SPICE) Part I. Scientific Background, CLIVAR Publication Series No. 111 , Technical report, CLIVAR Publication Series No. 111.
- Gattuso, J.P., Pichon, M., and Frankignoulle, M., 1995. Biological control of air-sea CO₂ fluxes: effect of photo- synthetic and calcifying marine organisms and ecosystems, *Marine ecology-progress series*, 129, 307–312.
- Geider, R. J. and J. L. Roche (2002). "Redfield revisited: variability of C [ratio] N [ratio] P in marine microalgae and its biochemical basis." *European Journal of Phycology* 37(01): 1-17.
- Geoscience Australia, 2009. Australian Bathymetry and Topography Grid, June 2009. Record 2009/21, Geoscience Australia, Canberra, Australia.

Gillibrand, P.A., Mongin, M., Tilbrook, B. In Prep. Coupled wave and hydrodynamic modelling of water circulation and exchange over Heron Island lagoon in the southern Great Barrier Reef. *Ocean Dynamics*.

C. Goyens, C. Jamet, T. Schroeder 2013. Evaluation of four atmospheric correction algorithms for MODIS–Aqua images over contrasted coastal waters. *Remote Sensing of Environment*, 131 (2013), pp. 63–75 <http://dx.doi.org/10.1016/j.rse.2012.12.006>.

Grant, D., Madsen, O., 1982. Movable bed roughness in unsteady oscillatory flow. *J. of Geophysical Research*, V. 87, N C1, pp. 469-481.

Griffin, D. A. and J. H. Middleton, 1986. Coastal trapped waves behind a large continental shelf island, southern Great Barrier Reef. *J. Phys. Oceanogr.*, 16, 1651 – 1664.

Griffin, D. A., J. H. Middleton and L. Bode, 1987. The tidal and longer-period circulation of Capricornia, southern Great Barrier Reef. *Aust. J. Mar. Freshw. Res.*, 38, 461 – 474.

Gustafsson, M. S., Baird, M. E. and Ralph, P. J. (2013) The interchangeability of autotrophic and heterotrophic nitrogen sources in Scleractinian coral symbiotic relationships: a numerical study. *Ecol. Model.* 250:183-194.

Hadley, S. Wild-Allen, K., MacLeod, C, (manuscript) Modelling macroalgae growth and nutrient dynamics for Integrated Multitrophic Aquaculture. *Ecological Modelling*:

Hamner, W., Hauri, I., 1981. Effect of island mass: water flow and plankton pattern around a reef in the Great Barrier Reef lagoon. *Limnology and Oceanography* 26, 1084–1102.

Hansen, P. J., P. K. Bjornsen and B. W. Hansen (1997). "Zooplankton grazing and growth: Scaling within the 2-2,000- μ m body size range." *Limnology and Oceanography* 42(4): 687-704.

Hardy, T. A., Mason, L.B., McConochie, J.D., 2000. A wave model for the Great Barrier Reef. *Ocean Engineering* 28, 45-70.

Harris, G. P. (2001). "Biogeochemistry of nitrogen and phosphorus in Australian catchments, rivers and estuaries: effects of land use and flow regulation and comparisons with global patterns." *Marine and Freshwater Research* 52(1): 139-149. Doi 10.1071/Mf00031.

Harris, P.T., Hughes, M.G., Baker, E.K., Dalrymple, R.W., Keene, J.B., 2004. Sediment transport in distributary channels and its export to the pro-deltaic environment in a tidally-dominated delta: Fly River, Papua New Guinea. *Continental Shelf Research*, 24, 2431-2454.

Hausler, G. (1991) Hydrology of north Queensland streams and their groundwaters. In Yellowlees (ed.) , *Land use patterns and nutrient loading of the Great Barrier Reef region* JCU Press, Townsville, 90-107.

Heil, C.A., Chaston, K., Jones, A., Bird, P., Longstaff, B., Costanzo, S., Dennison, W.C., (2004). Benthic microalgae in coral reef sediments of the southern Great Barrier Reef, Australia *Coral Reefs* (2004) 23: 336-343. DOI 10.1007/s00338-004-0390-1

Herzfeld, M., Andrewartha, J.R., Sakov, P., Webster, I., 2006. Numerical hydrodynamic modelling of the Fitzroy Estuary. Cooperative Research Centre for Coastal Zone, Estuary and Waterway Management (Coastal CRC), Technical Report 38, 94 pp.

Herzfeld, M., Waring J. R. (2008) SHOC: Sparse Hydrodynamic Ocean Code User's manual. CSIRO internal document. 128 pp.

- Herzfeld, M., 2006. An alternative coordinate system for solving finite difference ocean models. *Ocean Modelling*, 14, 174 – 196.
- Herzfeld, M., 200b. ROAM : Task 5 Model Description and Assessment / prepared for the Royal Australian Navy as part of the BLUElink project. Hobart, Tas.: CSIRO Marine and Atmospheric Research.
- Herzfeld, M., 2009a. The role of numerical implementation on open boundary behaviour in limited area ocean models. *Ocean Modelling*, 27, 18-32. [doi:10.1016/j.ocemod.2008.10.008](https://doi.org/10.1016/j.ocemod.2008.10.008)
- Herzfeld, M., 2009b. Improving stability of regional numerical ocean models. *Ocean Dynamics*, 59, 21- 46. <http://dx.doi.org/10.1007/s10236-008-0158-1>
- Herzfeld, M., Waring, J., Parslow, J., Margvelashvili, N., Sakov, P., Andrewartha, J. (2008) SHOC: Sparse Hydrodynamic Ocean Code Science manual. CSIRO internal document. 121 pp.
- Herzfeld, M., Schmidt, M., Griffies, S., Liang, Z. (2011) Realistic test cases for limited area ocean modelling. *Ocean Modelling*, 37, 1-34.
- Herzfeld, M., Jones, E., Margvelashvili, N., Mongin, M., Skerratt, J., Andrewartha, J., Rizwi, F., McAlister, T., Holmes, R., Barry, M., Weber, T., Teakle, I., 2012. SEQ Receiving Water Quality Model V3 Phase II. Final Report submitted to SEQ Healthy Waterways Partnership, 166 p.
- Herzfeld, M., J. Andrewartha, M. Baird, R. Brinkman, M. Furnas, P. Gillibrand, M. Hemer, K. Joehnk, E. Jones, D. McKinnon, N. Margvelashvili, M. Mongin, F. Rizwi, B. Robson, J. Skerratt, H. Tonin, K. Wild-Allen (2013). eReefs WP3 Marine Modelling: Milestone #1 Report, Dec. 2012, CSIRO, Hobart.
- Holthuijsen, L.H., 2007. *Waves in Oceanic and Coastal Waters*. Cambridge Univ. Press, Cambridge, UK, 387 pp.
- Howarth, R. W., R. Marino and J. J. Cole (1988). "Nitrogen fixation in freshwater, estuarine, and marine ecosystems. 2. Biogeochemical controls." *Limnology and Oceanography*: 688-701.
- Hughes, A. O., & Croke, J. C. (2011). Validation of a spatially distributed erosion and sediment yield model (SedNet) with empirically derived data from a catchment adjacent to the Great Barrier Reef Lagoon. *Marine and Freshwater Research*, 62(8), 962-973.
- Huthoff, F. and D. Augustijn (2006). Hydraulic resistance of vegetation. Predictions of average flow velocities based on a rigid-cylinders analogy. University of Twente, Faculty of Engineering Technology, Water Engineering and Management. The Netherlands. 77p.
- Ibelings, B. W. and S. C. Maberly (1998). "Photoinhibition and the availability of inorganic carbon restrict photosynthesis by surface blooms of cyanobacteria." *Limnology and Oceanography* 43(3): 408-419.
- Ikeda, T and M. Omori 1984 **Methods in Marine Zooplankton Ecology**, John Wiley and Sons, New York.
- Jaffrés, Jasmine B.D., and Heron, Malcolm L. (2011) Wave climate in the Southern Great Barrier Reef, Australia: evaluation of an ocean HF radar system and WaveWatch3. Proceedings of OCEANS 2011 OCEANS 2011 MTS/IEEE Kona. , 19-22 September 2011, Waikoloa, HI, USA.
- Jones, A. M., & Berkelmans, R. (2014). Flood impacts in Keppel Bay, southern Great Barrier Reef in the aftermath of cyclonic rainfall. *PloS one*, 9(1).

Jones, E. M., P. R. Oke, F. Rizwi and L. M. Murray (2012). "Assimilation of glider and mooring data into a coastal ocean model." *Ocean Modelling* 47: 1-13. DOI 10.1016/j.ocemod.2011.12.009.

Jørgensen, S. E. and International Society for Ecological Modelling. (1979). Handbook of environmental data and ecological parameters. Oxford Oxfordshire ; New York, Distributed throughout the world for the International Society of Ecological Modelling by Pergamon Press

Karl, D. M., R. Letelier, D. Hebel, D. Bird and C. Winn (1992). " *Trichodesmium* blooms and new nitrogen in the North Pacific gyre." *Marine pelagic cyanobacteria: Trichodesmium and other diazotrophs*: 219-237.

Katsaros, K.B. (1980). The aqueous thermal boundary layer. *Boundary Layer Meteorology*, 18, 107-127.

Key, R.M., A. Kozyr, C.L. Sabine, K. Lee, R. Wanninkhof, J. Bullister, R.A. Feely, F. Millero, C. Mordy, T.-H. Peng. (2004). A global ocean carbon climatology: Results from GLODAP. *Global Biogeochemical Cycles*, Vol. 18, GB4031

Kleypas, J.A., Anthony, K.R.N., Gattuso, J.P. 2011. Coral reefs modify their seawater carbon chemistry- case study from a barrier reef (Moorea, French Polynesia), *Global Change Biology*, 17, 3667–3678.

Kroon, F. J., P. M. Kuhnert, B. L. Henderson, S. N. Wilkinson, A. Kinsey-Henderson, B. Abbott, J. E. Brodie and R. D. R. Turner (2012). "River loads of suspended solids, nitrogen, phosphorus and herbicides delivered to the Great Barrier Reef lagoon." *Marine Pollution Bulletin* 65(4-9): 167-181. DOI 10.1016/j.marpolbul.2011.10.018.

Kuhnert P., Henderson B., Lewis S., Bainbridge Z., Wilkinson S., Brodie J. 2012. Quantifying total suspended sediment export from the Burdekin River catchment using the loads regression estimator tool. *Water Resour. Res.*, 48, W04533, doi:10.1029/2011WR011080.

Lambrechts, J., Harnet, E., Deleersnijder, E., Bernard, P.E., Legat, V., Remacle, J.F., Wolanki, E., 2008. A multi-scale model of the hydrodynamics of the whole Great Barrier Reef. *Estuarine, Coastal and Shelf Science* 79, 143e151.

Lanyon, J. M. and H. Marsh (1995). "Temporal changes in the abundance of some tropical intertidal seagrasses in North Queensland." *Aquatic Botany* 49(4): 217-237.

Larcombe, P., Woolfe, K., 1999. Increased sediment supply to the Great Barrier Reef will not increase sediment accumulation at most coral reefs. *Coral Reefs*, 18, 163-169.

Larcombe, P., Carter, R. 2004. Cyclone pumping, sediment partitioning and the development of the Great Barrier Reef shelf system: a review. *Quaternary Science Reviews* 23, 107–135.

Larkum, A.W.D., Kennedy, I.R., Muller, W.J., (1988). Nitrogen fixation on a coral reef. *Marine Biology* 98: 143-155.

Larcombe, P., Carter, R., 2004. Cyclone pumping, sediment partitioning and the development of the Great Barrier Reef shelf system: a review. *Quaternary Science Reviews*, 23, 107–135.

Lewis S., Olley J., Furuichi T., Sharma A., Burton J. 2014. Complex sediment deposition history on a wide continental shelf: Implications for the calculation of accumulation rates on the Great Barrier Reef. *Earth and Planetary Science Letters* 393, 146–158

- Lewis S., Bartley R., Bainbridge Z., Wilkinson, S., Burton J., Bui, E. (2015) Burdekin sediment story. Report No. 15/50 for the NQ Dry Tropics NRM, Centre for Tropical Water & Aquatic Ecosystem Research (TropWATER) Publication, James Cook University, Townsville, 42 pp.
- Leonard, B.P., Lock, A.P., MacVean, M.K., (1996) Conservative explicit unrestricted-time step multidimensional constancy-preserving advection schemes. *Monthly Weather review*, 124, 2588-2606.
- Lin, S-J., Rood, R.B., 1996. Multidimensional flux-form semi-lagrangian transport schemes. *Monthly Weather review*, 124, 2046-2070.
- Lin, S-J., Rood, R.B., 1997. An explicit flux-form semi-lagrangian shallow-water model on the sphere. *Q. J. R. Meteorol. Soc.*, 123, 2477-2498.
- Longuet-Higgins, M.S., and R.W. Stewart, 1961. The changes in amplitude of short gravity waves on steady non-uniform currents. *J. Fl. Mech.*, 10, 529-549.
- Luick, J.L., L. Mason, T. Hardy & M. J. Furnas (2007). Circulation in the Great Barrier Reef Lagoon using numerical tracers and in situ data. *Continental Shelf Research*, 27:757-778
- J.A. Maynard, P.A. Marshall, J. Johnson, O. Alves, G. Harris, L. Muller, G. R. Packer, C. Rathbone, A. Rea, G.P. Smith, C. Spillman, K. Suber, P. Tudman, and P.J. Turner, 2007. New and improved tools to forecast and monitor coral bleaching in the Great Barrier Reef and Coral Sea.
- Madsen, O.S., 1994. Spectral wave-current bottom boundary layer flows, in *Coastal Engineering 1994 Proceedings*, 24th International Conference Coastal Engineering Research Council/ASCE, pp. 384-398.
- Mann, N. H. and M. R. J. Clokie (2012). Cyanophages. *Ecology of Cyanobacteria II: Their Diversity in Space and Time*. B. A. Whitton, Springer: 535-557.
- Margvelashvili, N., Robson, B., Sakov, P., Webster, I. T., Parslow, J., Herzfeld, M., & Andrewartha, J. (2003). Numerical modelling of hydrodynamics, sediment transport and biogeochemistry in the Fitzroy Estuary. Cooperative Research Centre for Coastal Zone, Estuary and Waterway Management, Brisbane.
- Margvelashvili, N., Herzfeld, M., Webster, I., 2006. Modelling of fine sediment transport in the Fitzroy Estuary and Keppel Bay. Cooperative Research Centre for Coastal Zone, Estuary and Waterway Management (Coastal CRC), Technical Report 39, 38 pp.
- Margvelashvili, N., Saint-Cast, F., Condie, S., 2008. Numerical modelling of the suspended sediment transport in Torres Strait. *Continental Shelf Research*, 28, 2241-2256.
- Margvelashvili, N., C. Griffiths, C. Dyt, B. Robson and S. Nichol (2012). Coastal sediment-transport modelling and observational needs. *Australian Coastal and Oceans Modelling and Observations Workshop (ACOMO) 2012*. Canberra, Australia, IMOS
- Margvelashvili, N., Andrewartha, J., Herzfeld, M., Robson, B. J., and Brando, V. E., (2013). Satellite data assimilation and estimation of a 3D coastal sediment transport model using error-subspace emulators: *Environmental Modelling & Software*, v. 40, p. 191-201.

- Margvelashvili, N., and Campbell, E. P., (2012). Sequential data assimilation in fine-resolution models using error-subspace emulators: Theory and preliminary evaluation: *Journal of Marine Systems*, v. 90, no. 1, p. 13-22.
- Margvelashvili, Campbell, Murray, Jones (2014). Hierarchical Emulation & Data Assimilation into the Sediment Transport Model, *Procedia Computer Science*, v. 29, p. 2121–2126.
- Margvelashvili N., M. Herzfeld , F. Rizwi, M. Mongin, M. E. Baird, E. Jones, B. Schaffelke, E. King, T. Schroeder (2015) Emulator-assisted data assimilation in complex models. *Ocean Dynamics* (submitted).
- Marshall, S.M., (1933). The production of microplankton in the Great Barrier Reef region. *Scientific Reports of the Great Barrier Reef Expedition*, Vol. 2, pp. 111-157.
- Martin, J. H., K. H. Coale, K. S. Johnson, S. E. Fitzwater, R. M. Gordon, S. J. Tanner, C. N. Hunter, V. A. Elrod, J. L. Nowicki, T. L. Coley, R. T. Barber, S. Lindley, A. J. Watson, K. Vanscoy, C. S. Law, M. I. Liddicoat, R. Ling, T. Stanton, J. Stockel, C. Collins, A. Anderson, R. Bidigare, M. Ondrusek, M. Latasa, F. J. Millero, K. Lee, W. Yao, J. Z. Zhang, G. Friederich, C. Sakamoto, F. Chavez, K. Buck, Z. Kolber, R. Greene, P. Falkowski, S. W. Chisholm, F. Hoge, R. Swift, J. Yungel, S. Turner, P. Nightingale, A. Hatton, P. Liss and N. W. Tindale (1994). "Testing the Iron Hypothesis in Ecosystems of the Equatorial Pacific-Ocean." *Nature* 371(6493): 123-129. Doi 10.1038/371123a0.
- McWilliams, J.C. (1985) Submesoscale, Coherent Vortices in the Ocean. *Reviews of Geophysics*, 23(2), 165-182.
- Mehrbach, C., Culberso, C.H, Hawley, J., Pytkowic, R.M., 1973. Measurement of apparent dissociation-constants of carbonic-acid in seawater at atmospheric-pressure, *Limnology and Oceanography*, 18, 897–907.
- Mellor, G.L. (1992) User's guide for a three-dimensional, primitive equation, numerical ocean model. Princeton University, Princeton, NJ, 34pp.
- Middleton, J.H., Buchwald, V.T., Huthnance, J.M. (1984) The anomalous tides near Broad Sound. *Continental Shelf Res.*, 3, 359-381.
- Milgram, J. H. (1998). "Short wave damping in the simultaneous presence of a surface film and turbulence." *Journal of Geophysical Research-Oceans* 103(C8): 15717-15727. Doi 10.1029/98jc01191.
- Mitchell, A., J. Reghenzani, J. Faithful, M. Furnas and J. Brodie (2009). "Relationships between land use and nutrient concentrations in streams draining a 'wet-tropics' catchment in northern Australia." *Marine and Freshwater Research* 60(11): 1097-1108.
- Mongin, M., Baird, M., Tilbrook, B. Detailed modelling insight of the carbon chemistry variability inside a coral reef: Importance of photosynthesis versus calcification. *Biogeosciences Discussion* (submitted).
- Mongin, M., Baird, M. (2014) The interacting effects of photosynthesis, calcification and water circulation on carbon chemistry variability on a coral reef flat: a modelling study, *Ecological Modelling* 284, 19–34.
- Monismith, S.G (2007). Hydrodynamics of Coral Reefs. *Annu. Rev. Fluid Mech.*, 39:37-55

- Montoya, J.P., Holl, C.M., Zehr, J.P., Hansen, A., Villareal, T.A., Capone, D.G., (2004). High rates of N₂ fixation by unicellular diazotrophs in the oligotrophic Pacific Ocean. *Nature* 430: 1027-1031.
- Murray, A., J. Parslow, CSIRO. Environmental Projects Office. and Port Phillip Bay Environmental Study (1997). Port Phillip Bay integrated model : final report. Canberra, ACT, Port Phillip Bay Environmental Study, CSIRO Environmental Projects Office
- Murray, A. G., J. S. Parslow, S. J. Walker and J. R. Waring (2000). "The implementation of the ecosystem module of a coastal environmental model: Port Phillip Bay, Australia." *Environmental Modelling & Software* 15(4): 357-372.
- Mucci, A. 1983. The solubility of calcite and aragonite in seawater at various salinities, temperatures, and one atmosphere total pressure, *American Journal of Science*, 283, 780–799.
- Neil D., Orpin, A., Ridd, P., Yu, B., 2002. Sediment yield and impacts from river catchments to the Great Barrier Reef lagoon. *Mar. Freshwater Res.*, 53, 733-752.
- NOAA/EMC, 2012. <http://polar.ncep.noaa.gov/waves/wavewatch/>
- Oke, P. R.; Brassington, G. B.; Griffin, D. A. & Schiller, A. (2008). The BLUElink ocean data assimilation system (BODAS), *Ocean Modelling*, 21(1-2), 46-70.
- Oke, P. R.; Sakov, P.; Cahill, M. L.; Dunn, J. R.; Fiedler, R.; Griffin, D. A.; Mansbridge, J. V.; Ridgway, K. R. & Schiller, A. (2013). Towards a dynamically balanced eddy-resolving ocean reanalysis: BRAN3, *Ocean Modelling*, 67, 52-70.
- Oliver, R. L., D. P. Hamilton, J. D. Brookes and G. G. Ganf (2012). "Physiology, Blooms and Prediction of Planktonic Cyanobacteria." *Ecology of Cyanobacteria II*: 155-194.
- O'Kane, T. J.; Oke, P. R. & Sandery, P. A. (2011), Predicting the East Australian Current, *Ocean Modelling*, 38(3-4), 251-266.
- O'Neil, J. M. (1998). "The colonial cyanobacterium *Trichodesmium* as a physical and nutritional substrate for the harpacticoid copepod *Macrosetella gracilis*." *Journal of Plankton Research* 20(1): 43-59. DOI 10.1093/plankt/20.1.43.
- Olley J., Brooks A., Spencer J., Pietsch T., Borombovits D., Howley C., Curwen George (2013) "Geochemistry and provenance of sediments from Princess Charlotte Bay, Northern Great Barrier Reef", Appendix 12 of the Australian Rivers Institute and Griffith University report "An Empirically-based sediment budget for the Normanby Basin: Sediment Sources, Sinks & Drivers on the Cape York Savannah", Australian Government Caring for our Country - Reef Rescue initiative (<http://www.capeyorkwaterquality.info/references/cywq-229>).
- Orpin, A.R., Ridd, P.V., Stewart, L.K., 1999. Assessment of the relative importance of major sediment-transport mechanisms in the central Great Barrier Reef lagoon. *Australian Journal of Earth Science*, 46, 883 – 896.
- Paerl, H. W. (2012). "Marine plankton." *Ecology of Cyanobacteria II*: 127-153.
- Parslow, J., M. Herzfeld, J. Hunter, J. Andrewartha, P. Sakov and J. Waring (2001). "Mathematical modelling of the dispersion, fate and impact of newsprint mill effluent in an estuarine system." 55th Appita Annual Conference, Proceedings: 139-146.

- Parslow, J., N. Margvelashvili, D. Palmer, A. Reville, B. Robson, P. Sakov, J. Volkman, R. Watson and I. Webster (2003). The Response of the Lower Ord River and Estuary to Management of Catchment Flows and Sediment and Nutrient Loads: Final Science Report, CSIRO Marine Research / Land and Water Australia
- Priestley, A. (1993) A quasi-conservative version of the semi-Lagrangian advection scheme. *Mon. Wea. Rev.*, 121, 621-629.
- Prosser, I.P., P. Rustomji, W.J. Young, C.J. Moran and A.O. Hughes 2001 Constructing river basin sediment budgets for the National Land and Water Resources Audit. Technical Report 15/10, CSIRO Land and Water, Canberra.
- Qin, Y., Brando, V. E., Dekker, A. G., & Blondeau-Patissier, D. (2007). Validity of SeaDAS water constituents retrieval algorithms in Australian tropical coastal waters. *Geophysical Research Letters*, 34(21).
- Radke, L. C., Ford, P. W., Webster, I. T., Atkinson, I., Douglas, G., Oubelkheir, K., ... & Brooke, B. (2010). Biogeochemical zones within a macrotidal, dry-tropical fluvial-marine transition area: a dry-season perspective. *Aquatic geochemistry*, 16(1), 1-29.
- Reidenbach, M.A., F.R. Koseff, S.G. Monismith, J.V. Steinbuick and A. Genin (2006a). The effects of waves and morphology on mass transfer within branched reef corals. *Limnol. Oceanogr.*, 51(2):1134-1141
- Revelante, N., Williams, W.T., Bunt, J.S., (1982). Temporal and spatial distribution of diatoms, dinoflagellates and *Trichodesmium* in waters of the Great Barrier Reef. *Journal of Experimental Marine Biology and Ecology* 63: 27-45.
- Ridgway K.R., J.R. Dunn, and J.L. Wilkin (2002) Ocean interpolation by four-dimensional least squares -Application to the waters around Australia, *J. Atmos. Ocean. Tech.*, Vol 19, No 9, 1357-1375.
- Rood, R.B. (1987) Numerical advection algorithms and their role in atmospheric transport and chemistry models. *Reviews of Geophysics*, 25, 71 – 100.
- Rosman, J. H., and J. L. Hench (2011). A framework for understanding drag parameterizations for coral reefs, *J. Geophys. Res.*, 116, C08025, doi:10.1029/2010JC006892.
- Robson, B. J. (2005). Representing the effects of diurnal variations in light on primary production on a seasonal time-scale. *Ecological modelling*, 186(3), 358-365.
- Robson, B.J., Webster, I. T., Margvelashvili, N., & Herzfeld, M. (2006). Scenario modelling: Simulating the downstream effects of changes in catchment land use. CRC Coastal Zone Estuary and Waterway Management.
- Robson, B. J., I. T. Webster and U. Rosebrock (2006). Biogeochemical Modelling and Nitrogen Budgets for the Fitzroy Estuary and Keppel Bay. Australia, Cooperative Research Centre for Coastal Zone, Estuary and Waterway Management
- Robson, B. R., & Brando, V. E. (2007). Using satellite observations to improve biogeochemical modelling of the Fitzroy River Estuary. In *Proceedings of the MODSIM 2007 International Congress on Modelling and Simulation*. Modelling and Simulation Society of Australia and New Zealand.

Robson, B. J. and V. E. Brando (2008). Simulating the response of Keppel Bay coastal waters to potential changes in sediment and nutrient loads: Final report to the Fitzroy Basin Association

Robson, B. J., & Brando, V. E. (2008). Simulating the response of Keppel Bay coastal waters to potential changes in sediment and nutrient loads. CSIRO Water for a Healthy Country National Research Flagship.

Robson, B. J., M. A. Burford, P. S. Gehrke, A. T. Reville, I. T. Webster and D. W. Palmer (2008a). Response of the lower Ord River and Estuary to changes in flows and sediment and nutrient loads. Canberra, ACT, Water for a Healthy Country National research Flagship, CSIRO

Robson, B.J., Hamilton, D.P., Webster, I.T., and Chan, T., 2008. Ten steps applied to development and evaluation of process-based biogeochemical models of estuaries. *Environmental Modelling & Software* 23(4), 369-384.

Robson, B., N. Cherukuru and V. Brando (2010). Using satellite-derived optical data to improve simulation of the 3D light field in a biogeochemical model. International Environmental Modelling and Software Society (iEMSs) 2010 International Congress on Environmental Modelling and Software. D. A. Swayne, W. Yang, A. A. Voinov, A. Rizzoli and T. Filatova. Ottawah, Canada, International Environmental Modelling and Software Society (iEMSs)

Robson, B. J., & Dourdet, V. (2015). Prediction of sediment, particulate nutrient and dissolved nutrient concentrations in a dry tropical river to provide input to a mechanistic coastal water quality model. *Environmental Modelling & Software*, 63, 97-108.

Robson, B.J., Baird M., Wild-Allen, K. (2013) A physiological model for the marine cyanobacteria, *Trichodesmium*. 20th International Congress on Modelling and Simulation, Adelaide, Australia, 1-6 December 2013 www.mssanz.org.au/modsim2013.

Romanou, A., Rossow, W.B., Chou, S., (2006) Decorrelation scales of high-resolution turbulent fluxes at the ocean surface and a method to fill in gaps in satellite data products. *Journal of Climate*, 19, 3378 – 3393.

Ryan, D. A., B. P. Brooke, H. C. Bostock, L. C. Radke, P. J. W. Siwabessy, N. Margvelashvili and D. Skene (2007). "Bedload sediment transport dynamics in a macrotidal embayment, and implications for export to the southern Great Barrier Reef shelf." *Marine Geology* 240(1-4): 197-215. DOI 10.1016/j.margeo.2007.02.014.

Saha, S., and Coauthors, 2010: The ncep climate forecast system reanalysis. *Bull. Amer. Meteor. Soc.*, **91**, 1015–1057.

Sakov, P. & Oke, P. R. (2008), A deterministic formulation of the ensemble Kalman filter: an alternative to ensemble square root filters, *TELLUS SERIES A-DYNAMIC METEOROLOGY AND OCEANOGRAPHY* 60(2), 361-371.

Schaffelke, B., Carleton, J., Skuza, M., Zagorskis, E., Furnas, M., 2011. Water quality in the inshore Great Barrier Reef lagoon: Implications for long-term monitoring and management. *Marine Pollution Bulletin*, (in press) doi:10.1016/j.marpolbul.2011.10.031.

Schaffelke B, Carleton J, Doyle J, Furnas M, Gunn K, Skuza M, Wright M, Zagorskis I (2011) Reef Rescue Marine Monitoring Program. Final Report of AIMS Activities 2010/11– Inshore Water Quality Monitoring. Report for the Great Barrier Reef Marine Park Authority. Australian Institute of Marine Science, Townsville. (83 p.)

- Schmoker, C., Hernandez-Leon, S. and Calbet, A. (2013) Microzooplankton grazing in the oceans: impacts, data variability, gaps of knowledge, and future directions. *J. Plankton Res.*, 35, 691–706.
- Schroeder T., Behnert I., Schaale M., Fischer J. and Doerffer R. (2007) "Atmospheric correction algorithm for MERIS above Case-2 waters", *International Journal of Remote Sensing*, Vol 28 (7).
- Simpson, J.J. and T.D. Dickey (1981) The relationship between downward irradiance and upper ocean structure. *Journal of Physical Oceanography*, 11, 309 - 323.
- Spagnol, S., Wolanski, E., Deleersnijder, E. (2001). Steering by coral reef assemblages. In: Wolanski, E. (Ed.), *Oceanographic Processes of Coral Reefs: Physical and Biological Links in the Great Barrier Reef*. CRC Press, Boca Ralton, Florida, pp 145-160.
- Steinberg, C., 2007. Impacts of climate change on the physical oceanography of the Great Barrier Reef. Chapter 3, *Climate Change and the Great Barrier Reef*, eds. Johnson J.E. and Marshall P.A. Great Barrier Reef Marine Park Authority & Australian Greenhouse Office, pp 51-74.
- Steven, ADL, Hodge, J, Cannard, T, Carlin, G, Franklin, H, McJannet, D, Moeseneder, C, Searle, R, 2014. Continuous Water Quality Monitoring on the Great Barrier Reef. CSIRO Final Report to Great Barrier Reef Foundation, 1598pp
- Stephens, N., K. J. Flynn and J. R. Gallon (2003). "Interrelationships between the pathways of inorganic nitrogen assimilation in the cyanobacterium *Gloeotheca* can be described using a mechanistic mathematical model." *New phytologist* 160(3): 545-555.
- Stramma, L., Cornillon, L., Weller, R.A., Price, J.F., Briscoe, M.G. (1986) Large diurnal sea surface temperature variability: satellite and in situ measurements. *J. Phys. Oceanogr.*, 16, 827-837.
- Subramaniam, A., E. J. Carpenter and P. G. Falkowski (1999a). "Bio-optical properties of the marine diazotrophic cyanobacteria *Trichodesmium* spp. II. A reflectance model for remote sensing." *Limnology and Oceanography*: 618-627.
- Subramaniam, A., E. J. Carpenter, D. Karentz and P. G. Falkowski (1999b). "Bio-optical properties of the marine diazotrophic cyanobacteria *Trichodesmium* spp. I. Absorption and photosynthetic action spectra." *Limnology and Oceanography*: 608-617.
- SWAN Team, 2011a. SWAN User Manual. Delft University of Technology, 121 pp.
- SWAN Team, 2011b. SWAN Scientific and Technical Documentation. Delft University of Technology, 117 pp.
- Sweatman H, S Delean & C Syms (2011). " Assessing loss of coral cover on Australia's Great Barrier Reef over two decades, with implications for longer-term trends". *Coral Reefs*, 30:521-531. DOI 10.1007/s00338-010-0715-1
- Tartinville, B., E. Deleersnijder, J. Rancher, 1997: The water residence time in the Mururoa atoll lagoon: sensitivity analysis of a three-dimensional model. *Coral Reefs*, 16, 193 – 203.
- Thompson A., Schroeder T., Brando V., Schaffelke B. 2014. Coral community responses to declining water quality: Whitsunday Islands, Great Barrier Reef, Australia. *Coral Reefs* DOI 10.1007/s00338-014-1201-y

- Tolman, H. L., 2009. User manual and system documentation of WAVEWATCH III version 3.14. NOAA / NWS / NCEP / MMAB Technical Note 276, 194 pp.
- Trott, L. A. and D. M. Alongi (2000). "The impact of shrimp pond effluent on water quality and phytoplankton biomass in a tropical mangrove estuary." *Marine Pollution Bulletin* 40(11): 947-951. Doi 10.1016/S0025-326x(00)00035-7.
- Van Rijn, L. C. (1993). Principles of sediment transport in rivers, estuaries and coastal seas, Aqua publications Amsterdam
- Van Woessik, R. (1991). Immediate Impact of the January 1991 floods on the Coral Assemblages of the Keppel Islands (p. 33). Great Barrier Reef Marine Park Authority.
- Villareal, T. A. and E. J. Carpenter (2003). "Buoyancy regulation and the potential for vertical migration in the oceanic cyanobacterium *Trichodesmium*." *Microbial Ecology* 45(1): 1-10. DOI 10.1007/s00248-002-1012-5.
- Wang, S. D., Y. M. Shen, Y. K. Guo and J. Tang (2008). "Three-dimensional numerical simulation for transport of oil spills in seas." *Ocean Engineering* 35(5-6): 503-510. DOI 10.1016/j.oceaneng.2007.12.001.
- Wang, Y. G., P. Kuhnert and B. Henderson (2011). "Load estimation with uncertainties from opportunistic sampling data - A semiparametric approach." *Journal of Hydrology* 396(1-2): 148-157. DOI 10.1016/j.jhydrol.2010.11.003.
- Wanninkhof, R., 1992. Relationship between wind speed and gas exchange over the ocean. *J. Geophys. Res.* 97 (C5), 7373-7382.
- Wanninkhof, R., McGillis, W. R., 1999. A cubic relationship between air-sea CO₂ exchange and wind speed. *Geophys. Res. Letts.* 26, 1889-1892.
- Wachenfeld, D., 1998. State of the Great Barrier Reef World Heritage Area. 140 p. GBRMPA.
- Waters, DK, Carroll, C, Ellis, R, Hateley, L, McCloskey, GL, Packett, R, Dougall, C, Fentie, 2014, Modelling reductions of pollutant loads due to improved management practices in the Great Barrier Reef catchments – Whole of GBR, Technical Report, Volume 1, Queensland Department of Natural Resources and Mines, Toowoomba, Queensland (ISBN: 978-1- 7423-0999).
- Webster, I. T. and P. A. Hutchinson (1994). "Effect of Wind on the Distribution of Phytoplankton Cells in Lakes Revisited." *Limnology and Oceanography* 39(2): 365-373.
- Webster et al. (2003). Conceptual models of the hydrodynamics, fine sediment dynamics, biogeochemistry and primary production in the Fitzroy Estuary. CRC Coastal Zone Estuary and Waterway Management, 2003.
- Webster, I., V. Vicente-Beckett, I. Atkinson, H. Bostock, B. Brooke, G. Douglas, P. Ford, G. Hancock, M. Herzfeld, R. Leeming, C. Lemckert, N. Margvelashvili, R. Noble, K. Oubelkheir, L. Radke, A. Revill, B. J. Robson, D. Ryan, C. Schacht, C. Smith, J. Smith, K. Wild-Allen, Central Queensland University. Centre for Environmental Management. and Cooperative Research Centre for Coastal Zone Estuary and Waterway Management. (2006). The Fitzroy contaminants project a study of the nutrient and fine-sediment dynamics of the Fitzroy Estuary and Keppel Bay. Technical report 42. Indooroopilly, Qld., Cooperative Research Centre for Coastal Zone, Estuary and Waterway Management: x, 80 p.

- Webster, I.T., Brinkman, R., Parslow, J., Prange, J., Stevens, A.D.L., Waterhouse, J. 2008. Review and Gap Analysis of Receiving-Water Water Quality Modelling in the Great Barrier Reef. CSIRO Water for a Healthy Country Flagship. 137 p.
- Webster, I. T., & Ford, P. W. (2010). Delivery, deposition and redistribution of fine sediments within macrotidal Fitzroy Estuary/Keppel Bay: southern Great Barrier Reef, Australia. *Continental Shelf Research*, 30(7), 793-805.
- Weiss, R., 1970. The solubility of nitrogen, oxygen and argon in water and seawater. *Deep Sea Res.* 17, 721-735.
- Wild-Allen, K., Herzfeld, M., Margvelashvili, N., & Rosebrock, U. (2006). Fitzroy Estuary mudflat model. Cooperative Research Centre for Coastal Zone, Estuary and Waterway Management.
- Wild-Allen, K., CSIRO. Marine and Atmospheric Research and Derwent Estuary Program. (2009). "Derwent Estuary biogeochemical model : technical report." from <http://www.emg.cmar.csiro.au/www/en/emg/projects/Derwent/Derwent-CCI-Biogeochem.html>.
- Wild-Allen, K., Herzfeld, M., Thompson, P.A., Rosebrock, U., Parslow, J. and Volkman, J.K. 2010. Applied coastal biogeochemical modelling to quantify the environmental impact of fish farm nutrients and inform managers. *Journal of Marine Systems* 81: 134-147.
- Wild-Allen, K., P. A. Thompson, J. K. Volkman and J. Parslow (2011). "Use of a coastal biogeochemical model to select environmental monitoring sites." *Journal of Marine Systems* 88(1): 120-127. DOI 10.1016/j.jmarsys.2011.02.017.
- Willmott, C.J. (1981) On the validation of models. *Phys. Geogr.*, 2, 184-194.
- Wolanski E., I. Imberger and M.I. Heron (1984a). Island wakes in shallow coastal waters. *Journal of Geophysical Research*, 89:553-569.
- Wolanski E., G.L. Pickard and D.L.B. Jupp (1984b). River plumes, coral reefs and mixing in the Gulf of Papua and the northern Great Barrier Reef. *Estuarine, Coastal and Shelf Science*, 18:291-314.
- Wolanski, E., Hamner, W.M., 1988. Topographically controlled fronts in the ocean and their biological influence. *Science* 241, 177–181.
- Wolanski, E., 1994. *Physical Oceanographic Processes of the Great Barrier Reef*. CRC Press, Boca Raton, Florida, 194 pp.
- Wolanski E, T Asaeda, A Tanaka & E Deleersnijder (1996). Three-dimensional wakes in the field, laboratory experiments and numerical models. *Continental Shelf Reserach*, Vol. 16, No 11, pp. 1437-1452
- Wolanski, E., King, B., Spagnol, S., 1999. *Perspectives in Integrated Coastal Zone Management*. Springer-Verlag, Berlin, pp. 129–141.
- Wolanski, E., Spagnol, S. (2000). Sticky waters in the Great Barrier Reef. *Estuarine, Coastal and Shelf Science* 50, 27-32.
- Wolanski, E., Brinkmann, R., Spagnol, S., McAllister, F., Skirving, C.S.W., Deleersnijder, E., 2003a. Merging scales in models of water circulation: perspectives from the Great Barrier Reef. In: Lakhan, V. (Ed.), *Advances in Coastal Modeling*. Elsevier, pp. 411–429.

- Wolanski, E., Marshall, K., Spagnol, S., 2003b. Nepheloid layer dynamics in coastal waters of the Great Barrier Reef, Australia. *Journal of Coastal Research* 19, 748–752.
- Wolanski, E., Richmond, R., Davis, G., Deleersnijder, E., Leben, R., 2003c. Eddies around Guam, an island in the Mariana Islands group. *Continental Shelf Research* 23, 991–1003.
- Wolanski, E., Fabricius, K., Cooper, T., Humphrey, C., 2008. Wet season fine sediment dynamics on the inner shelf of the Great Barrier Reef. *Estuarine, Coastal and Shelf Science*, 77, 755-762.
- Wong, C.S., Yu, Z., Waser, N.A.D., Whitney, F.A., Johnson W.K., (2002). Seasonal changes in the distribution of dissolved organic nitrogen in coastal and open-ocean waters in the North East Pacific: sources and sinks. *Deep-Sea Research II* 49 (2002) 5759-5773.
- Yankovsky, A.E. (2000) The cyclonic turning and propagation of buoyant coastal discharge along the shelf. *Journal of Marine Research*, 58, 585-607.
- Young, I., Zieger, S., Babanin, A.V., 2011. Global Trends in Wind Speed and Wave Height. *Science*, 332, p. 451-455.
- Zeebe, R. E. and Wolf-Gladrow. D., 2001. *CO₂ in Seawater: Equilibrium, Kinetics, Isotopes*. Elsevier Oceanography Series, 65, Amsterdam, 346p.

8. Publications

- BAIRD, M. E., ADAMS, M. P., BABCOCK, R. C., OUBELKHEIR, K., MONGIN, M., WILD-ALLEN, K. A., SKERRATT, J., ROBSON, B., PETROU, K., RALPH, P. J., O'BRIEN, K. R., CARTER, A. B., JARVIS, J. C. & RASHEED, M. A. minor revisions-a. A physical representation of seagrass growth for application in a complex shallow-water biogeochemical model *Ecological Modelling*.
- BAIRD, M. E., CHERUKURU, N., JONES, E. M., MARGVELASHVILI, N., MONGIN, M., OUBELKHEIR, K., RALPH, P. J., RIZWI, F., ROBSON, B., SCHROEDER, T., SKERRATT, J., STEVEN, A. D. L. & WILD-ALLEN, K. A. minor revisions-b. Remote-sensing reflectance and true colour produced by acoupled hydrodynamic, optical, sediment, biogeochemical model of the Great Barrier Reef, Australia: comparison with remotely-sensed data *Environmental Modelling and Software Journal*.
- GILLIBRAND, P. A. & HERZFELD, M. minor revisions. A mass-conserving advection scheme for offline simulation of tracer transport in coastal ocean models. *Ocean Modelling*.
- HERZFELD, M. 2015. Methods for freshwater riverine input into regional ocean models. *Ocean Modelling*, 90, 1-15.
- HERZFELD, M. & GILLIBRAND, P. A. 2015. Active open boundary forcing using dual relaxation time-scales in downscaled ocean models. *Ocean Modelling*, 89, 71-83.
- JONES, E. M., DOBLIN, M. A., MATEAR, R. & KING, E. 2015. Assessing and evaluating the ocean-colour footprint of a regional observing system. *Journal of Marine Systems*, 143, 49-61.
- JONES, E. M., HERZFELD, M. & OKE, P. R. To be submitted Dec2015. Efficient estimation of coastal hydrodynamic model parameters. *Ocean Science Discussion*.
- MARGVELASHVILI, N., ANDREWARTHA, J., HERZFELD, M., ROBSON, B. & BRANDO, V. 2013. Satellite data assimilation and estimation of a 3d coastal sediment transport model using error-subspace emulators. *Environmental Modelling and Software Journal* 40, 191-201.
- MARGVELASHVILI, N., CAMPBELL, E., MURRAY, L. & JONES, E. M. 2014. Hierarchical emulation and data assimilation into the sediment transport model. *Procedia Computer Science*, 29, 2121-2126.
- MARGVELASHVILI, N., HERZFELD, M., F. RIZWI, M. M., M. E. BAIRD, E. JONES, , E. KING, T. SCHROEDE, RIZWI, F., MONGIN, M., BAIRD, M. E., JONES, E. M., SCHAFFELKE, B., KING, E. & SCHROEDER, T. Submitted. Emulator-assisted data assimilation in complex models. . *Ocean Dynamics (under review)*.
- MONGIN, M. & BAIRD, M. 2014. The impact of photosynthesis, calcification and water circulation on carbon chemistry variability above a coral reef: a modelling study. *Ecological Modelling*, 284, 19-34.
- MONGIN, M., BAIRD, M. E., TILBROOK, B., MATEAR, R., LENTON, A., HERZFELD, M., WILD-ALLEN, K. A., SKERRATT, J., MARGVELASHVILI, N., ROBSON, B., DUARTE, C. M., GUSTAFSSON, M. S. M., RALPH, P. J. & STEVEN, A. D. L. minor revisions. The exposure of the Great Barrier Reef to ocean acidification. *Nature Communications (in press)*.
- OKE, P. R., LARNICOL, G., JONES, E. M., KOURAFALOU, V., SPERREVIK, A. K., CARSE, F., TANAJURA, C. A. S., MOURRE, B., TONANI, M., BRASSINGTON, G. B., LE HENAFF, M., HALLIWELL, J., GEORGE R., ATLAS, R., MOORE, A. M., EDWARDS, C. A., MARTIN, M. J., SELLAR, A. A., ALVAREZ, A., DE MEY, P. & ISKANDARANI, M. 2014. Assessing the impact of observations

on ocean forecasts and reanalyses: Part 2, Regional applications. *Journal of Operational Oceanography*, issue?

ROBSON, B. 2014. When do aquatic systems models provide useful predictions, what is changing, and what is next? *Environmental Modelling & Software*, 61, 287-296.

ROBSON, B. J., BAIRD, M. & WILD-ALLEN, K. 2013. A physiological model for the marine cyanobacteria, *Trichodesmium*. *MODSIM2013, 20th International Congress on Modelling and Simulation, Modelling and Simulation Society of Australia and New Zealand*, 1652-1658.

ROBSON, B. J. & DOURDET, V. 2015. Prediction of sediment, particulate nutrient and dissolved nutrient concentrations in a dry tropical river to provide input to a mechanistic coastal water quality model. *Environmental Modelling & Software*, 63, 97-108.

ROBSON, B. J., SKERRATT, J., MONGIN, M., WILD-ALLEN, K. A. & BAIRD, M. E. 2014. Varying the temporal resolution of river nutrient boundary conditions to a coupled hydrodynamic-biogeochemical model of a coastal system has surprisingly little impact on model results. *Proceedings - 7th International Congress on Environmental Modelling and Software: Bold Visions for Environmental Modeling*, iEMSs Vol 1, 533-539.

SCHILLER, A., HERZFELD, M., BRINKMAN, R., RIZWI, F. & ANDREWARTHA, J. 2015. Cross-shelf exchanges between the Coral Sea and the Great Barrier Reef lagoon determined from a regional-scale numerical model. *Continental Shelf Research*, 109, 150-163.

SCHILLER, A., HERZFELD, M., BRINKMAN, R. & STUART, G. 2014. Monitoring, Predicting, and Managing One of the Seven Natural Wonders of the World. *Bulletin of the American Meteorological Society*, 95, 23-30.

STEVEN, A. D. L., HODGE, J., CANNARD, T., CARLIN, G., FRANKLIN, H., MCJANNET, D., MOESENEDER, C. & SEARLE, R. 2015. Continuous Water Quality Monitoring on the Great Barrier Reef. *CSIRO Final Report to Great Barrier Reef Foundation*. CSIRO, 159pp.

WEIJERMAN, M., FULTON, E. A., JANSSEN, A. B. G., KUIPER, J. J., LEEMANS, R., ROBSON, B. J., VAN DE LEEMPUT, I. A. & MOOIJ, W. M. 2015. How models can support ecosystem-based management of coral reefs. *Progress in Oceanography*.

8.1 Presentations

eReefs: Modelling the Great Barrier Reef. GODAE COSS-TT 2014 workshop, Puerto Rico, USA.

Model optimization through development: the eReefs example. ACOMO 2014. Canberra, Australia.

The eReefs data assimilation system. Ocean Sciences 2015. Honolulu, Hawaii.

The eReefs data assimilation system. ACOMO 2015. Canberra, Australia.

Margvelashvili (2014) "Towards fast and accurate emulators of complex ocean models"
Seminar presentation delivered at CMAR, Hobart, March 2014.

Margvelashvili (2014) "eDICE – emulation and data assimilation in computationally expensive models". Presentation delivered at CSIRO CSS TCP & eResearch Annual Conference & Workshops Melbourne Convention and Exhibition Centre 25-28 March 2014

Margvelashvili (2014) Assimilation into the Sediment Transport Model", Presentation delivered at International Conference on Computational Sciences, 2014, Cairns.

M. Herzfeld, R. Brinkman, P. Gillibrand, J. Andrewartha, F. Rizwi, H. Tonin, E. Jones, M. Hemer, K. Joehnk, E. Jones, N, Margvelashvili, K. Wild-Allen, B. Robson, M. Mongin, J. Skerratt, M. Baird, M. Furnas, D. McKinnon 2012. EReefs WP3 Marine Modelling: Milestone #1 Report p160

Robson, B.J., Skerratt, J., Mongin, M. and Baird, M. 2014. "Varying the temporal resolution of river nutrient boundary conditions to a coupled hydrodynamic-biogeochemical model has surprisingly little impact on model results". 7th Intl. Congress on Env. Modelling and Software

Robson, B. J., & Dourdet, V. (2013). Incorporating a generalised additive model of river nutrient concentrations into a mechanistic receiving water model. In MODSIM2013, 20th International Congress on Modelling and Simulation, Modelling and Simulation Society of Australia and (pp. 373-379).

Robson, B. J., Baird, M., & Wild-Allen, K. (2013). A physiological model for the marine cyanobacteria, *Trichodesmium*. In MODSIM2013, 20th International Congress on Modelling and Simulation. Modelling and Simulation Society of Australia and New Zealand, ISBN (pp. 978-0).

Robson, B.J., Herzfeld, M., Rizwi, F., Baird, M., Skerratt, J., Mongin, M., Wild-Allen, K., Jones, E., Margvelashvili, N. and Steven, A. 2014. The eReefs relocatable biogeochemical model (RECOM) and its parameter library.

Skerratt, J., Wild-Allen, K, Mongin, M Robson, B Baird M Herzfeld M Andrewartha J Gillibrand, P Rizwi, F Margvelashvili N 2013. A 4 km 3D hydrodynamic and biogeochemical model for the Great Barrier Reef- eReefs. AMSA Shaping the future Golden Jubilee Conference July 7-11 Gold coast – poster p 200.

Skerratt, J., Wild-Allen, K, Mongin, M Robson, B Baird M Herzfeld M Andrewartha J Gillibrand, P Rizwi, F Margvelashvili N 2013. A highly resolved 3D hydrodynamic and environmental model for the Great Barrier Reef-eReefs, AMSA, Brisbane 2013, 124p.

Skerratt, J., Baird M, Mongin, M Robson, B Wild-Allen K 2014 "Use of the eReefs Great Barrier Reef model to understand nutrient dynamics." AMSA Canberra July 6-10th 2014.

Skerratt, J., Baird M, Mongin, M Robson, B Wild-Allen K 2014 " Application of catchment load scenarios for management of coastal ecosystems", ACOMO conference 2014 6-8th October Canberra. p12

Skerratt, J., Baird M, Mongin, M Robson, B Wild-Allen K 2014 The CSIRO environmental modelling suite and possibilities for the inclusion of microbiological processes, Microbial II Friday 28th Nov. Hobart

Robson, B., Herzfeld, M., Rizwi, F., Geoffrey, L., Baird, M., Skerratt, J. (2014) The eReefs relocatable biogeochemical model (RECOM) and its parameter library. In: ACOMO 2014; 7-8 October 2014; Canberra. IMOS; 2014. 1.

Robson, Barbara; Skerratt, Jenny; Mongin, Mathieu; Wild-Allen, Karen; Baird, Mark. Varying the temporal resolution of river nutrient boundary conditions to a coupled hydrodynamic-biogeochemical model of a coastal system has surprisingly little impact on model results. In:

7th International Congress on Environmental Modelling and Software (iEMSS); 15-19 June 2014; San Diego, USA. San Diego, California, USA: iEMSS; 2014. 533-539.

Wild-Allen, Karen; Baird, Mark; Mongin, Mathieu; Robson, Barbara; Skerratt, Jenny; Jones, Emlyn; et al. Validation of the Great Barrier Reef and Coral Sea Biogeochemical Model. In: AMEMR; 29 June 2014 - 3 July 2014; Plymouth, UK. AMEMR Book of Abstracts: Plymouth University, UK; 2014. 106.

Wild-Allen, K. & Baird, M. 2014. The eReefs 3D Biogeochemical model of the GBR. Seminar at JCU, Townsville, 8th April 2014.

Wild-Allen, K. & Baird, M. 2014. The eReefs 3D Biogeochemical model of the GBR. Seminar at AIMS, Townsville, 9th April 2014.

Wild-Allen, K., MacDonald, L., Allen, S. 2014. High resolution nutrient observations off Heron Island. Poster presented at 6th EGO Meeting & Final Symposium of the COST Action ES0904 July 2014.

Wild-Allen, K. 2014. The eReefs Biogeochemical model of the GBR. Seminar at CSIRO, Floreat, 26 Sept 2014.

Mongin, M. & Robson, B. 2014. Seminar at AIMS, Townsville, 10th April 2014.

Baird, M., Wild-Allen, K., Ralph, P., Rizwi, F., & Steven, A. 2014. Including the package effect in the pigment synthesis term of a dynamic C:Chl model of microalgae. Oral Presentation at Advances in Marine Ecological Modelling Symposium, Plymouth, UK, June 2014.

Baird, Mark, Mathieu Mongin, Nugzar Margvelashvili Karen Wild-Allen, Jenny Skerratt, Emlyn Jones, Barbara Robson, Thomas Schroeder, Nagur Cherekuru, Russ Babcock, Kadija Oubelkheir (2014). Comparison of remotely-sensed surface reflectance with that calculated from a coupled hydrodynamic-ecological model of the Great Barrier Reef. AMSA 2014 Annual Conference.

Mongin, M. & Baird, M. 2014. The interacting effects of photosynthesis, calcification and water circulation on carbon chemistry variability on a coral reef flat: a modelling study. Oral Presentation at Advances in Marine Ecological Modelling Symposium, Plymouth, UK, June 2014.

DRAFT